



## DEFENSE TECHNICAL INFORMATION CENTER

*Information for the Defense Community*

DTIC® has determined on 

Month	Day	Year
12	15	2008

 that this Technical Document has the Distribution Statement checked below. The current distribution for this document can be found in the DTIC® Technical Report Database.

☒ **DISTRIBUTION STATEMENT A.** Approved for public release; distribution is unlimited.

☐ **© COPYRIGHTED.** U.S. Government or Federal Rights License. All other rights and uses except those permitted by copyright law are reserved by the copyright owner.

☐ **DISTRIBUTION STATEMENT B.** Distribution authorized to U.S. Government agencies only. Other requests for this document shall be referred to controlling office.

☐ **DISTRIBUTION STATEMENT C.** Distribution authorized to U.S. Government Agencies and their contractors. Other requests for this document shall be referred to controlling office.

☐ **DISTRIBUTION STATEMENT D.** Distribution authorized to the Department of Defense and U.S. DoD contractors only. Other requests shall be referred to controlling office.

☐ **DISTRIBUTION STATEMENT E.** Distribution authorized to DoD Components only. Other requests shall be referred to controlling office.

☐ **DISTRIBUTION STATEMENT F.** Further dissemination only as directed by controlling office or higher DoD authority.

*Distribution Statement F is also used when a document does not contain a distribution statement and no distribution statement can be determined.*

☐ **DISTRIBUTION STATEMENT X.** Distribution authorized to U.S. Government Agencies and private individuals or enterprises eligible to obtain export-controlled technical data in accordance with DoDD 5230.25.

SAND76-5122  
Unlimited Release

UC-21

EBRT  
75-1  
v.1  
c.1

Volume I

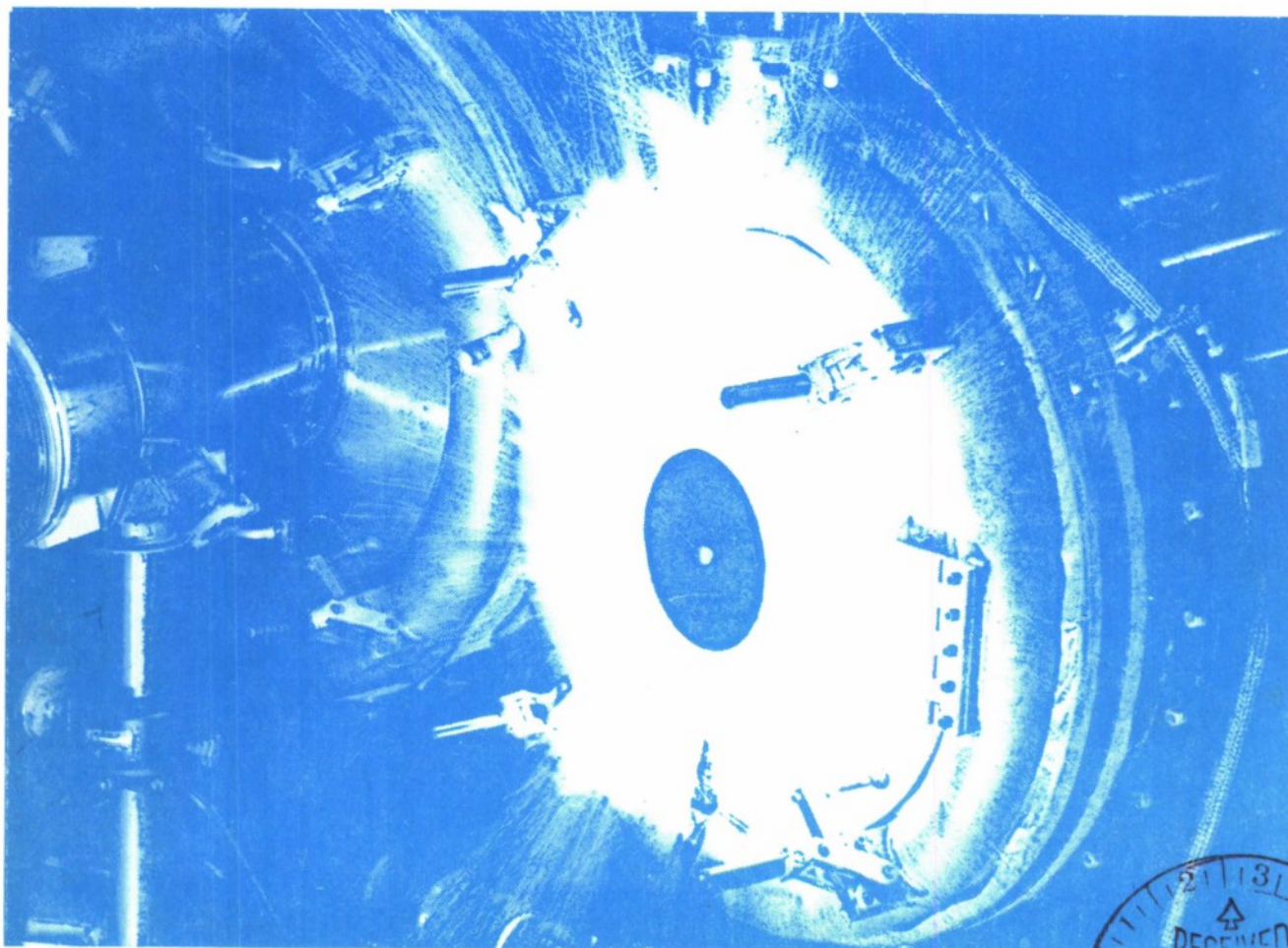
LOAN COPY: RETURN TO  
AFWL TECHNICAL LIBRARY  
KIRTLAND AFB, N. M.

# International Topical Conference on Electron Beam Research & Technology



Co-sponsored by Sandia Laboratories and the United States Energy Research and Development Administration.

Albuquerque, New Mexico  
November 3-5, 1975



20081120325





Issued by Sandia Laboratories, operated for the United States Energy Research and Development Administration by Sandia Corporation.

---

#### NOTICE

This report was prepared as an account of work sponsored by the United States Government. Neither the United States nor the United States Energy Research and Development Administration, nor any of their employees, nor any of their contractors, subcontractors, or their employees, makes any warranty, express or implied, or assumes any legal liability or responsibility for the accuracy, completeness or usefulness of any information, apparatus, product or process disclosed, or represents that its use would not infringe privately owned rights.

Printed in the United States of America

Available from  
National Technical Information Service  
U. S. Department of Commerce  
5285 Port Royal Road  
Springfield, Virginia 22161  
Price: Printed Copy \$17.25; Microfiche \$2.25

Add \$2.50 per copy for foreign price

SAND76-5122  
Unlimited Release

Distribution  
Category  
UC-21

Volume I of II

PROCEEDINGS OF THE INTERNATIONAL TOPICAL  
CONFERENCE ON  
ELECTRON BEAM RESEARCH AND TECHNOLOGY

November 3-6, 1975  
Albuquerque, New Mexico

Gerold Yonas, Editor

Co-sponsored by  
Sandia Laboratories  
and the  
United States Energy Research  
and Development Administration

Printed February 1976



## ACKNOWLEDGMENTS

### Conference Organizing Committee

Gerold Yonas, Sandia Laboratories -- Chairman

Thomas H. Martin -- Sandia Laboratories  
James B. Gerardo -- Sandia Laboratories  
Glenn W. Kuswa -- U. S. ERDA  
Bennett Miller -- U. S. ERDA

### Conference Coordinator

Sandra R. Hudson -- Sandia Laboratories

### Accompanying Persons Planning

Jo Toepfer  
Margaret Freeman  
Jane Yonas

### Conference Support

Jack Suttman  
Alan J. Toepfer  
Clara Taylor  
Eunice Vleck  
Milton J. Clauser  
Julia Polito

Jim Mitchell  
Edwina Kiro  
Carol Kaemper  
Marvin J. Beckett  
Fay Spellman  
Rosemary Teasdale













## CONTENTS

### VOLUME I

Acknowledgments . . . . .	3
---------------------------	---

#### Chapter 1 Pellet Fusion

"Stability and Symmetry Requirements of Electron and Ion Beam Fusion Targets." R. O. Bangerter, J. D. Lindl, C. E. Max, and W. C. Mead (Lawrence Livermore Laboratory) . . . . .	15
"Low Power Multiple Shell Fusion Targets for Use With Electron and Ion Beams." J. D. Lindl and R. O. Bangerter (Lawrence Livermore Laboratory) . . . . .	37
"Stable Confinement and Compression of Dense Thermonuclear Plasmas in a Detonation Driven Vortex." F. Winterberg (University of Nevada System) . . . . .	58
"A Study of REB Target Irradiation, Deposition, and Implosion." J. Chang, L. P. Mix, F. C. Perry, M. M. Widner, and J. W. Poukey (Sandia Laboratories) . . . . .	82
"Calculation of Pinched Beam Formation and Target Interaction." Z. Zinamon, S. Miller, E. Nardi, and E. Peleg (The Weizmann Institute of Science) . . . . .	99
"Seeded Mega-Gauss Turbulence in Dense Fusion Target Plasmas." D. A. Tidman (University of Maryland) . . . . .	115
"Charged-Particle Beam Implosion of Fusion Targets." M. J. Clauser and M. A. Sweeney (Sandia Laboratories) . . . . .	135
"Electron Beam Fusion Pellets." W. P. Gula and R. C. Kirkpatrick (Los Alamos Scientific Laboratory) . . . . .	158
"Interaction of Cylindrically-Symmetric Relativistic Electron Beams with Planar Targets and Plasmas: Theory and Applications." D. Mosher (Naval Research Laboratory) . . . . .	171



## Chapter 2 Beam Generation and Focusing

"Different Ways of Thinking About Beams." J. D. Lawson (Rutherford Laboratory) . . . . .	199
"Theory of Electron and Ion Flow in Relativistic Diodes." Shyke A. Goldstein and Ronald C. Davidson (University of Maryland) Roswell Lee and John G. Siambis (Naval Research Laboratory) . . . . .	218
"Processes Governing Pinch Formation in Diodes." A. E. Blaugrund and G. Cooperstein (Naval Research Laboratory) Shyke A. Goldstein (University of Maryland) . . . . .	233
" $Z < 1\Omega$ Pinched Electron Diodes." J. W. Poukey (Sandia Laboratories) . . . . .	247
"Pinching Limits and Scaling Laws for High Current Diodes." G. Ronald Hadley, Thomas P. Wright, and Archie V. Farnsworth, Jr. (Sandia Laboratories) . . . . .	255
"Anode Plasma and Focusing in REB Diodes." S. A. Goldstein, D. W. Swain, G. R. Hadley, and L. P. Mix (Sandia Laboratories) . . . . .	262
"Experimental Investigation of Focusing and Transportation of High-Current Electron Beams." E. I. Baranchikov, A. V. Gordeev, U. V. Koba, V. D. Korolev, V. S. Pen'kina, L. I. Rudakov, V. P. Smirnov, A. D. Sukhov, E. Z. Tarumov (I. V. Kurchatov Institute of Atomic Energy) . . . . .	284
"Electron and Plasma Flow in a Relativistic Diode Subjected to a Crossed Magnetic Field." G. Bekefi and T. J. Orzechowski (Massachusetts Institute of Technology) K. D. Bergeron (Sandia Laboratories) . . . . .	303
"REB Focusing in High Aspect Ratio Diodes." P. Spence, K. Triebes, R. Genuario, and D. Pellinen (Physics International Company) . . . . .	346
"Diode Behavior for a 1.7 Microsecond Generator." C. Stallings, R. Schneider and D. Cummings (Physics International Company) . . . . .	364
"Electron Beam Propagation and Focusing." Keith A. Brueckner (University of California) . . . . .	376
"High-Current Electron Beam Transmission Through Plasma Under Low Pressure." A. N. Didenko, Ye. T. Protasevich, V. V. Tikhomirov (Institute for Nuclear Physics) . . . . .	403

"Behaviour of the Self Focusing Relativistic Electron Beam Propagating Along the Interface of Different Media." A. N. Didenko, A. V. Petrov, A. I. Rjabchikov, V. A. Tusov, Yu. P. Usov (Institute for Nuclear Physics) . . . . .	409
--	-----

### Chapter 3 Accelerator Technology

"Proto-I Switching and Diode Studies." K. R. Prestwich, P. A. Miller, D. H. McDaniel, J. W. Poukey, M. M. Widner, S. A. Goldstein (Sandia Laboratories) . . . . .	423
"Proto-II - A Short Pulse Water Insulated Accelerator." T. H. Martin, J. P. VanDevender, D. L. Johnson, D. H. McDaniel M. Aker (Sandia Laboratories) . . . . .	450
"Approaches to the Generation of Hundred Megampere, Short Pulse Electron Beams." Ian D. Smith (Physics International Company) . . . . .	472
"Electron Beam Power from Inductive Storage." M. Cowan, G. J. Rohwein, E. C. Cnare, E. L. Neau, J. A. Mogford, W. K. Tucker, D. L. Wesenberg (Sandia Laboratories) . . . . .	490
"A Low Voltage Multi-Electron Beam Approach to Pellet Heating." R. G. Little, W. R. Neal, and J. R. Uglum (Simulation Physics Inc.) . . . . .	508
"TONUS-2 -- Intense Electron Beam Generator with Stored Energy of 0.2 MJ." V. M. Bistritsky, A. N. Didenko, I. S. Gleiser, G. A. Sterligov, B. V. Okulov, A. G. Gerlitsin, Yu. P. Usov, V. I. Tsvetkov, A. A. Shatanov (Institute for Nuclear Physics) . . . . .	529
"Nanosecond Switching of High Power Laser Activated Silicon Switches." O. S. Zucker, J. R. Long and V. L. Smith (Lawrence Livermore Laboratory) . . . . .	538

### Chapter 4 Ion Beams

"Experimental Investigations of Positive Ion Flow in a Double Diode." Marco Di Capua, Robert Huff and John Creedon (Physics International Company) . . . . .	555
"Intense, Pulsed, Ion-Diode Sources and Their Application to Mirror Machines." D. S. Prono, J. W. Shearer, and R. J. Briggs (Lawrence Livermore Laboratory) . . . . .	575

"Conversion of Intense Electron Beam Energy into Converging Ion Fluxes - Theoretical Studies." <i>John Guillory and Shyke A. Goldstein</i> (University of Maryland) . . . . .	590
"Injection, Compression and Stability of Intense Ion-Rings." <i>R. N. Sudan</i> (Cornell University) . . . . .	603
"Ion Beam Generation and Focusing." <i>P. A. Miller, C. W. Mendel, D. W. Swain, and S. A. Goldstein</i> (Sandia Laboratories) . . . . .	619
"Studies of a Reflex Triode." <i>J. Golden, C. A. Kapetanakis, and Roswell Lee</i> (Naval Research Laboratory) <i>Shyke A. Goldstein</i> (University of Maryland) . . . . .	635
"Use of Electronic Space Charge to Accelerate, Focus and Bunch Plasma Ions for Pellet Fusion." <i>J. T. Verdeyen, W. L. Johnson, D. A. Swanson, and B. E. Cherrington</i> (University of Illinois) . . . . .	657



# **CHAPTER 1**

## **PELLET FUSION**

STABILITY AND SYMMETRY REQUIREMENTS  
OF ELECTRON AND ION BEAM FUSION TARGETS\*

R. O. Bangerter, J. D. Lindl, C. E. Max, and W. C. Mead  
Lawrence Livermore Laboratory, Livermore, California 94550

Abstract

Considerations of hydrodynamic stability impose severe restrictions on the design of electron and ion beam imploded fusion targets. Furthermore, in order to obtain a sufficiently spherical implosion, many target designs require electron or ion beams having a high degree of spherical symmetry.

We have studied the stability and symmetry requirements of several recently proposed target designs by numerical simulation using the computer program LASNEX.

The ion beam targets we have studied are more vulnerable to instability than the electron beam targets.

\*Research performed under the auspices of the United States Energy Research and Development Administration, Contract No. W-7405-ENG-48, and Defense Nuclear Agency, Contract No. IACRO 75-825.

## I. Stability

The familiar phenomenon of Rayleigh-Taylor instability occurs when two fluids of density  $\rho_1$  and  $\rho_2$  ( $\rho_1 \neq \rho_2$ ) are placed in contact and accelerated in a direction normal to the interface and directed toward the denser fluid. Specifically, let us assume an acceleration  $a$  along the  $z$ -axis. If a perturbation of the form  $\eta_0 \sin kx$  is applied to an interface at  $z = z_0$  the amplitude  $\eta$  at time  $t$  is given by

$$\eta = \eta_0 e^{\gamma t}, \quad (1)$$

where  $\gamma = \sqrt{\alpha k a}$  (2)

and  $\alpha = \frac{\rho_2 - \rho_1}{\rho_2 + \rho_1}$

is the Atwood number. In this case we assume that the fluid of density  $\rho_2$  occupies the region  $z > z_0$  so that exponential growth occurs when  $\rho_2 > \rho_1$  and  $a > 0$ .

Equation (1) is valid for  $\eta \lesssim \lambda = 2\pi/k$ . For  $\eta \gtrsim \lambda$  the growth rate becomes more nearly linear in time.<sup>1</sup>

In this paper we consider only spherical fusion targets. In this case we expand the perturbation in spherical harmonics<sup>2</sup> of order  $\ell$  and replace  $k$  in Equation (2) by  $k \approx \ell/r$  where  $r$  is the radius of the interface.

There are at least three cases in typical electron and ion beam fusion targets where Rayleigh-Taylor instability is likely to play an important role. These are shown in Fig. 1.



Case I occurs when an initially uniform spherical shell is heated on the outside by an electron or ion beam. The region in which the beam is deposited expands, producing a low density medium which accelerates the denser material lying inside of the beam deposition region. It might be expected that Equation (2) would not be valid in this case, since one does not expect a density discontinuity but a more gradual density transition. If the density transition between  $\rho_1$  and  $\rho_2$  is exponential, such that

$$\rho = \begin{cases} \rho_1 & z \leq z_0 \\ \rho_1 e^{\beta(z-z_0)} & z_0 < z < z_1 \\ \rho_2 & z_1 \leq z \end{cases}$$

where  $z_1$  is chosen to insure the continuity of  $\rho$ , it can be shown<sup>3</sup> that one must make the replacement

$$k \rightarrow \frac{k\beta}{k+\beta} \quad (3)$$

in equation (2).

Case II can occur in target designs having an initial density discontinuity.

Case III occurs near the end of an implosion when the pressure in a relatively light fuel region becomes sufficiently great to decelerate the dense pusher surrounding the fuel.

In Cases I and II the effect of the instability depends on the wavelength. If the wavelength is sufficiently large the growth rate

will be too small to be of any consequence. If the wavelength is comparable to the shell diameter, the results will be gross shell distortion and are coupled to the symmetry requirements of the incoming beam. If the wavelength is much shorter than the shell thickness,<sup>4</sup> saturation of exponential growth will occur before the amplitude becomes of sufficient size to destroy the shell. The effects of turbulent transport and mixing could alter the implosion behavior, but these effects are not included in our treatment.

Perturbations having wavelengths comparable to the shell thickness are expected to be most destructive, since they can grow exponentially to amplitudes of the order of the shell thickness and cause shell break-up. Figure 2 illustrates these wavelength domains for a typical shell.

Similar comments apply to Case III instability if we replace shell thickness by fuel radius.

In fusion targets one might expect Equation (2) to be substantially modified by such things as thermal transport and ablation. We have, therefore, studied the behavior of a number of suggested target designs using the 2-dimensional Lagrangian computer code LASNEX,<sup>5</sup> written by George Zimmerman. This code includes electron and ion deposition, energy transport, and separate electron, ion, and radiation temperatures. As options one may also include multigroup photon and particle transport and magnetic field physics, although we have not done this in our simulations.

We believe the most serious deficiencies of our calculations involve the particle deposition. We have assumed classical energy loss

neglecting self-generated fields, plasma effects, and temperature dependence. Also in the current version of LASNEX, the deposition is calculated along the radial Lagrangian grid lines. This is incorrect when the mesh becomes distorted. These defects are currently being eliminated.

The five target designs<sup>6</sup> described in Figures 3a-e and Table I have been chosen as case studies. Using LASNEX we have been able to study instability Case I for all designs and Case II for design E. In most cases we impose a shell thickness perturbation equal to about 1 part in  $10^6$  of the initial shell radius using zoning similar to that shown in Fig. 4. This initial amplitude is sufficiently large to dominate over numerical noise and sufficiently small to allow large growth factors satisfying the conditions  $\eta \ll \lambda$ .

Test cases indicate that using only 4 angular zones per wavelength reduces the growth rate to about 0.8 times its analytic value.<sup>7</sup> Most of our conclusions are insensitive to this size of variation in growth rate. Also, using only 4 zones per wavelength effectively suppresses the growth of modes of higher order than the one under study. For these reasons, and for computer economy, most problems have been run with 4 zones per wavelength. The thickness  $\delta r$  of the radial zones must be chosen to satisfy the condition  $k\delta r < 1$ . This results from the fact that the perturbation extends a distance  $\sim 1/k$  beyond the unstable interface.

Figures 5 to 8 are frames from a movie showing the unsuccessful implosion of the low power target design A. In this case  $\ell = 200$  and only the outside shell is shown.

Figure 9 shows the shell thickness as a function of time together



with the r.m.s. amplitude<sup>8</sup> of the instability. The dashed curve is a simple calculation using equation (1) scaled by the ratio of the instantaneous density to the initial density in order to account for compressional effects. The growth is evidently catastrophic. Furthermore, we assumed an initial r.m.s. perturbation of only  $7\text{\AA}$ . This is rather small. In practice, it seems feasible to manufacture targets with surface perturbations between 50 and 100  $\text{\AA}$ , although  $\sim 10\text{\AA}$  may be possible.<sup>9</sup>

Figure 10 refers to target design B. Because of its small radius and large shell thickness, it is probably the most stable design of its type to appear in the literature. Our calculations indicate that this target survives Case I instability for  $\ell = 100$ . We have also simulated  $\ell = 200$  with the same conclusion. In these calculations we had difficulty in satisfying the  $k\delta r < 1$  criterion with a reasonable number of zones. Since the temperature effect on ion stopping power has not been taken into account, and since we may well start from a 100  $\text{\AA}$  perturbation, the survival of this target should be considered tentative.

Figures 11 and 12 illustrate the behavior of designs C and D. The behavior of these targets imploded by 1 MeV electrons is dramatically different than the ion imploded designs A and B. Figure 13 represents the deposition profiles for 10 MeV protons and 1 MeV electrons in gold. This difference in deposition profile results in rather different density profiles as shown in Fig. 14. Fig. 14 corresponds to a time about midway through the implosion. In the electron case  $k \gg \beta$  so that relation (3) gives  $k \rightarrow \beta$  and the growth rate becomes independent of  $\ell$ , as seen in Figs. 11 and 12. In fact, the lower order perturbations are shown growing slightly more rapidly than the higher order. We believe

this to be due to zoning difficulties associated with the  $k\delta r < 1$  criterion at late times. There is thus some point in time at which the validity of the calculation breaks down. Before this time the growth rates are in reasonable agreement with that predicted by Relation (3). Case I instability thus seems to be unimportant for 1 MeV electron beam implosions. Unfortunately the electron deposition profile that results in such benign instability is inefficient in terms of energy requirements.

Target design E survives both Case I and Case II instability. The Atwood number at the Fe-Au interface is 0.25 to 0.4 during most of the implosion, and furthermore, the acceleration is relatively low since the unstable interface is located relatively far out in the ablation region.

We now turn briefly to the question of Case III instability. This has been analyzed for electron and ion beam targets using the concept of the free-fall line. This model in its simplest form rests on the assumption that no material from a high Z pusher can achieve a velocity greater than the maximum velocity of the pusher, and thus can arrive at the center of the target no earlier than time  $t_0$  defined in Fig. 15. If ignition occurs before  $t = t_0$  it is assumed that the implosion will survive the instability. Fig. 15 corresponds to target C.

Roughly 2% of the yield of target C has occurred by  $t = t_0$ , at which time the temperature of the fuel was about 5 keV. Comparison with other targets is shown in Table II. We have been unable to quantify the degradation of burn caused by Case III instability, but the above analysis provides a rough comparison of the various targets.

## II. Symmetry

As mentioned above, the concepts of stability and symmetry are closely related. Shell thickness perturbations of  $\ell \sim 100$  quite clearly belong in the realm of stability problems, while shell thickness perturbations having  $\ell \sim 2$  are normally considered to be symmetry problems.

Low order symmetry perturbations can be produced by variations in radius, thickness, density, beam power, or time jitter in multiple beams. For example, one expects a two beam target irradiation scheme to have  $\ell = 1$  jitter asymmetry, as well as  $\ell = 1$  and  $\ell = 2$  beam power asymmetry.

Because of fuel turbulence induced by asymmetries, we have had some difficulty in studying this problem with our Lagrangian code LASNEX. However, our 2-D LASNEX calculations indicate that smoothing effects such as thermal conduction have little effect on an  $\ell = 2$  perturbation. Because of this fact it is possible to make some rather general statements.

We define convergence ratio as  $r_i/r_f$ , where  $r_i$  is the initial radius of the outermost pusher, and  $r_f$  is the final compressed radius of the fuel. Assume a small angle dependent variation  $\delta E$  in the energy  $E$  deposited in some region of target. From a variety of simple models one expects that the variation  $\delta V$  in pusher velocity  $V$  to be given by  $\delta V/V = c \delta E/E$  where  $c$  is of order unity.

In order to achieve a large convergence ratio the pusher must move a distance  $\sim r_i$ . Thus, a perturbation in velocity will result in a radial perturbation  $\delta r = r_i \delta V/V = cr_i \delta E/E$ . We expect degradation of the implosion when  $\delta r \sim r_f$  or  $r_f/r_i \sim c \delta E/E$ . We thus obtain the rule that the required energy symmetry is proportional to and roughly equals the



reciprocal of the convergence ratio. Similar arguments can be made for other types of asymmetries. An  $\ell = 2$  perturbation can be crudely simulated by running two 1-D LASNEX calculations representing slightly different input powers at the pole and equator of the target. By this method we obtain  $\delta r/r_f \sim 0.5$  for a 5% power difference on target B. This is shown in Fig. 16. The convergence ratio of target B is about 20, so that the LASNEX results are in agreement with our simple calculations for  $c \sim 1/2$ . The results for other targets are given in Table III.

In these examples it seems likely that an  $\ell = 2$  fractional energy perturbation of  $r_f/r_i$  would degrade but not destroy thermonuclear burn, however, considerably more work is needed in this area.

## Conclusions

We find that 1 MeV electron beam targets are rather invulnerable to stability problems. This is a result of the broad deposition profile which produces small density gradients and large shell thickness. By contrast, ion beams produce larger density gradients and thinner shells, and consequently suffer more severe instability damage.

Our preliminary symmetry results confirm the simple rule that the required energy symmetry is roughly equal to the reciprocal of the convergence ratio of the target. Thus symmetry requirements are more stringent for the large, low-power targets having high convergence ratios.

## ACKNOWLEDGMENTS

We are indebted to George Zimmerman for the use of LASNEX and gratefully acknowledge the encouragement and support of John Nuckolls.

## REFERENCES

1. An exact description of large amplitude Rayleigh-Taylor instability is extremely complex. See W. P. Crowley, University of California Report UCRL-72650 (1970).
2. M. S. Plesset, J. of Appl. Phys. 25, 96 (1954).
3. R. LeLevier, G. Lasher, and F. Bjorklund, University of California Report UCRL-4459 (1955).
4. In this paper we have arbitrarily defined shell thickness to be measured between the points where the density of the shell drops to 0.2 times its maximum value.
5. G. B. Zimmerman, University of California Report UCRL-74811 (1973).
6. Targets B, D, and E are described in the following references:  
M. J. Clauser, PRL 34, 570 (1975); M. J. Clauser, PRL 35, 848 (1975);  
M. A. Sweeney and M. J. Clauser, Applied Phys. Lett. 27, 483 (1975).  
Targets A and C were designed by our group at Lawrence Livermore Laboratory.
7. J. D. Lindl and W. C. Mead, PRL 34, 1273 (1975); W. C. Mead and J. D. Lindl, University of California Report UCRL-77057 (1975).
8. The amplitude is measured by calculating r.m.s. deviation of Lagrangian grid line from its mean radius along a symmetry direction.
9. Charles D. Hendricks, Lawrence Livermore Laboratory, private communication.

TABLE I  
Target Designs

Target	Beam	Voltage (MeV)	Outside radius (mm)	Peak power (TW)	Input energy (kJ)	Output energy (kJ)
A	Alpha	5	1.07	8	35	30
B	Proton	10	0.72	110	1070	1100
C	Electron	1	2.68	250	4400	5400
D	Electron	1	1.20	1200	6280	7700
E	Electron	1	1.44	400	3200	7860

TABLE II  
Free-Fall Analysis Shows Ion Beam Target and Multiple Shell  
Electron Beam Target Have Superior Ignition Characteristics

	Target	Beam	Percent yield at $t = t_0$	Fuel tem- perature at $t = t_0$
B	Single shell	10 MeV protons	2.6	4.4
C	Multiple shell	1 MeV electrons	2.1	5.4
D	Single shell	1 MeV electrons	0.55	3.1
E	Fe on Au shell	1 MeV electrons	0.48	3.0

TABLE III  
Results of Symmetry Calculations

Target	$\delta P/P$	$r_i/r_f$	$\delta r/r_f$	C
B	0.05	23	0.50	0.44
C	0.01	75	0.36	0.48
D	0.05	13	0.24	0.36
E	0.05	22	0.45	0.42



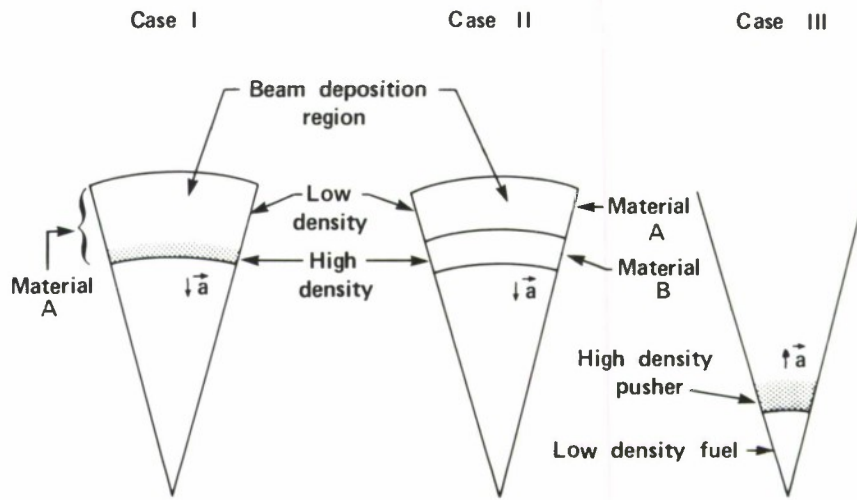


Figure 1. Three cases in which Rayleigh-Taylor instability can occur in electrons or ion beam fusion targets.

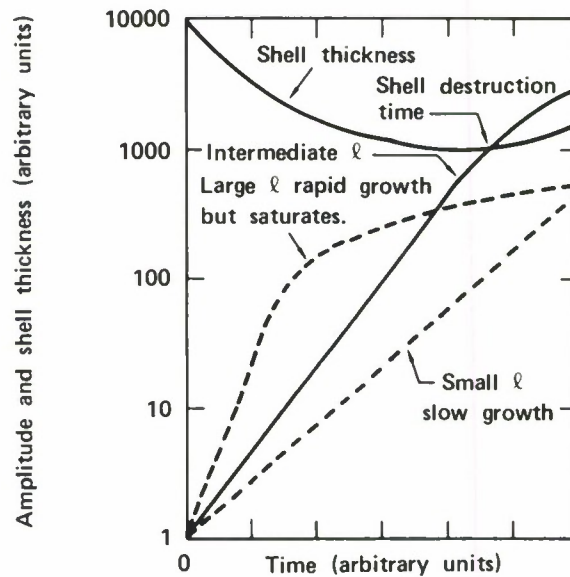
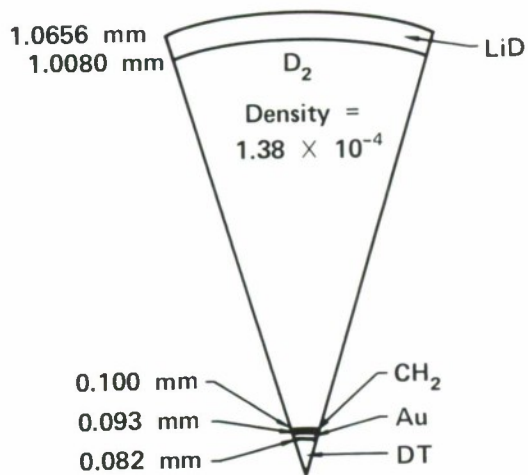
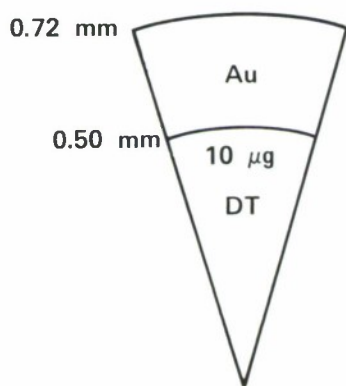
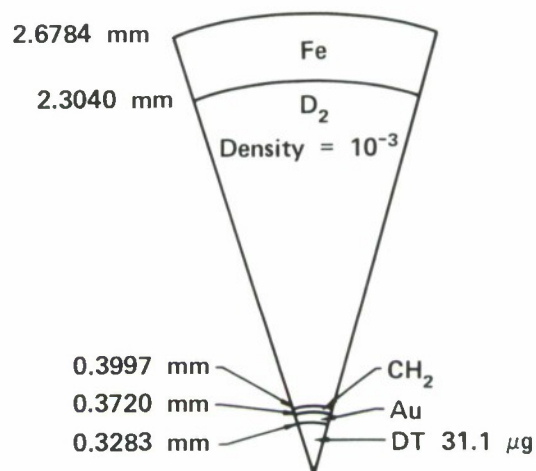


Figure 2. Behavior of small, intermediate, and large  $\ell$  perturbations, showing some intermediate  $\ell$  value to be the most destructive.



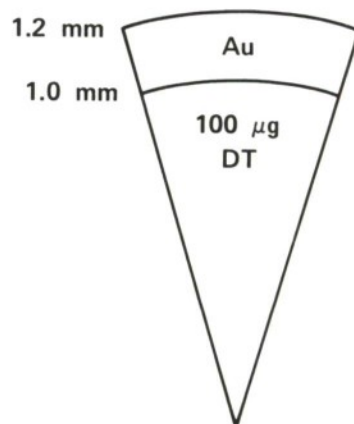
(a) 5-MeV alpha beam,  
target A

(b) 1-MeV electron beam,  
target C

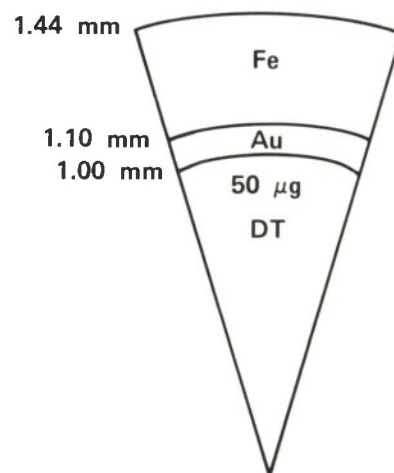


(c) 10-MeV proton beam,  
target B

Figure 3. Five target designs studied



(d) 1-MeV electron beam,  
target D



(e) 1-MeV electron beam,  
target E

Figure 3. (Cont.)

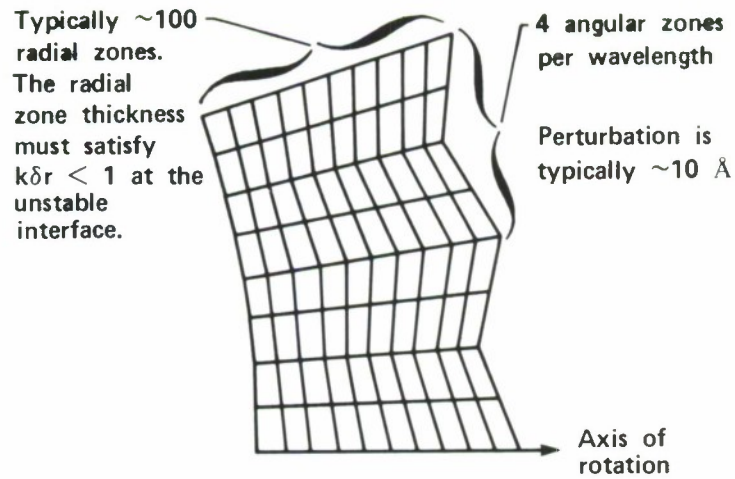


Figure 4. Lagrangian mesh for a typical problem. The perturbation is greatly magnified and only a few radial zones are shown.

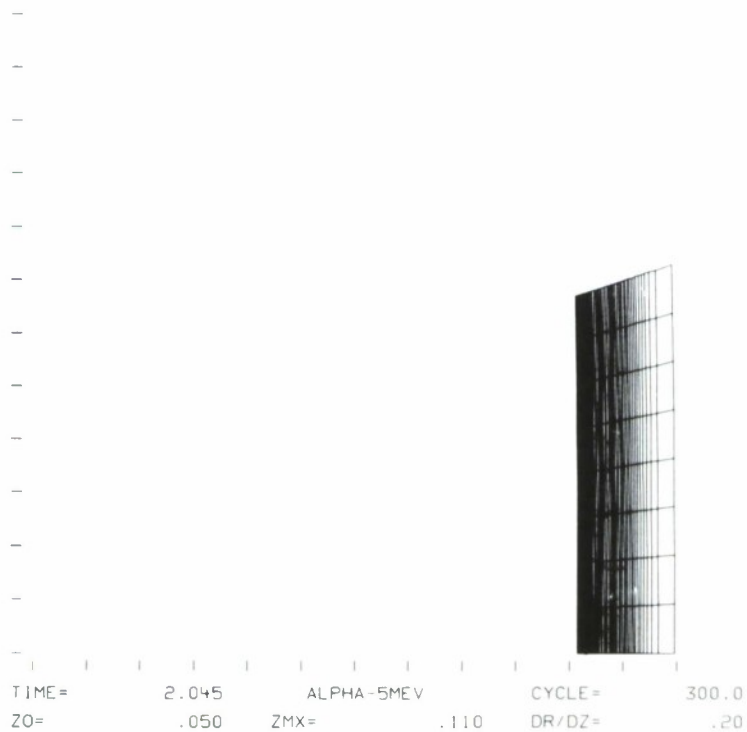


Figure 5. Frames from a movie to be presented with talk. The movie shows the unsuccessful implosion of target A.



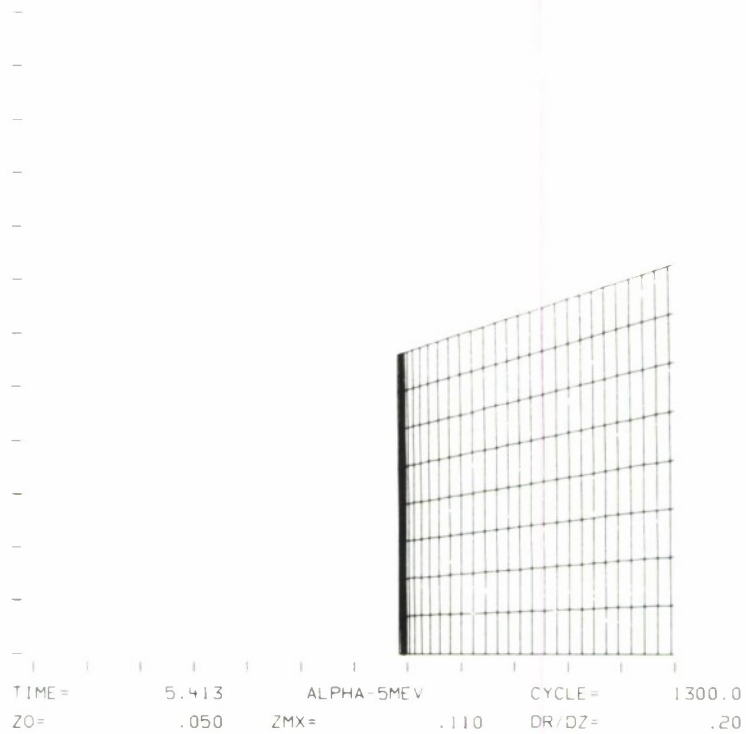


Figure 6. Frames from a movie to be presented with talk. The movie shows the unsuccessful implosion of target A

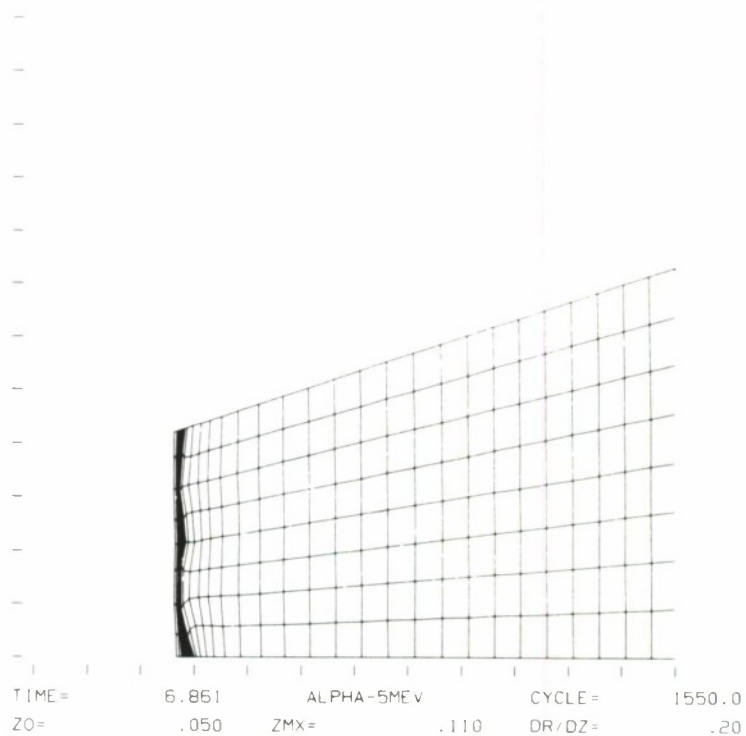


Figure 7. Frames from a movie to be presented with talk. The movie shows the unsuccessful implosion of target A

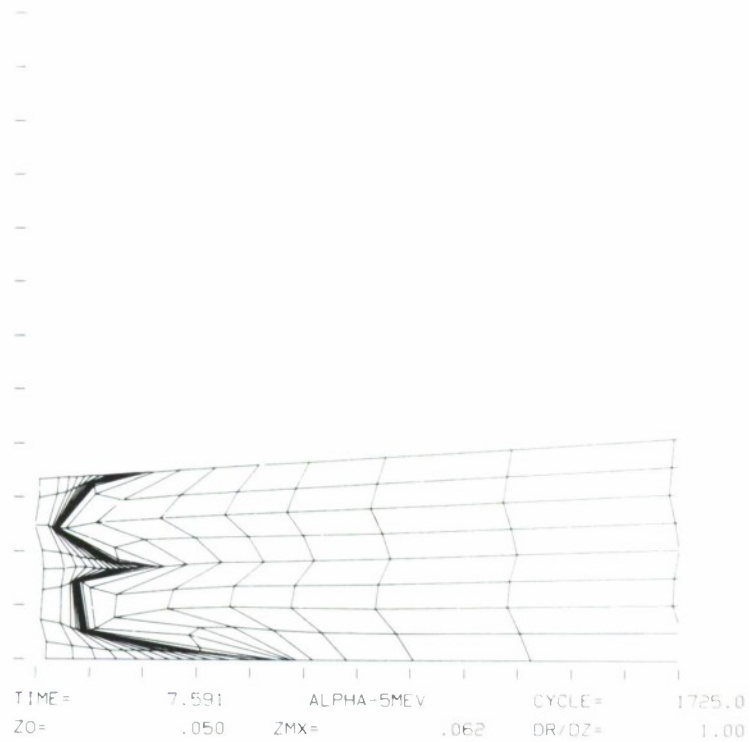


Figure 8. Frames from a movie to be presented with talk. The movie shows the unsuccessful implosion of target A

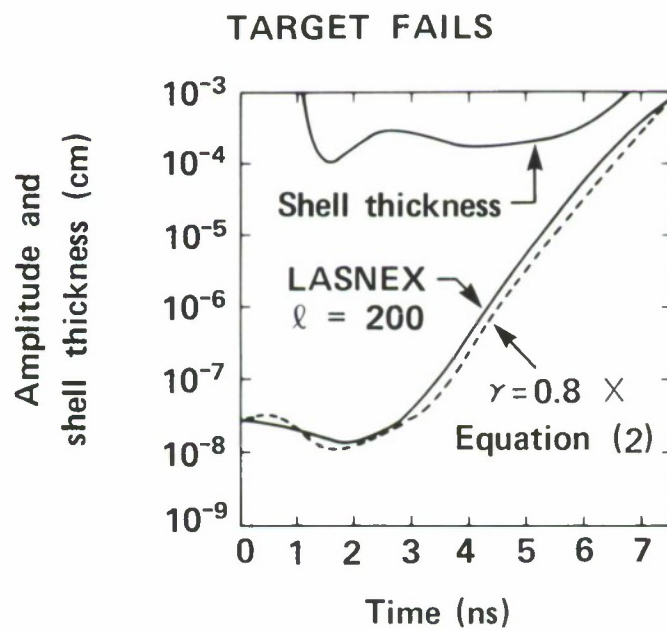


Figure 9. Perturbation amplitude (r.m.s.) and shell thickness as a function of time for target A.

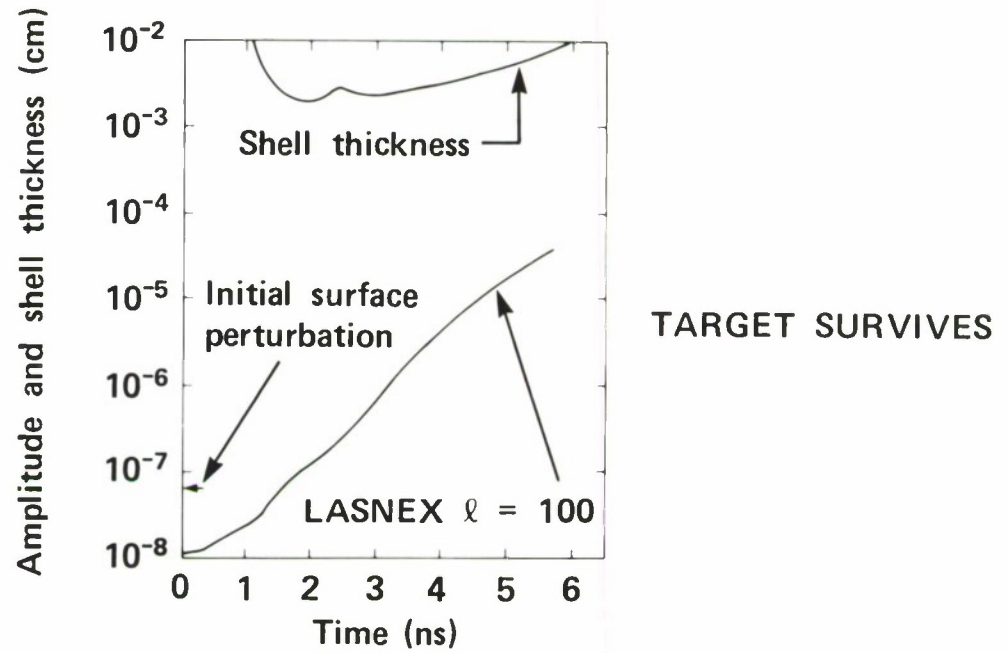


Figure 10. Perturbation amplitude (r.m.s.) and shell thickness as a function of time for target B. The amplitude is measured at a given mesh line. This results in a small amplitude at early times. The initial shell thickness perturbation is indicated by an arrow.

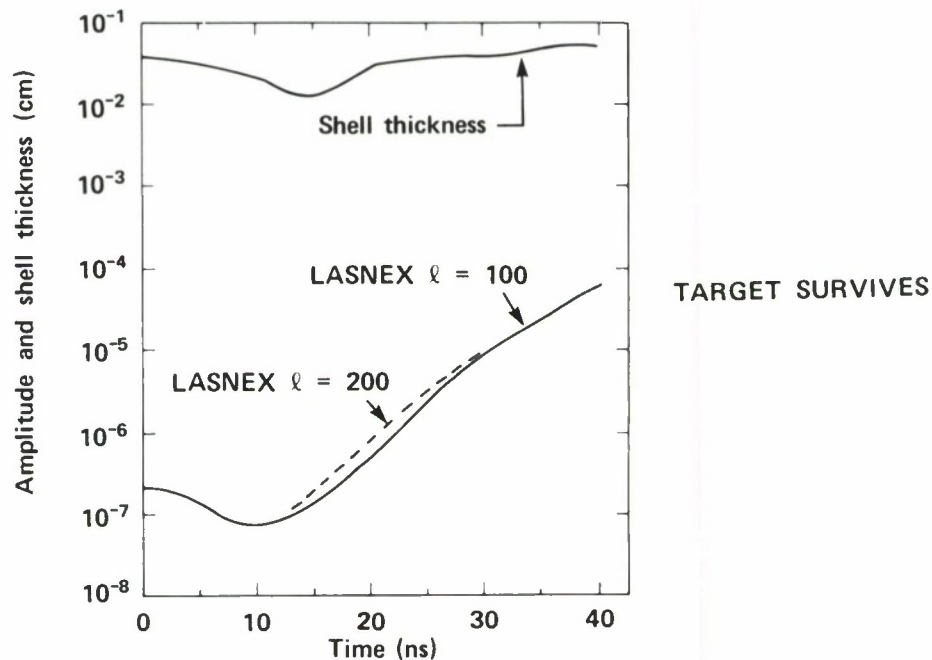


Figure 11. Perturbation amplitude (r.m.s.) and shell thickness as a function of time for target design C. The amplitude is the amplitude of the unstable interface and does not represent a fixed mesh line since the beam voltage varies as a function of time for this target design.

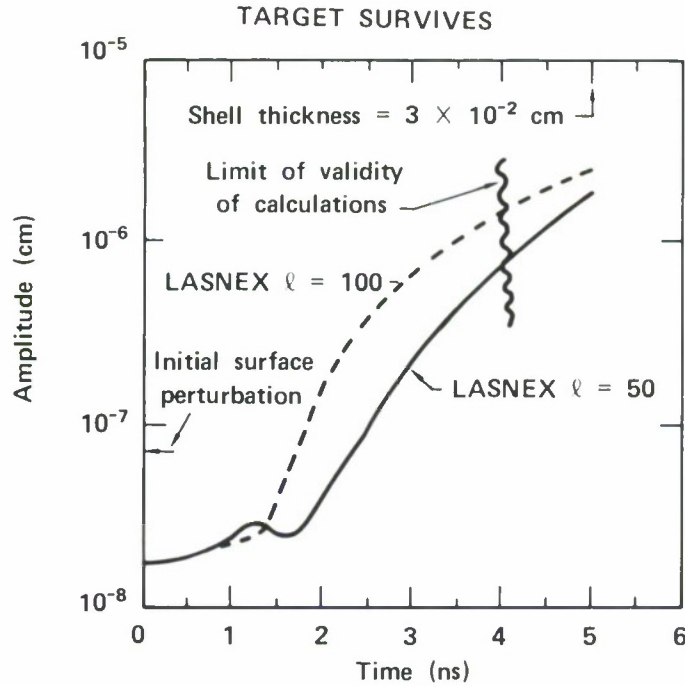


Figure 12. Amplitude (r.m.s.) of unstable interface for target design D. The wavy line represents the point at which the  $k \delta r < 1$  criterion is no longer satisfied.

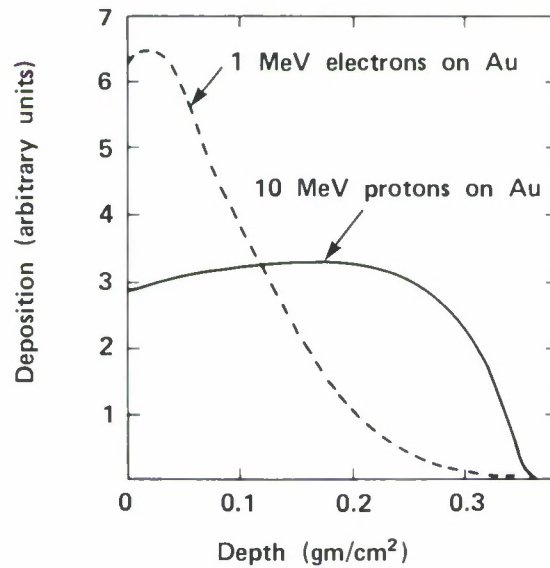


Figure 13. Deposition profiles for 1 MeV electrons and 10 MeV protons on gold. The incoming electrons were distributed as  $\cos\theta$  where  $\theta$  is the angle with respect to the radial direction. The angular distribution of protons corresponds to a proton beam temperature of 10 eV focused from a sphere 50 cm from the target.



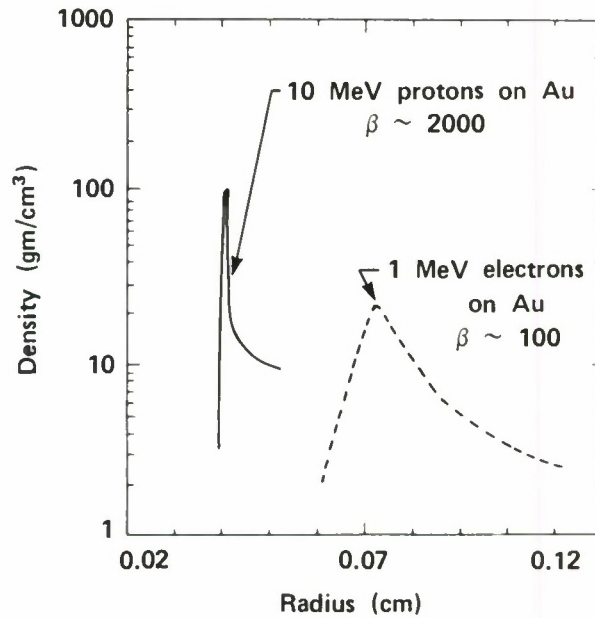


Figure 14. Density as a function of radius for targets B and D imploded with 10 MeV protons and 1 MeV electrons, respectively. These curves are taken at a time of 3.7 ns. This is roughly half way through the implosion.

PUSHER MATERIAL CAN REACH  $r = 0$  at  $t = t_0$ . IGNITION SHOULD OCCUR BEFORE  $t = t_0$ .

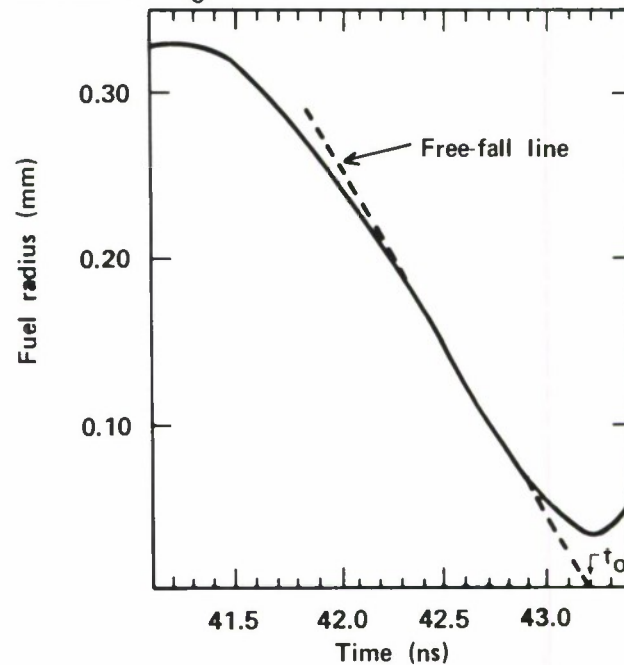


Figure 15. Outer radius of fuel as a function of time for target C. The slope of the free-fall line represents the maximum velocity of the pusher-fuel interface.

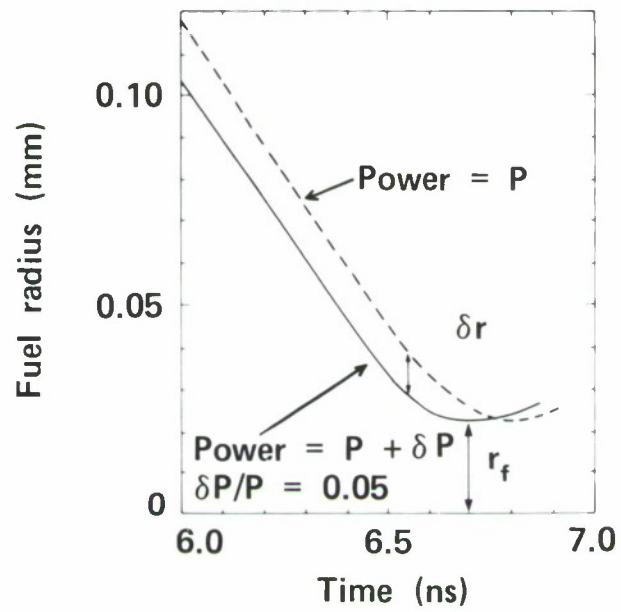


Figure 16. Outer radius of fuel as a function of time for power inputs  $P$  and  $P + \delta P$  differing by 5% on target B.

LOW POWER MULTIPLE SHELL FUSION TARGETS FOR USE WITH  
ELECTRON AND ION BEAMS\*

J. D. Lindl and R. O. Bangerter

University of California, Lawrence Livermore Laboratory  
Livermore, California, 94550

ABSTRACT

Use of double shell targets with a separate low Z, low density ablator at large radius for the outer shell, reduces the focusing and power requirements while maintaining reasonable aspect ratios. A high Z, high density pusher shell is placed at a much smaller radius in order to obtain an aspect ratio small enough to protect against fluid instability. Velocity multiplication between these shells further lowers the power requirements. Careful tuning of the power profile and intershell density results in a low entropy implosion which allows breakeven at low powers.

Ion beams appear to be a promising power source and breakeven at 10-20 Terrawatts with 10 MeV alpha particles appears feasible. Predicted performance of targets with various energy sources is shown and comparison is made with single shell targets.

\*Research performed under the auspices of the United States Energy, Research and Development Administration, Contract No. W7405-ENG-48, and Defense Nuclear Agency, Contract No. IACRO 75-825.

For a given mass of fuel and tamper, the minimum energy required to implode it to ignition will be approximately constant, for the best designs. One must do a certain amount of work per unit mass on the fuel tamper system in order to achieve ignition.

Since the efficiency with which one does this does not vary by a large factor between various low entropy designs, the input energy per unit mass is reasonably constant. This required energy is on the order of 1 Joule per nanogram of pusher and fuel.

$$E = \int \text{Power } dt = \bar{P}t = \frac{\bar{P}r}{\bar{V}}, \text{ where } r \text{ is the target radius,}$$

$\bar{P}$  the average power, and  $\bar{V}$  is the average velocity.  $\bar{V}$  is the average velocity required for ignition which is independent of design. For shell type targets  $\bar{P}$  is close to the peak power. For constant mass,  $E$  is approximately constant so  $\bar{P}$  varies as  $1/r$ . Hence, a larger radius allows you to drop the power. For such a target,  $\rho \Delta r$  varies as  $1/r^2$  or  $\Delta r \sim 1/\rho r^2$ . Since E-BEAM and I-BEAM targets have shells which are about 1 range thick, this means the range of the particle used has to vary as  $1/r^2$ . This scheme allows one to drop the power while keeping the yield and input energy the same.

If one is constrained to a particle with a given range, required power drops somewhat for decreasing radius.  $\bar{P}r \propto r^2$



for constant thickness shell so  $\bar{P} \propto r$ . However, since  $E \propto r^2$  and yield  $Y$  is proportional to  $M\rho r \propto r^4$  for a given compression, the yield ratio is proportional to  $r^2$  and drops rapidly as you shrink the size. This means that long range particles are going to require large-size targets, high powers, and large energies regardless of the design.

To minimize the input power required at a given input energy, one would like to use the highest aspect ratio shell possible. This aspect ratio is primarily determined by considerations of fluid instability and implosion symmetry. For a given aspect ratio shell,  $\bar{P}r \propto r^3$  or  $\bar{P} \propto 1/r^2$  so that decreasing the radius results in a rapid power drop. With  $Y \propto M\rho r$  or  $r^4$  and  $E \propto r^3$ , the yield rate drops only as  $r$  and gives the prospect of achieving breakeven at low powers and energies. This also requires that one go to short range particles since, for constant aspect ratio, the range of particle used must be proportional to  $r$ .

E-Beam and I-Beam targets have absorption shells about one range thick, essentially because there is no ablation front which propagates through the shell. This occurs for two reasons:

1. There is little density or temperature dependence in the range, so except for spherical convergence effects the beam deposits in the same mass throughout the implosion. Since some of the mass moves inward and

some moves outward, the convergence effects are small.

2. The matter temperatures achieved are only a few hundred eV at most and electron conduction is inefficient at carrying the energy beyond the matter where it is absorbed.

Single shells of high Z material can be used with particles like 1 MeV electrons, which have a long range to achieve fusion breakeven. For these long range particles, the thermal radiation generated by the hot plasma is substantially self-trapped, thus limiting the radiation losses. For example, in a typical target with 1 MeV electrons on gold, radiation losses are about 40% of the input energy. For 1 MeV electrons on iron, the losses are about 20%. On the other hand, for 100 keV electrons or 10 MeV  $\alpha$ 's on gold, virtually all of the input energy is radiated away as thermal x-rays. Such targets may be useful as x-ray sources but not for implosions. To limit the thermal x-ray losses to a tolerable value, these short range particles, which are necessary for breakeven at low energies and powers, must be absorbed in low Z and hence, low density materials. Even in  $\text{CH}_2$ , using 10 MeV  $\alpha$ 's, thermal x-rays result in about a 50% loss of input energy. This loss can be limited to about 20% by using LiD or LiH.

Low Z materials are very poor pushers and tampers. Unless one can design a target which achieves sufficient velocity to ignite without a pusher, one must have an added layer of high Z material for a pusher. With double shell targets, one can use a low Z, low density material for the outer shell. This allows one to increase the radius while keeping down the mass and maintaining a sufficiently small aspect ratio that fluid instabilities can be tolerated. The high Z pusher-tamper layer needed for ignition and efficient burn at the low velocities one is generally able to generate with E-Beams or I-Beams is placed at a much smaller radius. This keeps its thickness sufficient to survive fluid instability and also to act as a preheat shield against photons or high energy electrons and ions. If one tried to put a high Z pusher against a low Z exploding ablator, it would be very thin, making it very susceptible to preheat and fluid instability.

The larger radius of a double shell design at a given energy also reduces the focusing requirements of the beam. The penalty one pays for this advantage is a larger convergence ratio  $R_o/R_{min}$ . Here  $R_o$  is the initial radius of the outer shell and  $R_{min}$  is the minimum radius of the fuel. The convergence ratios for the various double shell designs given below are about 100, implying a one percent uniformity of deposition.

By contrast, convergence ratios of various single shell designs that have been published are 20-30, implying a uniformity of 3-5%.

The lowest power, double shell, ion beam breakeven target designed to date is shown in Figure 1. This target and all others to be presented here have been calculated using the LASNEX<sup>1</sup> computer code written by George Zimmerman of LLL. This target gives a theoretical yield of 65 KJ with 45 KJ of 9 MeV alphas which have a range of .0114 gm/cm<sup>2</sup>. It requires a peak power of 11 TW. The target performance characteristics and pulse shape are given in Table 1. The energy deposition profile includes range straggling and 5 milliradians of beam divergence at 10 cm from finite temperature and scattering at the source. Also, for this target, the range of the ions was varied linearly with the power, a crude attempt to model a constant impedance machine. For 3-T this feature of the deposition profile does not significantly affect the peak power required compared to that which would be required for a constant range profile. Its principal effect is to keep the higher energy thermal photons from leaking out of the outer shell and getting into the inner gold shell, thus degrading the implosion.

To achieve breakeven at this low power and energy, several features of the design must be closely controlled. These features will be examined for a target scaled upward 15% in radius from that in Figure 1. It used 11 MeV alphas, 15 TW peak power, and

72 KJ input energy. During the implosion, the LiD outer shell is nearly completely penetrated and exploded by the ions. This explosion drives the inner 228 $\mu$ gm of the LiD inward to a maximum velocity of 22.8 cm/ $\mu$ sec. The linear rise in power early in the ion pulse is designed so that a weak shock of about 1 cm/ $\mu$ cm is sent through this inner layer of LiD. This weak shock insures that the entropy of the LiD layer is low. A low entropy outer shell helps to provide an efficient collision with the inner gold shell.

In this collision, the gold receives a velocity of 32.5 cm/ $\mu$ sec. This is a velocity multiplication of 1.426. The formula for the elastic collision of two bodies of unequal mass gives a velocity multiplication of  $2/(1+x) = 1.61$  for the masses involved here so the collision was nearly elastic. X is the ratio of the Au mass to the LiD mass. The actual velocity imparted to the pusher is fairly insensitive to X, however. Although the energy transfer efficiency from the outer shell to the inner shell is proportional to X, the transfer of energy from the exploding ablator is inversely proportional to X. This is seen for a simple case of a rocket with constant blowoff velocity whose efficiency is given by

$$[m/M_0 - m] [\ln (m/M_0)]^2 ,$$



where  $M_0$  is the initial and  $m$  the final rocket mass. The velocity achieved by the gold as a function of the mass of LiD moving inward is shown in Figure 2.

The peak pressure between the shells is given approximately by  $1/2(\rho v^2)$  of the outer shell, just before it starts to slow down. This is the kinetic energy density in the shell that can be converted to pressure. If there is no material between the shells, this pressure will develop very early in the collision and a shock of this magnitude will be transmitted to the inner shell. Such a collision would result in a very high entropy pusher and hence a low pr, low density implosion, and poor efficiency. If there is material between the shells, it is shocked and heated by the incoming shell. By adjusting its density, one can control the arrival time and magnitude of the shock that is transmitted to the inner shell and achieve a nearly elastic collision. If that material density is too high, however, the pressure will rise too slowly and the implosion will be over before significant energy transfer can be achieved. Figure 3 shows the yield as a function of the intershell density. Figure 4 shows the pressure versus time history between the shells for the various density fills. The line A is the estimate for the peak pressure given above. For the lower density fills, the dip in pressure before the final rise is due to the fact

that the pressure starts to drop when the velocity of the inner shell exceeds that of the outer shell. The subsequent rise is due to spherical convergence. The degree of drop is essentially determined by the aspect ratio of the shell. The distance that the inner shell moves before it gets a velocity comparable to that of the outer shell is a few times its initial thickness.

A very simple analysis shows why this is reasonable. If  $V_1$  is the inner shell velocity and  $V_o$  is the outer shell velocity, then

$$V_1 = \int a \, dt = \bar{a} \Delta t \approx \frac{\bar{P}}{\rho_1 \Delta x_1} \Delta t$$

$$\sim \frac{1/2 \rho_o V_o^2}{\rho_1 \Delta x_1} \Delta t .$$

$V_o$  and  $\rho_o$  are measured at the time just before the outer shell starts slowing down. If the outer shell does not slow down much in accelerating the inner shell, then the pressure starts to drop when  $V_1 \sim V_o$ . Letting  $V_o \Delta t = x$ , the distance pushed, we get  $x/\Delta x_1 = 2\rho_1/\rho_o = 2-4$  for typical calculations.

When the pressure starts to drop, two competing effects act on the shell. The shell has an internal pressure about equal to the driving pressure. As the driving pressure starts to drop, the shell will start to decompress to be in pressure

equilibrium. This decompression can lead to a drop in the final  $\rho_r$  and hence in the effectiveness of the inner shell as a tamper. Acting to oppose the shell expansion is spherical convergence which acts to increase the density by constraining the mass to a smaller volume.

The compression of the shell at a time after the pressure starts to drop is given by the ratio of the volumes and is given approximately by

$$\begin{aligned}
 &= \frac{4\pi R_o^2 \Delta r_o}{4\pi R^2 \Delta r} \frac{R_o^2 \Delta r_o}{(R_o - Vt)^2 (\Delta t_o + V_s t)} \\
 &= \frac{1}{(1 - \frac{Vt}{R_o})^2 (1 + \frac{V_s t}{\Delta r_o})} ,
 \end{aligned}$$

where  $R_o$  and  $\Delta r_o$  are the radius and thickness of the shell at the start of the free fall,  $V$  and  $V_s$  are the shell velocity and sound velocity. Because of the quadratic dependence, spherical convergence eventually wins out. The decompression can be minimized by minimizing  $V_s/V$  and maximizing  $R/\Delta r_o$ .

In practice, spherical convergence starts dominating at a radius of a few times the shell thickness. The aspect ratio of the inner shell is pretty much determined by **considerations** of fluid instability. This limits one to aspect ratios of about ten. The yield is not terribly sensitive to the aspect ratio for the above design for aspect ratios from 8 to 17.5. The yield

was calculated with the mean pusher radius at 120, 140, and 160  $\mu$  for the same mass of Au and DT. At the smallest radius the fuel represented a solid DT fill. For the larger radii, the fuel was assumed to be frozen as a shell against the pusher. The targets with the larger radii worked somewhat better because the energy transfer from the outer shell was slightly more efficient and the fuel was put on a slightly better adiabat. These results are shown in Figure 5. At a given radius, the yield is not very sensitive to small changes in the pusher mass or thickness. The higher mass pusher will receive a smaller velocity but the pr will be larger and the fuel will have longer to ignite from the lower temperature achieved. With less mass, the velocity is higher, but the final pr is lower so the fuel ignites more rapidly but has less time to burn. The functional dependence of yield on pusher mass at a radius of 120  $\mu$  is shown in Figure 6.

Recent 2-D calculations indicate that the design shown in Figure 1 will not survive Rayleigh-Taylor instability. The target can be redesigned to have a more rapid early acceleration and a thicker outer shell. These modifications will probably result in about a factor 2 increase in required power but other comments above will not be affected.

In comparison with single shell targets for longer range particles, the advantage of a double shell target is not so

obvious. Since the outer shell must have the same  $\text{gm/cm}^2$  as the single shell target, its larger radius means it must have more mass. For example, the target shown in Figure 7 for use with 1 MeV electrons has about twice the radius of a breakeven single shell target. The iron mass is about 3 times that of the breakeven single shell in Figure 8. Because of the velocity multiplication on the gold, the average implosion velocity is about half and its radius twice that of the single shell, so one might expect similar power and a somewhat greater energy input than for the single shell. In fact, the calculations do show a slightly reduced power and increased input energy. With the target in Figure 8, Sweeney<sup>2</sup> achieves breakeven at about 350 TW. LASNEX calculations of the same target indicate a required power of 400 TW and 3 MJ, but gets twice breakeven. The double shell design in Figure 7 achieves a little over breakeven at 250 TW with 4.5 MJ input. Its performance characteristics are given in Table 2.

The performance of the pusher and fuel in the two cases is radically different. Figure 9 shows the pusher adiabat for the two types of target. Because of its low adiabat, the pusher uses what energy it gets very efficiently in the double shell target. But the transfer efficiency to the pusher from the beam is only 0.6%. This low efficiency occurs because of the large mass of iron that must be imploded inward to shield the Au pusher



from the bremsstrahlung tail of the 1 MeV deposition profile. This bremsstrahlung preheat is a serious effect if it penetrates the pusher because of the long time that the gold waits before being hit by the iron. In the one shell design, the transfer efficiency to the pusher is about 5%, but the entropy is very high because of the bremsstrahlung preheat.

Figures 10 and 11 show the single shell and double shell equivalents for 10 MeV protons. Clauser<sup>3</sup> calculates that, using a radial deposition profile, the single shell will break even at 60 TW. LASNEX calculations, using an ion deposition profile that includes range straggling and 5 milliradians of beam divergence at 10 cm due to finite temperature and scattering at the source, require 110 TW and 550 KJ. This only includes the energy that hits the target. Because of the beam divergence assumed, 15% of the beam energy misses the target. In the double shell target, the outer iron shell is about 25 times as massive as that for the single shell. However, the implosion efficiency is higher and the mass fraction imploded is smaller. The acceptance time is increased from 8 ns to 40 ns because of the increased radius. The overall result is an increase in the required energy by a factor of 3 to 1.65 MJ but a drop in power to 50 TW. The yield is about 6.0 MJ. Performance characteristics are given in Table 3. The calculations of Kirkpatrick,<sup>4</sup> et al., using a constant deposition profile are most nearly applicable to the

10 MeV proton results given here. The two sets of results are qualitatively consistent.

An interesting feature of E-Beam and I-Beam implosions is the fact that the implosion pressure in the ablator is not a monotonic function of power. Since the energy is being deposited in a constant mass whose density is dropping, the pressure can actually drop while the power is rising. This is seen in Figure 12 where pressure and power versus time are plotted for the 10 MeV protons deposited in the iron shell in Figure 11.

Other targets for implosion with 100 keV and 200 keV electrons are shown in Figures 13 and 14. Implosion characteristics are given in Tables 4 and 5. The powers are significantly lower than for 1 MeV electrons but the currents are about the same.

#### Conclusion:

Carefully tuned double shell targets can lower the power requirements for ion beam fusion breakeven to 10-20 TW with 10 MeV alphas. The focusing requirements are also reduced from those required for single shell targets. One pays for these advantages by an increased sensitivity to fluid instability and by more severe requirements on the required uniformity of energy deposition. Because convergence ratios are about 100 for typical double shell targets, the energy deposition must be uniform to about 1%.

For the longer range particles such as 1 MeV electrons and 10 MeV protons, one can achieve about a factor of 2 decrease in the power required for breakeven, although the energy required increases.

#### REFERENCES

1. G. B. Zimmerman, LLL Report, UCRL-74811, 1973.
2. M. A. Sweeney and M. J. Clauser, App. Phys. Lett., 11/1/1975.
3. M. J. Clauser, Phys. Rev. Lett., Vol. 35, No 13, pp. 848-851.
4. R. C. Kirkpatrick et al., Nuc. Fus. Vol. 15, No. 2.

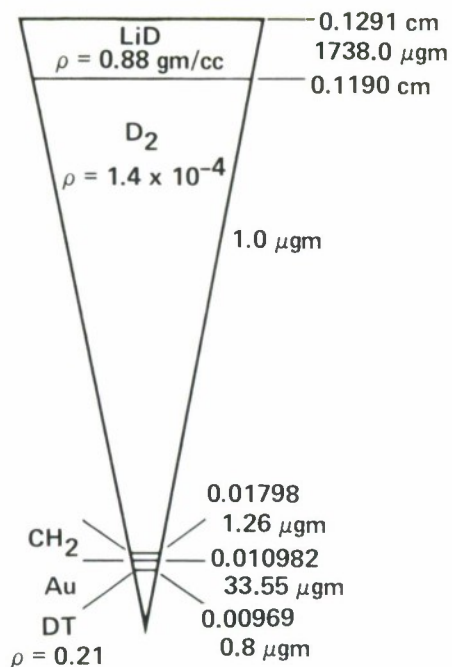


Figure 1. Pellet imploded with 9 meV  $\alpha$ 's

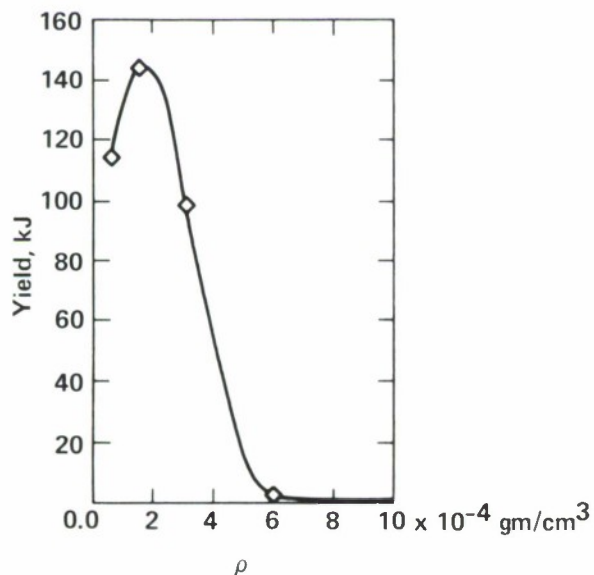


Figure 3. Yield versus gas fill density between LiD and Au shells

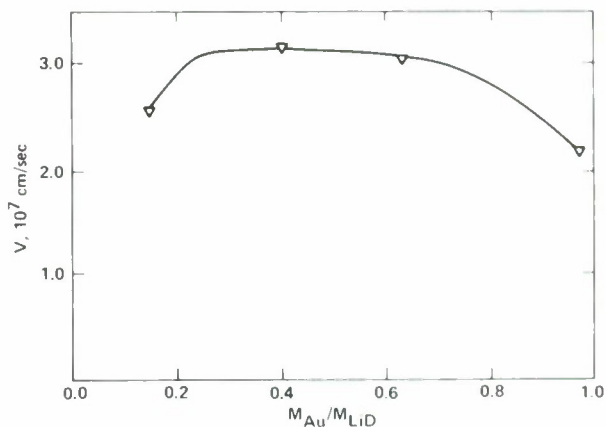


Figure 2. Velocity of gold pusher versus ratio of gold pusher mass to LiD pusher mass

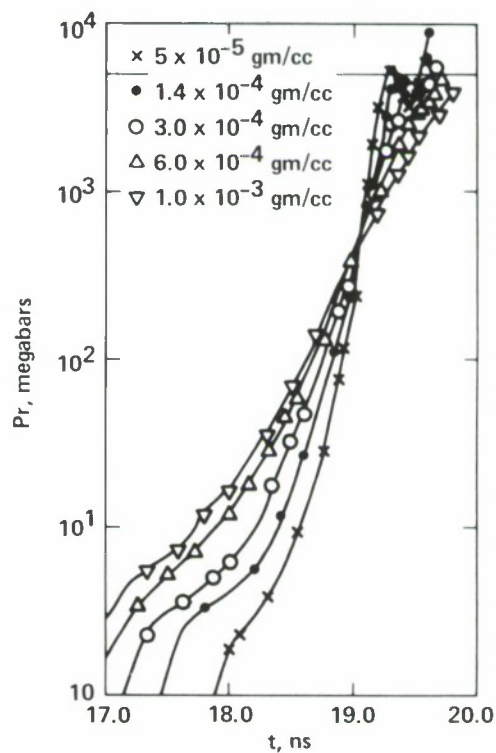


Figure 4. Pressure vs time between the LiD and Au shells for various gas fills between them

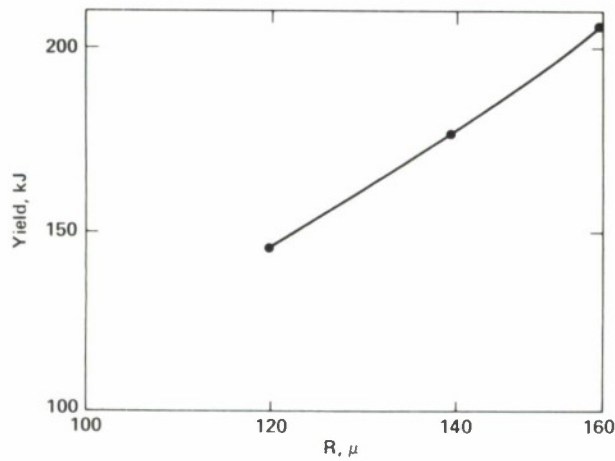


Figure 5. Yield versus gold pusher radius for constant gold and fuel mass

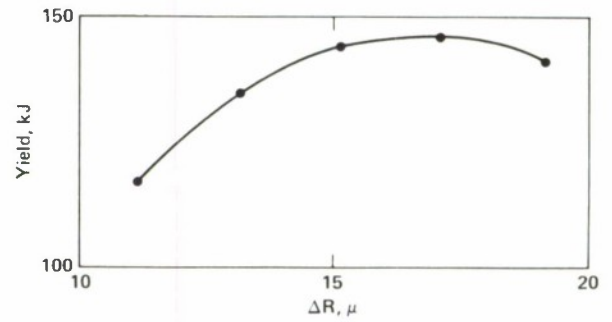


Figure 6. Yield versus gold shell thickness at a mean radius of  $120\mu$

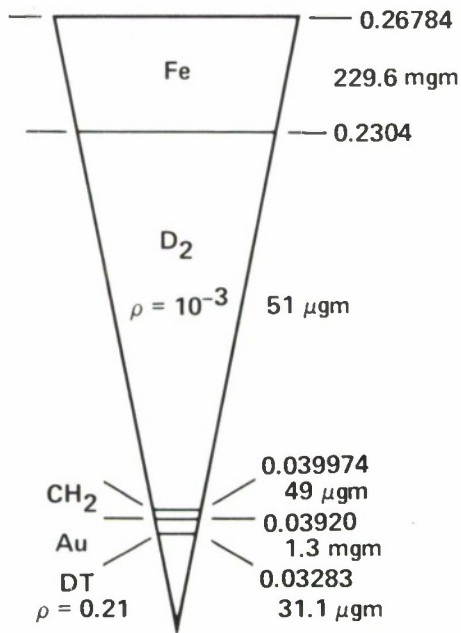


Figure 7. Double shell target driven by 1 MeV electrons

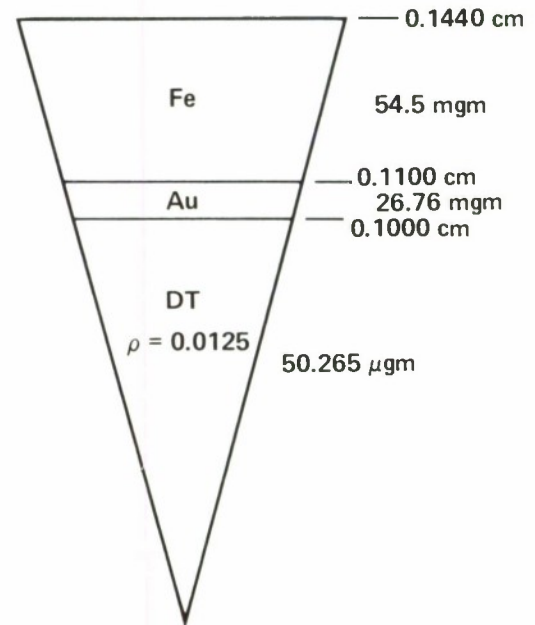


Figure 8. Single shell target driven by 1 MeV electrons



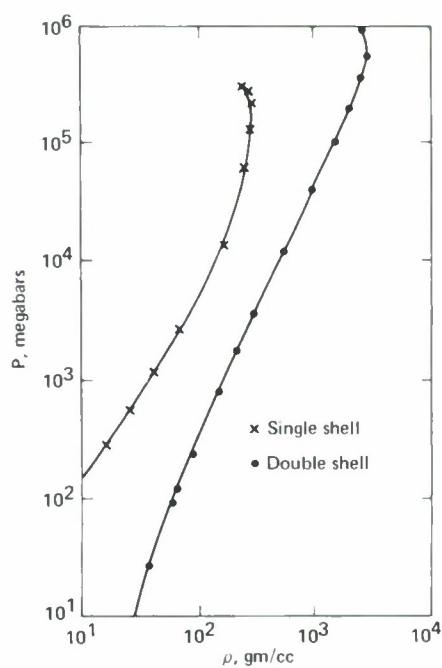


Figure 9. Pusher pressure versus density for 1 MeV electron targets

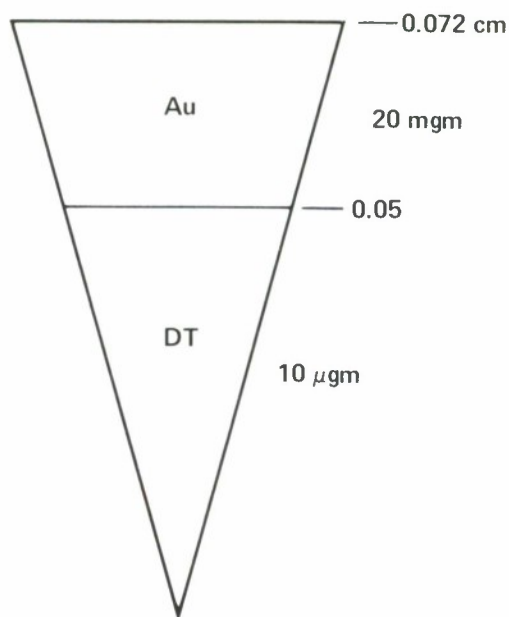


Figure 10. Single shell target driven by 10 MeV protons

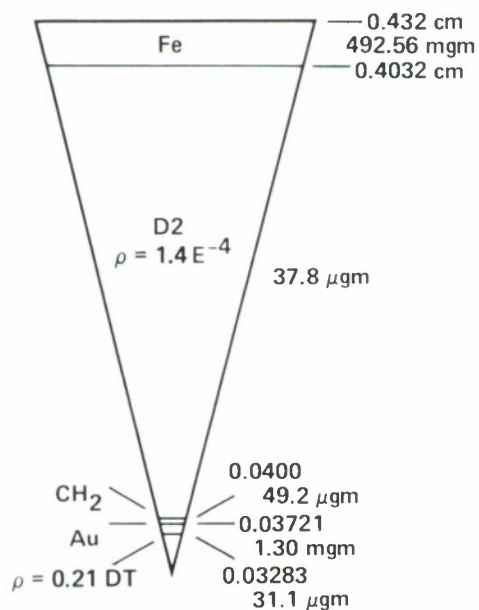


Figure 11. Double shell driven by 10 MeV protons

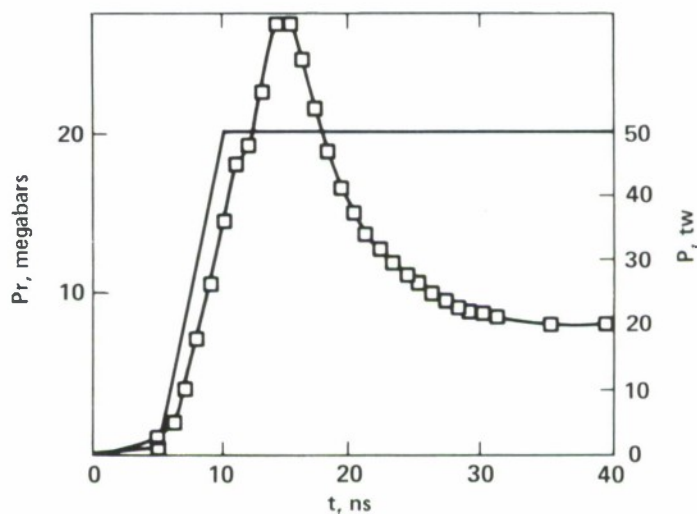


Figure 12. Power and pressure versus time for 10 MeV protons on iron

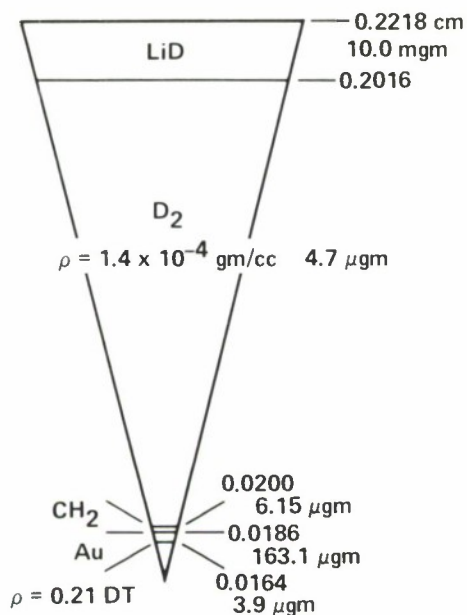


Figure 13. Double shell target imploded with 100 keV electrons

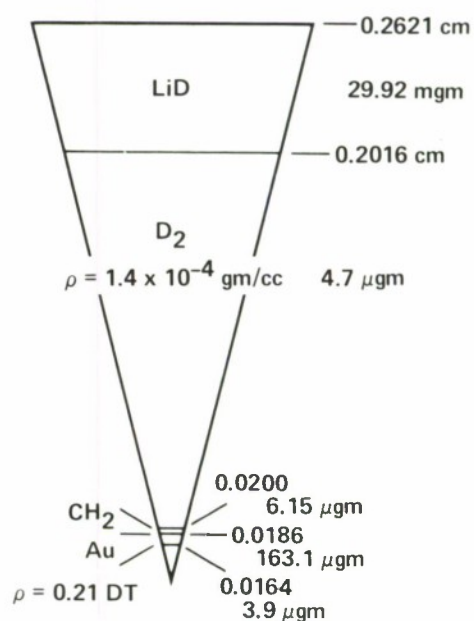


Figure 14. Double shell target imploded with 200 keV electrons

TABLE 1

Properties of 9 MeV alpha driven target

Time (ns)	Power (TW)	Range (gm/cm <sup>2</sup> )
0.0	0.11	0.000114
6.8	1.1	0.00114
13.6	11.1	0.0114

Power and range vary linearly between listed values

Input energy (kJ)	46.0
Yield (kJ)	66.0
$\rho r$ (DT) (gm/cm <sup>2</sup> )	0.33
$\rho r$ (Au) (gm/cm <sup>2</sup> )	2.0
$V_{\max}$ (Au) (cm/sec)	$3.20 \times 10^7$
$V_{\max}$ (LiD) (cm/sec)	$2.25 \times 10^7$
Burn temp (keV)	17.0 keV

TABLE 2

Properties of 1 MeV electron driven double shell target

Time (ns)	Power (TW)	Range (gm/cm <sup>2</sup> )
0.0	2.5	0.00471
35.0	250.0	0.471

Power and range vary linearly between listed values

Input energy (kJ)	4400
Yield (kJ)	5500
$\rho r$ (DT) (gm/cm <sup>2</sup> )	0.75
$\rho r$ (Au) (gm/cm <sup>2</sup> )	5.1
$V_{\max}$ (Au) (cm/sec)	$2.05 \times 10^7$
$V_{\max}$ (Fe) (cm/sec)	$1.22 \times 10^7$
Burn temp (keV)	34.0

TABLE 3

Properties of 10 MeV proton driven double shell target

Time (ns)	Power (TW)	Range (gm/cm <sup>2</sup> )
0.0	0.1	0.2238
5.0	1.0	0.2238
10.0	50.0	0.2238
40.0	50.0	0.2238

Power varies linearly between listed values

Input energy (kJ)	1630.0
Yield (kJ)	5800.0
$\rho r$ (DT) (gm/cm <sup>2</sup> )	0.84
$\rho r$ (Au) (gm/cm <sup>2</sup> )	5.45
$V_{\max}$ (Au) (cm/sec)	$1.99 \times 10^7$
$V_{\max}$ (Fe) (cm/sec)	$1.24 \times 10^7$
Burn temp (keV)	38.0

TABLE 4

Properties of 100 keV electron driven double shell target

Time (ns)	Power (TW)	Range (gm/cm <sup>2</sup> )
0.0	0.1	0.01953
5.0	1.0	0.01953
10.0	25.0	0.01953
15.0	25.0	0.01953

Power varies linearly between listed values

Input energy (kJ)	193.0 kJ
Yield (kJ)	553.0 kJ
$\rho r$ (DT) (gm/cm <sup>2</sup> )	0.48
$\rho r$ (Au) (gm/cm <sup>2</sup> )	3.32
$V_{\max}$ (Au) (cm/sec)	$2.59 \times 10^7$
$V_{\max}$ (LiD) (cm/sec)	$1.72 \times 10^7$
Burn temp (keV)	27.0

TABLE 5

Properties of 200 keV electron driven double shell target

Time (ns)	Power (TW)	Range (gm/cm <sup>2</sup> )
0.0	0.1	0.055
5.0	1.0	0.055
10.0	35.0	0.055
17.0	35.0	0.055

Power varies linearly between listed values

Input energy (kJ)	408.0
Yield (kJ)	516.0
$\rho r$ (DT) (gm/cm <sup>2</sup> )	0.485
$\rho r$ (Au) (gm/cm <sup>2</sup> )	3.35
$V_{\max}$ (Au) (cm/sec)	$1.39 \times 10^7$
$V_{\max}$ (LiD) (cm/sec)	$2.49 \times 10^7$
Burn temp (keV)	25.0

STABLE CONFINEMENT AND COMPRESSION OF DENSE  
THERMONUCLEAR PLASMAS IN A DETONATION DRIVEN VORTEX

F. Winterberg

Desert Research Institute, University of Nevada System, Reno, Nevada 89507

Abstract

In plane detonation waves of high explosives, pressures up to  $\sim 10^{12}$  dyn/cm<sup>2</sup>, corresponding to fluid velocities of  $\sim 10^6$  cm/sec, can be reached by the employment of implosion and explosive lens techniques. If such high explosives, having the shape of logarithmic spirals, are arranged around the shaft of a hollow cylinder and simultaneously ignited from their periphery, an ultrastrong vortex collapsing towards the axis of the cylinder will be generated. If thermonuclear material is placed in the center of this vortex and with a high current discharge passing through it, a stable high density pinch is formed. The stable confinement time of this pinch is only determined by the lifetime of the vortex and confinement times well above the Lawson value seem to be possible. The amount of explosives needed is rather small and in the order of 100 grams. Alternatively, the collapsing vortex may be also formed by replacing the explosive with some inert material which is externally bombarded and driven by either a laser-relativistic electron- or ion-beam. A Taylor-stable collapsing vortex cavity can be also used to confine and compress laser- or electron- (or ion-) beam produced dense thermonuclear plasmas.



## 1. Introduction.

During the early stages of the research efforts towards the controlled release of thermonuclear energy, great hope was placed on the linear pinch effect. Due to the highly unstable nature of this discharge mode, these hopes though were soon abandoned and the main thrust towards controlled thermonuclear fusion has since been shifted towards other approaches lacking the simple confinement geometry of the pinch effect. These early hopes resulted from the convincing simplicity of the pinch discharge and its close similarity to the arc discharge. With arc discharges, rather high temperatures have been produced and it is therefore quite natural to ask whether by a proper modification of this technique thermonuclear temperatures can be reached.

In contrast to a pinch discharge, which is surrounded by vacuum, an arc discharge under normal conditions is surrounded by a cooler gas and the magnetic pressure resulting from the arc current is always small compared to the gas pressure. It is for this reason that arc discharges do not exhibit the instabilities of the pinch discharge. Only if the arc current is raised to values at which the magnetic pressure becomes comparable or larger than the gas pressure of the surrounding medium is the stability destroyed, though due to the hydrodynamic coupling of the arc plasma with the surrounding gas the instabilities are less violent than in a pinch discharge. However, even for arc currents not sufficiently strong enough to produce these instabilities, an arc is never completely stable due to convective forces. Arcs operated at atmospheric pressure, as they are used for welding, operate at temperatures of several  $10^3$  °K.

In order to stabilize arc discharges and to reach higher temperatures three techniques have been successfully employed:

- 1) By increasing the pressure of the arc environment much higher temperatures can be obtained. In these so called high pressure arcs, which work at higher than atmospheric pressure, temperatures up to  $2 \times 10^4$  °K have been reached.

2) By confining the arc in a vortex, the arc is stabilized by the buoyant centripetal force acting on the lower density arc medium resulting from the centrifugal force within the vortex flow. This method of stabilizing the arc was first proposed by Schönherr.<sup>(1)</sup> In this original proposal the vortex was created by the flow of a gas. The method since then has been greatly improved by Gerdien et al.<sup>(2)</sup> who confined the arc in a water vortex. This method, known as the Gerdien arc, has been perfected more recently by Maecker.<sup>(3)</sup> It was shown<sup>(4)</sup> that by this technique, with an arc current of  $\sim 1500$  Amp and an arc voltage of  $\sim 500$  Volt/cm, temperatures of  $5 \times 10^4$  °K can be reached.

3) If a strong axial magnetic field is applied parallel to the arc discharge, the electronic heat conduction losses in the radial direction can be greatly reduced.<sup>(5)</sup> This method was originally proposed in an unsuccessful attempt to reach thermonuclear temperatures. The same method was subsequently applied to a hydrogen arc<sup>(6)</sup> reaching temperatures up to  $\sim 10^5$  °K, and it was estimated that for a 10 m long arc temperatures up to  $\sim 10^6$  °K may be attainable.

An attempt has been also made to reach higher arc temperatures by simultaneously stabilizing the arc in a gas vortex and reducing the electronic heat conduction losses by the application of a strong magnetic field,<sup>(7)</sup> but for a steady state thermonuclear reactor the energy losses due to radiation would be prohibitive. Rather than trying to reach higher arc temperatures, other attempts have been made to improve the pinch stability by embedding the high current discharge in a gas. Such proposals were made by Tidman<sup>(8)</sup> and the author.<sup>(9)</sup> In the scheme studied by Tidman the discharge occurs along the ionization trail left in the wake of a high power laser beam propagated through a dense gas placed in between the electrodes over which a large capacitor bank is subsequently discharged. In the method studied by the author, the pinch is produced by the self-magnetic field of a relativistic electron beam penetrating into a dense gas or solid target. In either case, because of the high plasma densities involved, the radiation losses are much less severe than for the previously considered steady state low density plasma configurations. In such a gas embedded z-pinch, the

magnetic pressure is much larger than the pressure of the surrounding gas, and the well known pinch instabilities reappear. However, because in the gas embedded z-pinch the discharge is strongly coupled to the gas environment, the growth rate for these instabilities can be greatly reduced. This fact is apparent from the observationally exhibited stability of a lightning discharge. For the large currents required in a thermonuclear pinch, the stabilizing effect of the surrounding medium at best is marginally sufficient if one goes to solid state densities,<sup>(10)</sup> although in the scheme studied by the author<sup>(9)</sup> this situation is considerably better since higher stability can be expected if the current is carried by a relatively small number of relativistic electrons with stiffer trajectories.

In order to overcome the outlined limitations we will show here that a rethinking of the different arc and pinch techniques will logically lead to an approach of substantial simplicity and much higher promise to reach conditions required for a positive thermonuclear energy balance.

The same technique can be also applied to the stable confinement and compression of laser- or electron- (or ion-) beam produced dense thermonuclear plasmas.

## 2. Thermonuclear Pinch in a Detonation Driven Vortex.

We listed three principal modifications to increase the arc temperature 1) higher pressure, 2) confinement in a vortex, and 3) application of a strong axial magnetic field, and furthermore 4) one modification aimed at increasing the stability of a pinch by surrounding it with a dense gas. We will now show that by a logical combination of these various modifications a stable thermonuclear pinch with a lifetime sufficiently long to ensure a positive thermonuclear energy balance can be established.

To 1): In order to obtain high pressures, the pinch channel filled with the thermonuclear material is to be surrounded by explosives which upon detonation create an environment of pressures up to and excess of  $\sim 10^{12}$  dyn/cm<sup>2</sup>.

To 2): By properly shaping explosive and inert material, whereby both have the shape of logarithmic spirals axially centered around the pinch discharge as shown in Fig. 1a, a detonation driven and collapsing vortex, as shown in Fig. 1c, is created upon simultaneously igniting the explosive from the periphery of the spirals. This vortex stabilizes the pinch discharge during the lifetime of the vortex.

To 3): By using a high current pinch discharge, a large azimuthal self-magnetic field is established, the effect of which on reducing the electronic heat conduction losses is similar to the effect of an axial magnetic field of the same strength.

To 4): By properly shaping the high explosive, the maximum vortex contraction will lead to a minimum core radius of the vortex which is equal to the pinch radius, thus embedding the pinch in a gas environment.

One may even try to make the pinch radius slightly smaller than the inner vortex radius, whereby the vacuum gap in between the outer pinch and inner vortex surface would be filled with a strong magnetic field. In this case the electronic heat conduction losses would be further reduced and, if the gap in between the outer pinch and inner vortex radius is small enough, the stability would be almost the same as without this gap.

The pinch discharge along the vortex axis can be triggered in optimal synchronisation with the vortex implosion. Preferably this may be done by a laser- or electron-beam trigger creating a preionized path over which a large capacitor bank is discharged.

During the implosive phase of the vortex, material is ablated from the outer part of the vortex, thereby creating a strong pressure causing the contraction of the vortex core. The ablated material carries angular momentum which by angular momentum conservation is equal and opposite to the angular momentum acquired by the vortex flow.

After the centrifugal force on the surface of the vortex core is equal to the pressure force, no further contraction takes place and the vortex from this moment on will remain quasi-stationary until all the detonated material is ablated. During the state of maximum contraction, the stream lines will form rather tight spirals around the vortex core.



A pinch enclosed in such a vortex will be stable if the stabilizing buoyancy force exceeds the destabilizing magnetic force. It will be shown below that with such an arrangement stable confinement times substantially in excess of the Lawson time are possible.

The discharge can take place as it is shown in Fig. 2. The cathode C is hollow to permit the passage of a laser- or electron-beam preionizing the channel passing through the core of the cylinder surrounded by the explosive charge and which becomes the core of the vortex. Over the thusly formed channel of ionized material is a large capacitor bank subsequently discharged. The easiest way to simultaneously ignite the high explosive charge from its periphery is by a convergent cylindrical laser-beam impinging and igniting the charge in the desired moment.

### 3. The Formation and Collapse of the Vortex.

In order to obtain a simple picture of the vortex formation, we will assume that the fluid flow in the vortex can be described by an incompressible fluid. This assumption implies that the vortex shall not change in times which are much smaller than the acoustic transit time. However, in the part of the vortex where the ablation process takes place the fluid is assumed to be compressible. Such a simplified model makes an otherwise very difficult problem tractable for an analytic treatment. It is likely that the real solution to the posed problem is in fact not too far off from the solutions obtained with such a model. We will therefore base the following estimates of the presented concept on this model.

We introduce cylindrical coordinates  $(r, \phi, z)$  with the cylindrical axis along the axis of the vortex (see Fig. 3). The inner radius of vortex core is defined by  $r = R_1$  and the radius at which the ablation process takes place by  $r = R_a$ . The Euler equations and equation of continuity in these coordinates have the form<sup>(11)</sup>



$$\frac{\partial v_r}{\partial t} + v_r \frac{\partial v_r}{\partial r} - \frac{v_\phi^2}{r} = - \frac{1}{\rho} \frac{\partial p}{\partial r} , \quad (1)$$

$$\frac{\partial v_\phi}{\partial t} + v_r \frac{\partial v_\phi}{\partial r} + \frac{v_r v_\phi}{r} = 0 , \quad (2)$$

$$\frac{\partial v_r}{\partial r} + \frac{v_r}{r} = 0 . \quad (3)$$

In eq. (1 - 3) we have assumed that  $\partial/\partial\phi = \partial/\partial z = 0$  and also that  $v_z = 0$ .

We are looking for a solution describing the physical situation of our posed problem and having simple analytical properties.

From eq. (3) we obtain

$$v_r r = F(t) , \quad (4)$$

and if we assume that  $\partial v_\phi/\partial t = 0$  we obtain from eq. (2)

$$\frac{\partial v_\phi}{\partial r} + \frac{v_\phi}{r} = 0 , \quad (5)$$

and hence

$$v_\phi r = \ell = \text{const.} \quad (6)$$

Eq. (4) of course expresses conservation of mass and eq. (6) conservation of angular momentum.

From eq. (4) and eq. (6) one obtains the equations for the streamlines at the time  $t$

$$\frac{v_r}{v_\phi} = \frac{F(t)}{\ell} , \quad (7)$$

hence

$$\frac{dr}{r d\phi} = \frac{F(t)}{\ell} , \quad (8)$$

or

$$r = R_i e^{(F(t)/\ell)\phi} , \quad (9)$$

Where  $R_i$  is the radius of the hollow vortex core at the time  $t$  (see Fig. 3). For the chosen particular solution, the streamlines at all times are logarithmic spirals. Especially for  $t = 0$  these logarithmic spirals have the form  $r = R_o e^{(F(0)/\ell)\phi}$ , where  $R_i = R_o$  is the core radius of the vortex at  $t = 0$ , and according to which the explosive charges and liners have to be shaped.

From eq. (4) we have

$$\frac{\partial v_r}{\partial t} = \frac{\dot{F}}{r} , \quad (10)$$

which upon substitution into eq. (1) together with eq. (6) yields

$$\frac{\dot{F}}{r} + v_r \frac{\partial v_r}{\partial r} - \frac{\ell^2}{r^3} = - \frac{1}{\rho} \frac{\partial p}{\partial r} , \quad (11)$$

Next we integrate eq. (11) from  $r = R_i$ , where  $p = 0$  and  $v_r = V_r$ , to  $r = R_a$ , where  $p = p_a$  and  $v_r = 0$ , with the result

$$\dot{F} \ln \left( \frac{R_a}{R_i} \right) - \frac{1}{2} V_r^2 - \frac{\ell^2}{2} \left( \frac{1}{R_i^2} - \frac{1}{R_a^2} \right) = - \frac{p_a}{\rho} . \quad (12)$$

The pressure  $p = p_a$  at  $r = R_a$  is caused by the explosion products ablated away from the vortex at a radius  $r > R_a$ . Since  $F(t) = R_i V_r$ , where  $V_r$  is the velocity of the inner core surface, and since  $\dot{R}_i = V_r$  we have

$$\begin{aligned}
 \dot{F} &= \dot{R}_i V_r + R_i \dot{V}_r \\
 &= V_r^2 + R_i \frac{dV_r}{dR_i} \dot{R}_i \\
 &= V_r^2 + \frac{R_i}{2} \frac{dV_r^2}{dR_i} .
 \end{aligned} \tag{13}$$

Eliminating  $\dot{F}$  from eq. (12) and eq. (13) results in

$$\begin{aligned}
 \frac{dV_r^2}{dR_i} + \frac{1}{R_i} \left( 2 + \frac{1}{\ln(R_i/R_a)} \right) V_r^2 \\
 + \frac{\ell^2}{R_i \ln(R_i/R_a)} \left( \frac{1}{R_i^2} - \frac{1}{R_a^2} \right) - \frac{2p_a}{\rho R_i \ln(R_i/R_a)} = 0 .
 \end{aligned} \tag{14}$$

Putting  $R_i \equiv x$ ,  $V_r^2 \equiv y$ , eq. (14) is seen to have the form of a linear first order differential equation with the standard form

$$y' + f_1(x)y + f_2(x) = 0 , \tag{15}$$

and the solution

$$y = e^{-\int f_1 dx} \left[ \text{const.} - \int f_2 e^{\int f_1 dx} dx \right] . \tag{16}$$

We thus obtain from eq. (14) after some simple integrations

$$V_r^2 = - \frac{1}{R_i^2 \ln(R_a/R_i)} \left[ \text{const.} + \ell^2 \ln \left( \frac{R_a}{R_i} \right) + \left( \frac{p_a}{\rho} + \frac{\ell^2}{2R_a^2} \right) R_i^2 \right] . \quad (17)$$

The constant of integration is determined by the initial condition at  $t = 0$  for which  $R_i = R_0$  and  $R_a = R_1$ . We put at  $t = 0$ ,  $V_r = V_r^{(0)}$  and  $V_\phi = V_\phi^{(0)}$ .  $V_\phi$  is the azimuthal velocity at the inner core surface. Introducing the angle  $\alpha = \alpha_0$  (see Fig. 3) which determines the slope of the logarithmic flow spiral at  $r = R_i = R_0$ , that is at  $t = 0$ , we have

$$\left. \begin{aligned} V_r^{(0)} &= c_0 \sin \alpha_0 \\ V_\phi^{(0)} &= c_0 \cos \alpha_0 \end{aligned} \right\} , \quad (18)$$

where  $c_0$  is the local fluid velocity at  $t = 0$ . Putting in eq. (17)  $V_r = V_r^{(0)}$ ,  $R_i = R_0$ ,  $R_a = R_1$  and  $p_a = p_1$ , we obtain the value for the constant of integration:

$$\begin{aligned} \text{const.} &= - R_0^2 \ln(R_1/R_0) c_0^2 \sin^2 \alpha_0 - \ell^2 \ln(R_1/R_0) \\ &\quad - \left( \frac{p_1}{\rho} + \frac{\ell^2}{2R_1^2} \right) R_0^2 . \end{aligned} \quad (19)$$

Furthermore, since  $\ell^2 = c_0^2 R_0^2 \cos^2 \alpha_0$  this expression reduces to

$$\text{const.} = -c_o^2 R_o^2 \ln(R_1/R_o) - \left( \frac{p_1}{\rho} + \frac{\ell^2}{2R_1^2} \right) R_o^2, \quad (20)$$

and one therefore obtains finally from eq. (17)

$$V_r^2 = \frac{1}{R_i^2 \ln(R_a/R_i)} \left[ c_o^2 R_o^2 \ln(R_1/R_o) + \left( \frac{p_1}{\rho} + \frac{\ell^2}{2R_1^2} \right) R_o^2 - c_o^2 R_o^2 \ln(R_a/R_i) \cos^2 \alpha_o - \left( \frac{p_a}{\rho} + \frac{\ell^2}{2R_a^2} \right) R_i^2 \right]. \quad (21)$$

Equation (21) can be approximated in a number of steps. First, the relative change in  $R_a$  resulting from the ablation process at the outer vortex surface is much smaller than the relative change of  $R_i$ , provided that  $R_1 \gg R_o$ . Therefore, one can put with sufficient accuracy  $p_a \approx p_1$  and  $R_a \approx R_1$ , resulting in

$$V_r^2 \approx \frac{1}{\ln(R_1/R_i)} \left( \frac{R_o}{R_i} \right)^2 \left[ c_o^2 \ln(R_1/R_o) - c_o^2 \ln(R_1/R_i) \cdot \cos^2 \alpha_o + \left( \frac{p_1}{\rho} + \frac{\ell^2}{2R_1^2} \right) \left[ 1 - \left( \frac{R_i}{R_o} \right)^2 \right] \right]. \quad (22)$$

Second, from Bernoulli's theorem one has  $p_1/\rho = c_o^2/2$ . But since  $\ell = c_o R_o \cos \alpha_o$  it follows that  $\ell^2/2R_1^2 = (c_o^2/2) (R_o \cos \alpha_o/R_1)^2$ . Therefore, if  $R_1 \gg R_o$ ,  $\ell^2/2R_1^2 \ll p_1/\rho$ . Third, if  $R_o \ll R_1$  and  $R_i \ll R_o$ , the last term



in the square bracket on the r.h.s. of eq. (22) may be neglected with sufficient accuracy in the framework of our goal to obtain some useful estimates. We therefore have finally

$$V_r^2 \approx \frac{c_0^2}{\ln(R_1/R_i)} \left( \frac{R_0}{R_i} \right)^2 \left[ \ln(R_1/R_0) - \ln(R_1/R_i) \cos^2 \alpha_0 \right] . \quad (23)$$

for this we can also write

$$V_r^2 \approx c_0^2 \left( \frac{R_0}{R_i} \right)^2 \frac{\ln \left[ (R_1/R_0) (R_i/R_1)^{\cos^2 \alpha_0} \right]}{\ln(R_1/R_i)} . \quad (24)$$

We are interested in the state of maximum compression which is reached at  $V_r = 0$ . If at this state  $R_i = R_m$ , then according to eq. (24) this implies that

$$\frac{R_1}{R_0} \left( \frac{R_m}{R_1} \right)^{\cos^2 \alpha_0} = 1 . \quad (25)$$

In case of maximum initial swirl  $\alpha_0 = 0$ , it follows that  $R_m/R_0 = 1$  which means the vortex does not contract. This of course means that the centrifugal force at the inner core surface prevents any further contraction. In order to obtain an appreciable contraction one must choose  $\alpha_0 > 0$ . If, for example,  $\alpha_0 = 45^\circ$  then  $\cos^2 \alpha_0 = 1/2$  and  $R_m/R_0 = R_0/R_1$ . A case coming close to the one of practical interest is given by a tenfold contraction  $R_0/R_m = 10$ , but with an outer radius not too large. Therefore let us put  $R_1 = 1.5$  cm and  $R_0 = 0.5$  cm,  $R_1/R_0 = 3$ . Inserting these values into eq. (25) gives a value for  $\alpha_0$ . Although this example violates our condition that  $R_1 \gg R_0$ , eq. (25) can probably still be used to obtain an estimate. One thus obtains  $\alpha_0 \approx 55^\circ$ .

As can be seen from eq. (9), the streamlines at the state of maximum contraction are circles, since at  $R_i = R_m$ ,  $F(t) = R_m V_r = 0$ .

The pressure distribution in the vortex can be easily obtained at the state of maximum contraction, for which we are primarily interested, by putting in eq. (11)  $v_r = 0$ , resulting in

$$\frac{dp}{dr} = \rho \left( \frac{\ell^2}{r^3} - \frac{\dot{F}}{r} \right). \quad (26)$$

For  $v_r = 0$  one has according to eq. (13)

$$\dot{F} = \frac{R_i}{2} \frac{dV_r^2}{dR_i} \bigg|_{R_i = R_m}. \quad (27)$$

Using eq. (24) one obtains

$$a = \frac{R_i}{2} \frac{dV_r^2}{dR_i} \bigg|_{R_i = R_m} = \frac{c_0^2}{2} \left( \frac{R_0}{R_m} \right) \frac{\ln(R_1/R_0)}{[\ln(R_m/R_1)]^2}, \quad (28)$$

for which, because of  $c_0 R_0 \cos \alpha_0 = c_{\max} R_m$ , and where  $c_{\max}$  is the maximum fluid velocity reached at the inner surface of the vortex core, we can also write

$$a = \frac{c_{\max}^2}{2 \cos^2 \alpha_0} \frac{\ln(R_1/R_0)}{[\ln(R_m/R_1)]^2}. \quad (29)$$

With this definition the equation for the pressure distribution is given by

$$\frac{1}{\rho} \frac{dp}{dr} = \frac{\ell^2}{r^3} - \frac{a}{r} . \quad (30)$$

If thus follows, that the pressure has a maximum at the position  $r_{\max} = \ell/\sqrt{a}$ . Since  $\ell = c_0 R_0 \cos \alpha_0$ , one obtains

$$r_{\max} = R_m \cos \alpha_0 \ln(R_m/R_1) \left[ 2/\ln(R_1/R_0) \right]^{1/2} . \quad (31)$$

By integrating eq. (29) with the boundary condition  $p = 0$  at  $r = R_m$  one obtains

$$\frac{p}{\rho} = \frac{\ell^2}{2} \left( \frac{1}{R_m^2} - \frac{1}{r^2} \right) - a \ln \left( \frac{r}{R_m} \right) . \quad (32)$$

For  $R_m \gg R_1$  the maximum pressure is approximately given by

$$p_{\max} \approx (1/2) \rho c_{\max}^2 , \quad (33)$$

and which is the stagnation pressure for the maximum fluid velocity reached at  $r = R_m$ . At this point we can make a remark regarding our incompressibility assumption. It is obvious, that the assumption would fail, if the local fluid velocity would exceed the velocity of sound. At the first sight this seems to be the case since  $c_{\max} \propto 1/R_m$ , during the contraction of the vortex, such that  $c_{\max} \gg c_0 = \sqrt{p_1/\rho}$  and where  $c_0$  is of

the same order of magnitude as the velocity of sound in the explosion products at  $t = 0$ . However, as can be seen from eq. (32), the contraction of the vortex is accompanied by a large buildup in pressure, with the maximum given by eq. (33) and from which  $c_{\max} = \sqrt{p_{\max}/\rho} \gg c_0$  follows. In effect, the compressibility will therefore result in a temperature increase according to  $c_{\max} \propto \sqrt{T_{\max}}$  such that  $T_{\max} \propto p_{\max}/\rho \propto 1/R_m^2$ , the temperature sharply rises in the inner part of the vortex during its contraction.

High explosives as they are considered here have typically detonation temperature of  $\sim 5 \times 10^3$  °K,<sup>(12)</sup> such that a tenfold vortex contraction would imply a temperature rise by a factor 100 that is  $5 \times 10^5$  °K.

At the vortex periphery where  $r = R_a \approx R_1$ , the pressure has dropped down to  $p_1 = (1/2)\rho c_0^2$  and which has to be balanced by the stagnation pressure of the ablated material.

The amount of material to be ablated which is required to form the vortex can be easily estimated. At the instance  $t = 0$ , the radial velocity distribution of the vortex obeys the law  $v_r = F(0)/r = c_0 R_0 \sin \alpha_0 / r$ . Therefore for a cylinder of length  $h$ , the radial momentum of the inward motion is given by

$$\begin{aligned}
 P_i &= 2\pi\rho h \int_{R_0}^{R_a} v_r r dr \\
 &= 2\pi\rho h c_0 R_0 \sin \alpha_0 \int_{R_0}^{R_a} dr \\
 &= 2\pi\rho h c_0 \sin \alpha_0 \cdot R_0 (R_a - R_0) .
 \end{aligned} \tag{34}$$

In computing the radial momentum of the material ablated in the outward direction one must observe that the velocity averaged over the half space is  $c_0/3$ . One thus has

$$\begin{aligned}
P_a &= 2\pi\rho h \frac{c_o}{3} \int_{R_a}^{R_1} r dr \\
&= (\pi/3) \rho h c_o (R_1^2 - R_a^2) .
\end{aligned} \tag{35}$$

It is obvious that the radial momentum of the motion directed inward must balance the radial momentum of the ablated material, that is,  $P_a = P_i$ .

This condition leads to

$$R_1^2 - R_a^2 = 6R_o(R_a - R_o) \sin\alpha_o . \tag{36}$$

Since  $v_\phi = \ell/r$ , it follows for the angular momentum of the vortex

$$\begin{aligned}
L_i &= 2\pi\rho h \int_{R_o}^{R_a} v_\phi r^2 dr \\
&= \pi\rho h \ell (R_a^2 - R_o^2) .
\end{aligned} \tag{37}$$

The angular momentum of the ablated material is given by

$$\begin{aligned}
L_a &= 2\pi\rho h \ell \int_{R_a}^{R_1} r dr \\
&= \pi\rho h \ell (R_1^2 - R_a^2) .
\end{aligned} \tag{38}$$



Conservation of angular momentum then requires that  $L_a = L_i$  which leads to

$$R_1^2 = 2R_a^2 - R_0^2 . \quad (39)$$

From combining eq. (36) and eq. (39) one obtains the conditions

$$R_a/R_0 = 6\sin^2\alpha_0 - 1 , \quad (40)$$

and

$$R_1/R_0 = \left[ 2(6\sin^2\alpha_0 - 1)^2 - 1 \right]^{1/2} . \quad (41)$$

For  $\alpha_0 = 55^\circ$ ,  $\sin\alpha_0 = 0.81$ , it follows that  $R_a/R_0 = 3.9$ ,  $R_1/R_0 = 6.8$ , and  $R_1/R_a = 1.75$ .

#### 4. Stability of Pinch Confined in Imploded Vortex.

We will now show that under certain conditions a pinched plasma confined in the core of the imploded vortex with the pinch radius equal to or slightly less than the core radius of the vortex, can be made absolutely stable during the lifetime of the vortex.

The density of the destabilizing force, acting on the confined plasma during a radial displacement of the pinch configuration from its equilibrium, with a wavelength  $\lambda$  of the disturbance, is given by

$$f_H = H^2/4\pi\lambda . \quad (42)$$

At the other hand, if the pinch discharge is displaced in the radial direction by penetrating into the vortex, it is subjected to a centripetal buoyancy force. If the density of the pinched plasma column is  $\rho_p$ , the density of this stabilizing force is given by

$$f_r = - \frac{dp}{dr} + \rho_p \frac{v_\phi^2}{r} . \quad (43)$$

With the help of eq. (30), where for  $r \approx R_m$  one can neglect the term  $-a/r$  and, by putting  $v_\phi = \ell/r$ , one obtains from eq. (43)

$$f_r = - (\rho - \rho_p) \frac{\ell^2}{r^3} . \quad (44)$$

We are considering cases for which typically  $\rho \gg \rho_p$  and displacements near the core of the vortex where  $r \approx R_m$ . After putting  $\ell = c_{\max} R_m$  we thus have

$$f_r = - \frac{\rho c_{\max}^2}{R_m} . \quad (45)$$

Therefore, the pinch discharge will be stable as long as

$$f_H + f_r < 0 , \quad (46)$$

or

$$H^2/4\pi\lambda < \rho c_{\max}^2/R_m . \quad (47)$$

The fastest growing instability has the smallest wavelength, and the smallest kink type disturbance which can cause instability has a wavelength  $\lambda \approx R_m$ . To prevent unstable growth for all wavelength one thus has to fulfill the condition

$$\frac{H^2}{8\pi} < \frac{1}{2} \rho c_{\max}^2, \quad (48)$$

which simply means that the magnetic energy density of the pinch must be smaller than the maximum kinetic energy density of the vortex flow. Because in a pinch discharge  $H^2/8\pi = 2NkT$ , where  $T$  is the temperature in the pinch, one can alternatively write for the stability criterion

$$2NkT < \frac{1}{2} \rho c_{\max}^2. \quad (49)$$

For shorter wavelengths  $\lambda \ll R_m$ , the  $m = 0$  instability may still pose a problem but could be suppressed by applying a strong axial magnetic field to be entrapped and compressed in the vortex. An initial axial field with a strength of  $2 \times 10^4$  Gauss, to be compressed by a tenfold decrease in the vortex radius, would lead to an axial magnetic field of  $2 \times 10^6$  Gauss. The initial field could thereby be provided by conventional iron core magnetic field coils.

##### 5. Vortex Lifetime and Pinch Confinement Time.

After formation and implosion of the vortex down to a core radius  $R_i = R_m$ , further material will be ablated from the vortex periphery at  $R = R_m$ , therefore extending the lifetime of the imploded vortex core. In this process the ablation velocity will increase as the ablation front propagates inward. The reason for this is that at  $R_i = R_m$ ,  $v_r = 0$ , but

for  $v_\phi$  one has  $v_\phi = c = \ell/r = c_{\max} R_m/r = c_o R_a/r$ . The ablation will result from the transformation at this ordered motion into disordered thermal motion at the ablation front and which propagates in the outward radial direction with the average velocity  $v_\phi/3 = c_o R_a/3r$ . The increase of the thermal ablation velocity in proportion to  $v_\phi = c$ , where  $c$  is the local fluid velocity, is consistent with the point made before that  $T \propto p/\rho \approx c^2$  in all parts of the vortex. During its inward propagation the ablation front will thus lead to an increasing reaction pressure which will balance the vortex pressure according to eq. (32) and will rise with decreasing values of  $r$ . The confinement time  $\tau$  of the vortex is thus given by

$$\tau = - 3 \int_{R_a}^{R_m} \frac{dr}{v_\phi} = \frac{3}{2} \frac{R_a^2 - R_m^2}{c_o R_a} . \quad (50)$$

But, since  $R_m \ll R_a$ , this simplified to

$$\tau \approx 3R_a/2c_o , \quad (51)$$

## 6. Practical Example Applied to a High Density Pinch.

In order to illustrate the foregoing analytical estimates, we take the following numerical example. The plasma density is given by  $N = 10^{21} \text{ cm}^{-3}$  and the plasma temperature by  $T = 10^8 \text{ }^\circ\text{K}$ . This then leads to a plasma pressure of  $p = H^2/8\pi = 2NkT \approx 3 \times 10^{13} \text{ dyn/cm}^2$ . The pinch magnetic field to confine the plasma is then given by  $H \approx 3 \times 10^7 \text{ Gauss}$ . If the pinch radius is  $r_p = R_m = 0.05 \text{ cm}$ , the discharge current to produce this magnetic field is  $I \approx 10^7 \text{ Amps}$  and which compares well with the pulsed currents produced by large megajoule capacitor banks.

High explosives have a detonation velocity which can be as high as  $v_o \sim 10^6$  cm/sec.<sup>(12)</sup> Therefore, if  $R_1 = 1.5$  cm and  $R_o = 0.5$ , the time to detonate all the material is  $\tau_o \sim (R_1 - R_o)/v_o \sim 10^{-6}$  sec. After the lapse of this time the vortex begins to ablate and contract from its initial core radius  $R_i = R_o$  with the initial velocity  $c_o$  to its final core radius  $R_i = R_m$  with the final velocity  $c_{max}$ . The detonation products have a density of  $\rho \sim 3$  g/cm<sup>3</sup> and move with an initial velocity of  $c_o \approx v_o/4 = 2.5 \times 10^5$  cm/sec. The detonation pressure is  $p_a = \rho v_o^2/4 = 5 \times 10^{11}$  dyn/cm<sup>2</sup>. We use the example  $R_1 = 1.5$  cm,  $R_o = 0.5$  cm,  $R_m = 0.05$  cm,  $\alpha_o = 55^\circ$ . Since the pressure in the vortex is approximately proportional to  $c^2$  and since  $c^2$  increases in proportion to  $R_i^{-2}$ , a decrease in the vortex core radius by the factor  $R_m/R_o = 0.1$  will lead to an increase of the maximum pressure by a factor  $10^2$  from  $5 \times 10^{11}$  dyn/cm<sup>2</sup> to  $5 \times 10^{13}$  dyn/cm<sup>2</sup>. Since  $p_{max} = (1/2)\rho c_{max}^2$ , stability of the pinch is assured if  $H^2/8\pi = 2NkT < 5 \times 10^{13}$  dyn/cm<sup>2</sup>. In our example  $H^2/8\pi = 2NkT = 3 \times 10^{13}$  dyn/cm<sup>2</sup>, so that stability is assured.

With the above obtained value of  $R_1/R_a = 1.75$  and  $R_1 = 1.5$  cm, one has  $R_a = 0.85$  cm. The confinement time according to eq. (51) is given by  $\tau = 3R_a/2c_o = 5 \times 10^{-6}$  sec. The Lawson value therefore is given by  $N\tau = 5 \times 10^{15}$  cm<sup>-3</sup> sec and which is well above the critical value of  $10^{14}$  cm<sup>-3</sup> sec.

We would like to estimate the amount of explosives needed. At the densities of  $N \sim 10^{21}$  cm<sup>-3</sup>, the minimum length of a pinched plasma to overcome the end losses would be  $h \approx 0.2$  cm. If the pinch has a length of  $h = 5$  cm, the energy to heat the pinch to thermonuclear temperatures would be  $2NkT\pi R_m^2 h \approx 10^{12}$  erg and which, including losses, could be drawn from a megajoule capacitor bank. If  $R_1 = 1.5$  cm,  $R_o = 0.5$ , the volume filled with explosives would be  $\pi(R_1^2 - R_o^2)h \approx 30$  cm<sup>3</sup>. With a density of  $\rho \sim 3$  g/cm<sup>3</sup> this would amount to  $\sim 100$  grams of high explosive. The cost of high explosives is about  $5 \times 10^{-4}$  \$/gram. Therefore, the amount of  $\sim 100$  grams of high explosives would amount to  $\sim 5$  cents. This value is not unreasonable if the energy delivered per pinch microexplosion is many megajoule and what seems to be possible in view of the long confinement times, is much better than in another scheme considered by Linhart.<sup>(13)</sup> Large yields, though,



may require to line the inner vortex wall with additional thermonuclear material into which a thermonuclear deflagration could proceed.

7. Other than Chemical Means by Which the Vortex Could be Produced.

It is quite obvious that the vortex could be also produced by bombarding some inert material with energetic particle beams, that is by beams of laser radiation, relativistic electron beams or bunched ion beams.<sup>(14)</sup> Especially in the latter case, it was shown that beams of enormous total energy output could be produced with a large variety of time behaviors. Such a method may be cheaper and more powerful than the use of high explosives. However, high explosives have the advantage of being easily available and it was the purpose to show that by their employment critical conditions in relation to the release of thermonuclear energy may arise. In case massive ion beams are used, the angular momentum needed to form the collapsing vortex can be directly transported by these beams to the pellet surface by giving the beam ions a finite impact parameter with regard to the pellet axis, thus eliminating the need for spiral liners. One of course, could also ablate the outer vortex material by the action of a powerful gas discharge to be in tandem with the pinch discharge.

8. Stable Confinement and Compression of Laser- or Electron-Beam Produced Plasmas in Collapsing Vortex Cavity.

One of the principal difficulties in implosion induced laser- or electron- (or ion-) beam fusion in the Taylor instability of the pusher material forming the collapsing cavity wall.<sup>(15)</sup> If the collapsing cavity has the form of a vortex, the inertial forces are primarily determined by the centrifugal forces. Since the centrifugal force is directed radially outward towards increasing material density, the collapsing vortex is Taylor stable. A collapsing vortex cavity can therefore be used to compress and heat thermonuclear material by placing it inside the vortex core. The compression and heating would then have to be accomplished by a) a convergent

cylindrical laser- or electron- (or ion-) beam and b) by two axial laser- or electron- (or ion-) beams. The convergent cylindrical beam would thereby compress the thermonuclear material radially and the two axial beams compress it axially.

#### References.

- 1) O. Schönherr, Elektrotechnische Zeitschrift 30 265 (1909).
- 2) H. Gerdien and A. Lotz, Z. technische Physik 4 157 (1923), 5 515 (1924).
- 3) H. Maecker, Z.f. Physik 129 108 (1951).
- 4) F. Burhorn, H. Maecker and T. Peters, Z.f. Physik 131 28 (1951).
- 5) H. Alfven, C. G. Fälthammer, R.B. Johannson, E.A. Smars, B. Wilner, E. Witalis, Nucl. Fusion Suppl. 1 33 (1962).
- 6) Von C. Mahn, H. Ringler, R. Wienecke, S. Witkowski and G. Zankl, Z. Naturforschg. 19a 1202 (1964).
- 7) J.C. Terlouw and B. Brandt, FOM Report IR 69/043 (Oct. 1969).
- 8) D. A. Tidman, Appl. Phys. Lett. 20 23 (1972).
- 9) F. Winterberg, Nuclear Fusion 12 353 (1972).
- 10) W.M. Manheimer, M. Lampe and J.B. Boris, Physics of Fluids 16 1126 (1973).
- 11) See for example. L.D. Landau and E.M. Lifshitz, Fluid Mechanics Pergamon Press, London 1959.
- 12) R. Schall, in Physics of High Energy Density, p. 230, Academic Press, New York 1971.
- 13) J. G. Linhart, Nuclear Fusion 10 211 (1970).
- 14) F. Winterberg, Nature 251 44 (1974), Plasma Physics 17 69 (1975).
- 15) F. Winterberg, Plasma Physics 10 55 (1968).

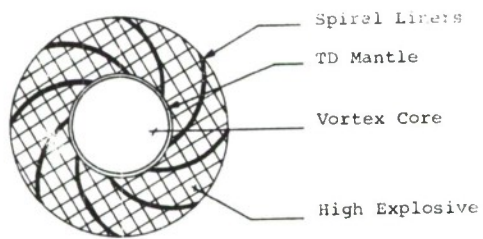


Figure 1A



Figure 1B

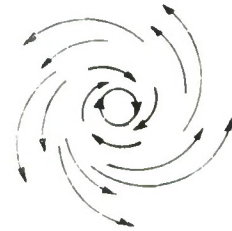


Figure 1C

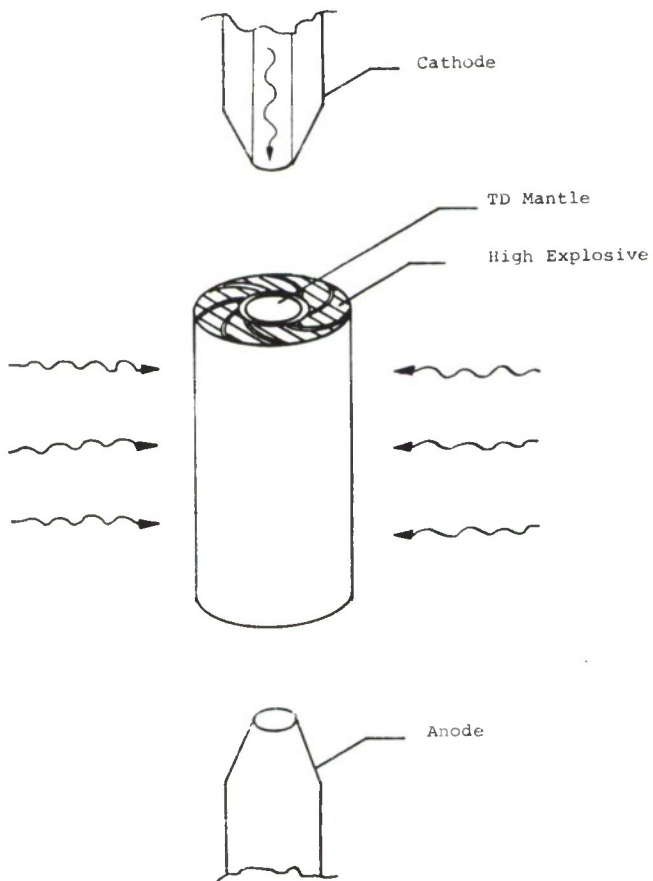


Figure 2

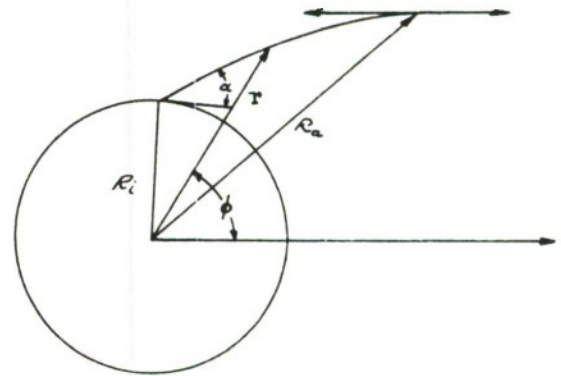


Figure 3

# A STUDY OF REB TARGET IRRADIATION, DEPOSITION, AND IMPLOSION\*

J. Chang, L. P. Mix, F. C. Perry, M. M. Widner, and J. W. Poukey

Sandia Laboratories, Albuquerque, New Mexico 87115

## ABSTRACT

We have irradiated flat targets, spheres, and hemispheres with intense REB ( $\sim 10^{11}$  W/cm<sup>2</sup>) from the Hydra machine to study target loading, ablation, and implosion. A wide variety of experimental techniques were used in these studies including x-ray pinhole photography, laser holography, laser velocimetry, and flash x-radiography. The energy absorption mechanism was found to be consistent with classical electron deposition. Variations in target loading and implosion symmetry have been observed and, in particular, symmetry of loading can be altered by changing the cathode geometry and anode-cathode spacing.

\*This work was supported by the U.S. Energy, Research and Development Administration.

## I. INTRODUCTION

In this paper we report the results of a series of experiments carried out to gain some insight to the general problem of REB target coupling. In particular our studies concentrate on the following areas:

- A. REB energy deposition.
- B. Target loading and implosion symmetry.

These experiments were all carried out on the Hydra machine with REB parameters of 750 kV, 300 kA, 100 ns. The targets were either the anode itself or 4 mm diameter hollow gold spheres or hemispheres with wall thicknesses of 0.2 mm mounted at the center of the anode. These pellet dimensions were chosen in agreement with the computed optimal ablation driven dense pusher pellet<sup>1</sup> for 1 MV electron energy. Two types of cathodes have been used. One was a 12.7 cm O.D. and 2.54 cm I.D. annular flat cathode with a 1 cm diameter thin-walled cylinder placed on axis protruding 0.05 cm beyond the cathode face.<sup>2</sup> The other cathode had the same O.D. and I.D. but did not have the cylinder on axis and in addition a 13° taper was cut on the cathode face.<sup>3</sup> Both of these cathodes have reliably produced highly focused REB's a few mm in diameter. The general experimental setup is illustrated in Fig. 1, where time integrated pinhole cameras and flash x-radiography (Appendix) were used simultaneously to observe the pellet loading and implosion. For other experiments these diagnostics were replaced by laser holography or laser velocimetry.

## II. EXPERIMENTS AND RESULTS

### A. Electron Energy Deposition

Although the possibility of other effects has been suggested,<sup>2</sup> calculations carried out to determine the optimal pellet design have generally assumed that electron deposition profile is consistent with classical-energy



deposition profile obtained from one-dimensional Monte Carlo electron-photon transport calculations.<sup>1</sup> To ascertain the validity of this assumption, two experiments were carried out.<sup>4</sup> In these experiments planar anodes were irradiated by self-focused Hydra REB, and the resulting shock transit time and average rear surface velocity were measured. By choosing the target material with a well known equation-of-state, in this case, 6061-T6 aluminum, these measurements can be directly compared with two-dimensional hydrodynamic calculations using CSQ.<sup>5</sup> To measure shock arrival and rear surface velocity, colinear reflections from the polished back surface of the anode and a beam splitter 1 mm away were monitored by a PMT. This arrangement is shown in Fig. 2. The oscilloscope traces in the same figure show data from the PMT and a PIN detector whose signal serves as a timing fiducial. The first reduction in light intensity occurred at 165 ns (corrected for cable length) after the start of the x-ray pulse. This was caused by the shock arrival destroying the reflecting surface. Two things happened when the aluminum rear surface impacted the beam splitter. First, the dielectric surface was destroyed and second, due to the high impact velocity, the quartz substrate would self-luminesce. This accounts for the apparent increase in light intensity at 325 ns and after that the self-luminosity decayed away. The rear surface velocity is therefore 0.65 cm/ $\mu$ s.

These results are compared with CSQ calculations with several different input conditions (1) classical deposition profile, (2) input energy reduced by 1/2, (3) electron range reduced by 1/3, and (4) energy reduced by 1/2 and range by 1/3. Of these, the one that gave the closest agreement with data ( $\pm 10\%$ ) was classical deposition. Another way to demonstrate the comparison of the "range shortened" effect with measurement is shown in Fig. 3. Here both the calculated and measured shock arrival time and the surface flight

time are plotted as a function of fraction of classical range. As shown, agreement is found near  $r_a/r_o = 1.0$ , again indicating classical deposition. From these measurements we conclude that energy deposition at Hydra power levels is consistent with classical energy deposition.

With a technique more sensitive to rear surface motion, in this case a VISAR<sup>6</sup> (Velocity Interferometer System for Any Reflector), an anomalous precursor to the shock arrival has been observed. This phenomenon is shown in Fig. 4 and it is not presently well understood. This precursor cannot be fully accounted for by in-depth bremsstrahlung heating nor by beam prepulse. An explanation can be constructed if a small fraction ( $\sim 1$  percent) of the beam current is to have twice the anode cathode potential. Although this anomalous high energy current has been observed elsewhere,<sup>7</sup> similar electron energy spectrum measurements have not been carried out on Hydra.

#### B. Pellet Loading

Several experimental methods have been used to determine the symmetry of REB loading of both spherical and hemispherical targets. Perhaps the most straightforward method used was the time-integrated x-ray pinhole photography. Two x-ray pinhole cameras each with a 0.34 mm pinhole were arranged as in Fig. 1, allowing observation of the pellet from orthogonal directions. Since the bremsstrahlung created by the beam electron stopping in the shell wall is directly related to the energy deposited, a measure of the optical density variation of the image provides information on loading symmetry. We have reported previously that, for a 18 mm A-K gap, symmetry of loading was found to be uniform within 20 percent.<sup>8</sup> We report now the effect of smaller A-K gaps on loading symmetry. We have observed a decrease in the uniformity of loading as the A-K gap spacing decreased. This effect is

illustrated in Figs. 5, 6, and 7. The results of changing the A-K gap to 11.4 mm is shown in Figs. 5 and 6. Here we show two views of an irradiated sphere. The horizontal line in the side view was caused by beam irradiation of the anode. Loading symmetry was determined by measuring the variation of the image brightness in terms of optical density along the circumference. The measurements indicate uniformity is no better than 30 percent. As the anode cathode gap was decreased to 9 mm, only the front half of the pellet was irradiated. Such a case is shown in Fig. 7. However in no case were we able to change the loading asymmetry in favor of the downstream side of the pellet with the cylinder on axis cathode. When the cathode was changed to the hollow cathode with a  $13^\circ$  taper, we found that it became possible to reverse the loading such that downstream side was loaded twice the amount as the front. An example of this phenomenon is shown in Fig. 8.

A four-exposure ruby laser ( $6943\text{\AA}$ ) holography system<sup>9</sup> has also been used to observe the blowoff plasma from the spherical target. In this system a 3 ns laser pulse is split into 4 pulses, of which three are delayed so that the interval between exposures is 16 ns. The four exposures are constructed on a single sheet of film with each at a different azimuth. The radial position of the interference fringes can provide a measurement of plasma blowoff velocity and from the velocity measurement, both the loading symmetry and the energy absorbed can be inferred. Fig. 9 shows a set of holographic reconstructions of an irradiated pellet and we note that the blowoff plasma is present nearly uniformly around the target surface and the supporting stalk. If we assume the blowoff plasma's ionic component is only of the target material, a comparison of the measured functional dependence of the fringes on time can be made with those calculated using a one-dimensional

hydrodynamic materials code, CHART D.<sup>10</sup> From this comparison, as is made in Fig. 10, we can estimate the energy absorbed by the pellet. In this case about 2 kJ were absorbed.

### C. Pellet Implosion

Measurements of the pellet implosion can provide information about implosion symmetry, implosion time, and energy absorbed. A flash x-radiography system (the details of which are discussed in the Appendix) was used to take a 3 ns shadowgram of the pellet as it imploded. The experimental setup is depicted in Fig. 1. A sequence of shadowgrams is shown in Fig. 11. A cylinder on axis cathode ("38") and 18 mm A-K gap were used for these shots. For each shot the flash x-radiography system was delayed by differing time intervals relative to the beginning of the Hydra pulse, thus providing a way to record the pellet in different phases of implosion. The pellet shadow's oblong shape is due to the projection onto a slanting surface (Fig. 1). The pellet is elevated 1 mm above the anode plane by a 0.5 mm diameter tungsten rod. This 1 mm spacing helps in achieving more uniform irradiation. Due to the flash x-ray camera's spectral response, for these shots, saturation of the recording film occurred at  $0.25 \text{ gm/cm}^2$  equivalent of gold. Therefore, the apparent dark core size in these pictures corresponds to an isodensity contour of  $0.25 \text{ gm/cm}^2$ . These core sizes are plotted and compared against calculated core sizes using CHART D.<sup>10</sup> (see Fig. 12). The three solid lines correspond to 2, 3, and 5 kJ absorbed by the pellet, and the experimental points are in qualitative agreement in the 2 and 3 kJ range. Based on this comparison, we estimate 2-3 kJ out of a total 10 kJ in the beam is absorbed by the pellet. To improve on the coupling efficiency, shorter A-K gaps and consequently smaller pinches were tried. Measurements indicate that, with the increased energy absorption, the degree of loading symmetry



decreased as already discussed in Section II, thus making meaningful comparisons of flash radiographic data with calculations impractical. A typical nonspherically imploding pellet is shown in Fig. 13. Here is a shadowgram of a pellet irradiated by an REB from a hollow-tapered cathode. As discussed before, the loading symmetry is 2:1 (back to front) and this image graphically demonstrates the kind of nonspherical implosion that can result. As shown, the downstream half of the pellet has already imploded and is exploding into the still slowly imploding upstream half. An additional evidence of the asymmetric loading is the rear surface motion of the thin anode plate, indicating that a large fraction of the beam energy is directly deposited in the plate.

For observing implosion of hemispheres, a laser reflection technique has been used. Figure 14 shows such an experimental setup. As the hemisphere implodes and as the imploded shell mass impacts the thin reflective membrane, a reduction of the reflected laser light will occur. This provides a direct measure of implosion time. Slightly later, after the imploded mass jets through the small opening in the anode and arrives at the beam splitter, a second change in light intensity occurs. From the arrival time of the jet, the average velocity of the imploded mass can be measured. The implosion time, average jet velocity, and the PMT output are also shown in Fig. 14. These measured quantities can be compared with calculations made with the CSQ code to determine the energy absorbed and symmetry of loading. These comparisons indicate about 5 kJ were absorbed by the target, about 1/3 the total beam energy, and to account for the jet velocity, a 2:1 asymmetric loading from pole to equator had to be assumed.



## II. DISCUSSION AND SUMMARY

In summary, we have found the following: (1) at Hydra power levels, REB energy deposition is consistent with classical deposition, (2) cathode-anode spacing and cathode configuration can independently effect symmetry of loading, and (3) between 25% to 33% of the total beam energy can be absorbed by the targets.

These target experiments can be best characterized as studies of electron flow into a prescribed target volume in an REB diode. In contrast, previous REB focusing studies dealt with beam flow onto an area of a flat anode. Thus, for target irradiation, the detailed beam electron trajectories in the diode have a significant effect on loading symmetry. The difference in pellet loading by a tapered hollow cathode and a cylinder on axis cathode is probably caused by the different beam flow patterns. For the tapered hollow cathode the beam flow may be predominantly in the radial direction and pinches at the base of the pellet, thus enhancing the loading of the base of the pellet. For the cylinder on axis cathode, the pinch may have formed near the front of the pellet, thus providing preferential loading of the front. As such, a detailed understanding of electron flow and beam pinch formation in the diode is essential if some degree of control of loading symmetry is to be achieved. Several possible mechanisms<sup>8,11</sup> have been suggested to explain the loading symmetry of a sphere irradiated by a single REB. These include (1) scattering from the high Z target, the anode face, or target blowoff and (2) irradiation of the sphere by a "hot beam." Such a "hot beam" has been predicted<sup>12</sup> and is characterized by a cylindrical current density shell containing a uniform density stagnated central region.

These results in themselves do not directly provide information for breakeven experiments, but they serve to indicate the direction of future research. It is clear that future deposition experiments have to be carried out with REB's in the  $10^{12}$  -  $10^{13}$  Watts range, and in order to optimize REB target coupling, we need to study mechanisms that control the detailed electron trajectories in the diode.

#### ACKNOWLEDGMENT

We would like to acknowledge the helpful technical assistance provided by P. F. McKay and R. W. Kessler and useful discussions with Drs. A. J. Toepfer, G. Yonas, and M. J. Clauser.

## APPENDIX

A useful diagnostic technique for REB driven pellet implosion studies must be an x-radiographic system that can discriminate against the intense REB bremsstrahlung pulse and yet at the same time be sensitive to a rather weak flash x-ray source. A prototype of such a device was built<sup>13</sup> and tested. In this camera, an input stage was made of a channel plate<sup>14</sup> which directly converts incident x-ray photons into low energy output electrons with a gain factor of  $\sim 10^3$ . The low energy output electrons are accelerated by a 90 percent transparent accelerating grid and guided by a longitudinal D.C. magnetic field of  $\sim 20$  gauss. These electrons in the magnetic field preserve the x-ray photon image and are further amplified by a second channel plate. The output electrons of the second channel plate are rendered visible by a phosphorous screen, and the visible image is directly coupled onto film via a fiber optic plate. To discriminate against the REB x-ray pulse, both channel plates are gated on after the REB pulse and the phosphorous screen and the film are protected by a lead shield as depicted in Fig. 1.

The quality of the shadowgrams depends on the flash x-ray source size, the distances between the source and the target, and the camera and the target, and magnetic focusing properties of the camera. With the prototype the shadowgrams were of low quality and from which it was difficult to extract quantitative data. The main shortcomings were the weak source and the operational difficulties encountered in achieving critical focus with the D.C. magnetic field.

The present system has a 1.4 mm diameter and 3 ns flash x-ray source, a 706 Febetron.<sup>15</sup> When operating, this source is placed 3 meters away from

the target and with the camera only 25 cm from the target. Thus, the penumbra is smaller than 0.14 mm. The D.C. magnetic field of the prototype camera was replaced by a pulsed magnetic field with a  $B_{\text{max}} \sim 4$  kG. This strong magnetic field effectively eliminates the need of critical focusing since now the inherent resolution of the camera is the gyrodiameter of the electrons. For a perpendicular component of  $\sim 40$  eV, which is typical of channel plate output, the gyrodiameter is  $\sim 0.1$  mm. A typical resolution test shot is shown in Fig. 15. This demonstrates that the resolution is better than 0.25 mm. In order to take advantage of this improved resolution and image contrast, a gold step wedge with  $0.098 \text{ gm/cm}^2$  steps is introduced into the shadowgram as in Fig. 16 for calibration purposes, thus permitting direct quantitative analysis. The shadowgram of Fig. 16 is read with a microdensitometer and the pellet areal density is plotted against the wedge (Fig. 17). It shows that the "gold" pellet has a double wall thickness of only  $\sim 0.64 \text{ gm/cm}^2$  which is approximately correct for a gold alloy of 15 percent (atm) copper as verified by an Auger spectrum analysis of the pellet.

## REFERENCES

1. M. J. Clauser, Phys. Rev. Lett. 34, 570 (1975).
2. G. Yonas, J. W. Poukey, K. R. Prestwich, J. R. Freeman, A. J. Toepfer, and M. J. Clauser, Nucl. Fusion 14, 731 (1974).
3. A. E. Blaugrund and G. Cooperstein, Phys. Rev. Lett. 34, 461 (1975).
4. F. C. Perry and M. M. Widner, to be published in J. Appl. Phys. (Dec. 1975).
5. S. L. Thompson, "CSQ-A Two Dimensional Hydrodynamic Program with Energy Flow and Material Strength" Sandia Report SAND-74-0122 (unpublished), (Aug. 1975).
6. L. M. Barker and R. E. Hollenback, J. Appl. Phys. 43, 4669 (1972).
7. S. P. Bugaev, V. I. Koshelev, and M. N. Timofeev, Sov. Phys. Tech., 19, No. 9, March 1975.
8. J. Chang, M. M. Widner, G. W. Kuswa, and G. Yonas, Phys. Rev. Lett. 34, 1266 (1975).
9. L. P. Mix, to be published.
10. S. L. Thompson, Sandia Laboratories Report SLA-73-0477 (1973).
11. M. J. Clauser et al., Seventh European Conference on Controlled Fusion and Plasma Physics Vol. 1, 85 (Sept. 1975).
12. G. R. Hadley, T. P. Wright, and A. V. Farnsworth Jr., Proceedings of International Topical Conference on Electron Beam Research and Technology (Nov. 1975).
13. G. W. Kuswa and J. Chang, Advances in X-ray Analysis 18, 107 (1974).
14. W. B. Colson, J. McPherson, J. I. King, Rev. Sci. Instrum. 44, 1694 (1973).
15. A 600 kV bremsstrahlung source manufactured by Hewlett Packard, McMinnville Division.



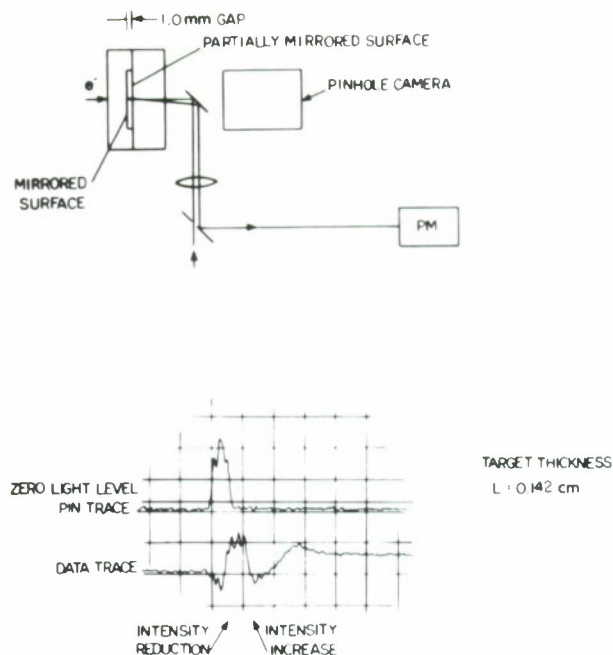
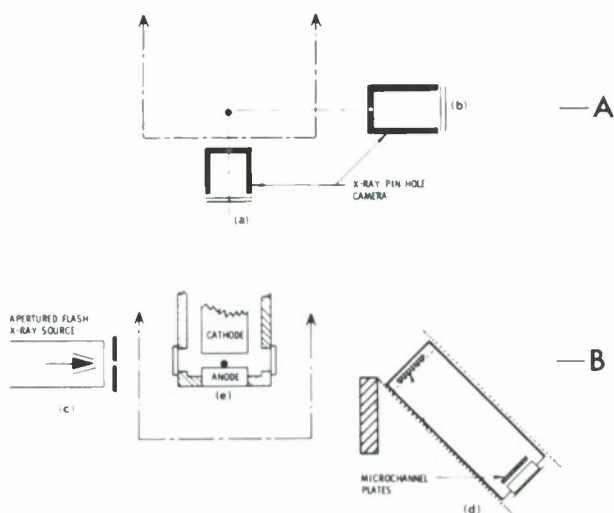


Figure 1. Experimental arrangement showing (A) x-ray pin-hole cameras and (B) flash x-radiography

Figure 2. Laser reflection experiment. The initial rise of the data is due to x-ray background. The intensity reduction corresponds to the arrival of the shock wave at 165 ns. The intensity increase corresponds to the arrival of the free surface at the beam splitter. This arrival is 325 ns.

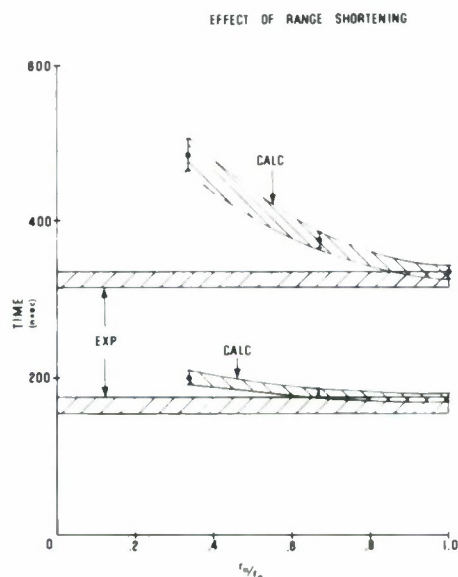


Figure 3. Experimental and calculated shock arrival times (lower curves) and free surface arrival times (upper curves) plotted against fractions of an electron range

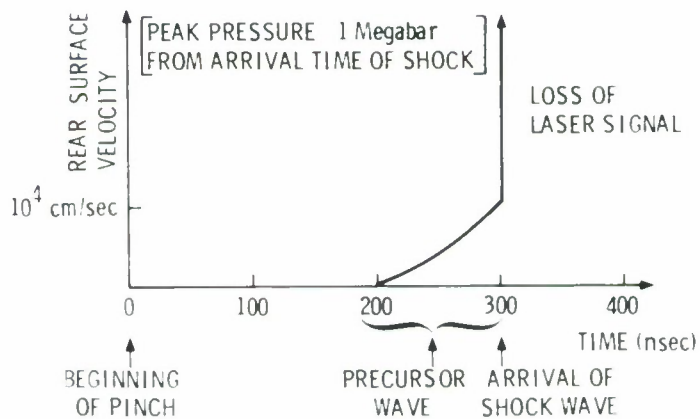


Figure 4. VISAR data showing precursor wave and shock arrival

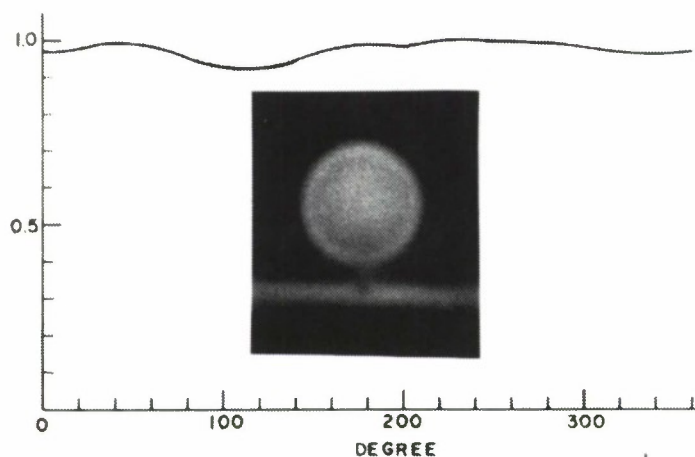


Figure 5. X-ray pinhole photograph of a spherical pellet (Au, 4 mm diam, and 0.2 mm wall thickness) showing side view. Normalized O. D. is plotted against angle. Zero degree is identified by the stalk. Uniformity is within 10%. A-K gap is 11.4 mm.

Figure 6. Same pellet as in Fig. 5. Viewed along the diode axis showing uniformity within 30%. A-K gap is 11.4 mm.

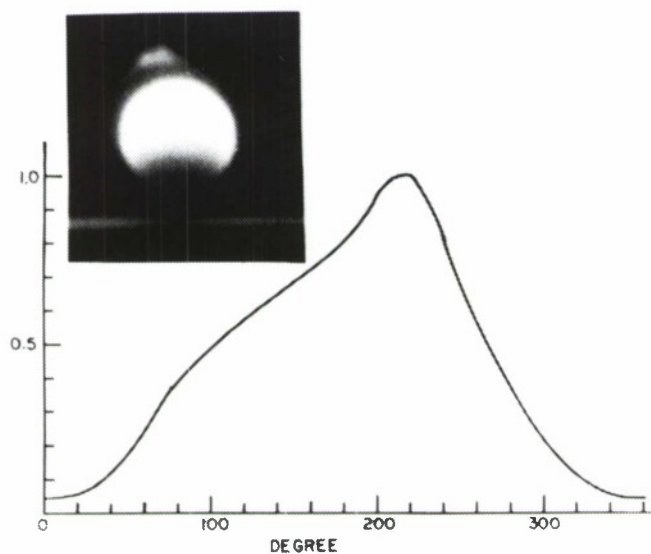
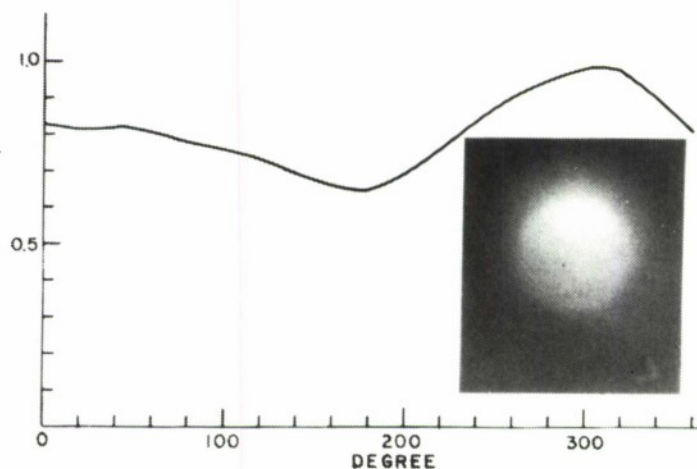


Figure 7. A-K gap is 9 mm. This sideview shows gross asymmetry in pellet loading. The back side is not irradiated.

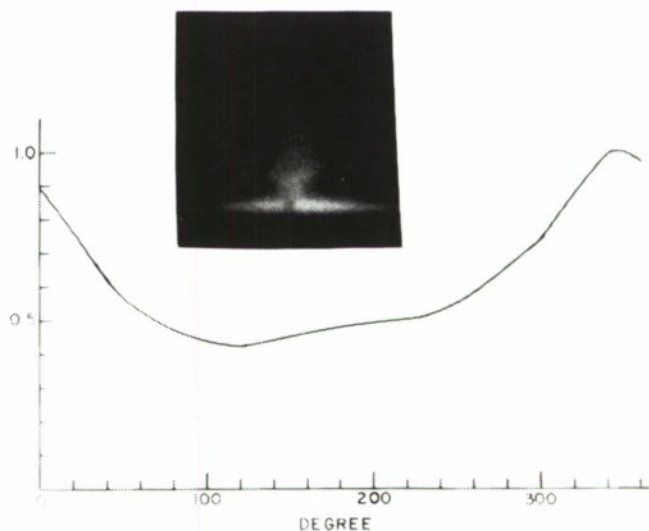


Figure 8. This shot was made with a tapered hollow cathode showing 2:1 preferential loading of the back side

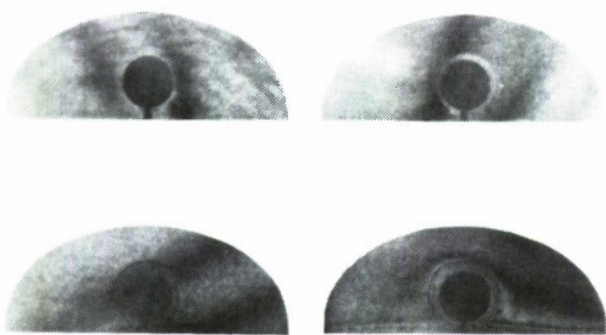


Figure 9. Four holograms of the pellet during irradiation. The interval between frames is 16 ns.

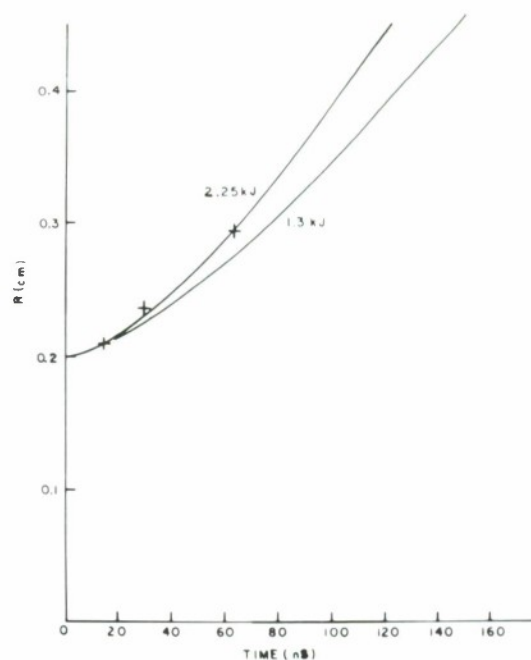


Figure 10. Experimental and calculated radial position of the first fringe plotted against time

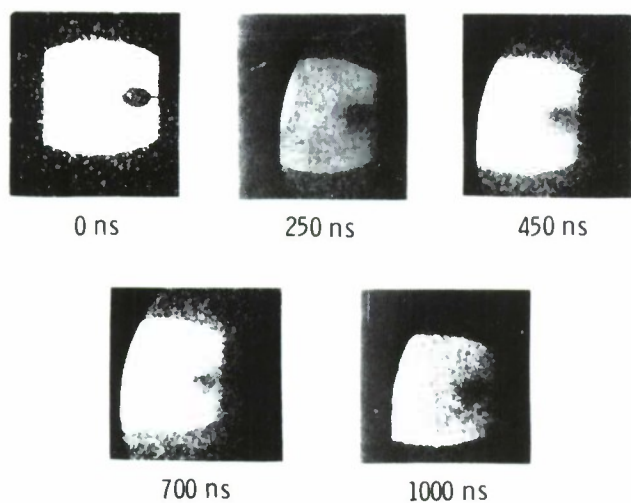


Figure 11. Flash x-ray shadowgrams taken at 5 delay times showing different stages of implosion

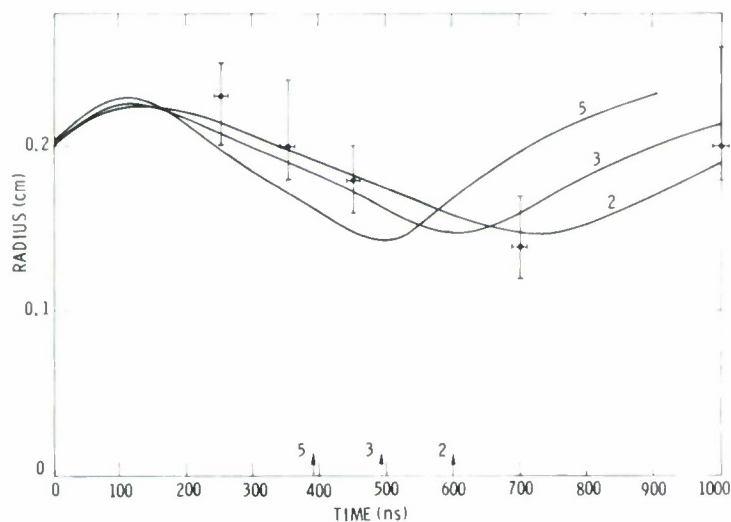


Figure 12. Variations in core size (areal density  $0.25 \text{ gm/cm}^2$ ) as a function of time. Solid curves are the calculated values for 2, 3, and 5 kJ absorbed by the target. The arrows mark the corresponding implosion times.

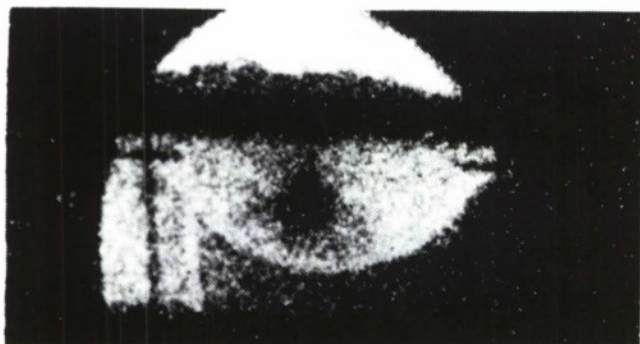


Figure 13. A shadowgram of a pellet undergoing asymmetric implosion. This shadowgram and the x-ray pinhole photograph shown in Fig. 8 were taken during the same shot.

Figure 14. Laser reflection technique used to measure hemisphere implosion and jet velocity

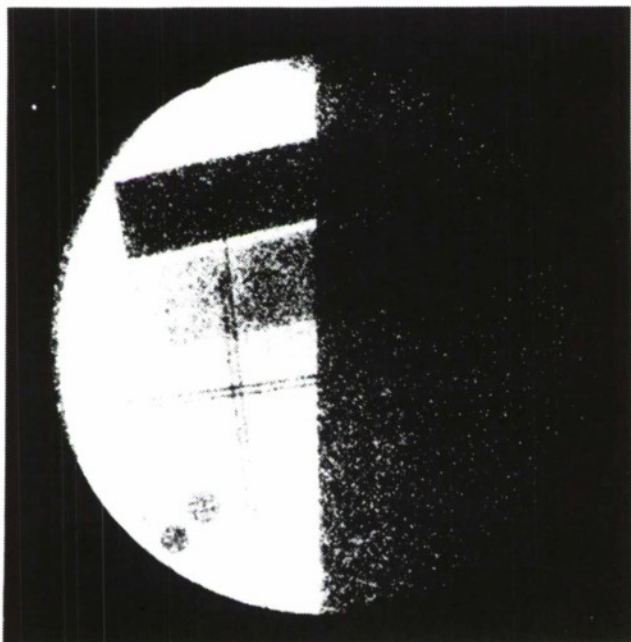
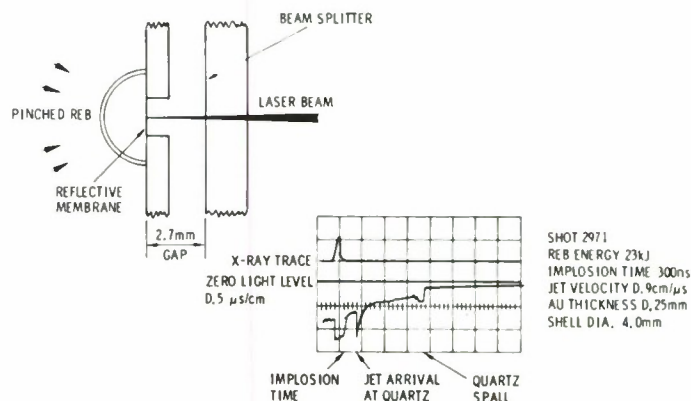


Figure 15

Resolution test of the x-ray shadowgraph camera. Half of the active area is covered with 0.5 mm thick Ta. Two broad stripes at the top are two Au step wedges. Step size is  $0.049 \text{ gm/cm}^2$ . 4 pairs of wire shadows are shown. The thicker wires are 0.5 mm dia. W wire separated by 0.5 mm. The thinner W wires are 0.25 mm dia. and separated by 0.25 mm. One pair of each is placed directly in front of the camera and the other 25 cm away. The round objects are two 4 mm dia. Au spheres and one 2 mm dia. Au sphere.



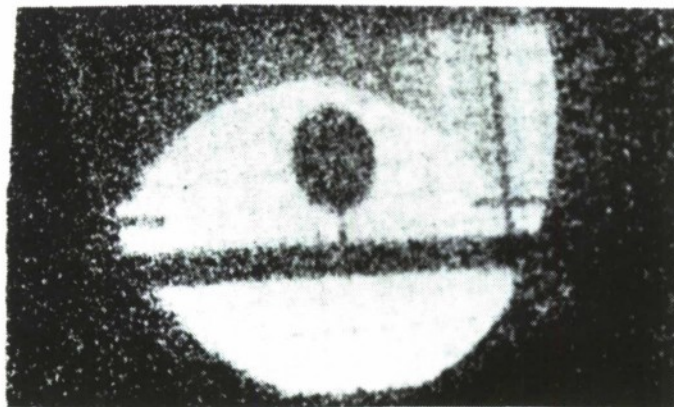


Figure 16. Shadowgram of a pellet mounted on a thin anode. Also showing are the fiducial marks and an Au stepwedge.

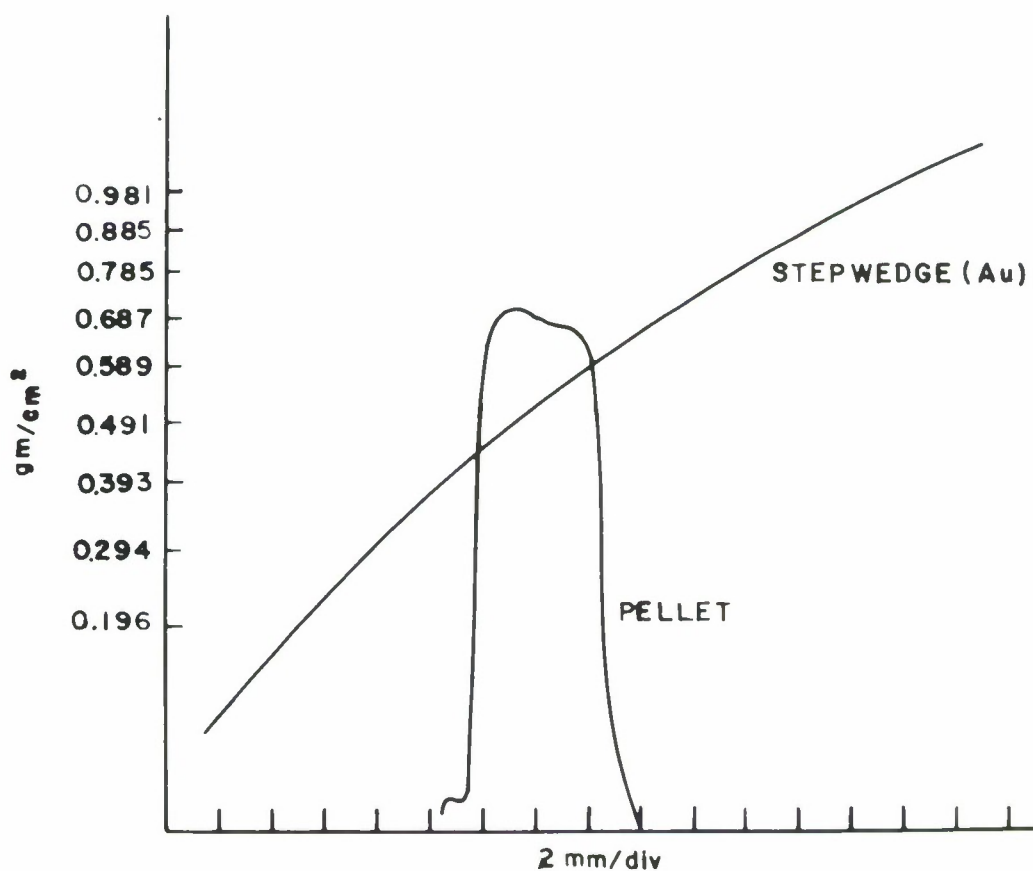


Figure 17. Densitometer scans of the stepwedge (Au) and gold copper alloy pellet.



## CALCULATION OF PINCHED BEAM FORMATION AND TARGET INTERACTION

Z. Zinamon, S. Miller, E. Nardi and E. Peleg

The Weizmann Institute of Science, Rehovot, Israel

### ABSTRACT

The dynamics of electron beams in large aspect ratio diodes is discussed. The role of plasma production and ion emission from anode targets is demonstrated by CIC calculations. The collapse of a hollow beam in the pinch process is simulated. The interaction of the pinched beam with a solid target is also calculated. Energy deposition is determined by the Monte Carlo method and the hydrodynamic expansion is calculated by the two dimensional particle-in-cell method. Bremsstrahlung emission is also calculated through the use of the Monte Carlo method. Self-magnetic-field effects are taken into account. It is found that the self-magnetic-field forces can considerably reduce the number of electrons escaping from the focal region by back-or side-scattering. The possibility of detecting self-magnetic-field effects by the bremsstrahlung angular distribution is discussed.

The application of electron beams to the achievement of inertially confined thermonuclear fusion requires focussing of such beams onto solid targets and generation of high-density and high-energy-density plasmas.<sup>1-4)</sup> The purpose of the work presented here is to study the generation and focussing of intense relativistic electron beams in high aspect ratio cold emission diodes and the processes governing the deposition of energy by such beams in solid targets.

The first stage in the chronological order of events in the diode is the generation and focussing of the electron beam. It is clear from the early work of Alfven<sup>5)</sup> and Lawson<sup>6)</sup> that the force of the self-magnetic field of the high current in the diode is responsible for the collapse of the electron beam and the self-pinch phenomenon. However, detailed numerical simulations of the electron flow in the diode done by Poukey et al.<sup>7)</sup> and by us indicate that a simple flow model is not valid. A straightforward calculation, assuming the cathode and anode are simple equipotential surfaces, vacuum in the gap and Langmuir-Child emission law, gives a "laminar" flow pattern of the electrons and no pinching in diodes which are experimentally known to produce pinched beams. Indeed, in the works of Alfven and Lawson, beam collapse was associated with the assumption of space-charge neutrality. It turns out that in the diode Coulomb forces dominate over the magnetic forces and prevent the collapse of the beam. To explain the pinch phenomenon the anode plasma model was suggested by Poukey et al.<sup>7)</sup> According to this model, electrons hitting the anode during the "laminar-flow" phase of the pulse produce an expanding plasma layer on the anode, into which the diode electric field cannot penetrate. In this plasma layer the magnetic force dominates and there the electron trajectories

are turned towards the center. In recent experiments Blaugrund and Cooperstein<sup>8)</sup> demonstrated that in a hollow cathode diode pinching proceeds as a collapse of a hollow beam at a velocity of the order of  $\sim 1$  mm/ns. At such a velocity there is not sufficient time to deposit enough energy in the anode in order to produce the plasma thermally, or even to evaporate a significant amount of anode material. On the other hand, it has been suggested quite a time ago<sup>9)</sup> that the anodes of e-beam diodes could be used as ion sources. More recently it has been suggested<sup>8,10-13)</sup> that these ions should have an important effect on the diode dynamics.

The pinch model we are trying to test numerically is as follows:

In the early phase of the pulse in a hollow cathode diode the electrons flow "laminarly" in a thick cylindrical shell and hit the anode nearly perpendicularly. At this stage the magnetic forces only slightly bend the electron trajectories. After some dwelling time ions start to be emitted from the anode. Even in this stationary stage there is not enough energy density on the anode surface to produce ions thermally, or even to evaporate enough of the anode material. Ions are produced by the primary beam electrons, by backscattered and secondary electrons. For the ions to be emitted they have to be produced in a gaseous material. In a recent work Blaugrund and Cooperstein<sup>12)</sup> showed that heating the anode has a damaging effect on the pinch, suggesting that emission of adsorbed or dissolved gases is involved. We assume that ion emission starts as soon as enough energy is deposited in a given surface element to liberate a significant amount of adsorbed gases.

The ions affect pinching in essentially two ways: Their space charge modifies the Coulomb fields such that the magnetic forces are more effective; and as soon as the ions reach the cathode their space charge enhances electron emission which in turn increases the magnetic force through the increase in current. These combined effects cause the initially laminar electron trajectories to bend and cross each other, and part of the current is driven into the inside of the cylindrical current sheet. There it is driven directly towards the anode by the diode field, thus hitting a new ring on the anode surface. The ions emitted from this new ring after a certain dwell time in which it is heated pull the electrons further in, and the beam collapse may proceed in this way. The model is essentially in agreement with the experimental results of Blaugrund and Cooperstein.<sup>8)</sup> The collapse velocity is a local function of the anode material and increases monotonically with the atomic number. The reason for this may be that surfaces of high Z targets heat up faster than low Z ones because of the shorter range of the primary electrons and because of the larger number of backscattered electrons. The nature of the anode material is determined by the upper layer of about 1  $\mu\text{m}$  thickness. This may be explained by the fact that at this thickness the time for the surface to reach the same temperature as the lower layer through heat conduction is shorter than the dwell time.

In the actual numerical calculations we tried to simulate the diode shown in Fig. 1. To simplify the calculations we used boundary conditions as also shown in Fig. 1: the recess in the cathode is simulated by suppressed emission up to a radius of 2.0 cm. The cathode tapering is

simulated by taking the gap to be 4 mm. Along the line from  $R=4$  to 5 cm a logarithmic drop of the potential is prescribed, as in the case of two coaxial infinite cylinders. Each simulation particle represents  $4 \times 10^{10}$  physical particles. The calculation is not strictly time dependent in the sense that the full time dependent equations are not actually solved. Instead, use is made of the facts that the system does not change significantly in a time interval of the order of 0.1 ns which is the order of transit time of information in the system, and that the flow is composed of slow ions and fast electrons. At each time step the electric fields in the diode are calculated from the charge distribution through the solution of Poisson's equation. From the simulation particle velocities the current distribution and the magnetic fields are obtained. The ion simulation particles are moved at time steps of 0.1 ns, and these represent the physical time intervals. The electron simulation particles are then moved by solving the relativistic equations of motion in a series of much shorter time steps, until relaxation to a quasi-stationary state is obtained. The ions are then moved again, and a new cycle begins.

The relativistic equations of motion for the electron simulation particles are given by

$$d(\gamma m_0 \vec{V})/dt = (e/c) [\vec{E} + (\vec{V} \times \vec{B})/c] , \quad (1)$$

where  $m_0$  is the electron mass,  $\vec{V}$  its velocity vector,  $c$  the velocity of light,  $\gamma = (1 - V^2/c^2)^{-1/2}$ ,  $e$  the electron charge,  $\vec{E}$  the electric field and  $\vec{B}$  the magnetic field. The actual solution is for the transformed variable  $\mathbf{p} = \gamma \mathbf{V}$ . A time step  $Dt$  is taken as follows: at first we assume



constant fields and  $\gamma$  and solve analytically for  $p$ . After finding the new approximate location of the particle the change in potential and the average fields are calculated. If necessary the time step  $\Delta t$  is divided into  $n$  sub-steps  $n\Delta t = \Delta t$  so that the change in potential will not exceed a given fraction of the particle energy and that  $\Delta t$  will not exceed a given fraction of the cyclotron period.

The emission law for both ions and electrons assumes space charge limited flow, and Langmuir-Child law corrected for two component flow is used<sup>14)</sup>. Ions can be emitted only from those regions on the anode which were hit by electrons in the last physical time step. Ion emission from a given element on the anode is suppressed until the electron energy density absorbed by that element is sufficient to heat it to a temperature of  $600^\circ\text{K}$ , when adsorbed gas release is assumed. This dwell time is an important parameter in determining the collapse velocity.

Results of the numerical calculations are shown in Figs. 2, 3. The calculation was followed only to a fairly early stage of the pinch, but some of the main features are already evident. As soon as ion emission starts to affect the flow in the diode, the trace of the beam on the anode shrinks down to a narrow ring in agreement with experimental results<sup>8)</sup> and beam collapse begins in accord with the model described above. A better agreement with experiment should be obtained if we choose a somewhat larger value for the gap to simulate the cathode taper. In this particular calculation the ions were assumed to be singly ionized carbon.

The next phase of events in the diode is the interaction of the pinched beam with the anode target. In calculating this we try to take into account the effects of the two dimensional hydrodynamic expansion on the process of

energy deposition. One might expect that these effects are important because during the energy deposition time the target expands to distances comparable with the focal radius. Indeed, previous calculations<sup>15)</sup> in which the effects of self-magnetic fields on the electron trajectories were neglected, indicated that the two dimensional nature of the system might reduce the efficiency of energy deposition. This reduction is caused by the fact that the rarefield plasma column expanding from the focal area is relatively "transparent" to electrons in the lateral direction. Therefore, electrons which are side-scattered in the expanded region have a good chance to escape without depositing their energy in the focal mass. It should be expected that the self-magnetic field of the beam current should affect the energy deposition process: The magnetic forces impede the escape of electrons from the beam. Also, if only partial current neutralization takes place in the rarefield target material, the effective range of the electrons will be shortened and more energy will be deposited in the outer layers.

To demonstrate magnetic field effects we examined two extreme cases:

Case I: Full current neutralization in the target material. Magnetic fields exist only due to those parts of the beam which are outside the expanding plasma column.

Case II: The rather unphysical model of no current neutralization throughout the target was used. The full magnetic field due to the beam current inside the target was assumed to exist for particle trajectories calculations. This model was calculated in order to see the maximum possible effect of the self-magnetic field.

In both cases a model of a "turbulent" converging beam was adopted: We assume a converging beam hitting the focal area with a conical contour line making an angle of  $20^\circ$  with the initial surface of the anode. At each point of entry the electron direction is chosen at random from a distribution bounded by a cone making the same angle with the initial surface. The electrical field was assumed zero everywhere inside the target material and equal to the ideal (nominal) diode field everywhere outside.

Energy deposition is calculated by the Monte Carlo method in a way similar to that described by Berger<sup>16)</sup> along the same lines as in ref. 15. In the case of full current neutralization in the target the magnetic field affects only back- and side-scattered electrons, while in the case of zero current neutralization it affects also the trajectories of electrons inside the target. In this case the electron trajectories between two Monte Carlo events are not straight lines as in usual cases, but rather bent by the magnetic forces. To follow these trajectories the relativistic equations of motion of the electrons were solved numerically, taking into account the magnetic force and the continuous slowing down between scattering events due to energy loss. The steps in the finite difference calculations were chosen to be limited by the smaller of the two characteristic lengths - one fourth of the distance between two multiple scattering events and one tenth of the Larmour radius at the local magnetic field. Each step is calculated by solving the linearized equations of motion with the local value of the magnetic field. In the case of zero current neutralization the actual trajectories of backscattered electrons were not followed exactly. The velocity vector and the magnetic field at the point of emergence of a back scattered electron are used to determine analytically whether it is going

to leave the target or return to it in its first cycle. If it does leave the plasma, conservation of energy allows us to calculate approximately the range of its return point.

In the case of full current neutralization in the target the Monte Carlo calculation is the same as in ref. 14. Full calculations of backscattered electron trajectories are performed by solving the relativistic equations of motion outside the plasma column, using the net current to calculate the magnetic fields.

The two dimensional hydrodynamic expansion of the target is calculated by the PIC method<sup>17)</sup>. The equation of state is essentially that of Altshuler et al.<sup>18)</sup> In order to avoid excessive computer time consumption, the Monte Carlo calculation was applied only each 60 hydrodynamic time steps, and between deposition calculations the power deposition was assumed to be a constant Lagrangian property of the hydrodynamic simulation particles. The mesh size used was  $dr = 0.003$  cm in the radial direction and  $dz = 0.0015$  cm in the axial direction. The cold target was  $50$  (radial)  $\times$   $20$  (axial) cells with 16 particles per cell.

Bremsstrahlung emission is calculated by the Monte Carlo method separately using density profiles obtained from the hydrodynamical calculation. The cross sections used are based on corrections to the Born approximation estimated from experimental work<sup>19-21)</sup>

Calculations were performed for the following system: a square pulse of  $(5\text{kJ})/(100\text{ ns})$  of 350 keV electrons hitting a focal area of 0.75 mm radius on the initial target surface. The anode material is tungsten.

Hydrodynamic profiles of the flow are shown in Fig. 4 for both cases. The flow was only followed to 14 ns. The effective range shortening in



case II results in more rapid expansion in that case. The magnetic field in case II also affects the energy density distribution in the target. Since range shortening is more effective at the edge of the plasma column, the energy density is peaked there. For example, at  $t = 13$  ns, the peak specific energy in the expanding material in case II is about 3 times that of case I. The calculation indicates that very little energy is lost from the focal area through back- and side-scattered electrons. Most of the scattered electrons are confined to the beam by the action of the magnetic forces.

The bremsstrahlung calculations were performed in order to see whether bremsstrahlung emission can be used as a diagnostic tool in investigating beam-target interaction processes. To this end bremsstrahlung angular distribution is shown in Figs. 5, 6 for cases I and II. The larger scatter in the points at small angles follows from the statistics of the Monte Carlo calculation. At the early stages there is not much difference between the two cases. The reason is that when the density of the target is still high, the electron trajectories in both cases are dominated by scattering processes. Later in the pulse the target material is rarefied and the electron trajectories in the outer layers in case II are dominated by the magnetic forces. At this stage the bremsstrahlung angular distribution of case II should be more isotropic than that of case I, as is indeed seen in Fig. 6.



## References

1. G. Yonas, J.W. Poukey, K.R. Prestwich, J.R. Freeman, A.J. Toepfer and M.J. Clauser, Nucl. Fusion 14, 731 (1974).
2. G. Cooperstein, J.G. Siambis and I.J. Condon, Bull. Amer. Phys. Soc. 19, 532 (1974).
3. W.C. Condit, Jr., D.O. Trimble, G.A. Metzger, D.G. Pelliuen, S. Heurlin and P. Creely, Phys. Rev. Lett. 30, 123 (1973).
4. L.I. Rudakov and A.A. Samarsky, in Proceedings of the Sixth European Conference on Controlled Fusion and Plasma Physics, Moscow, U.S.S.R., 1973 (U.S.S.R. Academy of Sciences, Moscow, U.S.S.R., 1973) p. 487.
5. H. Alfven, Phys. Rev. 55, 425 (1939).
6. J.D. Lawson, J. Electron, 3, 587 (1957).
7. J.W. Poukey, J.R. Freeman and G. Yonas, 12th Electron, Ion and Laser Beam Technology Symposium, Cambridge, Mass. (1973).
8. A.E. Blaugrund and G. Cooperstein, Phys. Rev. Lett. 34, 461 (1975).
9. S. Humphries, J.J. Lee and R.N. Sudan, Appl. Phys. Lett. 25, 20 (1974).
10. J.W. Poukey, Appl. Phys. Lett. 26, 145 (1975).
11. J.W. Poukey, SAND-75-5441, presented at the 13th Symposium on Beam Technology, Colorado Springs, May 1975.
12. A.E. Blaugrund and G. Cooperstein, private communication.
13. Shyke A. Goldstein and Roswell Lee, Phys. Rev. Lett. 35, 1079 (1975).
14. I. Langmuir, Phys. Rev. 33, 954 (1929).
15. Z. Zinamon, E. Nardi and E. Peleg, Phys. Rev. Lett. 34, 1262 (1975).
16. M.J. Berger, in Methods in Computational Physics, edited by B. Alder, S. Fernbach and M. Rotenberg (Academic, New York, 1963).
17. F.H. Harlow, in Methods in Computational Physics, edited by B. Alder, S. Fernbach and M. Rotenberg (Academic, New York, 1964) Vol. III.

18. L.V. Al'tshuller et al., Zh. Eksp. Teor. Fiz., 38, 790 (1960),  
[Sov. Phys. JETP 11, 573 (1960)].
19. J.W. Motz, Phys. Rev. 100, 1560 (1965).
20. J.W. Motz and R.C. Placious, Phys. Rev. 109, 235 (1958).
21. H. Aigingen, Z. Phys. (Leipzig) 197, 8 (1966).

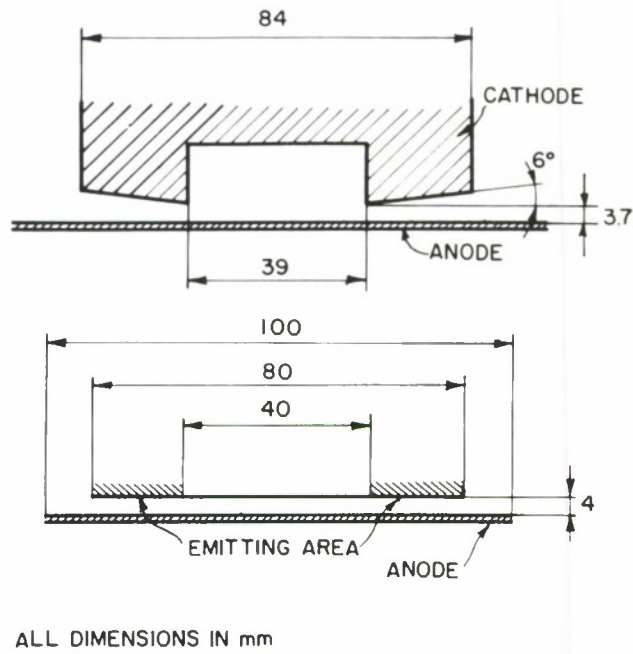


Figure 1. Actual (top) and simulation (bottom) diode structure

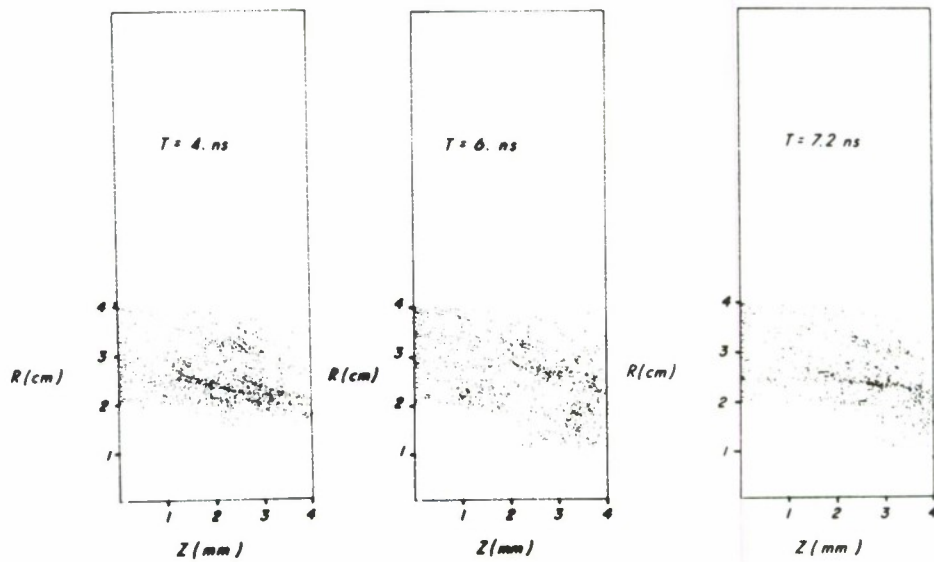


Figure 2. Electron charge distribution in the diode shown in Fig. 1

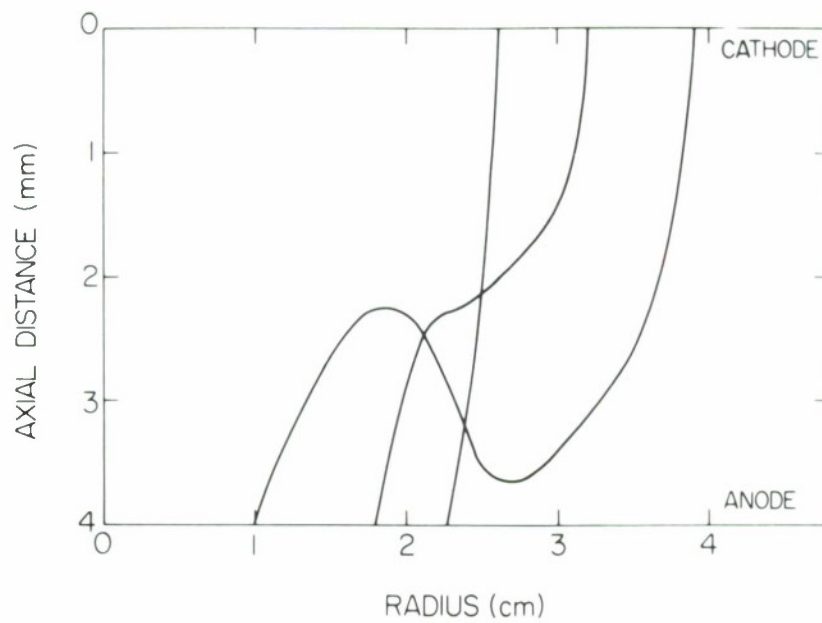


Figure 3. Typical electron trajectories in the diode shown in Fig. 1

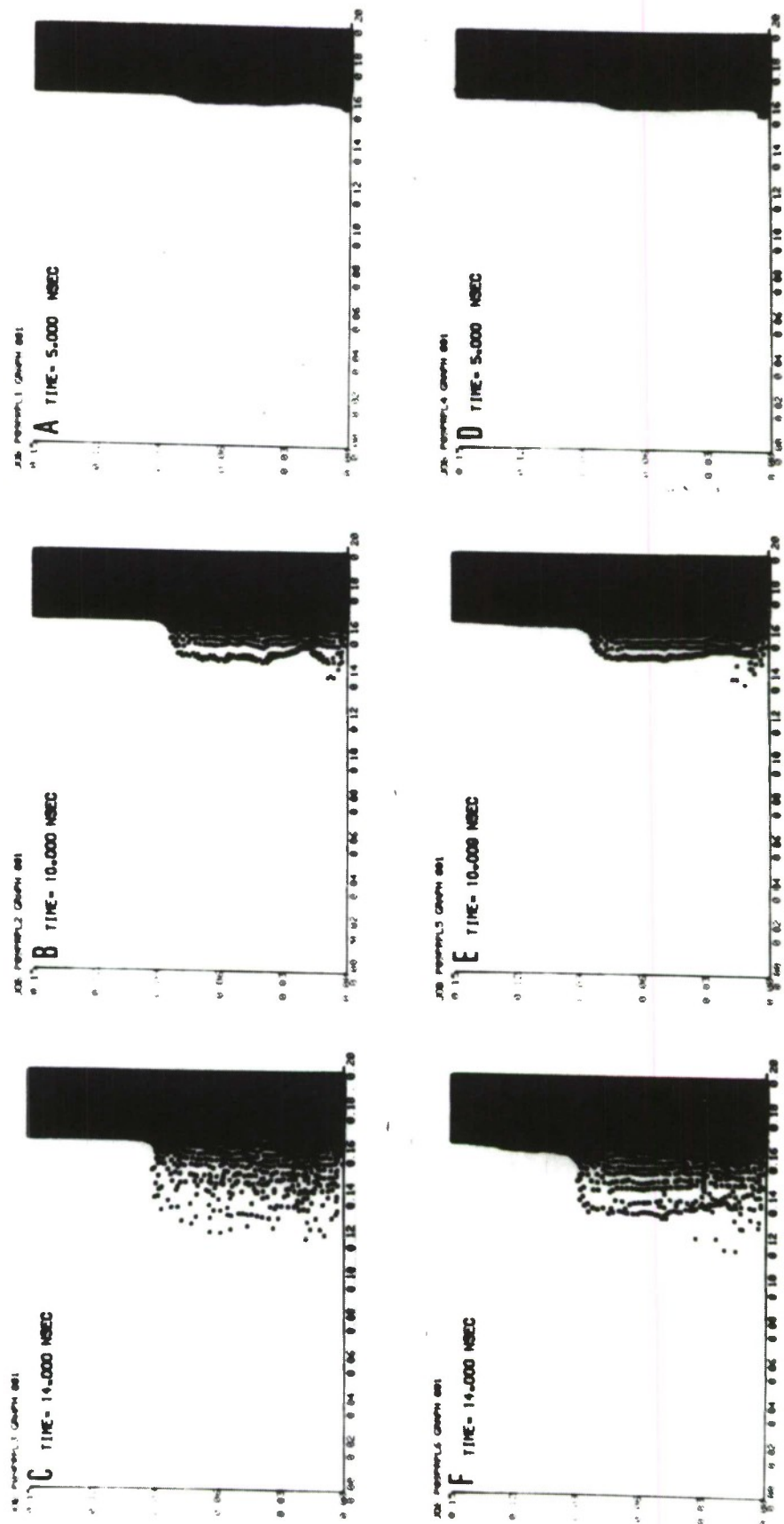


Figure 4. Successive snapshots of the hydrodynamic expansion at times 5, 10, 14 nsec from the start of the pulse. Zero current neutralization - a, b, c; full current neutralization - d, e, f.



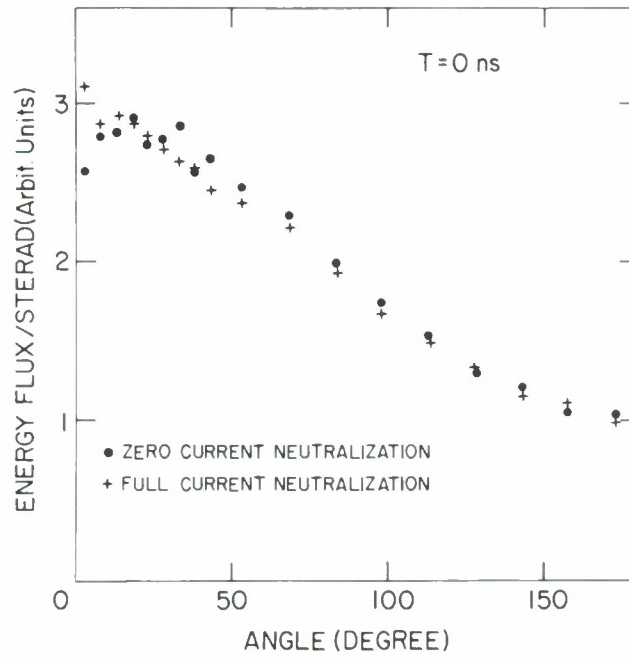


Figure 5. Angular distribution of bremsstrahlung emission from the focal mass at time 0

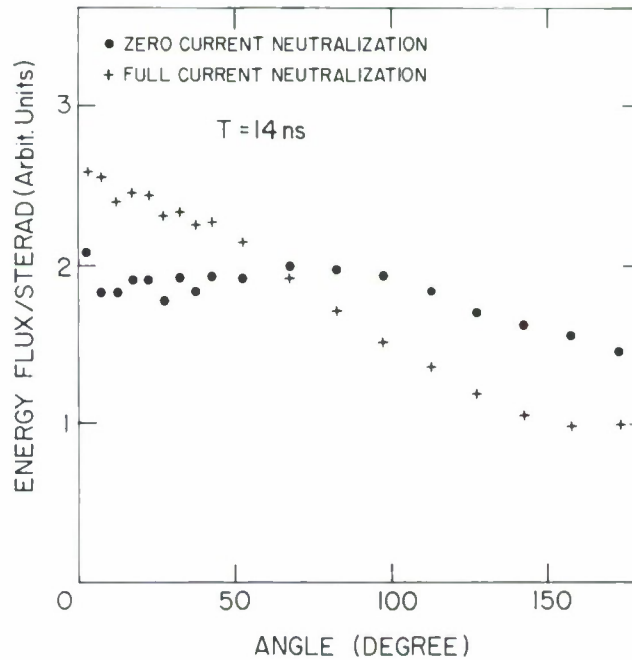


Figure 6. Angular distribution of bremsstrahlung emission from the focal mass at time 14 ns from the start of the pulse

SEEDED MEGA-GAUSS TURBULENCE IN DENSE FUSION  
TARGET PLASMAS<sup>\*</sup>

D.A. Tidman

Institute for Fluid Dynamics and Applied Mathematics  
University of Maryland  
College Park, Maryland  
20742

ABSTRACT

Fine scale variations in the chemical composition of a dense plasma target (such as a plasma produced by a focused laser or REB pulse) give rise to corresponding spatial fluctuations in the electron density which persist until dispersed by diffusive or turbulent mixing. In the presence of a sufficiently steep background temperature gradient these density fluctuations are expected to give rise to mega-Gauss magnetic field fluctuations for plasma temperatures of about a kilovolt. Composition fluctuations would also produce resistivity fluctuations in low-temperature targets and generate large fields in current-carrying plasmas. This phenomenon may be of interest in the design of targets for electron beam driven fusion.

\* Work supported in part by the Energy Research and Development Administration and National Science Foundation Grant ENG 74-15020.

## I. INTRODUCTION

The spontaneous growth of magnetic fields in laser-produced plasmas is now a well established phenomenon.<sup>1-6</sup> The same thermal sources of field (deriving initially from  $\nabla N_e \times \nabla T_e$ ) will be present in plasmas produced by relativistic electron beam pulses (REB's), in addition to the beam and return current fields in this case. It has also been pointed out that plasma composition jumps<sup>7-10</sup> are expected to provide a particularly potent source of magnetic flux in such situations.

In this paper we first note that a small grain of "impurity" plasma embedded in inhomogeneous dense collision-dominated plasma will set up a strong thermal source of B-field which derives from the electron density or temperature gradients associated with the grain. Following creation of the plasma by an electron or laser pulse, a diffusion wave of azimuthal magnetic field travels rapidly out from the grain and establishes a region of flux extending into the surrounding plasma (this field can be calculated fairly simply for a spherical grain in a background temperature gradient<sup>10</sup>). Thus, if for example a plasma is seeded with a distribution of such impurity grains, the plasma volume is predicted to rapidly fill out with fine-structure fields as shown in Fig. 1. For e-beam<sup>11-18</sup> or laser fusion target plasmas that reach the kilovolt temperature range, the microfields created by these thermal sources are expected to be above a mega-Gauss in some cases. Strong field fluctuations are also expected in low temperature current-carrying seeded plasmas due to resistivity fluctuations. This latter case will only be discussed briefly in Sec. VI of this paper.

Such a medium of random fields is of interest in that it has a scattering mean free path for a pulse of relativistic electrons much less than that due to Coulomb scattering for light or moderate atomic weight materials. Electrons undergo multiple scattering by the B-fields and in the course of their random walk also lose energy via Coulomb interactions.

Now the relatively simple picture illustrated in Fig. 1 omits several effects that can be expected to occur in most seeded plasma targets. First, in preparing such a grainy medium, the grain shapes and spatial distributions are likely to be irregular. Second, ion diffusion would cause a relatively slow mixing between the grain and background plasma, thereby erasing the source of field after some time. Further, kilovolt high density plasmas are often produced in highly accelerated states, such as in an ablation wave (unless heavily tamped). Such accelerations would result in a tendency of the grains to drift through the background plasma, which in turn would generate turbulence on the grain scale. This fluid turbulence may provide an important additional source of work on the magnetic turbulence by stretching the lines of force, but would also give rise to a more rapid turbulent mixing away of the grain sources (Sec. III C).

In view of these complexities we shall adopt a statistical approach in which we consider a plasma with small-amplitude fluctuations in chemical composition with their associated electron density, temperature, and velocity fluctuations. In the following sections we attempt to estimate the importance of these various field sources and in Sec. VI discuss some speculations for dense fusion target plasmas.

## II. FIELD FLUCTUATIONS

The equation for the magnetic field,  $\underline{B}$ , in a plasma is given in Braginskii's review paper<sup>19</sup> on fluid equations,

$$\begin{aligned} \frac{\partial \underline{B}}{\partial t} - \underline{\nabla} \times (\underline{V} \times \underline{B}) + \frac{c^2}{4\pi} \underline{\nabla} \times [\underline{r} \cdot (\underline{\nabla} \times \underline{B})] &= \underline{S} \\ &= - \frac{c}{eN_e} \underline{\nabla} N_e \times \underline{\nabla} T_e - \frac{c}{e} \underline{\nabla} \times \left( \frac{\underline{R}_T}{N_e} \right) - \underline{\nabla} \times \left[ \frac{c}{4\pi e N_e} (\underline{\nabla} \times \underline{B}) \times \underline{B} \right], \end{aligned} \quad (1)$$

where

$$\underline{r} = \underline{b} \underline{b} \sigma_{\parallel}^{-1} + (\underline{I} - \underline{b} \underline{b}) \sigma_{\perp}^{-1} \quad (2)$$

is the resistivity, and the thermal force  $\underline{R}_T$  is given by

$$\frac{\underline{R}_T}{N_e} = - \beta_o \underline{\nabla}_{\parallel} T_e - \left( \frac{\beta_1' x^2 + \beta_o'}{\Delta} \right) \underline{\nabla}_{\perp} T_e - \frac{x(\beta_1'' x^2 + \beta_o'')}{\Delta} \underline{b} \times \underline{\nabla} T_e \quad (3)$$

with  $x = \Omega_e \tau_e$ ,  $\Delta = x^4 + \delta_1 x^2 + \delta_o$ , and the various constants

$\beta_o = \beta_o' / \delta_o$ ,  $\beta_o'$ ,  $\beta_o''$ ,  $\beta_1'$ ,  $\beta_1''$ ,  $\delta_o$ ,  $\delta_1$  are as listed in Braginskii's

Table 2. In general the magnetic field equation should be solved self-consistently with the fluid equations for the density  $\rho$ , fluid velocity  $\underline{V}$ , and temperature  $T$  (e.g., Eqs. 6.5, 6.14, and 6.33 in Ref. 19).

Equation (1) applies to collisional plasmas, even for  $\Omega_e \tau_e \gg 1$ , provided gradient drift instabilities (which would modify  $\underline{r}$ ) do not occur. Although neo-classical and resonant-scattering transport of electrons across the fields may play a role,<sup>20</sup> and are not included in



Braginskii's equations, these processes modify the electron thermal conductivity, not the electrical conductivity in Eq. (1) (except indirectly through its T-dependence).

The parameter  $\Omega_e \tau_e$  can be written

$$\Omega_e \tau_e = 4.25 \times 10^{-6} \frac{B T_e^{3/2}}{Z^2 \ell n \Lambda} \left( \frac{N_s}{N_i} \right), \quad (4)$$

where  $N_s = 4.5 \times 10^{22}$  is a characteristic solid state density, and  $T_e$  is in keV. For "weak" fields ( $\Omega_e \tau_e \ll 1$ ) the source side of (1) simplifies to

$$\underline{S} \approx - \frac{c}{e N_e} \underline{\nabla} N_e \times \underline{\nabla} T_e + O(\Omega_e \tau_e), \quad (5)$$

so that for a situation in which  $\underline{B}(t=0) = 0$ ,  $\underline{\nabla} N_e \times \underline{\nabla} T_e$  is the term that initiates the field.

Now consider a grainy plasma in which the chemical composition variations have a characteristic scale  $\ell$  and the locally space-averaged plasma properties change on a scale  $L$  with  $L \gg \ell$ . The fluid variables then consist of an average part and a fluctuation,

$$\begin{aligned} \underline{B} &= \delta \underline{B}, \quad \rho = \langle \rho \rangle + \delta \rho, \\ \underline{V} &= \langle \underline{V} \rangle + \delta \underline{V}, \quad T_e = \langle T_e \rangle + \delta T_e, \end{aligned} \quad (6)$$

where we shall assume  $\underline{\nabla} \langle N \rangle$ ,  $\underline{\nabla} \langle T_e \rangle$ , and  $\langle \underline{V} \rangle$  to be parallel so that we can set  $\langle \underline{B} \rangle = 0$ . The resistivity can be written  $\underline{r} = \langle \underline{r} \rangle + \delta \underline{r}$  with  $\langle \underline{r} \rangle = \sigma^{-1} \underline{I} + \langle \Delta \underline{r} \rangle$ , where  $\sigma^{-1} = \langle r_{\perp} \rangle$ , and  $\Delta \underline{r} = \underline{b} \underline{b} (\sigma_{\perp} - \sigma_{\parallel}) / \sigma_{\perp} \sigma_{\parallel}$ , so that

$$\underline{\nabla} \times [\underline{\mathbf{r}} \cdot (\underline{\nabla} \times \delta \underline{\mathbf{B}})] = -\frac{1}{\sigma} \nabla^2 \delta \underline{\mathbf{B}} + \underline{\nabla} \times [(\langle \Delta \underline{\mathbf{r}} \rangle + \delta \underline{\mathbf{r}}) \cdot \underline{\nabla} \times \delta \underline{\mathbf{B}}] + O(L^{-1}) .$$

Dropping terms of order  $L^{-1}$  on the left side of Eq. (1) then gives

$$\left( \frac{\partial}{\partial t} + \langle \underline{\mathbf{v}} \rangle \cdot \underline{\nabla} - \frac{c^2}{4\pi\sigma} \nabla^2 \right) \delta \underline{\mathbf{B}} = \delta \underline{\mathbf{s}} , \quad (7)$$

where the source is

$$\delta \underline{\mathbf{s}} = \underline{\mathbf{s}} + \underline{\nabla} \times (\delta \underline{\mathbf{V}} \times \delta \underline{\mathbf{B}}) - \frac{c^2}{4\pi} \underline{\nabla} \times [(\langle \Delta \underline{\mathbf{r}} \rangle + \delta \underline{\mathbf{r}}) \cdot \underline{\nabla} \times \delta \underline{\mathbf{B}}] . \quad (8)$$

The terms in  $\delta \underline{\mathbf{s}}$  involve thermal sources, fluid turbulence, and fluctuations in the electrical resistivity.

### III. ESTIMATES OF SOURCE FLUCTUATION AMPLITUDES FOR A TWO-SPECIES GRAINY PLASMA

Equations (7) and (8) determine the field fluctuations,  $\delta \underline{\mathbf{B}}$ , in terms of  $\delta N_e$ ,  $\delta T_e$ , and  $\delta \underline{\mathbf{V}}$ , which have their origin in seeded chemical composition fluctuations of the plasma. In general the source (8) is extremely complicated. The purpose of this section is to make some order-of-magnitude estimates of the source fluctuation amplitudes in various cases. The temperature will be in keV in all practical formulas.

#### A. Electron Density Fluctuations

Consider a two-species plasma with light and heavy ion densities and charges  $N_\ell(\underline{\mathbf{x}})$ ,  $N_h(\underline{\mathbf{x}})$ ,  $Z_\ell$  and  $Z_h$  respectively, in which the heavy species plasma occupies a volume fraction  $\alpha$ . Suppose that the

ion charges and temperature  $T = T_i = T_e$  are assumed to be locally constant, and the L-scale fluid accelerations to be negligible, so that local pressure equilibrium prevails over the fluctuation scale,  $\ell$ . Under these circumstances one can show<sup>10</sup> that after ion-diffusive mixing has proceeded to the point where neighboring grains begin to merge (so that only a single fluctuation length is involved), the electron density fluctuation amplitudes are approximately given by

$$\frac{|\delta N_e|}{\langle N_e \rangle} \approx \frac{(0.5 - |0.5 - \alpha|) |Z_h - Z_\ell|}{[Z_\ell(1-\alpha)(1+Z_h) + \alpha Z_h(1+Z_\ell)]} . \quad (9)$$

For  $\alpha = 0.5$  and  $Z_h \gg Z_\ell$  this reduces to  $(1 + 2Z_\ell)^{-1}$ .

Note also that the mass density fluctuations  $\delta\rho$  can be relatively small in the case in which the pressure,  $P$ , and  $T$  are locally constant, provided also that the plasma is fully ionized. This can be seen by writing the atomic weights as  $A_{\ell,h} = 2Z_{\ell,h} + \Delta_{\ell,h}$ , in which case the mass density is

$$\rho = 2m_p \left[ PT^{-1} + N_\ell \left( \frac{\Delta_\ell}{2} - 1 \right) + N_h \left( \frac{\Delta_h}{2} - 1 \right) \right] . \quad (10)$$

If  $\Delta_\ell/2 \approx \Delta_h/2 \approx 1$ , then  $\delta\rho \approx 0$ .

## B. Temperature Fluctuations

If the plasma is optically thick, radiation diffusion tends to rapidly smooth the temperature over typical grain scales. Temperature fluctuations are most likely to arise for optically thin or grey plasmas in which the faster radiation rate of the high-Z plasma regions cools

them more rapidly than the low-Z regions, despite the smoothing effect of electron thermal conduction.

Consider the steady-state energy equation (with hydrodynamics frozen) for a single grain (ion species  $h$ ) embedded in a hot optically thin plasma,

$$\underline{\nabla} \cdot \underline{q}_e = -P_R + P_D, \quad (11)$$

where  $P_R$  is the radiation emission power density and  $P_D$  some spatially constant energy source that balances  $P_R$  in the background plasma (species  $l$ ). If the magnetic field is weak ( $x = \Omega_e \tau_e < 1$ ), the heat flux to order  $x$  is (using Braginskii's notation),

$$\underline{q}_e = -K_e \underline{\nabla} T_e - K_e \left( \frac{x \gamma_o''}{\gamma_o \delta_o} \right) \underline{b} \times \underline{\nabla} T_e - \frac{c \beta_o T_e}{4 \pi e} \underline{\nabla} \times \underline{B} + O(x^2), \quad (12)$$

where  $K_e = N_e T_e \gamma_o \tau_e / m$ , and the radiated power for a plasma of fully stripped ions is principally bremsstrahlung,

$$P_R \approx P_{Br} = 5.35 \times 10^{-24} N_1^2 Z^3 T_e^{1/2} \text{ ergs/cm}^3/\text{sec}. \quad (13)$$

Equation (11) relates the fluctuations in heat flux and radiation emission due to the grain, i.e.,  $\underline{\nabla} \cdot \delta \underline{q}_e = -\delta P_R$ . An order of magnitude estimate for  $\delta T_e$  then follows from (12) and (13) by writing  $\underline{\nabla} \sim \ell^{-1}$ , where  $\ell$  is the grain scale,

$$\frac{|\delta T_e|}{\langle T_e \rangle} \sim \frac{353 \ell^2 Z_h^4 \ell_{n\Lambda}}{\gamma_o T_e^3} \left( \frac{N_h}{N_s} \right)^2 \left\{ 1 + \frac{x \gamma_o''}{\gamma_o \delta_o} + 6.1 \times 10^{-5} (\ell_{n\Lambda})^2 \left( \frac{\beta_o x}{\gamma_o} \right) \frac{Z_h^3}{T_e^4} \left( \frac{N_h}{N_s} \right) \right\}^{-1}, \quad (14)$$

where  $T_e$  is in keV and we set  $\delta P_R \approx P_{Br,h}$ . This result only applies for an optically thin plasma, i.e., provided

$$\lambda_a = 116 \left\langle \frac{1}{Z^3} \left( \frac{N_s}{N_i} \right)^2 \right\rangle \frac{T_e^{7/2}}{\ell n \Lambda(v)} \geq \ell_T, \quad (15)$$

where  $\lambda_a$  is the plasma absorption length<sup>21</sup> of a thermal photon ( $h\nu = T_e$ ),  $\ell_T$  is the length scale on which  $\langle T_e \rangle$  changes, and  $N_s = 4.5 \times 10^{22} \text{ cm}^{-3}$ . Estimates for more general driven situations can similarly be obtained.

Taking  $\ell = 10^{-3} \text{ cm}$  we see that for low  $Z_h$ 's, or for  $N_h \ll N_s$ ,  $\delta T_e / \langle T_e \rangle$  is usually negligible. However, for  $Z \sim 10$  and  $T_e \sim 1 \text{ keV}$ ,  $\delta T_e / \langle T_e \rangle$  can become large and would then play a role as a source of B-field. The strong  $Z_h$ -dependence of (14) arises because of the increased bremsstrahlung and reduced thermal conduction for high ion charges.

### C. Velocity Fluctuations

The average plasma motion on the scale  $L$  often involves large accelerations. This would cause higher density grain regions,  $\delta\rho$ , to move through the lighter fluid and generate an  $\ell$ -scale turbulent velocity,  $\delta\mathbf{v}$ . For an order-of-magnitude guide as to when  $\delta\mathbf{v}$  is important, we consider a region in which the viscous force due to velocity gradients on the scale  $\ell$  is of order the inertial force  $\langle \dot{\mathbf{v}} \rangle \delta\rho$ , i.e.,  $\delta\rho \langle \dot{\mathbf{v}} \rangle \sim \eta_0 \delta v / \ell^2$ . Defining a characteristic time,  $\tau_L = \langle v \rangle / \langle \dot{v} \rangle$ , for



the accelerating large scale fluid motions, and using Braginskii's ion viscosity for  $\eta_0$ , then gives

$$\frac{\delta V}{\langle V \rangle} \sim 7.3 \times 10^{-5} \left\langle Z^4 \left( \frac{N_i}{N_s} \right) \left( \frac{m_i}{m_p} \right)^{\frac{1}{2}} \right\rangle \frac{\ell^2 \ln \Lambda}{\tau_L T^{5/2}} \left( \frac{\delta \rho}{\langle \rho \rangle} \right) . \quad (16)$$

For example, an ablation wave with  $\tau_L = 10^{-8}$ ,  $\ell = 10^{-3}$  cm,  $T = 1$  keV,  $\ln \Lambda \approx 7$ ,  $N_i/N_s = 0.1$ , gives  $\delta V/\langle V \rangle \sim 5 \times 10^{-3} Z^4 (m_i/m_p)^{\frac{1}{2}} (\delta \rho/\langle \rho \rangle)$ . We see that  $\delta V/\langle V \rangle$  can easily become large and lead to turbulence. This turbulence has two effects. First it may do additional work on the magnetic field by stretching the lines of force as represented in the source term  $\nabla \times (\delta \underline{V} \times \delta \underline{B})$  in Eq. (8). The problem of the partition of energy between the fluid kinetic energy density,  $\sim \frac{1}{2} \rho (\delta V)^2$ , and field energy in a turbulent dynamo is a fundamental one still under development<sup>22</sup>.

Second, if we consider a single spherical high-density grain region drifting through the background plasma, we see that it is likely to set up a convection cell within the grain plasma that may convect light plasma into the grain interior, thereby causing more rapid mixing away of the initial composition fluctuation source in highly accelerated situations. The net effect of these dynamo and mixing processes on the field is complicated, but could probably be clarified by use of an axisymmetric computer model for a single grain that includes the fluid and field dynamics self-consistently.

#### IV. SIMPLIFIED MODEL WITH DIFFUSIVE MIXING FOR THE CASE $\delta T_e \approx 0$ , $\delta \underline{V} \approx 0$ .

Consider Eq. (8) for the case  $\delta T_e = 0$ ,  $\delta \underline{V} = 0$ . The field sources remain complicated due to the thermal force contributions and the

field-dependent electrical conductivity. However, from (3) we see that  $\underline{R}_T/N_e \rightarrow -\beta_0 \underline{\nabla} T_e - (x\beta_0''/\delta_0) \underline{b} \times \underline{\nabla} T_e$  as  $x \rightarrow 0$ , so that for weak fields ( $x = \delta\Omega_e \tau_e \ll 1$ ),

$$\delta \underline{s} \rightarrow - \frac{c}{e \langle N_e \rangle} \underline{\nabla} \delta N_e \times \underline{\nabla} \langle T_e \rangle . \quad (17)$$

Equation (7) can be solved using this simplified source. It would give the correct initial growth of  $\delta \underline{B}$ , but becomes inaccurate for  $x \sim 1$ . A computer solution using the exact nonlinear source  $\delta \underline{s}$  (with  $\delta \underline{V} = 0$ ) will be given later.

Next, replacing  $\partial/\partial t + \langle \underline{V} \rangle \cdot \underline{\nabla}$  in (7) by  $\partial/\partial t$  (which can be regarded as the Lagrangian time derivative) and defining

$$\delta \underline{B}_{\underline{k}} = \int_{-\infty}^{\infty} d\underline{x} e^{i \underline{k} \cdot \underline{x}} \delta \underline{B} ,$$

(7) becomes

$$\left( \frac{\partial}{\partial t} + \frac{1}{\tau_B} \right) \delta \underline{B}_{\underline{k}} = \delta \underline{s}_{\underline{k}} , \quad (18)$$

where

$$\tau_B = \frac{4\pi\sigma}{c k^2} = \frac{7.8 \times 10^{-2} \langle T_e \rangle^{3/2}}{\langle Z \rangle k^2 \ln \Lambda} . \quad (19)$$

In order to obtain  $\delta \underline{s}_{\underline{k}}$  from (17), note that the "initial" fluctuation amplitudes are given by (9), but ion diffusive mixing proceeds to erase this source. The time scale for mixing away of composition fluctuations of scale  $\ell = \pi/k$  is given by the time taken for a light ion to diffuse a distance  $\ell$  through a medium of heavy ions, i.e.,

$$\tau_M = 5\pi^2 \times 10^{-5} \left( \frac{N_h}{N_s} \right) \frac{Z_h^2 Z_\ell^2}{\langle T \rangle^{5/2}} \frac{\ln \Lambda}{k^2} \left( \frac{m_\ell}{m_p} \right)^{1/2} . \quad (20)$$

A reasonable model for  $\delta N_{ek}(t)$  is thus

$$\delta \underline{s}_k = \frac{ic}{e} \underline{k} \times \underline{\nabla} \langle T_e \rangle \left( \frac{\delta N_{ek}}{\langle N_e \rangle} \right)_0 \exp \left[ - \int_0^t \frac{dt'}{\tau_M} \right] . \quad (21)$$

Assuming  $\delta \underline{B}_k(t = 0) = 0$ , (18) then integrates to give

$$\delta \underline{B}_k = \int_0^t dt' \frac{ic}{e} \underline{k} \times \underline{\nabla} \langle T_e \rangle \left( \frac{\delta N_{ek}}{\langle N_e \rangle} \right)_0 \exp \left[ \int_t^{t'} \frac{dt''}{\tau_B} - \int_0^{t'} \frac{dt''}{\tau_M} \right] . \quad (22)$$

In this equation  $\langle T_e \rangle$  and  $\langle N_h \rangle$  are in general functions of  $t$  and the slow space variable. Note also that the fields lie in planes perpendicular to  $\underline{\nabla} \langle T_e \rangle$ .

#### A. Field Amplitudes for Two Heating Models

In this section we list results for two heating models that provide formulas of value in obtaining estimates for applications. The first is

$$\frac{\langle T \rangle}{T_0} = \frac{N_0}{\langle N \rangle} = \left( \frac{t}{t_0} \right)^{2/3} , \quad (23)$$

which could be interpreted as a heated plasma undergoing expansion, or, writing  $t = \int dx / \langle v \rangle$ , as a parcel of plasma convected through a thermal front or ablation wave, etc. Using (23) in (22) gives (for  $T = T_e = T_i$ )

$$\begin{aligned}
\delta \underline{B}_{\underline{k}} &= \frac{ic}{e} \left( \frac{\delta N_{ek}}{\langle N_e \rangle} \right)_o \frac{k}{\tau} \times \frac{\nabla T_o}{\tau} \frac{t_o}{t_o/\tau_{Bo}} \int_0^\tau d\tau' \tau'^{\left(\frac{2}{3} + \frac{t_o}{\tau_{Bo}}\right)} \exp \left\{ - \left( \frac{\tau'}{t_o} \right)^{10/3} \right\} \\
&\approx \frac{ic}{e} \left( \frac{\delta N_{ek}}{\langle N_e \rangle} \right)_o \frac{k}{\tau} \times \frac{\nabla T_o}{\tau} t_o \left( \frac{t_o}{t} \right)^{t_o/\tau_{Bo}} \frac{\left( \frac{5}{3} + \frac{t_o}{\tau_{Bo}} \right)^y}{\left( \frac{5}{3} + \frac{t_o}{\tau_{Bo}} \right)}, \quad (24)
\end{aligned}$$

where  $y = \text{smaller of } \tau_o \text{ or } t/t_o$ ,  $\tau_{Bo} = \tau_B(T_o)$ ,  $\tau_{Mo} = \tau_M(T_o, N_o)$ ,  $\tau = t/t_o$ , and  $\tau_o = (10 \tau_{Mo}/3t_o)^{3/10}$ .

Equation (24) shows that  $\delta \underline{B}_{\underline{k}}$  grows from zero to a maximum value after which it slowly decays because the source has mixed away (Fig. 2). Defining a characteristic grain scale  $\ell = \pi/k$  and temperature gradient scale  $\ell_T = T_o/|\nabla T_o|$ , the growth of the field amplitude up to its maximum at  $t_{\max}$  is given by,

(model 1)

$$|\delta \underline{B}_{\underline{k}}| \approx 190 \left| \frac{\delta N_{ek}}{\langle N_e \rangle} \right|_o \frac{t_o T_o \sin \theta}{\ell \ell_T} \left\{ 1 + \frac{5.3 \times 10^{-7} \langle Z \rangle t_o \left( \frac{\ell n \Lambda}{7} \right)^{-1}}{T_o^{3/2} \ell^2} \right\} \left( \frac{t}{t_o} \right)^{5/3}, \quad (25)$$

for  $0 \leq t \leq t_{\max}$ , and

$$t_{\max} \approx 66 t_o^{7/10} \left( \frac{N_h}{N_s} \right)^{3/10} \frac{Z_h^{3/5} Z_\ell^{3/5} \ell^{3/5}}{T_o^{3/4}} \left( \frac{m_\ell}{m_p} \right)^{3/20} \left( \frac{\ell n \Lambda}{7} \right)^{3/10} \text{ nsec}, \quad (26)$$

where in these formulas the times  $t$ ,  $t_o$ , and  $t_{\max}$  are in nsec,  $T_o$  is in keV, and  $\theta$  is the angle between  $\underline{k}$  and  $\nabla T_o$ .

A second heating model has already been given in Ref. 9, namely

$$\langle T \rangle = T_o \left( \frac{t}{t_o} \right)^{2/3}, \quad \langle N \rangle = \text{const.} \quad (27)$$

The result for  $\delta B_{\vec{k}}$  is identical to (25), but the time to reach maximum in this case is longer,

(model 2)

$$t_{\max} \approx 173 t_o^{5/8} \left( \frac{N_h}{N_s} \right)^{3/8} \frac{Z_h^{3/4} Z_\ell^{3/4} \ell^{3/4}}{T_o^{15/16}} \left( \frac{m_\ell}{m_p} \right)^{3/16} \left( \frac{\ell n \Lambda}{7} \right)^{3/8} \text{ nsec.} \quad (28)$$

## V. RELATIVISTIC ELECTRON SCATTERING

The kinetic equation for a distribution,  $f(\underline{x}, \underline{p}, t)$  of relativistic electrons interacting with a plasma, has a Fokker Planck Coulomb collision term on the right which has recently been discussed by Mosher.<sup>16</sup> For a plasma containing magnetic field fluctuations we must add to this a term accounting for field-scattering of the electrons. In the case that the fluctuations make only a small orbit deflection over a fluctuation scale  $\ell$ , i.e.,  $\ell < r_B$ , where

$$r_B = \frac{mcv\gamma}{e\langle \delta B^2 \rangle^{1/2}} = \frac{1.7 \times 10^3 \gamma}{\langle \delta B^2 \rangle^{1/2}} \left( \frac{v}{c} \right), \quad (29)$$

their effect can be described by a diffusion term

$$C = \frac{\partial}{\partial \underline{p}} \cdot \left( \underline{D} \cdot \frac{\partial f}{\partial \underline{p}} \right), \quad (30)$$



where

$$\underline{\underline{D}} = - \frac{e^2}{8\pi^2 c^2} \int d\underline{k} \delta(\underline{k} \cdot \underline{v}) \underline{v} \times \underline{\underline{S}}_B \times \underline{v} , \quad (31)$$

and the field spectral density is defined by

$$\underline{\underline{S}}_B(\underline{k}) = \int d\underline{X} e^{i\underline{k} \cdot \underline{X}} \left\langle \delta B(\underline{x}) \delta B(\underline{x} + \underline{X}) \right\rangle . \quad (32)$$

This expression for  $\underline{\underline{D}}$  can be simplified for various cases.<sup>10</sup> If however the fields are of sufficient strength that  $r_B \sim \ell$ , then a different model for  $C$  is required.

For the case considered in Sec. IV, in which the fluctuations  $\delta \underline{B}$  are perpendicular to  $\underline{v} \langle T \rangle$ , the scattering mfp of a test particle follows from (31) as

$$\lambda_s = \text{larger of } \left\{ \frac{2}{3\sqrt{\pi} \ln(2r_B/\ell)} \left( \frac{r_B}{\ell} \right) \frac{r_B}{\cos^2 \theta} , \quad r_B \right. , \quad (33)$$

where  $\cos \theta = \underline{v} \cdot \underline{v} \langle T \rangle / v |\underline{v} \langle T \rangle|$ . If the fields become isotropized by  $\ell$ -scale fluid turbulence, then the  $\cos^2 \theta$  factor should be suppressed in (33).

For comparison the Coulomb scattering and energy-loss mean free paths,  $\lambda_s^c$  and  $\lambda_E^c$ , are also listed for the plasma,

$$\lambda_s^c = \frac{44(\gamma^2 - 1)^{3/2}}{\gamma \ell n \Lambda} \left( \frac{v}{c} \right) \left( \frac{N_s}{N_i} \right) \frac{1}{Z_i(Z_i + 1)} = \frac{2\gamma}{(Z_i + 1)} \lambda_E^c , \quad (34)$$

where  $N_i$  and  $Z_i$  are the local ion number density and charge, respectively.

## VI. DISCUSSION

As an example of the numbers given by formulas (25) - (28), consider the target deposition profile for a focused laser pulse in which a thermal wave penetrates ahead of the critical depth and moves in as target material is ablated. Suppose the ablator plasma consists of a 50/50 Al-Li mixture ( $\alpha = 0.5$ ) with a grain scale  $\ell = 5 \times 10^{-4}$  cm, and that the thermal wave has a thickness  $\ell_T = 10^{-2}$  cm and moves in at  $10^7$  cm sec $^{-1}$ . Plasma traversed by the wave is assumed to experience a temperature increase to say  $T_0 \approx 5$  keV in  $t_0 \approx 1$  nsec before being ejected. Using model 1 [Eqs. (9), (25), and (26)] with  $Z_h = 13$  and  $Z_\ell = 3$ , gives  $|\delta N_e / \langle N_e \rangle|_0 = 5/47$ ,  $|\delta B_k| = 8.03 \times 10^6 (t/t_0)^{5/3}$ , and  $t_{\max} = 2.49 (N_h/N_s)^{3/10}$ . Taking  $\langle N_e \rangle = 10^{21}$  at the critical depth gives  $(N_h/N_s) \approx 2.78 \times 10^{-3}$ , so that a maximum field of  $1.94 \times 10^6$  G is reached in a time  $t_{\max} = 0.426$  nsec.

The corresponding problem of the ablating deposition layer for an REB pulse is more difficult to discuss, even in a preliminary way, without further work. If we consider a relativistic electron cloud adjacent to a solid medium in which the Coulomb energy deposition mfp is  $\lambda_c^E$  and field scattering length is  $\lambda_s$ , the deposition "skin depth" is  $\sim (\lambda_E^c \lambda_s)^{1/2}$ , which can be less than the purely Coulomb deposition depth. However, using formulas (25) and (28) one can verify that, with a temperature gradient scale  $\ell_T \approx (\lambda_E^c \lambda_s)^{1/2}$ , the fields originating in the thermal sources considered in Sec. VI often tend to be rather weak.

An important aspect of the REB deposition problem for grainy plasmas, however, involves the fact that we have not considered all the source terms in (8) in calculating  $\delta B$ . At lower temperatures and longer

gradient scales,  $\ell_T$ , the most important source derives from fluctuations in the resistivity,  $r$  (due to its Z-dependence). For example an incident REB creates return currents which in turn interact with the resistivity fluctuations,  $\delta r$ , and give rise to  $\delta B$ 's. This would occur even in a cold metal. Calculations of the fields deriving from these sources (that dominate at low temperatures) will be given later. A preliminary estimate from Eq. (1) indicates that the field amplitudes could be of order  $\delta B \sim (4\pi\ell J/c)(\delta r/r)$ , where  $J$  is the return current density. For a grain scale  $\ell = 10^{-2}$  cm,  $\delta r/r \sim 1$ ,  $J = 10^8$  amps/cm<sup>2</sup>, this gives  $\delta B \sim 1.3 \times 10^6$  G.

In conclusion we note that if experimental support for the phenomenon discussed in this paper could be obtained, it would become worth investigating possible applications in detail. A number of speculations come to mind, the most obvious being the possibility of enhancing the coupling of REB's to fusion targets. For example, a relatively low-Z seeded ablator might be useful for driving pellet implosions and would have the advantage of decreasing the bremsstrahlung heating of the pusher.<sup>23</sup> Other examples to consider involve the direct REB heating of Li-seeded DT fuel in tamped spheres and other geometries. In the spherical case it might be possible to arrange for relativistic electrons to pass through the outer homogeneous tamper and then undergo a field-scattered random walk in the fuel region, thereby increasing their deposition power density in the fuel.

## REFERENCES

1. J.A. Stamper, K. Papadopoulos, R.N. Sudan, S.O. Dean, E.A. McLean , and J.M. Dawson, Phys. Rev. Lett. 26, 1012 (1971).
2. F. Schwirzke and L.L. McKee, Fifth European Conference on Controlled Fusion and Plasma Physics (Euratom CEA, Grenoble, 1972), Vol. 1, p.63.
3. G.A. Askar'yan, M.S. Rabinovich, A.D. Smir'nova, and V.B. Studenov, Zh. Eksp. Teor. Fiz., Pis'ma Red. 5, 116 (1967) [JETP Lett. 5, 93 (1967)].
4. J.A. Stamper and B.H. Ripin, Phys. Rev. Lett. 34, 138 (1975).
5. J.B. Chase, J.M. Leblanc, and J.R. Wilson, Phys. Fluids 16, 1142 (1973).
6. N.K. Winsor and D.A. Tidman, Phys. Rev. Lett. 31, 1044 (1973).
7. D.A. Tidman, Phys. Rev. Lett. 32, 1179 (1974).
8. D.A. Tidman, Thermally Generated Magnetic Fields in Laser-Driven Compressions and Explosions, Phys. Fluids (scheduled for Dec. 1975).
9. D.A. Tidman, Seeded Megagauss Turbulence in Dense Fusion Target Plasmas, Phys. Rev. Lett. (scheduled for Nov. 3, 1975).
10. D.A. Tidman, Megagauss Turbulence due to Seeded Composition Fluctuations in Dense Plasma, and Electron Beam Scattering, communicated to Phys. Fluids, August, 1975.
11. F. Winterberg, Phys. Rev. 174, 212 (1968).
12. G. Yonas, J.W. Poukey, K.R. Prestwich, J.R. Freeman, A.J. Toepfer and M.J. Clauser, Nucl. Fusion 14, 731 (1974).
13. K.M. Brueckner, IEEE Trans. Plasma Sci. 1, 13 (1973).
14. L.I. Rudakov and A.A. Samarsky in Proc. 6th Europ. Conf. on Controlled Fusion and Plasma Physics (Moscow 1973), p. 487.

15. M.J. Clauser, Phys. Rev. Lett. 34, 570 (1975).
16. D. Mosher, Phys. Fluids 18, 846 (1975).
17. S.A. Goldstein, R.C. Davidson, J.G. Siambis and R. Lee, Phys. Rev. Lett. 33, 1471 (1974).
18. A.E. Blaugrund and G. Cooperstein, Phys. Rev. Letters 34, 461 (1975).
19. S.I. Braginskii, in Reviews of Plasma Physics, edited by M.A. Leontovich (Consultants Bureau, New York, 1965), p. 205.
20. W.M. Manheimer, private communication of unpublished work.
21. T.W. Johnston and J.M. Dawson, Phys. Fluids 16, 722 (1973).
22. See for example R.H. Kraichnan and S. Nagarajan, Phys. Fluids 10, 859 (1967), U. Frisch, A. Pouquet, J. Léorat and A. Mazure, J. Fluid Mech. 68, 769 (1975), H.K. Moffatt, J. Fluid Mech. 57, 625 (1973), R.H. Kraichnan, J. Fluid Mech. 59, 745 (1973).
23. M.A. Sweeney and M.J. Clauser, Low-Z Ablator Targets for Electron Beam Fusion, Applied Physics Letters (scheduled for Nov. 1, 1975).



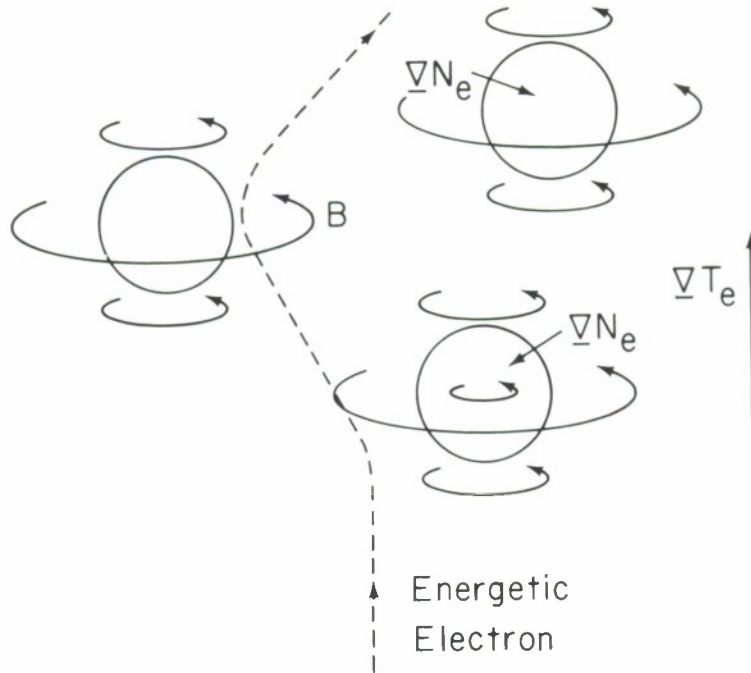


Figure 1. Azimuthal magnetic fields produced by spherical impurity grains embedded in a background dense plasma with a temperature gradient. The fields are perpendicular to  $\nabla T_e$ .

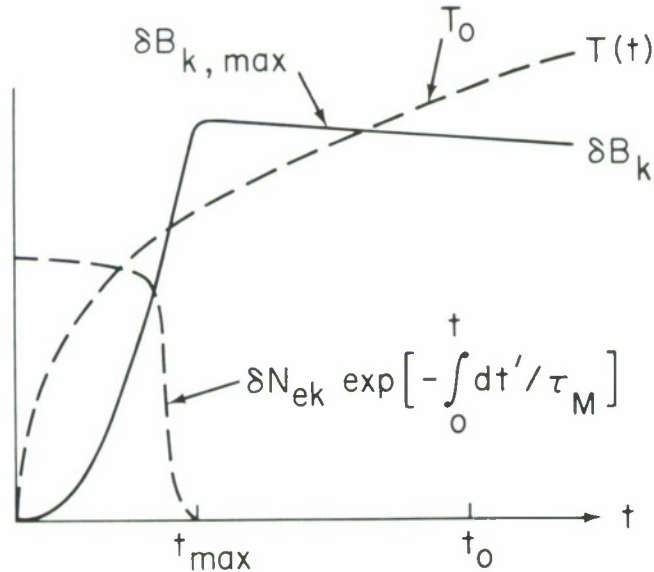


Figure 2. Time dependence of a field Fourier amplitude,  $\delta \underline{B}_k$ , for the plasma heating models in Sec. IVA. The field reaches a maximum as the electron density fluctuation source mixes away, and this maximum may occur either earlier or later than  $t_0$ .

## CHARGED-PARTICLE BEAM IMPLOSION OF FUSION TARGETS

M. J. Clauser and M. A. Sweeney  
Plasma Theory Division

Sandia Laboratories  
Albuquerque, New Mexico 87115

### Abstract

This paper discusses the calculated behavior of fusion targets consisting of solid shells filled with DT gas, irradiated by high power electron or ion beams. The current required for breakeven with gold shells is 500-1000 MA, independent of target radius and nearly independent of beam voltage in the  $\frac{1}{2}$  - 1 MeV range. Above 1 MeV the breakeven current increases because of the increased bremsstrahlung production by the beam electrons. By using a diamond ablator and a gold pusher, the breakeven current is reduced to 220 MA. The ion current required for breakeven (about 10 MA of protons) is independent of proton voltage above 10 MeV with gold shell targets. Below 10 MeV the range of the proton becomes too short for efficient coupling, and the required current increases, but the power does not. Various aspects of the symmetry and stability of the implosion are discussed. We find that the relatively long deposition lengths of electrons result in relatively small growths of the Rayleigh-Taylor instability during the acceleration of the pusher, resulting in a relatively stable implosion.

A number of different target designs have been proposed for electron and ion beam fusion.<sup>1-10</sup> These targets have varying degrees of complexity, ranging from simple spheres of DT to targets with several shells surrounding the fuel. If the main electron energy deposition mechanism is classical (collisional), then the simplest form of target that appears to be useful consists of a high density spherical shell containing DT fuel, as shown in Fig. 1. Other mechanisms which have the effect of shortening the range of the electrons may also play a role in the energy deposition. Two mechanisms currently being considered are return current heating<sup>3,11</sup> and thermoelectrically generated magnetic fields.<sup>12</sup> As these mechanisms are still poorly understood, our target studies during the past few years have assumed only collisional deposition. The principal results of our studies that have been published previously<sup>4,8,9</sup> are:

(1) The optimum shell is thick enough that few electrons reach the inner surface of the shell. Except for stability and symmetry considerations, the optimum shell thickness is essentially independent of the target radius and fuel mass and depends only on the electrons' range.<sup>4</sup>

(2) Breakeven with a simple gold shell requires that about 800 MA of 1 MeV electrons deposit their energy in the target.<sup>4</sup>

(3) The low-level bremsstrahlung produced by the beam in the outer part of the shell has a significant, detrimental effect on the performance of the inner surface of the pusher.<sup>4</sup>

(4) By using a shell with an iron ablator and a gold pusher, the bremsstrahlung is reduced and the power required for breakeven is decreased by more than a factor of two.<sup>8</sup>

(5) With proton beams irradiating gold shell targets,<sup>9</sup> breakeven is achieved with about 10 MA or  $10^{14}$  W of 10 MeV protons, and with a volume compression ratio around  $3 \times 10^3$ .

In this paper, we present further results of studies of this general type of target.

(1) The current required for breakeven with gold shells is 500-1000 MA, independent of target radius and more or less independent of beam voltage in the  $\frac{1}{2}$ -1 MeV range.<sup>7</sup> Above 1 MeV the current required for breakeven increases, perhaps linearly, with voltage.

(2) By using a high density carbon (diamond,  $3.5 \text{ g/cm}^3$ ) ablator and a gold pusher, the power required for breakeven with a 1 mm fuel-radius target is reduced to 220 TW with a 1 MeV electron beam. However, with a graphite ablator the performance of these small targets is apparently no better than with an iron ablator.

(3) Various aspects of the symmetry and stability of the implosion will be discussed. Of particular interest, we find that the relatively long deposition lengths of electrons and ions result in a much less severe problem of Taylor stability during the acceleration of the pusher than is generally expected for laser-fusion targets.

#### Electron Beam Fusion

Figure 2 shows the thermonuclear energy production calculated for several different targets as a function of the electron beam power deposited in the targets. In all cases the radius of the DT fuel is 1 mm, and the targets were irradiated by 1 MeV electrons. The mass of the DT fuel is

indicated for each curve. Four different shells were used: "C/Au" consisting of a high density carbon (diamond) ablator with a gold pusher; "Fe/Au" consisting of an iron ablator and a gold pusher; "Au" with an all gold shell; "Fe" with an all iron shell. In each case the thickness of each material has been optimized. The nearly straight line labeled  $P_{eb} \times t_i$  is the electron beam energy deposited in the Fe/Au targets up to the implosion time (time of maximum compression) and is approximately equal to the energy required for the implosion. Thus, breakeven for the C/Au targets occurs near 220 TW; for the Fe/Au targets, near 360 TW; for the Au targets, near 800 TW; and for the Fe targets, not at all.

The lower-Z ablators generally produce better results: lower power is required to initiate burn of the fuel and more complete burn-up of the fuel occurs once ignited. This appears to be primarily due to the lower level of bremsstrahlung produced by the interaction of the electron beam with the lower-Z ablators. This bremsstrahlung is more penetrating than the electrons and can penetrate to the inner surface of the pusher, preheating it, setting it on a higher adiabat, and thereby decreasing its effectiveness as a pusher. The desirability of having the pusher be of as high density as possible is demonstrated by the poor performance of the all-iron shell.

With a lower density carbon (graphite) ablator, the target performance is generally worse than with the iron ablator for targets of this size. The graphite ablator occupies 93% of the total volume of the target, evidently resulting in inefficient coupling of beam energy into the implosion of the pusher and fuel. With a larger fuel radius this effect is mitigated: increasing the fuel radius to 1.5 mm produces breakeven at 450 TW. The optimum radius may be somewhat larger.



Figure 3 shows how the performance of gold-shell targets varies with fuel radius for 1 MeV beams.<sup>7</sup> At each point on the curves, the fuel mass is optimized to give the maximum yield. The optimum mass is shown at various points along the curves. The  $r = 1$  mm curve is thus the envelope of the Au curves in Fig. 2. As can be seen, the beam power (or current) required for breakeven is nearly independent of the target radius (it increases roughly as  $r^{1/6}$ ).

Figure 4 shows how the target performance varies with beam voltage for targets with a fuel radius of 1 mm. As in Fig. 3, the fuel mass has been optimized at each point along the curves. Note that the curves are plotted here as a function of beam current rather than power. At lower voltages, the current required for breakeven is somewhat lower, and the power is significantly lower. At lower voltages the shells have a lower  $\rho r$  which decreases their effectiveness both as pushers and as tampers. With a 200 keV electron beam the shells are so thin that the largest output calculated is under 100 kJ for a  $\frac{1}{2}$ -mm radius target. At 3 MeV the bremsstrahlung degrades the performance of all but the targets with the largest fuel mass. This, combined with the larger thermonuclear energy required to produce breakeven, causes the current required for breakeven to rise to about 2000 MA. In the intermediate range of  $\frac{1}{2}$ -1 MeV, the current required for breakeven is relatively constant, 600-800 MA.

The energy loss  $dE/dx$  of relativistic electrons is relatively independent of beam voltage. The pressure produced in the ablator is proportional to  $J dE/dx$ , where  $J$  is the current density, and hence, is also independent of voltage. Thus, for different beam voltages, we would expect similar

target performance for the same beam current. This argument, however, neglects the effect of bremsstrahlung, which becomes increasingly severe as the voltage is raised. By using a low-Z ablator, the bremsstrahlung can be kept at a tolerable level up to higher voltages. We would thus speculate that the use of low-Z ablators would extend the voltage range over which the breakeven current remains relatively constant. Recent results obtained by Poukey<sup>13</sup> indicate that a beam voltage of 17 MeV or more is required to obtain a pinched electron current of 100 MA per diode. Target behavior at these voltages is currently being investigated.

If the deposition length of the electrons at these high currents is substantially shorter than the collisional deposition lengths used in these calculations, breakeven conditions will be considerably easier to attain.<sup>7</sup> For example, if a 5 MeV electron beam deposited its energy in the same fashion as we have assumed for 1 MeV electrons, then a target that is calculated to break even with a 1 MeV, 350 MA beam would break even with a 5 MeV, 70 MA beam, which appears to be achievable.

### Ion Beam Fusion

During the past year considerable progress has been made in the efficient production of ion beams.<sup>14,15</sup> A number of methods of producing and focusing ion beams have been suggested,<sup>15-22</sup> some of which appear to be capable of accelerating heavy ions.<sup>16,18,19,21</sup> Using beams of ions to implode fusion targets offers several distinct advantages over the use of electron beams:<sup>9</sup>

(1) Ions having the same range as electrons will have higher energies (voltages). Thus higher voltage, lower current beams will have the same power and deposition length as electron beams, presumably simplifying the task of producing the high power beams required for fusion.

(2) Ions produce essentially no bremsstrahlung, eliminating the pusher preheat problem encountered with electron beams.

(3) Ions undergo very little scattering in the target so that there are no "reflection" losses of ion beam energy.

(4) For ions normally incident on the target surface, the ions have a significantly higher energy loss rate near the end of their range. This results in better coupling of the ion beam energy into pusher kinetic energy than for electron beams or lasers where the deposition is peaked at the surface (see Figure 5).

While ion beams are clearly preferable from the standpoint of target behavior, these advantages are largely offset at the present time by the relatively large uncertainties concerning the feasibility of efficiently producing and focusing a high power ion beam. By contrast, efficient production and focusing of high power electron beams has been demonstrated; likewise, symmetric irradiation of spherical targets by electron beams has been demonstrated.<sup>23</sup>

Protons with energies greater than 1 MeV have a range-energy relation in gold given approximately by<sup>9,24</sup>

$$E = 19 x^{0.61},$$

where  $E$  is the proton energy in MeV and  $x$  is the range in  $\text{g/cm}^2$ . The energy loss ( $dE/dx$ ) of any ion of a given velocity is proportional to  $Z^2$  where  $Z$  is its charge state. From this, it follows that the range-energy relation for an arbitrary ion is given approximately by

$$\frac{E}{A} = 19 \left( \frac{Z^2 x}{A} \right)^{0.61},$$

where  $A$  is the atomic weight of the ion. Thus 10 MeV protons, 13 MeV deuterons, 40 MeV  $\text{He}^4$  ions and 10-20 GeV uranium ions all have about the same

range and, moreover, the same shape deposition profile. Consequently, target calculations for proton beams are equally valid for beams of other ions having the same beam power.

Calculations for a number of ion beam targets were presented in Ref. 9, primarily for 10 MeV protons. Figure 6 shows the behavior of these targets as the voltage is varied. For each voltage, the thickness of the gold shell is optimized. It was found that the pusher thickness (the unheated portion of the shell) is essentially constant, 0.05 mm, independent of beam voltage. There would appear to be an optimum voltage for these targets around 10 MeV: for higher voltages the current required for breakeven is essentially constant. (However, it may be easier to produce the required current and rise times at the higher voltage.) In order to utilize the higher voltage beams, it is necessary to use additional gold, primarily to reduce the proton energy to 10 MeV, thereby throwing away the energy above 10 MeV. Below 10 MeV the outer part of the shell is cut away, reducing the tamping effect of this part of the shell. As can be seen, this increases the current (but not the power) required for breakeven and reduces the thermonuclear energy produced by the target.

It has been suggested<sup>6</sup> that a further advantage of ion beams is that their momentum is considerably larger than for electron beams. It can be shown, for the cases of interest here, that the beam momentum produces a negligible effect on the implosion. The momentum fluence of the beam is

$$p_b \approx \phi/v,$$

where  $\phi$  is the energy fluence and  $v$  is the ion velocity (we neglect factors of order unity). The momentum per unit area imparted to the pusher by the pressure produced in the ablator is

$$p_p \approx P \Delta t,$$

where the pressure  $P$  is

$$P \approx \phi/r$$

and the time during which the pressure acts on the pusher is

$$\Delta t \approx r/c.$$

Here  $r$  is on the order of the ion range in the ablator, and  $c$  is the sound speed in the material. Thus, we have

$$\frac{p_b}{p_p} \approx \frac{c}{v}.$$

The temperature in the ablator is  $\frac{1}{2}$  to 1 keV so that any material used is well ionized, and the ratio of momenta can be written

$$\frac{p_b}{p_p} \approx \left( \frac{T_a}{T_b} \right)^{1/2},$$

where  $T_a$  is the ablator temperature and  $T_b$  is the energy per nucleon of the ion beam, both measured in eV. For  $T_a = 1$  keV and  $T_b = 10$  MeV, the beam momentum is about 1% of the pusher momentum.

### Symmetry and Stability

A central problem in laser fusion is the growth of Rayleigh-Taylor instability in the region of the ablator/pusher interface.<sup>25-27</sup> As will be seen it is of somewhat less concern in electron and ion beam targets. The growth rate  $n$  of the Rayleigh-Taylor instability can be written

$$n^2 = \alpha g k$$

in a number of situations.<sup>28</sup> Here  $g$  is the acceleration,  $k$  is the wave number,



and  $\alpha$  may be a function of density, wavenumber, etc., and is generally of order unity or less. For the classical case of an interface between two incompressible fluids,  $\alpha$  is equal to the Atwood number  $A$ ,

$$A = (\rho_1 - \rho_2)/(\rho_1 + \rho_2).$$

for an exponentially varying density,  $\alpha$  is given approximately by

$$\alpha \approx 2(2k/\beta + \beta/2k)^{-1},$$

where  $\beta = (\partial\rho/\partial z)/\rho$ . For  $\beta \approx 2k$ ,  $\alpha$  is largest and decreases on either side.

When a slab or pusher of finite thickness  $\tau$  is accelerated by a lower density ablator, the instabilities of the interface are attenuated by a factor  $\exp(-k\tau)$  at the surface of the pusher away from the ablator. This means that instabilities which are the most damaging to the fuel-pusher interface are those with a wavenumber  $k \approx \tau^{-1}$ . Shorter wavelength instabilities are attenuated outside of the unstable region, and they saturate (i.e., they have a linear rather than exponential growth) when their amplitude approaches their wavelength. Longer wavelengths grow more slowly and are thus less damaging. After being accelerated for a time  $t$ , an initial disturbance will have grown by an amount  $\exp(nt)$  where  $nt$  is

$$nt \approx t(g/\tau)^{1/2}.$$

The pusher will have moved a distance  $\ell$  given by

$$\ell = 1/2 g t^2$$

from which we may obtain

$$nt \approx (2\ell/\tau)^{1/2}.$$

This result gives rise to the rule-of-thumb that a pusher can not be accelerated over distances  $\ell$  greater than several times its thickness  $\tau$  before instabilities damage it. Of course, the allowable values of  $\ell/\tau$  depend on the size of the initial perturbation and on how large a distortion of the front surface can be tolerated. It is also apparent that spherical shells with large aspect ratios  $r/\tau$  can be imploded more successfully if they are accelerated during the initial part of the implosion rather than throughout the implosion.<sup>29</sup>

A plot of pressure and density profiles for one of our e-beam target calculations is shown in Figure 7. The region between the peak density and the peak pressure is unstable. For the purpose of estimating instability growth rates, we will use the relation

$$n^2 = 1/2 \, g \, \beta$$

for an instability of wave number  $k = 1/2 \, \beta$ . This can be written

$$n^2 = -1/2 \, \frac{1}{\rho} \, \frac{\partial \rho}{\partial r} \, \frac{1}{\rho} \, \frac{\partial \rho}{\partial r}.$$

A plot of the resulting values of  $n$  and  $\int n \, dt$  are shown in Figure 8 for an e-beam target. An initial perturbation would grow by a factor  $\exp \int n \, dt \approx 10$  by the time of the implosion at 7.8 ns. These constitute estimates of the upper limits instability growth: We have ignored the effects of convective stabilization, compressibility, changing wavenumber of maximum instability, and finite thickness of the unstable region. From the rather small growths seen here, it would appear that larger aspect ratio targets could

be used with little danger of their being destroyed by instabilities. For the ion beam targets the growth is somewhat larger, however both ion and electron beam targets of the type considered here seem to be rather stable by comparison with laser targets where more than 10 exponentiations ( $\exp(10) = 2 \times 10^4$ ) have been calculated.<sup>27</sup>

In attempting to compare the merits of various targets, it is necessary to consider not only the power required, but the symmetry or uniformity of irradiation that is required. In general, the higher the compression of the fuel, the higher the symmetry of the implosion must be. While a detailed analysis of the symmetry requirements is rather difficult, even with modern two-dimensional computer codes, a fairly simple approximate method can be used to estimate the symmetry requirements.<sup>30</sup> Unlike laser implosions, electron and ion beam implosions probably can not rely on thermal conduction to symmetrize the deposition. Thus the uniformity of irradiation can be related directly to the spread of implosion velocities:

$$\frac{2\Delta v}{v} \approx \frac{\Delta E}{E},$$

where  $v$  is the implosion velocity and  $E$  is the beam energy flux on the target. This velocity spread will result in a difference in the radial positions of the pusher at the implosion time (i.e., at turnaround) given by

$$\Delta r = \Delta v t_i$$

This radius error should be smaller than the calculated turnaround radius  $r_t$  to obtain a reasonable implosion. Combining these relations, we find the approximate symmetry condition

$$\frac{\Delta E}{E} \leq \frac{r_t}{r_i} = \left( \frac{V_t}{V_i} \right)^{1/3},$$

where  $V_i$  is the initial radius of the pusher,  $r_i = vt_i$ , and  $V_i$  and  $V_t$  are the fuel volumes initially and at turnaround. Thus a volume compression ratio ( $V_i/V_t$ ) of 1000 would require that the uniformity of illumination be about 10% or better.

Figure 9 represents an attempt to display both the power and symmetry requirements of various targets on a single graph. Each curve represents a given target type, with only the fuel mass being varied as one moves along the curve. Thus, increasing the fuel mass increases the power required to ignite the fuel, as we have seen before, but decreases the compression ratio and the symmetry requirement. The three curves marked "Au 0.5 mm," "Au 1 mm," and "Au 2 mm" are for gold shell targets irradiated by 1 MeV electrons and having an initial fuel radius  $r_i$  of 0.5, 1, and 2 mm. Comparing these curves, it is apparent that one should use as small a target as is consistent with the e-beam focal spot size and pulse length in order to minimize symmetry problems. The curve marked Fe/Au 1 mm is for the targets having iron ablaters and gold pushers. It would appear that these targets are better than gold shells of the same radius only for the higher compression ratios. Indeed the reason they perform better than the gold shells is that they can achieve a higher compression with a given fuel mass. Another feature that is not apparent in the graph is that the iron/gold shells produce higher thermonuclear gain for a given compression ratio. The curves marked 10 MeV protons are for proton beam targets which are very similar to the Au 0.5 mm and 1 mm electron beam

targets. Here there is clear advantage over the e-beam targets. In terms of beam current rather than power, the proton beam targets appear even more advantageous.

One of our major concerns is the Taylor instability of the pusher-fuel interface near maximum compression. This could cause some of the pusher to mix with the fuel, reducing the burn. One way of estimating the effect of this instability is to calculate the yield before the free fall line shown in Figure 10 reaches the center. While this is a relatively crude method, there does not appear to be any other method in use that has significantly greater accuracy. For the case shown in Figure 10 most of the yield occurs after this "fall time," however, this is not always the case.

Figure 11 shows a comparison of the total thermonuclear yield with the thermonuclear yield obtained prior to the fall time. This graph is for 200  $\mu\text{g}$  of fuel. For smaller fuel mass the difference between the curves is greater; for larger fuel masses the curves are closer together. If the Taylor instability of the inner surface of the pusher is indeed a serious problem, then the beam power required for breakeven is roughly doubled in this case. Similar results are also obtained for other types of targets. In general, the beam power must be increased by a factor of  $1\frac{1}{2}$  to 2 in order to have the thermonuclear burn occur before the fall time.



## References

1. F. Winterberg, Phys. Rev. 174, 212 (1968); F. Winterberg, in Physics of High Energy Density, Academic Press, New York (1971) 370.
2. M. V. Babykin, E. K. Zavoiskii, A. A. Ivanov, and L. I. Rudakov, in Plasma Physics and Controlled Thermonuclear Fusion Research (Proc. 4th Int. Conf. Madison, 1971) 1, IAEA, Vienna (1971) 635; L. I. Rudakov and A. A. Samarsky, in Controlled Fusion and Plasma Physics (Proc. 6th Europ. Conf. Moscow, 1973) Moscow (1973) 487.
3. G. Yonas, J. W. Poukey, J. R. Freeman, K. R. Prestwich, A. J. Toepfer, M. J. Clauser, and E. H. Beckner, in Controlled Fusion and Plasma Physics (Proc. 6th Europ. Conf. Moscow, 1973) Moscow (1973) 483; G. Yonas, J. W. Poukey, K. R. Prestwich, J. R. Freeman, A. J. Toepfer, and M. J. Clauser, Nuclear Fusion 14, 731 (1974).
4. M. J. Clauser, Bull. Am. Phys. Soc. 19, 856 (1974); Phys. Rev. Letters 34, 570 (1975).
5. R. C. Kirkpatrick, C. C. Cremer, L. C. Madsen, H. H. Rogers, and R. S. Cooper, Postdeadline Paper presented at the Amer. Phys. Soc. meeting, in Albuquerque, November 1974; R. C. Kirkpatrick, et al., Nuclear Fusion 15, 333 (1975).
6. J. W. Shearer, "Ion Beam Compression of Thermonuclear Pellets," UCRL-76519, (1975). Submitted to Nuclear Fusion.
7. M. J. Clauser and M. A. Sweeney, 2nd Int'l. Conf. on Plasma Sci., Ann Arbor, 1975.
8. M. A. Sweeney and M. J. Clauser, Appl. Phys. Letters 27, 483 (1975) and Bull. Am. Phys. Soc. 20, 1272 (1975).
9. M. J. Clauser, Phys. Rev. Letters 35, 848 (1975).

10. J. D. Lindl, R. O. Bangerter, and D. Meeker, Int'l. Topical Conf. on E-Beam Res. and Tech., Albuquerque, 1975.
11. D. Mosher, 2nd Int'l. Conf. on Plasma Sci., Ann Arbor, 1975; Phys. Rev. Lett. 35, 851 (1975).
12. D. A. Tidman, submitted to Phys. Rev. Letters.
13. J. W. Poukey, Int'l. Topical Conf. on E-Beam Res. and Tech., Albuquerque, 1975.
14. S. Humphries, J. J. Lee, and R. N. Sudan, Appl. Phys. Lett. 25, 20 (1974); J.A.P. 46, 187 (1975); S. Humphries, Jr., R. N. Sudan, and W. C. Condit, Jr., Appl. Phys. Lett. 26, 667 (1975).
15. P. A. Miller, C. W. Mendel, D. W. Swain, and S. A. Goldstein, Int'l. Conf. on E-Beam Res. and Tech., Albuquerque, 1975.
16. J. T. Verdeyen, D. A. Swanson, B. E. Cherrington, and W. L. Johnson, Appl. Phys. Lett. 27, 380 (1975).
17. J. W. Poukey, Proc. 13th Symposium on Electron, Ion, and Photon Beam Technology, Colorado Springs, May 1975; J. W. Poukey, J. R. Freeman, M. J. Clauser, and G. Yonas, submitted to Appl. Phys. Lett.; Bull. Am. Phys. Soc. 20, 1382 (1975).
18. R. L. Martin, Bull. Am. Phys. Soc. 20, 209 (1975); IEEE Trans. on Nucl. Sci. NS-22, 1763 (1975); R. Arnold and R. Martin, Int'l. Conf. on Radiation Test Facilities for the CTR Surface and Materials Program, Argonne, 1975.
19. A. W. Maschke, Particle Accel. Conf., Washington, D. C., 1975.
20. Shyke A. Goldstein and Roswell Lee, Phys. Rev. Lett. 35, 1079 (1975); Shyke A. Goldstein and John Guillory, Phys. Rev. Lett. 35, 1160 (1975).

21. C. L. Olson, Bull. Am. Phys. Soc. 20, 1382 (1975); Int'l. Topical Conf. on E-Beam Res. and Tech. Albuquerque, 1975.
22. K. D. Bergeron, Bull. Am. Phys. Soc. 20, (1975).
23. J. Chang, L. P. Mix, F. C. Perry, M. M. Widner, and J. W. Poukey, Int'l. Topical Conf. on E-Beam Res. and Tech., Albuquerque, 1975.
24. W. Whaling, Handbuch der Physik 34, 193 (1958); W. H. Barkas and M. J. Berger, "Tables of Energy Losses and Ranges of Heavy Charged Particles" in Studies in Penetration of Charged Particles in Matter, Nuclear Science Series, Report No. 39, Nat'l. Acad. of Science, Nat'l. Res. Council, Wash., D. C. (1964), p. 103.
25. D. B. Henderson and R. L. Morse, Phys. Rev. Lett. 32, 355 (1974); D. B. Henderson, R. L. McCrory, and R. L. Morse, Phys. Rev. Lett. 33, 205 (1974).
26. J. N. Shiau, E. B. Goldman, and C. I. Weng, Phys. Rev. Lett. 32, 352 (1974).
27. J. D. Lindl and W. C. Mead, Phys. Rev. Lett. 34, 1273 (1975); W. C. Mead and J. D. Lindl, Proceedings of Orbis Scientiae II, Coral Gables, Florida, Jan. 19-24, 1975.
28. S. Chandrasekhar, Hydrodynamic and Hydromagnetic Stability, Oxford University Press, London (1961), pp. 428-480.
29. G. S. Fraley, W. P. Gula, D. B. Henderson, R. L. McCrory, R. C. Malone, R. J. Mason, and R. L. Morse, 5th IAEA Conf. on Plasma Physics and Cont. Nuc. Fusion Res., Tokyo, 1974.
30. J. Nuckolls, L. Wood, A. Thiessen, and G. Zimmerman, Nature (London) 239, 139 (1972).

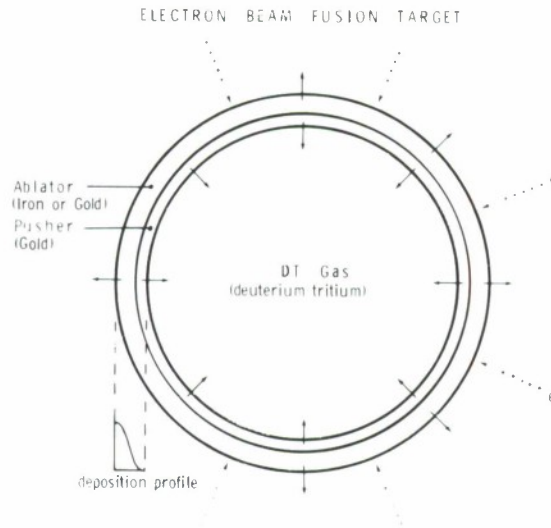


Figure 1. Schematic diagram of electron beam fusion target.

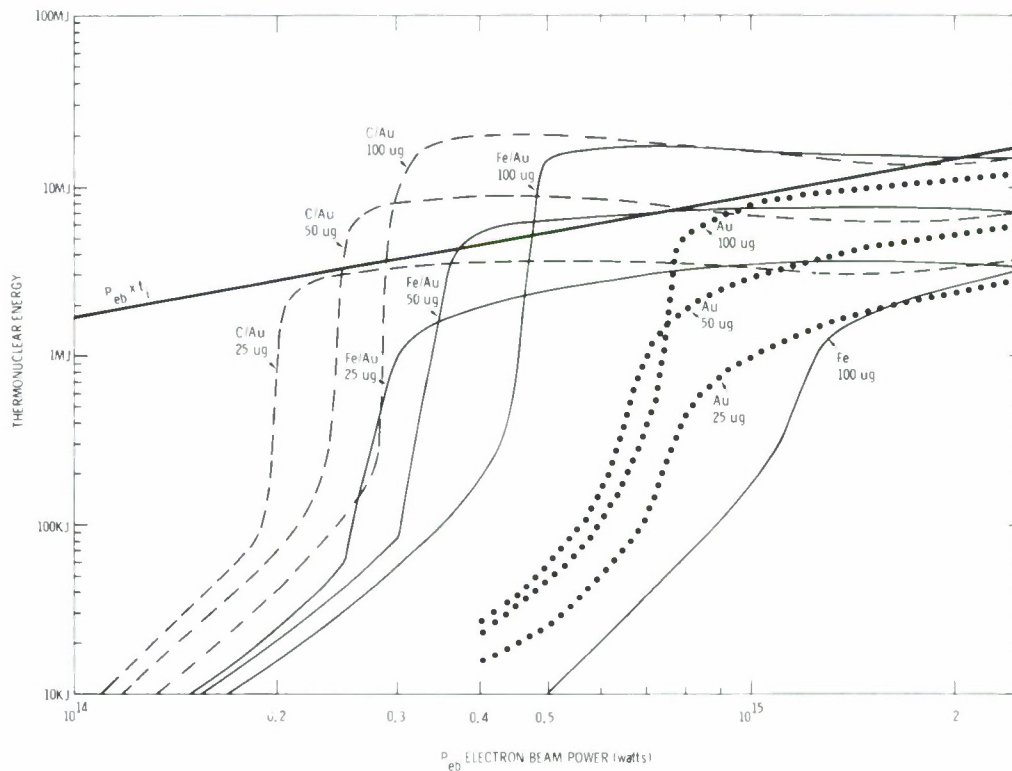


Figure 2. Thermonuclear energy production, calculated for various electron beam targets. All targets had a DT fuel radius of 1 mm and were irradiated by 1 MeV electrons. Each curve is labeled by the mass of DT fuel and by the composition of the shell - C/Au denotes a carbon (diamond) ablator and a gold pusher. The straight line labeled  $P_{eb} \times t_i$  is the product of the electron beam power and the implosion time for the Fe/Au targets, and is an approximate upper limit on the energy required to implode the targets.

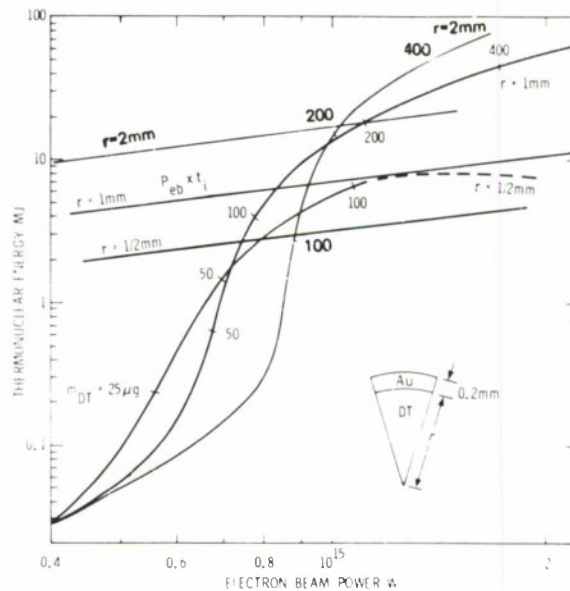


Figure 3. Thermonuclear energy production calculated for electron beam targets of various radii. All targets have an all-gold shell, 0.2 mm thick, and are irradiated by 1 MeV electrons. For each point on the curves the fuel mass is optimized, and the optimal fuel mass is denoted at various points along the curves.

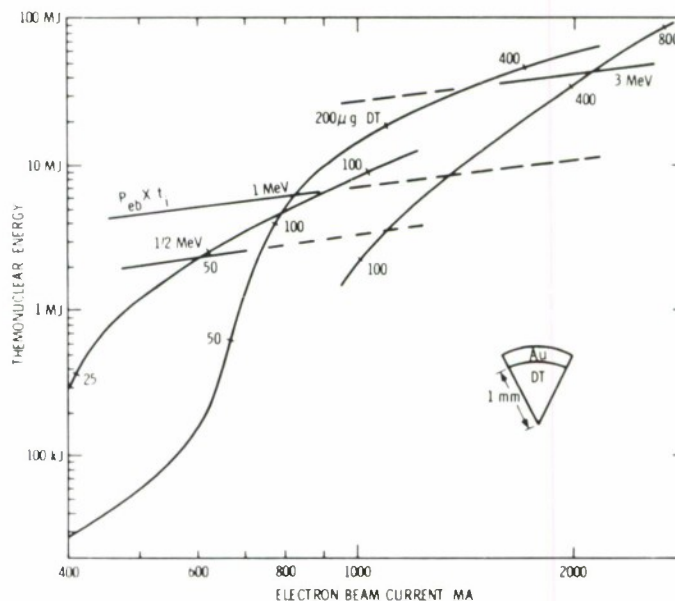


Figure 4. Thermonuclear energy production calculated for electron beam targets irradiated by electron beams of various voltages. All targets have an all-gold shell with thickness optimized for each voltage. The fuel radius is 1 mm in all cases.



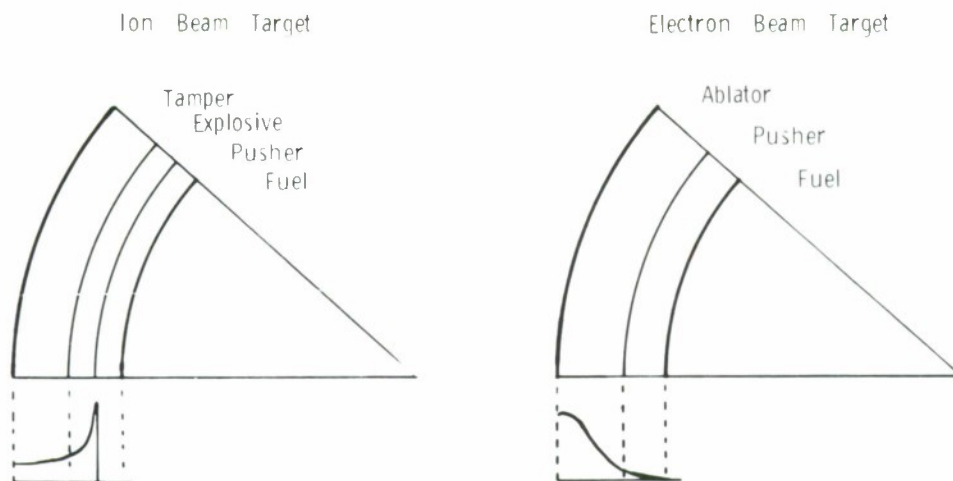


Figure 5. Schematic comparison of ion and electron beam targets. The curves beneath each diagram are energy deposition profiles.

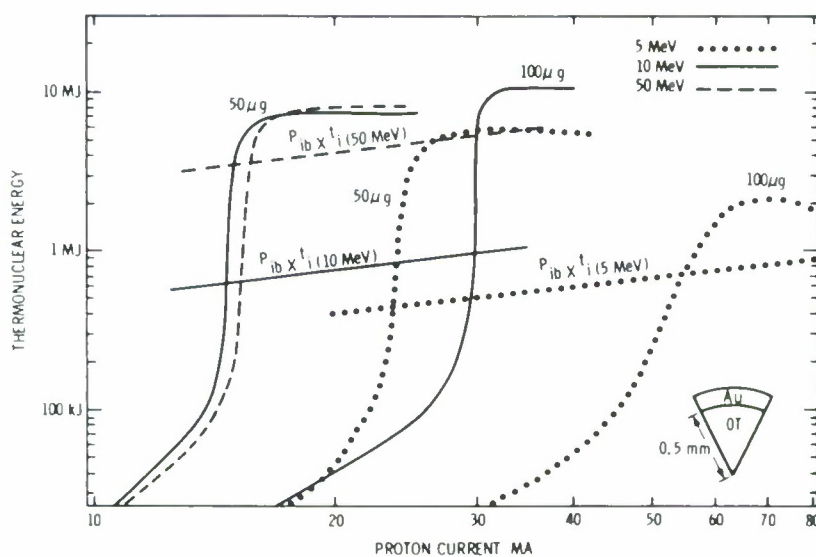


Figure 6. Thermonuclear energy production calculated for various ion beam targets. All targets have a fuel radius of 0.5 mm and a gold sheath with a thickness optimized for the proton beam voltage. The DT fuel mass is indicated for each curve.

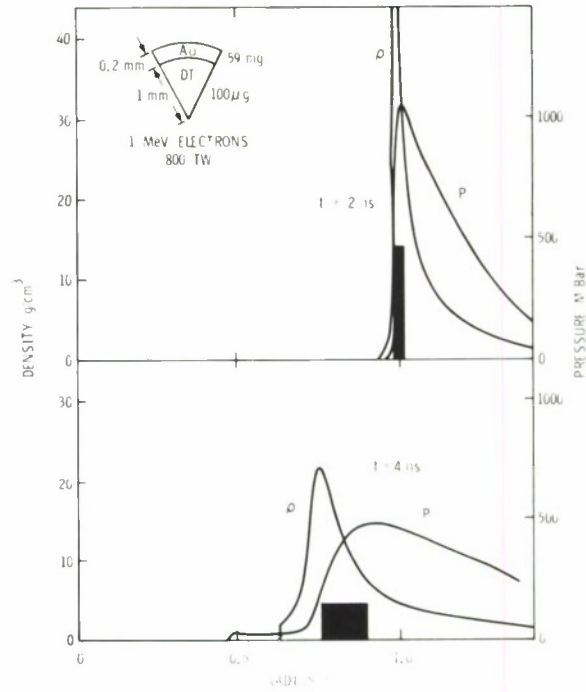


Figure 7. Pressure (P) and density ( $\rho$ ) profiles calculated for an electron beam target (see insert) at 2 ns and 4 ns after the beginning of the pulse. The width of the solid bar in each graph denotes the Taylor-unstable region, and the height of the bar is proportional to the instantaneous growth rate.

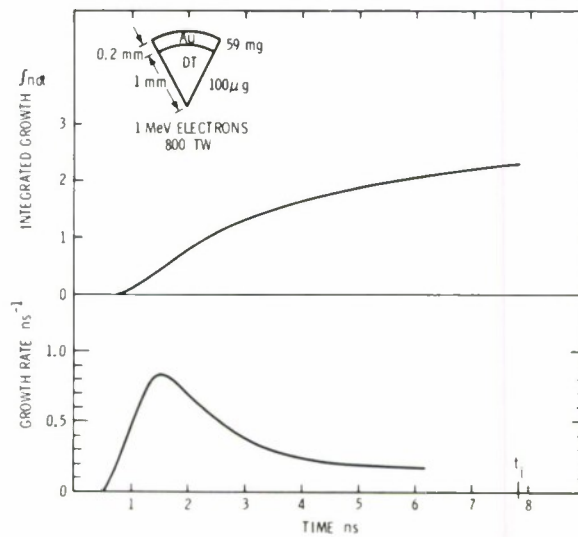


Figure 8. Instantaneous growth rate and time-integrated growth of the Rayleigh-Taylor instability of the target in Fig. 7.

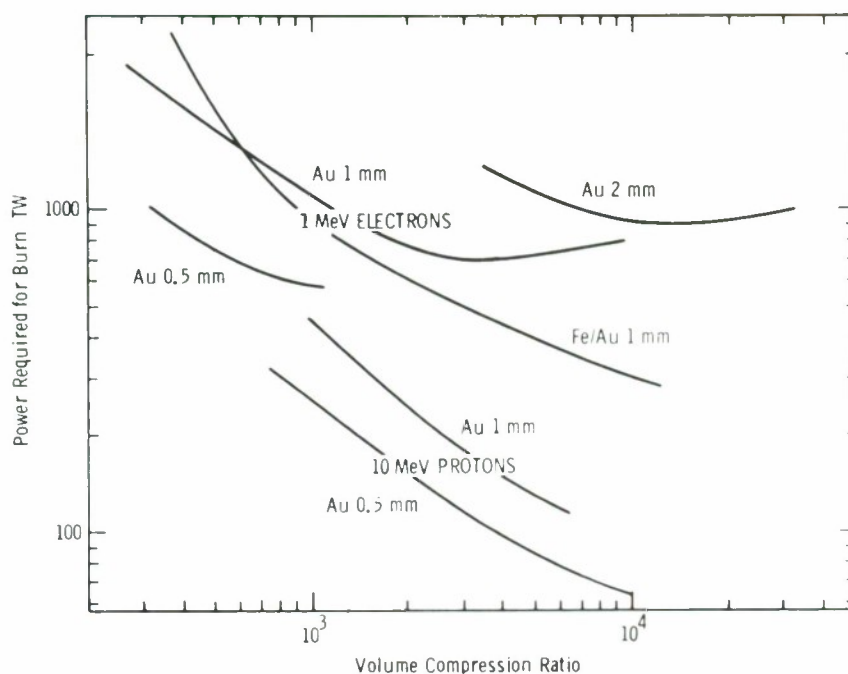


Figure 9. Beam power required to initiate burn in various targets plotted versus the volume compression ratio of the fuel. The upper curves are for 1 MeV electron beam targets with all-gold (Au) and iron-over-gold (Fe/Au) shells. The lower curves are for 10 MeV proton beam targets. The dimension (0.5 mm, etc.) denotes the fuel radius. For each curve the fuel mass increases towards the left.

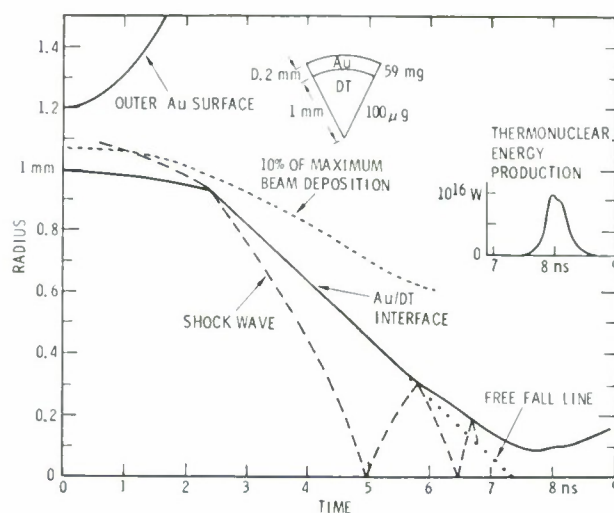


Figure 10. Plot of the radius of various parts of an electron beam target as a function of time (see ref. 4). The "Free Fall Line" has the maximum velocity of the Au/DT interface.

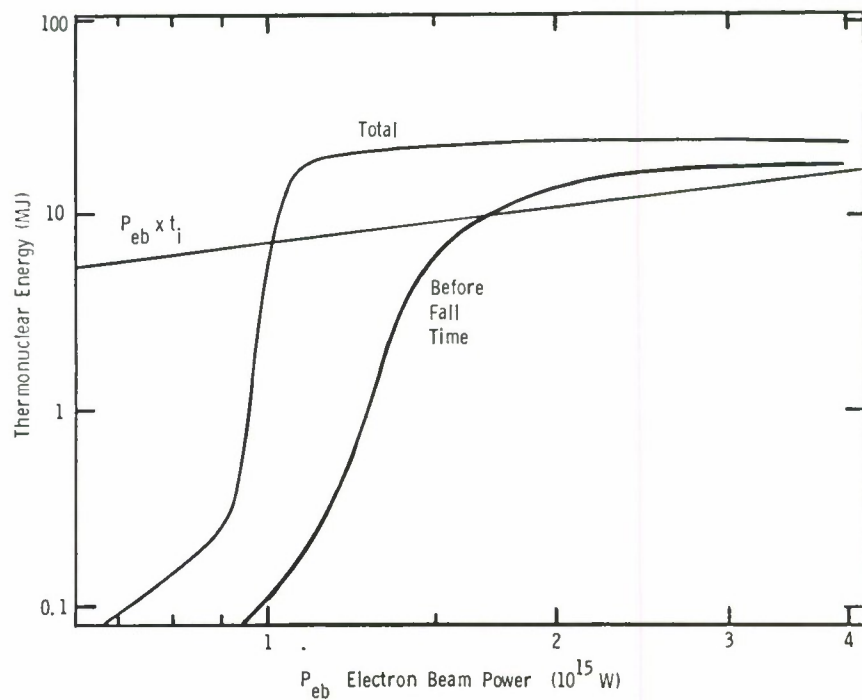


Figure 11. Comparison of total thermonuclear yield and yield produced before the fall line in Fig. 10 reaches the target center. The targets in these calculations are the same as in Figure 10 except that the DT fuel mass is 200  $\mu\text{g}$  here.

# ELECTRON BEAM FUSION PELLETS\*

by

W. P. Gula and R. C. Kirkpatrick

University of California  
Los Alamos Scientific Laboratory  
Los Alamos, New Mexico 87545

## ABSTRACT

Double shelled pellets seem attractive for the current generation of relativistic electron beam machines such as HYDRA because of the low density of the energy deposited in the relatively heavy shell. This low energy density yields implosion speeds of the order of 1 cm/ $\mu$ sec, which is insufficient to compress and heat the fuel to fusion conditions. Because of the expectation that the inner shell of a double shelled pellet would move at a greater implosion velocity than the outer shell, an investigation was made with computer simulation codes to determine whether such a pellet could produce neutrons, what would be the best design of such a pellet for the HYDRA device, and what problems we might expect.

Our studies indicate that fuel ion temperatures of a few hundred electron-volts can be reached and that a measurable number of neutrons should be produced.

One problem, in particular, that might cause difficulty is the preheating of the inner shell, either by bremsstrahlung or by the relativistic electrons themselves.

Various simulation results will be presented.

---

\*This work was performed under the auspices of the United States Energy Research and Development Administration.



Papers have already been published concerning requirements for relativistic electron beam fusion pellets.[1-3] In this paper we are concerned only with pellet design for the HYDRA relativistic electron beam machine which will provide neutrons for diagnostics. Experiments with this machine have already indicated that irradiation of a 0.2 mm thick gold hemishell of 4 mm inner diameter filled with 100 atm of  $D_2$  gas does not produce neutrons. Indeed, measurements show that the implosion velocity of the shell is on the order of  $10^6$  cm/sec, which is insufficient to heat DT fuel to fusion temperatures. [4]

We are searching for pellet designs that will give neutrons using the present HYDRA machine. The reasons are 1) we want to demonstrate that relativistic electron beam fusion can occur and 2) the neutrons are the only diagnostic capable of telling us what is happening in the fuel. The low implosion velocity in the experiment cited above led us to consider the possibility of velocity multiplication from the use of multiple shells. In practice we have limited our present calculations to double shell pellet designs in order to limit the size of the parameter space under consideration and to make life easier for the pellet fabrication group.

We have also put several other constraints upon our design considerations. For the most part we have used a 12 kJ, 85 nsec pulse with a constant power of  $1.41 \times 10^{11}$  W. We feel that this is a reasonable pulse to simulate the output of the HYDRA machine. Most of the calculations have used an outer shell of gold with a density of  $19.3 \text{ g/cm}^3$ , an inner diameter of 3 mm, a thickness of 0.2 mm, and a mass of 125 mg. The fuel has been DT gas with a density of  $0.0238 \text{ g/cm}^3$ . Figure 1 shows a cutout wedge diagram of a double shell design. Our parameter variation has dealt mainly with the

position, mass, and material of the inner shell and with the form of the energy absorption.

One rather important result of these calculations is the fact that the quality of the implosion is very sensitive to the tail of the energy absorption function, a result that has been previously noted by Clauser[2] for single shell targets. A typical function used is shown in Figure 2 as specific energy vs. radius and in Figure 3 as energy absorbed vs. radius for a specific time in one calculation. The function is actually a function of  $\rho r$  and so it varies with time when presented as a function of radius. Figures 4 and 5 show the specific energy vs  $\rho r$  and the energy absorbed vs  $\rho r$ . One can see that very little energy is absorbed inside the inner surface of the outer shell. However, when the energy function is truncated at the point where  $\rho r = 0.753 \text{ g/cm}^2$  which is the classical range of a 1 MeV electron in gold, the behavior of the system improves dramatically. For one design, for instance, the number of neutrons produced by the truncated absorption is up by almost two orders of magnitude while the fuel peak average ion temperature and density are up by factors of 2 and 4 respectively. This energy deposition tail is due mainly to the bremsstrahlung produced by the 1 MeV electrons as they stop in the gold outer shell. This degradation of performance was also noted by Clauser [2] in his breakeven calculations when he let a truncated electron-only profile penetrate the shell. At least two means of reducing this problem have been suggested. One is to have a double layered outer shell composed of an iron ablator over a gold pusher. [5] Since the conversion efficiency of electron kinetic energy to x-rays is less in iron than in gold, this would help alleviate the problem by producing fewer x-rays to be absorbed by the inner portions of the pellet. Since the absorption

rate of x-rays by iron is less than that by gold, the second means suggested to reduce the tail absorption problem is to have the inner shell be of iron or some other material of lower Z than gold. At this time, however, it is not clear whether the advantage of reduced x-ray absorption by the inner shell is outweighed by the disadvantage of a lower density inner shell.

We have varied the position of the inner shell. In these studies the mass of the inner shell has been kept constant at 12.5 mg, thus giving a 10:1 mass ratio between the outer and inner shells. The cushion gas is hydrogen at  $0.0238 \text{ g/cm}^3$  initially. For these calculations the optimum inner diameter of the inner shell is less than 0.2 mm. This is with the absorption tail. If the absorption is truncated at  $\rho r = 0.753 \text{ g/cm}^2$  the optimum inner diameter is 0.75 mm. The number of neutrons predicted by these different calculations are  $2 \times 10^5$  and  $2 \times 10^6$  respectively. The minimum number of neutrons that can be detected by the current instrumentation at the HYDRA machine is  $10^4$ .

The variation in the implosion as the inner radius of the inner shell is varied as shown in figures 6-9. They show the number of neutrons produced, the peak average fuel ion temperature, the peak average fuel density, and the maximum implosion velocity of the inner shell. At this time these curves are not completely understood. The improvement in the maximum implosion speed of the inner shell shown in figure 9 as the shell radius becomes smaller is partly the result of a longer runup time and partly because of the lower conversion of implosion energy to internal energy in the inner shell.[1] The improvement in the fuel ion temperature shown in figure 7 results from the improved implosion speed. The relative flatness

of the fuel density curve of figure 8 indicates that most of the improved neutron yield of figure 6 is due to the increased heating. The dip in the neutron yield shown in figure 6 in spite of a temperature rise seems to be the result of the diminishing fuel mass and a shorter burn time. In any case, more points need to be calculated, especially at smaller radii.

The implosion itself proceeds as shown in figures 10-15. They show temperature, pressure, density, and velocity profiles 1) at an early stage when the energy is being absorbed, 2) when the outer shell is up to its peak implosion speed, 3) when the two shells are at their point of closest approach, 4) when the inner shell is at its peak implosion speed, 5) when the fuel is at peak compression, and 6) at disassembly.

Figure 10 shows a blowoff region being formed and the acceleration of the outer shell to  $\sim 10^6$  cm/sec. At this point a little more than half the energy has been absorbed. In figure 11 all the energy has been absorbed and the outer shell has attained its maximum implosion speed. Figure 12 shows the point of closest approach of the "collision" of the two shells. The implosion speed at this time is  $\sim 0.75 \times 10^6$  cm/sec. The fuel is still relatively cold and uncompressed. Figure 14 is at the peak compression. At this time the average fuel density is  $10.5 \text{ g/cm}^3$  and the fuel average ion temperature is 45 eV. The peak fuel density is  $12.9 \text{ g/cm}^3$  and the peak fuel ion temperature is 107 eV. This particular run was not very successful in producing neutrons. Only the center of the fuel (less than 1% of the fuel mass) became hot enough to exceed the burn calculation threshold. In figure 15 the entire system is expanding.

In short, we have started and are continuing an investigation of double shell targets in order to design them for experiments on the HYDRA machine at Sandia Laboratories in Albuquerque. The calculations presented here

have been done with a one dimensional spherically symmetric ideal gas code and since more realistic equations of state reduce the implosion velocities somewhat, these results should be treated with some caution. However, we feel that these calculations show that the double shell experiments are worth doing on HYDRA. It is highly desirable from a theoretical point of view that two dimensional calculations and stability calculations be done and some preliminary work has been started along these lines. In any case, the current delivery date of the first double shell pellets to Sandia is late January or early February. Hopefully, we will have experimental data to compare with our calculations soon after that.

#### REFERENCES

1. R. C. Kirkpatrick, C. C. Cremer, L. C. Madsen, H. H. Rogers, and R. S. Cooper, Nuclear Fusion 15, 333 (1975).
2. M. J. Clauser, Phys. Rev. Lett. 34, 570 (1975).
3. L. I. Rudakov and A. A. Samarsky, in Proceedings of the Sixth European Conference on Controlled Fusion and Plasma Physics, Moscow, U.S.S.R., 1973, (U.S.S.R. Academy of Sciences, Moscow, 1973), p. 487.
4. A. J. Toepfer, Private Communication.
5. M. A. Sweeney and M. J. Clauser, Appl. Phys. Lett. 27, 483 (1975).



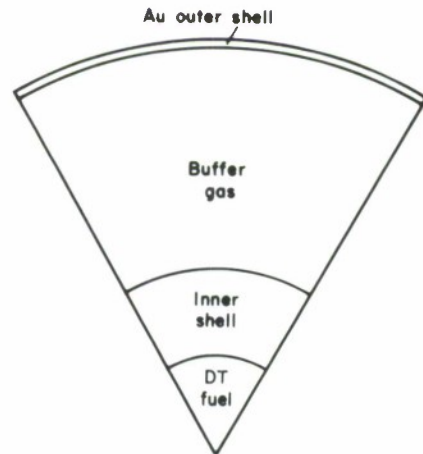


Figure 1. Wedge coutout diagram showing double shell pellet construction.

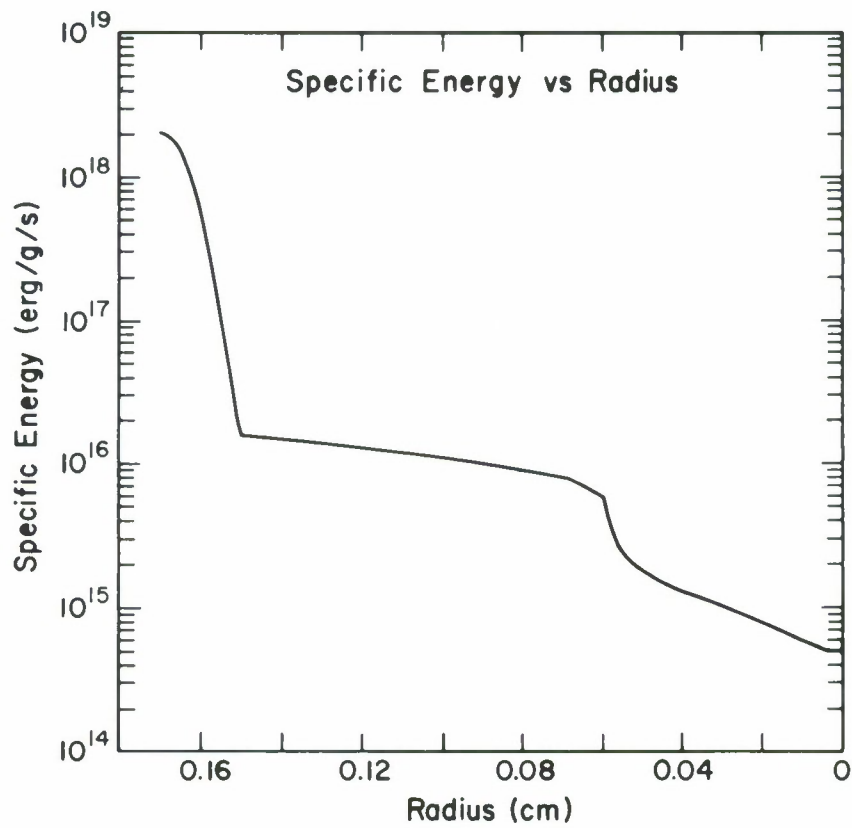


Figure 2. Specific energy vs radius for a typical design.

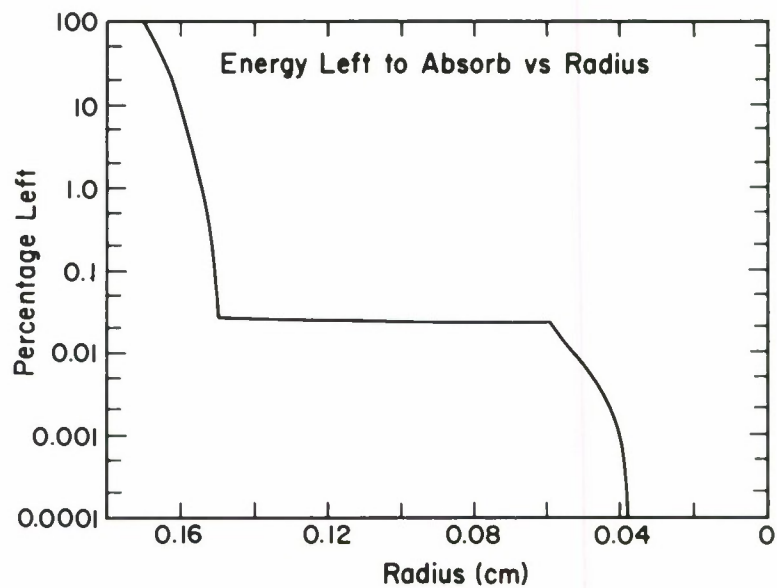


Figure 3. Energy left to absorb vs radius for a typical design.

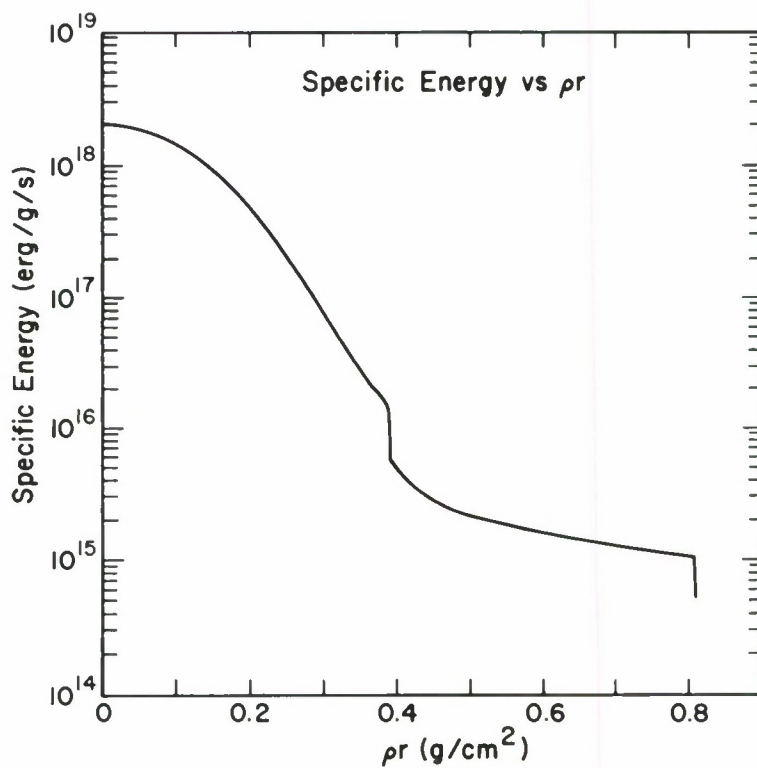


Figure 4. Specific energy vs  $\rho r$  for a typical design.

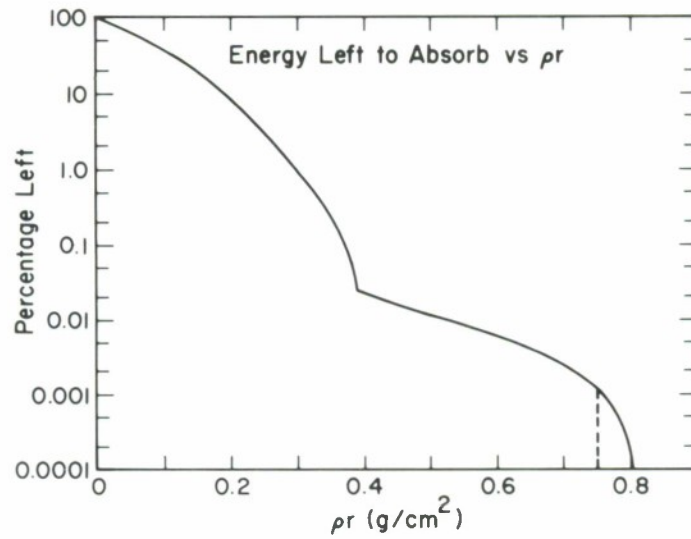


Figure 5. Energy left to absorb vs  $\rho r$  for a typical design. The dashed line at  $\rho r = 0.753 \text{ g/cm}^2$  is where the absorption was truncated for some of the calculations.

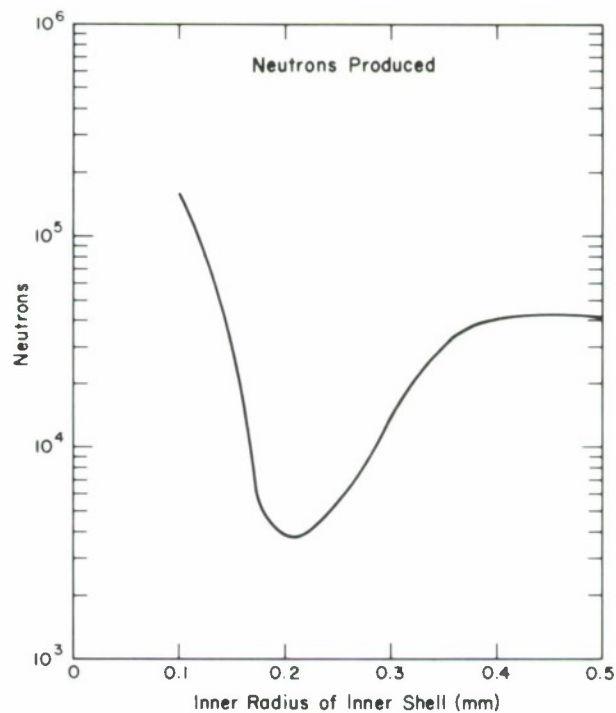


Figure 6. Neutrons produced vs the inner radius of the inner shell.

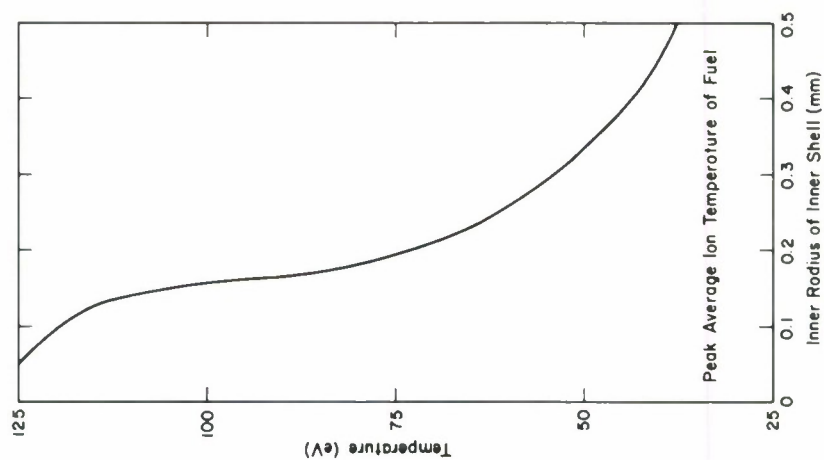


Figure 7. The peak space averaged ion fuel temperature vs the inner radius of the inner shell.

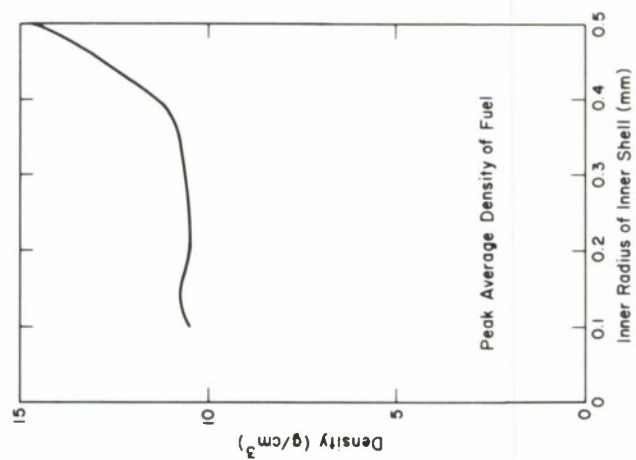


Figure 8. The peak space averaged fuel density vs the inner radius of the inner shell.

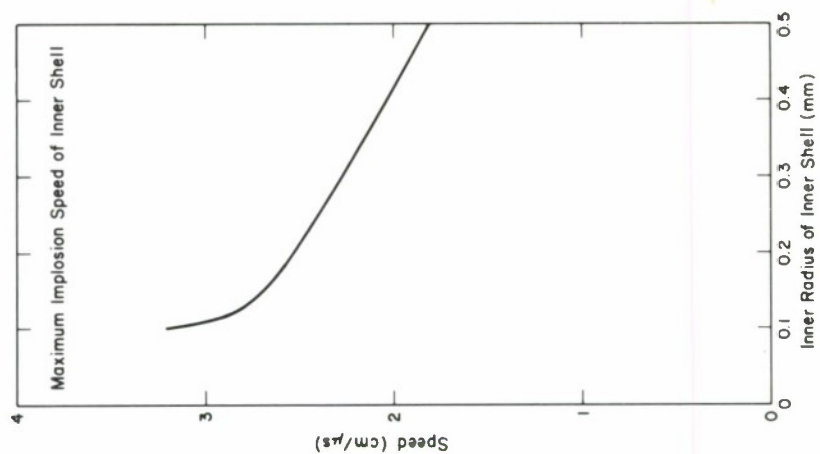


Figure 9. The maximum implosion speed of the inner shell vs the inner radius of the inner shell.

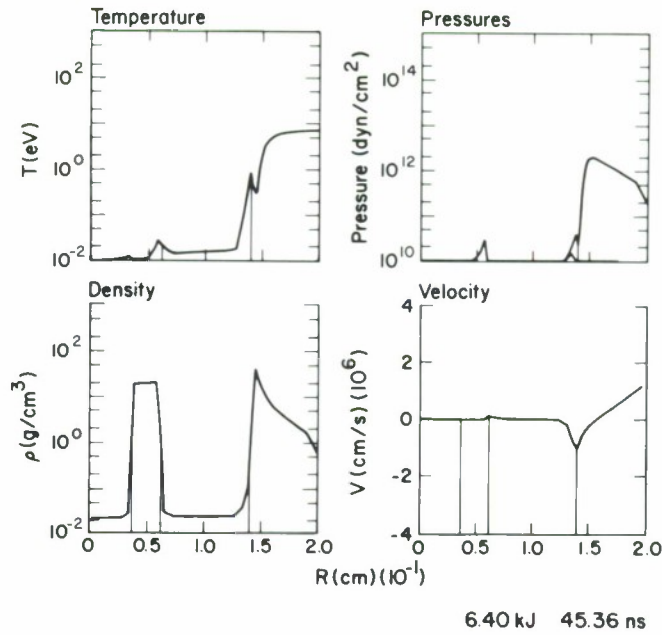


Figure 10. Temperature, pressure, density, and velocity profiles of the pellet 45 nsec after the start of the e-beam pulse. The vertical lines are the material boundaries. The upper curve (marked by T's) of the pressure graph is the total pressure. The lower curve (marked by V's) is viscous pressure which indicates where shock heating occurs.

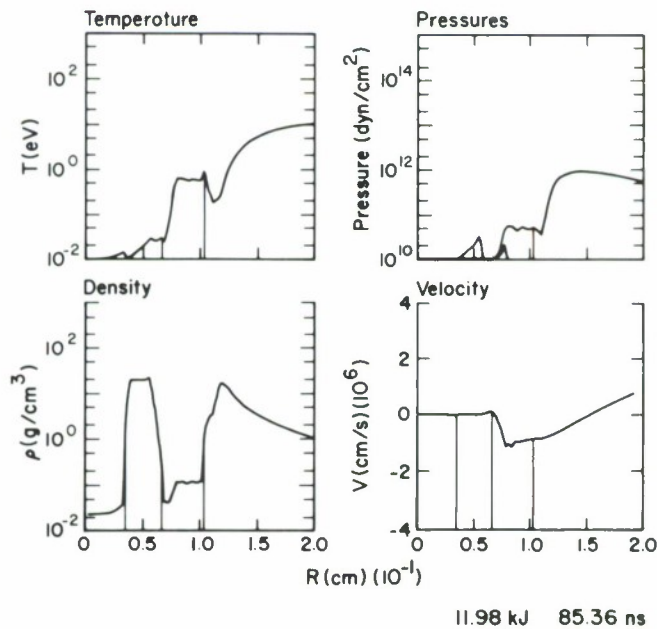


Figure 11. Temperature, pressure, density, and velocity profiles of the pellet 85 nsec after the start of the e-beam pulse. The vertical lines are the material boundaries. The upper curve (marked by T's) of the pressure graph is the total pressure. The lower curve (marked by V's) is viscous pressure which indicates where shock heating occurs.



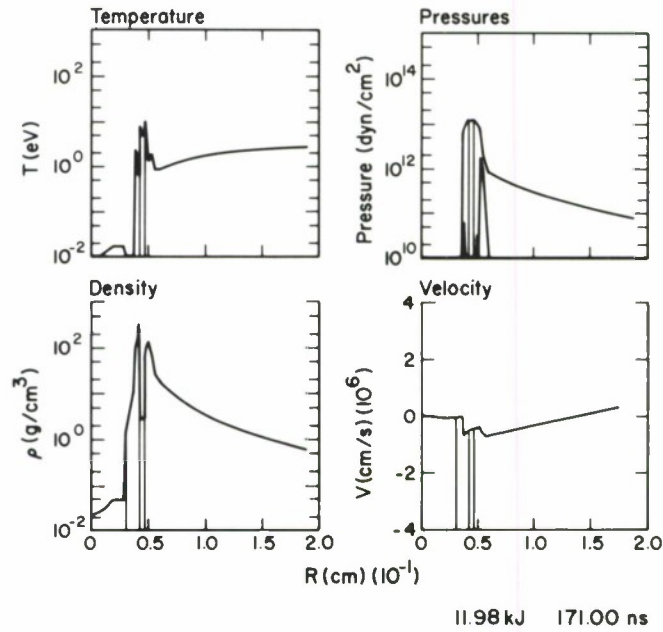


Figure 12. Temperature, pressure, density, and velocity profiles of the pellet 171 nsec after the start of the e-beam pulse. The vertical lines are the material boundaries. The upper curve (marked by T's) of the pressure graph is the total pressure. The lower curve (marked by V's) is viscous pressure which indicates where shock heating occurs.

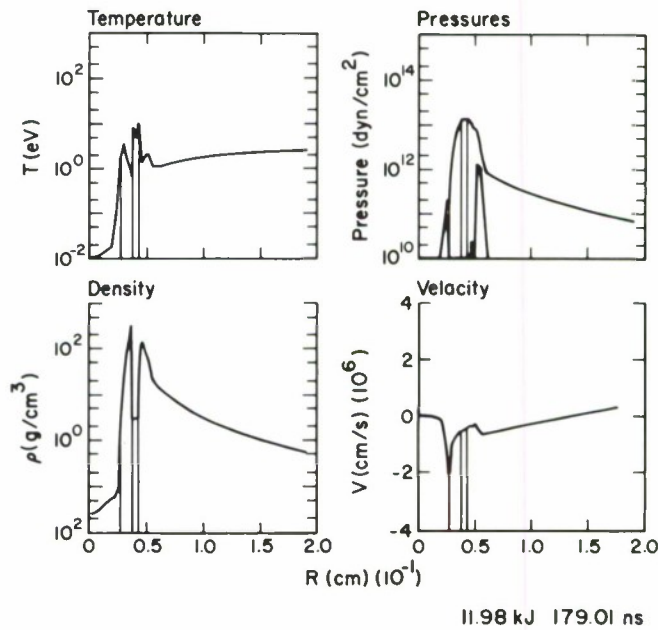


Figure 13. Temperature, pressure, density, and velocity profiles of the pellet 179 nsec after the start of the e-beam pulse. The vertical lines are the material boundaries. The upper curve (marked by T's) of the pressure graph is the total pressure. The lower curve (marked by V's) is viscous pressure which indicates where shock heating occurs.

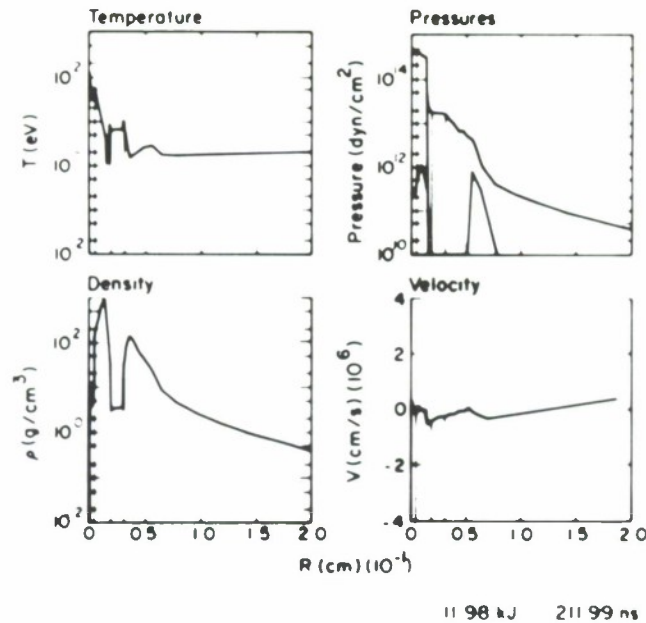


Figure 14. Temperature, pressure, density, and velocity profiles of the pellet 212 nsec after the start of the e-beam pulse. The vertical lines are the material boundaries. The upper curve (marked by T's) of the pressure graph is the total pressure. The lower curve (marked by V's) is viscous pressure which indicates where shock heating occurs.

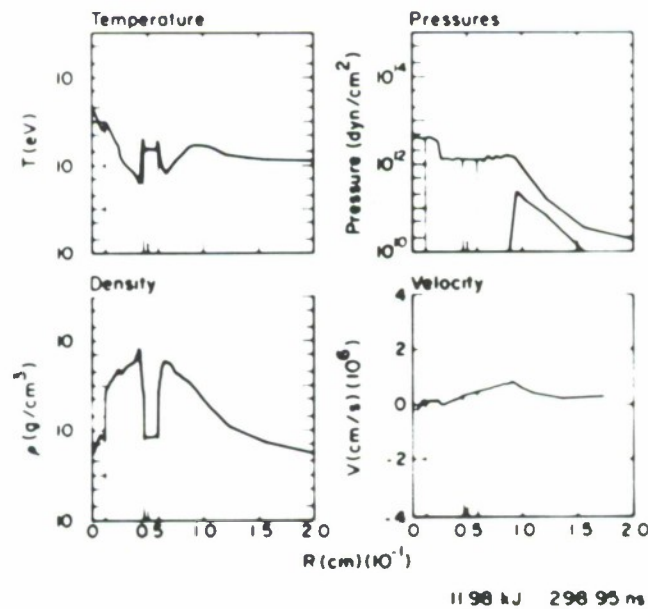


Figure 15. Temperature pressure, density, and velocity profiles of the pellet 299 nsec after the start of the e-beam pulse. The vertical lines are the material boundaries. The upper curve (marked by T's) of the pressure graph is the total pressure. The lower curve (marked by V's) is viscous pressure which indicates where shock heating occurs.

INTERACTION OF CYLINDRICALLY-SYMMETRIC RELATIVISTIC ELECTRON  
BEAMS WITH PLANAR TARGETS AND PLASMAS:  
THEORY AND APPLICATIONS

D. Mosher

Naval Research Laboratory, Washington, D. C. 20375

ABSTRACT

A diffusion theory for the collisional interaction of relativistic electron beams with high-atomic-number plasmas\* is used to develop analytical expressions for the beam-momentum distribution function in a slab target or plasma for the case of a normally-incident, well-collimated, monoenergetic beam with any radial profile. Moments of the distribution function are calculated for a Gaussian incident profile of arbitrary width. Using these, contour plots of energy deposition and current flow are determined. Bremsstrahlung intensity profiles corresponding to pinhole photographs of tightly-pinched beams are presented for various ratios of incident beam width to electron range. Theoretical deposition profiles, current transmission, and energy coupling of beam to target are compared with the results of Monte Carlo calculations.

---

\*D. Mosher, Phys. Rev. Lett. 35, 851 (1975).

## I. INTRODUCTION

Computer codes which model the hydrodynamic response of initially-solid targets to pinched relativistic-electron-beam deposition are used to diagnose existing experimental beams<sup>1</sup> and to predict pellet-fusion feasibility.<sup>2</sup> To one degree or another, target heating in these codes is determined by the results of Monte Carlo calculations which model the collisional interaction of beam electrons with solid and ensuing plasma portions of the target. One-dimensional hydro-codes employ Monte Carlo-generated energy deposition profiles and beam transmission coefficients which scale with target density. Thus, the results of a single particle-in-cell (PIC) calculation can be used continuously as the target density profile changes. Unfortunately, inclusion of realistic beam scattering in higher-dimension codes require either that they be coupled to a PIC code or that some other model for the beam-target interaction be included. Coupling of hydro and Monte Carlo codes has been successfully carried out.<sup>3</sup> However, this procedure usually requires lengthy, and therefore costly, computer calculations which may be inappropriate for routine numerical research such as parameter studies. It is therefore desirable to have available an analytical model for the coulomb-scattering and energy-loss aspects of the beam-plasma interaction which can be incorporated into hydrodynamic calculations. Such a model is the subject of this paper. The relativistic Boltzmann equation with a Fokker-Planck collision term is solved assuming that elastic scattering characterizes the shortest time

scale of the beam plasma system. Selected moments of the relativistic-electron distribution function then yield the desired beam-plasma coupling coefficients and energy-deposition characteristics.

The momentum-distribution function of the beam electrons is determined from<sup>4</sup>

$$\frac{\partial f}{\partial t} + \frac{\vec{p}}{m\gamma} \cdot \nabla f - e \left( \vec{E} + \frac{\vec{p} \times \vec{B}}{m\gamma} \right) \cdot \nabla_p f = \nabla_p \cdot \left[ \nu_S(p) (p^2 \vec{I} - \vec{p}\vec{p}) \cdot \nabla_p f \right] + \nabla_p \cdot \left[ \nu_E(p) \vec{p} f \right], \quad (1)$$

where  $\gamma^2 = 1 + p^2/(mc)^2$ . The quantities  $\nu_S$  and  $\nu_E$  are scattering and energy-loss frequencies

$$\nu_S = \Omega_S \gamma / (\gamma^2 - 1)^{3/2} \quad ; \quad \nu_E = \epsilon \gamma \nu_S, \quad (2)$$

where  $\Omega_S = 2\pi n_i r_o^2 c (Z^2 + Z) \ln \Lambda$  and  $\epsilon = 2/(Z + 1)$ . Here,  $n_i$  is the plasma ion density,  $r_o$  is the classical electron radius,  $c$  is the velocity of light,  $Z$  is the plasma atomic number, and  $\ln \Lambda$  is about 10.

Equation (1) has been solved with the assumption that the elastic-scattering time  $\nu_S^{-1}$  is the shortest characteristic time of the beam-plasma system.<sup>5</sup> This assumption required that  $\epsilon$  be small compared with 1 so that solutions apply only to the interaction of a relativistic electron beam with high-atomic-number plasmas and targets. In that case

$$f = f_0 + f_1 + f_2 + \dots = O(1) + O(\epsilon^{\frac{1}{2}}) + O(\epsilon) + \dots$$

was given by

$$f_0 = f_0(p, \vec{x}, t), \quad (3)$$

that is,  $f_o$  is isotropic in momentum space and

$$f_1 = \vec{A} \cdot \vec{p} \quad (4)$$

$$f_2 = \frac{1}{6v_S} \left( \frac{e\vec{E}}{p} \frac{\partial \vec{A}}{\partial p} - \frac{1}{m\gamma} \nabla \vec{A} \right) : \vec{pp} + \frac{e}{2v_S m\gamma} (\vec{B} \times \vec{A}) \cdot \vec{p} , \quad (5)$$

where

$$\vec{A} = \frac{1}{2v_S} \left( \frac{e\vec{E}}{p} \frac{\partial f_o}{\partial p} - \frac{1}{m\gamma} \nabla f_o \right) . \quad (6)$$

Setting secular terms in the second-order equation to zero resulted in

$$\frac{\partial f_o}{\partial t} + \frac{p^2}{3m\gamma} \nabla \cdot \vec{A} = \frac{1}{p^2} \frac{\partial}{\partial p} \left[ p^3 (v_E f_o + \frac{1}{3} e\vec{E} \cdot \vec{A}) \right] . \quad (7)$$

Since it is desired to incorporate results of this analysis with hydrodynamic codes describing target dynamics, moments of  $f$  which yield the beam-electron and energy fluxes are of primary interest. To lowest significant order in  $\epsilon$ , these are

$$\vec{\Phi} = \int \frac{\vec{p}}{m\gamma} f_1 d^3p = \int \frac{\vec{pp}}{m\gamma} \cdot \vec{A} d^3p \quad (8)$$

$$\vec{Q} = \int mc^2(\gamma-1) \frac{\vec{p}}{m\gamma} f_1 d^3p = mc^2 \int (\gamma-1) \frac{\vec{pp}}{m\gamma} \cdot \vec{A} d^3p. \quad (9)$$

The rate at which energy is transferred from the beam to a unit volume of plasma is obtained by taking the divergency of Eq. (9) and substituting from Eq. (7). In the steady state,



$$Q = -\nabla \cdot \vec{q} = e\vec{E} \cdot \vec{\Phi} + 4\pi \int_0^\infty \frac{p^4 v_E}{m\gamma} f_O dp . \quad (10)$$

In the same way, Eq. (8) yields

$$\nabla \cdot \vec{\Phi} = -4\pi(p^3 v_E f_O)_{p=0} = -4\pi \epsilon \Omega_S (mc)^3 f_O(0, \vec{x}) . \quad (11)$$

The right-hand-side of Eq. (11) represents the merging of beam electrons, slowed by dynamic friction to very low energies, with the cold plasma-electron background.

An explicit analytical form for  $f$  has been obtained in the limit that electron slowing down is dominated by return-current-generated electric-field deceleration.<sup>5</sup> Here, solutions will be developed which apply to the interaction of the beam with high-density plasma and solid portions of the target where dynamic-friction dominates over field effects.<sup>6</sup> All electric and magnetic field terms are therefore set equal to zero in Eqs. (3) through (7). Additionally,  $v_S \tau \gg 1$  in high-density regions, where  $\tau$  measures the time over which macroscopic beam parameters vary. Only steady-state solutions of Eq. (7) will then be considered. With these approximations, Eq. (7) reduces to

$$a(\vec{x}) \nabla \cdot \left[ a(\vec{x}) \nabla (\gamma^2 f_O) \right] = - \frac{\gamma^4}{(\gamma^2 - 1)^3} \frac{\partial}{\partial \gamma} (\gamma^2 f_O) , \quad (12)$$

where  $a(\vec{x}) = c / [\sqrt{\epsilon} \epsilon \Omega_S(\vec{x})]$ , and Eq. (2) has been used to write the equation in terms of  $\gamma$ . The quantity  $\Omega_S$  may depend on  $\vec{x}$  through the

spatial variation of  $n_i$ . For convenience, 'a' will be treated as constant<sup>7</sup> so that Eq. (12) may be written in the form of the age equation<sup>8</sup>

$$a^2 \nabla^2 \psi = \frac{\partial \psi}{\partial \tau} . \quad (13)$$

In the above,

$$\psi(\vec{x}, \gamma) = \gamma^2 f_0(p, \vec{x}) , \quad (14)$$

$$\tau = \int_{\gamma}^{\gamma_0} \frac{(\gamma^2 - 1)^3 d\gamma}{\gamma^4} = \Gamma(\gamma_0) - \Gamma(\gamma), \quad (15)$$

and

$$\Gamma(\gamma) = \frac{(\gamma^2 - 1)(\gamma^4 - 10\gamma^2 + 1)}{3\gamma^3} .$$

The quantity  $\gamma_0$  is the value of  $\gamma$  associated with the incident electron beam. In terms of the new variables, the electron flux and volumetric heating rate may be written

$$\vec{\Phi} = -\nabla S \quad ; \quad S = \frac{2\pi}{3} \frac{m^3 c^2}{\Omega_S} \int_0^{\tau_1} \psi d\tau , \quad (16)$$

where  $\tau_1 = \Gamma(\gamma_0) - \Gamma(1)$ , and

$$Q = 4\pi m^4 c^5 \epsilon_0 \int_1^{\gamma_0} \psi d\gamma . \quad (17)$$

The body of this work is concerned with evaluation of Eqs. (16) and (17) using specific solutions of Eq. (13). Simple one-dimensional

planar solutions will be presented in Section II. Two-dimensional solutions corresponding to cylindrically-symmetric beams interacting with planar targets are developed in Section III. Using these, contours of constant S and Q for an incident Gaussian beam shape are evaluated. The effect of pinched-beam scattering in the target on the bremsstrahlung x-ray signature is also calculated. In Section IV, one-dimensional results are compared to predictions of Monte Carlo calculations for normally and isotropically incident beams. Sophistications in the theory which improve the model are also presented. Results are summarized in Section V.

## II. ONE-DIMENSIONAL SLAB SOLUTIONS

The plane  $x = 0$  is chosen to divide a semi-infinite, uniform plasma<sup>7</sup> occupying the region  $x > 0$  from a vacuum. A monoenergetic beam of relativistic electrons (particle flux  $\phi_i$ ) propagating in the vacuum is incident on the plasma. In this section, a solution of Eq. (13) is sought which satisfies the simplest reasonable boundary condition:  $f_0$  has the same energy distribution at  $x = 0$  as the incident beam, i.e.,  $f_0(p, 0) \sim \delta(\gamma - \gamma_0)$ . The required solution is<sup>8</sup>

$$\psi = \gamma^2 f_0 = \frac{\psi_0 x}{2\pi^{1/2} a \tau^{3/2}} \exp\left(-\frac{x^2}{4a^2 \tau}\right). \quad (18)$$

Note that

$$\lim_{x \rightarrow 0} \psi = \psi_0 \delta(\tau).$$

At any point  $x$ , the number of electrons with energies between  $\gamma$  and  $\gamma + d\gamma$  is  $4\pi(mc)^3 \gamma(\gamma^2 - 1)^{\frac{1}{2}} f_0 d\gamma$  and is therefore proportional to

$g(\gamma) = (1-1/\gamma^2)^{\frac{1}{2}}\psi$ . This relative energy spectrum is plotted for  $\gamma_0 = 3$  and various values of  $x/a$  in Fig. 1.

The variation of particle flux with  $x$  can now be determined by substitution of Eq. (18) into either Eqs. (11) or (16) with the result

$$\Phi(x) = \Phi_0 \exp\left(-\frac{x^2}{4a^2\tau_1}\right) \quad ; \quad \Phi_0 = \left(\frac{8\pi\epsilon}{3\tau_1}\right)^{\frac{1}{2}} m^3 c^4 \psi_0. \quad (19)$$

Substitution into Eq. (17) yields

$$Q = \frac{mc^2\Phi_0}{a} \frac{x\tau_1^{\frac{1}{2}}}{2a} \int_1^{\gamma_0} \exp\left(-\frac{x^2}{4a^2\tau}\right) \frac{d\gamma}{\tau^{3/2}}, \quad (20)$$

where  $\psi_0$  has been evaluated using Eq. (19). The variation of  $Q$  with  $x/a$  for various values of  $\gamma_0$  is shown in Fig. 2.

The transmission coefficient of beam current at the interface can be estimated by equating  $\Phi_i$  with the positive-going beam current there.<sup>9</sup>

$$\Phi_i = 2\pi \int_0^1 d\mu \int dp \, p^2 f \frac{p\mu}{m\gamma} = \pi m^3 c^4 \int_1^{\gamma_0} \frac{(\gamma^2-1)\psi(0,\gamma)d\gamma}{\gamma^2} + \frac{\Phi_0}{2} \quad (21)$$

correct to first order, where  $\mu = \vec{p} \cdot \vec{e}_x / p$ . Substituting for  $\psi$  and integrating results in a transmission coefficient given by

$$T_C = \Phi_0 / \Phi_i = \left[ \frac{1}{2} + \left( \frac{3\pi}{8\epsilon} \right)^{\frac{1}{2}} \frac{\gamma_0^2 \tau_1^{1/2}}{(\gamma_0^2-1)^2} \right]^{-1}. \quad (22)$$

For  $\gamma_0 = 3$ ,  $T_C$  ranges from .75 for aluminum to .40 for gold.

The energy transmission coefficient is given by

$T_E = q(o)/[(\gamma_o - 1)m_o c^2 \Phi_i]$ . Integrating Eq. (20) over all  $x$  to obtain  $q(o)$  yields

$$T_E = T_C \cdot \frac{\tau_1^{1/2}}{\gamma_o - 1} \int_1^{\gamma_o} \frac{d\gamma}{\tau^{1/2}} \quad (23)$$

which is always greater than  $T_C$ . For  $\gamma_o = 3$ ,  $T_E/T_C = 1.4$ .

### III. A TWO-DIMENSIONAL SOLUTION

Here, solutions corresponding to the interaction of cylindrically-symmetric beam with the slab target of Section II are developed. Equation (13) is solved with the aid of the Green's function for diffusion<sup>8</sup> associated with the infinite half-space  $x \geq 0$ .

$$G(\vec{x}, \tau | \vec{x}_o, \tau_o) = \frac{1}{2\pi^{1/2} a (\tau - \tau_o)^{3/2}} \exp \left\{ -[(y - y_o)^2 + (z - z_o)^2] / 4a^2 (\tau - \tau_o) \right\} \\ \times \left\{ \exp[-(x - x_o)^2 / 4a^2 (\tau - \tau_o)] - \exp[-(x + x_o)^2 / 4a^2 (\tau - \tau_o)] \right\}. \quad (24)$$

The solution  $\psi(\vec{x}, \tau)$  for which  $\psi_S = \psi(o, y, z, \tau)$  is specified is given by<sup>8</sup>

$$\psi(\vec{x}, \tau) = \lim_{\delta \rightarrow 0^+} \frac{1}{4\pi} \int_0^{\tau + \delta} d\tau_o \int dy_o dz_o \psi_S(y_o, z_o, \tau_o) \left. \frac{\partial G}{\partial x_o} \right|_{x_o=0}. \quad (25)$$

A solution is desired for the case of a cylindrically-symmetric, mono-energetic incident beam, i.e.

$$\psi_S(y, z, \tau) = \Psi(\rho) \delta(\tau), \quad (26)$$

where  $\rho^2 = y^2 + z^2$ . Transforming the  $(y, z)$  and  $(y_o, z_o)$  variables into

cylindrical coordinates  $(\rho, \theta)$  and  $(\rho_0, \theta_0)$ , substituting from Eq. (26) into Eq. (25), and integrating over  $\tau_0$  and  $\theta_0$  leads to

$$\begin{aligned} \psi(\vec{x}, \tau) = & \frac{x}{4\pi^{1/2} a^3 \tau^{5/2}} \exp[-(x^2 + \rho^2)/4a^2\tau] \\ & \times \int_0^\infty \exp(-\rho_0^2/4a^2\tau) I_0(\rho\rho_0/2a^2\tau) \Psi(\rho_0) \rho_0 d\rho_0, \end{aligned} \quad (27)$$

where  $I_0$  is the modified Bessel function of zero order. Equation (27) can be used to determine  $\psi(\vec{x}, \tau)$  for an incident beam of any radial cross-section by numerical integration. Fortunately, the integral can be determined analytically for the interesting case of a Gaussian profile

$$\Psi(\rho) = \psi_0 \exp[-\rho^2/R^2].$$

Performing the integration over  $\rho_0$  results in

$$\psi(\vec{x}, \tau) = \frac{\psi_0}{2\pi^{1/2}} \frac{x}{a\tau^{3/2}} \frac{R^2}{R^2 + 4a^2\tau} \exp[-x^2/(4a^2\tau) - \rho^2/(R^2 + 4a^2\tau)]. \quad (28)$$

Note that in the limit  $R \gg a$  (beam radius  $>$  electron range), Eq. (28) reduces to the one-dimensional energy distribution of Section II with a Gaussian radial profile. In the opposite limit,  $\psi$  reduces to the form for an incident point beam expanding in a semi-infinite medium.<sup>8</sup>

The particle flux and volumetric heating rates can now be obtained by substituting from Eq. (28) into Eqs. (16) and (17) and integrating over  $\tau$  numerically. Results for three values of  $R/a$  and  $\gamma_0 = 3$  are displayed in Figs. (3) through (5) in the form of contours of constant  $S$  and  $Q$ . The contour values shown are values of  $S/S_0$  and  $Q/Q_0$  where



$$S_o = \frac{2\pi m^3 c^5}{3\Omega_S} \psi_o \quad ; \quad Q_o = \frac{4\pi m^4 c^5 \epsilon \Omega_S \psi_o \gamma_o^4}{(\gamma_o^2 - 1)^3} .$$

When the vacuum magnetic field does not penetrate into the high-density region of the target plasma, the beam is fully current neutralized. An electric field

$$\vec{E} = \eta_e \vec{\Phi} = -\eta_e \nabla S$$

is then established, where  $\eta$  is the target resistivity. In that case, constant  $S$  contours are seen to be identical to equipotentials of the return-current electric field.

The quantity  $\psi_o$  can be determined in terms of the total current flowing normal to the interface. Substituting for  $\psi$  from Eq. (28) into the x-component of Eq. (16) and integrating over  $\rho$  and  $\tau$  in the limit of small  $x$  leads to

$$\frac{J_o}{\pi R^2} = \left( \frac{8\pi\epsilon}{3\tau_1} \right)^{\frac{1}{2}} m^3 c^4 \psi_o , \quad (29)$$

where

$$J_o = 2\pi \int_0^\infty \Phi_x(o, \rho) \rho d\rho . \quad (30)$$

Note that the mean particle flux just inside the interface obeys the same relation to  $\psi_o$  as the one-dimensional flux defined in Eq. (19). A current-transmission coefficient can be defined by first integrating the two-dimensional form of Eq. (21) over  $\rho$  as in Eq. (30). The resulting expression for  $T_C$  is identical to Eq. (22) where now  $T_C = J_o/J_i$  and  $J_i$  is the total beam current incident on the target.

Observation of the radial distribution of thick-target bremsstrahlung radiation produced when pinched relativistic electron beams enter target anodes is a primary diagnostic used to determine the beam diameter.<sup>10</sup> When the beam diameter is smaller than the electron range, scattering in the target will cause the beam to expand as it diffuses into the target (see Figs. 3 through 5). In these cases, the observed x-radiation profile will not accurately reflect the incident beam profile. Using Eq. (28), the effect of scattering on the x-ray signature is now determined for a Gaussian beam shape.

The rate at which an electron loses energy due to bremsstrahlung radiation may be written<sup>11</sup>

$$\left. \frac{dT}{dt} \right|_{\text{rad}} = n_i m_o c^3 \sigma_{\text{RAD}} (\gamma^2 - 1)^{\frac{1}{2}} \quad , \quad (31)$$

where  $\sigma_{\text{RAD}}$  depends on the target material and may be treated as constant. The energy radiated per unit volume is obtained by integrating this expression over the electron distribution function (see discussion following Eq. (18)).

$$P_{\text{RAD}}(\vec{x}) = 4\pi m^4 c^6 \sigma_{\text{RAD}} n_i \int_1^{\gamma_o} \psi \frac{(\gamma^2 - 1)}{\gamma} d\gamma \quad . \quad (32)$$

Since the beam is highly scattered, the radiation may be considered to be isotropically emitted. The radial distribution of radiation intensity viewed normal to the target is then obtained by integrating  $P_{\text{RAD}}$  over  $x$ . Radiation reabsorption is unimportant for beams and targets of experimental interest.<sup>10</sup> For targets thicker than an electron range

$$I(\rho) = \int_0^\infty P_{\text{RAD}} dx = 4\pi^{\frac{1}{2}} m^4 c^6 \sigma_{\text{RAD}} n_i a \psi_0 \int_1^{\gamma_0} \frac{R^2}{R^2 + 4a^2 \tau} \exp\left(-\frac{\rho^2}{R^2 + 4a^2 \tau}\right) \frac{(\gamma^2 - 1) d\gamma}{\gamma \tau^{1/2}} . \quad (33)$$

The relative variation of  $I$  with  $\rho$  for various values of  $R/a$  is shown in Fig. 6 for  $\gamma_0 = 3$ . As expected,  $I(\rho)$  is essentially Gaussian for large-diameter beams. Beams which are small compared to an electron range exhibit large-radius wings of low x-radiation intensity.

Experimentally, the size of small beams may then be overestimated when the radiation intensity is sufficiently high to cause pinhole photographs to be saturated at the center of the image.

The quantity 'a' may be related to the electron range  $R_e$  by<sup>4</sup>

$$\frac{R_e}{a} \approx \sqrt{3}(Z + 1)^{\frac{1}{2}} [(\gamma_0^2 - 1)^{\frac{1}{2}} - \cos^{-1}(1/\gamma_0)] . \quad (34)$$

Size estimates will be in error for  $R/R_e \leq (R_e/a)^{-1}$ . Corrections for scattering for millimeter-radius beams are then important for (1) high-energy beams ( $\gamma \geq 5$ ), (2) low-atomic-number targets, and (3) long-duration beams for which the target may expand to densities significantly lower than solid.

#### IV. IMPROVEMENTS AND HIGHER-ORDER CORRECTIONS IN ONE DIMENSION

Figure 7 compares the deposition profile calculated in Sec. II with the results of Monte-Carlo calculations<sup>12</sup> for the case of a 1 MeV beam interacting with a gold slab target. The two numerical calculations correspond to (1) beams which are well-collimated and normally incident and (2) beams which have an isotropic angular distribution of

incident velocities. All profiles have been normalized to the absorbed beam power per unit area. The error bars indicate statistical deviation due to the finite electron number chosen in the numerical calculation. The normalized x-coordinate for the Monte-Carlo-generated profiles is determined by numerical evaluation of 'a' using a value of  $\ln \Lambda$  determined from<sup>4,13</sup>

$$\Lambda = (\gamma_0 - 1)(\gamma_0 + 1)^{\frac{1}{2}} \frac{mc^2}{I_z} ; \quad I_z = 9.1 (1 + 1.9Z^{-\frac{2}{3}}) . \quad (35)$$

Alternately, Eq. (34) can be used with the same results.

The theory of Sec. II is seen to agree satisfactorily with the isotropic-incidence calculation but not with that of normal incidence. This result should be expected since the theory assumes that the beam is nearly isotropic (i.e.  $f_0$  is isotropic) even for small values of  $x$ . In part A of this section, a scattering source function is added to the equation describing  $f_0$  which simulates scattering of a well-collimated incident beam in order to more-nearly approximate the numerical calculation for that case. In parts B and C, higher-order corrections to the transmission equation and an improved boundary condition are considered as means to improve the evaluation of beam transmission.

#### A. A Solution with a Scattering Source Function

Here, it is desired to improve the form for  $f_0$  for the case of a normally-incident electron beam. Rather than determine  $f_0$  exclusively from the beam distribution function in the vacuum, it is assumed that  $f_0$  is "fed" by that portion of the beam which is scattered out of the incident normal direction. Thus, by introducing a source term into

the diffusion-like equation governing  $f_0$ , the existence of a scattering boundary-layer<sup>9</sup> is approximated.

If  $\Phi_i$  electrons/unit area/sec cross the interface at  $x=0$ , a number  $\Phi_i \exp(-x/\lambda) dx/\lambda$  can be considered to be scattered into the distribution function per unit volume/sec between  $x$  and  $x + dx$ . Here,  $\lambda$  is a measure of the elastic-scattering mean-free-path for incident electrons. An appropriate form for the source term feeding  $f_0$  is then<sup>8</sup>

$$\mathcal{S} = \frac{\delta(p-p_0)}{4\pi p^2 \lambda} \Phi_i \exp(-x/\lambda)$$

to be added to the right-hand-side of Eq. (7). In this expression,  $p_0 = mc(\gamma^2 - 1)^{\frac{1}{2}}$  is the momentum of incident electrons. Note that it is assumed that source electrons do not degrade in energy with  $x$  since, for high-atomic-number targets, electrons are scattered on a shorter length scale than required to appreciably slow them. In terms of the variables defined by Eqs. (13)-(15), the relation to be solved takes the form

$$a^2 \frac{\partial^2 \psi}{\partial x^2} = \frac{\partial \psi}{\partial \tau} - \frac{\Phi_i \delta(\tau) \exp(-x/\lambda)}{4\pi (mc)^3 \epsilon_0 \lambda} , \quad (36)$$

The solution of interest can be written<sup>8</sup>

$$\begin{aligned} \psi = & \frac{\Phi_i}{8\pi (mc)^3 \epsilon_0 \lambda} \exp(a^2 \tau / \lambda^2) [\exp(-x/\lambda) \operatorname{erfc}(a\tau^{\frac{1}{2}}/\lambda - x/2a\tau^{\frac{1}{2}}) \\ & - \exp(x/\lambda) \operatorname{erfc}(a\tau^{\frac{1}{2}}/\lambda + x/2a\tau^{\frac{1}{2}})] + \frac{\psi_0 x}{2\pi^{\frac{1}{2}} a \tau^{\frac{3}{2}}} \exp(-x^2/4a^2 \tau) . \end{aligned} \quad (37)$$

In the limit of  $\lambda \rightarrow 0$ ,  $\psi$  reduces to the form given in Sec. II. The quantity  $Q(x)$  can be determined by substitution<sup>14</sup> into Eq. (17).

$$Q(x) = \frac{mc^2 \Phi_i}{a} \int_1^{\gamma_0} \psi d\gamma / \psi_s ; \quad \psi_s = \frac{\Phi_i}{4\pi(mc)^3 \epsilon \Omega_s a} . \quad (38)$$

The absorbed heat flux is calculated by integrating  $Q$  over  $x$ . Thus,

$$q = mc^2 \Phi_i \int_1^{\gamma_0} \left[ K(a\tau_1^{\frac{1}{2}}/\lambda) + \frac{\psi_0}{\psi_s} \cdot \frac{1}{\pi^{\frac{1}{2}} \tau_1^{\frac{1}{2}}} \right] d\gamma , \quad (39)$$

where  $K(w) = \exp(w^2) \operatorname{erfc}(w)$ . The quantity  $\Phi_0$  is most easily determined by substituting<sup>14</sup> from Eq. (37) into Eq.(11) and integrating over  $x$ .

$$\Phi_0 = \Phi_i \left[ K(a\tau_1^{\frac{1}{2}}/\lambda) + \frac{\psi_0}{\psi_s} \cdot \frac{1}{\pi^{\frac{1}{2}} \tau_1^{\frac{1}{2}}} \right] . \quad (40)$$

The system of equations is completed by substituting the present form for  $\psi$  into Eq. (21).

$$\Phi_i = \frac{1}{\sigma} \Phi_0 + \Phi_i \cdot \frac{\psi_0}{\psi_s} \frac{\gamma_0^2}{(\gamma_0^2 - 1)^2} \left( \frac{3}{8\epsilon} \right)^{\frac{1}{2}} . \quad (41)$$

The quantity  $\lambda$  is chosen to be some fraction of the scattering mean-free-path  $\lambda_i = p_0 / [m\gamma_0 v_s(\gamma_0)]$ , so that

$$\frac{\lambda}{a} = \sigma(6\epsilon)^{\frac{1}{2}} \frac{(\gamma_0^2 - 1)^2}{\gamma_0^2} , \quad (42)$$

where  $0 \leq \sigma \leq 1$  is the familiar "fudge factor" and  $\sigma = 0$  corresponds to the solutions of Sec. II. The normalized deposition profiles  $aQ(x)/q$



are plotted in Fig. (8) for several values of  $\sigma$  for a gold target and  $\gamma_0 = 3$ . Also plotted is the normal-incidence profile for the same case from Monte-Carlo calculations. The choice  $\sigma = .6$  is seen to provide a good fit to the numerical calculation. Figure (9) displays a similar comparison for an aluminum target. No choice of  $\sigma$  provides a good fit to the numerical results in this case.

#### B. Evaluation of Transmission Coefficients to Second Order

Equations (4) and (41) yield the current-transmission coefficient  $T_c = \Phi_o/\Phi_i$  when solved simultaneously for  $\Phi_o/\Phi_i$  and  $\Psi_o/\Psi_s$  after which substitution for  $\Psi_o/\Psi_s$  into Eq. (39) yields the energy transmission coefficient  $T_E = q/[(\gamma_0 - 1)mc^2\Phi_i]$ . Here, we calculate the second-order correction to Eq. (41) in order to improve accuracy for lower-atomic-number materials. To the same order of accuracy,  $q$  and  $\Phi(x)$  are unaffected since the contribution of  $f_2$  to these quantities is zero;  $f_2$  being an even function of  $\mu$ .

For a 1D slab with all fields set equal to zero,  $f_2$  may be written in the form

$$f_2 = \frac{\mu^2}{2p^2v_s} \left[ \frac{1}{p^2} \frac{\partial}{\partial p} (p^3 v_e f_o) + \mathcal{S} \right], \quad (43)$$

where  $\frac{\partial A}{\partial x}$  from Eq. (7) with the source term  $\mathcal{S}$  has been substituted into Eq. (5). Including  $f_2$  in the evaluation of forward current leads to<sup>14</sup>

$$\Phi_i = \frac{1}{2}\Phi_o + \frac{\Psi_o}{\Psi_s} \frac{\gamma_o^2}{(\gamma_o^2 - 1)^2} \left( \frac{3}{8\epsilon} \right)^{\frac{1}{2}} \left[ 1 + \frac{\epsilon(\gamma_o^2 + 1)}{2\gamma_o} \right], \quad (44)$$

where the second term within the bracket represents the second-order correction to Eq. (41). Simultaneous solution of Eqs. (44) and (40) yield the corrected value of  $T_c$ . Table I displays results of this calculation for 1 MeV electron beams interacting with gold and aluminum and compares current and energy transmission with Monte-Carlo results.

Table I -- Current and Energy Transmission for a 1 MeV Electron Beam  
Incident on a Slab Target

Target	Beam	$\sigma$	$T_c$		$T_E$	
			Theory	Monte-Carlo	Theory	Monte-Carlo
Au	Normal	.6	.68	.53	.86	.65
Au	Isotropic	0	.39	.33	.56	.45
Al	Normal	.3	.93	.90	> 1	.95

### C. A First-Order Boundary Condition

Here, an additional complication which may bring the 1D theory into better agreement with Monte-Carlo results is discussed. Rather than associate  $f_0$  with the incident electron energy distribution,  $f = f_0 + f_1$  evaluated at  $x = 0$  in the forward direction ( $\mu = 1$ ) is chosen for this identification. In the variables chosen here, this relation takes the form

$$\left[ \psi - \frac{\lambda}{2} \frac{\partial \psi}{\partial x} \right]_{x=0} = v^2 f_i, \quad (45)$$

where  $f_1$  is the momentum distribution function for the incident electron beam. In the absence of sources, the solution of Eq. (13) subject to Eq. (45) can be written<sup>8</sup>

$$\psi(x, \gamma) = \frac{1}{\beta} \int_0^{\infty} \exp(-w/\beta) \psi^*(x+w, \gamma) dw, \quad (46)$$

where  $\beta = \lambda_1/2$  ( $= \lambda/a$  of Eq. (42) with  $\sigma = .5$ ) and  $\psi^*$  is the solution of  $\psi^*(0, \gamma) = \gamma^2 f_1$ . For an incident monoenergetic beam;  $\psi^*$  is given by Eq. (18) so that

$$\psi(x, \gamma) = \frac{\psi_0 a}{\beta} \left[ \frac{1}{\pi^{\frac{1}{2}} \tau^{\frac{1}{2}}} \exp(-x^2/4a^2\tau) - \frac{a}{\beta} \exp\left(\frac{x}{\beta} + \frac{a^2\tau}{\beta^2}\right) \operatorname{erfc}\left(\frac{x}{2a\tau^{\frac{1}{2}}} + \frac{a\tau^{\frac{1}{2}}}{\beta}\right) \right]. \quad (47)$$

Using this form for  $\psi$  and neglecting the second-order corrections of part B of this section,

$$\frac{aQ(x)}{q} = \int_1^{\gamma_0} \left[ \quad \right] d\gamma / \int_1^{\gamma_0} K(a\tau^{\frac{1}{2}}/\beta) d\gamma, \quad (48)$$

$$T_c^{-1} = \frac{1}{2} + \left(\frac{3}{8\epsilon}\right)^{\frac{1}{2}} \int_1^{\gamma_0} \frac{\gamma^2 - 1}{\gamma^2} \left[ \frac{1}{\pi^{\frac{1}{2}} \tau^{\frac{1}{2}}} - \frac{a}{\beta} K(a\tau^{\frac{1}{2}}/\beta) \right] d\gamma / K(a\tau_1^{\frac{1}{2}}/\beta), \quad (49)$$

and

$$T_E = \frac{T_c}{\gamma_0 - 1} \int_1^{\gamma_0} K(a\tau^{\frac{1}{2}}/\beta) d\gamma / K(a\tau_1^{\frac{1}{2}}/\beta), \quad (50)$$

where the square bracket in Eq. (48) contains the expression of Eq. (47).

This calculation results in values of  $T_c$  and  $T_E$  closer to those predicted by Monte-Carlo techniques (.39 and .46 for gold and an isotropically-incident 1 MeV beam). The deposition profile of Eq. (48) is monotonically decreasing for this case (as is the Monte-Carlo result) but is too strongly-peaked for small values of  $x$  to improve agreement with numerical calculations ( $aQ(0)/q \approx .28$  as compared with .22 from the histogram of Fig. 7).

## V. CONCLUSIONS

The use of a diffusion theory describing the collisional interaction between a relativistic electron beam and a high-atomic-number target has been investigated. Analytic solutions for one- and two-dimensional beams interacting with slab targets have been obtained. In its simplest form, energy deposition profiles derived from the theory approximate those obtained using Monte-Carlo codes for the case of incident beams whose angular distribution is isotropic (Sec. II). By employing a scattering source function, theoretical deposition profiles for normally-incident beams interacting with very-high- $Z$  targets such as gold can be made to agree well with numerical calculations (Sec. IV). However, this technique does not yield accurate profiles for lower-atomic-number targets such as aluminum. It is reasonable that in this case, the expansion parameter  $\epsilon$  ( $1/7$  for aluminum) is insufficiently small to be able to separate scattering and energy-loss lengths as required by the theory.

Current and energy transmission coefficients are found to be in error by about 25% for the case of gold targets. Although an improved

boundary condition reduces this discrepancy somewhat, agreement between theoretical and numerical desposition profiles is also reduced. It is believed that further refinements in the model (such as combining realistic boundary conditions with energy-dependent source functions) and inclusion of secondary-electron effects can improve its accuracy. However, the benefits are probably not worth the added complication.

An interesting result of the cylindrically-symmetric 2-D solution is the prediction of radial x-ray profiles for various diameter beams (Sec. III). Results indicate that most x-ray pinhole photographs obtained in present experiments accurately reflect the actual beam diameter. However, these data may overestimate beam size when long-duration or high-voltage beams are employed or when low-atomic-number anodes are used.

Finally, it should be mentioned that many of the limitations discussed do not apply when the age equation, Eq. (12), is solved numerically. Complex geometries for the beam and plasma-blowoff, and sophisticated source functions and boundary conditions can be incorporated. Even when all these 'goodies' are included, meaningful physical results can be obtained using a small fraction of computer time and storage required for Monte-Carlo calculations.

## VI. ACKNOWLEDGMENTS

The author wishes to thank Dr. Milton J. Clauser for providing the Monte-Carlo results and for associated fruitful discussions. This work was supported by the Defense Nuclear Agency.

## VII. REFERENCES

1. M. M. Widner and S. L. Thompson, Sandia Lab. Rep. SAND-74-351 (1974).
2. G. Yonas, J. W. Poukey, K. R. Prestwich, J. R. Freeman, A. J. Toepfer and M. J. Clauser, Nucl. Fusion 14, 731 (1974).
3. Z. Zinamon, E. Nardi and E. Peleg, Phys. Rev. Lett. 34, 1262 (1975).
4. D. Mosher, Phys. Fluids 18, 842 (1975).
5. D. Mosher, Phys. Rev. Lett. 35, 851 (1975).
6. From Ref. 5, dynamic friction will dominate over electric field deceleration when  $J_i < 10^{-15} n_i \theta^{3/2}$  A/cm<sup>2</sup>, where  $J_i$  is the incident current density and  $\theta$  is the plasma temperature in eV.
7. For many applications involving existing electron beams,  
 $a = \text{constant} = \text{solid material value}$  may be assumed. For one dimensional problems where 'a' varies spatially the change-of-variable  $x' = \int \frac{dx}{a(x)}$  brings Eq. (12) to the desired form. In higher dimensions, Eq. (13) is approximately correct when  $|\nabla a| \ll 1$ , otherwise, numerical solution of Eq. (12) is required.
8. P. M. Morse and H. Feshbach, "Methods of Theoretical Physics" (McGraw-Hill, New York, 1953), Chaps. 2, 7, and 12.
9. H. A. Bethe, M. E. Rose and L. P. Smith, Proc. Amer. Phil. Soc. 78, 573 (1938).
10. A. E. Blaugrund and G. Cooperstein, Phys. Rev. Lett. 34, 461 (1975).
11. R. D. Evans, "The Atomic Nucleus" (McGraw-Hill, New York, 1955), Chap. 20.
12. M. J. Clauser, Informal Communication.
13. E. Segre, "Nuclei and Particles" (W. A. Benjamin, New York, 1965), p. 28.



14. When taking an energy integral of the source term, the procedure is to calculate

$$\lim_{\delta \rightarrow 0^+} \int_1^{\gamma_0 - \delta} \mathcal{L} \cdot F(\gamma) d\gamma = 0$$

since, in reality, no electrons with  $\gamma = \gamma_0$  exist for  $x > 0$  although artificially introduced by  $\mathcal{L}$ .

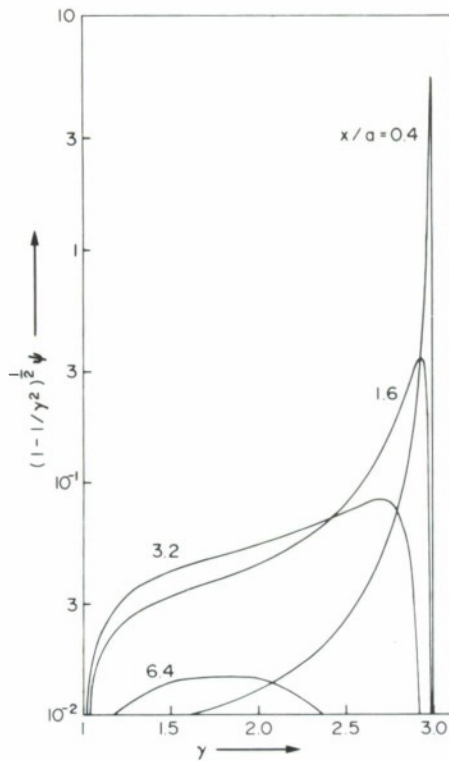


Figure 1. Distribution of electrons with energy for various values of  $x/a$  and a 1 MeV incident beam. Ordinate is proportional to the number of electrons per increment  $dy$

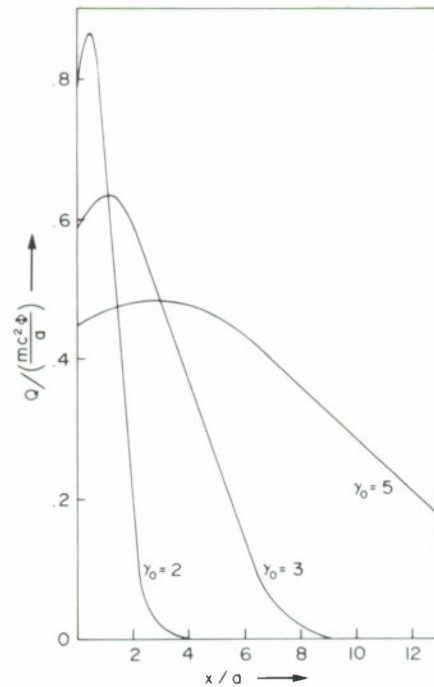


Figure 2. Energy deposition profiles in a slab geometry for three values of incident electron energy

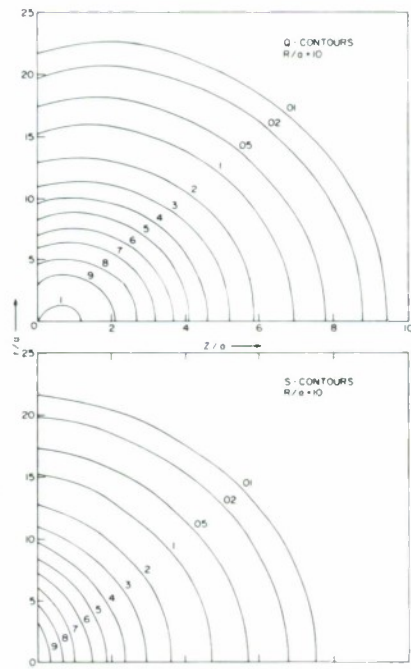


Figure 3. Contours of constant  $Q$  and  $S$  for  $R/a = 10$  for a 1 MeV incident beam of Gaussian profile

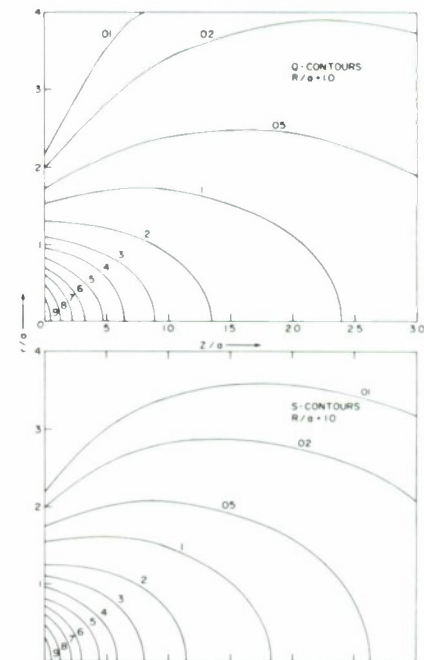


Figure 4. Contours of constant  $Q$  and  $S$  for  $R/A = 1$  for a 1 MeV incident beam of Gaussian profile

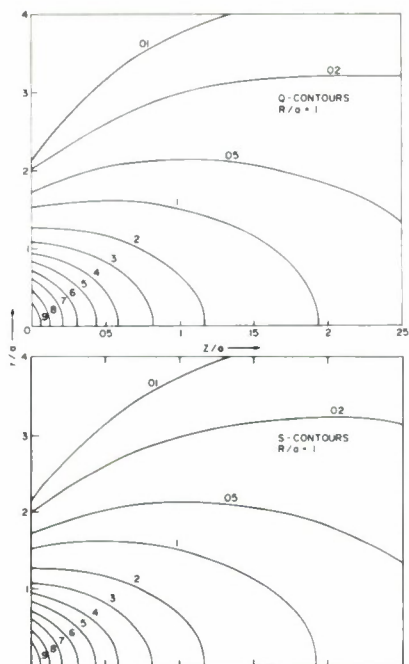


Figure 5. Contours of constant  $Q$  and  $S$  for  $R/a = .1$  for a 1 MeV incident beam of Gaussian profile

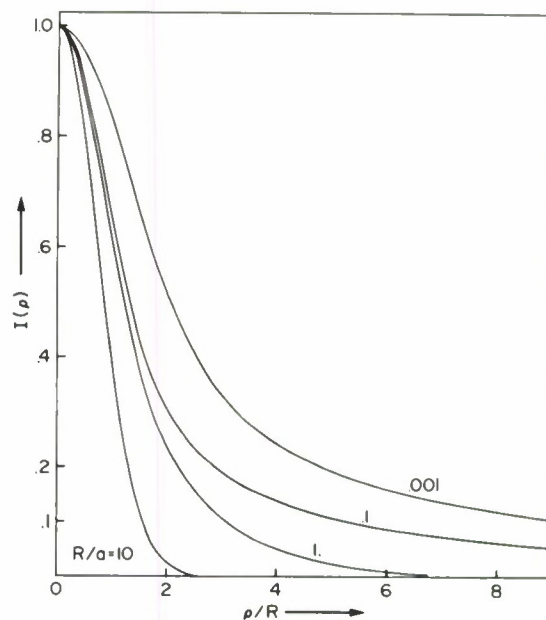


Figure 6. Radial variation of bremsstrahlung intensity for a  $\gamma_0 = 3$  Gaussian incident beam and various values of  $R/a$

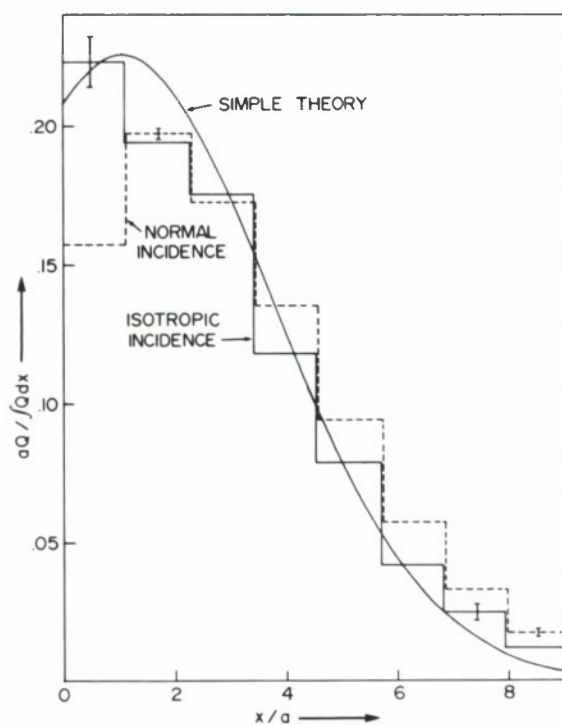


Figure 7  
Comparison of simple-theory deposition profile with the results of Monte-Carlo calculations for normally and isotropically incident beams. Case shown is for a 1 MeV beam incident on a gold target.

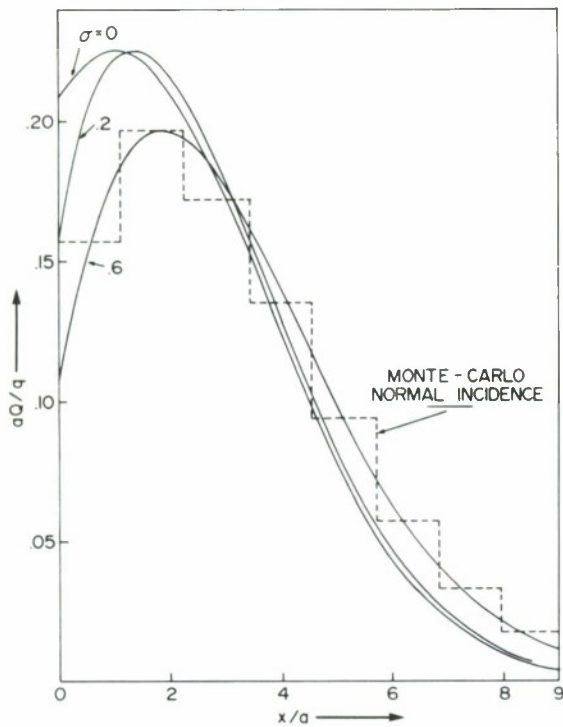
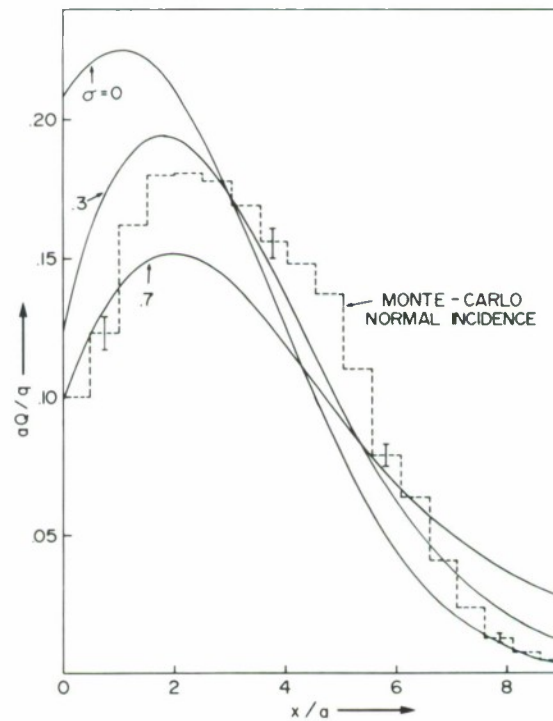


Figure 8

Comparison of Monte Carlo calculation for a normally-incident 1 MeV beam on gold with theoretical deposition profiles using a scattering source function of various scattering strengths

Figure 9

Comparison of Monte Carlo calculation for a normally-incident 1 MeV beam on aluminum with theoretical deposition profiles using a scattering source function of various scattering strengths



## **CHAPTER 2**

# **BEAM GENERATION AND FOCUSING**

## DIFFERENT WAYS OF THINKING ABOUT BEAMS

J.D. Lawson

Rutherford Laboratory, Chilton, Oxon, England

### Abstract

Some of the characteristics of particle beams used in various fields such as electron microscopy, microwave tubes, particle accelerators and various aspects of fusion research, are contrasted and compared.

Starting with a discussion of the very simplest type of beam in paraxial approximation, the concepts of emittance and perveance are introduced. These characterize respectively the degree of disorder of the beam, and the effect of the smoothed out self electric and magnetic fields of the particles. Simple models illustrate some of the types of behaviour encountered in more complex systems.

Alternative descriptions of some of these phenomena are discussed, and some effects associated with "negative mass" instability in annular systems are described.



## 1. INTRODUCTION

During the past fifty years charged particle beams have been studied by different groups of people with different applications in mind. Different viewpoints are obviously required for different situations; it is clear for example that an optical approach, valid in the design of electron microscopes, is useless for the sort of beams we are hearing about at this conference, which are perhaps best thought of as non-equilibrium plasmas with a highly unsymmetrical distribution in velocity or momentum space. Nevertheless it is of interest to see how these two extreme points of view merge in the intermediate domain occupied by the study of particle accelerators and microwave tubes. The distribution function in six dimensional phase space forms a fundamental common description of all types of beam; this is unwieldy for many purposes however, and subsidiary concepts have been introduced. In beams, emittance on the one hand and temperature on the other characterize the same sort of property, but the relation between them is not simple.

In table 1, four fields of interest are represented, and the importance of various aspects of beam behaviour indicated.

Relevant concepts are shown in table 2; where these are unambiguous their relative importance is indicated, but where their manifestation is different, the appropriate "key-word" is shown.

In addition to the applications listed, there are of course many others, such as ion-implantation, welding, rock-breaking etc, but it is workers in the four fields listed who have contributed most to our fundamental understanding of the properties of beams.

## 2. PARAXIAL TRAJECTORY EQUATION

To introduce some of these ideas we start by considering a very simple situation, and bring in complications gradually. The paraxial approximation assumes:

1. Orbits make small angles with the axis.
2. Longitudinal field components are constant across the beam cross section.
3. Transverse field components are proportional to the displacement from the axis.

This is a good approximation in at least the first three fields in the table. We take the  $z$  axis as the beam axis; this may be straight, or curved, as in an accelerator or spectrometer. In the transverse direction it is convenient to use co-ordinates  $x$  and  $y$ , even if the system has axial symmetry.

We consider now the motion of a single particle in external focusing fields with axial symmetry; there are components of  $E$  and  $B$  in the  $x$ ,  $y$  and  $z$  directions, but  $B_\theta$  and  $E_\theta$  are zero.

In the presence of a component of magnetic field  $B_z$  along the orbit, the  $x$  and  $y$  motions are coupled. This is normally removed by transforming to the "Larmor frame", rotating about the axis with angular velocity  $\Omega_L = \frac{1}{2}\omega_c$ . In this frame the field and canonical angular momentum are transformed as

$$1. \quad B_z \rightarrow -2E_r / r\Omega_L$$

$$2. \quad P_\theta = p_\theta + qA_\theta r \rightarrow p_\theta$$

For any set of fields satisfying the conditions specified, the equation of motion of a particle in the Larmor frame may be written

$$\ddot{x} + \alpha(z)x' + \frac{x}{\chi^2(z)} = 0 \quad (1)$$

where

$$\begin{aligned} \alpha &= \gamma' / \beta^2 \gamma \\ \chi^{-2} &= -\frac{qE_x}{\gamma m_0} + \frac{q^2 B_z^2}{4\gamma m_0^2} \end{aligned} \quad (2)$$

In these expressions  $m_0$  is the mass of the charge,  $\beta = v/c$ , and  $\gamma = (1-\beta^2)^{-1/2}$ .

The normalized energy gradient  $\gamma'$  is equal to  $qE_z/m_0 c^2$ .

If  $E_z$  is zero, then  $\alpha$  is zero; if in addition the focusing is uniform, so that  $\chi$  is independent of  $z$ , the trajectory is a sine wave with wavelength  $2\pi\chi = \lambda$ .

It is possible always to remove the  $x'$  term by introducing new "reduced" variables  $x = (\beta\gamma)^{1/2} \tilde{x}$ ; to preserve simplicity appropriate to a half-hour talk however we shall retain  $x$  and  $y$ , and assume  $E_z = 0$ . Eqn 1 becomes

$$\ddot{x} + x/\chi^2(z) = 0 \quad (3)$$

This is a second order equation, in which the values of  $x$  at two values of  $z$  are related as

$$\begin{pmatrix} x_2 \\ x_2' \end{pmatrix} = \begin{pmatrix} u(z) & u'(z) \\ v(z) & v'(z) \end{pmatrix} \begin{pmatrix} x_1 \\ x_1' \end{pmatrix} \quad (4)$$

where  $u(z)$  and  $v(z)$  are the "principal solutions", that is, those which, at  $z_1$ , have initial conditions  $(x, x')$  equal to  $(1, 0)$  and  $(0, 1)$  respectively. The absence of the term in  $x'$  implies that determinant of this matrix is unity.

### 3. A BEAM AS A BUNDLE OF TRAJECTORIES

The matrix elements  $u$  and  $v$ , found by solving eqn 3 with the appropriate initial conditions, allow us to map points from the  $x \ x'$  plane at  $z = z_1$  to a similar plane at  $z = z_2$ . Each orbit may be represented as a point on the  $x \ x'$  plane, which moves as  $z$  varies. Let us now consider a beam represented by points in this plane which lie with uniform density within an elliptical contour.

The following theorems may be simply proved by invoking the theory of second order linear differential equations,

Th. 1) As  $z$  varies, the bounding contour remains elliptical, but can change shape and orientation.

Th. 2) The area of the ellipse remains constant.

The second of these theorems is essentially Liouville's theorem; it remains true even in the presence of non-linearities in eqn 3; these cause "aberrations". In the presence of aberrations however the contour no longer remains elliptical.

In Fig 1 the  $x'x'$  plane ellipses of a beam being focused by a lens are plotted.

In Fig 2 the distortions of an ellipse arising from an array of lenses with spherical aberration are shown.

In Fig 3 a typical "practical"  $x'x'$  plane plot is shown<sup>(1)</sup>. The distribution does not have a sharp edge, and the fraction of current within the various contours is indicated.

The area of the ideal ellipse divided by  $\pi$  is known as the "emittance"  $\epsilon$  of the beam. Further, it may be shown by algebraical arguments that the envelope equation of the beam of finite emittance is

$$a'' + \frac{a^2}{x'^2(z)} - \frac{\epsilon^2}{a^3} = 0 \quad (5)$$

It is readily verified that in the absence of focusing, ( $x'^{-2} = 0$ ), the solution of eqn 5 is a hyperbola. The trajectories are all straight lines, and the "waist" is the circle of least confusion. We discuss later the meaning of emittance in non-ideal situations.

#### 4. THE MICROCANONICAL DISTRIBUTION OF KAPCHINSKIJ AND VLADIMIRSKIJ

It is relevant to enquire into the nature of the distribution function which produces a uniform distribution of charge across the beam. Such a distribution has been described by Kapchinskij and Vladimirsky<sup>(2)</sup>; it is sometimes known as the microcanonical distribution. For a beam uniform in the z-direction it may be written

$$\frac{x^2 + y^2}{a^2} + \frac{a^2 (\dot{x}^2 + \dot{y}^2)}{\epsilon^2} = 1 \quad (6)$$

This represents a three dimensional shell in four dimensional  $xy\dot{x}\dot{y}$  space. By an extension of the theorem of Archimedes, two dimensional projections of this hyper-ellipsoid have uniform density within an elliptical contour. Projections of the four dimensional orbits on the  $x\dot{x}$  and  $xy$  planes are shown in Fig 4.

This distribution function is highly artificial; it has nevertheless some nice properties and is useful for model-building and general orientation. At a radius  $r = (x^2 + y^2)^{\frac{1}{2}}$  all the particles have the same value of  $\dot{x}^2 + \dot{y}^2$ . It is readily seen that the radial energy of the particles is a function of  $r$  only

$$\begin{aligned} \frac{1}{2}\gamma m_0 (\dot{x}^2 + \dot{y}^2) &= kT = \frac{1}{2}\beta^2 c^2 \gamma m_0 (\dot{x}^2 + \dot{y}^2) \\ &= \frac{1}{2}\beta^2 c^2 \gamma m_0 \left(1 - \frac{r^2}{a^2}\right) \frac{\epsilon^2}{a^2} \end{aligned} \quad (7)$$

The temperature, which is highly non-Maxwellian, decreases parabolically with radius from  $\frac{1}{2}\beta^2 c^2 \gamma m_0 \epsilon^2 / a^2$  on the axis to zero at the beam edge.



The temperature gradient implies a pressure gradient; since the density is uniform -  $dT/dr$  is proportional to  $r$ .

So far our approach has been purely optical; as an alternative we could adopt a hydrodynamic starting point, in which the force on a small element of the beam, rather than on a single particle, is calculated.

By evaluating the appropriate pressure tensor it is readily verified that the emittance term now represents a force arising from the pressure gradient. Indeed, we can regard the beam as a two dimensional gas; at a waist,  $T$  is large and  $V$  is small, whereas at a maximum the converse is true. The adiabatic gas law

$$T(\pi a^2)^{\gamma-1} = \text{const}, \quad \gamma = \frac{1}{2}(2+2) = 2 \quad (8)$$

can readily be deduced from the geometry of the ellipses and orbits.

## 5. SELF-FIELD EFFECTS

The microcanonical distribution is ideal for studying self-field effects such as beam spreading and pinching, which occur when the beam density is no longer negligible. Electrostatic pinching and magnetic focusing produce forces on a charge proportional to  $r$  but inversely proportional to  $a^2$ . At the edge particle of the beam the force is proportional to  $a^{-1}$ , and we can add a further term to eqn 5

$$a'' + \frac{a}{\chi^2(z)} - \frac{e^2}{a^3} - \frac{K}{a} = 0 \quad (9)$$

K is the 'perveance', and for a beam with neutralization fraction f

$$K = \frac{2v}{\beta^2 \gamma} (1-f-\beta^2) \quad (10)$$

where  $v = Nr_0$ , the number of particles per unit length multiplied by the classical electron radius. For some special limiting situations

$$\begin{array}{ll} K = \frac{2v}{\beta^2} & ) \\ & ) \text{ non-relativistic,} \\ & ) \\ \propto I/V^{3/2} & ) \text{ unneutralized} \end{array} \quad (11)$$

$$\begin{array}{ll} K = - \frac{2v}{\gamma} & ) \\ & ) \text{ relativistic,} \\ & ) \\ = - \frac{2I}{I_{\text{Alfvén}}} & ) \text{ fully neutralized} \end{array} \quad (12)$$

$$K = 0 \quad \text{when } f = \gamma^{-2}, \text{ (Budker condition)} \quad (13)$$

For the paraxial approximation to be valid,  $K \ll 1$ . The condition  $|K| \approx 1$  corresponds to "limiting perveance" for an unneutralized beam, and the "Alfvén limit" for a neutral beam.

Equation 9 exhibits a wide range of phenomena; by taking pairs of terms special situations can be illustrated. These are shown in Table 3.

## 6. NON-UNIFORM RADIAL PROFILES, MAXWELLIAN TRANSVERSE VELOCITIES

In linear external fields, self consistent radial profiles for distributions which are not microcanonical may be found (eg by the Vlasov technique). The most interesting velocity distribution is the Maxwellian. For a pinch this gives the Bennett distribution. For a system with external focusing, the form depends on  $\lambda_D/a$ , the ratio of Debye length to beam radius, as shown in Fig 5.

## 7. EMITTANCE IN NON-LINEAR SYSTEMS

The emittance was defined in connection with the very special microcanonical distribution. Various definitions are possible when the density distribution is not uniform and the boundary not elliptical<sup>(3)</sup>. A practical approach, relevant to the design of beam handling systems, is to specify the smallest ellipse which can be drawn to enclose say 95% of the points. For a system showing filamentation, such as may be seen in Fig 2, the emittance defined in this way increases along the length of the beam. The profile of a beam undergoing this type of filamentation is shown in Fig 6.

Ultimately the emittance settles down to a roughly constant value as the phases of the oscillations of individual particles become mixed. On a fine enough scale the occupied area of phase space remain constant; in practice however the whole area is effectively occupied, the free space is "whipped in" with the occupied area.

A formal way to describe this effect is to divide the phase space into cells and take the entropy of the distribution<sup>(4)</sup>. For the microcanonical distribution it is found that the entropy  $S$  is the logarithm of the emittance,

minus a constant which depends on the cell size. If such a distribution becomes filamented because of aberrations, then  $S$  remains constant provided that the cell size is small compared with the structure of the filamentation. If however this is not so,  $S$  increases as the filamentation proceeds, as illustrated in Fig 7.

It would seem reasonable to take the cell size appropriate to the resolution of the apparatus of interest.

Not surprisingly, this entropy can be related to the thermodynamic entropy of the beam regarded as a two dimensional gas. For a beam with structure, such as an electron microscope beam capable of forming an image, increase of entropy, arising from aberrations, implies loss of information.

## 8. NON-PARAXIAL SYSTEMS

Paraxial systems are particularly simple to study by virtue of the fact that the transverse and longitudinal phase space are not coupled. This is not so for many of the beams discussed at this meeting; indeed the Kapchinskij-Vladmirskij distribution is the paraxial limit of that studied by Hammer and Rostoker<sup>(5)</sup>. Nevertheless, a thorough understanding of paraxial systems helps one to visualize more effectively the properties of the more complicated general distributions.

It is interesting to note finally that the Bennett distribution holds for both paraxial beams and non-paraxial plasma streams.

## 9. WAVE PROPERTIES OF BEAMS

The topic of wave propagation on beams is extensive, and cannot be considered in this short review. In considering the properties of such waves, the Debye length is an important parameter. In many situations the Debye length is large compared with the beam radius and small compared to its length, so that only propagation characteristics along the beam are of interest. The transverse dimensions however enter into the dispersion relation; for example in an infinite  $B_z$  field  $\omega_p$  for an infinite medium is replaced by  $\omega_q$ , which is a function of  $\omega_p$ , transverse dimensions, and  $k_z$ .

In this context it is important clearly to appreciate how quantities such as temperature transform when moving with the beam. Transverse temperatures are invariant, but characteristic longitudinal temperatures are considerably less than energy spreads measured in the laboratory frame, especially in the relativistic regime. Beams in annular systems (such as storage rings) can show negative mass, and consequently negative temperature effects. Since negative temperatures are hotter than positive temperatures, energy diffuses continuously from longitudinal to transverse motion in such devices. Since the mass is negative, the effective plasma frequency  $\omega_q$  is pure imaginary; in the absence of sufficient energy spread to cause Landau damping, this gives rise to the characteristic "negative mass" instability.

## 10. CONCLUSION

Time has permitted only a brief look at one aspect of the connection between viewpoints in different fields suggested in Tables 1 and 2. Although no new results have been presented, and the analysis has been confined to trivially simple examples, the speaker hopes that the insights gained by this type of presentation will help to provide a fuller understanding of the possibilities and limitations of the very much more complicated beams that we shall be hearing about during the next few days.



## REFERENCES

Most of the material of this review, and the appropriate detailed references, are contained in the paper "Optical and Hydrodynamical Approaches to Charged Particle Beams", Plasma Physics, 17, 567 (1975). Numbered references are:

1. T.J.L. Greenway and H.R.M. Hyder. Proc. Symposium on Ion Sources and Formation of Ion Beams, Brookhaven National Laboratory, NY, (1971).
2. I.M. Kapchinskij and V.V. Vladimirskij. Proc. CERN Conference on High-Energy Accelerators and Instrumentation, Geneva (1959).
3. P. Lapostolle. Proc. 2nd International Conference on Ion Sources and Ion Beams, Vienna, p.133 (1972).
4. J.D. Lawson, P.M. Lapostolle and R.L. Gluckstern. Particle Accelerators 5, 61 (1973).
5. D.A. Hammer and N. Rostoker. Physics of Fluids 13, 7 (1970).

TABLE 1

Phenomenon	Degree of interest			
	Electron Optics	Microwave Tubes	Accelerators and Storage Rings	Fusion Research Applications
Focusing by external fields	XXX	XX	XXX	X
Space charge	0	XXX	XX	XXX
Self-magnetic field	0	0	XX	XXX
Interaction with walls	0	XXX	XX	XX
Wave properties, and stability	0	XXX	XX	XXX
Interparticle scattering	X	0	X	XX
Charge exchange and ion formation	0	X	X	XXX

TABLE 2

Concept	Application			
	Electron Optics	Microwave Tubes	Accelerators and Storage Rings	Fusion Research Applications
Geometrical Optics	XXX	X	XX	0
Liouville's theorem ) Phase space ) Gas laws )	Normalized brightness	0	Emittance, Entropy	Pressure, Temperature
Self-field effects	0	Perveance	Tune shift	$v/\gamma$ , $I/I_A$
+ and - energy waves	0	XXX	X	X
Beam-environment interaction	0	XXX	XX	XXX
Hydrodynamic description	0	Sometimes useful	Possible, but not useful	Useful
Interparticle scattering	Boersch effect	0	Touschek effect	XX

TABLE 3

Terms in eqn 9	Situation described
1, 2	Focused laminar beam
1, 3	Crossover
1, 4, K + ve	Space charge spread
1, 4, K - ve	Laminar pinch
2, 3	) Matched beam
2, 3, 4	
2, 4	Brillouin flow
3, 4 K - ve	Pinch

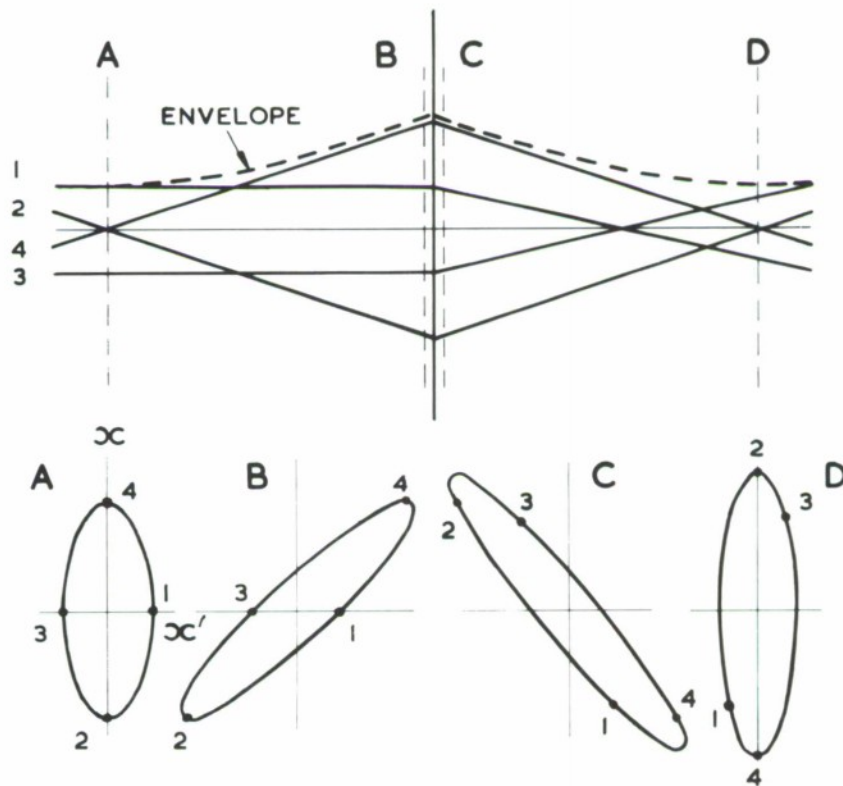


Figure 1. Bundle of orbits focusing by a perfect lens. Four orbits lying on an ellipse in the  $xx'$  plane are shown at various positions in the system. The ellipse area is invariant. The beam envelope corresponding to the presence of all the orbits represented by the ellipse is shown dotted.

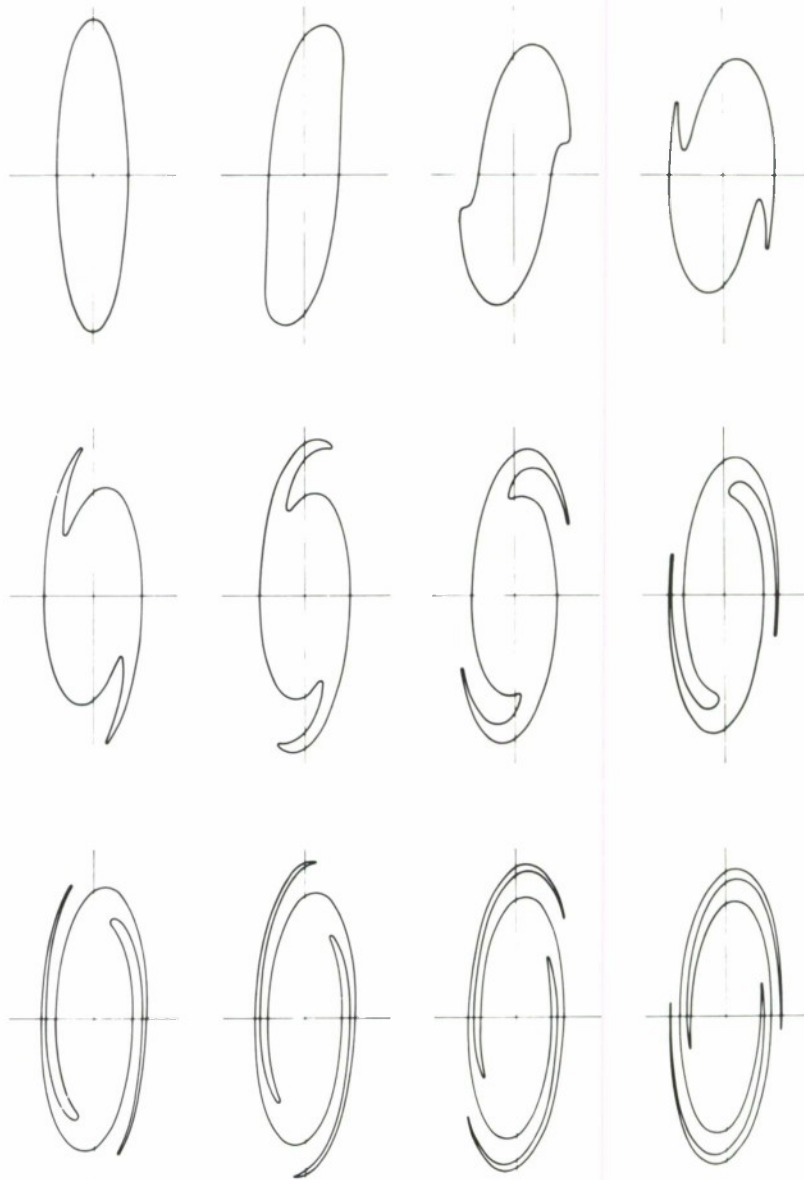


Figure 2. Progressive distortion of the ellipse caused by focusing through an array of lenses in which spherical aberration is present. The curve is drawn at successive points corresponding to an integral number of wavelengths of the particle orbit; between these points rotation occurs as in Fig. 1.

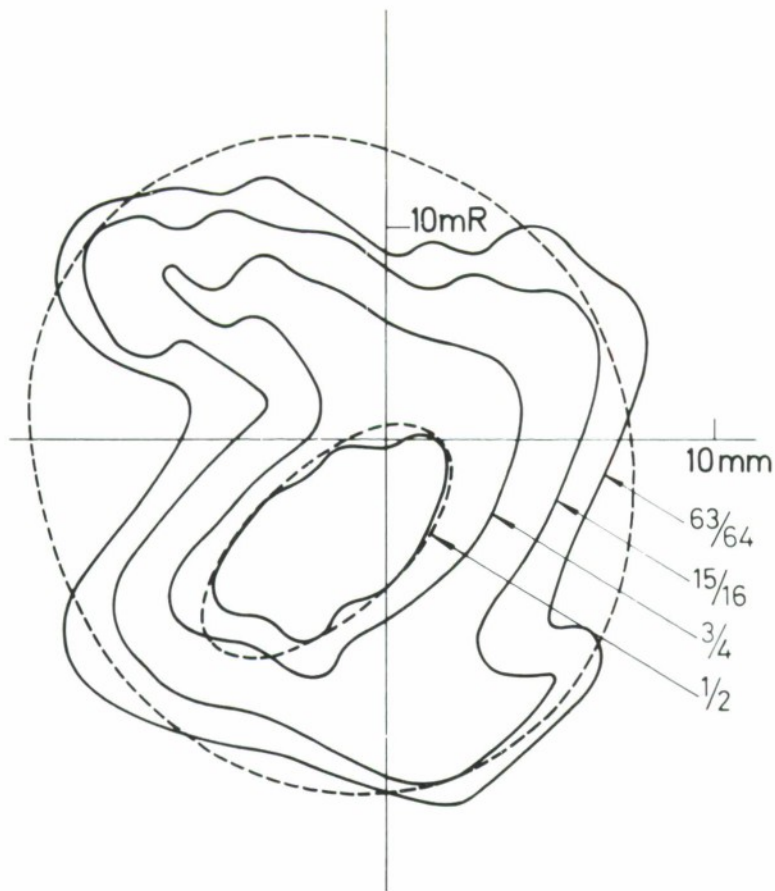


Figure 3. A typical 'practical' emittance plot from an ion source. The numbers denote the fraction of current contained within the appropriate isodensity contour.

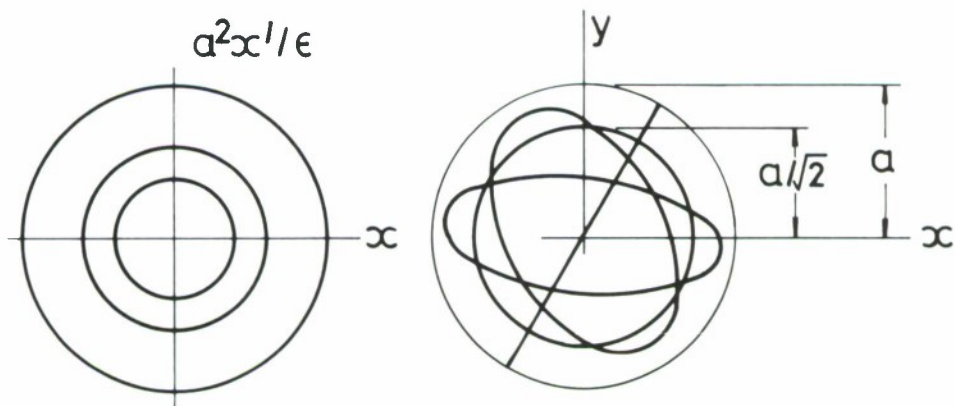


Figure 4. Projections of the orbits associated with the Kapchinskij-Vladimirskij distribution on the (renormalized)  $xx'$  plane and the  $xy$  plane.

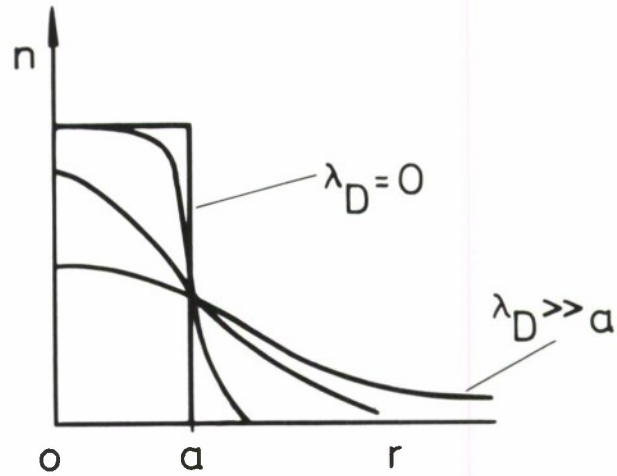


Figure 5. Self-consistent beam density profile in a parabolic potential well, corresponding to uniform external focusing. When  $\lambda_D = 0$ , the space charge and focusing forces exactly balance; when  $\lambda_D \gg a$ , the solution is that of the standard "atmosphere" problem, and the profile is gaussian.

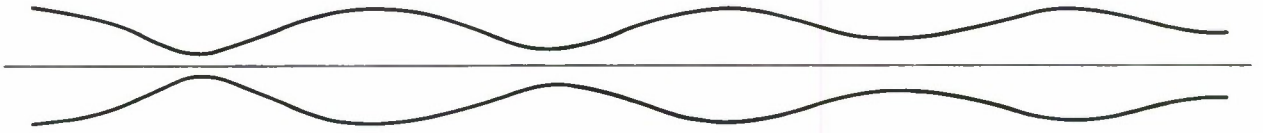


Figure 6. Progressive loss of structure in the envelope of a beam undergoing phase space filamentation in a uniform focusing channel.

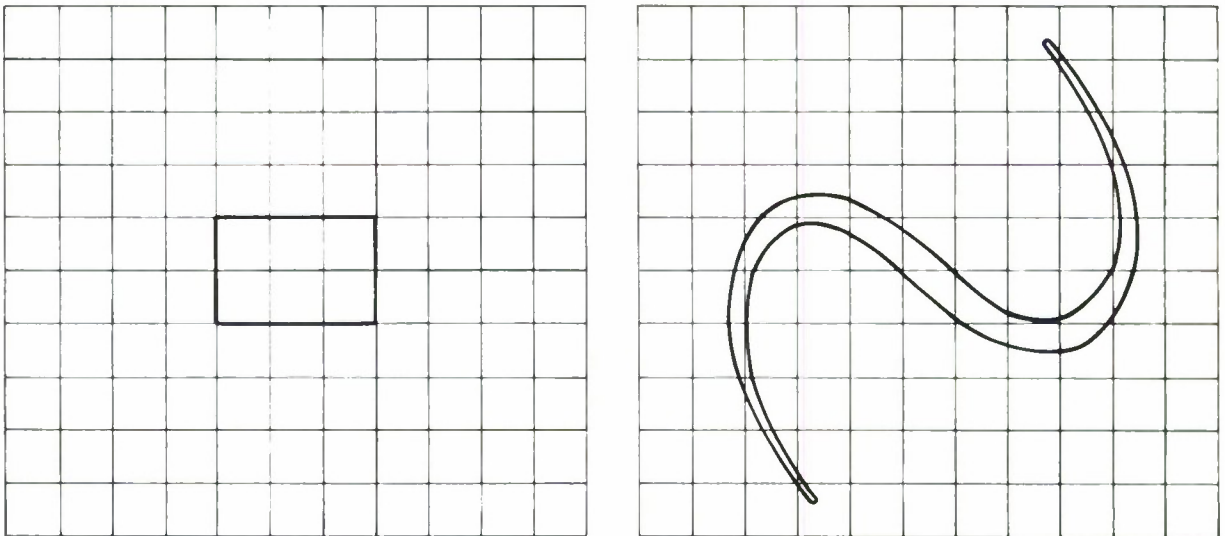


Figure 7. Two distributions with the same area in phase-space, but different entropies. If the cell sizes were reduced by a factor of 100 the entropy difference would be much reduced.



# THEORY OF ELECTRON AND ION FLOW IN RELATIVISTIC DIODES\*

Shyke A. Goldstein and Ronald C. Davidson  
University of Maryland, College Park, Md. 20742

Roswell Lee and John G. Siambis  
Naval Research Laboratory, Washington, D. C. 20375

## ABSTRACT

The time dependent evolution of electron and ion flow in large aspect-ratio relativistic diodes is studied by analytic models and computer simulation. Four distinct phases are considered: (1) Pure electron flow at low voltages, (2) Weak pinching at large voltages, (3) Collapsing pinch due to time dependent ion emission from anode plasma and (4) Steady-state pinched electron flow and laminar ion flow. The physics incorporated in a new, time dependent, simulation code is outlined and the simulation results are compared to the analytic predictions. In particular, we find that in phase (4) the ion current may be larger than the electron current and present day accelerators may thus produce mega-ampere ion currents.

---

\*Work supported by the Office of Naval Research under the auspices of the joint University of Maryland-Naval Research Laboratory plasma physics program.

When high voltage is applied to a large aspect ratio diode, plasma is formed on the cathode surface and space charge limited electron emission takes place. The combination of self magnetic field and space charge effects defines the flow pattern in a given diode geometry. As long as ion effects are not present (no anode plasma formation) it can be shown that only weakly pinched electron flow will exist. At low voltages,  $\sim 100$  kV, the well known Child-Langmuir derivation has been commonly used. At higher voltages, it was realized that self magnetic field effects are of importance at large radii. It was assumed, however, that these effects are of little importance at small radii. A self consistent derivation now shows the need to include the magnetic field effects even near the axis of a cylindrically symmetric diode at high voltages and also at large radii for low voltages, the reason being that the electron flow lines decrease in radius from cathode to anode, thus increasing the current density. The current density on the anode plane is thus larger by a factor of order 2 from the Child-Langmuir prediction.

In the case of cold electron flow (no orbit crossing) the mechanical momentum field of the electrons completely characterizes the relativistic steady-state flow. The system of relativistic fluid-Maxwell equations is reduced to one second-order partial differential equation for the electron momentum in the limit that the energy is constant, not only along current flow lines, but also constant across current flow lines in the diode region. The treatment is fully self-consistent and includes the influence of self-field effects on the relativistic electron flow. The equations describing steady-state flow are given by

$$\nabla \cdot (n\vec{u}) = 0 \quad , \quad (1)$$

$$\vec{u} \cdot \nabla \vec{p} = e(\vec{E} + \vec{u} \times \vec{B}/c) \quad , \quad (2)$$

$$\nabla \cdot \vec{E} = 4\pi en \quad , \quad \vec{E} = -\nabla\phi \quad , \quad (3)$$

$$\nabla \cdot \vec{B} = 0 \quad , \quad \nabla \times \vec{B} = 4\pi \vec{J}/c = 4\pi en\vec{u}/c \quad , \quad (4)$$

$$\vec{p} = m\vec{u} \quad , \quad m = m_0 / \left(1 - (u/c)^2\right)^{1/2} \quad ,$$

$$\gamma^2 = 1 + p^2/m_0^2 c^2 \quad , \quad (5)$$

where  $n$  is the electron density,  $\vec{u}$  is the mean velocity of an electron fluid element,  $\vec{E}$  and  $\vec{B}$  are the electromagnetic fields,  $c$  is the speed of light in vacuo,  $m_0$  and  $e$  are the electron rest mass and charge, respectively, and cgs electrostatic units are used throughout the present analysis. The energy constant of the motion implied by Eqs. (1) - (4) is given by

$$\vec{J} \cdot \nabla(e\phi + (\gamma - 1)m_0 c^2) = 0 \quad , \quad (6)$$

and reduces to the form  $e\phi + (\gamma - 1)m_0 c^2 = \text{const}$  in the present analysis. From Eqs. (2), (3), (5) and (6) and the vector identity,  $\nabla(G^2/2) = \vec{G} \times (\nabla \times \vec{G}) + (\vec{G} \cdot \nabla)\vec{G}$ , it follows that  $\vec{p} \times (\nabla \times \vec{p} + e\vec{B}/c) = 0$ . For azimuthal symmetry ( $\partial/\partial\theta = 0$ ) and no  $\theta$  rotation, we find

$$\nabla \times \vec{p} = -e\vec{B}/c \quad . \quad (7)$$

Combining Eqs. (3) - (7), it is straightforward to show that

$$\nabla \times (\nabla \times \vec{p}) = -\vec{p}(\nabla^2 \gamma)/\gamma \quad . \quad (8)$$

Equation (8) and the boundary conditions on  $\vec{p}$  and the electromagnetic fields constitute the basic equations to be solved. The solution of Eq. (8) at low voltages contains the Child-Langmuir solution as one of its terms and shows that it is dominant only for radii smaller than

$$\Delta = D \cdot \frac{9}{4} \cdot \frac{(\gamma_0 + 1)^{1/2}}{\gamma_0 - 1} \quad ,$$

where  $D$  is the cathode-anode gap spacing and  $\gamma_0$  is at the anode. At larger radii the self magnetic fields limit the electron emission. The general solution of Eq. (8) is rather complicated,<sup>1</sup> and only very near the cathode does it resemble the Child-Langmuir solution. At higher voltages,  $\sim 1$  MV, the exact relativistic Child-Langmuir derivation holds nowhere!

The electrons flow mainly in the radial direction and pinch weakly on the anode plasma at a radius  $r_c/\gamma_0$  where  $r_c$  is the radius of origin from the cathode. The total current depends on the specifics of the cathode and anode geometry, mainly near the outer cathode radius. For a hollow cathode, the solution to Eq. (8) shows that when the radial thickness of the cathode is larger than  $\Delta$ , then magnetic effects are dominant. Crossing of electron orbits may take place near the inner corner of the cathode and the solution of Eq. (8) describes the flow only approximately.

In the past, it was assumed that the electrons from large radii can ExB drift to the diode axis and form a tight pinch on the anode plane. This view led to the invention of the parapotential flow model.<sup>2</sup> In this model, the electrons flow radially in a region of an axial scale length much smaller than the radial length. However, without an external current flowing on the diode axis the axial electric field is always larger than the magnetic field. This can be shown by integrating Eqs. (3) and (4) across the flow in the axial direction. One then has

$$E_z(z) = E_z(z_1) + 4\pi e \int_{z_1}^z n_e(z) dz \quad ,$$

$$B_0(z) = B_0(z_1) + 4\pi e \int_{z_1}^z \frac{V_r(z)}{c} n_e(z) dz \quad ,$$

where we choose  $z_1$  such that  $B_\theta(z_1) = 0$ . The radial electric field will not contribute to the integral since it is shorted out near the anode. Thus since  $V_r(z)/c$  is always less than unity it is clear that  $|E_z|$  will always be



greater than  $|B_0|$ . In this case the average axial velocity is not zero and the electrons are driven into the anode plane after traversing a radial distance of the order of one Larmor radius. Thus a tight pinch cannot form in vacuum.

Computer simulations using the code DIODE-1 are in good agreement with the laminar flow theory described above. Figure 1 shows current and potential contours for a simulation with  $\gamma_0 = 2$ ,  $R/D = 10$ , and are typical of results showing the weak pinch.<sup>1</sup> Figure 2 shows a comparison of the theoretically predicted axial density profile and the results of simulation. Similar results have also been obtained for hollow cathodes and they also show only a weak pinch is formed.

We thus conclude that phase 1 of electron flow at low voltages and phase 2 of flow at high voltages are generally understood for flat cathodes and anodes. Different diode geometries, like conic cathodes or conic anodes and their corner effects are presently under investigation.

The laminar flow model<sup>1</sup> is the basis for the following discussion and will be referred to as GDSL.

The electrons striking the anode plane may generate a plasma which acts as a source of ions. Depending on the accelerator characteristics and on the anode material, the time of anode plasma formation may occur during phase 1 (low voltage) or phase 2 (high voltage). During phase 1, one may change Eq. (8) to include the ion charge effects and the solutions to the new equation contain the Langmuir solution for the bipolar flow with corrections as long as the cathode radius is smaller than  $\Delta$ . For larger radii, there is no solution to the equation; the reason being that electron orbits do drift radially to form a pinch. Hence, a new model that allows for reflection of electron orbits near the anode plane has to be constructed. Furthermore, due to the slow ion motion, one needs a time dependent description of the dynamics of pinch formation. If the anode plasma is produced during phase 2, the Langmuir bipolar solution does not apply at all. We thus describe phase 3 of the flow during which pinch formation takes place.

During phase 2, the heating of the anode material is more efficient at large radii due to the grazing incidence of electrons on the anode plane. A dense anode plasma is thus expected to form there first. The initial motion of the ions, accelerated from the anode plasma, forms an ion sheath which modifies the electric field. We will follow the dynamics of the ion sheath as a function of time and show that the electric field drops (linearly in the sheath) from its value given outside the sheath by GDSE, to zero on the anode plasma. This linear drop of the electric field across the ion sheath is in sharp contrast to the steady-state Child situation where the electric field goes to zero as  $x^{1/3}$ , where  $x$  is the distance from the anode plasma. This is not surprising since the initial ion motion is far from steady state.

While the anode plasma contains a diamagnetic electron flow which excludes the magnetic field, no such effect exists in the ion sheath allowing for the full penetration of the magnetic field. When an electron enters the ion sheath with grazing incidence (i.e.,  $p_z/p_r \ll 1$ ) it will be reflected back into the diode by the unaffected magnetic field but reduced electric field. These electrons then move radially inwards until they reach a radius where no dense anode plasma has yet been produced. There, the enhanced electron flow hits the anode plane until enough ions are formed to allow further radial drift of the electron flow from large radii. The necessary ion sheath thickness to provide such electron reflection is reached in times which are short enough ( $< 1$  nsec) to explain the fast collapsing pinch. Also, a qualitative explanation for the collapsing hollow ring, as observed experimentally<sup>3</sup> for hollow cathodes, is provided by the above picture. The following quantitative analysis applies only for solid cathodes at large radii.

The dynamics of the ion sheath and electron orbits are now computed under the following assumptions. Using the electrostatic approximation to solve for the time dependent electric field as a function of the distance  $x$



from the anode plasma with  $E(x = 0) = 0$ , we find for  $t > 0$ ,  $E(x, t) = \int_0^x 4\pi\rho(x', t) dx'$ , where  $t = 0$  is the time of anode plasma generation. This plasma is assumed to be dense enough to provide a sufficient reservoir of ions so as to reduce the diode electric field to zero in the anode plasma. The electric field in the diode is of order  $\sim 1$  MV/cm and thus prevents anode plasma electrons from following the ions. We follow the ion motion only for short times so that the ion front  $x_F(t) \ll D$ . Since the electric field is zero on both the cathode and anode plasmas, the total charge of the ions is nearly equal to the charge of the electrons present in the diode gap. The fraction of the electron charge in the very thin ion sheath is thus negligible compared to the ion charge. Outside the ion sheath, the electron charge dominates and results in an electric field  $E(x_F)$  which is nearly constant in time. The total number of ions in the sheath during its early expansion is thus fixed. Solving the dynamics of  $N$  test ions, with equal intervals of space charge between them, one finds for the  $i$ 'th ion that

$$x_i(t) = x_i^0 + v_i^0 \cdot t + \frac{1}{2} a_i t^2 \simeq \frac{1}{2} a_i t^2$$

where

$$a_i = (i/N) \cdot ZeE(x_F)/M \quad ,$$

and the ions are ionized  $Z$  times and have mass  $M$ . The ion ordering remains unchanged only after the acceleration term becomes dominant. This, together with the constancy of  $E(x_F)$ , makes  $a_i$  time independent in this Lagrangian picture. The last approximate equality holds since the expansion due to the acceleration during 1 nsec is of order of 1 mm and is much larger than the thermal ion expansion of  $\sim 10^{-2}$  mm. At a given time, therefore, the ion distances are spaced in proportion to  $i$  which means a uniform ion density,  $n$ , for  $0 \leq x \leq x_F(t)$ . This density decreases as a function of time,  $Zen = E(x_F)/(4\pi x_F)$ , where  $x_F(t) = x_N(t)$ . An estimate

for  $E(x_F)$  is provided by GDSL and is:

$$E(x_F) = \frac{V_0}{D} \cdot \left( \frac{\gamma_0 + 1}{\gamma_0 - 1} \right)^{1/2} \cdot \ln \left( \gamma_0 + (\gamma_0^2 - 1)^{1/2} \right). \quad (9)$$

It is easy to see that inside the constant density ion sheath the electric field drops linearly to zero from its value  $E(x_F)$ . The axial ion current density profile and its time dependence have also been derived but will be given elsewhere.

We follow the orbit of an electron that enters at  $x_F$  with velocity  $v_z/c \ll 1$  and large radial momentum. For a thin ion sheath we may neglect relative changes in the radial momentum and the magnetic field along the electron trajectory. The magnetic force is thus equal to  $eE(x_F)$ . The electron also undergoes little change of potential energy hence,  $\gamma \simeq \gamma_0$ . Since the transit time of an electron in the ion sheath is  $\sim 10^{-10}$  sec, only small changes of ion density will occur and the fields may thus be viewed as time independent for the electron. The axial force equation for an electron is thus:

$$\gamma_0 m_0 \frac{dv_z}{dt} = e \left( \vec{E} + \frac{\vec{v} \times \vec{B}}{c} \right)_z. \quad (10)$$

Substituting the expressions for the fields in Eq. (3) we find:

$$\gamma_0 m_0 \frac{dv_z}{dt} = eE(x_F) \cdot \frac{z + x_F - D}{x_F}, \quad (11)$$

which can be readily integrated since it is a harmonic oscillator. Electrons entering the ion sheath with an axial velocity  $v_0$  will be reflected if their

turning point lies inside the ion sheath. The turning point distance is easily computed from Eqs. (9) and (11) and is less than  $x_F$  when

$$x_F > D \cdot \left(\frac{v_0}{c}\right)^2 \cdot \frac{\gamma_0}{\left(\gamma_0^2 - 1\right)^{1/2} \ln\left(\gamma_0 + \left(\gamma_0^2 - 1\right)^{1/2}\right)} . \quad (12)$$

This ion sheath thickness is achieved for typical diodes, during  $\sim 1$  nsec for  $v_0/c < 1/6$  and  $D \sim 0.5$  cm. The electrons then follow complicated orbits inside the diode, drifting radially inwards with multiple reflections until the diode axis is reached and a tight pinch results. Thus, at small radii, the electron flow pattern includes accumulation of charge and the GDSL model does not apply any more. For the electron trajectories at small radii none of the above stated assumptions apply and Eq. (12) should not be used there. Also, for typical diode parameters, the inductive electric field becomes comparable to the static electric field and the time dependent Maxwell's Equations must be solved at small radii. The electron and ion motion, before steady state is achieved, is presently under investigation using a time dependent computer code. Preliminary results confirm the transition of electron flow from GDSL to pinched flow by very thin ion sheaths.

As yet no analytic theory exists describing the evolution of the electron and ion flow towards steady state. We can, however, draw a few conclusions about the flow properties in steady state. When calculating the ratio of ion current to electron current in the steady state the following considerations apply. The current for each species is equal to the amount of its charge inside the diode divided by its average crossing time. For space charge limited flow the total charge inside the diode is nearly zero. The current ratio is, therefore, inversely proportional to the crossing times. For strict one dimensional motion of electrons from cathode and ions from anode, the crossing length is equal to  $D$ , the anode cathode gap,

and the ratio of crossing times depends only on the species velocities, giving:

$$T_e/T_i = (\langle D/v_e \rangle)/(\langle D/v_i \rangle) = \sqrt{\frac{m_e}{M}}$$

which is the well known Langmuir result for nonrelativistic electrons. The relativistic correction introduces a factor  $\sqrt{(\gamma_0 + 1)/2}$  to the above expression. Now, for strongly pinched electron flow, the ion crossing length remains equal to  $D$  (as long as ion pinching is prevented!), while the electrons move radially inwards and their crossing length scale is of the order of the diode radius ( $R$ ). The crossing time for the electrons is thus longer by a factor  $R/D$  relative to the one dimensional flow. The ratio of the ion current to the electron current, being proportional to the ratio of crossing times, is thus enhanced by the factor  $R/D$  giving:

$$\frac{I_i}{I_e} \approx \frac{R}{D} \frac{\langle 1/v_e \rangle}{\langle 1/v_i \rangle} \quad (13)$$

which may clearly be above unity. If a very hollow cathode is used instead of the solid cathode, ions may move in trapped orbits due to virtual anode formation. Also,  $D$  is then the gap distance in the hole. Both effects reduce the ion current. A more rigorous computation of the electron-ion current ratio is given by finding a lower bound for the ion charge density as a function of radius. For a large aspect ratio diode, with conducting boundaries, the radial electric flux is negligible. For space charge limited flow from the cathode and the anode the electric field is zero at both surfaces and hence the electric flux there is also zero. This then gives zero net charge at every radius.

$$\int_0^D \rho_i \, dz \approx \int_0^D |\rho_e| \, dz \quad . \quad (14)$$

We have shown that the electrons emitted at large radius reach the anode plane at small radius within the pinch. These electrons constitute the major contribution to the electron current. For radii  $r > R_p$ , where  $R_p$  is the radius of the pinch on the anode, the current flux through a cylinder of radius  $r$  and length  $D$  is

$$I_e = \int_0^D 2\pi r \rho_e v_{er} dz = 2\pi r c \int_0^D \frac{v_{er}}{c} \rho_e dz . \quad (15)$$

Since  $|v_{er}/c| < 1$  (in reality this fluid velocity may be much smaller than  $c$ ) we have

$$I_e < 2\pi r c \int_0^D |\rho_e| dz . \quad (16)$$

For steady-state ion flow, the axial ion current density  $J_i$  is only a function of radius. This gives the ion charge density, assuming no trapped ions (no virtual anodes):

$$\int_0^D \rho_i dz = \int_0^D \frac{J_i}{v_i} dz = J_i \left\langle \frac{D}{v_i} \right\rangle . \quad (17)$$

Using Eqs. 14, 16 and 17 we have

$$J_i > \frac{I_e}{2\pi r} \frac{\langle (v_i/c)^{-1} \rangle^{-1}}{D} . \quad (18)$$

This  $1/r$  dependence (excluding  $r < R_p$ , of course) gives the ratio of the ion current emitted from a disk of radius  $r$  to the total electron current:

$$\frac{I_i(r)}{I_e} > \frac{r}{D} \langle (v_i/c)^{-1} \rangle^{-1} \quad (19)$$



which increases linearly with  $r$  unlike Langmuir flow which scales as  $r^2$ . The maximum value of  $r$  is the radius of the anode plasma which is somewhat smaller than the cathode radius as described earlier. The average of the inverse ion velocity depends on the specifics of the voltage distribution inside the diode. For a nearly constant electric field that drops to zero near the cathode and anode on a distance scale much smaller than  $D$ , the ion velocity scales as  $v_i \sim (D - z)^{1/2}$  and this gives

$$\langle (v_i/c)^{-1} \rangle^{-1} = \frac{1}{2} \beta_i = \frac{1}{2} \sqrt{\frac{2eV_0}{Mc^2}} \quad (20)$$

The total ion current from Eqs. (19) and (20) is therefore

$$\frac{I_i}{I_e} > \frac{1}{2} \frac{R}{D} \beta_i \quad (21)$$

If the accelerated ions are protons and  $V_0 \approx 2\text{MV}$  then a diode with aspect ratio  $R/D \approx 20$  will generate an ion to electron current ratio of the order:

$$\frac{I_i}{I_e} > 0.65 \quad .$$

The total diode current consists of the sum of the electron and ion current and is self limited by the total magnetic field. If the electron current is greater than the ion current, then the properties of the electron flow at large radii  $r > R_1$  (Fig. 3), where no ions flow, are well described by GDSL which predicts the total magnetic field. Thus, the total magnetic field is unchanged and the diode current is the same, irrespective if a large ion current, in addition to electron current, exists inside the diode or pure electron flow takes place. The ion current only reduces the



electron current. For the above numerical example the total current is above 1MA giving about 0.5 MA of ion current.

The above estimates clearly indicate the possibility of using high power electron beam accelerators to efficiently generate ion beams. A plasma jet will, of course, be formed if these MeV ions are extracted through a meshed cathode. This plasma jet may be focused geometrically by using different diode geometries. Possible applications of such ion beams may prove far reaching.<sup>4</sup>

It should be noted that highly accurate computer simulation is needed in order to follow the dynamic pinch formation and the detailed electron and ion motion. In a fully time dependent simulation one has to include the complete set of Maxwell equations and a time dependent anode plasma generation with the appropriate emission of ions from it, as well as the time dependent effects on the emission from the cathode plasma. At present, some of these effects are being investigated by a time dependent code which neglects radiation type effects but includes time dependent electron and ion emission from the plasmas (with zero electric fields).

## References

1. S. A. Goldstein, R. C. Davidson, J. G. Siambis and R. Lee, Phys. Rev. Lett. 33, 147 (1974).
2. John M. Creedon, J. Appl. Phys. 46, 2946 (1975).
3. A. E. Blaugrund and G. Cooperstein, Phys. Rev. Lett. 34, 461 (1975).  
For more details see: A. E. Blaugrund, G. Cooperstein and Shyke A. Goldstein, these proceedings.
4. Shyke A. Goldstein and Roswell, Phys. Rev. Lett. 35, 1079 (1975).  
Shyke A. Goldstein and John U. Guillory, Phys. Rev. Lett. 35, 1159 (1975) and also these proceedings. For more preliminary data and schemes see: Bull. Am. Phys. Soc. 20, 1252 (1975): R. Lee and S. A. Goldstein; A. E. Blaugrund, G. Cooperstein, J. R. Boller and S. A. Goldstein; S. A. Goldstein, R. Lee, G. Cooperstein, and A. E. Blaugrund.

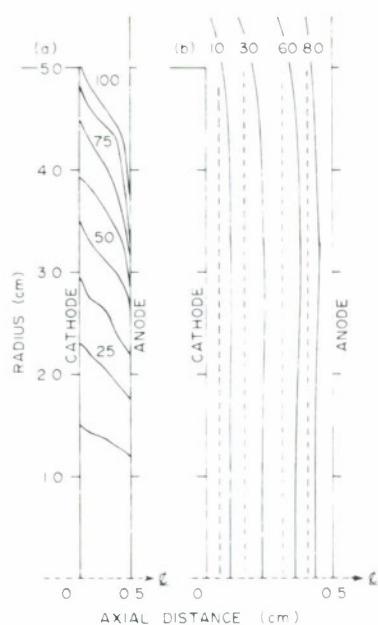
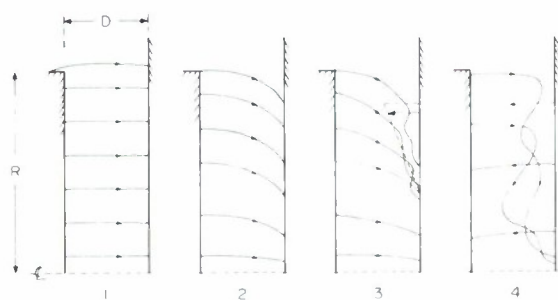


Figure 1. Steady state current contours and equipotentials for a diode with an aspect ratio  $R/D = 10$ . The applied voltage is 0.511 MV.



1 CHILD-LANGMUIR ELECTRON FLOW AT LOW VOLTAGE  
2 ELECTRON FLOW AT HIGH VOLTAGE - WEAK PINCH  
3 ION INDUCED COLLAPSING RING  
4 STEADY STATE ELECTRON AND ION FLOW

Figure 3. Schematic presentation of the four distinct phases of the evolution of charge flow in a large aspect ratio diode.

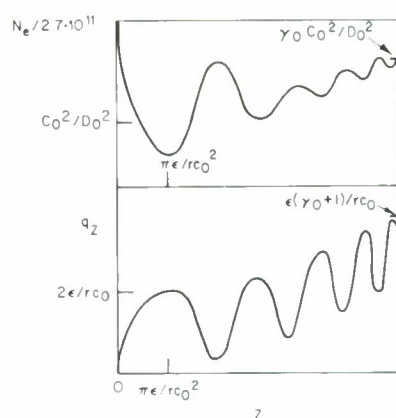


Figure 2. (a) Sketch of density  $n$  and normalized to  $m_e c$  axial momentum  $q_z$  versus  $z$ , at large radii inside the diode.

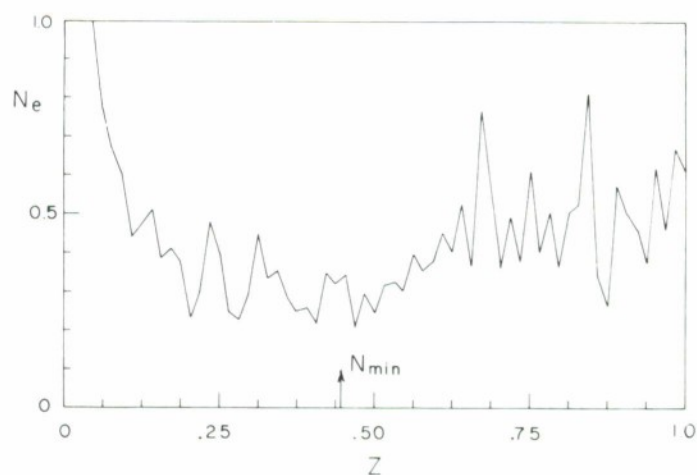


Figure 2. (b) Typical density profile variation versus  $z$  as found in computer simulation. The theoretical prediction for the location of the first minimum is indicated on the  $z$  axis.

## PROCESSES GOVERNING PINCH FORMATION IN DIODES

A. E. Blaugrund\* and G. Cooperstein  
Naval Research Laboratory, Washington, D. C. 20375

and

Shyke A. Goldstein  
University of Maryland, College Park, Md. 20742

### ABSTRACT

The process of pinch formation in large aspect ratio diodes has been studied by means of streak photography and time-resolved x-ray detectors. A tight pinch is formed at the anode center by a collapsing thin hollow electron beam. The collapse velocity depends, amongst other things, on the type of material in the top  $1\text{ }\mu\text{m}$  layer of the anode. In a tentative model it is assumed that an anode plasma is at least partially created from gases released from the surface layer of the anode by the heating action of the beam. These gases are ionized by primary, backscattered, and secondary electrons. Ions emitted from this plasma modify the electron trajectories in the diode leading to a radial collapse of the hollow electron beam. The observed monotonic dependence of the collapse velocity on the atomic number of the anode material can be explained by the smooth dependence on  $Z$  of both the specific heat and the electron backscatter coefficient. In the case of high- $Z$  anodes the ion expansion time appears to be the factor limiting the collapse velocity. Detailed experimental data are presented.

---

\*Permanent address: The Weizmann Institute of Science, Rehovot, Israel.

The interest in pellet fusion and in dense hot plasmas in general, has caused many groups to search for efficient methods of focusing intense relativistic electron beams. So far the most promising approach seems to be the self-pinching of the electron beam within the accelerator diode. In this paper we present a series of experiments designed primarily to investigate the transient phase leading to the formation of a tight pinch. We limit ourselves to low impedance ( $Z < 4\Omega$ ) diodes with hollow, tapered cathodes and flat anodes. This type of diode produces a stable pinch at the center of the anode. By proper choice of the cathode dimensions more than  $2/3$  of the diode current can be focused within the pinch region<sup>1</sup>. In these diodes pinching occurs through the formation and subsequent collapse of a thin hollow ring of electrons. This has the advantage that a small target placed at the center of the anode undergoes practically no heating until the collapsing electron ring reaches it. Power risetimes in the pinch region are of the order of 1 nsec. A stable and intense pinch can also be obtained in diodes employing a preformed plasma or a current channel on the diode axis<sup>2</sup>. However, in these cases power risetimes in the pinch region are comparable to the diode power risetime, i.e., 20 - 30 nsec at present.

The experiments presented here were done primarily on the Gamble I machine<sup>3</sup> using a very hollow tapered cathode (I.D. = 69 mm, O.D. = 84 mm,  $6.3^\circ$  taper). This rather hollow cathode does not produce as intense a pinch as the less hollow one. It was chosen because it produces a large diameter hollow beam which takes a relatively long time to contract. This is convenient when one wants to investigate the processes affecting the collapse of the hollow beam leading to the formation of the pinch. The total electron

beam energy was 8-9 kJ/pulse and the peak diode power as  $1.5 \times 10^{11}$  W. The anode-cathode spacing was 6.0 mm (at outer diameter of the cathode) corresponding to a diode impedance of approximately  $3 \Omega$ . The streak photography technique described in ref. 1 served as the main diagnostic tool. In this technique the outside of the anode plate is covered by a thin sheet of fast plastic scintillator (see Fig. 1). The anode plate is just thick enough to prevent the electrons from reaching the scintillator. The light signal is generated by the bremsstrahlung radiation emitted from the anode. Thus, at any given time, the light pattern in the scintillator reflects the distribution of electrons striking the anode. The spatial resolution of the method depends on the thickness of the anode and on the x-ray absorption coefficient of the anode material. This resolution varied from about 4 mm for light elements like carbon to less than 2 mm for tantalum or gold. The scintillator light was recorded by fast image converter cameras (TRW model 1D) operating in frame and streak modes. In the streak mode the object slit was positioned along a diameter of the anode. The streak duration and length were 100 nsec/50 mm and the time resolution was approximately 3 nsec. The center 20 mm diameter of the scintillator was covered with an optical neutral density filter which attenuated the light by a factor of three. This made possible the observation of the very bright pinch region in the center together with much less bright parts of the scintillator. In addition, the size of the filter provided a convenient scaling length on the streak record. Figure 1 shows such a streak photograph time correlated with the voltage and current waveshapes. The time correlation was obtained by observing the time of arrival of the pinch on axis by means of a collimated x-ray scintillation



detector. It can be seen that the streak picture is somewhat distorted by the camera. Therefore, a fixed grid of equally spaced thin lines was placed across the slit. These lines which can be seen in the streak photograph practically eliminate errors due to camera distortion. In this picture a thin hollow ring can be seen forming early in time. The initial radius (36 mm) of this ring is slightly larger than the inner radius of the cathode. This ring contracts slowly until it reaches a radius of approximately 33 mm. There, an abrupt change - a jump - occurs. The existing intense ring fades and a new ring is formed at a smaller radius. This new ring contracts in an accelerated motion into a tight pinch at the center of the anode. The light observed outside the collapsing ring is due to a fraction of the electron flow not contained in the ring. The details of this light distribution will be presented elsewhere.

Figure 2 shows similar photographs taken with anodes made of aluminum and brass. It can be seen that in both cases the behaviour is qualitatively similar but the time scales are different. In the case of brass the abrupt transition occurs earlier, it is accompanied by a very clear discontinuity, and the subsequent collapse proceeds at a higher speed. Experiments with anode materials ranging from carbon to lead seem to indicate that the collapse velocity increases monotonically as a function of the atomic number. Figure 3 shows the collapse velocity for anodes made of graphite, aluminum, brass, tantalum and gold as a function of the atomic number  $Z$ . The velocity plotted in this figure is the areal velocity  $d(\pi r^2)/dt$  where  $r$  is the radius of the electron ring. Experimentally, the areal velocity is found to be reasonably constant and the justification for this will be discussed later.

By coating high Z anodes with thin layers of low Z materials and vice versa it was found that the collapse velocity was largely determined by the top 1  $\mu\text{m}$  layer. Figure 4 shows the effect of totally or partially coating a brass anode with approximately 1  $\mu\text{m}$  of carbon (aquadag). For comparison Fig. 4a again shows a streak photograph taken with an uncoated brass anode. The streak in Fig. 4b was taken with a brass anode fully coated with carbon. In this latter case the initial phase before the jump is much longer than for bare brass and the subsequent collapse much slower. In Fig. 4c only the inner region  $r < 29.5 \text{ mm}$  was coated with aquadag. It can be seen that here the jump occurs early but once the hollow beam lands on the carbon coating it collapses slowly starting with a very low velocity. The complementary experiment is shown in Fig. 4d where the outer region  $r > 25.5 \text{ mm}$  was coated with carbon. Here, a long time elapsed before the jump occurred but once the hollow beam landed on the bare brass it collapsed with a very high speed towards the center. These experiments show that the movement of the beam over the anode surface is locally determined by the type of anode surface.

Figure 5 shows a streak photograph taken with a brass anode, the lower half of which had been coated with aquadag. The behaviour of the electron beam on the two halves of the anode is distinctly different. Initially, the electron ring forms at the same radius on both halves and the slow movement inwards is similar. Then, after some 20 nsec the jump occurs on the brass side only, and a new and brighter ring is formed at a smaller radius. So far this behaviour is typical of brass and other high Z materials. However, after the jump the new ring is brighter and collapses with a much lower velocity than normally found for brass. The electron ring on the aquadag

side contracts slowly in a way typical for aquadag-coated brass anodes. The final pinch is formed off center on the brass half of the anode. This rather unexpected behaviour can be explained as follows: The formation of the electron ring and its initial slow contraction can be understood in the framework of the laminar flow model<sup>4,5</sup> and is confirmed by computer simulation. As the electrons hit the anode the local temperature rises. The rate of temperature rise at the surface depends on the specific heat of the surface layer, on the electron angle of incidence, and on the electron backscatter coefficient. Because of these factors the surface temperature on the brass side rises faster than on the aquadag side. The rising temperature causes adsorbed and dissolved gases to be released and these gases are ionized by primary, backscattered, and secondary emission electrons. The ions move towards the cathode and increase the electron emission. The rising magnetic field increases the incidence angle of the electrons and thereby the backscatter coefficient and surface heating, which, in turn, cause more gas to be released and ionized. Eventually, these gases may even be ionized by electrical breakdown. The resulting ion cloud affects the electron trajectories, causing the "jump", and produces an increased electron current density on the brass side. This current is further augmented by additional gap closure due to anode plasma motion. The resulting magnetic field is no longer azimuthally symmetric (see Fig. 5). On the brass side there now exists an additional magnetic field inside the electron ring. The direction of this field is such as to oppose the motion of electrons toward the diode axis. This field is responsible for the unusually slow collapse of the electron ring on the brass side and causes the pinch to be formed off center. The above model can also

be used to explain a similar behaviour observed when the asymmetry is due to a non-parallel anode-cathode geometry.

Surface heating, release of gas, creation of ions and their expansion, are believed to be the mechanisms responsible for the pinch formation. It has been shown<sup>5,6</sup> that an expanding sheath of ions emitted from the anode is necessary and sufficient for the formation of a pinch by the collapse of a hollow beam\*. The motion of these ions is practically unaffected by the magnetic field and they move in the axial direction from the anode to the cathode. In our tentative model surface gases are released by the heating action of the beam. These gases are then ionized by the electrons. When the ions move fast enough a thick ion sheath is created which enables the electrons to drift towards the axis. When they reach a radius where there are no ions the electrons are driven towards an as yet unheated region of the anode. Under the bombardment by the electrons this ring-shaped region eventually starts emitting ions and the electrons can move to smaller radii. If the surface energy deposition rate is constant during the collapse phase this model leads to a constant areal velocity  $d(\pi r^2)/dt$ . Therefore, anode materials with lower specific heat and higher electron reflection coefficients (i.e., higher atomic numbers) are expected to have a higher collapse velocity. However, at higher collapse velocities the finite expansion time of the ions becomes a limiting factor. The areal collapse velocity in this case can be shown to be proportional to  $I \Delta(r)$  when  $I$  is the current

\* Not enough time and energy is available for the creation of a thick enough plasma layer as assumed in previous models.<sup>7</sup>



contained in the ring and  $\Delta(r)$  is the ring thickness. If this product changes little with the radius  $r$  then again a constant areal velocity can be expected. Figure 3 shows that indeed the areal velocity increases with the atomic number  $Z$ . For carbon and aluminum the areal velocity seems to be limited by the heating rate of the anode material. It is clear however that for high  $Z$  materials the observed areal velocity is much too low to be explained by the heating mechanism. We assume that in these cases the ion expansion time limits the collapse velocity. In the majority of cases, the constant areal velocity is experimentally observed. An example of this is shown in Fig. 6 when  $\pi r^2$  is plotted as a function of time for carbon and gold anodes.

If one assumes that  $\gtrsim 10^{16}$  atoms/cm<sup>2</sup> are released in the form of gas from the anode surface, enough ions will be created to satisfy the requirements of the above model. Experiments with various coating thicknesses have shown that the properties of the material in the top 1  $\mu$ m layer largely determine the pinching behaviour. It is easy to show that on a time scale of  $\sim 10^{-9}$ s indeed a minimum thickness of  $\sim 10^{-6}$  m is required in order for the surface temperature to be determined by the coating rather than by the substrate. The collapse velocity will also to some extent be affected by electron backscattering by the substrate.

The role of surface gases in the pinch formation was confirmed by experiments in which the anode was either heated or cooled. Because of experimental limitations only temperatures of +120<sup>o</sup> C and -90<sup>o</sup> C were employed. The heated anode showed almost no "jump" and a slightly lower collapse velocity while cooling had the opposite effect.

On the Gamble II<sup>8</sup> accelerator streak photographs were taken at beam powers of approximately  $10^{12}$  W with an identical diode geometry. These photographs also showed the hollow ring formation and the collapse into a very tight pinch. The areal collapse velocity seems to be proportional to the electron current in the collapsing ring as predicted by our model. The presence of copious quantities of ions during the pinch formation was demonstrated<sup>9</sup>.

So far all our observations are consistent with the described model. However, additional experiments and theoretical work are required to verify and refine the model's various aspects.



## REFERENCES

1. A. E. Blaugrund and G. Cooperstein, Phys. Rev. Lett. 34, 461 (1975).
2. G. Yonas, K. R. Prestwich, J. W. Poukey and J. R. Freeman, Phys. Rev. Lett. 30, 164 (1973); P. A. Miller, J. Chang and G. W. Kuswa, Appl. Phys. Letters 23, 423 (1973); G. Cooperstein, J. J. Condon and J. R. Boller, Bull. Am. Phys. Soc. 18, 585 (1973) G. Yonas in SAND 74-0439, March 1975.
3. G. Cooperstein, J. J. Condon and J. R. Boller, J. Vac. Sci. Technol. 10, 961 (1973).
4. S. A. Goldstein, R. C. Davidson, J. G. Siambis and Roswell Lee, Phys. Rev. Lett. 33, 1471 (1974).
5. S. A. Goldstein, R. C. Davidson, R. Lee and J. G. Siambis, this conference.
6. S. A. Goldstein and R. Lee, Phys. Rev. Lett. 35, 1079 (1975).
7. G. Yonas, J. W. Poukey, K. R. Prestwich, J. R. Freeman, A. J. Toepfer and M. J. Clauser, Nucl. Fusion 14, 731 (1974).
8. L. S. Levine and I. M. Vitkovitsky, IEEE Trans. Nucl. Sci. 18, No. 4, 225 (1971).
9. A. E. Blaugrund, G. Cooperstein, J. R. Boller and S. A. Goldstein, Bull. Am. Phys. Soc. 20, 1252 (1975).

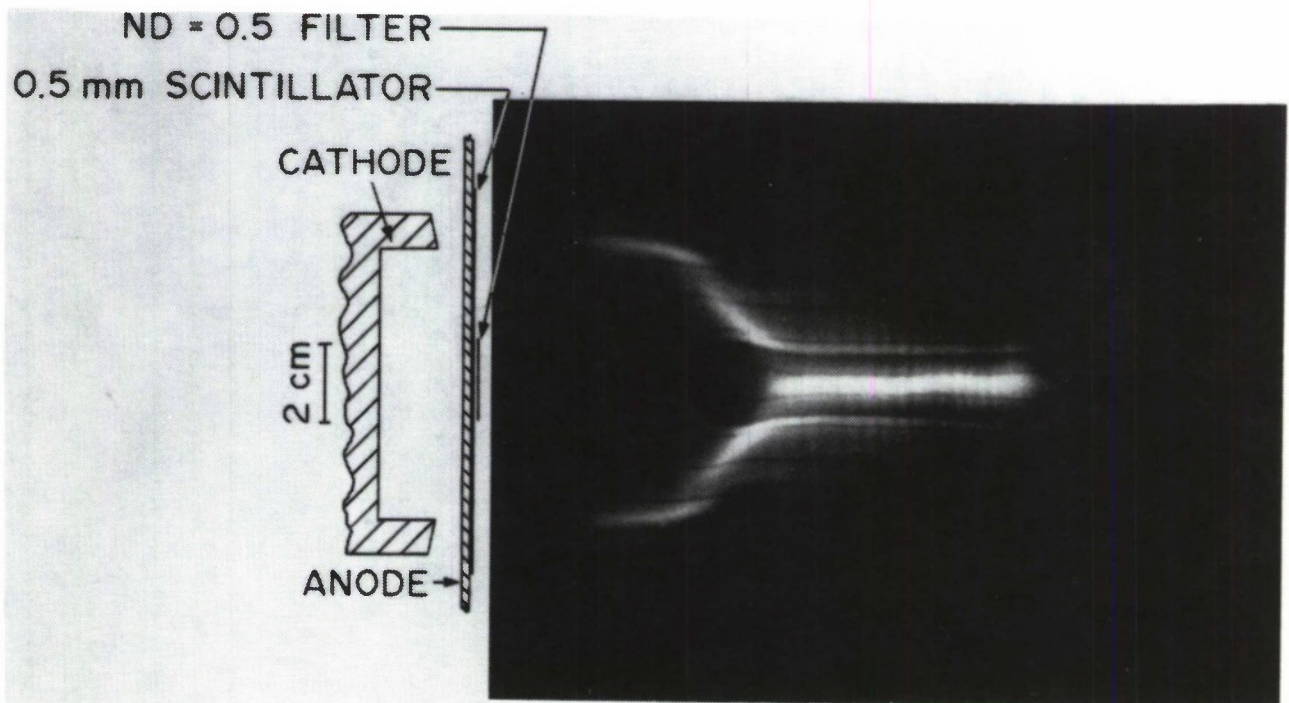
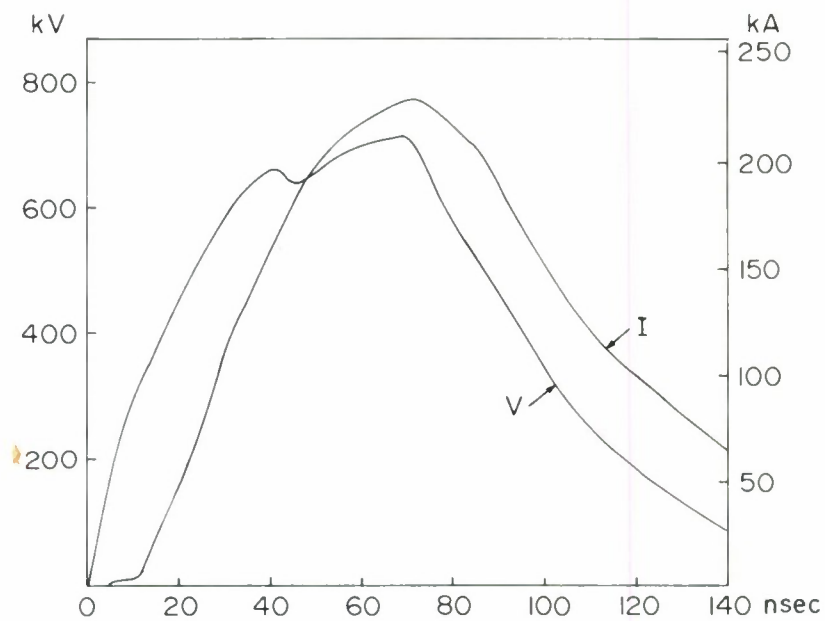
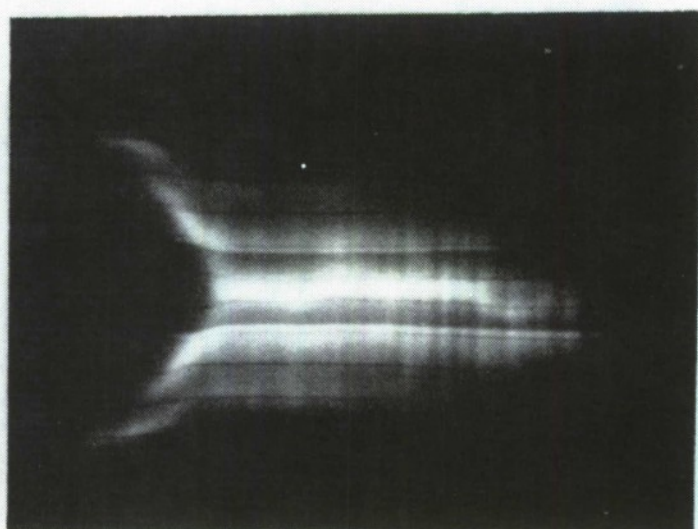
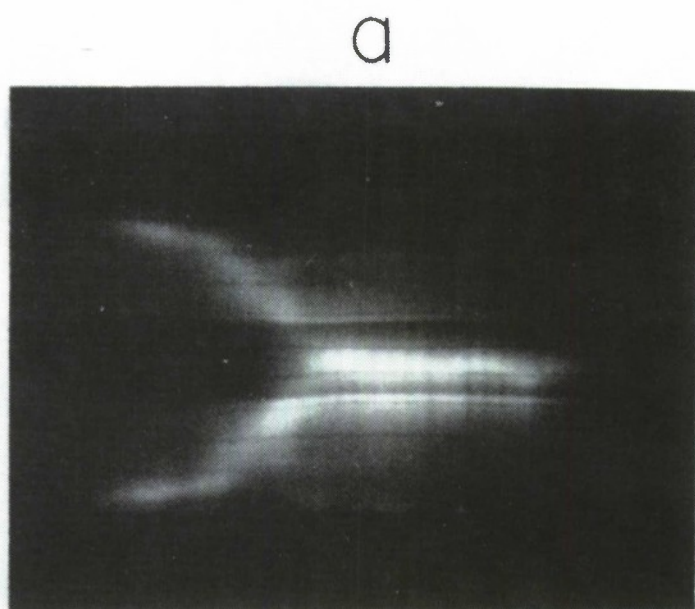


Figure 1. Voltage and current waveforms time correlated with a streak photograph (Ti-hydride anode). The voltage shown has been corrected for the inductive part. The diode geometry, the scintillator and the optical filter are also shown.



b

20 nsec

Figure 2. Streak photographs taken with anodes made of aluminum (a), and brass (b).

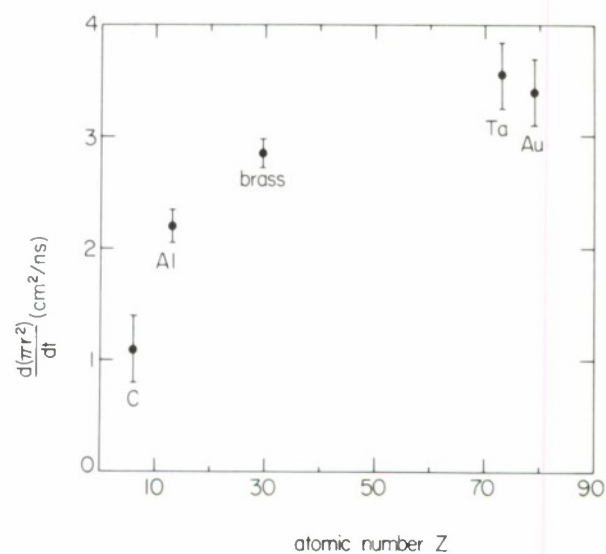


Figure 3. The areal velocity  $d(\pi r^2)/dt$  as a function of the atomic number of the anode material.

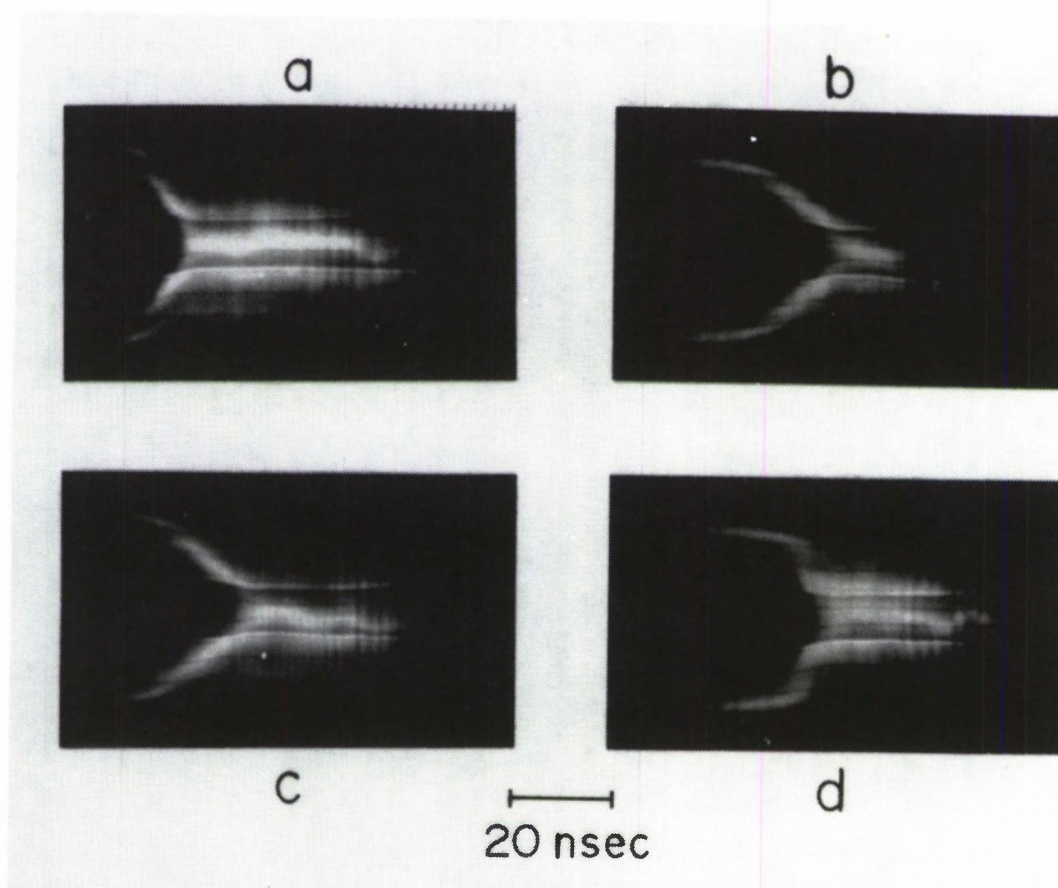


Figure 4. The effect of thin carbon layers on the behaviour of the electron ring (a) uncoated brass anode, (b) brass anode fully coated with carbon, (c) the center of a brass anode,  $r < 29.5$  mm, coated with carbon, (d) the outer region of a brass anode,  $r > 25.5$  mm, coated with carbon.



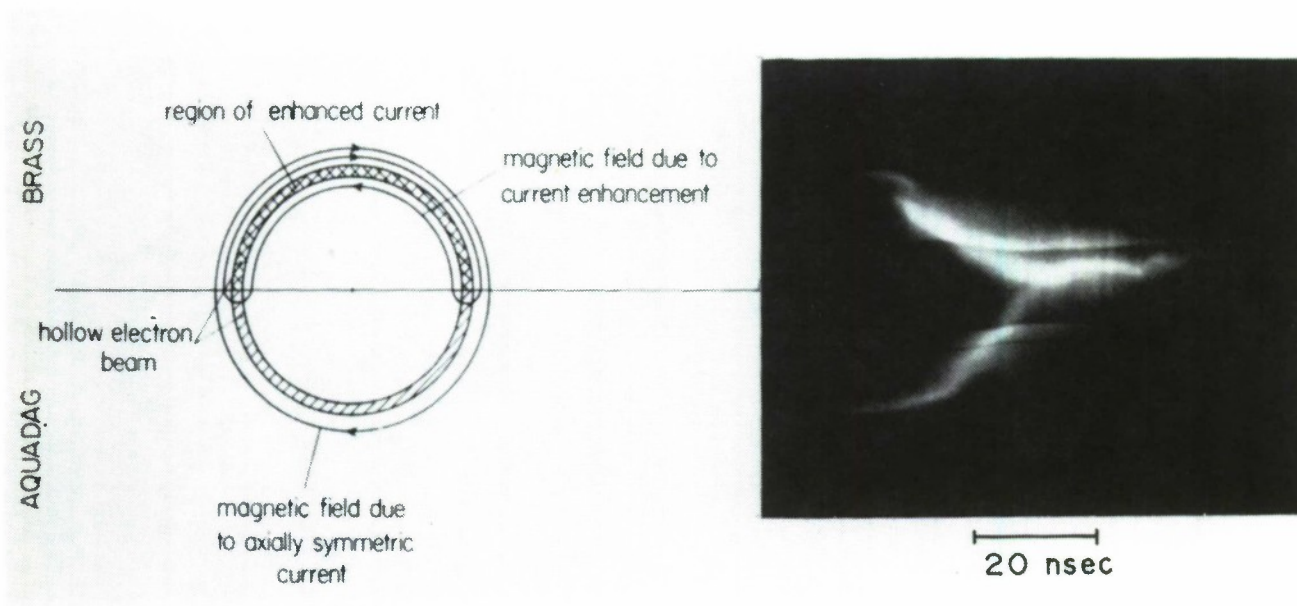


Figure 5. Streak photograph taken with a brass anode, the lower half of which had been coated with a thin layer of carbon. The drawing at left shows schematically the electron ring at the anode plane, the region of enhanced current, and the magnetic fields due to the azimuthally symmetric part of the electron beam and to the beam enhancement.

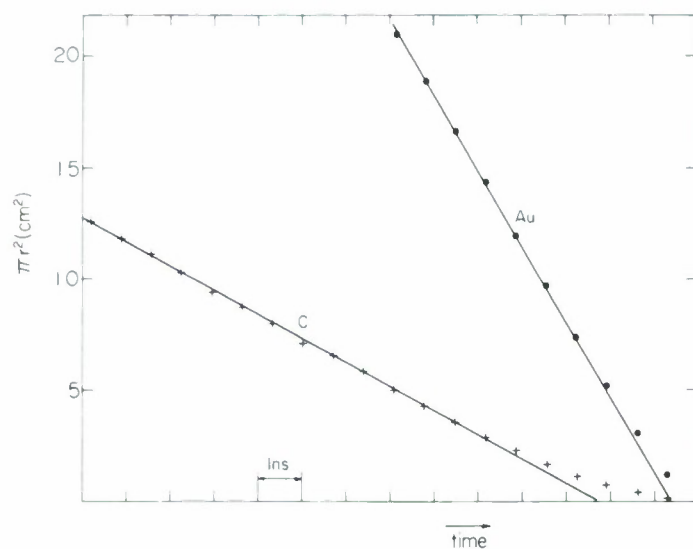


Figure 6.  $\pi r^2$  as a function of time for solid carbon and gold anodes.

$Z_e < 1\Omega$  PINCHED ELECTRON DIODES\*

J. W. Poukey  
Plasma Theory Division

Sandia Laboratories  
Albuquerque, New Mexico 87115

ABSTRACT

High current pinched electron flow in diodes is shown to be self-limiting in the sense that for given diode voltage the electron current approaches a limiting value as  $R/d$  (cathode radius/gap)  $\rightarrow \infty$ . The consequence is that in order to achieve electron impedances  $Z_e < 1\Omega$ , one may have to inject high-atomic-weight plasma into the diode.

\* Work supported by the United States Energy Research and Development Administration.



Previous computational work on relativistic diodes has shown that the electrons in relativistic diodes may be made to pinch using exploded wires,<sup>1</sup> thick anode plasmas,<sup>2</sup> or by emitting space-charge-limited ion currents from a thin anode plasma produced by electron bombardment of the anode<sup>3</sup> or by separate plasma injection into the diode.<sup>4</sup> It was also shown that the pinching electron beam causes displacement of the equipotentials towards the anode, leading to ion currents which may exceed the electron currents.<sup>3,5</sup> In this paper we consider the problem of obtaining large ( $\sim$  MA) pinched electron currents in the presence of space-charge-limited ion flow. The reason this is a problem is that high current pinched electron flows in diodes tend to be self-limiting; i.e., large negative space charge in the diode tends to "shut off" the cathode and put more current into the ions. For a given diode in the steady state, let  $V$ ,  $R$ ,  $d$ ,  $I_e$ , and  $I_i$  be voltage, cathode radius, vacuum gap, electron current, and ion current, respectively. Let  $\gamma = 1 + eV/mc^2$  and (in kA)  $I_p = 8.5 \gamma \ln(\gamma + \sqrt{\gamma^2 - 1}) R/d$ , the parapotential current.<sup>6</sup> We consider only steady states with space-charge-limited ions emitted for  $r < R$ , and only states with good electron pinching. Since we wish to consider cathodes with various degrees of "hollowness," we let  $\Delta R$  be the width of the cathode annulus (so  $\Delta R = R$  means a solid cathode).

The particle simulation diode code has in the past consistently refused to produce solutions with  $Z_e \equiv V/I_e \leq 1$ . A summary of some of the latest runs is shown in Table I. For all runs shown, the ions were protons. Note that  $I_p$ , while far from exact, agrees rather well with the sum of  $I_e$  and  $I_i$  as calculated by the code, except in the spherical cases where the  $I_p$  formula cannot be expected to apply (even here the scaling looks right). We tentatively conclude that for all pinched, bipolar, cylindrically symmetric,

planar diodes (whether solid or hollow, using  $d$  = plasma-to-plasma gap if plasma is present);

$$I_e + I_i = I_p . \quad (1)$$

As Shyke Goldstein points out,<sup>7</sup> for solid-cathode diodes with space-charge-limited electrons and ions there should be nearly equal numbers of  $e$  and  $i$  present in the gap, so current  $\propto$  (transit time)<sup>-1</sup> or

$$I_i/I_e = \beta_i R/d \beta_e = \frac{.033}{\sqrt{A}} \frac{\gamma}{\sqrt{\gamma+1}} \frac{R}{d} \quad (2)$$

where  $\beta_i = \sqrt{2(\gamma-1) m_e/m_i} = .033 \sqrt{\gamma-1}/\sqrt{A}$ , and  $A$  is the atomic weight of the ions of mass  $m_i$ . As can be seen from the table by comparing runs for which only  $R/d$  was changed, this relation is approximately satisfied for diodes where  $\Delta R/R \geq 1/2$ , but is not valid for very hollow diodes. From Eqs. (1) and (2), we have for solid-cathode diodes

$$I_e = \frac{I_p}{1 + \beta_i R/d \beta_e} . \quad (3)$$

For fixed  $V$ , the largest possible  $I_e$  is ( $R/d \rightarrow \infty$ )

$$I_{\max}^e = 258 \sqrt{A} \sqrt{\gamma+1} \ln(\gamma + \sqrt{\gamma^2-1}) (\text{in kA}) . \quad (4)$$

We see from the table that the only case with  $\Delta R/R \geq 1/2$  where  $I_e$  comes within a factor 2 of  $I_{\max}^e$  is the 2 MV case with  $R/d = 51$ . Defining  $Z_{\min}^e \equiv V/I_{\max}^e$ ,

$$A^{1/2} Z_{\min}^e = \frac{2(\gamma-1)}{\sqrt{\gamma+1} \ln(\gamma + \sqrt{\gamma^2-1})} (\text{in } \Omega) \quad (5)$$

From Fig. 1, we see that for  $A^{1/2}Z_{\min}^e < 1$  we need  $\gamma < 2.5$ , or  $V < .77$  MV. The only case in the table (when ions are protons) for which  $V/I_e$  even comes close to unity is the 500 kV hollow case ( $V/I_e = 1.25 \Omega$ ). To achieve  $.1 \Omega$  or less at 1 MV one must use anode plasma composed of ions with  $A > 125$ .

Going to very hollow diodes (small  $\Delta R/R$ ) reduces  $I_i/I_e$  somewhat, but the reduction is smaller at larger  $V$  (in Table I, compare the pairs of runs at .5, 1, and 2 MV). If one is willing to work at lower  $V$ , say 500 kV, Table I suggests that using very hollow diodes will lower  $Z_{\min}^e$  by a factor of about 3. This would allow one to achieve a given  $Z_e$  with much lighter ions. This work on hollow diodes is preliminary, and Eqs. (2)-(5) may not apply when  $\Delta R/R < 1/2$ . Thus our somewhat pessimistic conclusion concerning the difficulty of achieving  $Z_e < 1 \Omega$  (when ions are protons) should be regarded as tentative for hollow diodes. Also, one must keep in mind the possibility that the ion emission may be supply-limited, rather than space-charge-limited, in which case our conclusions do not apply for any diode.

To study the increase of  $I_e$  with  $A$ , the code was used to repeat the 2 MV,  $R = 51$  cm,  $d = 1$  cm case but with  $A = 100$  (instead of protons). One would expect  $I_i/I_e$  to be reduced by a factor 10, from 4 to .4, and from Eq. (3),  $I_e$  should be increased (from .8 MA) to 2.7 MA. The results were in fact slightly better than these predictions:  $I_e = 3.0$  MA,  $I_i/I_e = .2$ , suggesting that going to heavy ions buys one somewhat more than Eq. (2) would suggest (insofar as reducing the power put into the ions is concerned).

The conclusion of this work is that in order to produce low- $Z_e$  diodes (with good pinching), one may have to inject high- $A$  plasma into the diode. The alternative is to use the lower-current electron beam pinch to make

large currents of ions and then to direct the ions themselves onto a fusion target.<sup>8,9</sup> From Eqs. (1) and (2), the solution for  $I_i$  is

$$I_i = I_p / (1 + \beta_e d / \beta_i R) \quad . \quad (6)$$

There is no limit here; as  $R/d \rightarrow \infty$ ,  $I_i \sim R/d$ . At least from the impedance point of view, ion diodes may be easier to design.

The computational result for a 20 MV spherical diode is shown in Fig. 2. This result was obtained using a new spherical coordinate version of the diode simulation code.<sup>9</sup> The computed  $I_i$  of 9 MA exceeds  $I_e$  by a factor 3 so that most of the power is being used to accelerate ions. The anode is outside the cathode so the emitted ions converge radially inwards. The electrons pinch to the symmetry axis; note the large displacement of the equipotentials there towards the anode. This case should be of real interest for ion beam fusion studies,<sup>8</sup> although there are problems in actually focusing the ions onto a mm-sized target located at the center of the sphere.

#### Acknowledgment

The helpful comments of M. M. Widner and G. Yonas are acknowledged.

## REFERENCES

1. G. Yonas, K. R. Prestwich, J. W. Poukey, and J. R. Freeman, Phys. Rev. Lett. 30, 164 (1973); G. Yonas, J. W. Poukey, K. R. Prestwich, J. R. Freeman, A. J. Toepfer, and M. J. Clauser, Nucl. Fusion 14, 731 (1974).
2. J. W. Poukey, J. R. Freeman, and G. Yonas, J. Vac. Sci. Technol. 10, 954 (1973); J. W. Poukey and A. J. Toepfer, Phys. Fluids 17, 1582 (1974).
3. J. W. Poukey, 13th Symposium on Electron, Ion, and Photon Beam Technology, Colorado Springs, Colorado, May 1975 (to be published).
4. P. A. Miller, J. W. Poukey, and T. P. Wright, Phys. Rev. Lett. 35, 940 (1975).
5. J. W. Poukey, Appl. Phys. Lett. 26, 145 (1975).
6. J. M. Creedon, J. Appl. Phys. 46, 2946 (1975).
7. S. A. Goldstein and R. Lee, Phys. Rev. Lett. 35, 1079 (1975).
8. M. J. Clauser, Phys. Rev. Lett. 35, 848 (1975).
9. J. W. Poukey, J. R. Freeman, M. J. Clauser, and G. Yonas, to be published.

TABLE I  
SUMMARY OF COMPUTATIONAL DIODE STUDIES

V (MV)	$\Delta R/R$	R (cm)	d (cm)	$I_e$ (MA)	$I_i$ (MA)	$I_p$ (MA)	$I_{max}^e$ (MA)	$\frac{I_i}{I_e} \frac{d}{R}$	$\frac{\beta_i}{\beta_e}$
.4	1	5.1	.44	.14	.07	.21	.51	.043	.035
.5	1	19	.8	.28	.30	.53	.58	.045	.038
.5	1/3	19	.8	.40	.14	.53	.58	.015	.038
.625	1/3	6.4	.6	.26	.04	.29	.67	.014	.041
1	3/4	10	1.5	.2	.06	.29	.90	.045	.049
1	3/16	10	1.5	.2	.04	.29	.90	.030	.049
1.4	1/2	10	2	.25	.05	.33	1.1	.040	.056
1.5	1	19	2	.34	.23	.66	1.2	.07	.06
1.5	1	19	1.5	.40	.34	.88	1.2	.07	.06
1.5	1	19	.75	.50	.90	1.7	1.2	.07	.06
2	1/2	51	1	.8	3.2	4.8	1.4	.078	.067
2	1/8	51	1	.8	3.2	4.8	1.4	.078	.067
3	5/16	19	.8	.8	1.8	3.6	1.9	.095	.081

WITH THICK ANODE PLASMA

1.25	7/16	15.2	1.5	.40	.13	.57	1.0	.032	.054
1.25	"	15.2	2	.25	.085	.43	1.0	.045	.054
1.7	"	15.2	2.8	.25	.09	.43	1.3	.066	.062
1.7	"	15.2	3.5	.21	.06	.34	1.3	.066	.062

SPHERICAL DIODES

10		R/d = 4		.7	.5	2.7	4.5	.18	.15
10		R/d = 9		1	1.6	6	4.5	.18	.15
20		R/d = 9		1.6	4.7	14	7.3	.33	.21



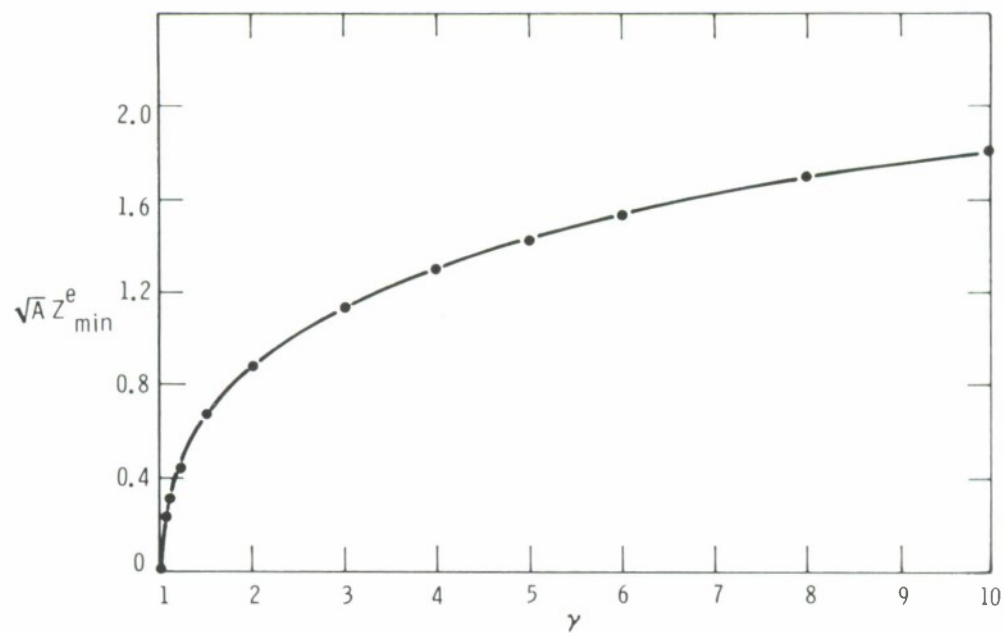


Figure 1. Plot of  $A^{1/2} Z_{min}^e$  vs.  $\gamma$ , from Eq. (5)

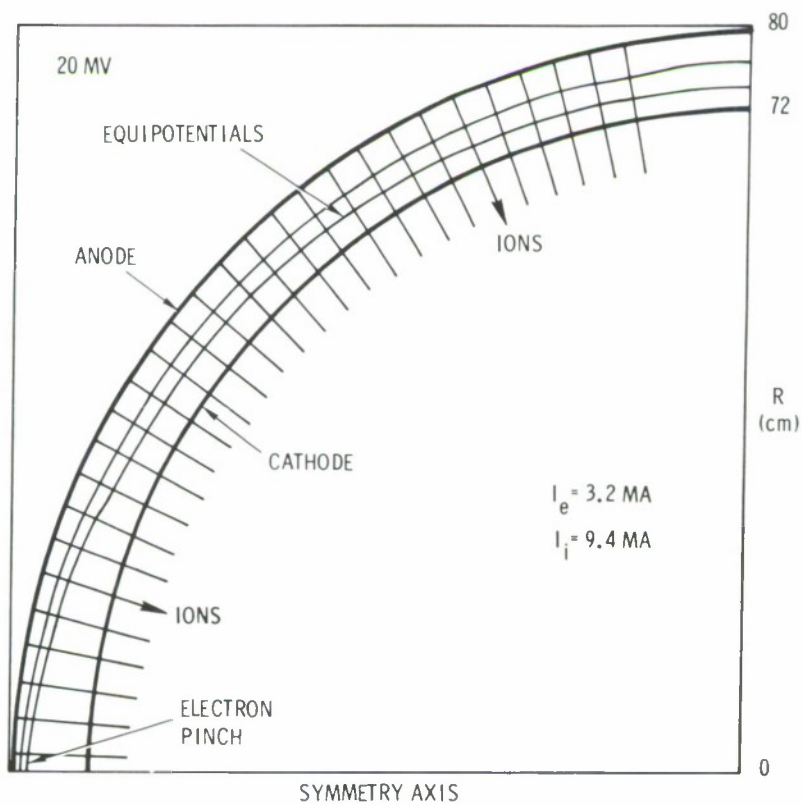


Figure 2. Computer Simulation of 20 MV Spherical Diode

## PINCHING LIMITS AND SCALING LAWS FOR HIGH CURRENT DIODES\*

G. Ronald Hadley, Thomas P. Wright, and Archie V. Farnsworth, Jr.  
Plasma Theory Division - 5241

Sandia Laboratories  
Albuquerque, New Mexico 87115

### ABSTRACT

A maximum current density achievable in a diode has been determined from a previously obtained steady state relativistic constant of the motion for the beam fluid. This current density limit has been used together with the purely radial and purely axial flow limits of the fluid equations to establish a minimum pinch radius for the beam which can be expressed in terms of macroscopic diode parameters. This expression has been combined with a Child-Langmuir emission law to obtain a necessary condition for optimal pinching. In this paper we list and discuss several electron beam machines, both present and proposed, in the light of this pinching condition.

---

\*Work supported by the United States Energy Research and Development Administration.

This paper describes the modeling of high current electron beam flow by the use of relativistic fluid equations. These equations have been described elsewhere<sup>1</sup> and that description will not be repeated here except to list the equations and give a brief summary of their derivation. First, an infinite set of fluid equations is obtained in the usual way by taking moments of the Vlasov equation. At the next step our approach to closure differs from the conventional one of ignoring all moments higher than, say, the momentum flux tensor, and consists instead, of the assumption of an analytical form for the distribution function. Since in most parts of a high current diode an electron's energy is a unique function of position, we have chosen a mono-energetic distribution function with which to close the equations. The specific form we use allows for beam temperature through the use of a variable angular spread in velocity space. The resulting set of time-dependent equations may be further simplified by neglecting time derivatives and at this point two constants of the motion may be derived, one involving total fluid energy and the other fluid internal energy which determines an equation of state for the fluid. The steady state, fluid-Maxwell equations, thus obtained, are shown below.

$$\frac{e\mathbf{B}}{mc} = \nabla \times (\mathbf{F}_m \gamma \beta) \quad (1)$$

$$W_M = \gamma - \frac{e\phi}{mc^2} \quad (2)$$

$$Q_M = \frac{na}{w\gamma} \frac{e^{a/b}}{\sinh a} \quad (3)$$

$$\nabla \times \mathbf{B} = -\mu_0 c en \beta (1 - f_M) \quad (4)$$

---

1. T. P. Wright and G. R. Hadley, Bull. Am. Phys. Soc. 20, 583 (1975).

$$\nabla^2 \phi = \frac{en}{\epsilon_0} (1 - f_e) \quad (5)$$

where  $b \equiv \coth a - \frac{1}{a} = \beta \frac{\gamma}{w}$

$$F_M = (1 - 3b/a)/b^2 \quad (7)$$

$$w = \sqrt{\gamma^2 - 1} \quad (8)$$

and  $W_M$  and  $Q_M$  are the above-mentioned constants of the motion.

A direct consequence of the constant  $Q_M$  is the establishment of upper bounds on three important quantities: beam number density, beam current density, and kinetic pressure. Formulas for these quantities are given below:

$$n_{\max} = e^{-3} w_A \gamma_A Q_M \quad (9)$$

$$J_{\max} = 1.4 \left( \frac{w_A}{w_c} \right)^2 J_c \quad (10)$$

$$P_{\max} = \frac{1}{3} \frac{w_A^2}{\gamma_A} n_{\max} \quad (11)$$

where the subscripts A and c refer to anode and cathode values, respectively, and  $w_c$  is computed from the electron "temperature" at the cathode by

$$w_c = \sqrt{\frac{kT_c}{mc^2}}.$$

For a three megavolt diode with a cathode plasma temperature of three electron volts ( $w_c = .0024$ ),  $J_{\max} = 10^7 \times J_c = 10^{10} \text{ A/cm}^2$  for a value of  $J_c = 10^3 \text{ A/cm}^2$ .

Next we shall investigate properties of z-independent flow at high  $v/\gamma$ . This may be done by setting radial velocities and z-derivatives equal to zero

in the steady state momentum equation (1), resulting in the equation

$$\frac{dp_{\perp}}{dr} = ecn\beta_z B_{\theta} , \quad (12)$$

where  $p_{\perp}$  is the pressure transverse to the beam flow. The addition of Ampere's law (4) to (12) results in the pressure balance condition

$$\frac{B_{\theta}^2(r)}{2\mu_0} = \frac{2}{r} \int_0^r p_{\perp}(r') r' dr' - p_{\perp}(r) \quad (13)$$

From previous solutions<sup>1</sup> to high current pinches we note that such pinches are characterized by a hot uniform density core at maximum density and pressure. Using equation (11) we may then approximate the pressure profile in equation (13) by a step function to obtain an expression for the beam radius

$$\frac{\pi r_b^2}{A_c} = \sqrt{\frac{9}{8\pi}} \left( \frac{I}{I_A} \right) \left( \frac{w_c}{w_A} \right)^2 . \quad (14)$$

Using values of current and voltage appropriate to the Hydra accelerator (1 MV, .5 MA) and the value of  $w_c$  used above we obtain  $r_b = .15$  mm. This is an order of magnitude below the pinch radii obtained in the laboratory for Hydra. This indicates that either Hydra is not optimally pinched, or an effective value of  $T_c$  should be used which is much larger than 3 eV. Although this question is presently unresolved, some rough arguments may be made for a higher  $T_c$  than the actual temperature of electrons in the cathode plasma. It seems reasonable that any mechanism which gives rise to a "random" radial or azimuthal electric field component of magnitude larger than .1% of the gap field would serve to justify a  $T_c$  of  $\sim 1$  kV. Some possible mechanisms might be 1) cathode tilt, 2) cathode surface imperfections, or 3) cathode plasma

imperfections. An effective temperature of 1 kV inserted in the formula for  $r_b$  gives a result which is then comparable to the Hydra pinch size. We have proposed experiments to test this hypothesis as well as the former hypothesis that Hydra is not optimally pinched.

Although the expression for  $r_b$  was derived only for the case of  $z$ -independent equilibrium, an interesting consequence of the constancy of  $Q_M$  is that in fact for the case of purely self-consistent fields with no perturbing objects present, diode flow cannot pinch to a radius less than or equal to  $r_b$  even when the flow is two dimensional. This statement is based on the maximum for kinetic pressure obtained earlier. A property of the  $z$ -independent solutions is that here both  $n$  and  $p_{kin}$  are at their maximum values in the pinch core. A pinch tighter than  $r_b$  implies higher magnetic pressure. However, the kinetic pressure cannot increase any further and so no steady state solution for  $r < r_b$  is possible.

One may now ask under what conditions a diode may achieve a  $z$ -independent equilibrium pinch. Although this question cannot be answered in full at present, a partial answer can be found by considering the momentum equation (eq. 1), expressed in non-dimensional variables:

$$a_b \frac{\partial}{\partial \tilde{z}} (F_M \tilde{\gamma} \tilde{\beta}_r) - \frac{\partial}{\partial \tilde{r}} (F_M \tilde{\gamma} \tilde{\beta}_z) - 2 \left( \frac{I}{I_A} \right) \tilde{B} = 0$$

with  $a_b \equiv \frac{r_b}{z_0}$ . If a  $z$ -independent pinch is approached, then in that region the last two terms in the above equation approximately cancel, leaving

$a_b \frac{\partial}{\partial \tilde{z}} (F_M \tilde{\gamma} \tilde{\beta}_r) \ll 1$ . But we have chosen a scale length  $z_0$  defined so that  $z$

derivatives are of order unity, and thus,  $a_b \ll 1$ . The condition  $a_b \ll 1$

is thus a necessary condition for obtaining a  $z$ -independent equilibrium pinch.



We may carry this one step further since  $a_b \equiv \frac{r_b}{z_o} \ll 1$  together with  $z_o \leq d$  then gives the condition of interest  $\frac{r_b}{d} \ll 1$ .

The above condition may now be examined for different machines of interest by using an impedance law to eliminate  $A_c$  in the expression for  $r_b$ . We shall choose the parapotential law as an example, although others could be used as well. The impedance law provides an expression for the diode aspect ratio  $\frac{R}{d}$  which may be substituted in the  $r_b$  equation if we write

$$A_c = \alpha \pi R^2 \quad (15)$$

where  $\alpha = 1$  for solid cathodes.

An expression for  $\frac{r_b}{d}$  is then obtained as a function of  $I$  and  $V$  only. Shown in Figure 1 are lines of constant  $\frac{r_b}{d}$  along with load lines for various machines. For a given point on a load line one may then determine an approximate value for  $\frac{r_b}{d}$ . Notice that machines running at high current have generally higher  $\frac{r_b}{d}$  indicating more difficulty in achieving minimum pinching. In addition the figure provides an estimate of how much over critical current a machine is run by the use of lines for  $I = I_c$  at different aspect ratio. Thus, if a machine is being run at  $\frac{R}{d} = 100$  at a point above the critical current line for  $\frac{R}{d} = 100$ , it is then operating above critical current. From the graph it appears that all machines shown can be operated above critical current.

The overall results obtained to date, then, from the fluid formulation just presented consist of constants of the motion, maxima in the beam density, beam current density and kinetic pressure, a minimum pinch radius for 2-D flow, and a necessary condition which must be met in order to approach the z-independent solution. Progress is now being made towards a numerical solution of the two-dimensional equations, which will give more detailed information including sufficient conditions for pinching.

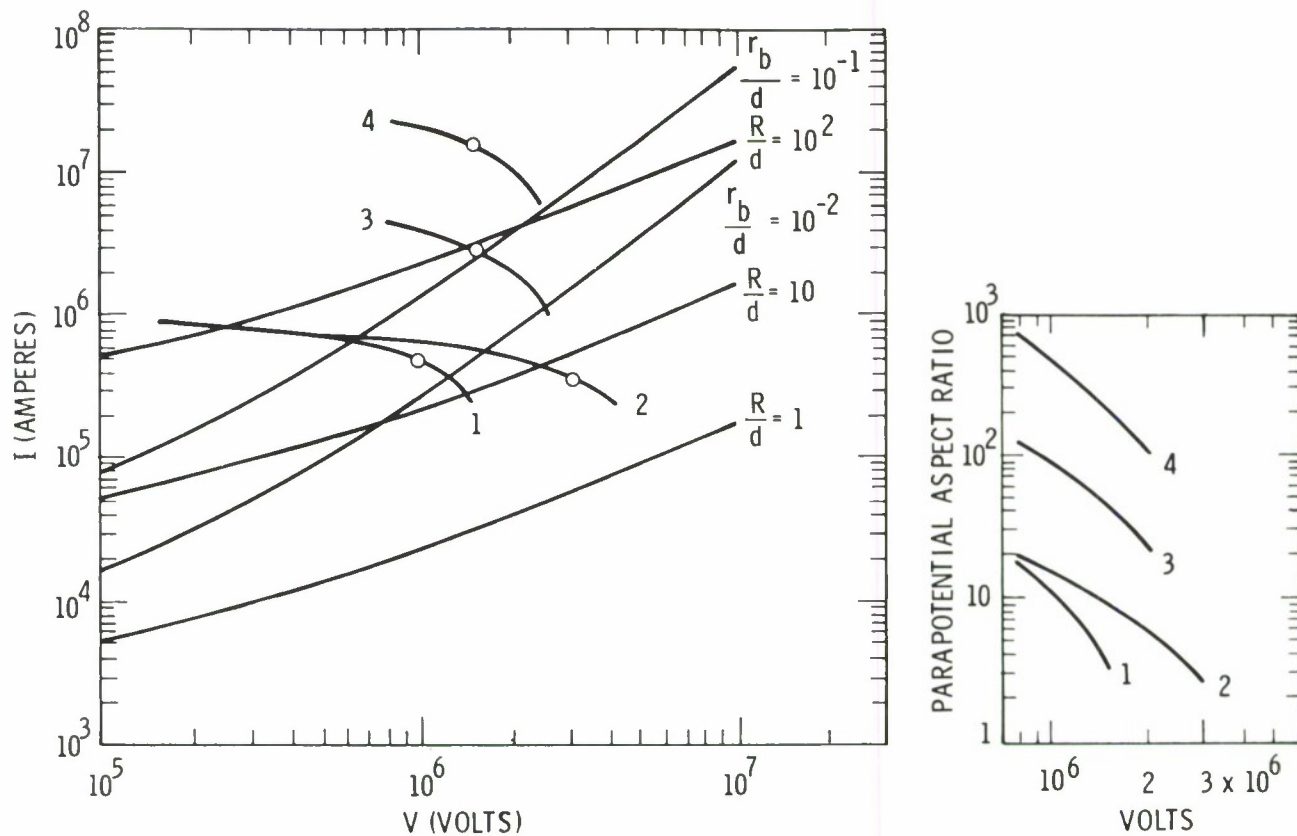


Figure 1. Diode scaling using parapotential law. Accelerator (one side):  
 1. HYDRA, 2. PROTO-I, 3. PROTO-II, 4. Conceptual 0.1 ohm matched load accelerator.

## ANODE PLASMA AND FOCUSING IN REB DIODES\*

S. A. Goldstein, D. W. Swain, G. R. Hadley, and L. P. Mix

Sandia Laboratories, Albuquerque, New Mexico 87115

### ABSTRACT

The use of electrical, optical, x-ray, and particle diagnostics to characterize the production of anode plasma and to monitor its influence on beam generation and focusing are reviewed. Studies using the Nereus accelerator show that after cathode turn-on, deposition of several kJ/gm on the anode is necessary before ions from hydrocarbons, adsorbed gases, and heavier metallic species are detected. The actual time at which ions are liberated depends on several factors, one of which is the specific heat of the anode substrate. Once formed, anode ions cross the A-K gap (with an energy equal to the diode voltage) and interact with the cathode to produce an axially peaked beam profile, a "pinch" which does not follow the critical current criterion. Experiments with externally generated anode plasma show that this type of pinch can be attracted to localized areas on the anode. Preliminary observations on Hydra indicate the anode plasma composition is similar to that on Nereus. The effect of this plasma on pinch dynamics currently is under investigation.

\*This work was supported by the U.S. Energy Research and Development Administration.

## I. INTRODUCTION

Although the importance of ions from electrodes in high voltage D.C. electron accelerators has been under investigation for some time,<sup>1</sup> the significance of ions in nanosecond pulsed accelerator diodes employed in focused electron beam driven fusion studies has only recently been appreciated. After initial observations of anode and cathode plasma in these diodes,<sup>2</sup> REB diode theory was modified to account for ion flow. Anode plasma was found to affect both the diode impedance (allowing the current to exceed the Child's law predicted value) and the electron trajectories (by decreasing E fields near the anode and modifying the  $\bar{E} \times \bar{B}$  drift), leading to prediction of tighter focusing and higher beam densities.<sup>3</sup> Indeed, preliminary experiments employing localized, externally generated space-charge neutralizing anode plasmas have demonstrated improvements in pinch size, centering, and stability.<sup>4</sup> In spite of these promising results, it was obvious that to reach the power densities required to initiate thermonuclear burn in electron beam target materials,<sup>5</sup> significant additional beam concentration was necessary. To this end, further experimental work has been performed to better understand the mechanism of anode plasma production, to characterize its geometry and composition, and to determine the influence of plasma on the dynamics of electron focusing. This information will assist in the development of more accurate 2-D, time dependent codes for predicting diode behavior and will indicate experimental conditions for optimum beam generation and focusing.

In this talk we will review several electrical, optical, x-ray, and particle diagnostics developed and used to monitor plasma composition, density, and motion. Application of these techniques to the Nereus

accelerator has lead to a relatively complete description of the diode behavior.<sup>6,7,8</sup> Recent results from studies on plasmas on the Hydra and Proto I machines also will be presented.

## II. CHARACTERIZATION OF ANODE PLASMA PROPERTIES

### A. Diagnostic Techniques

Most of the plasma diagnostic techniques used in this work have been described in detail elsewhere.<sup>8</sup> Consequently, only a brief review will be given here.

#### 1. Diode Impedance

By measuring diode voltage and current, and correcting for inductive effects, the time-dependent impedance could be calculated and used to obtain the velocity of diode closure, assuming planar electron flow.<sup>9</sup> From impedance alone, the time of diode shorting could be determined, and in experiments employing plasma-filled diodes,<sup>10</sup> the degree to which the machine and diode impedances were matched (or mismatched as desired) could be monitored on a shot-to-shot basis. Differences in calculated closure velocities and those measured by other techniques (e.g., holography and time-resolved photography) furnished qualitative data on anode plasma motion and geometry. Using this technique, Kelly et al., obtained some of the first experimental data on the influence of anode surface composition on beam generation.<sup>6</sup>

#### 2. PIN Diode Arrays

The configuration used to measure electron current density profiles on the anode is shown at the top of Fig. 1. A linear array of three PIN diodes was located a short distance from the anode plane; each



diode viewed a portion of the anode through a small hole in a lead aperture plate. By moving the array between successive shots, the relative x-ray output vs. radius could be measured, and a plot of current density vs. radius could be obtained. A 22 element diode array also has been developed for more extensive beam mapping.<sup>11</sup>

### 3. Ion Detectors

The Faraday cup and Thomson parabola apparatus are shown in the center and bottom of Fig. 1. Although use of either detector for anode plasma monitoring required reversing the machine polarity (cathode grounded and anode pulsed positive), no difference in diode behavior between reversed and normal configurations could be detected. The Faraday cup was used to measure the production time of ions which originate at the anode, accelerate across the anode-cathode gap during the beam pulse, and pass through a small hole in the cathode. A seven element Faraday cup array recently has been constructed for precise spatial and temporal profiling of ions leaving the anode.<sup>12</sup> The Thomson parabola employed parallel  $\vec{E}$  and  $\vec{B}$  fields to deflect ions of constant  $E/Z$  into parabolic paths in order to identify the charge to mass ratio and energy.

### 4. Multiple-Pulsed Holography

A pulsed holography system<sup>13</sup> capable of generating four successive interference holograms (0 to 16 nsec delay between pulses) during a single shot was used to record both anode and cathode plasma distributions. The minimum detectible plasma density of  $\sim 3 \times 10^{17} \text{ cm}^{-3}$  with this system represented several orders of magnitude less sensitivity than the Faraday cup detectors. Consequently, holograms could be expected to show plasma fronts somewhat behind those observed with Faraday cups.



## 5. Time-Resolved Photography and Optical Spectroscopy

Time and space profiling of radiating anode and cathode plasma fronts was accomplished using a Quantrad Model 77A image intensifier camera in both framing and streaking modes. Time-resolved spectroscopy was performed by coupling the streak camera to a Spex Minimate spectrometer. The S-20UV photocathode response of the image converter tube allowed spectral scanning from 2000 to 9000 Å. The tube required  $\geq 10^{17}$  emitters/cm<sup>3</sup> before light could be detected and therefore had a response similar to the holography system.

### B. Experimental Results

A synopsis of events occurring in the Nereus diode will be given with the aid of Fig. 2, in which important time regions are indicated along typical diode corrected voltage and current waveforms. At point one, from 20 to 25 nsec into the voltage pulse, the electron beam just begins to concentrate on axis, as evidenced by the development of a distinct peak in the current density profile (Fig. 3). This high axial current density has a duration of about 15 nsec and begins to decay, at 40 nsec, with a simultaneous drop in the diode impedance attributable to gap closure (to be discussed shortly).

At point two,  $25 \pm 2$  nsec, ions originating from an axial region on an aluminum anode surface are first produced, as indicated by Faraday cup time-of-flight data (Fig. 4). The four ion peaks a through d were nearly identical in appearance for a variety of anode materials. Thomson parabola mass-energy analysis of the peaks identified ion species of  $M/Z$  1, 2, 6, 12, 16, with all species being monoenergetic, having an energy equal to the diode voltage at the extrapolated ion production time. Hence, during the

pinch, the anode ion current was composed primarily of  $H^+$  (peak a) and  $H_2^+$  (b), some  $C^{+2}$ ,  $C^+$  (c), and  $O^+$  (d), with ions of the anode material appearing at later times. Faraday cup signal amplitudes showed the plasma profile to be highly peaked on axis. The maximum axial proton current density of  $1 \text{ kA/cm}^2$  (corresponding to an ion density of  $\sim 10^{13} \text{ cm}^{-3}$ ) was within a factor of two of the value calculated assuming space-charge limited flow. At 4 mm off axis, ions appeared about 8 nsec later than on axis, and the peak current density fell to  $\sim 3\%$  of the axial value.

At point three and beyond (30 to 46 nsec), a higher density ( $\geq 10^{17} \text{ cm}^{-3}$ ), axially peaked plasma front from both anode and cathode was observed by holography (Fig. 5) and photography (Fig. 6) to propagate across the gap. Both radial and axial expansion velocities from  $2.5$  to  $5 \times 10^6 \text{ cm/sec}$  for each plasma were measured. At much later times, four, (55 nsec) and five (65 nsec), the high density fronts, now containing significant amounts of metallic electrode species (as detected by optical spectroscopy, Fig. 7), coalesce in the gap.

The significance of the results in Figs. 3 through 7 is that a plasma of low Z materials, such as adsorbed gases (e.g.,  $CO_2$ ), water vapor, and diffusion pump oil, is produced at a localized area on the anode during the time the electron beam commences and continues to pinch. A model has been proposed which successfully explains the production of this plasma and its blowoff into the gap.<sup>8</sup> Of several possible production mechanisms postulated to be active in vacuum diodes,<sup>14</sup> electron heating of the anode substrate, subsequent desorption of surface impurities, and rapid ionization by either beam electrons, secondaries, or photoionization by the cathode plasma is consistent with our observations.

The effect of electron deposition heating can be studied by converting the current density profiles of Fig. 3 to energy deposition profiles. Assuming normally incident electrons of 200 keV energy, the average energy loss rate for aluminum over the first 25% of the range is  $5.25 \text{ MeV-cm}^2/\text{gm}$ ; <sup>16</sup> a current density of  $1 \text{ kA/cm}^2$  deposits energy into the anode at a rate of  $5.25 \times 10^9 \text{ W/gm}$ . Integrating  $j_-(r,t)$  with respect to time and multiplying by the above factor gives the curves shown in Fig. 8. An axial ion production time of  $25 \pm 2 \text{ nsec}$  corresponds to a deposition of  $2 - 4 \text{ kJ/gm}$ , while the  $4 \text{ mm}$  off axis value is about  $1.2 \text{ kJ/gm}$ . It therefore appears that between  $1$  and  $3 \text{ kJ/gm}$  is necessary to remove surface gases. Although this initially appears to be a large energy requirement for simple desorption, it must be remembered that we are requiring material removal within only a few nanoseconds. Hadley<sup>15</sup> has shown that typical monolayer desorption times at room temperature can be significantly longer than the time scale of interest here, whereas for temperatures of several thousand degrees, desorption within nanoseconds can occur. These temperatures are sufficient to melt and partially vaporize most commonly used anode materials, and suggests that the anode is molten during the desorption process. The energy required to melt and begin vaporizing aluminum ( $1.1 \text{ kJ/gm}$  and  $3.0 \text{ kJ/gm}$ , respectively, from Reference 28) is in fact delivered by the beam after  $25 \text{ nsec}$ . Once one or more monolayers of neutral vapor have been removed from the anode surface, the processes of primary ionization and avalanching, although resulting in only a small ionization fraction, have been found to produce sufficient plasma to account for the observed space charge limited ion and electron flow.

On a nanosecond time scale, transport of heat by thermal conduction is negligible. On the anode, the local rate of temperature rise and the time at which surface materials are desorbed and ionized consequently should exhibit a dependence on some thermodynamic property of the anode substrate. Such a dependence is shown in Fig. 9, where  $H^+$  and  $C^+$  ions detected 4 mm off axis are seen to be produced earlier for anode materials of low specific heat. Because of the rapid change in deposition rate on Nereus (Fig. 8), the exact functionality cannot be determined, but the differences in ion production time are statistically significant.

Due to the comparatively small A-K gaps used in the Nereus diode, the large axial flux of energetic ions is capable of rapidly traversing the gap and depositing sufficient energy to locally vaporize the cathode surface (see curve in Fig. 8). The local plume of cathode plasma thus formed expands rapidly toward the anode. The resultant gap closure causes increased axial electron current density which, in turn, will result in increased axial anode plasma production and increased anode damage. Consequently, the Nereus pinch, and possibly pinches on other machines employing small gaps and pointed cathodes,<sup>17</sup> is a result of a thermal instability mechanism and does not satisfy the critical current criterion describing conventional pinched flow, where electrons from large radii on the cathode focus down to a small spot on the anode.

To test the idea that the initial site of anode ion emission develops into the center of a thermal instability pinch, an experiment was performed in which plasma ( $\sim 10^{14}$  ions/cm<sup>3</sup>) externally generated by a pulsed ruby laser was allowed to expand into a small hole in the anode at various off axis locations (Fig. 10). By timing the laser pulse such that the front of



the plasma reached the anode surface coincident with the application of voltage to the diode, the pinch was observed to occur directly over the hole at positions up to 7 mm off axis. In contrast, when a similar experiment was set up on Hydra, where "supercritical" pinched flow is known to occur, damage patterns far off axis could not be induced by locally injected plasma.

Although the Nereus pinch is fundamentally different from those on larger machines, recent results indicate the anode plasma production mechanism active on Nereus may be common to other accelerators. For example, the dependence of ion production time on specific heat (Fig. 9) can be used to rationalize the dependence of pinch velocity on anode surface layer composition observed on Gamble I by Blaugrund and Cooperstein,<sup>18</sup> in that earlier desorption and ionization of impurities from high Z anodes could result in both earlier pinch formation and faster collapse velocities. The specific relationship will depend on the initial beam profile and deposition rate.

Although anode plasma in diodes on larger accelerators has not yet been diagnosed as thoroughly as that in Nereus, preliminary observations on Hydra indicate the sequence of events in this diode runs a course similar to that in Nereus, as seen with the aid of Fig. 11. At point one, 67 nsec into the voltage pulse, ions are first detected by Faraday cup. Time-of-flight data analysis identified the ion species to be the same low Z surface impurities seen in Nereus. At point two (72 nsec), continuum radiation first is detected, indicating propagation of higher density plasma into the gap, and at point three (80 to 95 nsec) the beam begins to collapse, as monitored by PIN diodes. Also during this time (point four, 91 nsec), spectral line radiation from the anode metal is first detected, suggesting that plasma now emerging has a high metal atom content.

Hydra current density profiles for parameters under which ion experiments were conducted have not yet been measured. Consequently, conversion from current density on the anode to energy deposition similar to that between Figs. 3 and 8 is not possible. However, using the same conditions as in the Nereus case, i.e., normal incidence and constant voltage, and assuming initial uniform emission from the whole cathode surface, integration of a typical Hydra power curve gives an energy of 2.6 kJ delivered by the beam at 67 nsec into the pulse, when ions are detected. For  $\sim 600$  kV electrons this corresponds to a deposition of 60 J/gm, a factor of 20 less than the deposition requirement found on Nereus. Several factors may help explain this discrepancy. First, as the current approaches critical current (typically 100 kA for our conditions), the beam may begin to weakly pinch and the angle at which electrons strike the anode may increase from near zero to near grazing incidence.<sup>19</sup> This is not the case on Nereus, where emittance angles of 3-4 degrees have been measured.<sup>20</sup> The anode dose will increase significantly with incidence angle, and a factor of 3 to 5 can be accounted for if reflection and recapture of electrons is considered.<sup>21</sup> Second, if the beam does begin to collapse, the current density will no longer be uniform and the anode deposition will increase. If weak pinching were to commence at  $\sim 45$  nsec (100 kA) and proceed at a rate of 2 mm/nsec, the deposition rate at 67 nsec could be a factor of 2 higher than the calculated value. And third, some of the cathodes used in the ion studies employed irregular surfaces for enhanced pinching (e.g., "38" and "parapotential" cathodes). These geometries have been observed experimentally to generate non-uniform deposition on the anode,<sup>18,22</sup> presumably by a local field enhancement mechanism, and this effect has not yet been considered in our treatment.



Preliminary diode experiments on Proto I, described in more detail by Prestwich,<sup>10</sup> have furnished additional data on the relationship of anode plasma and pinching. Experiments employing 20 cm diameter "38" cathodes and larger solid and hollow cathodes produced only little anode damage, presumably because the current density, and consequently the energy deposition on the anode, was too low to generate anode plasma until late in the pulse. Significant improvement in focusing and reasonably successful pinching with large diameter (e.g., 30 cm) cathodes was accomplished using externally generated low density ( $10^{12} \text{ cm}^{-3}$ ) plasma filling the entire diode. The collisionless plasma sheaths which form over the electrodes upon application of the diode voltage<sup>23</sup> appear to circumvent any desorption rate limitations on plasma formation and, in producing centimeter diameter pinches, have enhanced beam collapse velocities from typical mm/nsec values to greater than 1 cm/nsec. Since further concentration of the  $\sim 300 \text{ kA}$ , 3.8 cm diameter beam (corresponding to  $n_e = 3 \times 10^{12} \text{ cm}^{-3}$ ) by neutralization from the fill plasma was not possible, experiments injecting higher density ( $10^{15} \text{ cm}^{-3}$ ) axial plasma directly on the anode surface in conjunction with the fill plasma were begun, and results will be forthcoming.

### III. SUMMARY

Anode plasma production by electron deposition heating, desorption, and ionization of surface impurities appears to be active in many REB diodes. Although anode ions were present at the earliest indications of focusing and throughout the pinch, timing accuracy, the simultaneity with which multiple diagnostics could be used, and shot-to-shot reproducibility have somewhat limited real-time experimental study of how these ions specifically

influence the beam dynamics. Qualitative indications that anode plasma is necessary for tight pinching were reported. Additional analysis must be performed before a definitive statement of plasma generation requirements is made.

It can be concluded that the physically larger, higher power accelerators being designed to meet fusion requirements, although incapable of self-producing anode ions, can be made to pinch with externally generated plasmas.

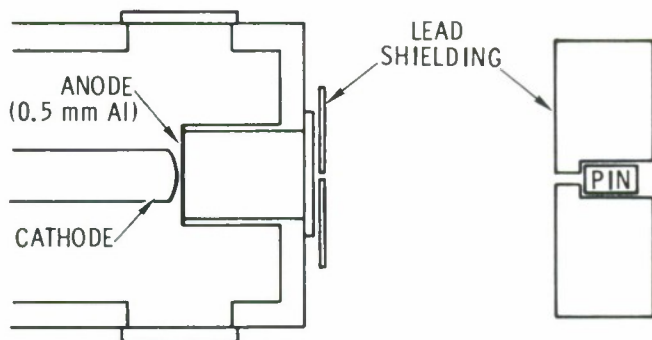
#### ACKNOWLEDGMENTS

The authors would like to thank J. G. Kelly, P. A. Miller and G. Yonas for helpful discussion, and P. R. Johnson, H. L. Myers, and L. W. Kruse for experimental assistance.

## REFERENCES

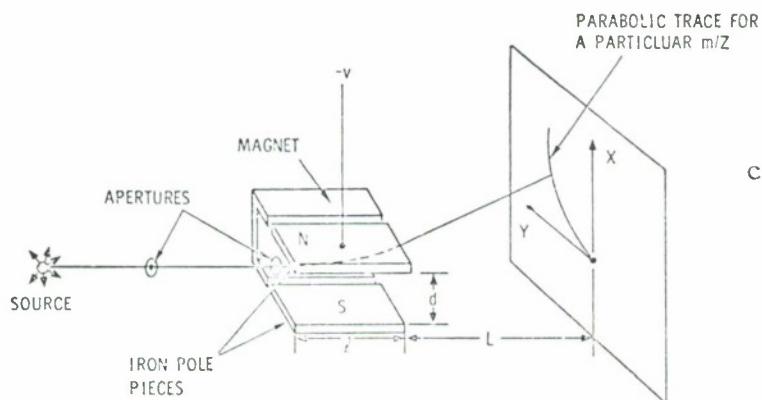
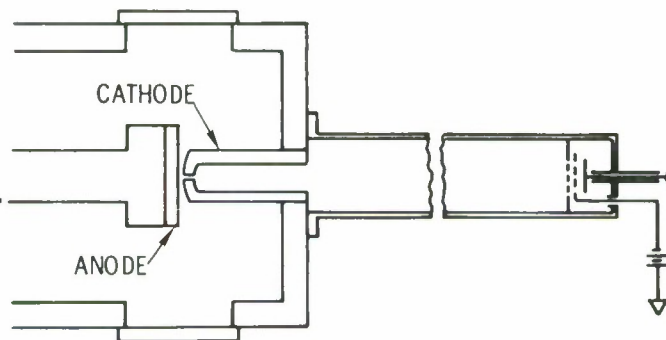
1. For example, Van Atta, Van de Graaf, and Barton, *Phys. Rev.* 43, 158 (1933); W. K. Mansfield and R. L. Fortescue, *Brit. Journ. Appl. Phys.* 8, 73 (1957); W. K. Mansfield, *Brit. Journ. Appl. Phys.* 11, 454 (1960).
2. L. P. Mix, J. G. Kelly, G. W. Kuswa, D. W. Swain, and J. N. Olsen, *J. Vac. Sci. Technol.* 10, 951 (1973); J. G. Kelly and L. P. Mix, *Journ. Appl. Phys.* 46, 1084 (1975).
3. J. W. Poukey, J. R. Freeman, and G. Yonas, *J. Vac. Sci. Technol.* 10, 954 (1973); J. W. Poukey and A. J. Toepfer, *Phys. Fluids* 17, 1582 (1974); J. W. Poukey, *Appl. Phys. Lett.* 26, 145 (1975).
4. P. A. Miller, J. Chang, and G. W. Kuswa, *Appl. Phys. Lett.* 23, 423 (1973); G. Yonas, K. R. Prestwich, J. W. Poukey, and J. R. Freeman, *Phys. Rev. Lett.* 30, 164 (1973).
5. M. J. Clauser, *Phys. Rev. Lett.* 34, 570 (1975).
6. J. G. Kelly, S. A. Goldstein, and D. W. Swain, to appear in *J. Appl. Phys.* 46, (1975).
7. D. W. Swain, S. A. Goldstein, J. G. Kelly, and G. R. Hadley, to appear in *J. Appl. Phys.* 46, (1975).
8. D. W. Swain, S. A. Goldstein, J. G. Kelly, G. R. Hadley, and L. P. Mix, submitted to *J. Appl. Phys.*
9. R. K. Parker, R. E. Anderson, and C. V. Duncan, *J. Appl. Phys.* 45, 2463 (1974).
10. See paper by K. R. Prestwich, P. A. Miller, D. H. McDaniel, J. W. Poukey, M. M. Widner, and S. A. Goldstein, this conference.
11. L. P. Mix and J. Chang, *Bull. Amer. Phys. Soc.* 20, 583 (1975).
12. D. W. Swain, S. A. Goldstein, and L. P. Mix, *Bull. Amer. Phys. Soc.* 20, 1250 (1975).

13. L. P. Mix, Rev. Sci. Instr. (in preparation for publication).
14. G. R. Hadley, Bull. Amer. Phys. Soc. 19, 870 (1974).
15. G. R. Hadley, Bull. Amer. Phys. Soc. 20, 1251 (1975).
16. R. Multgren, R. Orr., P. D. Anderson, and K. K. Kelly, Selected Values of Thermodynamic Properties of Metals and Alloys, John Wiley and Sons, Inc., New York (1968).
17. D. L. Morrow, J. D. Phillips, R. M. Stringfield, Jr., W. O. Doggett, and W. H. Bennett, Appl. Phys. Lett. 19, 441 (1971); W. C. Condit, Jr., D. O. Trimble, G. A. Metzger, D. G. Pellinen, S. Heurlin, and P. Creeley, Phys. Rev. Lett. 30, 123 (1973).
18. A. E. Blaugrund and G. Cooperstein, Phys. Rev. Lett. 34, 461 (1975); Private communication; see paper, this conference.
19. See for example, Shyke A. Goldstein and Roswell Lee, Phys. Rev. Lett. 35, 1079 (1975).
20. L. P. Bradley, Rev. Sci. Instr. 46, 673 (1975).
21. J. A. Halbleib, private communication.
22. J. Chang, L. P. Mix, F. C. Perry, M. M. Widner, J. W. Poukey, this conference.
23. P. A. Miller, J. W. Poukey, and T. P. Wright, Phys. Rev. Lett. 35, 940 (1975).



- a. Linear 3 element PIN diode array for  $j_-(r,t)$  profiling. Machine is operated with normal polarity.

- b. Faraday cup ion detector for ion arrival time measurement and  $j_+(r,t)$  profiling. Machine is operated with reversed polarity.



- c. Thomson parabola mass-energy analyzer for identifying ion species by  $M/Z$ .

Figure 1

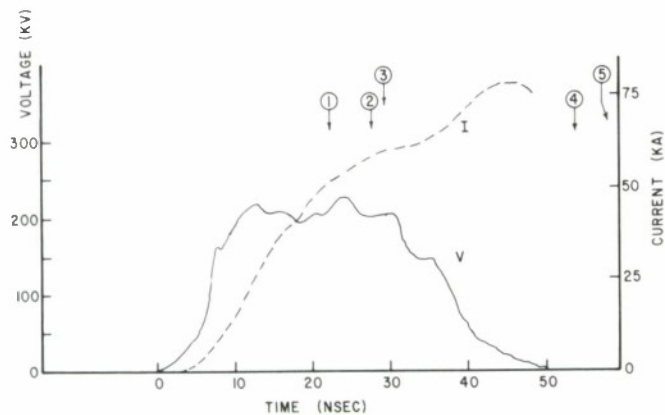


Figure 2. Synopsis of events in the Nereus diode.

- 1: 20-25 nsec, beam just begins to pinch (PIN diode data)
- 2: 25 nsec, ions first detected (Faraday cup).
- 3: 30 nsec, high density anode plasma propagates across A-K gap (holography, spectroscopy data).
- 4, 5: 55 nsec and later, high density fronts coalesce.

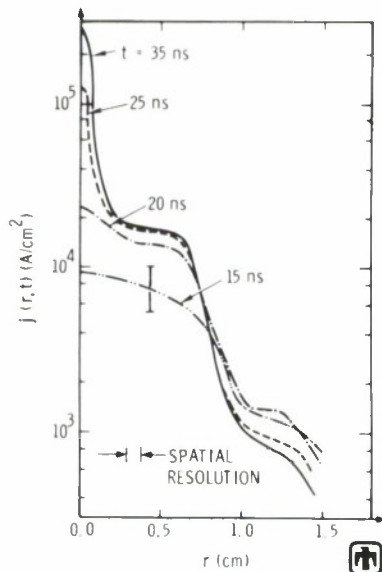
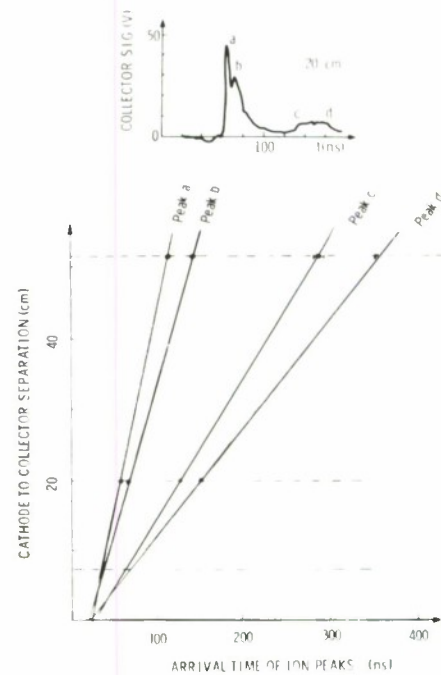


Figure 3.  $j(r,t)$  profiles after normalization and calibration.



- a. Typical Faraday cup ion signal for cm ion flight path.
- b. Time-of-flight extrapolation to obtain ion production time.

Figure 4



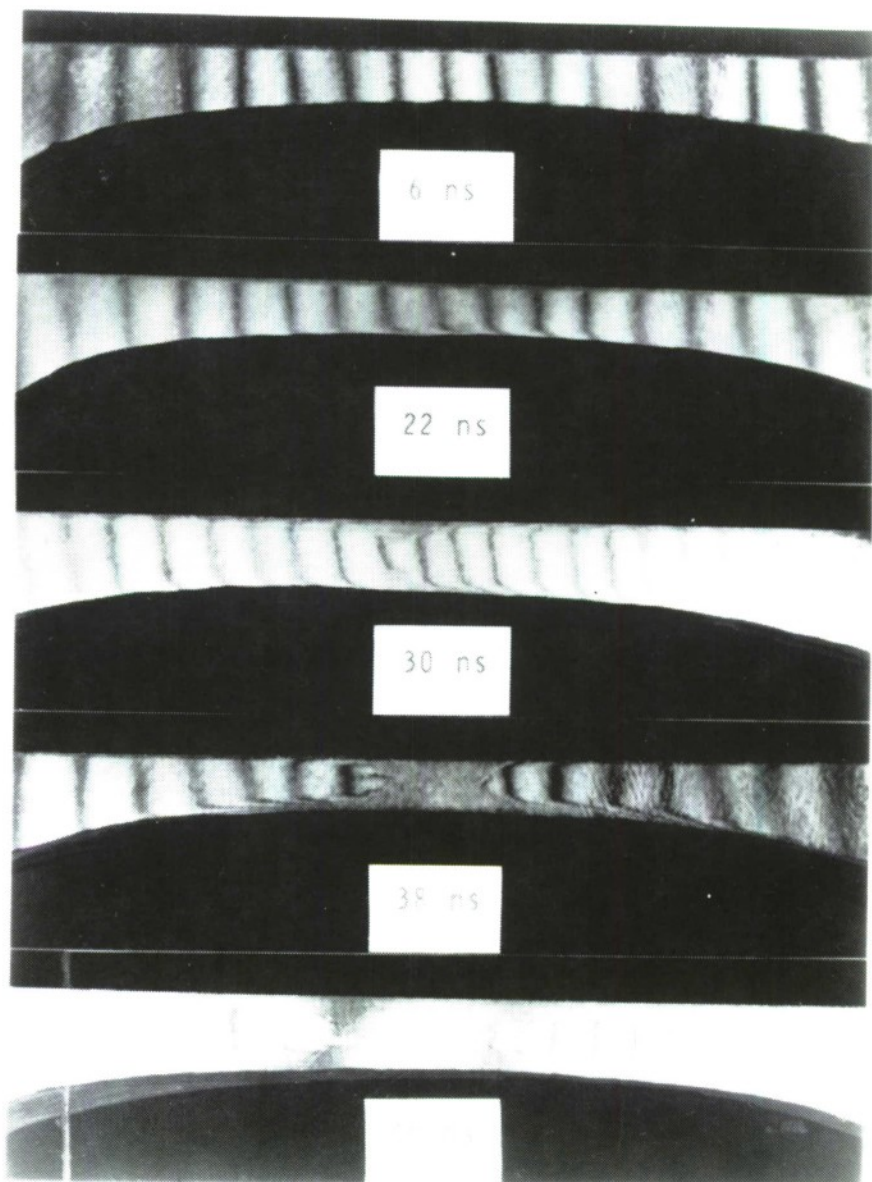
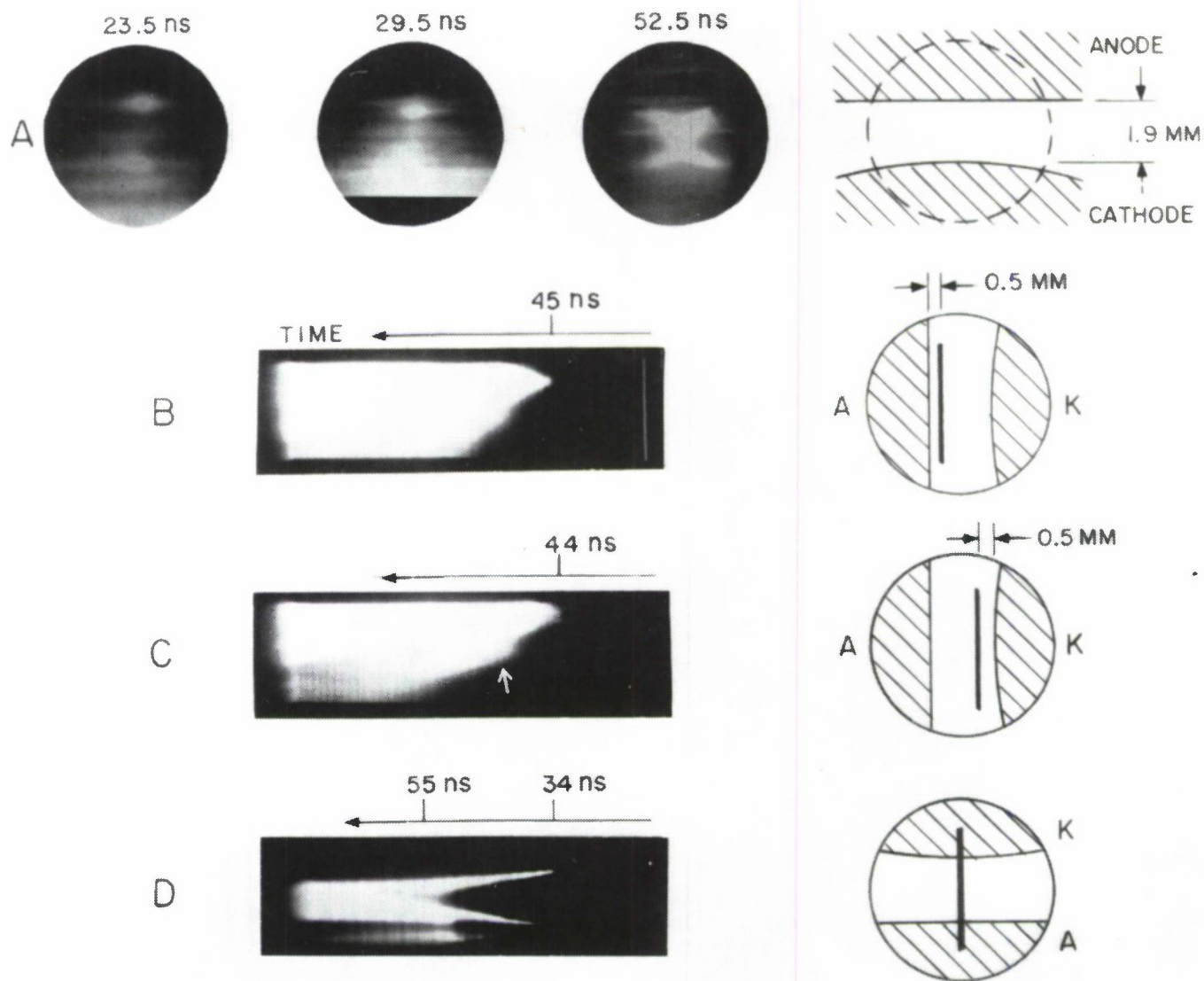
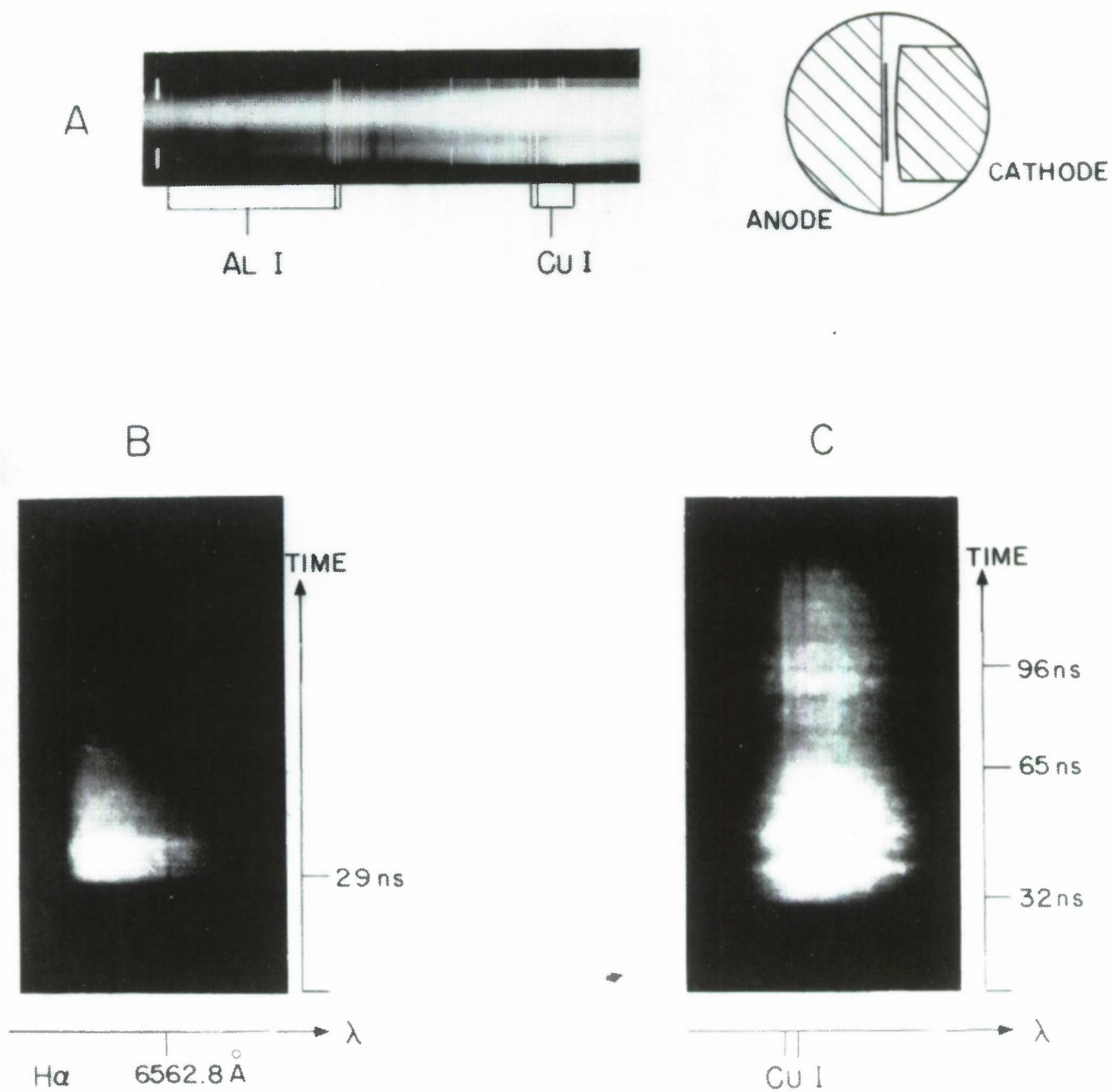


Figure 5. Interference holograms (3 nsec exposure) showing plasma between anode (top) and cathode. Plasmas first appear on axis by 22 nsec and close gap by 38 nsec. Plasma velocity from each surface is measured to be  $> 5 \times 10^6$  cm/sec.



- A. 5 nsec exposures showing 1 mm diameter plasma plumes crossing gap.
- B,C. Streaks showing radial expansion of plasmas off anode and cathode.  
At both locations,  $V \sim 5 \times 10^6$  cm/sec.
- D. Axial expansion of plasma fronts.  $V_k = 2.6 \times 10^6$  cm/sec.  
 $V_a = 2.9 \times 10^6$  cm/sec.

Figure 6. Frame (top) and streak photographs of visible radiation from diode plasma.



A. Time integrated spectrum vs radius.

B,C. Time resolved spectra at two wavelength regions.

Note last time appearance of lines from electrode material.

Figure 7. Optical spectra of diode radiation.

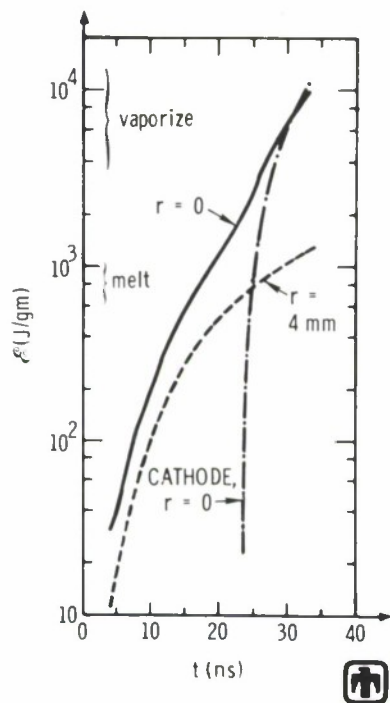
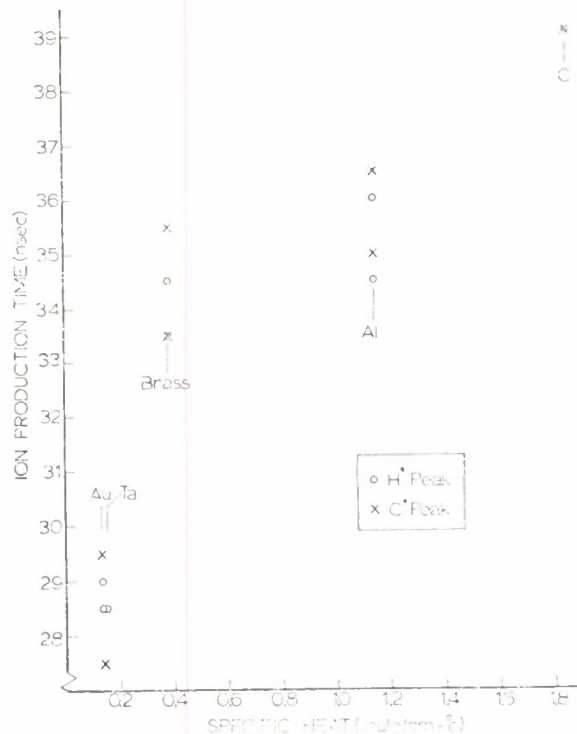
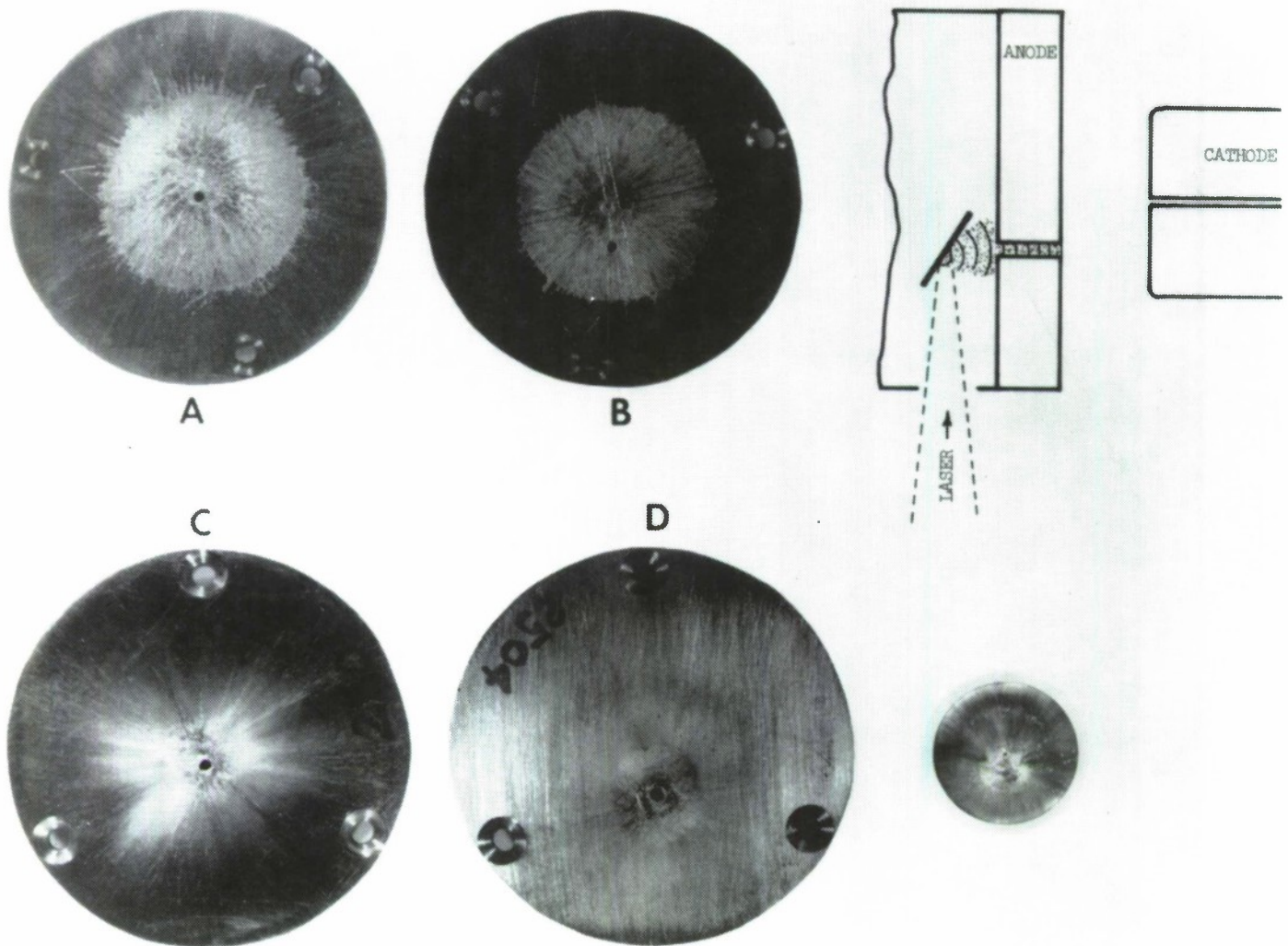


Figure 8. Nereus energy deposition vs time on anode ( $r=0$  and  $r=4$ mm). Deposition on cathode ( $r=0$ ) by  $1 \text{ kA/cm}^2$  proton beam traversing the gap is also shown.

Figure 9. Dependence of  $\text{H}^+$  and  $\text{C}^+$  production time on specific heat of anode substrate (evaluated at  $600^\circ\text{C}$ ).



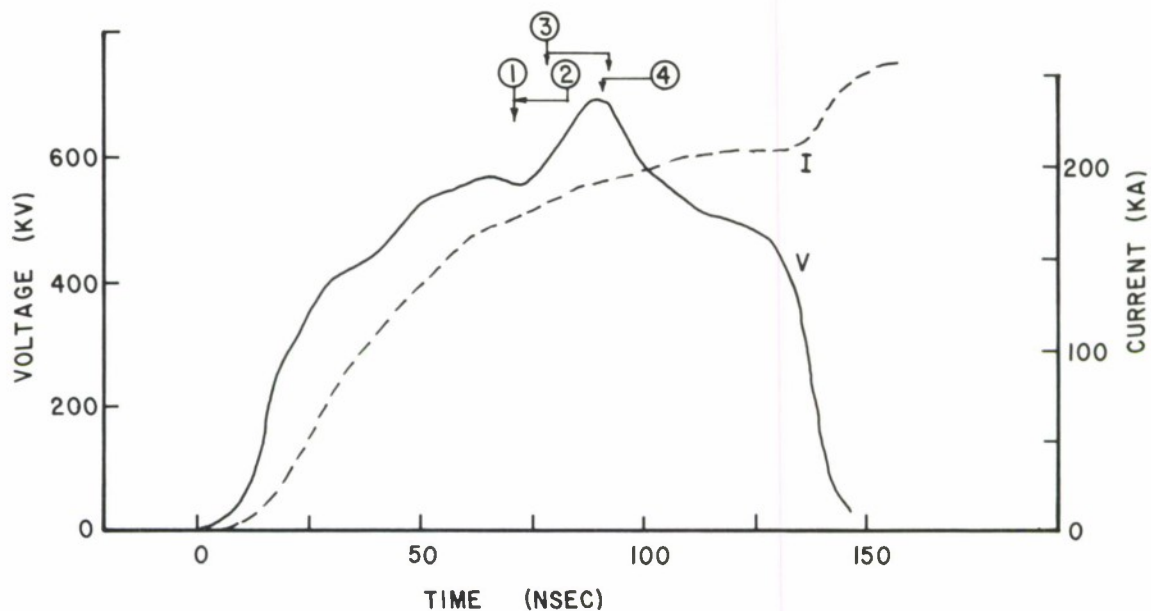




A,B. No plasma present in off axis holes. Damage pattern is centered on anode.

C,D. Plasma of  $10^{12} - 10^{14}$  ions/cm<sup>3</sup> in off axis holes. Damage pattern is now centered over holes. Diode impedance was 2 ohms lower than cases A and B but showed characteristic pinching behavior.

Figure 10. Laser generated anode plasma experiment.



1. 67 nsec, ions first detected.
2. 72 nsec, optical radiation from higher density plasma detected.
3. 80-95 nsec, beam begins to collapse (PIN diode data).
4. 91 nsec, line radiation from anode substrate detected.

Figure 11. Synopsis of events in the Hydra diode.



EXPERIMENTAL INVESTIGATION OF FOCUSING AND  
TRANSPORTATION OF HIGH-CURRENT ELECTRON BEAMS

E. I. Baranchikov, A. V. Gordeev, U. V. Koba,  
V. D. Korolev, V. S. Pen'kina, L. I. Rudakov,  
V. P. Smirnov, A. D. Sukhov, E. Z. Tarumov  
I. V. Kurchatov Institute of Atomic Energy, Moscow, USSR

Recent investigations showed that high current REB's may be effectively focused in the accelerating gap of a diode [1,2]. Achieved values of the electron-beam energy density have permitted model experiments on the implosion of spherical shells for compression and heating of D-T pellets up to fusion conditions [2,3,4]. The realization of pellet ignition according to such a scheme may be accompanied by the destruction of the diode. Therefore it is preferable to focus the electron beam on the target placed at a sufficient distance from a diode. However, until now, the necessary beam focusing in a drift space has not been achieved.

Another possible solution of the problem of the beam transportation to the target was proposed by L. I. Rudakov.

If the relativistic electrons of the pulse duration  $\tau$  are accumulated in a form of a cloud of radius  $R$  around a target of radius  $r$  the criterion for most of them to hit the target can be written as follows:

$$R \leq r \left( \frac{c\tau}{2r} \right)^{1/3}$$

( $c$  -- velocity of light).

In this case the target irradiation will be sufficiently uniform. For the cloud formation L. I. Rudakov and E. Z. Tarumov suggested the use of a cusp magnetic field geometry with the injection of the beam through the equatorial hole. The use of the cusp geometry seems to be rather natural for reaching the goal mentioned.

The first experimental results confirming the possibility of such focusing and transportation of electrons to the region of trapping are presented in the second part of this paper.

The first part of it is devoted to the theoretical and experimental results of the beam propagation across magnetic fields.

#### I. HIGH CURRENT REB PROPAGATION ACROSS MAGNETIC FIELD

It was shown theoretically and experimentally [5,6] that the trajectory of motion of REB across magnetic field is close to Larmor circle. The character of the beam propagation changes significantly when the beam is injected in the plasma channel directed across magnetic field [7]. If the injected REB current is sufficiently high then it propagates along the plasma channel.

For explanation of a beam confinement in the channel we shall suppose electric and magnetic neutralization of a beam in a plasma. The beam electrons under the influence of the external magnetic field are turned around and try to leave the channel. As a result of this, charges and currents will arise on the channel surface, and the electric and magnetic fields will be generated in vacuum around the channel. Because of electric neutrality of a system the electric field confines the beam

electrons and keeps the leakage current at some limiting level. The leakage current value depends also on the magnetic field generated by the beam. For example, in the examined system, the magnetic field arises when there exists a vacuum gap between the plasma channel and the target on which is hit by the beam, that is less than Debye length for the beam electrons. Then the magnetic field generated around the channel by the injection current returns the electrons back into the channel.

In another possible case the channel and the target are electrically connected and the beam current in the channel is compensated by the current flowing from the target along the channel. It means that the confinement force vanishes on the leaving electrons layer's boundary. For that reason the leakage current and associated with it magnetic field arise. In this situation at least the part of the beam may be confined in the channel.

For a good understanding of the physical picture of a beam propagation along a plasma channel two simple plane models were theoretically analyzed. In the first case, the behavior of the electrons having no angular divergence from the channel under the influence of only external magnetic field was considered. It was shown that the beam propagates along the plasma channel if the self-magnetic field of the beam  $H_I$  is greater than the external magnetic field  $H_0$ , and the transverse size of the channel

$$d \ll R = \frac{\gamma m c v}{e H_0}$$

Because the size of the output region of the beam from the channel is about

$$\sqrt{R d} \gg d$$

the dependence of all physical quantities on the longitudinal coordinate is weak. This allows one to obtain an analytical solution of the problem.

With an increase of the external magnetic field  $H_0$ , the beam width  $D$  grows as

$$D \sim \frac{H_1 H_0}{(H_1 - H_0)^2} \frac{d}{\gamma^2}$$

the beam is spreading and the propagation efficiency decreases.

In principle it is possible to form the homogeneous layer along the channel. In this case the single electron goes into the channel and leaves it many times and the trajectories of different particles intersect each other. The propagation of such a layer can be described by the magnetic insulation theory [8]. With the increasing of the external magnetic field  $H_0$  the layer width grows. In this case it is necessary to take into account the appearance of induced currents and induced charges in the walls of the drift chamber and in the plasma channel. We must note that in both models it is essential to account for the electrical fields around the plasma channel.

The experiments were carried out on MS accelerator with the beam parameters,  $I_0 \leq 35 \text{ kA}$ ,  $U \leq 350 \text{ kV}$ ,  $\tau = 40 \text{ nsec}$ . The scheme of experimental device is shown on Fig. 1. The graphite cathode of the accelerator was placed directly in the drift chamber. The voltage pulse from the pulse forming line was transmitted to the diode gap along a vacuum coaxial line about 40 cm long, with a 2.5 cm outer tube radius and 1.1 cm inner tube radius. The electron beam was injected into a vacuum sealed cylinder 15-30 cm long, 2.1 - 4.8 cm in diameter of 12  $\mu$  thick aluminum foil through its end

covered with 30  $\mu$  aluminum anode foil. The cylinder was filled with an air at 0.5 torr pressure and placed radially in a ceramic chamber of 45 cm inner diameter. The small thickness of the foil allows one to neglect the energy losses of electrons and moreover ensures absence of the image current. The plasma in the cylinder may be created as a result of gas ionization by the injected beam.

The ceramic chamber was filled with an air in the range of pressures from  $5 \cdot 10^{-4}$  to 1 torr. The solenoidal magnetic field of  $H_0 \geq 2$  kG was directed along the chamber axis.

At a distance of 3-5 mm behind the further end of the cylinder was placed a Faraday cup combined with a calorimeter. The Faraday cup of 6.5 cm in diameter was electrically connected with the accelerator either by copper strips or by a plasma channel. In the first case, the return current in the channel induced by the injected current was short-circuited by the surface current flowing in the skin-layer of a plasma channel. This current induced the magnetic field around the channel. In the second case the beam current was compensated by the return current flowing from the collector and the magnetic field around the channel was created only as a result of a leakage current. The efficiency of transportation of the beam in the case of vacuum gap existence between the Faraday cup and the channel was determined as a ratio of the Faraday cup current to the beam current  $I_C/I_0$  is shown in Fig. 2 as a function of  $H_0$ . As one can see the efficiency is rather high, namely more than 80% even for the magnetic field strength of 300 - 500 G. At these fields the Larmor radius of electrons of the beam is greater than the length of the cylinder by 2-4 times. The injected current for all the cases shown is 24 kA.



An increase of the injected current up to 30 kA results in essential growth of the transport efficiency for magnetic field,  $H_0 \geq 500$  G. The measured values of the ratio  $I_C/I_0$  and that of the beam energy transfer to the target when it was directly connected to the end of the channel are shown in Fig. 3. An essential peculiarity in this data a leakage current of  $\approx 25\%$  from the channel even in the absence of the applied magnetic field that can be explained by angular divergence of the beam.

The beam propagation for  $H > 0$  was accompanied by damage of a side surface of the cylinder. The character of damage depended on the magnetic field strength and the gas pressure in the vacuum chamber. At pressures less than  $10^{-2}$  torr in the cylinder we observed holes with a transverse dimension roughly corresponding to the beam diameter. The beam position in the collector plane was determined from darkening and damage to the glass and lucite plates (Fig. 4). The photograph of the plates were obtained by contact method. The beam contours on Figs. 4.1 and 4.2 can be seen as light traces. Darkening of the central region is connected with the burnoff or surface destruction owing to its overheating by the beam. It can be witnessed from Fig. 4.3 where uniform damage of lucite plates are shown.

From Fig. 4.1 one can see that for  $H = 0$  the beam occupies practically all the plasma channel, and for  $H = 750$  G it is displaced down and partially comes out beyond the limits of the channel. We must note, that these photographs were obtained in the conditions when the diameter of the beam at the entrance of the channel ( $\phi = 2.2$  cm) practically coincides with the cylinder diameter. The increase of cylinder's diameter to 4.6 cm leads to the propagation efficiency decrease of 20%. A series of experiments were

also carried out in which copper and tungsten wires were used as a channel. These wires were placed between the anode foil and Faraday cup [9]. The beam current was carried away from Faraday cup by copper strips. As one can see from Fig. 5, the effectiveness of the transport was determined by the initial wires resistance and turned out to be essentially worse than that for the plasma channel.

As it follows from aforementioned results, the beam transportation along the channel can be realized only when the self-magnetic field of the beam  $H_I$  is greater than the outer magnetic field  $H_0$ . This may be explained with the help of following physical considerations. In the absence of the plasma channel the average magnetic field in the beam region is equal to  $H_0 > 0$ . In the presence of the channel the situation is changed essentially. Although self-magnetic field of the beam changes the sign, when crossing the beam but at the edge of the plasma channel arises the electrical field that has such a sign and a value, that the average effective magnetic field in the beam region is equal  $-H_I + H_0 < 0$ . It must be noted that this result is connected with the presence of the electrical field out of the plasma channel. Therefore the air pressure increase outside the plasma channel must lead to the partial decrease of the electric field and the beam transport along the channel. In Fig. 6 is shown the change of the efficiency of the beam transport as a function of the air pressure in the vacuum chamber. For the physical interpretation of experimental results we have supposed that the magnetic field around the plasma channel is not equal to zero. However, in the absence of the gap between the channel and the collector the magnetic field is generated only in the presence of the leakage current. The losses connected with it are equal in our experiments

to about 25% and this is inevitable payment for the transportation along the plasma channel of the rest of the beam in the physically more interesting case of direct electric connection between the cylinder and the collector.

## II. INJECTION AND TRANSPORT OF A RING SHAPED RELATIVISTIC ELECTRON BEAM THROUGH A CUSP-TYPE MAGNETIC TRAP

As it was mentioned already, the problem of beam energy transfer to a target is one of the most serious subjects in the program of REB application to pulsed fusion. For this reason it was decided to carry out scaling experiments on multi-module radial injection of beams to a target placed in the center of the cusped type magnetic trap.

Having this in mind the high current electron accelerator "URAL" [7] was adapted for generation of a ring shape beam and radial injection of it into a cusp type magnetic trap along its equatorial plane.

As can be seen from the schematic view of experimental device shown in Fig. 7 inside the hollow cathode shank of a high voltage diode was inserted a lucite 80 mm diameter cup (1) with a 10 mm wide gap in the equatorial plane sealed with the aluminum foil (12 - 15  $\mu$  thick) that was electrically connected to ground by means of copper foils and which served as the anode of the accelerator (see Fig. 11). Air pressure inside the cup can be varied from  $10^{-4}$  to a few torr. A stainless steel ring with a sharp inner edge of 92 mm in diameter was used as a cathode (2). A pulsed magnetic field was created by means of two copper coils (4) with inner diameter of 87 mm, outer diameter 115 mm and 10 mm wide. The distance between coils L was 20 or 40 millimeters. The coils were energized by a current generator of 10  $\mu$  sec wave period. The magnetic field strength in the cusp hole and the mirror hole at the moment of beam injection for the

coil distance  $L = 40$  and  $20$  mm was  $10$  and  $4$  kG correspondingly. In Fig. 8 are shown the typical oscillograms of a current and a voltage across the diode (a) measured by means of resistive divider and low inductance current shunt and x-ray detector signal (b) with a self rise time of the detector less than  $5$  nsec.

The beam energy determined from typical oscillograms shown in Fig. 8 and corrected for an inductive part of the diode voltage is about  $420$  joules. In addition, the input energy of the electron beam at the entrance of the magnetic trap was determined by means of the thin walled ( $100\text{ }\mu$  thick) calorimetric cylinder made of titanium and provided with a thermocouple and arranged coaxially in the trap. The measurements of the mean energy behind the anode foil by a  $40$  mm diameter and  $40$  mm long calorimeter give the value of about  $320$  joules for  $p = 0.3$  torr and  $I = 20$  mm. Also was measured the energy transferred to two  $60$  mm disk calorimeters located at each throat of the magnetic trap perpendicularly to the axis of it. It was found that the two streams of energy are almost equal and the total energy thus measured amounts to  $190$  joules for  $L = 20$  mm.

Thus, we can conclude that about  $40\%$  of the beam energy, which passed through the anode foil went to the central part of the cusped trap. According to calorimetric measurements made for the trap with  $L = 40$  mm, the part of the energy that is transported into the zero field region increases in this case and reaches more than  $50\%$ .

Experiments on energy transfer to a target put in the center of the cusped magnetic trap were carried out at two ranges of air pressure:

- a) high pressure -- a few torr
- b) low pressure --  $10^{-3}$  torr or less.

In the first case, we can expect full space charge neutralization of the beam and partial compensation of the beam current by the current flowing in the plasma created in the trap and the effect of self-focusing of a disc shape beam in a total magnetic field [10]. In the second case the absence of space charge neutralization and current compensation.

Determination of the energy that is transferred to a target placed in the central region of the trap was made by the measurement of the amount of evaporated matter and the heating of various probe bodies which were irradiated by the relativistic electrons. The heat transfer to probes were measured by means of thermocouples (5). We must bear in mind, however, that the energy transfer measured in such a way may be lowered, because the evaporated matter can be additionally heated by the beam after evaporation takes place. Indeed, the photographs taken by a high speed camera show a rather high level of energy contained in a vaporized matter that leaves the surface of the lead sphere (see Fig. 10).

For determination of the character of propagation of a ring shaped electron beam in the trap, the trace of the beam was photographed by means of x-ray pinhole camera (6). In Fig. 9 is shown the pictures related to different parts of the trap. From Fig. 9a (the trace of the beam at the anode made of titanium) it follows that the distribution of the beam current along the ring is not uniform. The figures 9b, 9c were obtained at a high pressure regime ( $p = 1.3$  torr) by means of conical converter made of



tantalum (100  $\mu$  thick) with a half cone angle equal to  $60^\circ$ , placed coaxially in the center of the trap. It is seen that due to self-magnetic field effect of the beam it remains the shape of a ring, traveling radially inside the trap (Fig. 9b - after 8 mm of travel, Fig. 9c - after 20 mm). Finally on Fig. 9d is shown the x-ray photography of the lead sphere of 8 mm in diameter, hanging on a thin wire in the center of the trap ( $p = 4$  torr).

Measurements of the energy transferred to the copper discs, 0.5 mm thick placed in the center of the trap in its equatorial plane obtained by thermocouples give the following values 15, 40, 63 joules for discs with 6, 10 and 15 mm radius corresponding to  $L = 20$  mm,  $p = 4$  torr. Determination of energy transferred to the 8 mm diameter sphere of graphite placed in the center of the trap obtained from heat measurements only gave the value of about 60 joules for  $p = 3 \div 5$  torr and  $L = 20$  or 40 mm.

At low pressures ( $p \leq 10^{-3}$  torr) the character of energy transfer to a target is somewhat different. X-ray radiation from a surface of a probe body placed inside the trap as well as the erosion traces are much more uniform compared with the high pressure case and indicates significant beam scattering. As the measurements have shown, the energy transferred to the 6 mm diameter aluminum sphere placed in the center part of the trap with  $L = 40$  mm is equal to 120 joules, which exceeds the results of high pressure case. This comprises about 75% of the energy that is transported to the central part of the cusped magnetic trap or 40% of the energy that goes out through the anode foil. The erosion traces on the surface of aluminum spheres also indicate rather symmetric irradiation.

Energy determination by heat transfer only to the 8 mm diameter spheres of graphite placed in the center of the trap at low pressures and for  $L = 40$  mm gives a somewhat lesser value, namely, about 70 joules. On



Fig. 10 is shown the picture of the blowoff from the surface of the lead sphere in equatorial plane of the trap at  $p = 3.5 \cdot 10$  torr. Symmetrical irradiation and high efficiency of energy transport in the case of low pressure with highly scattered beam can be explained in terms of sufficient trapping effect of relativistic electrons in the cusped field with equatorial hole closed by electric and magnetic fields of the diode and with the low level of leakage through the mirror holes. The electrons that enter such a trap can be concentrated and form a cloud in the region with zero magnetic field. It seems reasonable to suppose that for the formation of a cloud, several travels of electrons across the trap would be enough. Therefore for the trap examined ( $R_{\text{cloud}} \approx 2$  cm) the mean time of trapping for an individual electron may be of the order  $10^{-9}$  sec. If a target is put into such a cloud it experiences uniform heating as a result of irradiation by relativistic electrons. The criterion for transfer of greater part of the energy contained in a cloud to the target immersed in it was already mentioned in the introduction.

Thus the preliminary experimental results show that the efficiency of energy transfer by the ring shape beam to the target placed in the center of the chamber in the zero field region of the cusped trap can reach 40% for the ratio of the radius at the entrance of beam into the trap to the radius of the target of more than 10.

## REFERENCES

1. G. Yonas, J. W. Poukey, K. R. Prestwich, J. R. Freeman, A. J. Toepfer, M. J. Clauser, Nuclear Fusion 14, No. 5, 731 (1974).
2. U. V. Koba, V. I. Liksonov, V. S. Pen'kina, L. I. Rudakov, Y. L. Sidorov, V. P. Smirnov, A. D. Sukhov and E. Z. Tarumov, Fifth Conference on Plasma Physics and Controlled Nuclear Fusion Research, Tokyo (1974).
3. L. I. Rudakov and M. A. Samarsky, Sixth European Conference on Controlled Fusion and Plasma Physics, Moscow, Vol. 2, 487 (1973).
4. M. J. Clauser, et al., Seventh European Conference on Controlled Fusion and Plasma Physics, Lausanne, Vol. 1, 85 (1975).
5. E. Ott and R. N. Sudan, Phys. Fluids 14, No. 6, 1226 (1972).
6. I. I. Bzura, T. I. Fessenden, H. H. Fleishmann, D. A. Phelps, A. C. Smith and D. M. Woodall, Phys. Rev. Lett., 29, 256 (1972).
7. L. I. Rudakov, et al., Sixth European Conference on Plasma Physics and Controlled Thermonuclear Fusion, Moscow, Vol. 2, 430 (1973).
8. A. V. Goordeev, V. D. Korolev, Y. L. Sidorov and V. P. Smirnov, Annals of the New York Academy of Sciences, Vol. 251, pp. 668 (1975).
9. M. Friedman and M. V. Vitkovitsky, Appl. Phys. Lett, Vol. 25, No. 5, 259 (1974).
10. M. V. Babykin, E. K. Zavoisky, A. A. Ivanov and L. I. Rudakov, Plasma Physics and Controlled Nuclear Fusion Research, Vol. 1, 635 (1971), Vienna.

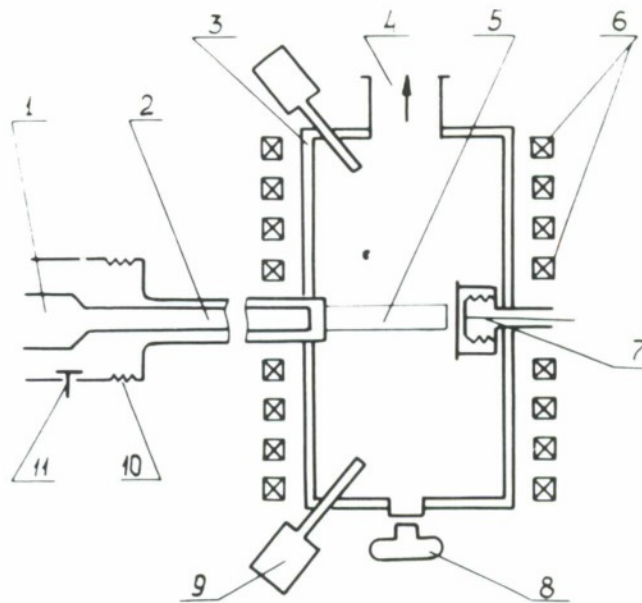


Figure 1. Schematic view of experimental device  
 1 - accelerator, 2 - vacuum line, 3 - drift chamber, 4 - vacuum pump, 5 - cylindrical shell, 6 - coils, 7 - Faraday cup - calorimeter, 8 - camera, 9 - scintillator detector, 10 - shunt, 11 - capacitor divider.

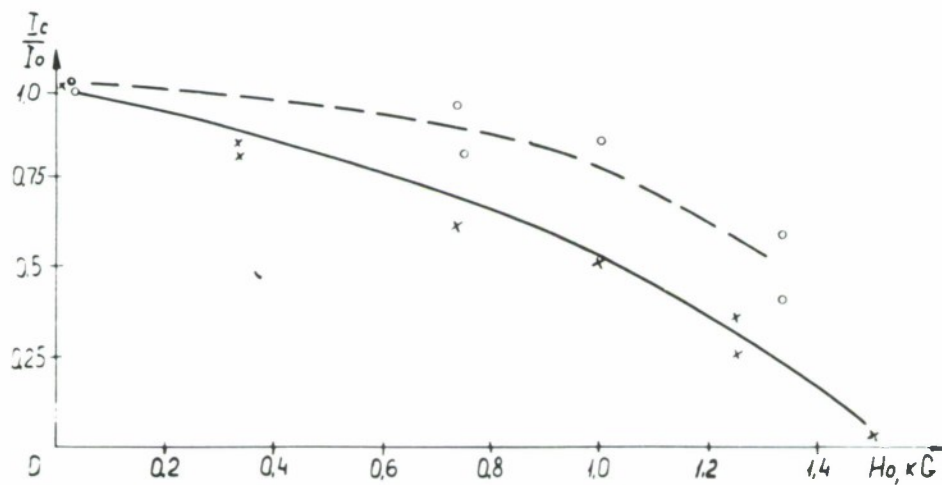


Figure 2. Dependences of the current ratio  $I_c/I_0$  on magnetic field for different beam currents in the case of vacuum gap for  $p = 5 \cdot 10^{-4}$  torr.  
 $I_0 = 24$  kA,  $U = 350$  kv  
 $I_0 = 30$  kA,  $U = 270$  kv

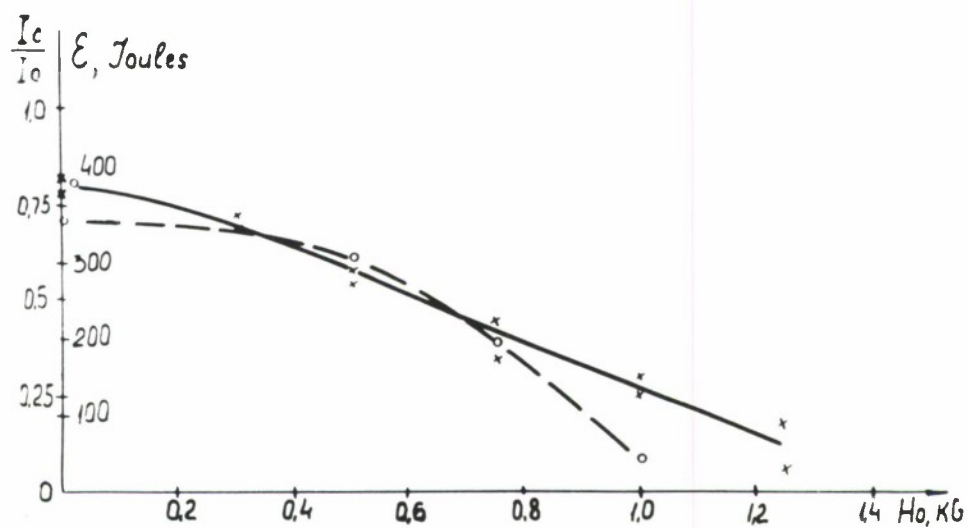


Figure 3. Dependences of the current ratio  $I_c/I_0$  (solid curve - cylinder length 15 cm) and the beam energy  $E$  (dashed curve) on magnetic field in the case with electrical contact between channel and collector for  $p = 5 \cdot 10^{-4}$  torr.

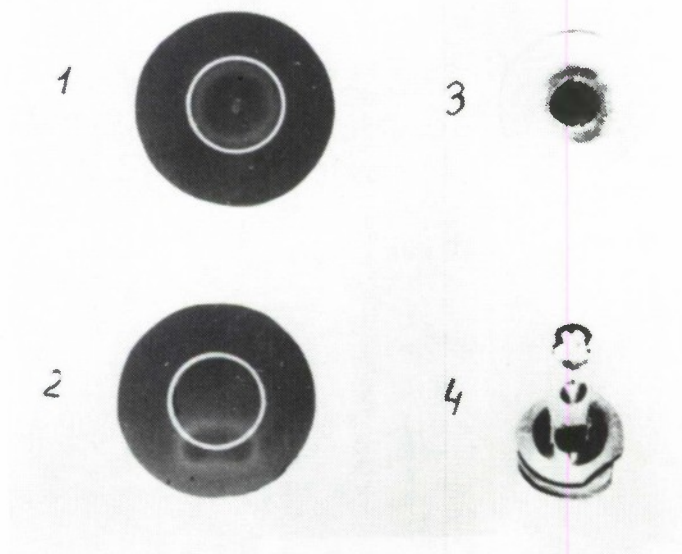


Figure 4. Electron beam damage of glass surface for  $H = 0$  (1) and for  $H = 750$  G (2); of lucite surface for  $H = 0$  (3) and of side surface of cylinder shell (4).

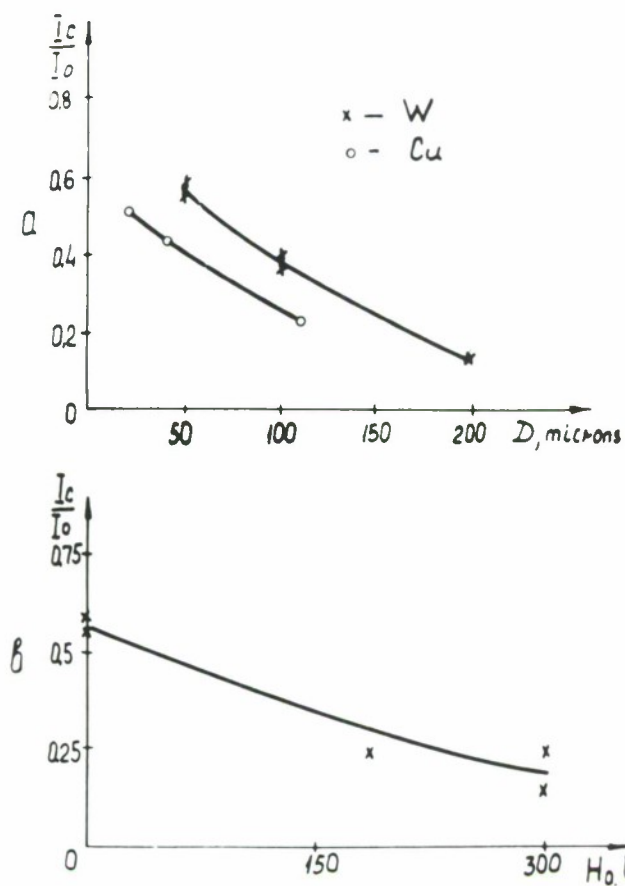
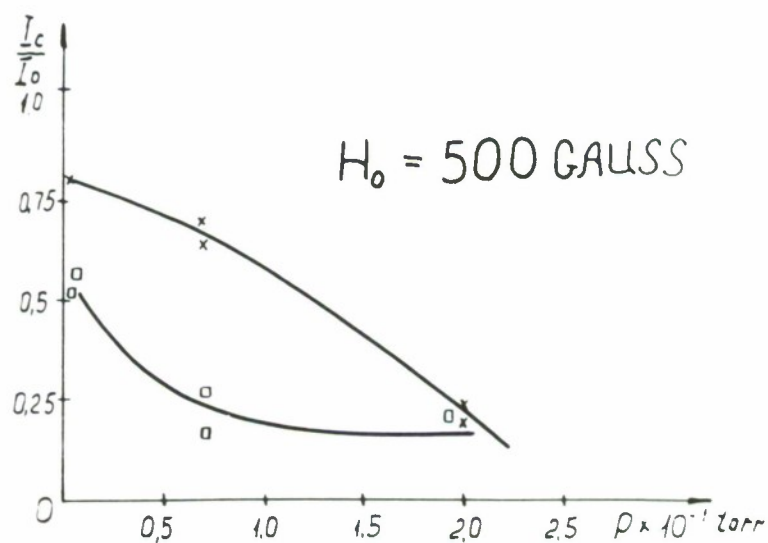


Figure 5. a - Dependence of current ratio  $I_c/I_0$  on wire diameter  $D$  for  $p = 5 \cdot 10^{-4}$  torr with return current conductors for  $H = 0$  (x) - tungsten wires; (o) - copper wires; b - Dependence of current ratio  $I_c/I_0$  on magnetic field for tungsten wire ( $D = 50$  microns) with return current conductors.

Figure 6. Dependence of current ratio  $I_c/I_0$  on the drift chamber pressure: upper curve for the case with a gap between channel and collector, lower for the case with contact between channel and Faraday cup.



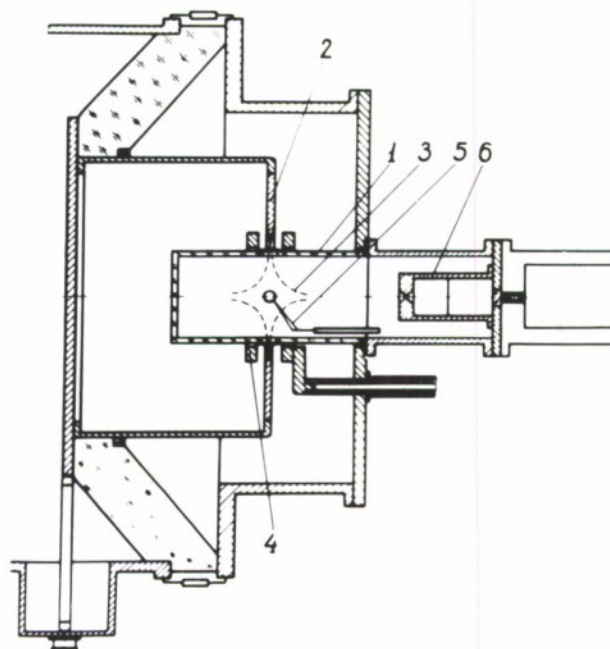


Figure 7. Schematic view of experiment  
 1 - lucite cup, 2 - stainless steel ring cathode, 3 - lines of magnetic field, 4 - magnetic coil, 5 - thermocouple, 6 - pin-hole camera.

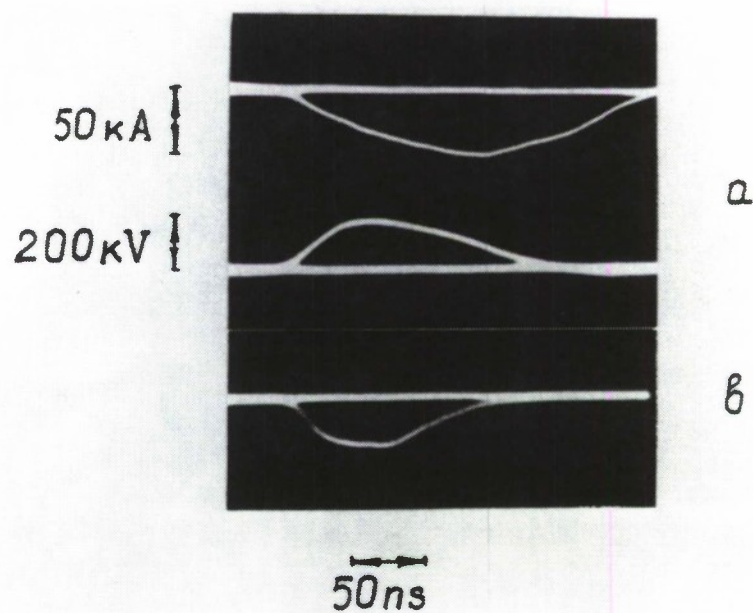


Figure 8. Typical oscillograms of diode current and voltage (a) and X-ray signal (b).



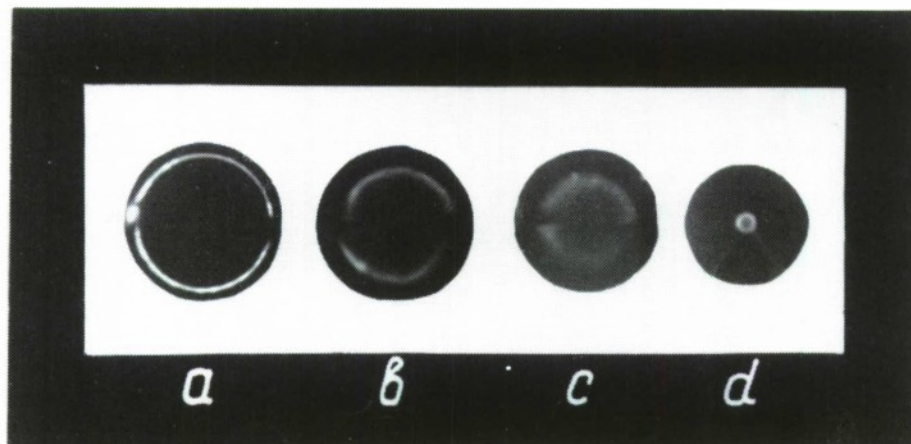


Figure 9. Pinhole X-ray photography of electron traces.

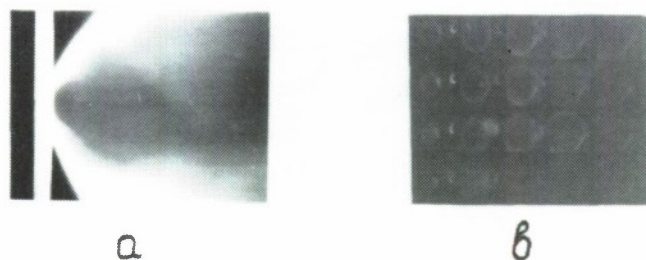


Figure 10. High speed photography of the blowoff from a lead sphere surface at  $p = 3,5 \cdot 10^{-4}$  torr a) gap scanning (speed of luminous front -  $6 \times 10^5$  cm/sec), b) picture scanning (time interval between pictures -  $0.4 \mu\text{sec}$ ).

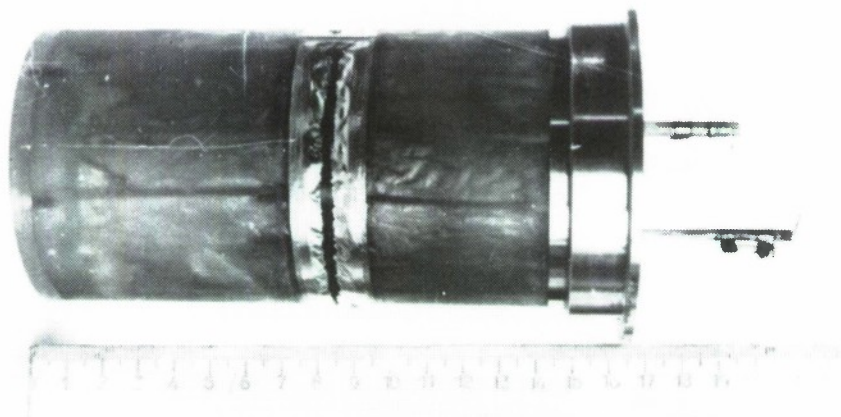


Figure 11. Lucite cup with circular foil gap for radial injection of an electron beam. On the anode foil is distinctly seen the burn through trace left after a beam passage.

ELECTRON AND PLASMA FLOW IN A RELATIVISTIC DIODE  
SUBJECTED TO A CROSSED MAGNETIC FIELD\*

G. Bekefi and T. J. Orzechowski  
Massachusetts Institute of Technology, Cambridge, Massachusetts 02139  
and

K. D. Bergeron  
Sandia Laboratories, Albuquerque, New Mexico 87115

ABSTRACT

The behavior of a cylindrical field emission diode (radial potential  $\sim 200\text{kV}$ ) is studied in the presence of an externally applied axial magnetic field  $B \leq 16\text{kG}$ . Observations made of the space-charge limited electron current ( $\sim 50\text{kA}$ ) compare favorably with theory which takes into account the presence of both the external axial magnetic field and the azimuthal self-magnetic field generated by current flow in the cathode. At magnetic fields exceeding the critical field necessary for cutoff, small but not insignificant current flows persist. The associated microwave emission suggests that this residual current is being driven by an as yet unidentified high frequency instability. Time-resolved measurements of the diode current and voltage lead to a determination of the expansion velocity of the cathode and anode plasmas. It is found that an external magnetic field of  $\sim 5\text{kG}$  suffices to stop plasma motion. This is in agreement with magnetohydrodynamic computations for a hydrogen plasma having an initial temperature of a few eV. Spectroscopic measurements of the diode plasma show that hydrogen is indeed the dominant ion species. Stark broadening of the spectral lines yields their number density.

---

\*Work supported in part by the United States Energy Research and Development Administration and in part by the National Science Foundation.

## I. INTRODUCTION

A transverse magnetic field acting on a vacuum, field-emission diode can play one of several roles. It can bend around the paths of the beam electrons and, at sufficiently large field strengths, it can prevent the electrons from reaching the anode. Such "magnetic insulation"<sup>1,2,3</sup> is utilized to inhibit electrical breakdown in high voltage diodes and associated transmission lines;<sup>4,5</sup> it can also be used to prevent electron flow in certain types of ion diodes.<sup>6,7</sup> Secondly, the transverse magnetic fields self-generated by the intense current flows in the diode gap itself can result in large  $\vec{E} \times \vec{B}$  forces and thus to pinching of the electron beam, a technique which is being exploited<sup>8,9,10</sup> to achieve beam focussing. And thirdly, a transverse magnetic field may slow down<sup>10,11</sup> the motion of cathode and anode generated plasmas which, if left to themselves, move rapidly across the diode gap causing an undesirable electrical shorting of the system (i.e., diode closure).

In this paper we examine electron and plasma motions in a cylindrical diode under conditions where beam pinching does not occur, and where the external magnetic field is provided by a solenoid. We will show that observations of the space-charge limited electron current compare favorably with theory which takes into account the presence of both the external axial magnetic field and the azimuthal "self-magnetic field" generated by the longitudinal current flow in the cathode. At magnetic fields exceeding the critical field necessary for cutoff, small but not insignificant currents persist. The associated microwave emission suggests that this residual current is being driven by an as yet unidentified instability. Finally, time-resolved measurements of the diode current and voltage lead to a determination of the expansion velocity of the cathode and anode plasmas. It

is found that an external magnetic field of  $\sim 5\text{kG}$  suffices to stop plasma motion. This is in agreement with magnetohydrodynamic computations for a hydrogen plasma having an initial temperature of a few eV. Spectroscopic measurements of the diode plasma show that hydrogen is indeed the dominant ion species. Stark broadening of the spectral lines yields their number density.

## II. THE EXPERIMENTAL ARRANGEMENT

### The diode

A schematic of the cylindrical vacuum diode is illustrated in Fig. 1a. The outer stainless steel anode is a cylinder 4.44 cm in diameter and 4.0 cm long. It is polished and has rounded edges to minimize local field enhancement and arcing. The inner coaxial cathode is machined from dense, fine-grained graphite [POCO Graphite<sup>T.M.</sup>]. A number of cathodes with diameters varying between 3.36 cm to 3.98 cm is used, thus providing diodes having gaps with spacings  $d_0$  ranging from 2.3 mm to 5.4 mm. The cathode is connected via a stainless steel shank to the inner conductor of the water filled coaxial capacitor which serves as the transmission line of the 4 ohm Nereus high voltage facility [maximum voltage  $\sim 600\text{ kV}$ ]. The anode is connected via a current viewing probe to the outer, grounded wall of the capacitor. The system is continuously pumped by means of a 4 inch metal diffusion pump to pressures better than  $3 \times 10^{-5}$  Torr.

### The axial magnetic field $B_z$ .

The axial magnetic field  $B_z$  acting on the diode is generated in a



solenoid energized by a capacitor bank whose rise time is approximately 2 msec. The discharging of this bank is timed in such a way that  $B_z$  reaches its peak value when Nereus fires. Thus, the magnetic field is virtually constant in time over the duration of the  $\sim 40$  nsec voltage pulse applied across the diode. The thin-walled, stainless steel construction of the diode ensures good penetration of the pulsed magnetic field into the diode interior. A magnetic field as high as 16 kG can be generated; its strength is controlled by the charging voltage on the capacitor bank. The solenoid current is monitored by means of a precision current probe. The system is initially calibrated by passing a known dc current through it and simultaneously measuring with a Hall gauss meter the magnetic field in the diode gap. In this way a determination of  $B_z$  to an accuracy of better than  $\sim 2$  percent is achieved.

#### The azimuthal magnetic field $B_\theta$

Even when the externally applied magnetic field  $B_z$  is zero, there is an azimuthal self-field  $B_\theta$  in the gap generated by the axial "feed" current  $I_z(z)$  flowing along the cathode and cathode shank. At the far end of the cathode (call this  $z = L$ ),  $I_z(L)$  is zero and therefore  $B_\theta(L)$  is zero or very small. However, as one approaches the shank [see Fig. 1],  $I_z(z)$  increases and the associated magnetic field  $B_\theta$  is expected to come close to  $B_\theta = \mu_0 I / 2\pi r$ , a value one obtains for current flow in an infinitely long cylinder. In view of the fairly complicated geometry caused by the discontinuity at the cathode-shank connection ( $z = 0$ ), we found it advisable to verify the aforementioned expectations experimentally. We proceeded as follows. We filled the cathode-anode gap with an aqueous

solution of copper sulphate and we adjusted the concentration to yield the nominal  $4\Omega$  impedance of the actual diode. We then passed a small dc current ( $\sim 4\text{A}$ ) through the diode and measured  $B_\theta(z)$  as a function of  $z$  by means of a small Hall probe; as expected,  $B_\theta(z = L)$  was very close to zero at the far end of the cathode, then rose and reached its peak value at  $z \approx 0$  where the shank joins onto the cathode. The value  $B_\theta(z = 0)$  that was measured there was equal, within experimental accuracy, to the theoretical value  $B_\theta = \mu_0 I / 2\pi r$ . The measurements are illustrated in Fig. 2. We expect similar results when later we shall scale the current in the mock-up diode to the actual currents ( $\sim 50\text{ kA}$ ) drawn from the relativistic diode.

#### Measurements of the diode current and voltage

The diode current is measured with a rapidly responding, low-inductance current viewing probe [T&M Research Products Inc.] shown in Fig. 1. Its output is displayed on a fast oscilloscope. The diode voltage is obtained from the signal delivered by a calibrated copper-sulphate voltage divider network (not shown) which is housed within the system, and is likewise displayed on an oscilloscope. There is an unwanted inductive contribution to this voltage which is subtracted out by a technique proposed by Swain. Prior to a run, the diode is physically shorted by inserting a graphite cylinder into the diode gap. A signal from a magnetic ( $\dot{B}$ ) probe located in the diode, attenuated and phase shifted, is added to the signal from the voltage probe. The attenuation and phase are adjusted, until there is zero net signal on the oscilloscope. Then, with the diode unshorted and in normal operation, the observed signal yields



the true diode voltage [of course, no further adjustment must be made in the setting of the attenuation and phase shift on the  $\dot{B}$  probe].

Typical oscilloscope voltage and current traces are illustrated in Fig. 3 for three different values of applied magnetic field; they are characteristic of the kind of results that are obtained for other intermediate values of magnetic field used [in a given run, it was not uncommon to make measurements in steps 300 gauss or less]. The sharp spike shown dashed in the voltage trace represents electrical breakdown of the prepulse switch which is in series with the diode. We use this spike as a convenient fiducial time marker. The same time marker (also shown dashed), but delayed by 71 nsec is seen in each of the current traces. To display it, we split off part of the diode voltage signal, delay it in time and superpose it on the current trace. This enables us to determine accurately the current  $I(t)$  and the corresponding voltage  $V(t)$  at the same instant of time  $t$ . The error in the relative timing of the currents and voltages does not exceed 3 nsec.

There are two important advantages to the cylindrical diode geometry used in our experiments. The first is that in this geometry any diamagnetic current (i.e. aximuthal current) caused by  $(\vec{E} \times \vec{B})_\theta = \hat{\theta} E_r B_z$  drifts can flow freely. In this way the undesirable space charge gradients caused by charge accumulation found in the case of planar diodes are avoided.<sup>6</sup> In the latter, charge accumulation at the edges of the cathode can result in a buildup of a space charge electric field  $\vec{E}_s$  parallel to the surface of the cathode. Unless this field is shorted out by a sufficiently high conductivity of the cathode (or the cathode plasma covering it), an undesirable  $\vec{E}_s \times \vec{B}$  drift of electrons towards the anode will

take place. Indeed, the difficulty of achieving good magnetic insulation in planar geometry (private communication by R. N. Sudan) is blamed on precisely this drift. Secondly, the radially flowing electron current has no self-magnetic field associated with it. Therefore, there is no beam pinching of the kind found in many planar diodes. To be sure, there is an azimuthal magnetic field  $B_\theta$  within the diode gap (see above) generated by the axial "feed" current  $I_z$  flowing in the cathode cylinder and in the cylindrical shank to which it is connected. The role played by this "self-field" will be discussed later.

#### The anode shield

Careful coaxial alignment of the cathode and anode is mandatory for satisfactory and reproducible operation of the diode. This is achieved by inserting into the gap an accurately machined spacer equal in size to the gap width, and then centering the diode. Subsequently, the spacer is removed and the system is pumped out. During a run, the alignment is checked visually by viewing the gap through the polystyrene window shown in Fig. 1. Despite all care taken, slight misalignments are unavoidable; and their effect can be quite pronounced. For example, a slight tilt of the cathode axis relative to the anode axis causes an appreciable component of the diode electric field to be collinear with  $\vec{B}$ . The electrons are then accelerated in the axial direction, an effect similar to that obtained in a magnetron injection gun.<sup>12,13</sup> Electrons traveling along  $\vec{B}$  would normally be collected by the current viewing probe, and their current would be indistinguishable from the radially flowing current. Even if the alignment could be made perfect, electron flow in the  $z$  direction

may well take place as a result  $\vec{E} \times \vec{B}$  drifts. The field  $B_\theta$  crossed with the radial electric field  $E_r$  induces electron motion along the positive  $z$  direction, towards the plexiglass window shown in Fig. 1. To ensure that none of these currents are received by the current viewing probe, an anode shield was constructed to protect the probe from the unwanted signal. The shield is illustrated schematically in Fig. 1a and in more detail in Fig. 1b. Thus, while the axial currents are allowed to flow freely, they pass directly to ground and are therefore not detected by the current measuring equipment. We note that their magnitudes are typically 10 percent of the total diode current.

### III. ELECTRON FLOW

Results for the three magnetic fields shown in Fig. 3 represent interesting regimes of diode operation. At zero external magnetic field (the first set of traces), a current of approximately 46 kA is drawn; the corresponding voltage is approximately 180 kV. The diode has an impedance of 3.9 ohm and is well matched to the nominal 4 ohm impedance of the Nereus facility. The current pulse has a long tail suggesting that significant current flows even though the voltage has fallen considerably below its peak value. This is indicative of diode closure caused by moving plasma, a phenomenon that will be discussed in Section IV.

At a magnetic field of 5810 G (the second set of traces) the diode is quite strongly mismatched to the transmission line; the diode voltage has risen, the current has fallen, and the impedance at peak current is

approximately 11 ohms. The fall in current has to do with the dynamics of the electron motion in the diode gap. The electron paths no longer follow straight lines directed radially outward, but curve in the magnetic field. As a result, the electrons lose some of their forward (radial) momentum and the space charge density near the anode increases. The consequence is a reduced electron current.

The magnetic field strength of ~5800 G is not quite large enough to completely stop the electron flow. Cutoff occurs at a slightly higher magnetic field  $B_z = B^*$  corresponding to the case for which the electron orbit just grazes the anode plane. This occurs when (approximately) the Larmor radius equals to the cathode-anode gap width. In the case of a uniform transverse magnetic field one finds that<sup>14,15,16,17</sup> the critical value of  $B^*$  necessary for cutoff is, in MKS units, given by

$$B^* = \frac{m_o c}{ed_e} \left[ \left( \frac{2eV}{m_o c^2} \right) + \left( \frac{eV}{m_o c^2} \right)^2 \right]^{1/2} \quad \text{Webers/m}^2 \quad (1)$$

where  $V$  is the diode voltage and  $d_e$  is the effective anode-cathode gap spacing. In planar geometry,  $d_e$  equals the physical gap width, but in cylindrical geometry it is defined as

$$\begin{aligned} d_e &= (R^2 - r^2)/2R \\ &= d_o [1 - (d_o/2R)] \quad ; \quad (d_o = R - r) \end{aligned} \quad (2)$$

where  $R(>r)$  is the radius of the outer anode and  $r$  is the radius of the inner cathode [note that if the cathode is the larger of the two cylinders having radius  $R$ , one then finds<sup>17</sup> that in place of Eq. (2),  $d_e = (R^2 - r^2)/2r$ ].

The last trace of Fig. 3 represents conditions for which  $B_z \gg B^*$ .

The current should be completely cut off. We observe that although it is small, it is not zero, a result which will be discussed at greater length later.

Details of the current flow in the aforementioned regimes are conveniently discussed in terms of the perveance  $P$ , defined as the ratio  $I(t)/[V(t)]^{3/2}$ . As we shall see in Sect. IV, motion of plasma across the diode makes  $P$  time dependent. For the present we avoid the difficulties of time dependence by defining  $P$  at a time  $t = t_0$  during the pulse when maximum current is drawn from the diode. One finds that at this time plasma motion is still so small that the anode-cathode gap is almost exactly equal to the initial physical separation between conductors. Figure 4 shows a plot of the perveance  $P(t_0)$  as a function of the normalized magnetic field  $B/B^*$ , for diodes with different gap widths. We see that the perveance is virtually independent of magnetic field for  $B_z \ll B^*$  and that magnetic fields begin to manifest themselves only when  $B_z$  becomes comparable to or exceeds  $B^*$ . For that reason it is convenient to divide our discussion into the following three cases.

Case (a): Zero external magnetic field ( $B_z = 0$ )

Reasonably good models of the space charge limited flow in pulsed relativistic diodes is afforded by time independent theories. Thus, for example, in the absence of a magnetic field one expects the Child-Langmuir law to hold. For cylindrical geometry, and when relativistic effects are not important, the case of our experiment, one has that<sup>18</sup>

$$\begin{aligned}
 P &= \frac{I}{V^{3/2}} = \frac{8}{9} \pi \epsilon_0 \left(\frac{2e}{m}\right)^{1/2} \frac{L}{R\alpha^2} \\
 &= 14.66 \times 10^{-6} \frac{L}{R\alpha^2} \text{ Amp-Volt}^{-3/2}
 \end{aligned}
 \tag{3}$$



where  $L$  is the length of the diode,  $R$  the radius of the anode and

$$\alpha = \{\ln(R/r) - 0.4 [\ln(R/r)]^2 + \dots\} \quad (r = R-d) \quad (4)$$

with  $r$  as the cathode radius. In Table I is shown a comparison between the measured perveance at maximum current  $[P(t_o)]$  and that computed from Eqs. (3) and (4). It is seen that for all four gap spacings  $d_o$  studied, the agreement is better than 10 percent.

The good agreement just mentioned may appear somewhat surprising in view of the fact that although  $B_z = 0$ ,  $B_\theta$  is not. To be sure,  $B_\theta$  is zero at the end of the cathode  $z = L$ , but then it rises (see Fig. 2) and reaches its full value  $B_\theta = \mu_o I(\text{diode})/2\pi r$  near the joint ( $z = 0$ ) between cathode and the cathode shank. On scaling the current in the mock-up diode discussed in the previous section to the actual current flowing in the system, one finds, for all gap spacings  $d$ , that  $B_\theta(z = 0)$  equals within experimental accuracy,  $B^*$  of Eq. (1). Why then do we see no experimental evidence of the effect of  $B_\theta$  on the perveance  $P(t_o)$ ? This is in large part due to the fact that  $B_\theta(z)$  decreases with increasing  $z$  and thus falls below  $B^*$  over most of the cathode surface. Nonetheless, a partial reduction in current can be expected. That none is seen may well be due to  $\vec{E} \times \vec{B}$  drifts. The field  $B_\theta$  crossed with the radial electric field  $E_r$  induces electrons born near  $z = 0$  to drift along the positive  $z$  direction towards the far end of the cathode where  $B_\theta$  is weak and where therefore the electrons can move towards the anode under the action of the electric field  $E_r$ . Indeed, there is experimental evidence indicating that a large fraction of the electrons do ultimately leave the cathode at its far end,  $z = L$ . Examination of the anode surface after many firings



reveals a very pronounced damage pattern in the form of a narrow circular groove situated at position  $z \approx L$ . The discoloration of the cathode, on the other hand, shows clear evidence that emission occurred uniformly over its entire surface. In addition, there is also the possibility of space charge accumulation at the cathode end; an axial electric field can be established which when crossed with  $B_\theta$ , forces electrons to drift radially outwards towards the anode.

The fact that  $B_\theta(z = 0) \approx B^*$  is no fortuitous accident. The point is that for fixed parameters  $V$ ,  $d$ , etc. one cannot draw a diode current greater than that given by  $B^* = B_\theta(z = 0) = \mu_0 I(\text{diode})/2\pi r$ , because as  $I$  increases, so does  $B_\theta$  until the critical magnetic field is reached. In this situation electrons are emitted from the cathode up to distances  $z$  from the end not exceeding a certain distance  $L_c$ ; but none will be emitted from regions beyond  $z = L_c$  where the system self-insulated itself. To obtain an estimate of  $L_c$  one substitutes  $B^*$  from Eq. (1) into  $B^* = \mu_0 I/2\pi r$ , and then eliminates the current  $I$  between this equation and Eq. (3), with the result that

$$L_c \approx \{2.25 r R \alpha^2 / d_e\} \left[ eV / m_o c^2 \right]^{-1} \left[ 1 + \left( eV / 2 m_o c^2 \right) \right]^{1/2} \quad (5)$$

Since all quantities on the right-hand side of this equation are known from experiment,  $L_c$  can be found; its values are listed in the last column of Table I. It is seen that  $L_c$  comes close to the physical cathode length  $L = 1.90$  cm. That  $L_c \approx L$  (or is even a little larger than  $L$ ) is an indication that emission over the full length of the cathode cylinder took place. Had it been otherwise, measurements of  $P$  would not agree with Eq. (31). It is also noteworthy that  $L_c$  remains constant for all four gap

spacings studied, and that the diode voltage (over which one has little control) appears to adjust itself so as to make  $L \approx L_c$ , thus allowing for full electron emission from the entire available surface. Observe from the Table that the diode voltage varies by more than a factor of two as one goes from the smallest to the largest gap. This is so despite the fact that the voltage on the transmission line is maintained the same throughout the experiments.

Case (b):  $B_z \leq B^*$

Figure 4 illustrates that, with increasing magnetic field, a well-defined cutoff in the current is achieved experimentally. To obtain actual values of the critical magnetic field, one can extrapolate the horizontal (plateau) part of each curve and the steeply falling part, and take the intersection of the two curves as the definition of  $B^*$ . The last column of Table II tabulates such experimentally determined values of  $B^*$  for different gap widths. The fourth column gives the appropriate theoretical results; the overall agreement is seen to be good.

With increasing  $B_z$ , cutoff does not set in discontinuously, but there is a gradual falling off of the diode current as the critical magnetic field is approached. This is seen more clearly in Fig. 5 where we plot on a linear scale the normalized current  $I/I_L$  as a function of the normalized magnetic field  $B/B^*$  [ $I_L$  is the Child-langmuir current obtained in the limit  $B_z \rightarrow 0$ ]. The solid line of Fig. 5 represents the theoretical predictions<sup>19,20,21</sup> computed for a planar diode subjected to a uniform magnetic field oriented parallel to the electrode surfaces. The physical reason in the computed reduction of  $I$  with increasing  $B$  is

as follows. As  $B$  is increased from zero, the electron paths become curved and as a result, the electrons lose some of their forward directed velocity (that is, they lose speed in the direction of the accelerating electric field). This leads to space-charge accumulation in the vicinity of the anode surface. This additional space charge due to the presence of  $B$ , over and above the familiar "Child-Langmuir" space charge near the cathode, causes the current reduction seen in the solid curve of Fig. 5.

It will be noted that the measured current is consistently lower than the current computed by the above mentioned theory. We believe that the observed discrepancy is to a large part due to the presence of the "self-magnetic" field  $B_\theta$  generated by the axial current flowing in the cathode. The inclusion of  $B_\theta$  in a self-consistent computation is difficult because of the strong variation this field experiences with distance  $z$  along the cathode (see Fig. 2), and no such computations are presently available.<sup>22</sup> However, a crude "back of the envelope" calculation may proceed as follows. For a given  $B_z$ , and a given diode voltage  $V$  there is a critical current  $I$  just large enough to generate a  $B_\theta = \mu_0 I / 2\pi r$  which satisfies the cutoff condition  $(B_\theta^2 + B_z^2)^{1/2} = B^*$ . On combining these two relations it follows that

$$I = \frac{2\pi r B^*}{\mu_0} \left[ 1 - \left( \frac{B_z}{B^*} \right)^2 \right]^{1/2} \quad (6)$$

where  $r$  is some radius that lies between the anode and the cathode; for convenience we shall take it to be the cathode radius. Now, the point is that one cannot draw any more current than the one just computed since as was already discussed earlier, the axial current increases from zero (at  $z = L$ ), and reaches its maximum value at  $z \approx 0$ . For  $z < 0$ , the

radial flow of current is magnetically self-insulated and thus the longitudinal current remains fixed at the value  $I$  given by Eq. (6). Use of Eqs. (1) and (3) allows one to rewrite the foregoing result in terms of the length  $L$  of the cathode and the critical length  $L_c$  defined by Eq. (5). One then finds that the normalized current is given by

$$\frac{I}{I_L} = \frac{L_c}{L} \left[ 1 - \left( \frac{B_z}{B^*} \right)^2 \right]^{1/2} \quad (7)$$

where, once again,  $I_L$  is the current obtained in the limit as  $B_z \rightarrow 0$ .

It will be recalled that in the absence of the external magnetic field  $B_z$ , the ratio  $L_c/L$  is about unity and remains constant for all four gap spacings  $d_0$  studied [see Table I]. In the presence of  $B_z$ , the diode voltage changes somewhat and so does  $L_c$ . However, in view of the crude nature of these calculations, we may as well neglect this effect and write that  $I/I_L \approx [1 - (B_z/B^*)^2]^{1/2}$ , a result which is plotted in Fig. 5 by the dashed curve. Allowing for the scatter in the experimental data, the agreement with the computed curve is judged to be fair.

#### Case (c): $B_z > B^*$

None of the theories presently available permit the existence of electron flow for values of magnetic field exceeding the critical field  $B^*$ . Nonetheless Fig. 4 shows clearly the presence of a "hot tail" extending beyond  $B^*$ . Electrons can exist in this forbidden region only if their energy exceeds the energy  $eV$  gained in crossing the gap. How did they gain this energy which in our experiments amounts to 3 to 4 times  $eV$ , or equivalently to 600-800 kV? It is suggested that an instability causes

auto-acceleration of a small but by no means negligible fraction of the primary electrons. The nature of the instability is as yet not known. It is interesting to note that an apparently similar "hot tail" (but of much smaller energy) was discovered<sup>23</sup> more than five decades ago in the so-called "smooth bore magnetron" whose geometry was much like that shown in Fig. 1 above. A number of experimental studies have been reported<sup>24,25,26</sup> with the view of unraveling the nature of the "hot tail" and of the associated instabilities occurring in smooth bore magnetrons. Some of the existing theories are based on models for unneutralized electron clouds;<sup>26</sup> others<sup>27</sup> claim that under normal working vacuum conditions the electron cloud is well neutralized and that, therefore, the instability is in the neutral electron-ion plasma. We point out that in the present experiments where short pulses ( $\leq 40$  nsec) and low base pressures ( $p \lesssim 3 \times 10^{-5}$  Torr) are employed, neutralization is not likely to occur, and that here therefore the instability is probably associated with unneutralized electrons.

Our studies are concentrated on exploring the microwave spectrum. Here we report observations made in the X-band range of frequencies. The experimental arrangement is illustrated in Fig. 6. Radiation emitted from the diode at frequencies between 7 GHz and 12 GHz (the X-band regime) is received by a microwave horn and then detected by a calibrated crystal whose output is connected to a fast oscilloscope. With the horn fixed in one position (at an axial distance of 15 cm from the polystyrene window) the microwave output was measured as a function of the axial magnetic field  $B_z$  applied to the diode. The results are illustrated in Fig. 7. It is seen that there is no evidence of microwave emission for magnetic field strengths below about 3.5 kG. But, with increasing magnetic field,



and just as the current begins to cut off, the microwave emission rises steeply and reaches its peak value somewhat beyond the nominal cutoff value  $B_z = B^* \approx 6300\text{G}$ . As the magnetic field is increased further, the emission falls off more gradually. The power levels reached are well above those that can be derived from single particle emission processes.<sup>28</sup> Of these the strongest is cyclotron emission. Setting  $I = 45\text{ kA}$ ,  $V = 200\text{ kV}$  and from a knowledge of the diode dimensions, one obtains an average electron density  $N \approx 6 \times 10^{11}\text{ cm}^{-3}$  and an upper limit of  $9 \times 10^{-2}$  watts for the single particle cyclotron radiation. This is more than three orders in magnitude smaller than the measured power levels from the cutoff diode, a fact which impels one to conclude that one is indeed dealing with some form of collective emission by the electron cloud.

To obtain the radiation spectrum, the signal received by the horn is dispersed by passage through 155 meters of dispersive X-band waveguide, and is then detected with a calibrated crystal whose output is displayed on an oscilloscope. The time delay  $t$  suffered by the signal relative to the time ( $t = 0$ ) of the arrival of the undispersed signal, allows one to decompose the measurements into the various frequency components by means of the familiar waveguide dispersion formula

$$\omega = \frac{\omega_c}{\sqrt{1 - (\ell/ct)^2}} \quad (8)$$

Here  $\omega_c$  is the waveguide cutoff frequency and  $\ell$  the length of waveguide. A typical spectrum is illustrated in Fig. 8 for the case when the axial magnetic field  $B_z$  equals 8900 G; this corresponds to the situation for which the emission is maximum (see Fig. 7). Two peaks are observed, one



at approximately 9.5 GHz and the other at ~11.5 GHz. When the magnetic field  $B_z$  is varied, the signal amplitudes change but the main features of the spectrum remain largely unaltered. That is to say, the frequency of the peaks does not "track" with  $B_z$ . This insensitivity to magnetic field (once  $B_z$  exceeds  $B^*$ ) rules out most resonant cyclotron instabilities (see for example Ref. 29). In fact there is no obvious, clearly discernable characteristic mode of oscillation which would fall into the frequency regime of the peaks shown in Fig. 8. With cyclotron effects probably ruled out, the frequency that comes closest is the electron plasma frequency  $\omega_p = \sqrt{Ne^2/m\epsilon_0}$ . Setting  $N$  equal to the average density of  $6 \times 10^{11} \text{ cm}^{-3}$  computed earlier, one obtains that  $\omega_p/2\pi \approx 7 \text{ GHz}$ . This suggests that one may have here a form of unstable Langmuir oscillations. Since the electron density varies with the radial position  $r$ , so does  $\omega_p$ , which may explain the rather broad feature of the observed frequency spectrum.

The angular distribution of the emitted power is determined by rotating the receiving horn along an arc of a circle whose origin coincides with the center of the diode. The arc radius is 40 cm at which distance the transmitter and receiver are in each others distant (i.e. radiation) zones. The measured H-plane radiation pattern is shown in Fig. 9; the corresponding E-plane pattern is found to be very similar. From the radiation pattern and from the known antenna gain of the receiving horn one calculates that the power emitted by the diode is ~100 watts, a result which agrees well with the near field measurements shown in Fig. 7.

#### IV. PLASMA FLOW

There is circumstantial evidence from the work of several laboratories<sup>10,11</sup> that a transverse magnetic field inhibits plasma motion across

the diode gap, and therefore reduces the speed at which the diode closes electrically. We shall now demonstrate conclusively that such is indeed the case. A closing diode is characterized by a time dependent cathode-anode separation  $d(t)$ . We can write this as

$$d(t) = d_0 - \int v(t)dt \quad (9)$$

where  $d_0$  is the initial spacing between the metal electrodes, and where  $v(t)$  is the combined velocity of cathode and anode plasmas. As the gap width  $d(t)$  decreases with time, the diode perveance  $P(t)$  rises. Therefore a study of the time dependence of  $P(t)$  serves as a convenient way of deriving information about  $v(t)$ , a fact which was first exploited by Parker et al<sup>30</sup> for the case of zero external B field.

Figure 10 shows the time history of  $P(t)$  for several different values of applied magnetic field B. The results were obtained from raw data like that shown in Fig. 3. The top left-hand diagram illustrates conditions in the absence of any transverse magnetic field. The rapid increase of perveance with time is indicative of plasma motion. This motion can be unfolded by inserting Eq. (9) in Eqs. (3) and (4), and demanding that the measured and theoretical perveances agree at all times. Figure 11 shows a plot of the velocity  $v(t)$  as a function of time thus deduced. Initially, the cathode and anode plasma stands still. It then begins to accelerate and at 40 nsec into the pulse, it reaches a velocity of  $\sim 16$  cm/ $\mu$ sec. The velocity  $v(t)$  averaged over the entire duration of the pulse is approximately 6 cm/ $\mu$ sec. The fact that the plasma accelerates is not unexpected; it is being continuously heated by

the diode current  $I$  flowing through it. The energy dissipated in Joule heating is then converted into plasma expansion.

Figure 10 shows that at  $B_z = 2390$  G the expansion velocity has decreased. At  $B_z = 4410$  G the perveance is virtually time independent and plasma expansion must have ceased altogether. Measurements made at a magnetic field of 5810 G represent conditions just prior to cutoff (i.e.  $B \approx B^*$ ). The remaining two sets of measurements shown in Fig. 10 are in the cutoff regime for which  $B_z \gg B^*$ . Observe that for  $B_z = 6850$  G, there is an increase in  $P(t)$  at late times. This suggests that some plasma [possibly of high atomic weight] is trying to close the gap.

To aid us in the interpretation of the above results, we developed<sup>31</sup> a one-dimensional magnetohydrodynamic computer code which gives the space-time history of a plane, infinite plasma slab expanding against a uniform, transverse magnetic field. The pertinent dynamic equations are the particle, momentum, and energy conservation equations.<sup>32,33</sup> If the expansion is taken along the  $x$ -axis and the magnetic field is assumed to be oriented along the  $z$ -axis, the equations take the form

$$\frac{d\rho}{dt} = -\rho \frac{dv_x}{dx} \quad (10)$$

$$\rho \frac{dv_x}{dt} + \frac{dp}{dx} = J_y B_z \quad (11)$$

$$\frac{3}{2} \frac{dp}{dt} + \frac{5}{2} \rho \frac{dv_x}{dx} = \frac{J_y^2}{\sigma} + \beta \frac{dp}{dx} \quad (12)$$

where  $\rho$ ,  $p$ ,  $J$ , and  $\sigma$  are the mass density, pressure, current density, and plasma conductivity, respectively. The operator  $d/dt = \partial/\partial t + v_x \partial/\partial x$

is the usual total time derivative. Ohmic heating ( $J_y^2/\sigma$ ) and thermal conduction ( $\beta dp/dx$ ) are allowed for in the energy conservation Eq. (12). Indeed, since thermalization of electrons and ions to a common temperature is often incomplete during the times of interest, we employ two energy equations, (but for the sake of brevity we do not show them explicitly): one equation for electrons and one for ions, each of which contains on the right-hand side appropriate energy equilibration rates.<sup>33</sup> To complete the foregoing equations, we require the generalized Ohm's law

$$J_y = -\sigma v_x B_z. \quad (13)$$

Maxwell's equations which govern the configuration of the magnetic field are not used. Rather,  $B_z$  appearing in Eqs. (11) through (13) is taken to be the unperturbed, externally applied magnetic field. The reason is that for the parameters of interest here, the magnetic Reynolds number proves to be sufficiently small, and the magnetic field diffusion time sufficiently fast, that the back-reaction of the plasma on the field can be safely neglected. In addition to  $J_y$ , there is the diode current  $J_x$  flowing from anode to cathode. This current can be comparable in magnitude with  $J_y$ . We have studied its effect, but all results given in this paper are for the case  $J_x = 0$ .

The computer program does a Lagrangian calculation of the magnetohydrodynamic equations described above. The plasma is divided into a fixed number of slabs (40 in all) each containing a fixed mass; no material is allowed to cross the slab boundaries. Motion of the plasma is determined by calculating the net force exerted on the boundaries between slabs. The thermal conduction between two slabs is calculated by

averaging the transport coefficient in the slabs and allowing heat to flow.

Initially, the slabs are all of uniform density and are all at the same temperature. Also, the electrons and ions are assumed to have the same temperature. At  $t = 0$  the plasma begins expanding at the expense of its own energy. During the computation, the variables in the system ( $N, T, V$ , etc.) are calculated at each position in the plasma, and the boundaries are adjusted to account for the forces exerted on them. After each cycle, the time is incremented and the calculations are redone. In this manner, the entire spatial and temporal evolution of the plasma is determined. In order to limit the possible development of steep gradients such as shock waves an artificial viscosity is introduced which smooths out the steepness.<sup>34</sup> We note that there is no provision in the program for instabilities. In particular if the plasma suffers from a Rayleigh-Taylor gravitational type of instability, our one dimensional computer model may well be too restricted. However, many magnetohydrodynamic instabilities, including the last named, have growth rates that are much too slow to have any noticeable effect during the  $\sim 40$  nsec lifetime of our plasma.

The plasma is assumed to be fully ionized, with an initial density<sup>35</sup> in the range  $10^{17}$ - $10^{19}$   $\text{cm}^{-3}$  and an initial temperature in the range 1-10 eV. Processes such as recombination, diffusion, and radiation are neglected since they prove to be negligible on the time scale ( $\sim 100$  nsec) being considered here. In the program an initial density  $N_0$  and temperature  $T_0$  are inputted into a plasma slab assumed to be  $10\mu$  thick. There is no further energy input beyond the initial one of magnitude  $N_0 k T_0$ . The



space-time development  $N(x,t)$  and  $T(x,t)$  of the expanding plasma is then observed. In the absence of a magnetic field, the program shows that the plasma expansion is almost exactly adiabatic in accord with expectations, that is  $N(x,t)/T^{3/2}(x,t) = \text{constant}$ . Typically, the plasma front reaches its terminal velocity in a matter of 1 to 2 nsec, and then continues expanding at a constant speed given by

$$v = \alpha \sqrt{\frac{\kappa T_o}{M}} \quad (14)$$

where  $M$  is the mass of the ion and  $\alpha$  is a number whose value lies between 3 and 5 [see Table III]. The density and temperature of the plasma front fall with time as  $N \propto t^{-1}$ ,  $T \propto t^{-2/3}$ ; the electron and ion temperatures remain equal to one another. [When current with density  $J_x$  is allowed to flow, heating followed by plasma acceleration occurs,<sup>31</sup> in accord with the observations discussed earlier.]

In the presence of a transverse magnetic field the plasma is decelerated as a result of the  $\vec{J} \times \vec{B}$  force acting on it. The development of the density and temperature is illustrated in Figs. 12 and 13, for a hydrogen plasma in a magnetic field of 5 kG, having an initial density of  $10^{19} \text{ cm}^{-3}$  and an initial electron and ion temperature of 5 eV. At early times, when the plasma is dense and hot, it travels unhindered by the magnetic field. The magnetic field begins to assert itself at those times (and in those locations) for which the plasma pressure  $N\kappa(T_e + T_i)$  becomes about equal or less than the magnetic pressure  $B^2/2\mu_o$  [i.e., when the "plasma  $\beta$ " becomes less than unity]. The sharp spikes in the density traces and the corresponding jumps in the temperature traces seen in Figs. 12 and 13 represent, what we believe to be the manifestation of a shock. [The shock is not observed in the absence of the magnetic field.] The details of the shock are illustrated in Fig. 14.

Figure 15 shows motion of the plasma front with no magnetic field; in a 5 kG field, and in a 10 kG field. When B is zero, the velocity is seen to be constant. The slope of the straight line gives a velocity equal to 7.8 cm/ $\mu$ sec. In a 5 kG magnetic field there is clear indication that the plasma is slowed down and actually stops moving at a time of approximately 100 nsec. In some cases the plasma is seen to bounce, that is it stops, goes backward, and then forward again.

The effect of magnetic field on plasmas composed of heavier ions (carbon, steel) is much less pronounced as is illustrated in Table IV which gives the velocities under different conditions. Thus, for example, a 5 eV carbon plasma requires a 10 kG magnetic field to reduce its velocity by less than a factor of two.

The foregoing computations prove to be a helpful guide toward a better understanding of the experiments described earlier. From these experiments two pieces of valuable information emerge. First, in the absence of a magnetic field we find that the average plasma velocity must be approximately 6 cm/ $\mu$ sec. And second, a magnetic field of  $\sim 4500$  G virtually stops plasma motion. The experiments are consistent with the computer modeling of an expanding hydrogen plasma having an initial density of the order of  $10^{19}$  cm<sup>-3</sup> and an initial temperature of the order of 5 eV. The experiments would not be consistent, for example, with the model of a moving carbon plasma. There are two reasons; first, because the measured velocity in the absence of magnetic field is too high compared with the prediction from Eq. (14); and second, because the measured magnetic field required to stop plasma motion is too low [compared

with values of  $v$  for carbon given in Table IV]. The fact that a hydrogen plasma rather than, for example, a carbon plasma from the carbon cathode appears to be flowing across our diode may not be too surprising. Monolayers<sup>39</sup> of diffusion pump oil back-streaming from the pump and/or vacuum grease from the diode insulators undoubtedly cover all of the diode surfaces. Moreover, since the carbon cathode has not been previously baked, occluded water vapor may well be another source of hydrogen. If there is carbon plasma moving, its velocity is presumably slower and the time for closure longer. The necessary magnetic field for stoppage must be correspondingly higher.

To check out some of these ideas, we undertook a series of spectroscopic measurements of the diode plasma. The light from the gap, after passage through the polystyrene window shown in Fig. 1 is focused onto the slits of a 1.5 meter Wadsworth grating spectrograph (Jarrell-Ash Model 78-090). This instrument is provided with a film strip situated in its focal plane: the overall dispersion is  $10.8 \text{ \AA/mm}$ . In order to obtain sufficient light intensity, the slits are opened to a width of  $100 \text{ }\mu\text{m}$ , and the light from 10 successive shots is superposed on the same film strip. Thus, only time-integrated effects are being observed in these experiments.

By far the most prominent line seen is the Balmer  $\alpha$  line of hydrogen at  $6563 \text{ \AA}$ , and, to a lesser extent, the Carbon II doublet at  $6578 \text{ \AA}$  and  $6583 \text{ \AA}$ . A Balmer  $\beta$  line and a host of other very faint carbon lines are also seen, but they are too weak to be used for diagnostic purposes. Figure 16 is an enlarged photograph of the aforementioned three lines.

Significant line broadening is clearly evident; it is caused by the electric field of the ambient ions and electrons of the diode plasma. Since such plasma Stark broadening is governed by the charged particle density  $N$  (it is insensitive to the temperature  $T$ ), it can be exploited to obtain a reliable value of the time integrated density of our diode plasma. Film strips like those shown in Fig. 16 were scanned with a photodensitometer [Fig. 17]. After subtraction of the instrumental broadening, the full line width  $\Delta\lambda(1/2)$  at the half power points was recorded. The density was then determined using tabulated values<sup>37</sup> which relates  $N$  and  $\Delta\lambda(1/2)$ . To obtain good shot-to-shot reproducibility of our spectroscopic data, the following procedure was adopted. The diode was pumped out and then filled with hydrogen to almost an atmosphere of pressure. Time was allowed for the hydrogen to be adsorbed by the diode surfaces and after several minutes it was pumped out until a base pressure  $\sim 3 \times 10^{-5}$  Torr was again achieved. The procedure was followed after each firing of the Nereus facility. Good, reproducible line broadening was thus achieved. We note, however, that the line intensities were not very reproducible and they varied significantly from one run to the next. This implies that whereas the electron density remained quite invariant, the density of the radiating atoms was fairly erratic.

One sees from Fig. 16 that the line width, (and thus the density  $N$ ) varies with the up and down position on the photographed spectral line. This simply says that the plasma density is somewhat inhomogeneous -- being denser near the cathode and less dense near the anode. Photodensitometer scans were taken at three positions, one near the cathode, one

near the anode, and one midway between the two. The results are recorded in Table V. We note that the determination of  $N$  from the broadening of the  $H\alpha$  line is in good agreement with the determination of  $N$  from the C II line, thus adding confidence concerning the reliability of this technique. However, the determination of  $N$  from the C II line is much less accurate in view of the fact that the instrumental line broadening in this case becomes comparable with the Stark width of the line.

It is seen from Table V that when the diode is acted upon by a strong axial magnetic field, the measured plasma density is reduced by about a factor of ten. It is this reduction which is undoubtedly responsible for the fact that diode closure discussed earlier is inhibited by the presence of the  $B_z$  field. However, one important question remains unanswered. Is the observed reduction in the time-integrated  $N$  due to the fact that the  $\vec{J} \times \vec{B}$  forces are so strong as to prevent plasma from leaving the immediate vicinity of the cathode (and is thus unobservable by us because of limitation in spatial resolution of the optical setup); or does the magnetic field  $B_z$  inhibit in some way or other the initial formation of plasma? Better spatial resolution, together with time-resolved determinations of the Stark broadening would be required to answer this question.

#### ACKNOWLEDGMENTS

We wish to thank Mr. I. Mastovsky for technical assistance. The computer codes were run in the M.I.T. Computer Center and at Sandia Laboratories. We also wish to thank Dr. Fader for making available to us his laser-plasma codes.



## REFERENCES

1. R. Miller, N. Rostoker, and I. Nebenzahl, Bull. Am. Phys. Soc. 17, 1007 (1972).
2. G. Bekefi, T. J. Orzechowski, and J. Golden, Bull. Am. Phys. Soc. 19, 534 (1974).
3. J. Golden, T. J. Orzechowski, and G. Bekefi, J. Appl. Phys. 45, 3211 (1974); also T. J. Orzechowski, Ph.D. Thesis, M.I.T. 1975 (unpublished).
4. T. H. Martin, IEEE Trans, Nucl. Sci. NS-16, 59 (1969).
5. N. Rostoker, Bull. Am. Phys. Soc. 17, 1005 (1972).
6. R. N. Sudan and R. V. Lovelace, Phys. Rev. Lett. 31, 1174 (1973).
7. P. Dreike, C. Eichenberger, S. Humphries, and R. Sudan, Appl. Phys. Letters (to be published).
8. B. Ecker, Bull. Am. Phys. Soc. 16, 1249 (1971).
9. K. R. Prestwich and G. Yonas, Bull. Am. Phys. Soc. 17, 981 (1972).
10. G. Cooperstein and J. J. Condon, J. Appl. Phys. 46, 1535 (1975).
11. J. Credon, P. Spence, and R. Huff, Bull. Am. Phys. Soc. 18, 1310 (1973); G. Bekefi and T. J. Orzechowski, Bull. Am. Phys. Soc. 20, 584 (1975).
12. G. S. Kino and N. Taylor, IEEE Trans. Electron. Devices ED-9, 1 (1962).
13. M. Friedman and M. Ury, Rev. Sci. Instrum. 41, 1334 (1970).
14. A. W. Hull, Phys. Rev. 18, 31 (1921).
15. L. Page, Phys. Rev. 18, 58 (1921).
16. A. Ron, A. A. Mondelli, and N. Rostoker, IEEE Plasma Sci. PS-1, 85 (1973).

17. R. V. Lovelace and E. Ott, Phys. Fluids 17, 1263 (1974).
18. I. Langmuir and K. T. Compton, Rev. Mod. Phys. 3, 191 (1931).
19. L. Tonks, Phys. Sowjetunion 8, 572 (1936).
20. R. V. Lovelace (to be published).
21. K. D. Bergeron and J. W. Poukey, Appl. Phys. Letters 27, 58 (1975).
22. V. S. Voronin and A. N. Lebedev, Zh. Tekh. Fiz 43, 2591 (1973) [Sov. Phys., Tech. Phys. 18, 1627 (1974)].
23. I. Langmuir, Phys. Rev. 26, 585 (1925).
24. E. G. Linder, Proc. IRE 26, 346 (1938); J. Appl. Phys. 9, 331 (1938).
25. C. D. Sims and D. Gabor, J. Electron 1, 231 (1955); R. L. Jepsen and M. W. Muller, J. Appl. Phys. 22, 1196 (1951); G. D. Sims, article in Crossed Field Microwave Devices (Academic Press), 1961.
26. D. Gabor, Proc. Roy. Soc. A183, 436 (1945).
27. V. I. Farenik, V. V. Vlasov, A. M. Rozhkov, K. N. Stepanov, and V. A. Suprunenko, Zh. Tekh. Fiz. 42, 1625 (1972) [Sov. Phys. Tech. Phys. 17, 1298 (1973)]; also Zh. Eksp. Teor. Fiz. Pis. Red. 10, 71 (1969) [J.E.T.P. Lett. 10, 46 (1969)].
28. G. Bekefi, Radiation Processes in Plasmas (J. Wiley & Sons) 1966.
29. M. Frieman and M. Herndon, Phys. Rev. Lett. 28, 210 (1972); 31 752 (1973); Y. Carmel and J. A. Nation, Phys. Rev. Lett. 31, 806 (1973); 33, 1278 (1974); V. I. Granatstein, M. Herndon, R. K. Parker, and P. Sprangle, IEEE J. Quant. Electron. QE-10, 651 (1974).
30. R. K. Parker, R. E. Anderson, and C. V. Duncan, J. Appl. Phys. 45, 2463 (1974).
31. T. J. Orzechowski and G. Bekefi, Bull. Am. Phys. Soc. 20, 584 (1975).

32. I. B. Bernstein and W. J. Fader, Phys. Fluids 11, 2209 (1968).
33. S. I. Braginskii, in Reviews of Plasma Physics edited by M. A. Leontovich (Consultants Bureau, New York, 1965), Vol. 1 p. 205.
34. J. Von Neumann and R. D. Richtmyer, J. Appl. Phys. 21, 232 (1950).
35. L. P. Mix, J. G. Kelley, A. J. Toepfer, and C. F. Perry, Bull. Am. Phys. Soc. 18, 1309 (1973); 19, 857 (1974).
36. A. J. Toepfer (private communication).
37. H. R. Griem, Spectral Line Broadening by Plasmas (Academic Press) 1974.

Table I. Measured and theoretical diode perveances  $P$  for different gap spacings. The external magnetic field  $B_z$  is zero. The values of  $I$ ,  $V$ , and  $P$ (experimental) correspond to measurements made at a time of maximum current flow ( $t = t_0$ ).

$d_0$ (cm)	$I$ kA	$V$ kV	$P$ (experiment) $AV^{-3/2} \times 10^6$	$P$ [from Eq. (3)] $AV^{-3/2} \times 10^6$	$L_c$ cm
0.23	49.9	131	1052	1149	2.07
0.34	46.2	183	589	522	2.18
0.44	36.5	231	329	310	2.23
0.54	30.8	285	202	205	2.20

Table II. Comparison of the measured and calculated magnetic fields  $B^*$  necessary to cutoff radial current flow in a cylindrical diode of gap width  $d_0$ .  $V$  is the diode voltage (at the given  $B_z$ ) averaged over many shots.

$d_0$ (cm)	$d_e$ (cm)	$V(t=t_0)$ (kV)	$B^*$ (Eq. 1) (gauss)	$B_z^*$ (experiment) (gauss)
0.23	0.218	204	7651	7500
0.34	0.314	271	6288	6050
0.44	0.396	303	5337	5070
0.54	0.474	363	4990	4790

Table III. Calculated velocity of the plasma vacuum boundary of an unmagnetized plasma slab.

Hydrogen			
temperature (eV)	velocity of plasma boundary (cm/ $\mu$ sec)	$\sqrt{KT_0/M}$ (cm/ $\mu$ sec)	$\alpha$
1	3.92	.98	4.00
5	7.80	2.19	3.56
10	10.21	3.10	3.29
Carbon			
1	1.09	0.28	3.89
5	2.62	0.63	4.16
10	4.03	0.89	4.53
Steel			
1	0.43	0.13	3.31
5	1.30	0.29	4.48
10	2.10	0.41	5.12



Table IV. Computed velocities of hydrogen, carbon and steel plasmas at various times  $t$  (given in cm/ $\mu$ sec) during their expansion. The initial plasma density is  $10^{19}$  cm $^{-3}$  and the initial temperature is 5 eV.  $B$  is the externally applied transverse magnetic field (in kG). A negative velocity implies that the plasma has been stopped and is moving back.

Hydrogen				
$t$	$B$	0 kG	5 kG	10 kG
3 nsec		7.8	8.3	7.8
20		7.8	3.4	1.3
65		7.8	0.87	-0.26
98		7.8	0	-0.26
Carbon				
3		2.6	3.8	3.1
20		2.6	3.2	2.7
65		2.6	2.6	2.0
98		2.6	2.1	1.9
Steel				
3		1.3	1.3	1.3
20		1.3	1.3	1.3
65		1.3	1.3	1.3
98		1.3	1.3	1.3

Table V. Time integrated plasma density at three positions of the diode gap determined from the Stark broadening of the H $\alpha$  line and the C II 6578  $\text{\AA}$  line.  $\Delta\lambda$  is the measured full half-width at the half power point and  $B_z$  is the axial magnetic field applied to the diode.  $d_o = 3.4$  mm

$B_z = 0$			
Spectral line	Near cathode	Midway between cathode and anode	Near anode
H $\alpha$	$N = 1.8 \times 10^{17}$ $\Delta\lambda = 14.5 \text{ \AA}$	$N = 1.7 \times 10^{17}$ $\Delta\lambda = 13.3 \text{ \AA}$	$N = 1.1 \times 10^{17}$ $\Delta\lambda = 10.0 \text{ \AA}$
C II(6578)	$N = 1.6 \times 10^{17}$ $\Delta\lambda = 1.7 \text{ \AA}$	$N = 1.8 \times 10^{17}$ $\Delta\lambda = 1.9 \text{ \AA}$	$N = 0.9 \times 10^{17}$ $\Delta\lambda = 0.94 \text{ \AA}$

$B_z = 14$ kG			
Spectral line	Near cathode	Midway between cathode and anode	Near anode
H $\alpha$	$N = 1.4 \times 10^{16}$ $\Delta\lambda = 1.6 \text{ \AA}$	$N = 0.9 \times 10^{16}$ $\Delta\lambda = 1.1 \text{ \AA}$	$N = 0.7 \times 10^{16}$ $\Delta\lambda = 0.8 \text{ \AA}$

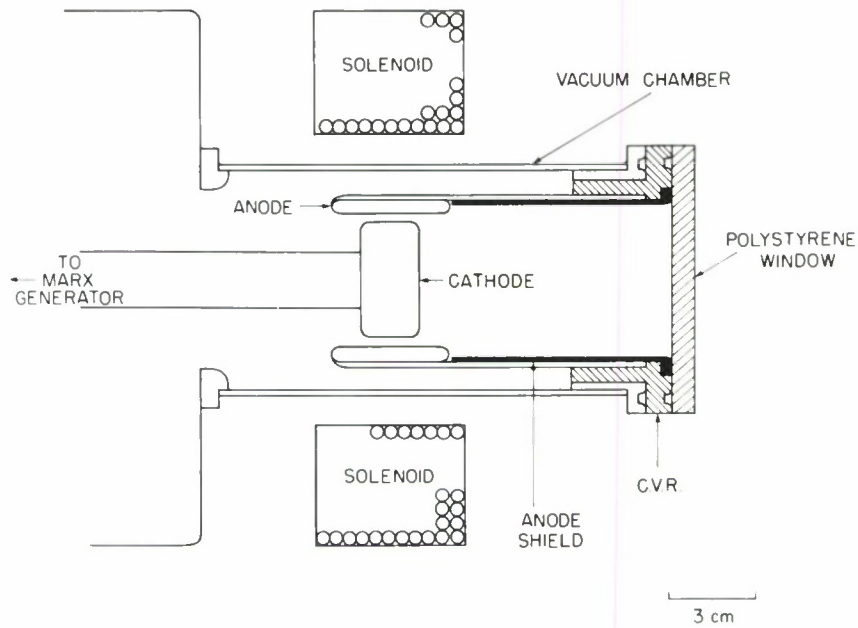


Figure 1a. Schematic drawing of the cylindrical diode.

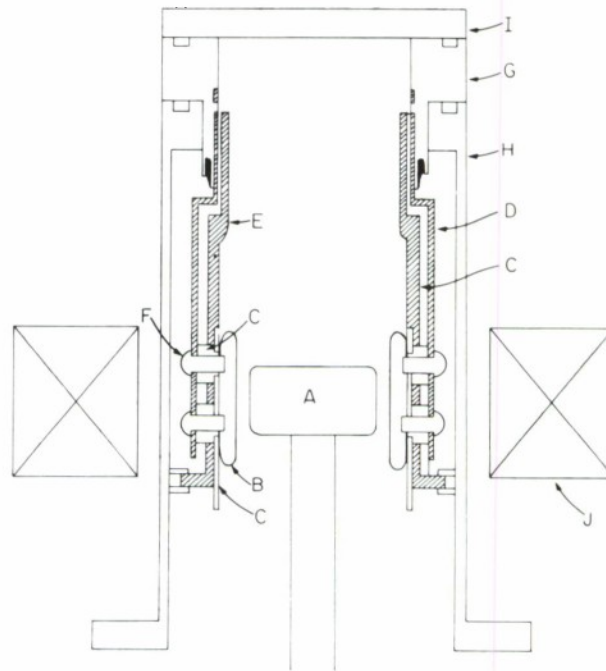


Figure 1b. More detailed drawing of diode showing placement of the anode shield and of the current viewing probe. A-cathode; B-anode; C-insulator; D-anode connection to the current viewing probe; E-anode shield; F-stainless steel screws connecting B to D; G-current viewing resistor; H-vacuum envelope; I-polystyrene window; J-solenoid.

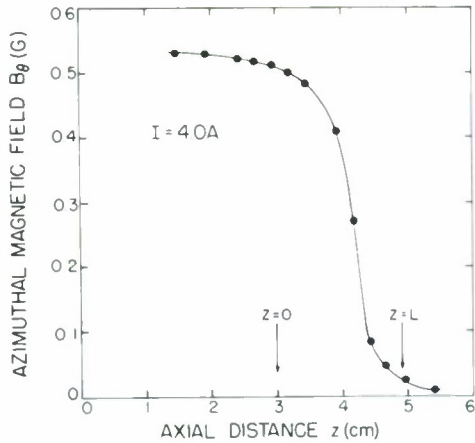


Figure 2. Axial variation of the azimuthal magnetic field in a mock-up cylindrical diode drawing 4A of current.  $z = L$  refers to the far end of cathode;  $z = 0$  refers to the near end where the cathode connects onto the shank. Measurement at radial distance of 1.5 cm.

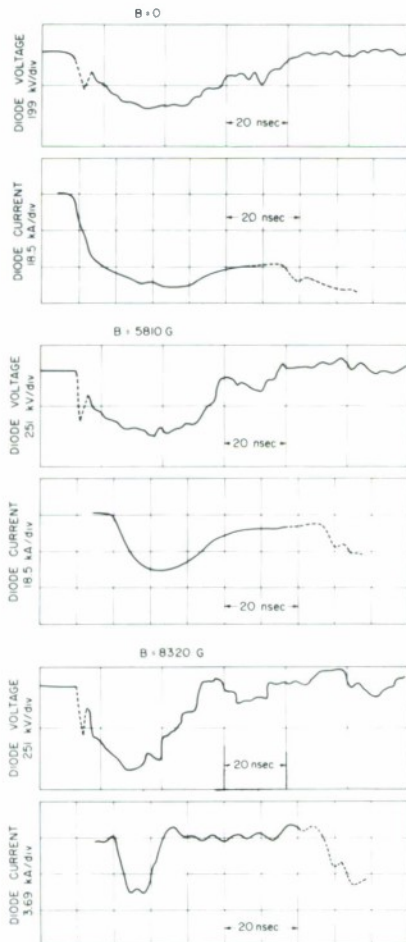


Figure 3. Oscilloscope traces of the diode voltage and current for three different values of externally applied magnetic field  $B_z$ . The dashed lines represent fiducial time makers. The diode gap  $d_0 = 3.4$  mm. The voltage traces shown represent signals after subtraction of the unwanted inductive contribution.  $V$  and  $I$  increase downwards. Zero  $V$  and zero  $I$  are given by the initially horizontal parts of traces.

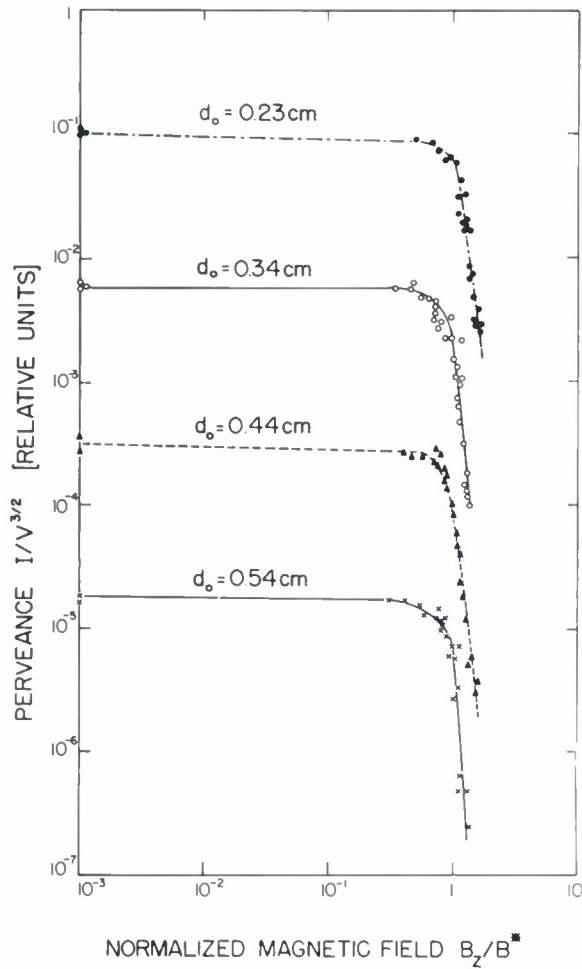


Figure 4. Diode perveance as a function of the normalized magnetic field  $B_z/B^*$ , for different gap widths  $d_0$ . The curves for the different gap widths are displaced vertically with respect to one another by a fixed interval, for easier visual presentation. The absolute value of the perveance for each gap is given in Table I for the case  $B_z \rightarrow 0$ . To normalize the abscissa, we computed the appropriate  $B^*$  from Eq. (1) for each experimental point, from the known value of  $V(t_0)$ .

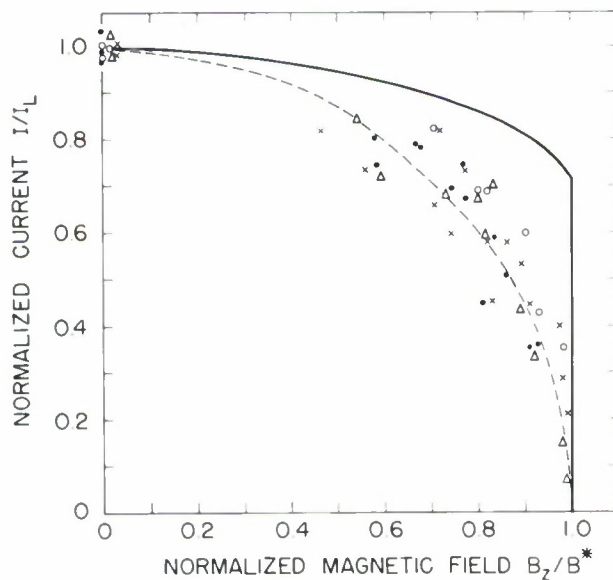


Figure 5. Normalized electron current  $I/I_L$  as a function of the normalized magnetic field  $B_z/B^*$ . The "hot tail" at  $B_z > B^*$  has been omitted from this figure for the sake of clarity. The various points are experimental values obtained for different gap widths:  $\circ \circ$   $d_0 = 2.3$  mm;  $\bullet \bullet$   $d_0 = 3.4$  mm;  $\times \times$   $d_0 = 4.4$  mm;  $\Delta \Delta$   $d_0 = 5.4$  mm. The solid line is from nonrelativistic theory<sup>19,20,21</sup> for a planar diode in a uniform magnetic field. The dashed curve is from Eq. (7).



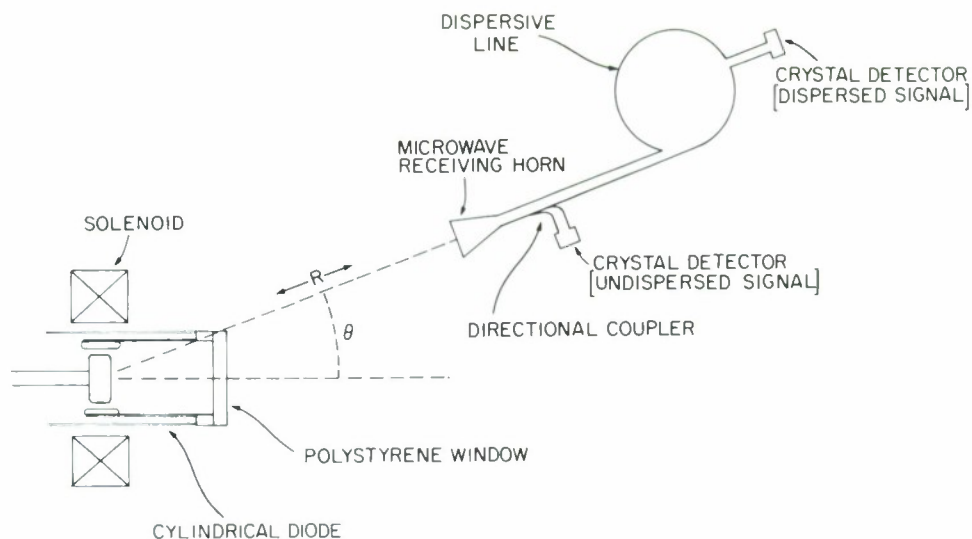


Figure 6. Diagram of the experimental setup used in the study of the microwave emission from the cutoff diode.

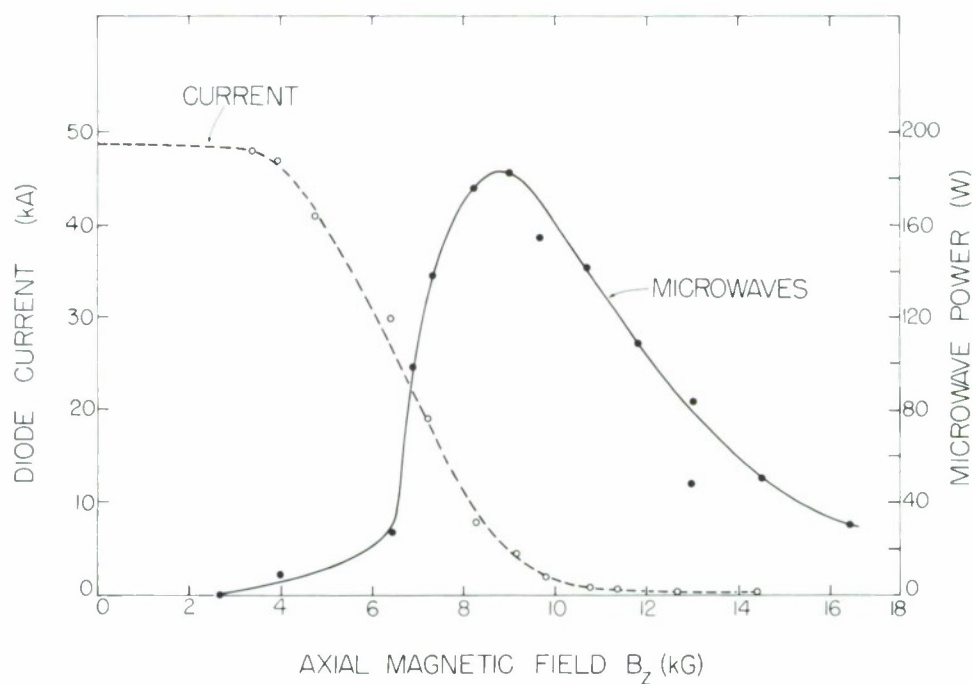


Figure 7. The total microwave power emitted in the X-band frequency range, and the diode current, plotted as a function of the applied axial magnetic field. The microwave emission is the sum total for the two orthogonal polarization of the electric vector.  $d_0 = 3.4$  mm.

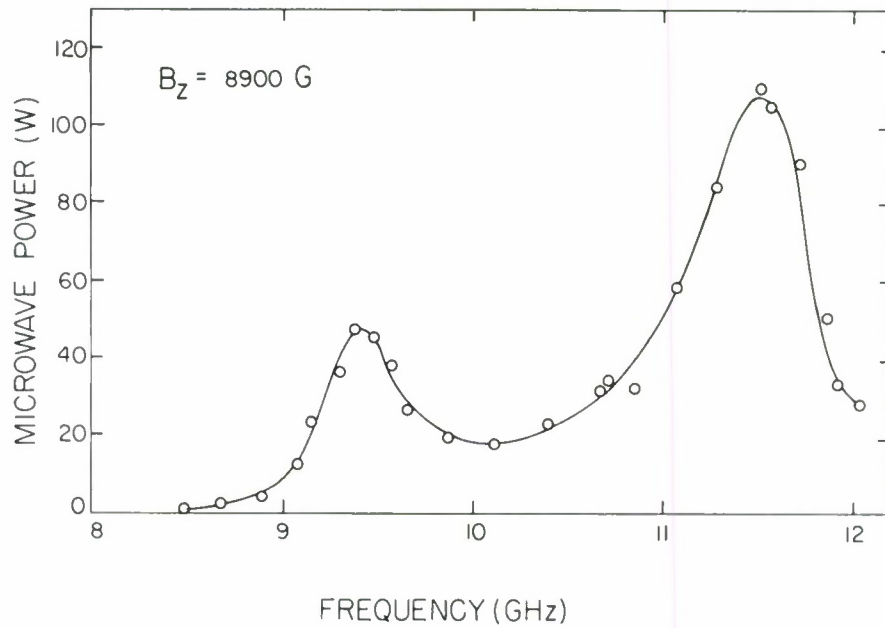


Figure 8. The X-band microwave spectrum observed at a fixed axial magnetic field  $B_z = 8900$  G;  $d_0 = 3.4$  mm. One polarization only.

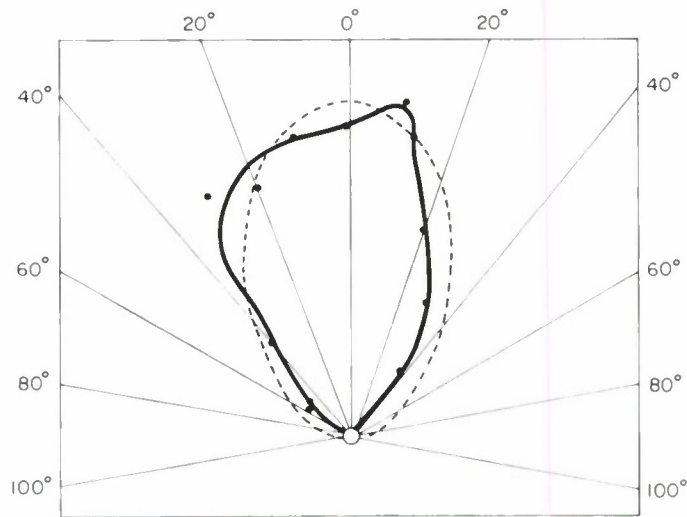


Figure 9. The H-plane radiation pattern of the emitted microwaves (solid points, solid line). The dashed line shown for comparison is the theoretical radiation pattern of an open cylindrical waveguide equal in radius to our vacuum can and excited in the  $TE_{11}$  mode. The emitted power is that integrated over the entire X-band frequency range. The E-plane pattern is similar. The observations suggest that multimode waveguide excitation of the cylindrical vacuum can is taking place, rather than single mode excitation.  $d_0 = 3.4$  mm.

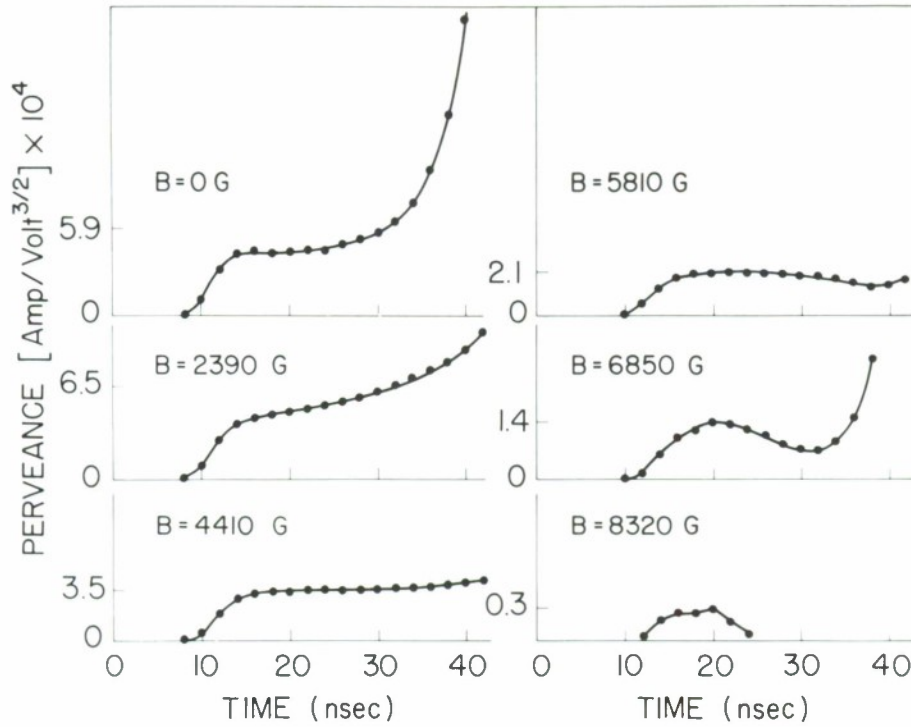


Figure 10. The measured perveance as a function of time, for various transverse magnetic fields applied across the diode  $d_0 = 3.4$  mm. When  $B_z > 6300$  G, the electron current is cut off [see Table II]; in this regime, the meaning of perveance has little physical content.

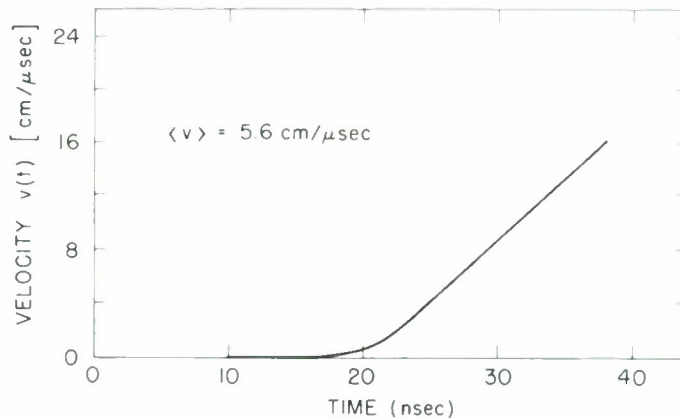


Figure 11. The net velocity of the cathode and anode plasmas for  $B_z = 0$ , as determined from  $P(t)$  of Fig. 10. The plasmas accelerate probably as a result of the ohmic heating  $J_r^2/\sigma$  from the radially flowing current.  $d_0 = 3.4$  mm.

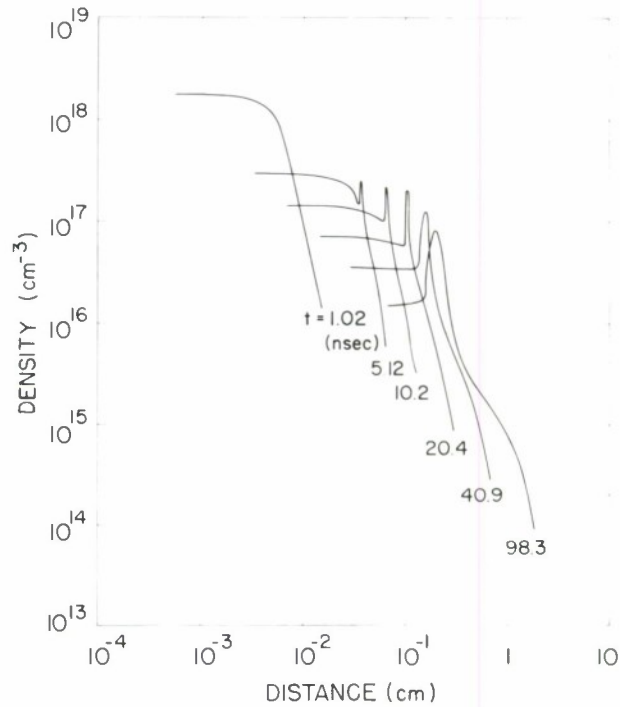


Figure 12. The computed space-time density variation of a fully ionized hydrogen plasma traveling across a uniform magnetic field of 5 kG. The initial density  $N_0 = 10^{19} \text{ cm}^{-3}$  and the initial temperature  $T_0 = 5 \text{ eV}$ .

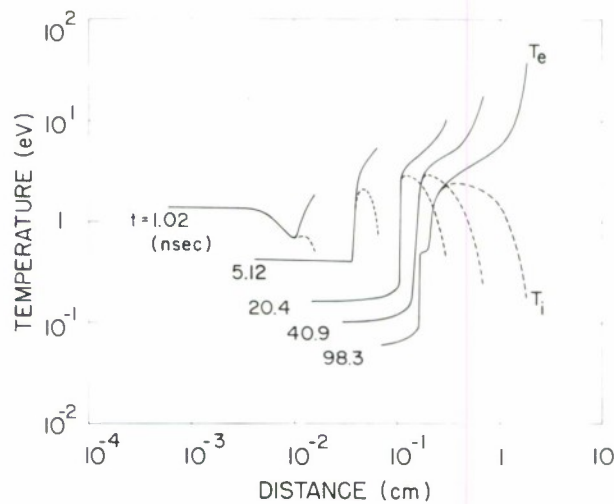


Figure 13. The computed space-time temperature development of the plasma described in the caption to Fig. 12.

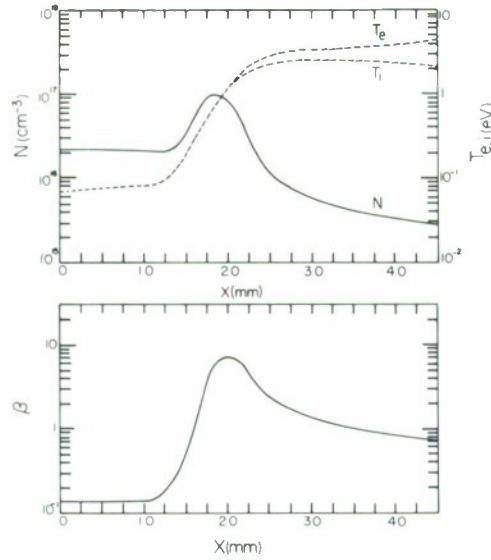


Figure 14. Detail picture of the density and temperature "jumps" across the shock (above); the plasma  $\beta \equiv 2N(\kappa T_e + \kappa T_i)\mu_0/B^2$  across the shock (below). Hydrogen plasma,  $N_0 = 10^{19} \text{ cm}^{-3}$ ,  $T_0 = 5 \text{ eV}$ . Time of observation  $t = 65 \text{ nsec}$ .

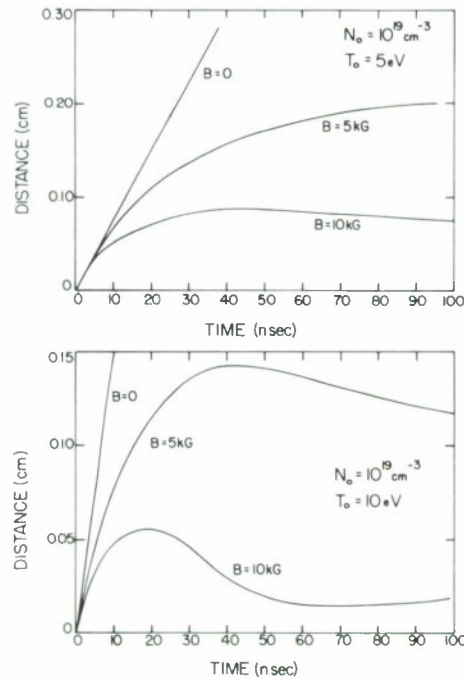


Figure 15. The computed position of the plasma front as a function of time during the first 100 nsec of its expansion. Fully ionized hydrogen plasma with  $N_0 = 10^{19} \text{ cm}^{-3}$ ,  $T_0 = 5 \text{ eV}$  and  $10 \text{ eV}$ . When the slope of the curve is negative, the plasma is moving backwards.



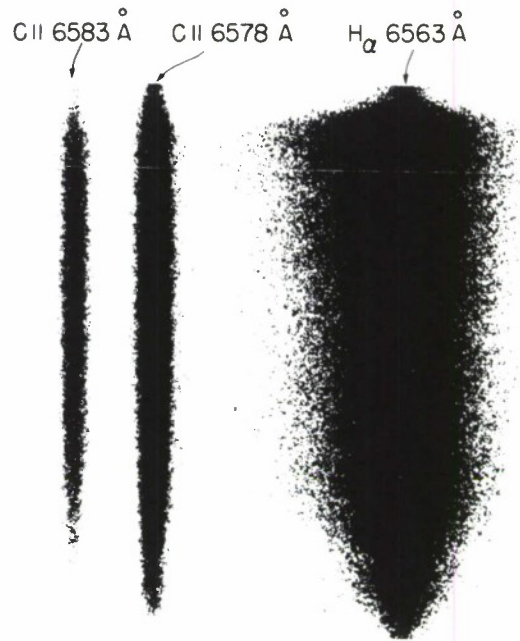


Figure 16. A section of the time integrated optical spectrum from the diode plasma. The lines are Stark broadened.  $d_0 = 3.4$  mm  $B_z = 0$ .

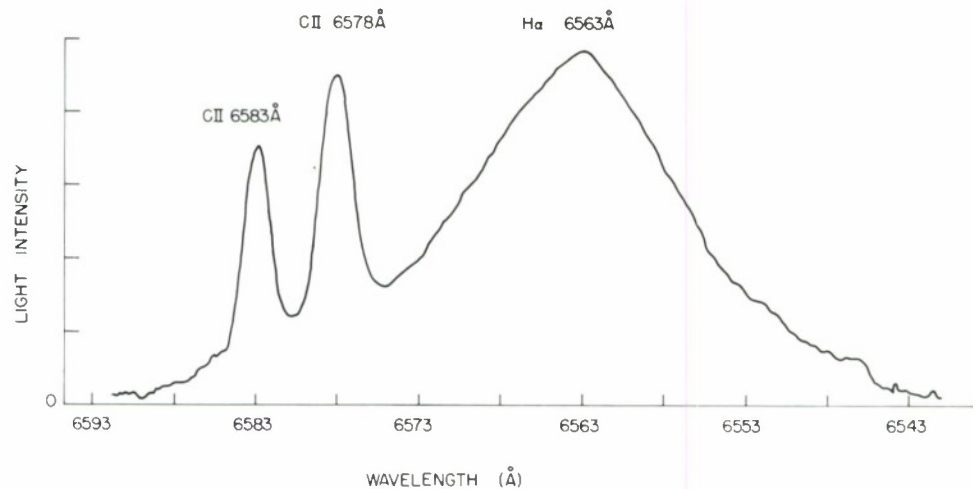


Figure 17. Photodensitometer trace of the spectrum shown in Fig. 16, scanned across that portion of the line which corresponds to the region of the gap situated near the cathode.

## REB FOCUSING IN HIGH ASPECT RATIO DIODES\*

P. Spence, K. Triebes, R. Genuario, and D. Pellinen  
Physics International Company  
San Leandro, California 94577

### ABSTRACT

Typical current-voltage "trajectories" in pinched electron beam diodes have been characterized by a sequence of phases beginning with cathode plasma formation and expansion, a Langmuir-Childs phase, transition to and operation in a focussed beam mode (where the cathode plasma is contained in the  $B_0$  fields and forced back toward the cathode), and a final impedance collapse phase [1]. Recent experiments with tapered hollow cathodes have addressed the transition phase and indicate that formation of an anode plasma is required (in addition to the current exceeding the Friedlander and Jory critical current,  $I_c$ ) before the impedance deviates from a Langmuir-Childs trajectory. Time correlated measurements of beam pinch collapse initiation, proton beam generation, and pinch arrival on axis are given. Once the pinch is formed the impedance is found to be within  $\pm 15$  percent of the saturated parapotential value for the remainder of the driving pulse. Comparison with previous data indicates that a 300 to 450 J/gm dose is required to form the anode plasma (brass and copper anodes) and suggests that  $\approx$  simultaneous achievement of  $I \approx I_c$  and anode plasma formation produces a longer-lived, more stable pinched flow phase.

\*Work supported by Defense Nuclear Agency

## I. INTRODUCTION AND BACKGROUND

Efficient extraction and concentration of energy from low impedance, short pulse, electron beam accelerators is central to their eventual use in heating and compressing pellets. Pinched-beam vacuum diodes, i.e., configurations in which the electron beam is drawn from a relatively large diameter cathode (large radius to gap spacing ratio,  $R/d$ ) and focuses during transit across the anode-cathode gap, have received much experimental and analytical study in recent years. Such diodes have proven to give electron current densities in excess of  $10^6$  A/cm<sup>2</sup> at voltages from 0.5 to 1.0 MV for timescales of tens of nanoseconds. In addition sharpened current risetimes due to the delayed arrival (on axis) of the radially collapsing pinched beam have been observed [2,3].

Figure 1 gives a generalized diode impedance versus time history showing the five distinct phases typical of much of the existing experimental data. Shortly following application of the voltage pulse a cathode plasma is thought to be produced via explosion of whiskers on the cathode surface which coalesce to form a conducting plasma layer over the cathode surface [4,5]. Once formed, the cathode plasma initially expands at an apparently constant velocity across the anode cathode gap and a current

consistent with Langmuir-Childs electron flow (corrected for a time decreasing gap spacing) is drawn by the diode [5-7]. Cathode plasma closure velocities inferred from impedance characteristics of unpinched diodes (including high current cases where pinching is prevented by use of an external axial magnetic field) have been observed at PI to depend on cathode material. Previously unpublished data is given in Figure 2 where cathode plasma closure velocities are seen to range from  $6-8 \times 10^6$  cm/sec for carbon to about  $2.5 \times 10^6$  cm/sec for tungsten. The approximate dependence of closure velocity on the square root of the material vaporization dose suggests that the cathode plasma front may be represented by the high velocity tail of the distribution frozen in at the time of whisker vaporization.

The next phase in the impedance history is one of transition from Langmuir-Childs to pinched beam flow. This transition phase has been the subject of much recent work. Initially the pinched phase was considered to begin when the diode current exceeded the Friedlander and Jory [8] critical value. Blaugrund, et al. [3] have shown experimental evidence that the anode material can also influence the pinch time and pinch collapse velocity. Their suggestion of the importance of an anode plasma layer was also pointed out in particle simulation code calculations by Poukey [9]. More recent analytical work has considered the role of ions drawn

from this anode plasma [10] and has incorporated the existence of ion flow to explain the rapid pinch collapse velocities [11].

Following the transition from Langmuir-Child's impedance and the radial pinch collapse the diode impedance remains relatively stable past the end of the driving pulse or until the time of impedance collapse. Of the two current analytical models describing the pinched phase [1, 12] a wide range of impedance data is consistent with the parapotential value described by Creedon. In cases where the cathode plasma has expanded to partially fill the diode gap before transition to pinch flow, the observed impedance time histories suggest that the plasma is pushed back to the cathode surface and contained by the magnetic fields associated with the pinched flow [13].

The impedance collapse phase is not well understood. The slowly decreasing impedance behavior following the power pulse peak may be simply due to the decreasing beam magnetic field and its inability to continue to contain the diode plasmas. The sometimes evident catastrophic collapse behavior may result from instabilities or jets in the otherwise contained diode plasmas or alternatively an avalanche arc condition where regenerative coupling between ion and electron flow is initiated in a region of high current density.



The experiments discussed in the remainder of this paper were designed to examine in more detail the transition phase from Langmuir-Childs to pinched flow. Section II details the experimental configuration and diagnostic hardware. Results are given in Section III and compared with previous data. Conclusions follow in Section IV.

## II. EXPERIMENTAL SETUP

The experiments were performed on the Pulserad 225W (alias CAMEL) generator which can deliver up to 12 kJ at 1 MV into a matched (5 ohm) load. The power pulse duration is 60 to 65 nsec FWHM. For these experiments the generator was operated into an undermatched (1 to 2 ohm) load, giving diode voltages of 300 to 500 kV and energy output levels of  $\sim 6$  kJ.

Figure 3 is a schematic drawing of the experimental configuration and diagnostics. Tube voltage was directly measured with a resistive monitor and A-K gap voltage was obtained by subtracting the inductive component ( $\propto dI/dt$ ) from the tube voltage on a separate scope. Current monitors (Rogowski coils) used to monitor tube current and current reaching the anode plane indicated that magnetic insulation was sufficient to prevent shank loss. Other diagnostics included (1) an X-ray pinhole camera which recorded

the spatially resolved (0.25 mm resolution), time averaged, electron bremsstrahlung radiation pattern produced by electrons striking the anode plane, (2) an array of collimated PIN diodes which viewed spatially separated  $0.75 \text{ cm}^2$  areas of the anode plane and recorded the time resolved electron bremsstrahlung pattern, (3) a TRW streak camera in a configuration similar to that used by Blangrund [3] to record the radial collapse rate of the hollow annular electron beam, and (4) a Faraday cup with sweeping magnet which could be moved to various positions inside the hollow cathode well and used to record ion current waveforms. A transit-time isolator was used to allow electrical access to the ion diagnostics which were at cathode potential. Anode heating hardware also shown in Figure 3 was available but not used in the initial experiments reported below.

Experiments to date with the above apparatus have utilized a hollow, tapered ( $\sim 5^\circ$  taper), stainless steel cathode with an outer diameter of 10 cm and an inner diameter of 5 cm. Anode-cathode gap spacings of 1.4 to 2.0 mm (at the inner diameter) have been used to give diode aspect ratios ( $R/d$ ) from 12.5 to 17.9. Data were taken for both carbon and brass anodes.

### III. RESULTS AND DISCUSSION

A typical set of output waveforms is given in Figure 4, in this case for a brass anode shot at 2.0 mm A-K gap. Time phasing of the various diagnostic outputs was accomplished by use of fiducial markers superimposed on each trace which reduced the phasing uncertainty to at most 2 to 3 nsec. The TRW streak camera record is shown in Figure 5 and time phased with respect to the current waveform to within a  $\pm 5$  nsec uncertainty in relative phasing.

Cathode plasma formation leading to onset of diode current is seen to require about 10 to 15 nsec after which time the current rises sharply. The on-axis collimated PIN diode and streak camera photograph both record the arrival of the pinch on axis at about 25 nsec following the start of current flow. The ion collector cup placed at a distance of 25 cm from the anode plane recorded an ion pulse arrival time consistent with the ions being protons from the anode plane generated within  $\pm 5$  nsec of pinch arrival on-axis and having a voltage of 400 kV, the diode voltage at that time. (Experiments will be continued to confirm the existence of protons and to calibrate the ion current cup using a nuclear activation technique.)

The time averaged FWHM beam diameter was 5 to 6 mm as determined from the X-ray pinhole photos and the final sweep-in velocity approached 4 to 5 mm/nsec. Similar data was also collected for carbon anodes where FWHM beam diameters of 2 to 3 mm were typical and the final sweep-in velocities were 2 to 3 mm/nsec. The collimated PIN diode data was used in conjunction with the SANDYL code (which calculates the electron bremsstrahlung generation and transport through the anode) to estimate peak current densities in excess of  $10^6$  A/cm<sup>2</sup>.

A better view of the time evolution of the diode impedance phases is given for the brass anode data in Figure 6 where the I vs V "trajectory" is given. The data points, plotted at 5 nsec time intervals, clearly show the ~ 10 to 15 nsec cathode plasma turn-on phase followed by (1) a ~ 7 nsec long Langmuir-Childs law impedance phase, (2) a 10 to 15 nsec long pinch collapse phase in which the impedance follows the parapotential value, (3) a stable impedance phase (falling within  $\pm 15$  percent of the parapotential value) continuing for about 55 nsec, and (4) a slow transition to zero impedance over a final 20 to 25 nsec time period.

In Figure 7 this behavior is compared to the I-V trajectory typical of past data on the OWL II generator [14] for a hollow tapered steel cathode and copper anode. In this case the beam

was observed to pinch to  $\sim 1$  cm FWHM and the pinched phase ended abruptly by impedance collapse 80 to 90 nsec after current turn-on. The data points, plotted here at 10 nsec intervals show (1) a  $\sim 10$  nsec cathode plasma formation phase, (2) a  $\sim 37$  nsec long trajectory along a Langmuir-Childs impedance path. (Note that the Langmuir-Childs line superimposed on the data was not corrected for cathode plasma motion. A plasma front expansion of  $\sim 1$  mm would be expected after  $\sim 30$  nsec giving  $\sim 20$  percent more current than the uncorrected Langmuir-Childs line, in better agreement with the data), (3) a 5 to 10 nsec long pinch collapse phase in which the trajectory starts to approach the parapotential line, (4) a 40 to 45 nsec long pinched beam phase where the current continues to approach the parapotential line, and (5) a sudden  $\lesssim 10$  nsec transition to zero impedance. The relatively stable pinched phase appears to be shorter in duration than the recent (Figure 6) data despite the over threefold difference in A-K gap. In addition the current appears to follow a Langmuir-Childs trajectory well above both the critical current and parapotential flow limits.

The observation of ions time correlated with the pinch formation process in the present experiments suggests that formation of an anode plasma is a necessary step before the impedance can begin to deviate from the Langmuir-Childs trajectory.



Estimates of the dose delivered to the anode during the LC phase are made below:

$$\text{Dose} = \int_0^t V(t)J(t)\eta \, dt \quad (1)$$

where  $J(t)$  is assumed to be the Langmuir-Childs current density  $[2.34 \times 10^3/d^2 V_{MV}^{3/2} \text{ A/cm}^2]$  and  $\eta$  is the dose/fluence coupling coefficient which can be approximated in the voltage range 100 kV to 1 MV by

$$\eta = \frac{4 \text{ to } 5}{V_{MV}^{3/2}} \text{ (cm}^2/\text{gm)} \quad (2)$$

Equations (1) and (2) give:

$$\text{Anode Dose (t)} = (9 \text{ to } 12 \times 10^9) \int_0^t \frac{V_{MV}}{d^2} \, dt \text{ (J/gm)} \quad (3)$$

$$0.1 \leq V \leq 1.0 \text{ MV}$$

This approximation yields nearly equal anode dose levels at the end of the Langmuir-Childs impedance phase of 300 to 400 J/gm and 350 to 450 J/gm for the Pulserad 225W and OWL shots, respectively which suggests that dose levels of 300 to 450 J/gm are required to produce anode plasma in the case of initially unheated brass and copper anodes. Similar analysis of the carbon anode

data indicates 450 to 650 J/gm required before departure from Langmuir-Childs impedance.

Thus the initiation of the transition phase apparently requires not only current in excess of the critical current but anode dose levels of 300 to 450 J/gm (in brass or copper) to give sufficient anode plasma.

Although no analytical solutions describing electron flow dynamics during the transition phase presently exist, the data presented here suggest that the impedance tends toward the parapotential flow model prediction as the pinch begins to arrive on axis. Comparison of the OWL and Pulserad 225W shots suggests in addition that longer impedance lifetime, stable pinched flow may be associated with a smooth transition into parapotential flow (i.e., production of anode plasma near the time that the LC trajectory approaches the parapotential one) as opposed to a transition which begins when the current is already considerably above either  $I_c$  or  $I_p$ .

If this hypothesis is true, its implications can be summarized by use of the following simple example: assuming a planar hollow cathode geometry where the degree of hollowness is represented by a filling factor,  $f$ , equal to the cathode emission

area  $\pi(R_{\text{outer}}^2 - R_{\text{inner}}^2)$  divided by  $\pi R_{\text{outer}}^2$ , one can write the following expression for the ratio of the critical current to the Langmuir-Childs current:

$$\frac{I_{\text{LC}}}{I_{\text{C}}} \approx f (R/d)^{0.35} V_{\text{MV}}, \quad 0.1 \leq V \leq 1.0 \quad (4)$$

If we also assume (a) minimal expansion of cathode plasma during the Langmuir-Childs phase [i.e.,  $u \cdot \tau \leq d/10$ , where  $u$  = cathode plasma closure velocity  $\approx 3 \times 10^6$  cm/sec for steel and  $\tau$  = time until formation of anode plasma], (b) a 300 J/gm critical dose for anode plasma formation, (c) a desired ratio of  $I_{\text{LC}}/I_{\text{C}} = 1.5$  at  $t = \tau$ , and (d) a linearly rising voltage waveform in Eq. (3): then Equations (3) and (4) reduce to

$$f (R/d) \cdot d \lesssim 2.5 \quad (5)$$

The implications of Eq. (5) can be summarized as follows: as pinched flow diodes are scaled to either lower impedance levels (i.e., larger  $R/d$ ) or to higher voltages (where  $d$  must generally be larger due to higher prepulse), a decreased filling factor,  $f$ , will be required to preserve approximate simultaneity in anode plasma production) when the current crosses  $I_{\text{C}}$ . The relevance of this simultaneity to pinch stability and the formation of anode plasma by means other than electron beam heating will be addressed in future experiments.

#### IV. CONCLUSIONS

The experiments reported here with tapered hollow cathodes have shown, as in the past [1, 15, 16], a general agreement with--or tendency to approach--the saturated parapotential current levels as formulated by Creedon [1]

$$I_p = \left(\frac{R}{d}\right) 8500 \gamma \ln [\gamma + (\gamma^2 - 1)^{\frac{1}{2}}] \quad (6)$$

during the pinched flow phase. Ions contribute an as yet unquantified portion of the measured total diode current.

The transition phase from Langmuir-Childs parapotential appears to be the most critical one. Transition onset requires  $I > I_c$  and delivery of  $\gtrsim 300$  to 450 J/gm to brass and copper anodes and present results suggest more stable, longer lifetime pinched flow when the two conditions are met near the same point in time. Critical dose levels of 450 to 650 J/gm have been inferred for carbon anodes.

The authors would like to acknowledge the contributions of John Creedon and Ian Smith, who participated in numerous helpful discussions, Kendall Childers who helped develop the cathode plasma expansion velocity analysis, Norm Albright who ran the SANDYL calculations, and John Kishi who assisted with the design and fabrication of the recent experimental hardware.

## REFERENCES

1. J. Creedon, J. Appl. Phys. 46, 2946 (1975).
2. B. Ecker, PIIR-13-72, Physics International Company, San Leandro, CA. (1972).
3. A. E. Blaugrund and G. Cooperstein, Phys. Rev. Letters 34, 461 (1975).
4. G. Mesyats, et al., Proc. 4th Int. Sym. on Insulation of High Voltages in Vacuum, University of Waterloo, Ontario, Canada (1970).
5. R. Parker, et al., J. Appl. Phys. 45, 2463 (1974).
6. P. Flynn, Proc. Phys. Soc. London B69, 748 (1956).
7. G. Loda and P. Spence, Bull. Am. Phys. Soc. 15, 1401 (1970).
8. F. Friedlander, et al., Varian Report No. DASA 2173 (1968).
9. J. Poukey, J. Vac. Sci. Technol. 10, 954 (1973).
10. J. Poukey, Proceedings of 13th Symposium for Electron, Ion, and Photon Technology, Colorado Springs, Colorado (1975), to be published.
11. S. Goldstein and R. Lee, Phys. Rev. Letters 35, 1079 (1975).
12. S. Goldstein, et al., Phys. Rev. Letters 33, 1471 (1974).
13. J. Creedon, et al., Bull. Amer. Phys. Soc. 18, 1310 (1973).
14. G. Frazier, Proceedings of 13th Symposium for Electron, Ion, and Photon Technology, Colorado Springs, Colorado (1975), to be published.
15. B. Ecker, et al., Record of 11th Symposium on Electron, Ion, and Laser Beam Technology, R. F. M. Thornley, editor, San Francisco Press, San Francisco, CA (1971), p. 433.
16. M. Di Capua, et al., (to be published).

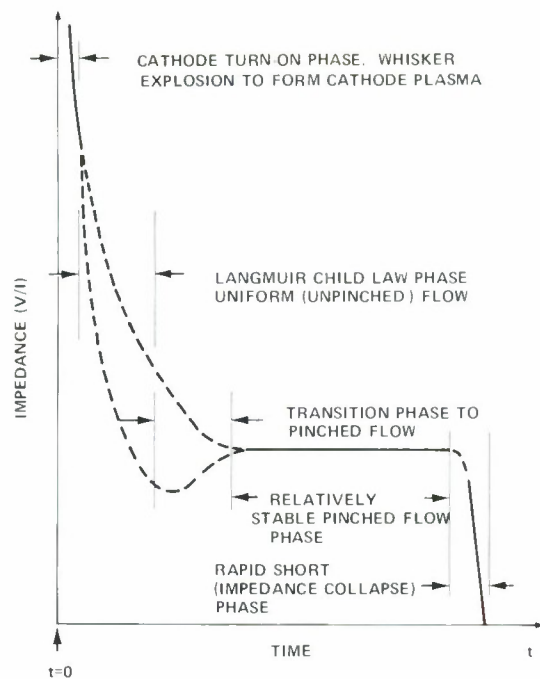


Figure 1. Generalized Diode Impedance Characteristics Focused Beam Mode

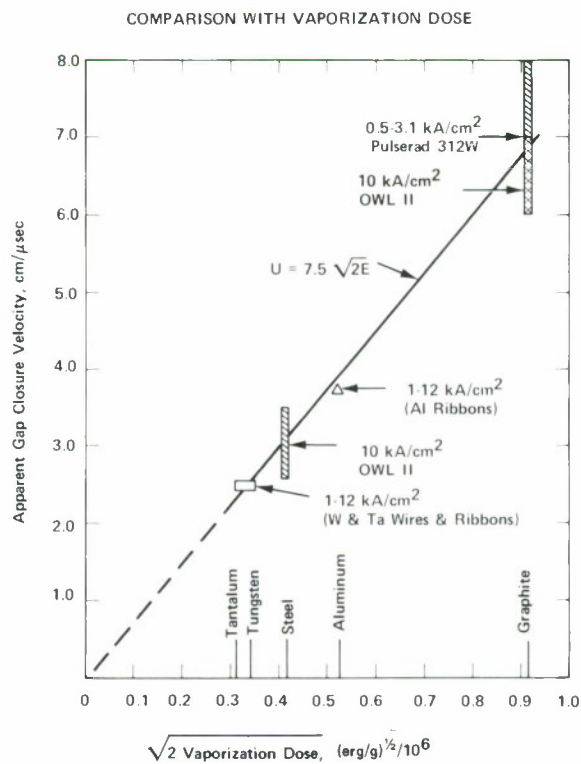


Figure 2. Gap Closure in Langmuir-Childs (unpinched) Diodes



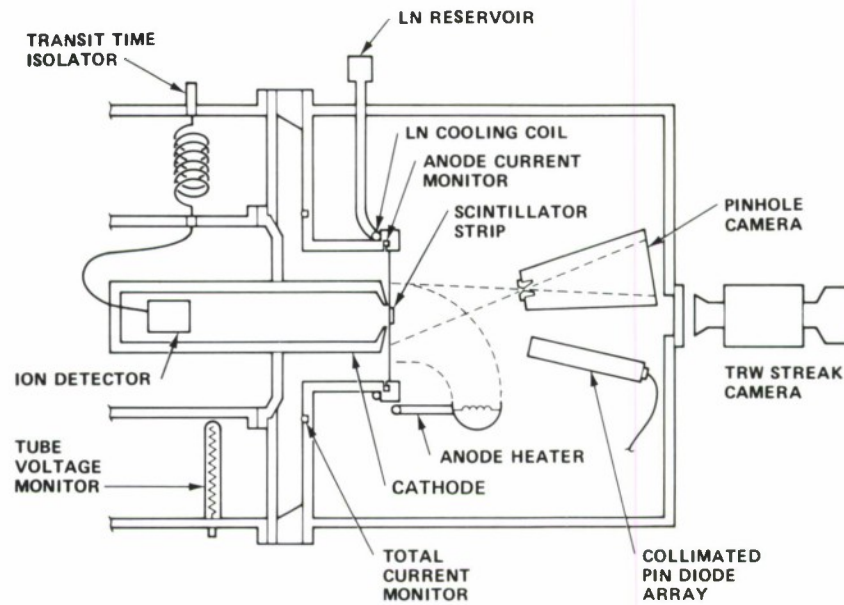


Figure 3. Experimental Setup

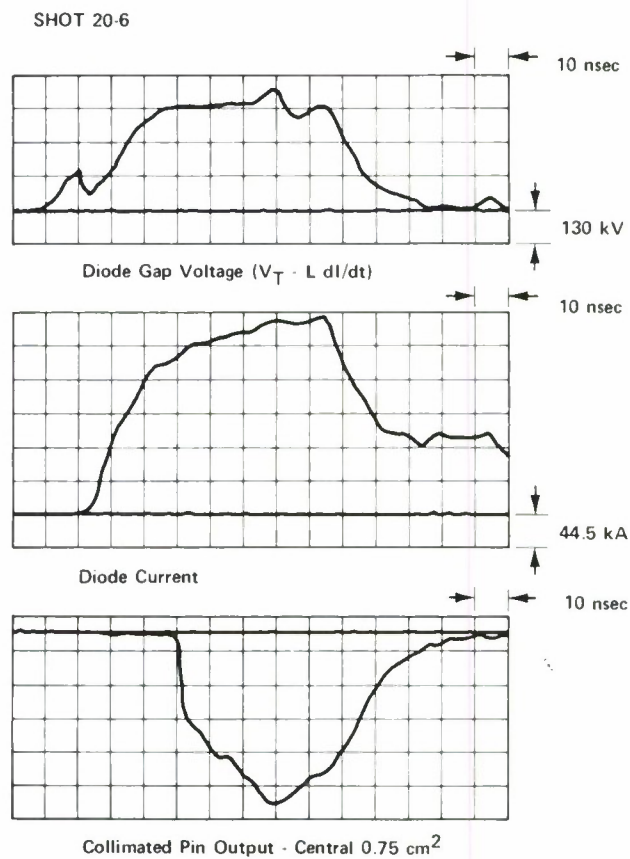


Figure 4. Diode Diagnostic Waveforms

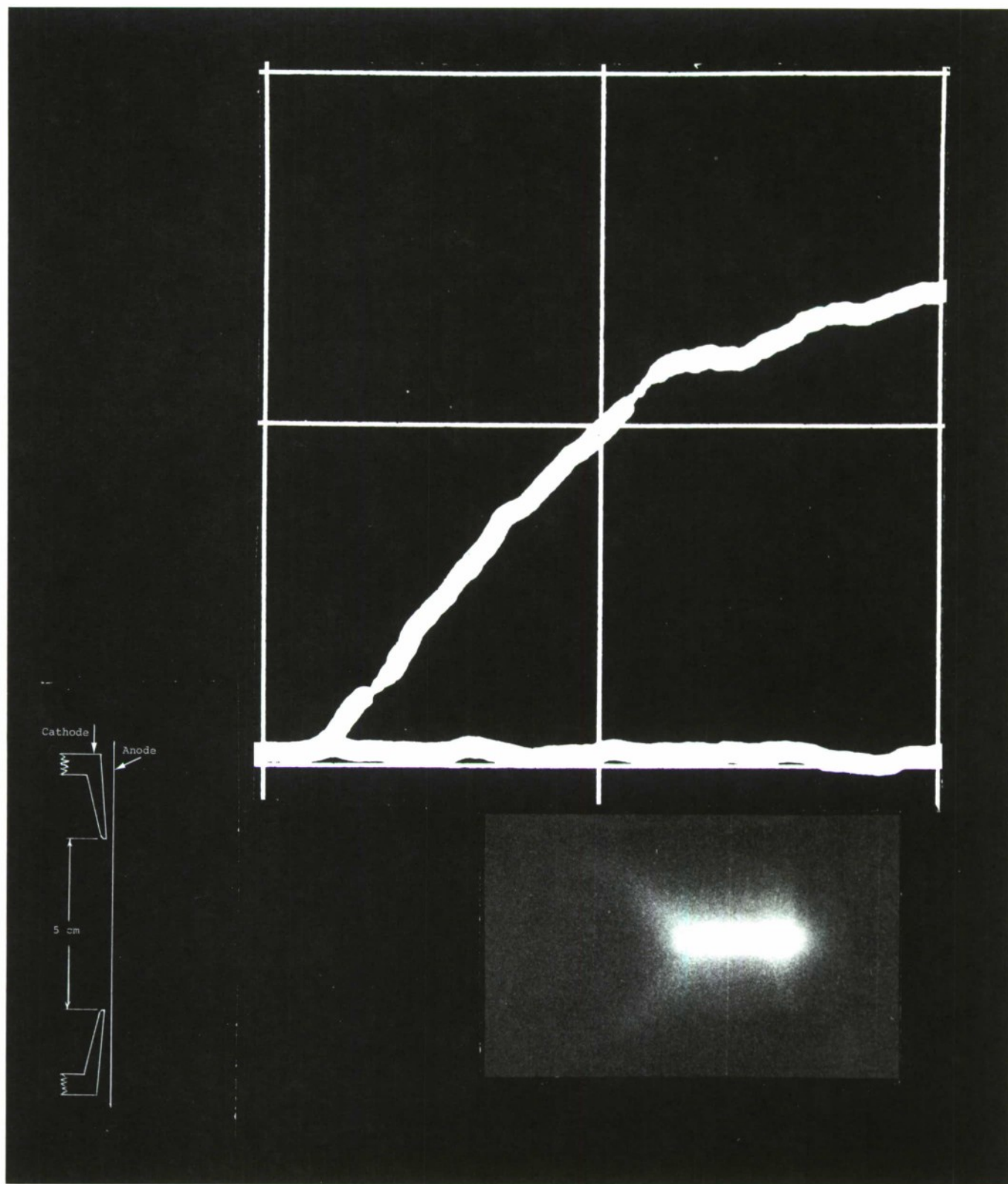


Figure 5. Diode Current and Streak Records, 20 nsec/div.

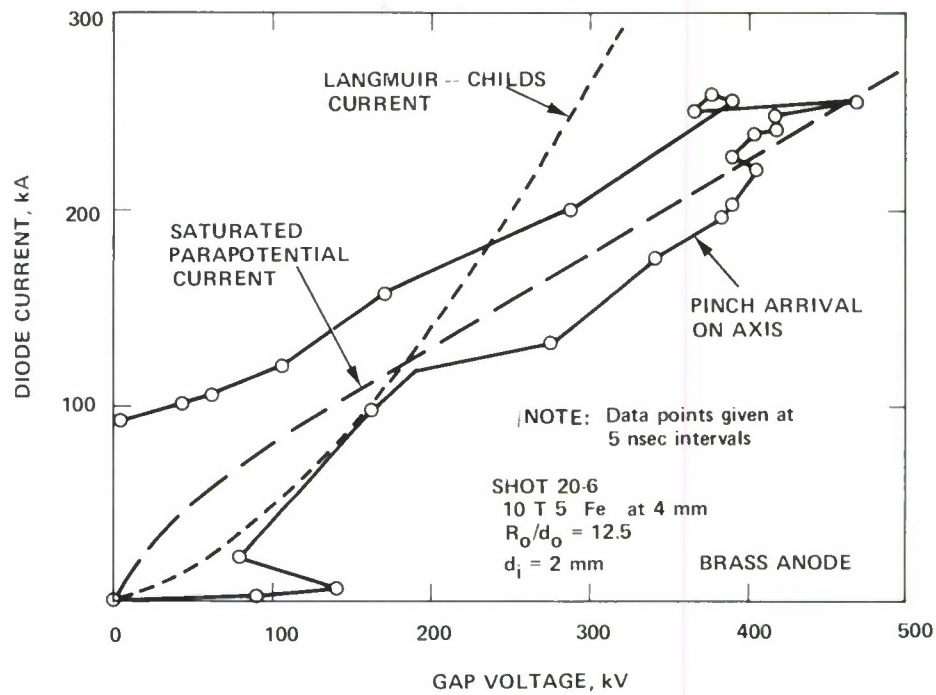


Figure 6. Diode Current-Voltage Trajectory

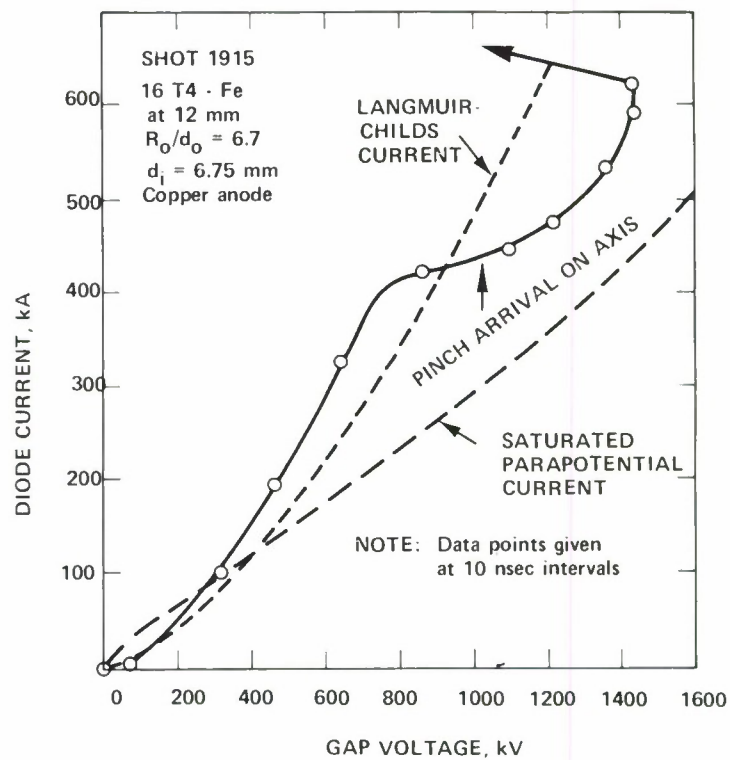


Figure 7. Diode Current-Voltage Trajectory

## DIODE BEHAVIOR FOR A 1.7 MICROSECOND GENERATOR

C. Stallings, R. Schneider and D. Cummings  
Physics International Company  
San Leandro, California 94577

### ABSTRACT

The Pulserad 1140 (a 4 MeV, 45 nsec, 35 ohm generator) was converted to a 2 MeV, 1.7  $\mu$ sec, 80 ohm machine by replacing the Blumlein with a lumped element pulse forming network. This generator was used to study diode behavior for microsecond pulses. Typical waveforms will be presented. The diode closure with a foil anode can be interpreted as a moving plasma front that reduced the anode cathode spacing. Experiments have been carried out to determine this closure velocity as a function of magnetic field and cathode material. The impedance as a function of time and magnetic field are also presented for a foilless diode.

Several potential applications of intense electron beams such as long solenoid fusion reactors [1] and laser stimulation [2] require large total energy input but do not require the high power levels normally associated with the present 50-100 nsec generators. For many applications energy can be delivered over times greater than 1  $\mu$ sec thereby decreasing beam current to a  $v/\gamma$  less than 1 [3]. These longer pulses are also more efficient in the transfer of energy from the Marx generator to the beam. The major technical problems inherent in this approach are associated with the impedance lifetime of the diode.

To study the diode behavior for a 1.7  $\mu$ sec diode, the Pulserad 1140 machine at Physics International Company was converted from a 4 MeV, 45 nsec, 35 ohm generator to a 2 MeV, 1.7  $\mu$ sec, 80 ohm machine. This change was accomplished by replacing the inner conductors of the oil Blumlein with a lumped element pulse forming network (shown schematically in Figure 1) of similar size. Figure 2 shows how this PFN fits inside the machine. This technique allows the machine to be used in either mode with minimal conversion time.

Typical diode waveforms are shown in Figure 3. The beam current is measured at the anode with a combination calorimeter-Faraday cup. The voltage risetime is approximately 100 nsec

with a roughly comparable current risetime. The voltage full width at half maximum is 1.2  $\mu$ sec for this shot which is somewhat shorter than the 1.7  $\mu$ sec full width into a matched load. This is due to the time dependent impedance which decreases with time (Figure 4). The impedance was typically very erratic for the first 400 to 500 nsec and then settled down to a smooth decay. This rapidly, time-varying impedance at early times is not well understood but is present on most shots.

The theoretical maximum transfer of Marx energy to beam energy is 96 percent between the half maxima points of voltage. In practice, only 40 to 60 percent of the Marx energy was in the beam. Part of this loss can be attributed to the time-varying impedance which only matches the generator on the average: most of the loss is due to a loss of current from the cathode stalk rather than an inherent electrical inefficiency in the system. The anode current monitor typically measured 50 percent of the current measured by a monitor 50 cm before the anode. The large "shank current" occurred even though the electric field on the shank was always less than 160 kV/cm. This electric field is a reasonable design value for 100 nsec pulses but large shank currents were obtained in these experiments with electric fields as small as 70 kV/cm.

The cathodes were machined as a series of sharp pyramids, 1 cm on a side at the base. These were then mounted on cathode



stalks in a cylindrical geometry (Figure 5). The cathode material and diameter could be changed to study the diode behavior.

To understand the diode behavior, it was necessary to determine if any of the current entering the anode current monitor was due to shank current. Calorimeter maps of beam fluence showed a beam that was consistently the cathode radius plus one electron gyroradius in the applied magnetic field. Even when the cathode stalk was larger than the emitting cathode (Figure 5) and the applied magnetic field was strong enough to stop beam pinching (if any), no beam fluence was detected outside the cathode radius plus one gyroradius. In addition, a polyethylene witness plate was placed around the small shank immediately behind the cathode. This witness did not show any evidence of damage. These two experiments imply a shank current approximately equal to the cathode current that does not flow across the anode-cathode gap. This result is probably due to the applied magnetic field. The field is uniform within  $\pm 10$  percent in the anode-cathode gap but it diverges back from the cathode surface. The diode current is approximately half the current needed for magnetic insulation. This means that any shank current must enter a converging magnetic field to reach the cathode. A more favorable path for the shank current is across the spacing between the cathode shank and the outer ground cylinder; therefore, it appears that the shank current did not influence current flow in the anode-cathode gap.

The anode-cathode spacing  $d$  and the magnetic field  $B$  were varied to develop a semi-empirical formula for diode impedance (Figure 6) [4]. To generate this formula the diode impedance was measured early in time before plasma motion became important.

$$Z = \frac{117d^2V}{\left\{ r_o + \frac{(V + 2mc^2V)^{\frac{1}{2}}}{CB} + \alpha d \right\}^2 \left\{ \left( \frac{V}{mc^2} + 1 \right)^{\frac{1}{2}} - 0.8471 \right\}^2}$$

This expression is simply the relativistic Child's law impedance [5] with a modification to the beam radius to account for the larger beam due to a large aspect ratio and electron gyration in the magnetic field. It was assumed that the self magnetic field is small compared to the applied field and that the electron gyroradius can be approximated by  $(V+2mc^2V)/CB^{\frac{1}{2}}$ . This implies that the electron velocity vector has a large angle with respect to the applied magnetic field. The experimentally determined constant  $\alpha$  is related to the diode aspect ratio. Note that when  $\alpha d$  is small compared to the beam radius plus a gyroradius, this semi-empirical formula has a simple  $Z$  proportional to  $d^2$  dependence similar to Child's law. When the cathode radius is large compared to both the electron gyroradius and the anode-cathode spacing this expression reduces to the relativistic Child's law.

After current flow is initiated a plasma forms at the cathode and anode. This plasma expands and this effectively closes the anode cathode spacing causing the diode impedance

to decrease with time. This decrease in impedance can be characterized by using  $d = d_0 - vt$  in the expression for impedance where  $d_0$  is the initial anode-cathode spacing and  $v$  is a velocity of plasma expansion. This velocity of expansion is the core of the problem in building longer pulse diodes. To efficiently transfer energy the diode impedance should not vary more than a factor of 3 or 4 during the pulse and should approximately match the generator impedance.

A study was made of the impedance time history for several cathode materials and two magnetic fields. The data were analyzed by assuming an impedance that was proportional to  $d^2$  (for the anode cathode spacings used the semiempirical model mentioned above and Child's law flow both have this dependence). This analysis typically gave a linear relationship between  $d$  and  $t$  from 500 nsec to 2000 nsec. The slope of this line was taken to be the characteristic diode closure velocity for that shot. Figure 7 is a plot of these velocities for several materials and two magnetic fields using an ATJ graphite anode. These data show a trend of higher closure velocities (faster impedance collapse) for higher  $Z$  anodes. The trend is rather gentle and data scatter is large but nevertheless it is clear that lower  $Z$  cathodes on the average had a longer impedance lifetime and therefore are superior for the long pulse diode.

An additional study used a foilless diode shown in Figure 8 to investigate the feasibility of this type of diode for these pulse length and total beam energies [6, 7]. The peak magnetic field was approximately at the calorimeter with field lines parallel to the cathode surface. Two monitors were used, one current monitor 50 cm from the end of the cathode and a calorimeter 20 cm past the end of the cathode. The calorimeter typically read 50 to 60 percent of the  $\int IV dt$  measured upstream with an applied magnetic field of 6 to 7 kG. This implies that 40 to 50 percent of the current flows from the cathode or cathode stalk across to the outer coaxial cylinder.

A typical impedance time history is shown in Figure 9. This impedance is well behaved and does not collapse until after the generator voltage has fallen well below half maximum. However, the impedance is too low to efficiently transfer energy from the Marx to the beam. To get maximum energy transfer the average impedance should have been approximately 80 ohms.

The actual energy delivered to the calorimeter was a function of the applied magnetic field (Figure 10). Less than 200 calories were delivered below 3 kG while a maximum of 1600 to 2000 calories were delivered for the two fields tested at 6 and 7.4 kG.

In conclusion two types of diodes have been tested on a 1.7  $\mu$ sec generator with 120 kJ of energy stored in the Marx. In the normal diode with an anode foil collapse velocities of 2.5 to 5.5 cm/ $\mu$ sec have been measured. There is a suggestion that this collapse velocity depends on cathode material but the scatter from shot to shot is less than the variation between materials. A foilless diode has been successfully used but its impedance is too low to efficiently extract energy from this machine.

## REFERENCES

1. James Benford, *Laser Focus II*, 45 (July 1975).
2. R. Aprahamian, J. H. S. Wang, J. A. Betts, and R. W. Barth, *Appl. Phys. Letters* 24, 239 (1974).
3. J. D. Lawson, *Part. Accel.* 1, 41 (1970).
4. R. Schneider, C. Stallings and D. Cummings, *J. Vac. Sci. Technol.* 12, 6, Nov./Dec. (1975).
5. F. Friedlander, R. Hechtel, H. Jory and C. Mosher, *DASA 2173*, Varian ASSociates (1968).
6. M. Friedman and M. Ury, *Rev. Sci. Instr.* 41, 1334 (1970).
7. M. Friedman and M. Ury, *Rev. Sci. Instr.* 43, 1659 (1972).



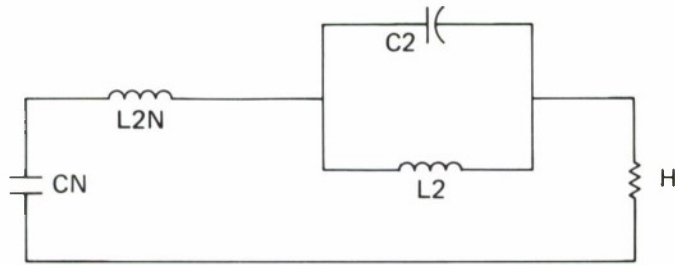


Figure 1. Circuit Diagram for the Long Pulse Generator

Figure 2. The Pulse Forming Network Replacing the Blumlein

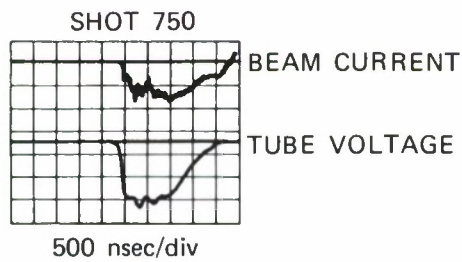
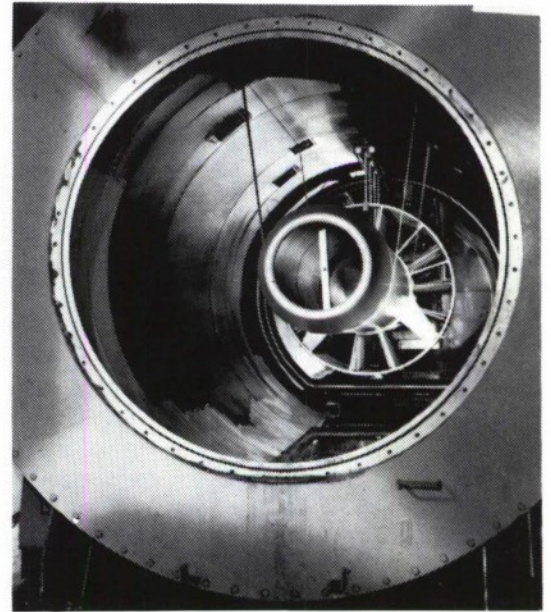
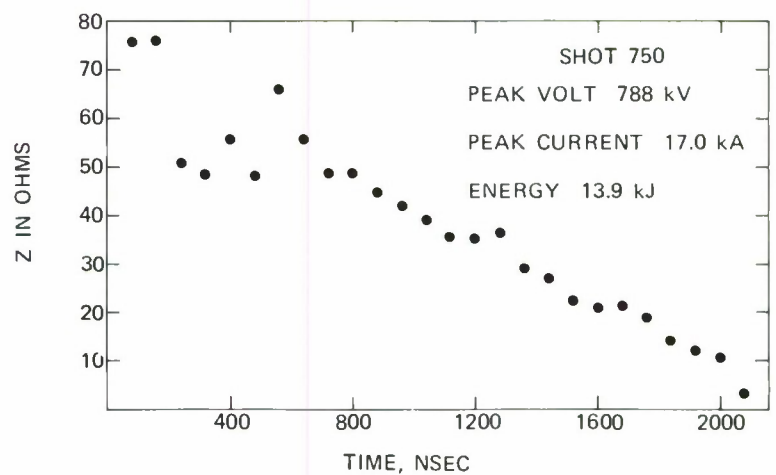


Figure 3. Typical Diode Waveforms

Figure 4. Typical Diode Impedance Versus Time



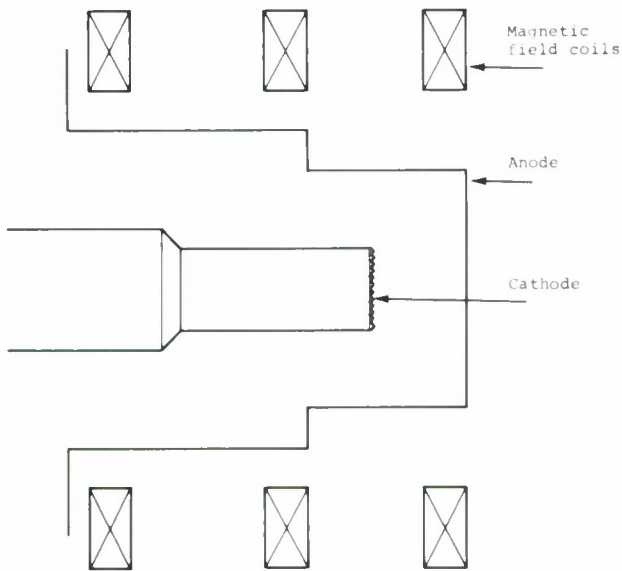


Figure 5. Schematic Diagram of the Experiment of Diode Closure Velocity

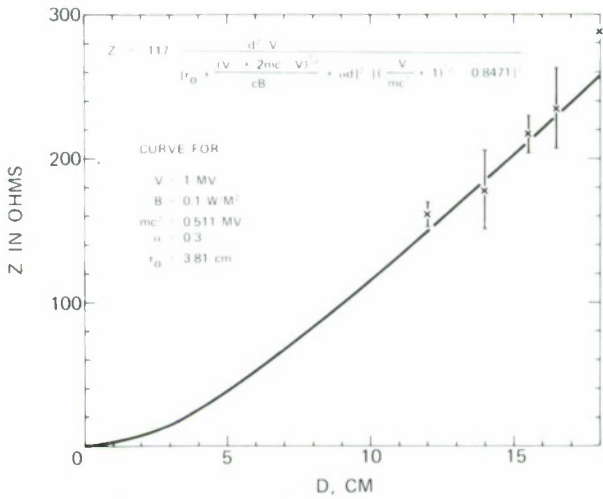


Figure 6. Impedance as a Function of Anode-Cathode Spacing. The solid line is the semi-empirical model.

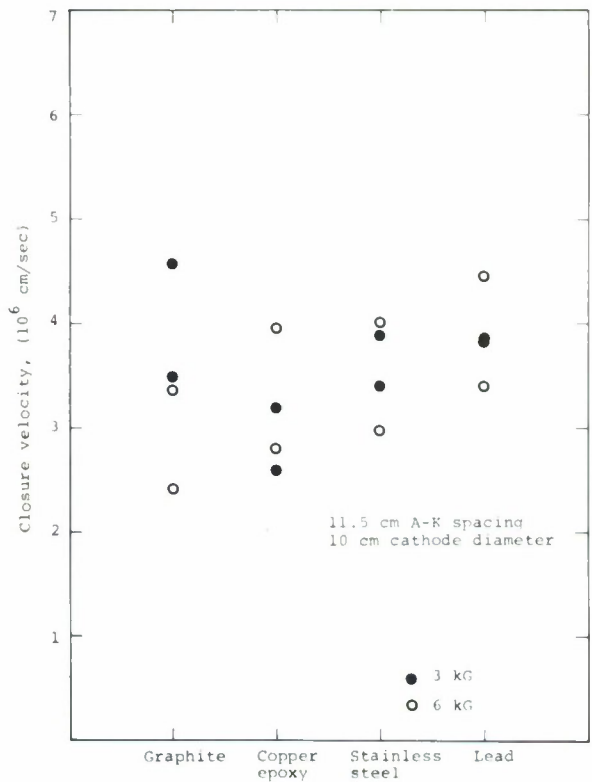


Figure 7. Diode Closure Velocity for Four Materials and Two Magnetic Fields

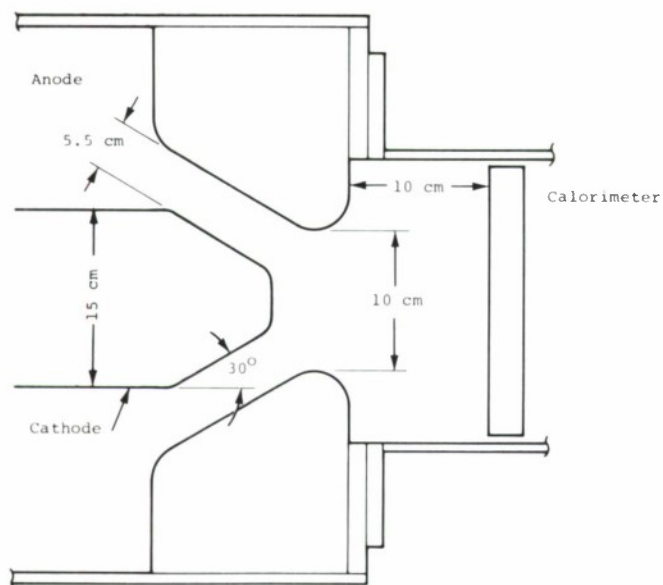


Figure 8. Schematic Diagram of the Foilless Diode

Figure 9. Typical Impedance Time History for the Foilless Diode

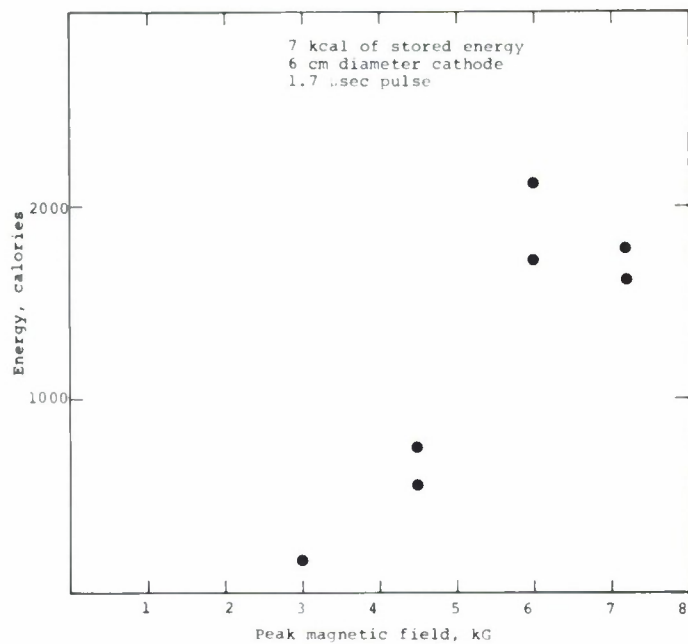
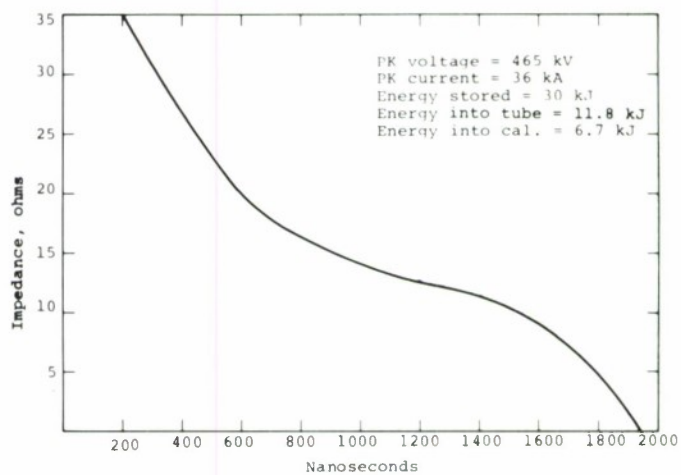


Figure 10. Energy Delivered to a Calorimeter by the Foilless Diode

## ELECTRON BEAM PROPAGATION AND FOCUSING

Keith A. Brueckner

Department of Physics, University of California, San Diego  
La Jolla, California 92093

### ABSTRACT

Energy transfer by a relativistic electron beam is restricted by the interaction of the electrons with the magnetic fields produced by the total beam and plasma current. In the absence of plasma current, various proposed configurations of current have an effective limit for energy carried by the electrons approximately equal to the conventional Alfven limit. This restriction appears to prevent establishment of energy transport sufficient for fusion application.

If plasma currents are included, the total current may lie within the Alfven limit. Analytic models have been developed which predict the rate of radial collapse of the beam current, which is very slow if classical plasma conductivity is assumed. The beam is initially very unstable against breakup into fine current filaments and, as pinching occurs, to other unstable modes of development of transverse structure. Those affect overall current concentration and focusing.

## I. INTRODUCTION

The formation of very high current electron beams for fusion-pellet implosions is of considerable present interest. The conditions for producing a fusion reaction are analyzed in order-of-magnitude in Section II. The beam may produce large transient plasma currents which neutralize the beam current and allow beam currents in excess of the Alfvén limiting current. The beam contraction is then determined by the decay of the plasma currents. The nature of this transient behavior is analyzed in Section III. In the absence of plasma currents but with charge neutrality assumed, a high current beam can be formed using a configuration proposed by Yoshikawa.<sup>1</sup> His analysis is summarized in Section IV and some comments given. A theory of superpinched relativistic beams, as given by Poukey and Toepfer<sup>2</sup> of Sandia Laboratories, is summarized in Section V. Their analysis shows a strong pinch occurring in a charge-neutralized beam. The pressure balance is, however, maintained at the pinch maximum by very strong beam heating, reducing or eliminating the feasibility of the beam for fusion pellet heating. A proposal by Hammer and Rostoker<sup>3</sup> is summarized in Section VI. Their analysis shows that an arbitrary current can be carried in a very thin current sheet in which electrons are reflected, moving with  $v_z \approx 0$  in the rest of the beam. This configuration is highly singular; the problems of beam formations and stability have not been considered.

In the proposals by Yoshikawa and Poukey and Toepfer, the magnetic energy is very large compared with the energy in the

internal and directed energy of the beam. This presents severe problems for efficient coupling to a fusion pellet. The problem is reviewed in Section IV.

Some concluding remarks are given in Section VII.



## II. SCALING LAWS

The deposition of energy in a dense shell is efficient if the electron range for nuclear scattering is less than the shell thickness. If this condition is satisfied, the penetration of the shell can be kept small, and direct heating of the contained thermonuclear fuel reduced or eliminated. The beam will still not be fully coupled to the shell which will have a finite albedo for reflecting the beam. The beam electrons rapidly lose energy by collisions with the electrons of the material, with a corresponding rapid decrease in their range for nuclear scattering. Consequently the albedo is low; a quantitative determination of the coupling efficiency requires solution of the transport and diffusion problem for the beam electrons. In the following estimate we neglect the back scattering and penetration of the beam.

The mass per unit area of the shell which is finally imploded after the ablation process is complete must be approximately

$$\begin{aligned}\Delta m &= \rho_0 \lambda_s(\mathcal{E}) \\ &= \frac{Am_1}{Z^2 \sigma_{\text{coul}}(\mathcal{E})} \\ &\cong 5.5 \frac{A}{Z^2} \mathcal{E}^2 \text{ gm/cm}^2, \quad \mathcal{E} \text{ in mev.}\end{aligned}\tag{2.1}$$

The kinetic energy in the shell imploded with velocity  $v$  is

$$\begin{aligned}E_s &\cong 2\pi r_0^2 \Delta m v_{\text{imp}}^2 \\ &= 2\pi (r_0/\Delta r)^2 v_{\text{imp}}^2 / \rho_0^2 (\Delta m)^3.\end{aligned}\tag{2.2}$$

The electron beam energy must be approximately a factor of ten greater than the implosion energy, the rest of the energy being carried off in ablation products. As an example, we assume

$$v_{\text{imp}} = 3 \times 10^7 \text{ cm/sec}$$

$$\rho_0 = 20 \text{ gm/cm}^3$$

$$A = 200$$

$$Z = 80$$

giving

$$\Delta m = 0.172 \epsilon^2 \text{ gm/cm}^2$$

$$E_s = 7.15 (r/\Delta r)^2 \epsilon^6 \text{ kilojoules} \quad (2.3)$$

$$E_B = 71.5 (r/\Delta r)^2 \epsilon^6 \text{ kilojoules.}$$

The aspect ratio  $r/\Delta r$  of the shell must be determined by implosion studies of tamper efficiency; a reasonable choice is  $r/\Delta r = 10$ , giving

$$E_B = 7.15 \epsilon^6 \text{ megajoules.} \quad (2.4)$$

Thus at a beam energy of one Mev ( $\epsilon = 1$ ), the beam energy is 7.15 megajoules.

The pulse length is approximately

$$\begin{aligned} t_{\text{imp}} &\cong 2r/v_{\text{imp}} \\ &= (r/\Delta r)^2 m/\rho_0 v_{\text{imp}} \end{aligned} \quad (2.5)$$

for the parameters used above,

$$t_{\text{imp}} = 0.57 r/\Delta r \epsilon^2 \text{ nanoseconds.} \quad (2.6)$$

The beam power is

$$\begin{aligned} P_B &= E_B/t_{\text{imp}} \\ &= 1.26 (r/\Delta r) \epsilon^4 10^{14} \text{ watts} \end{aligned} \quad (2.7)$$

For  $r/\Delta r = 10$  and  $\epsilon = 1 \text{ Mev}$ , the beam power is  $1.26 \times 10^{15}$  watts. The beam current is  $1.26 \times 10^9$  amperes. The pulse length is 5.7 nanoseconds and the initial pellet radius 0.86 millimeters. The current density is

$$I_B/4\pi r^2 = 1.35 \times 10^{10} \text{ amp/cm}^2 \quad (2.8)$$

corresponding to an incident power of  $1.35 \times 10^{16} \text{ watts/cm}^2$ .

The estimates given above are only correct in order-of-magnitude. They show the strong dependence of the energy and power requirements on the beam energy and on the aspect ratio of the imploded shell. The principal problem of interest to this proposal is the control and focussing of the electron-beam on the fusion pellet. The nature of the beam-handling problem is described in the next section.

### III. BEAM PINCH IN THE PRESENCE OF PLASMA CURRENTS

The desired concentration of beam power on the fusion pellet can be achieved only by a controlled pinch of the beam, using the self-magnetic field of the beam. A beam can pinch only if partially charge neutralized: we assume that sufficient plasma is present to give charge neutrality. We first consider the case of a plasma with high resistivity, so that the plasma current can be neglected. For a uniform beam, the condition of pressure balance at the beam edge is

$$B^2/8\pi \cong n_B \epsilon_{\perp} . \quad (3.1)$$

The magnetic field is

$$B = I_B/5r \quad (3.2)$$

with  $I$  in amperes. The current is

$$I_B = 10\pi r^2 n_B e v_{||} / c . \quad (3.3)$$

Eqs. (3.1), (3.2), and (3.3) combine to give

$$I_B = 20 \frac{\epsilon_{\perp}}{e} \frac{c}{v_{||}} = 6.4 \times 10^4 \frac{c}{v_{||}} \epsilon_{\perp} (\text{Mev}) \text{ amperes} . \quad (3.4)$$

The beam current required for fusion is much greater than that given by Eq. (3.4); such an intense beam can propagate only if partially compensated by plasma current. The present experiments appear to be in the regime where Eq. (3.4) can be satisfied; these conditions however are not relevant to the fusion current levels.

Ivanov and Rudakov<sup>4</sup> have estimated conditions in a plasma in which the beam current is initially compensated by a plasma current. The decay of the plasma current then causes beam contraction. We first give an estimate of the rate of beam contraction, using a model based on a different approximation from that given in Ref. 1. We suppose that the beam current with radius  $r$  is partially cancelled by a uniform plasma current with radius  $R-x$ . The magnetic field is

$$B \cong \frac{2I_B}{cr} \frac{2x}{r} . \quad (3.5)$$

The pressure balance is

$$\frac{B^2}{8\pi} = n_B \mathcal{E}_\perp = \frac{R^4}{r^4} \frac{\mathcal{E}_\perp(0)}{ec} j_0 . \quad (3.6)$$

Eq. (3.5) and Eq. (3.6) combine to give

$$x^2 = \frac{\mathcal{E}_\perp(0)}{2\pi n_B(0)e^2} . \quad (3.7)$$

The beam electrons move in a field-free region for  $r < R - x$  and are reflected at the beam edge by the magnetic field. For consistency, the penetration distance of the electron into the magnetic field should be of order  $x$ . If the electron enters the magnetic with angle  $\theta$ , measured from the beam direction, the penetration depth is

$$d \approx \frac{1}{2} r_L \theta^2$$

$$\approx v_{\perp}/v_{\parallel}$$
(3.8)

where  $r_L$  is the Larmor radius. The ratio of  $d$  to  $x$  is

$$d/x = \frac{\frac{1}{2} r_L (v_{\perp}/v_{\parallel})^2}{x}$$

$$= \frac{1}{2} \frac{\gamma m c^2}{e B x} (v_{\perp}/v_{\parallel})^2.$$
(3.9)

Using Eqs. (3.5) for  $B(R)$  and (3.7) for  $x$  we find

$$d/x = j c / n_B v_{\parallel}^2 e.$$
(3.10)

The current is

$$j = n_B e v_{\parallel}$$
(3.11)

so that

$$d/x = c/v_{\parallel} \approx 1$$

Thus the penetration distance is consistent with the skin depth.

The skin depth  $x$  is determined by the diffusion equation for the magnetic field,

$$\nabla^2 B = \frac{4\pi}{c} \sigma \frac{\partial B}{\partial t}.$$
(3.12)

We obtain an estimate for the rate of change of beam radius by replacing the Laplacian in Eq. (3.12) by  $x^{-2}$ .



The conductivity varies as  $T^{3/2}$ . The plasma temperature is given by

$$\begin{aligned} \frac{3}{2}n_0 \frac{dT}{dt} &= \frac{j_p^2}{\sigma} \\ &= \frac{j_0^2}{\sigma_0} \left(\frac{T_0}{T}\right)^{3/2} \frac{R^4}{r_0^4} \end{aligned} \quad (3.13)$$

giving

$$T = T_0 \left(1 + \frac{5}{3} \frac{j_0^2}{\sigma_0 n_0 T_0} \int_0^t dt' \frac{R^4}{r_0^4}\right)^{2/5}. \quad (3.14)$$

Eq. (3.12) may then be written

$$\frac{B}{x^2} = \frac{4\pi\sigma_0}{c^2} \left(1 + \frac{5}{3} \frac{j_0^2}{\sigma_0 n_0 T_0} \int_0^t dt' \frac{R^4}{r_0^4}\right)^{3/5} \frac{\partial B}{\partial t}. \quad (3.15)$$

Using Eq. (3.6) for B, Eq. (3.15) may be written

$$\frac{\partial}{\partial t} \left( \frac{R^2}{r_0^2} \frac{1}{\frac{\partial}{\partial t} \frac{R^2}{r_0^2}} \right)^{5/3} = \frac{5}{3} \frac{j_0^2}{\sigma_0 n_0 T_0} \frac{R^4}{r_0^4} \left( \frac{4\pi\sigma_0 x^2}{c^2} \right)^{5/3}. \quad (3.16)$$

This allows a similarity solution

$$r_0/R = (\tau/t)^{1/6} \quad (3.17)$$

with the characteristic time  $\tau$  given by

$$\begin{aligned}\tau &= \left\{ \frac{j_0^2}{\sigma_0 n_0 T_0} \left( \frac{4\pi\sigma_0 x^2}{3c^2} \right)^{5/3} \right\}^{3/2} \\ &= \left( \frac{\sigma_0 n_0 T_0}{j_0^2} \right) \left( \frac{2n_B(0)\epsilon_\perp}{3n_0 T_0} \right)^{5/2}.\end{aligned}\quad (3.18)$$

The analysis by Ivanov et al.<sup>4</sup> proceeds along a somewhat different line. We repeat the main features of his analysis, simplifying his results, and apply them to the fusion beam.

The magnetic field is given by

$$\begin{aligned}B &= -c \nabla \times E \\ &= -c \nabla \times j_p / \sigma\end{aligned}\quad (3.19)$$

giving

$$B_\phi = -c \frac{\partial}{\partial r} \int_0^t \frac{j_p(t')}{\sigma(t')} dt'. \quad (3.20)$$

The conductivity is again determined by Eq. (3.13). The magnetic pressure on the beam is

$$\begin{aligned}p_B &= \int dr \quad B_\phi j_B / c \\ &\approx j_0^2 \frac{R^2}{r_0^2} \int_0^t \frac{R^2}{r_0^2 \sigma} dt' \\ &= j_0^2 \frac{R^2}{r_0^2} \frac{1}{\sigma_0} \int_0^t \frac{R^2 / r_0^2 dt'}{\left[ 1 + \frac{5}{3} \frac{j_0^2}{\sigma_0 n_0 T_0} \int_0^{t'} dt'' \frac{R^4}{r_0^4} \right]^{3/5}}.\end{aligned}\quad (3.21)$$

Pressure balance gives

$$\begin{aligned}
 p_B &= n_B \mathcal{E}_\perp \\
 &= \frac{R^4}{r_0^4} \frac{j_0}{2ec} \mathcal{E}_\perp^{(0)} .
 \end{aligned} \tag{3.22}$$

Eqs. (3.7) and (3.22) combine to give

$$\begin{aligned}
 \frac{j_0}{\sigma_0} \int_0^t \frac{R^2/r_0^2 dt'}{\left[ 1 + \frac{5}{3} \frac{j_0^2}{\sigma_0 n_0 T_0} \int_0^t dt'' \frac{R^4}{r_0^4} \right]^{3/5}} \\
 = \frac{R^2}{r_0^2} \frac{1}{2ec} \mathcal{E}_\perp^{(0)} .
 \end{aligned} \tag{3.23}$$

This can be transformed into a differential equation

$$\begin{aligned}
 \frac{y}{\left[ 1 + \frac{5}{3} \frac{j_0^2}{\sigma_0 n_0 T_0} \int_0^t dt' y^2 \right]^{3/5}} \\
 = \dot{y} \frac{\mathcal{E}_\perp^{(0)} \sigma_0}{2ec j_0}
 \end{aligned} \tag{3.24}$$

$$y = \frac{R^2}{r_0^2}$$

and

$$y^2 = \frac{3\sigma_0 n_0 T_0}{5j_0^2} \left( \frac{2ec j_0}{\mathcal{E}_\perp^{(0)} \sigma_0} \right)^{5/3} \frac{d}{dt} (y/\dot{y})^{5/3} . \tag{3.25}$$

Eq. (3.25) has a similarity solution

$$y = \alpha t^k . \quad (3.26)$$

The coefficients  $\alpha$  and  $k$  are

$$\alpha = \left[ \frac{\sigma_0 n_0 T_0}{j_0^2} \left( \frac{2ecj_0}{\mathcal{E}_\perp(0)\sigma_0} \right)^{5/3} \right]^{1/2} \quad (3.27)$$

$$k = 1/3 .$$

Eq. (3.26) can therefore be written

$$\frac{r}{R} = (\tau/t)^{1/6} \quad (3.28)$$

with the characteristic time  $\tau$  given by

$$\tau = \frac{\sigma_0 n_0 T_0}{j_0^2} \left( \frac{n_B(0)\mathcal{E}_\perp}{2n_0 T_0} \right)^{5/2} . \quad (3.29)$$

Eq. (3.28) and (3.29) are the same as Eqs. (3.17) and (3.18), except for a numerical factor of order unity.

The beam contracts very slowly; for  $r$  to decrease from one meter to one millimeter requires a time of  $10^{18}\tau$ .

The final transverse beam energy is

$$\mathcal{E}_T(t) = \mathcal{E}_T(0) \left( \frac{R}{r_0} \right)^2 . \quad (3.30)$$

Thus, if the final transverse energy is 1 Mev and  $R/r_0 = 10^3$ , the initial transverse energy must be 1 ev. As an example, we consider

$$\begin{aligned}
I_0 &= 3 \times 10^8 \text{ amperes} \\
R &= 100 \text{ cm} \\
j_0 &= 3 \times 10^4 \text{ amperes} \\
&= 9 \times 10^{13} \text{ cgs} \\
n_0 &= 10^{18}/\text{cm}^3 \\
T_0 &= 1 \text{ ev} \\
\sigma_0 &= 10^{13} \text{ sec}^{-1}
\end{aligned} \tag{3.31}$$

giving  $\tau = 3.35 \times 10^{-23} \text{ sec}$ . The beam collapse time to one millimeter is  $t = 10^{18} \tau = 3.35 \times 10^{-5} \text{ sec}$ . The collapse time to one centimeter is  $3.35 \times 10^{-8} \text{ sec}$ .

The energy deposited in the gas per unit length is

$$\begin{aligned}
U_{\text{gas}} &= \int_0^t \pi r^2 \frac{j^2}{\sigma} dt \\
&= \frac{\pi R^2}{\sigma_0} j_0^2 \int_0^t \frac{R^2}{r^2} \left( \frac{T_0}{T} \right)^{3/2} dt .
\end{aligned} \tag{3.32}$$

Using Eqs. (3.14) for  $T/T_0$  and (3.17) for  $R^2/r^2$ , we find

$$\begin{aligned}
U_{\text{gas}} &= \frac{\pi R^2 j_0^2 \tau}{\sigma_0} \left( \frac{3}{5} \frac{n_0 \sigma_0 T_0}{j_0^2 \tau} \right)^{3/5} \int_0^t \frac{dt}{\tau} (\tau/t)^{4/15} \\
&= \frac{\pi R^2 j_0^2 \tau}{\sigma_0} \left( \frac{3}{5} \frac{n_0 \sigma_0 T_0}{j_0^2 \tau} \right)^{3/5} \frac{15}{11} (R/r)^{22/5} .
\end{aligned} \tag{3.33}$$

Using Eq. (3.18) for  $\tau$ , the result is (we drop a numerical factor of order of unity)

$$U_{\text{gas}} = \pi R^2 n_{B,0} \mathfrak{E}_{1,0} (R/r)^{22/5} . \tag{3.34}$$

The ratio of energy in the gas to the beam input power is

$$\frac{U_{\text{gas}}}{P_{\text{beam}}} = \frac{\epsilon_{\perp,0}}{c \epsilon_{||,0}} (R/r)^{22/5} . \quad (3.35)$$

Thus if  $\epsilon_{\perp,0}/\epsilon_{||,0} = 10^{-6}$  and the beam power is  $10^{15}$  watts,

$$U_{\text{gas}} = \frac{1}{30} (R/r)^{22/5} \text{ joules/cm} . \quad (3.36)$$

This is equal to one megajoule per centimeter if the beam contracts by a factor of 50, which is a prohibitively large energy loss to the gas.

The results given above are very schematic since the dynamics of the beam collapse are not included. The simple treatment of the plasma is also incorrect since expansion will occur under the strong prolonged heating by the plasma current. Radiative and inductive loss also must be included. The possibility of anomalous plasma resistivity due to the two-stream instability, which would change the rate of beam contraction, also must be considered.

The beam may also be subject to various hydrodynamics instabilities. The most serious is the interaction between the beam, if slightly displaced, and the plasma current. The opposed currents are repulsive, leading to rapid lateral ejection of the beam from the plasma channel. Less serious are the hose and sausage instabilities. Another possibility, mentioned by Ivanov and Rudakov,<sup>4</sup> is the breakup of the beam and plasma current into inter-penetrating filaments with average zero current. They assert that this mode is absent if the plasma density is sufficiently high.



#### IV. THE YOSHIKAWA CONFIGURATION

Yoshikawa<sup>1</sup> considers a beam in which the electrons move on helices with  $v_r = 0$ . He assumes a current configuration for which  $B_r = 0$  and the fields are independent of  $z$  and  $\theta$ . The force balance then is

$$\begin{aligned} \frac{\gamma m v_\theta^2}{r} &= \frac{e}{c} (\mathbf{v} \times \mathbf{B})_r \\ &= \frac{e}{c} (v_\theta B_z - v_z B_\theta) . \end{aligned} \quad (4.1)$$

The current is related to  $\mathbf{B}$  by

$$\begin{aligned} \vec{\nabla} \times \vec{B} &= \frac{4\pi}{c} \vec{j} \\ &= -\frac{4\pi}{c} (ne\vec{v}) \end{aligned} \quad (4.2)$$

giving

$$\begin{aligned} \frac{dB_z}{dr} &= \frac{4\pi}{c} nev_\theta \\ \frac{1}{r} \frac{d}{dr} (rB_\theta) &= -\frac{4\pi}{c} nev_z . \end{aligned} \quad (4.3)$$

Eqs. (4.1) and (4.3) combine to give

$$\frac{\gamma m}{r} \frac{c^2}{4\pi ne^2} \left( \frac{dB_z}{dr} \right)^2 - B_z \frac{dB_z}{dr} = \frac{B_\theta}{r} \frac{d}{dr} (rB_\theta) . \quad (4.4)$$

Eq. (4.4) can be solved by any radial variation of  $B_z$  which satisfies the boundary conditions. A simple choice is

$$B_z = B_0 (1 - r^2/a^2) \quad (4.5)$$

giving

$$B_\theta^2 = B_0^2 \frac{r^2}{a} \left(1 - \frac{2}{3} \frac{r^2}{a} + \alpha\right) \quad (4.6)$$

$$\alpha = \gamma mc^2 / 2\pi ne^2 a^2 .$$

The parameter  $\alpha$  is

$$\alpha = I_A / I \quad (4.7)$$

with the Alfvén current given by

$$I_A = \frac{1}{2} \gamma \frac{mc^2}{e} \bar{v}_z \quad (4.8)$$

and the beam current by

$$I = \pi ne a^2 \bar{v}_z . \quad (4.9)$$

The magnetic field at  $r = a$  is

$$\begin{aligned} B_\theta(a) &= B_0 \left(\frac{1}{3} + \alpha\right)^{1/2} \\ &= \frac{2}{ca} I . \end{aligned} \quad (4.10)$$

Eqs. (4.6) and (4.10) are solutions for any value of  $B_0$  and hence of beam current.

The pitch of the magnetic field is determined by

$$\frac{B_\theta}{B_z} = \frac{\frac{r}{a} \left(1 - \frac{2}{3} \frac{r^2}{a} + \alpha\right)^{1/2}}{(1 - r^2/a^2)} . \quad (4.11)$$

The pitch of the electron motion is

$$\begin{aligned} \frac{v_{\theta}}{v_z} &= - \frac{\frac{dB_z}{dr}}{\frac{1}{r} \frac{d}{dr} (rB_{\theta})} \\ &= \frac{\frac{r}{a} (1 - \frac{2}{3} \frac{r^2}{a^2} + \alpha)^{\frac{1}{2}}}{1 - (r^2/a^2) + \alpha} . \end{aligned} \quad (4.12)$$

Thus, for  $I \gg I_A$  or  $\alpha \rightarrow 0$ , the electron motion is parallel to the magnetic field except for  $r/a$  very close to unity. At  $r = a$ ,  $B_z$  vanishes but  $v_z/v_{\theta} = \alpha/(1/3 + \alpha)^{\frac{1}{2}}$ . The electrons at  $r = a$  therefore move in a very flat helix, with the magnetic field lines closed circles.

Although the magnetic field and electron motion given by the above equations are a formal solution to the beam equation, they are a highly specialized configuration and probably very difficult to produce. The beam stability has not been analyzed and may present severe problems if the initial beam configuration can be produced.

The overall energy of the beam resides almost entirely in the magnetic field. The kinetic energy in the electrons is

$$E_e \approx \pi a^2 \gamma m c^2 n \approx \frac{j m c}{e} I \quad (4.13)$$

while the magnetic energy for  $r > a$  is

$$\begin{aligned}
 E_B &= \frac{1}{8\pi} (2I/c)^2 \int_a^{R_{\max}} \frac{1}{r^2} 2\pi r dr \\
 &= \frac{I^2}{c^2} \ln \frac{R_{\max}}{a} .
 \end{aligned} \tag{4.14}$$

Thus,

$$\begin{aligned}
 \frac{E_B}{E_e} &= \frac{I_c}{\gamma m c^3} \ln R_{\max}/a \\
 &\cong \frac{2I}{I_A} \ln R_{\max}/a .
 \end{aligned} \tag{4.15}$$

The coupling to a fusion pellet of a beam with the energy primarily in the magnetic field has not been analyzed. The magnetic energy can be deposited in the pellet only if the beam current is reduced, requiring very large plasma currents with the associated problem of delayed beam contraction, as discussed in Section III.

## V. THE SANDIA ANALYSIS

Poukey and Toepfer<sup>2</sup> analyze the equations for a relativistic beam with a Maxwellian velocity distribution in the rest frame of the electrons. They consider the special case of a stationary configuration and derive equations for the beam radius, making the simplifying assumptions of a constant beam shape and with the velocity independent of radial position. The basic equation they obtain for a square beam the case of no external electric field and, with the beam charge neutralized but no plasma current, is

$$\gamma \beta^2 \frac{F dx}{dz} + \frac{1}{\gamma} F_{\xi} \left[ \frac{4(1+x^2)}{R \left( \frac{L_{\xi}}{L} + \frac{F_{\xi}}{F} \right)} - x \frac{d\xi}{dz} \right] = -2 \frac{v\beta}{R} (1+x^2) \quad (5.1)$$

with

$$\begin{aligned} x &= \frac{dR}{dz} \\ \beta^2 &= (\gamma^2 - 1) / \gamma^2 (1+x^2) \\ \xi &= mc^2 / T_0 \\ F &= K_3(\xi) / K_2(\xi) \\ \frac{L_{\xi}}{L} &= -\xi F_{\xi} - \frac{1}{\xi} \\ v &= -eI / mc^3 \end{aligned} \quad (5.2)$$

The constants of the motions are

$$\begin{aligned} Q &= nL(\xi) / \gamma \\ W &= \gamma F(\xi) \\ I &= -\pi enR^2 \beta c \end{aligned} \quad (5.3)$$

The beam contracts to a minimum at  $x=0$  and  $d\xi/d\tau=0$ . The minimum radius is at  $dx/dz=0$ , for which

$$\frac{\frac{F_\xi}{L_\xi + \frac{F_\xi}{F}}}{L_\xi} = -\frac{1}{2}v\beta\gamma = -\frac{1}{4} \frac{I}{I_A}(\gamma^2-1) \quad (5.4)$$

if the internal energy of the beam electrons is much less than  $mc^2$ ,  $F_\xi/F = -\frac{5}{2\xi^2}$ ,  $L_\xi/L = 3/2\xi$ ,  $F = i + 5/2\xi$ , giving

$$v\beta\gamma\xi = 5/6$$

or

$$\frac{T_0}{mc^2} = 1/\xi = 3/5 \frac{I}{I_A} (\gamma^2-1). \quad (5.5)$$

As observed by Poukey and Toepfer,<sup>2</sup> Eq. (5.5) can also be written

$$\begin{aligned} \frac{5}{3} \frac{nT_0}{\gamma} &= -\frac{1}{2}\beta v mc^2 \\ &= -\frac{1}{2} \frac{\beta e I n}{c} \\ &= + \frac{1}{2\pi R^2} \frac{I^2}{c^2} \\ &= B(R)^2/8\pi. \end{aligned} \quad (5.6)$$

Thus, the beam internal energy measured in the laboratory system, with  $T = T_0/\gamma$ , satisfies a simple pressure balance condition. Eq. (5.5) shows that very strong beam heating must occur if  $I \gg I_A$ .



In the relativistic limit, with  $T_0/mc^2 = \xi^{-1} \gg 1$ ,  $F = 4/\xi$ ,  $F_\xi/F = -1/\xi$ ,  $L_\xi/L = 3/\xi$ , and Eq. (5.11) gives

$$\gamma v \beta \xi = 4 . \quad (5.7)$$

This may be rewritten

$$\begin{aligned} T &= mc^2 / \gamma \xi \\ &= (I/8I_A) \gamma mc^2 . \end{aligned} \quad (5.8)$$

The corresponding pressure balance is

$$\frac{2nT_0}{\gamma} = \frac{B^2}{8\pi} . \quad (5.9)$$

In this limit, the internal energy of the beam becomes very large if  $I \gg I_A$ . These results are already indicated in the Poukey-Toepfer<sup>2</sup> paper, since they found the same result for a beam condition independent of  $z$ .

The usefulness of the superpinched beam produced under these conditions is probably seriously diminished since the beam electrons are very strongly heated and energy coupling to the pellet is accordingly reduced as shown in Section II.

The pinched beam, as in the Yoshikawa case, has most of the energy in the magnetic field, again raising the problem of coupling the magnetic energy to the pellet.

## VI. THE HAMMER-ROSTOKER CONFIGURATION

Hammer and Rostoker<sup>3</sup> consider an axisymmetric beam with all electrons having the same total energy and canonical momentum along the beam. In the absence of an applied electric field, they find a solution with constant electron density and with electron velocity varying with radius as

$$v_z(r) = v_z(0) I_0(r/L_e) \quad (6.1)$$

for a characteristic depth  $L_e$  and where  $I_0$  is the modified Bessel function of order 0. For high current,  $L_e \ll b$  and

$$v_z(r) = v_z(0) \frac{\exp r/L_e}{\sqrt{2\pi r/L_e}} . \quad (6.2)$$

Then the beam current is concentrated near  $r = b$  with a characteristic depth of  $L_e$ .

The essential features of this result may be obtained for a simple mode in which the electrons move with  $v_z = 0$  within a hollow cylinder of current in which they are reflected, re-emerging with  $v_z = 0$ . The current depth  $\delta$  must be of the order of the Larmor radius in the average magnetic field, i.e., (for  $v \approx c$ )

$$\frac{\gamma mc^2}{\delta} = eB = \frac{2eI}{cb} . \quad (6.3)$$

The current is generated entirely within  $\delta$  where the electrons turn,

$$\begin{aligned}
 I &= ne\overline{v_z} 2\pi b\delta \\
 &\cong \frac{1}{2} nec 2\pi b\delta .
 \end{aligned}
 \tag{6.4}$$

Thus,

$$\begin{aligned}
 j &\cong \frac{1}{2} nec = \frac{I}{2\pi b\delta} \\
 &= \frac{I^2 e}{\delta \pi b^2 mc^3} \\
 &= \frac{I}{I_A} \frac{I}{\pi b^2} .
 \end{aligned}
 \tag{6.5}$$

Thus, for a given beam radius, the current density  $j$  increases as  $I^2$ . The sheath thickness is

$$\frac{\delta}{b} = \frac{\gamma mc^3}{2eI} = \frac{I_A}{I} .
 \tag{6.6}$$

For this configuration, the energy in the electrons per unit length is

$$E_{\text{elect}} \cong \pi b^2 n \gamma mc^2
 \tag{6.7}$$

while the magnetic energy is

$$E_{\text{mag}} = \int_b^{R_{\text{max}}} \frac{B^2}{8\pi} 2\pi r dr = \frac{I^2}{c^2} \ln \frac{R_{\text{max}}}{b} .
 \tag{6.8}$$

Using Eq. (6.5) for  $n$ , Eq. (6.7) becomes

$$E_{\text{elect}} = \frac{2I^2}{c} .
 \tag{6.9}$$

Thus,

$$\frac{E_{\text{mag}}}{E_{\text{elect}}} = \frac{1}{2} \ln \frac{R_{\text{max}}}{b} . \quad (6.10)$$

The average flow velocity is of the order of

$$\overline{v_z} \approx \frac{\delta}{b} c = \frac{I_A}{I} c . \quad (6.11)$$

Thus the ability of the beam to carry energy is very low.

The results of this simple model, as given in Eqs. (6.3)-(6.11), are in all essentials identical with the Hammer-Rostoker<sup>3</sup> results. They show that the high current beam has a singular structure, i.e., a very thin current sheath in which reflection of electrons occurs and in which the entire beam current flows. The stability and formation of this beam have not been discussed. In addition, the magnetic energy is relatively large and the energy flow in the beam very low. This clearly raises serious questions of coupling of beam energy into a pellet.

## VII. SUMMARY

Electron beams in the power and energy range for driving a fusion pellet present severe and unsolved problems in beam handling. If the beam is charge-neutralized but plasma currents are assumed to be absent, the force-balance in the beam requires highly specialized current configurations (the Yoshikawa or Hammer-Rostoker proposals) or very high internal beam energy to provide pressure balance. In either case the magnetic energy is very large compared with the beam kinetic energy and can be coupled to the fusion pellet only if the beam current is cancelled by return currents in the plasma. This transient problem has not been analyzed.

A more realistic treatment of the plasma currents produced as transients during the beam pinching shows considerable delay in the final pinch and large energy deposition in the plasma. This configuration may also be very unstable due to interaction between the beam and plasma currents. The dynamics of the plasma responding to the enormous heating power of the beam also can markedly modify the pinch

In any case, the delivery of energy by an intense electron beam at power levels of  $10^{14}$  to  $10^{15}$  watts and  $10^{16}$  watts/cm<sup>2</sup> to the fusion pellet is a difficult and inadequately studied problem. A plausible "scientific scenario" for beam delivery remains to be produced.

#### REFERENCES

1. S. Yoshikawa, Phys. Rev. Lett. 26, 295 (1971).
2. J. W. Poukey and A. J. Toepfer, Phys. Fluids 17, 1582 (1974).
3. D. A. Hammer and N. Rostoker, Phys. Fluids 13, 1831 (1970).
4. A. A. Ivanov and L. I. Rudakov, Sov. Phys. JETP 31, 715 (1970).



HIGH-CURRENT ELECTRON BEAM TRANSMISSION THROUGH  
PLASMA UNDER LOW PRESSURE

A. N. Didenko, Ye. T. Protasevich, V. V. Tikhomirov

Institute for Nuclear Physics, 634050, Tomsk-50,

P.S. Box 25, USSR.

ABSTRACT

In this paper is showed a possibility of effective (up to 75%) transmission of a high-current electron beam through a pre-ionized gas ( $p = 10^{-4} + 10^{-5}$  torr). Optimal beam transmission was observed with  $f = n_i/n_{eb} \approx 10$  and total compensation of the beam current with  $c/\omega_p \sim 0.1r_b$ .

High-current relativistic electron beams are now widely used in various spheres. Using such beams one faces the problem of elaborating effective transmission methods of them. It is known that high-current beams will focus and transmit through a gas medium with  $p = 10^{-1} + 10^{-2}$  torr [1]. Under this pressure charge neutralization is assured by the beam itself through residual gas ionization. Known are also methods of transmission by applying an external strong magnetic field [2]. However, in a number of cases we have to transmit beams through vacuum media ( $p = 10^{-4} + 10^{-5}$  torr) without any magnetic field [3].

In this paper we speak of transmission of beams under low pressure under condition of almost full residual gas pre-ionization.

The experiments were carried out in silica tubes of diameter  $d = 8 + 9$  cm and of length  $l = 100$  cm. Full ionized plasma was produced by a discharge. With power input of about 30 kW the level of ionization reached about ~90%. Electron beams had the following parameters: 1.  $E = 1.5$  MeV,  $I = 30$  kA,  $t = 50$  ns; 2.  $E = 0.4$  MeV,  $I = 5$  kA,  $t = 30$  ns.

To increase the plasma density and to shorten its decay time we applied an external weak constant axially symmetrical magnetic field  $B_0$  ( $B_0 \ll B_\phi$ , wherein  $B_\phi$  is the internal beam field). In Fig. 1 the experimental apparatus is presented in schematic illustration.

Fig. 2. represents in relative units current dependencies at the tube output with respect to plasma density. It is seen that when charge ionization is insufficient (left curve branches) no transmission of the

beams is observed. The beam transmission takes place only when the neutralization factor  $f$  increases. The transmission factor has its maximum with  $f = n_i/n_{e,b} \approx 10$  makes 75%. A considerable self-focusing of the beam is observed in Fig. 3 showing the beam shape in cross-section at the input (3-1) and at the output (3-2) of the drift tube. With a further increase of the plasma density (right curve branches) the transmission efficiency begins to decrease and the beam diameter at the output increases because of its partial magnetic neutralization. With  $c/\omega_p \sim 0.1r_b$ , where  $c$  is the speed of light,  $\omega_p$  is the Langmuir plasma frequency and  $r_b$  is the beam diameter, a total compensation of the beam current ( $B_\phi \approx 0$ ) is supposed to set up and then the beam diameter under the action of a transverse pulse increases to such an extent that the beam strikes the walls of the drift tubes.

In paper [4] a total current compensation was observed also when  $c/\omega_p \approx 0.15r_b$ , if  $B_0 \gg B_\phi$ .

With external magnetic field  $B_0$  the efficiency of transmission decreases. This may be explained by the fact that, due to growing nonuniformity of the radial plasma density distribution, charge neutralization on the beam periphery turns out to be insufficient.

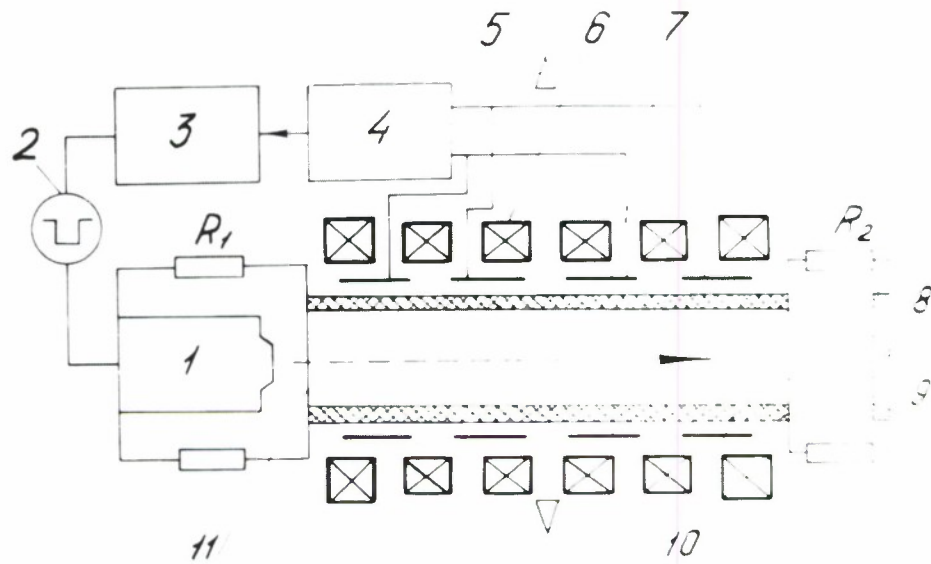
Fig. 4 gives typical oscillograms of the beam current. It is seen that in the process of transmission the pulse shape at the output undergoes no appreciable changes in comparison to the pulse shape at the input.

Consequently, the transmission of a high-current electron beam through a pre-ionized gas medium may find a wide application in many fields of science and engineering, where there is a need to assure an effective transmission of a beam under low pressure.

The authors express their gratitude to V.P. Grigoryev and Yu.P. Usov for discussing the results of the work and to A.I. Ryabchikov, S.L. Semyonov, A.A. Solovyov and V.A. Tuzov for assistance in carrying out the experiments.

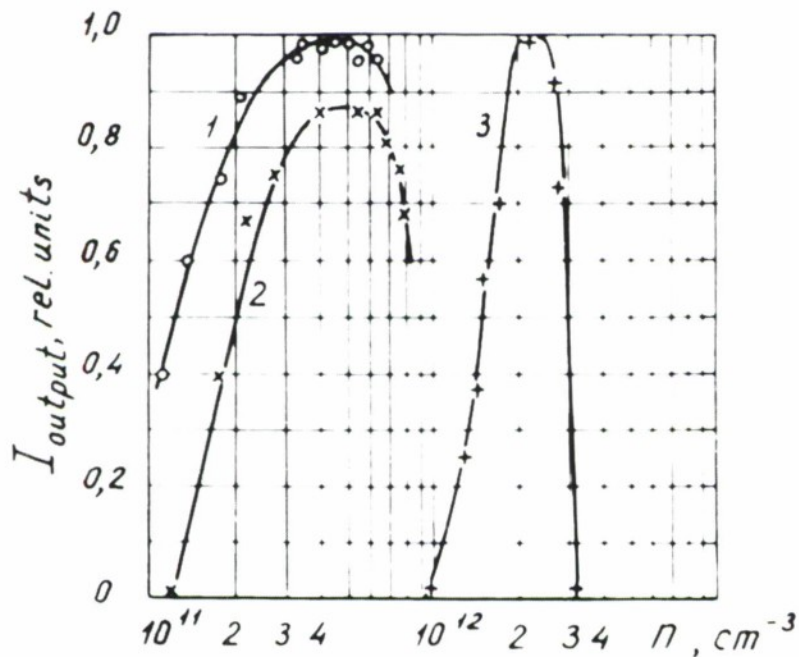
#### REFERENCES

1. L.I. Rudakov, V.P. Smirnov, A.M. Spektor. Pisma Zh.Eksp. Teor. Fiz., 15, 9, 540, 1972.
2. A.V. Agafonov. Atomnaya Tekhnika za Rubezhom, 10, 31, 1973.
3. A.N. Didenko, G.P. Fomenko. Trudy Nauchno-issledovatel'skogo Instituta Yadernoi Fiziki, Elektroniki i Avtomatiki pri Tomskom Polytekhnicheskom Institute. Vyp.4, 37, 1974, M. Atomizdat.
4. O.D.Klok, V.D. Krementsov, P. Strelkov, A.G. Shkvarunets. Zh. Eksp. Teor. Fis., 67, 1401, 1974.



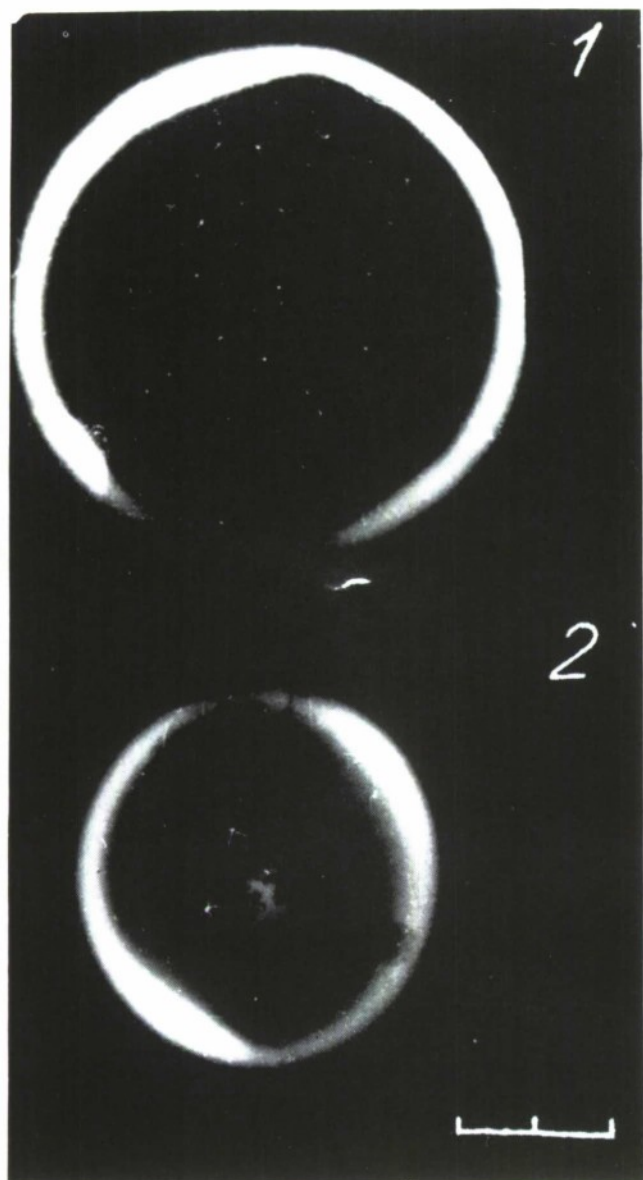
- |   |                           |
|---|---------------------------|
| 1. cathode  | 6. solenoid               |
| 2. generator                                      | 7. ring electrodes        |
| 3. delay scheme                                   | 8. Faraday cup output     |
| 4. RF-generator ( $F=37$ Mc,<br>$\tau = 10$ msec) | 9. foil (aluminum, 200 m) |
| 5. antenna  | 10. silica tube           |
|   | 11. anode foil            |

Figure 1. Scheme of experimental apparatus



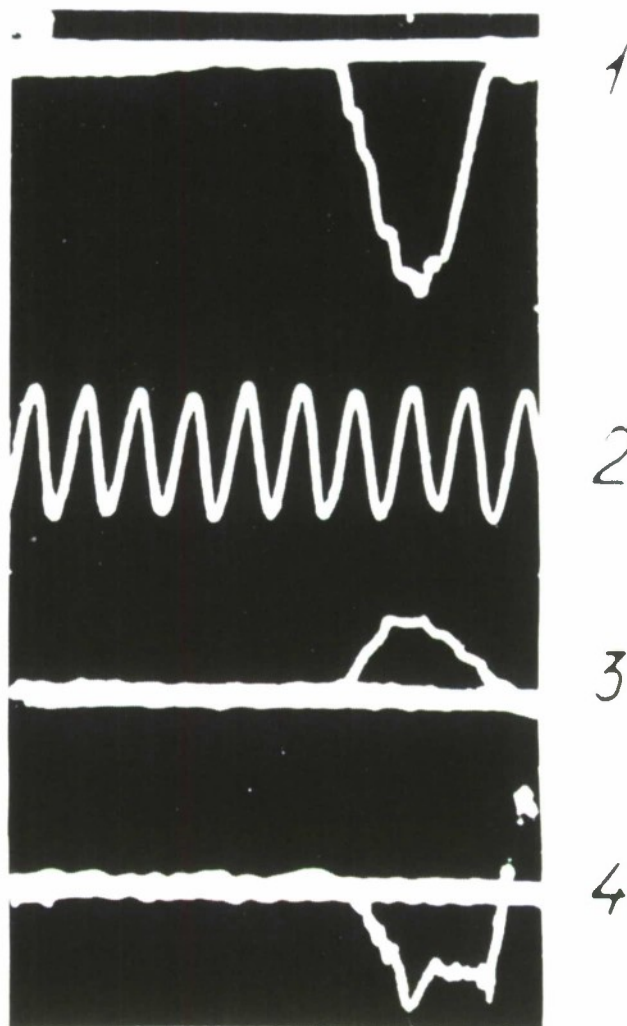
1. for  $N_{e,b} = 6.6 \times 10^{10} \text{ cm}^{-3}$   
( $\epsilon = 0.4$  MeV,  $I = 5$  kA,  
 $\tau = 30$  ns) if  $d = 9$  cm and  
 $B_0 = 80$  Oersted.
2.  $B_0 = 125$  Oersted.
3. for  $N_{eb} = 2.3 \times 10^{11} \text{ cm}^{-3}$   
( $\epsilon = 1.5$  MeV,  $I = 30$  kA,  
 $\tau = 50$  ns) if  $d = 8$  cm,  
 $B_0 = 95$  Oersted.

Figure 2. Current dependencies at tube output with respect to plasma density



for  $N_{e,b} = 2.3 \times 10^{11} \text{ cm}^{-3}$  (scale:  
1 division - 1 cm) 1 - input,  
2 - output, when  $N_{eb} = 2.7 \times 10^{11} \text{ cm}^{-3}$

Figure 3. Beam shape in cross-section



1. input
2. gradiating curve ( $f = 100 \text{ Mc}$ )
3. Faraday cup output
4. reverse current shunt output

Figure 4. Typical oscillograms of Beam current



BEHAVIOUR OF THE SELF FOCUSING RELATIVISTIC  
ELECTRON BEAM PROPAGATING ALONG THE  
INTERFACE OF DIFFERENT MEDIA

A. N. Didenko, A. V. Petrov, A. I. Rjabchikov, V. A. Tusov, Yu. P. Usov

Institute for Nuclear Physics, 634050,

Tomsk-50, P. O. Box 25, USSR

ABSTRACT

Self focusing relativistic electron beam propagating along the surface of ferromagnetic plate is attracted to it and reflected in the case of the diamagnetic plate.

Self-focusing properties of intense relativistic electron beams propagating through the gas with low pressure and their abilities to propagate on considerable distances are shown in [1] and in a number of more recent works cited, for instance, in [2]. The behaviour of the intense relativistic electron beam propagating along the interface of two different media is the subject of many investigations. Indeed, in [3] the ability of reflecting of the intense electron beam from the conducting surface is shown. Investigations of this effect carried in [4] cleared a number of main features of such a reflection. The first experimental results of the intense relativistic electron beam interaction with the ferromagnetic surface are given in [5]. The wide possibilities of practical applications of this phenomenon highly stimulated investigations of it. The problem of interaction of charges and currents with different media can be treated properly by the method of the "mirror" image [6,7]. If we have direct current in the media with  $\mu_1$  on the certain distance from media with  $\mu_2$  then for the image current  $I'$  the expression  $I$  is valid:

$$I' = I \left( \mu_2 - \mu_1 \right) \left( \mu_2 + \mu_1 \right)^{-1}. \quad (I)$$

In the case of pulse current propagating along the metal surface near it we must take into consideration induced AC which cause the seeming decrease of the metal magnetic permeability. Using the "mirror" image method it is convenient to introduce the so-called quasimagnetic permeability [8].

The metals with high conductivity and relative magnetic permeability  $\mu_2 = 1$  behave in the fields of high frequency as diamagnetics with quasipermeability  $0 \leq \mu_q < 1$ . In the case of superconductor  $\mu_q = 0$ . The value of quasipermeability of ferromagnetics is also dependent on the frequency of the

alternating field, its intensity and can take values of  $\mu_2 > \mu_q > 0$ . The force applied to the unit of the conductor length with the current  $I$  located on the distance "d" from the interface of a medium with magnetic quasipermeability is equal:

$$F = \frac{\mu_0 I}{2\pi d} (\mu_q - \mu_1)(\mu_q + \mu_1)^{-1}$$

So the force of the current interaction with the interface of two given media isn't single-valued. Its value and sign depend upon the electrodynamic and geometric parameters of the system under investigation, the intensity of electromagnetic field and rate of the changing of pulse currents. It should be taken into consideration several peculiarities of intense beams when you investigate their behaviour during the propagation along the interface of two different media. Existing intense relativistic beams are characterized by the high rate of the current increase (approximately  $10^{13} - 10^{14}$  A/s) and high values of self electric and magnetic fields. When propagating in the gas or prematurely generated plasmas which are needed for the self focusing of these beams the partial neutralization of the beam charge takes place and a reverse current  $I_0$  flowing in the beam channel is induced which neutralizes the magnetic field of the beam.

In this paper we report about the experimental investigation of the intense self focusing electron beam interaction with the copper plate and ferromagnetic surface.

The scheme of the experimental set up is shown in Fig. 1. The electron beam 1 generated from the cathode 2 of the beam generator TONUS [9] was transmitted through the 50 micron titanium foil 3 into the drift chamber 4. Dimensions of the chamber were  $500 \cdot 500 \cdot 200 \text{ mm}^3$ . The energy of electrons was 1 MV, the beam current was 47 kA, the pulse duration was 50 ns, the rise time was 20 ns, the beam diameter was 30 mm. The copper reflecting plate 8 of 1 mm thickness was installed on movable supports so that the location of the copper plate can be changed without disturbing of vacuum inside of the chamber. During the measurements of the reflected beam current the Faraday cup was installed on the curve 10 and the beam reflected on the various angles drifted along equal distances before falling on the Faraday cup. The reflecting plate was electrically connected with the drift chamber. The upper lid of the chamber was made of plastic; the inner surface was covered with copper net-liner. Throughout, photographing of the integral luminosity of the beam was fulfilled. The residual pressure of the gas in the drift chamber varied from  $10^{-3}$  to 5 Torr. The photos of the beam luminosity in different conditions of the gas focusing during the reflection from copper plate are given in Fig. 2.

The value of current losses of the reflected electron beam is the question of special interest. Obviously the minimal losses are predicted when the focusing forces dominate over external repel forces. In our case it takes place in the range of angle of the beam entering from  $0^\circ$  to  $30^\circ$  when there are no visible changes in the structure of the beam in the point of the beam interaction with the surface (see, for instance, Fig. 2, b).

The stabilization of the trajectory when the current is changing is obviously connected with the appearance of the conducting channel after the gas breakdown. A similar effect was observed in [10].

The measurement of losses during the reflection was carried out by the measurements of the beam current after its reflection from the metal plate and by the comparison with the current in the absence of the reflecting plate. In both cases the lengths of drift ways were equal. The results of these measurements are given in Fig. 3. In the region between curves 2 and 3 all current values corresponding to the condition with and without the reflecting are located. For the angles  $\alpha$  between  $0^\circ$  and  $30^\circ$  the value of losses of electrons due to the reflection is not bigger than the experimental error, i.e., 10%.

The maximum incident angle at which the reflection takes place without considerable losses depends on parameters of the beam and gas focusing conditions which determines the degree of the charge and current neutralization and the beam radius. The critical angle in our experiments at which the complete stopping of the beam took place was varied with the pressure of residual gas from  $35^\circ$  to  $48^\circ$ . The critical angle value for fixed energy of beam electrons and fixed value of the beam current was increased with the pressure decrease. With the pressure decrease the whole current value was increased and accordingly to that the interaction between the beam and plate was increased too. The effectiveness of the beam reflection vs pressure of residual gas is given in Fig. 4. The angle values of the reflection " $\beta$ " at  $\alpha = 0^\circ$  vs the initial distance between the beam axis and the reflecting plate for several pressure values are also given. Experimental

investigations demonstrated that  $\beta$  angle depended on the values of the incident  $\alpha$  angle and it was always less than  $\alpha$ . The difference between angles  $\alpha$  and  $\beta$  is increasing with the incident angle. The reason of this may be the increase of the interaction between the incident and reflected beams with the increase of the angle  $\alpha$ .

In this case the equation of the electron motion of the incident beam in the field of the image current can be written in the form:

$$\gamma m \frac{d^2 X}{dt^2} = \frac{\beta^2 N e^2}{X} \left( \frac{1 + \cos 2\alpha}{2} \right)$$

and for the reflected beam electrons with the correction on the interaction with incident beam we have an equation:

$$\gamma m \frac{d^2 X}{dt^2} = \frac{\beta^2 N e^2}{X} \left\{ \frac{1 + \cos 2\alpha}{2} - \frac{\sin \beta \cos \beta [1 - \cos(\alpha + \beta)]}{\sin(\alpha + \beta)} \right\}$$

Solving this equation we have the angle values  $\alpha$  and  $\beta$  which are given in Table I. Observed values of "B" are somewhat smaller than cited ones in Tables. For instance, for angles  $\alpha = 15^\circ, 20^\circ, 25^\circ$  and  $30^\circ$  the angle  $\beta$  is consequently  $13^\circ, 16^\circ, 20^\circ$  and  $24^\circ$ . Other reasons for the decrease of the angle  $\beta$  may be the generation of free oscillations of the beam diameter suggested in [11] and the influence of the drift chamber walls.

The photo of the self focusing beam attracted to the ferromagnetic plate is given in Fig. 5. The beam was injected in the direction parallel to the ferromagnetic surface on different distances  $d$ . In Table II



different values of  $\ell$  in the case of the ferromagnetic surface are given with  $d = 40$  mm and 70 mm and different pressures in the drift chamber.  $\ell$  is the distance along the plate at which the beam strikes it. The net current value is decreased with the increase of the pressure in the given pressure range [2] and it is the explanation of  $\ell$ -dependence (which characterizes the attractive force of the plate) from the pressure in the chamber for  $c = 70$  mm. Nevertheless, the attractive force of the plate for  $d = 40$  mm is approximately independent of  $P$ . The possible explanation of this can be the nonlinear dependence of the magnetic permeability of the frequency and the amplitude of the magnetic field of beam the phenomena of the magnetic saturation.

According to these experimental results, the application of the reflecting and attraction effect for the organizing of the complex trajectories of self focusing intense electron beams and their capture on closed orbits can be discussed.

# REFERENCES

1. S. Graybile, S. Nablo, Appl. Phys. Letters, 8, 18, 1966.
2. A. V. Agafonov. Atomnaya tekhnika za Rubejom, 10, 31, 1973.
3. W. Link, IEEE Trans. NS-14, N°3, 777, 1967.
4. A. N. Didenko, A. I. Rjabchikov, V. A. Tuzov, Yu. P. Usov, Zhurnal Techn. Fiz., 44, 2613, 1974.
5. A. N. Didenko, A. V. Petrov, A. I. Rjabchikov, V. A. Tuzov, Yu. P. Usov, Pisma v Zhurnal Techn. Fiz., 1, 11, 538, 1975.
6. L. P. Landau, E. M. Lifshits, "Electrodinamika Sploshnih sred", M., Izdat. "Nauka", 1973.
7. V. Smyte, Electrodinamika i electrostatika, Perevod c angliyskogo, M., Izdat. Inostr. Literatury, 1974.
8. Ia. T. Turovskiy, Technicheskaya electrodinamika, M., Izdat. Energia, 1974.
9. I. Z. Gleyzer, A. N. Didenko, L. P. Dronova, A. G. Gerlitsin, G. I. Kotliarevsky, B. V. Okulov, V. S. Pak, N. S. Rudenko, G. E. Remnev, V. I. Smetanin, V. A. Tuzov, Yu. P. Usov, A. A. Shatanov, Atomnaya Energia, 36, 5, 378, 1974.
10. M. Friedman, I. M. Vitkovitsky. Appl. Phys. Lett., 25, Sept., 1, 1974.
11. K. V. Hodataev, Atomnaya Energia, 32, 5, 379, 1974.

TABLE I

$\mathcal{L}$	$5^{\circ}$	$10^{\circ}$	$15^{\circ}$	$20^{\circ}$	$25^{\circ}$	$30^{\circ}$	$35^{\circ}$	$40^{\circ}$
$\beta$	$4,75^{\circ}$	$9,5^{\circ}$	$14^{\circ}$	$18,5^{\circ}$	$23^{\circ}$	$26^{\circ}$	$30,5^{\circ}$	$34^{\circ}$

TABLE II

p, Torr d, mm	0.1	0.15	0.2	0.35
40	320	285	305	280
70	430	445	465	500

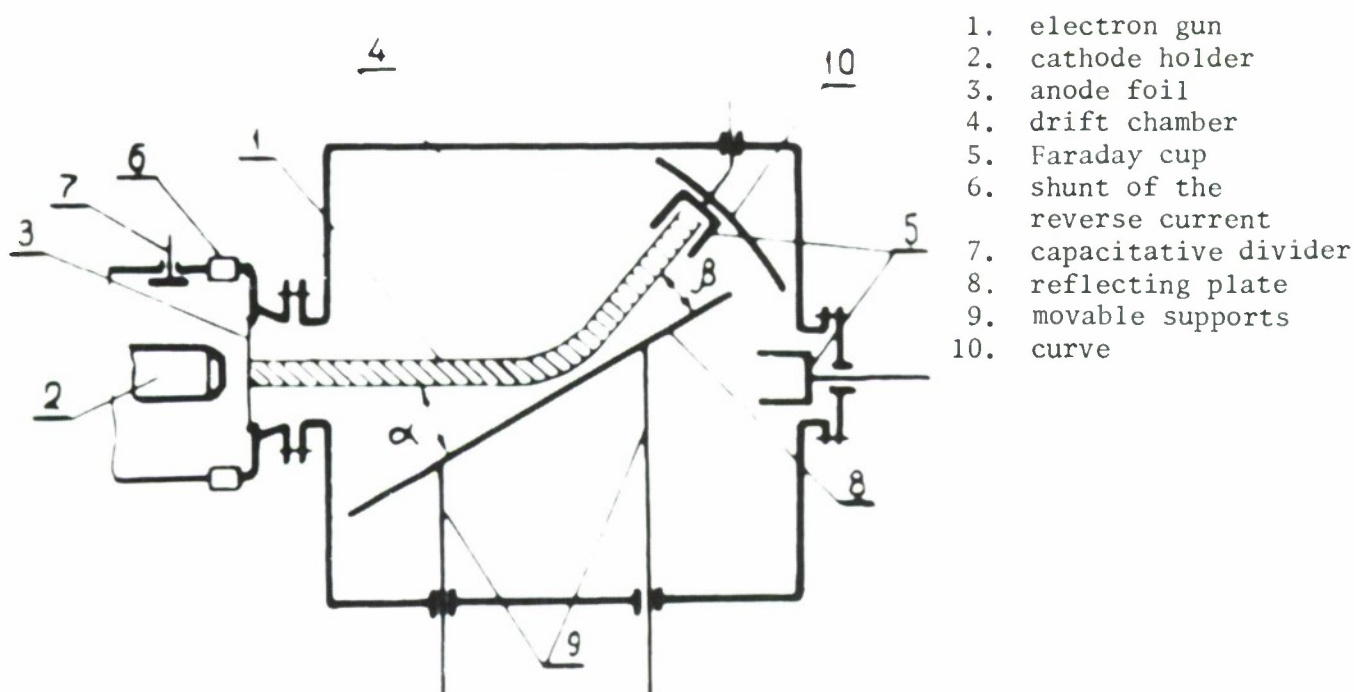
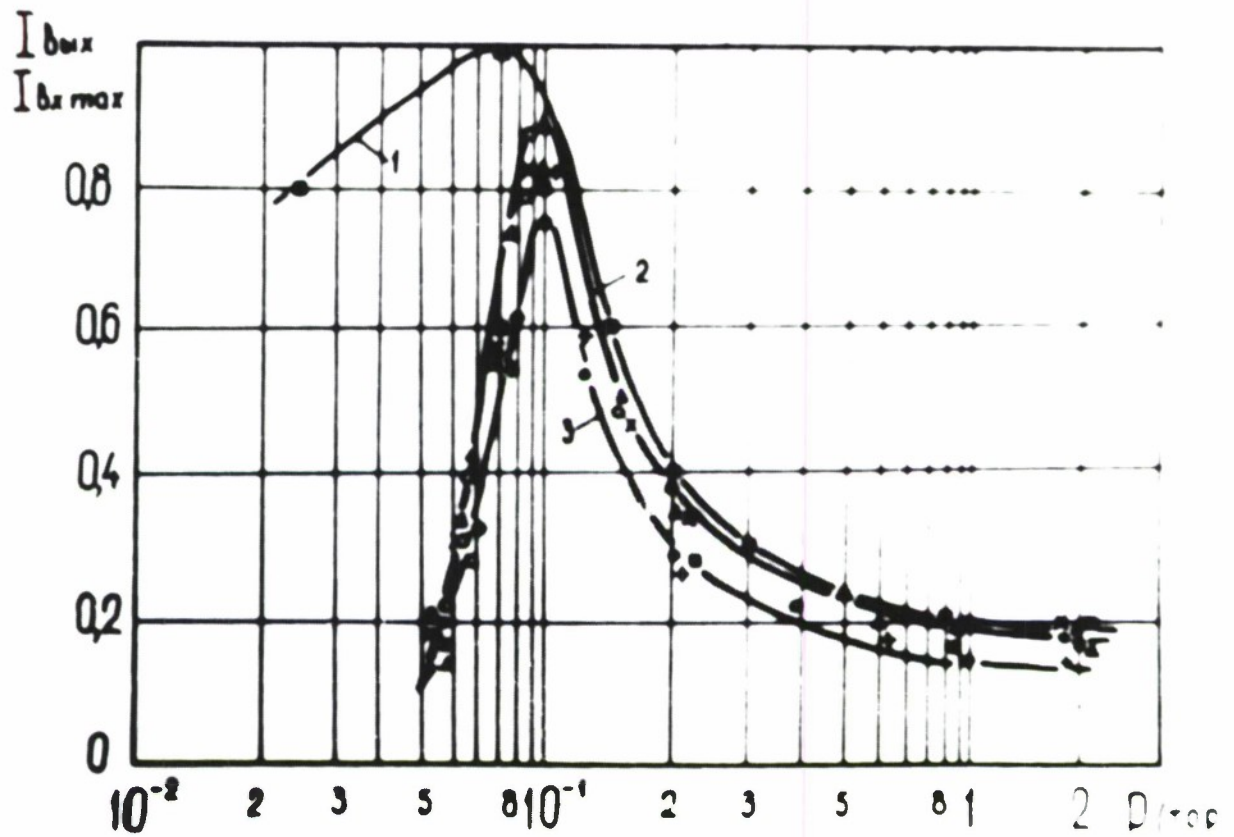


Figure 1. The scheme of the experimental set up.

The pressure of the residual gas, in Torr: a - 2; b,c, d - 0.1; e - 0.2.  
The incidence angle  $\alpha$ , in degrees:  
a - 0; b - 15; c,d - 35; e - 45.



Figure 2, The photos of the reflected beam trajectory.

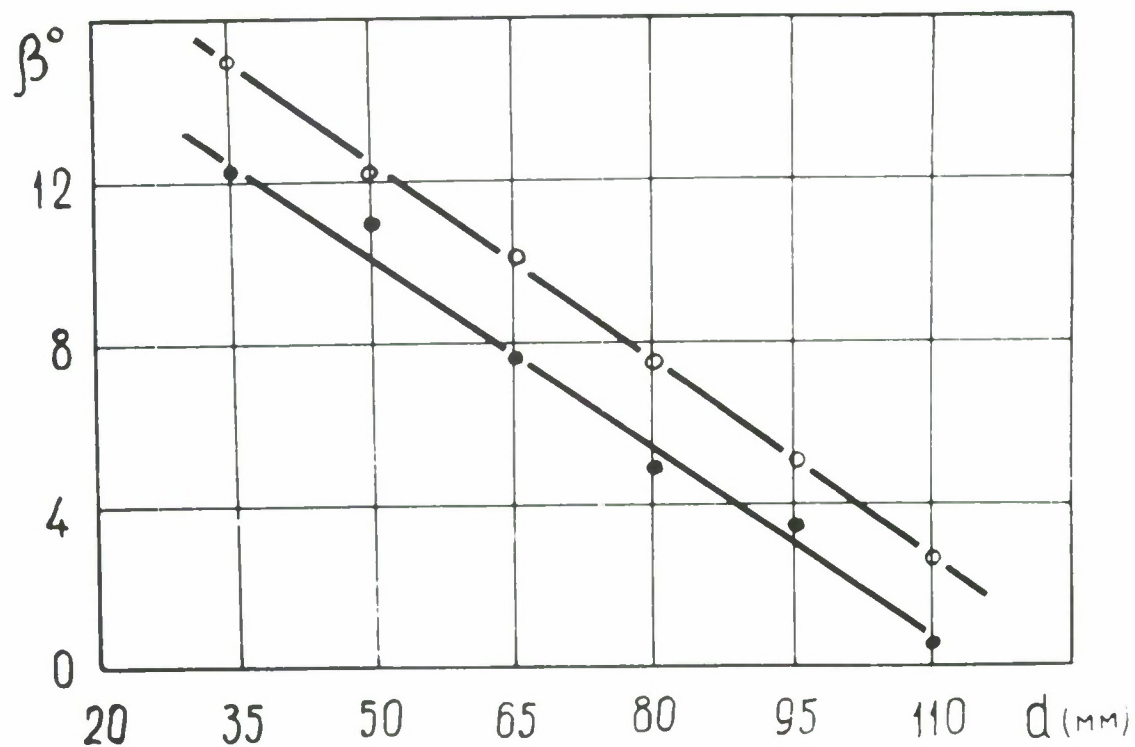


1- on the entrance of the chamber,

2-3 - for angles  $\alpha$ :  $\Delta$  -  $0^\circ$ ,  $\times$  -  $5^\circ$ ,  $\circ$  -  $10^\circ$ ,  $+$  -  $15^\circ$ ,

$\blacktriangle$  -  $20^\circ$ ,  $\blacksquare$  -  $25^\circ$ ,  $\bullet$  -  $30^\circ$ .

Figure 3. The dependence of the whole current on the pressure of the residual gas.



The pressure of the residual gas, Torr: o - 0.69; ● - 1.2

Figure 4. The dependence of the reflection angle for the incident angle  $\alpha=0^\circ$  vs the initial distance from the axis of the beam to the metal surface.

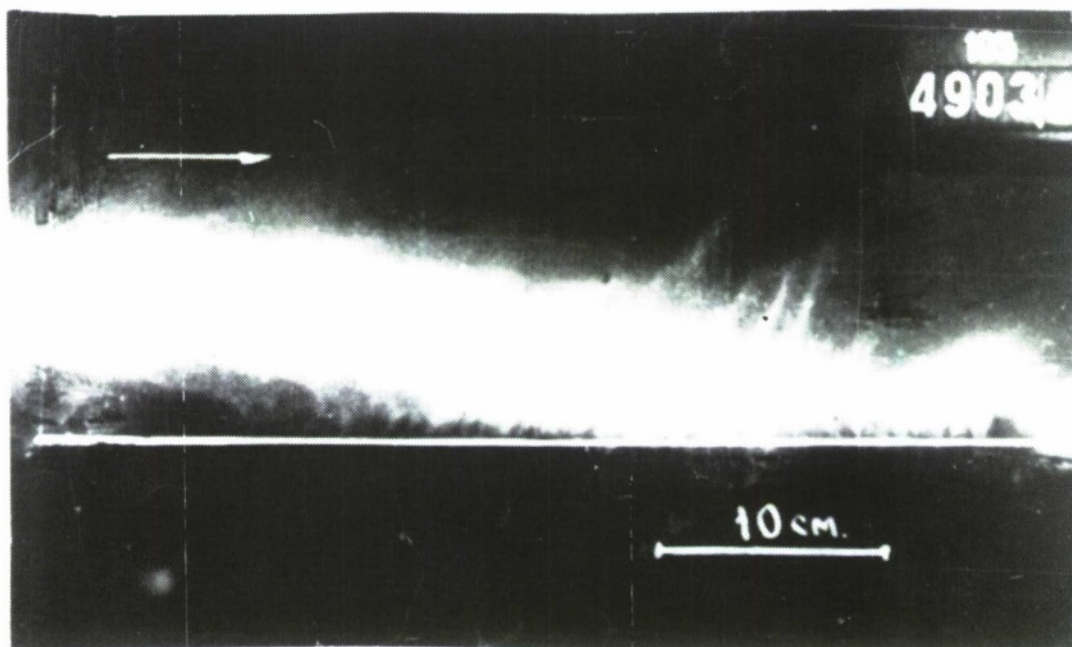


Figure 5. The photo of the attracted beam trajectory.



# **CHAPTER 3**

## **ACCELERATOR TECHNOLOGY**

## PROTO-I SWITCHING AND DIODE STUDIES\*

K. R. Prestwich, P. A. Miller, D. H. McDaniel, J. W. Poukey,  
M. M. Widner, S. A. Goldstein

Sandia Laboratories, Albuquerque, New Mexico 87115

### ABSTRACT

Proto-I is a 3 MV, 800 kA, 24 ns electron beam accelerator that is under development at Sandia Laboratories. It represents an initial effort to develop a scalable technology that is applicable to accelerators for electron beam driven, inertial confinement fusion studies. Energy is supplied to each of the two diodes from six oil-dielectric Blumlein transmission lines (PFL) operating in parallel. A Marx generator charges three intermediate storage, water-dielectric capacitors which subsequently transfer the stored energy to the PFL. The discharge of the PFL is initiated by the simultaneous closure of 12 triggered oil-dielectric rail switches. Data are presented on the operation of these multichannel switches. The two diodes have a common anode. Cathode diameters can be varied from 10 to 60 cm. Results of initial diode experiments and comparisons with theory are discussed. Plasma filled diode experiments are also reported, indicating pinch collapse velocities in excess of  $10^9$  cm/s.

\*This work was supported by the Energy Research and Development Administration.

## INTRODUCTION

The electron beam fusion program<sup>1,2</sup> will require high power electron beams ( $\sim 10^{14}$  W) with pulse duration of 10-20 ns for breakeven experiments. A research and development program with long-range goals of reaching these levels has been initiated at Sandia and is proceeding on two parallel paths; the first uses transformer oil as the primary dielectric and the second includes an investigation of the feasibility of using water for the fast energy storage dielectric. Proto-I represents the initial efforts to develop an accelerator<sup>3</sup> that could be scaled to substantially higher powers<sup>4</sup> and which utilizes transformer oil as the principal dielectric. The water dielectric approach will result in an accelerator called Proto-II and is discussed elsewhere in these Proceedings.<sup>5</sup>

Proto-I design goals are 3 MV, 800 kA (two 400 kA beams), and 24 ns. At the present time it has been operated at 2 MV, 530 kA, 24 ns level and is now undergoing a planned upgrade to its full design level.

## ACCELERATOR DESIGN

Figure 1 is a block diagram outlining the major components of Proto-I and the interaction of these components. As indicated, the accelerator has two diodes with a common anode to facilitate two-sided irradiation of targets. Energy is fed into each of these two diodes from six sets of parallel plate, pulse forming transmission lines (PFL) connected in parallel around the periphery of the diode. These transmission lines can be charged either directly by a Marx generator or by an intermediate storage capacitor. The discharge of these transmission lines into the diode is initiated by the nearly simultaneous closure of twelve multichannel oil-dielectric rail switches. For low jitter operation of these three electrode switches, a

large amplitude ( $\sim 2$  MV) trigger pulse is required. The trigger pulse is generated by discharging a water dielectric PFL into a set of oil-dielectric transmission lines that transmit the pulse to all twelve switches. This water dielectric PFL is positively charged by another Marx generator.

Figure 2 is an artist's drawing of the accelerator, and Fig. 3 is a photograph of the transmission lines and diode area during the early stages of construction. As shown in Fig. 3, there are six stacks of transmission lines, each stack consisting of five  $120\text{ cm} \times 240\text{ cm}$  and  $10\text{ cm}$  electrodes. The twelve sets of parallel plate transmission lines are configured as Blumleins with six of these connected in parallel around each diode.

The center electrode is common to both the upper and lower sets of transmission lines and becomes the high voltage electrode during discharge of the transmission lines. These center electrodes are attached to the common anode of the two diodes. Three  $4\text{ }\mu\text{H}$  inductors connected at the diode end of the PFL ground these center electrodes during charge. The impedance of each transmission line is  $22\text{ }\Omega$ . The effective impedance feeding each diode is  $7.2\text{ }\Omega$ , and the capacitance of each transmission line including fringing fields is about  $0.7\text{ nF}$ . Thus, the total capacity of the 24 transmission lines is  $17\text{ nF}$ . The initial pulse power and diode experiments were conducted with one Marx generator directly charging the PFL in  $760\text{ ns}$ . With this charge rate, the self-breakdown voltage of the PFL is  $2.5\text{ MV}$ . About two hundred shots have been fired near the  $2.0\text{ MV}$  level with only a few minor problems.

Three water-dielectric, intermediate storage capacitors are being added to the system. These  $8.4\text{ nF}$  capacitors will be charged by the Marx generator in about  $900\text{ ns}$ . The lower capacitance and inductance of the network, composed of one of these capacitors, one-third of the PFL, and a gas switch, will allow

the PFL to be charged in 180 ns. Because of the time dependence of the oil dielectric strength, the estimated transmission line breakdown voltage is increased to 3.8 MV. The new operating level will be 3 MV.

The switch in these circuits is composed of 3 MV sulfur hexafluoride trigatrons<sup>6</sup> developed at Sandia Laboratories for the Hydra accelerator.<sup>7</sup> This switch requires a 150 kV trigger pulse rising in 70 ns for operation with < 1 ns r.m.s. jitter. This same switch is used in the trigger pulse generator. The trigger pulse for all four switches will be generated from a single, 150 kV pulse generator.

The Proto-I Marx generators are constructed in the same manner as the Marx generator developed for the Hydra electron beam accelerator. Eight capacitors and four spark gaps hang in a row. During the 2 MV operation, both the positive and negative Marx generators had 5 rows consisting of 38 capacitors and 19 spark gaps. During 3 MV operation a sixth row will be added to the negative Marx (46 capacitors) that charges the PFL. The SF<sub>6</sub> insulated spark gaps are the type developed by the Physics International Company for the Aurora accelerator.<sup>8</sup> The negative Marx erects 60 ns faster than the positive one. The r.m.s. jitter of each Marx generator was measured to be 20 ns. The trigger PFL capacitance is in series with an inductor to adjust the peak voltage to occur at the appropriate time for the trigger pulse to close the oil switches when the PFL voltage is 85-90 percent of its peak value.

#### TRIGGER PULSE GENERATOR

The positive Marx charges the water-dielectric PFL that generates the trigger pulse to 2.7 MV. The 7  $\mu$  water dielectric transmission line is then discharged into a 20  $\mu$  section of oil dielectric transmission line generating

a 2 MV trigger pulse with a 30 ns, 10-90 risetime. These transmission lines provide equal propagation length from the trigger PFL to each of the twelve switches. The ends of these transmission lines are separated from the rail switch trigger electrodes by isolating resistors and switches. The 80  $\Omega$  isolation resistors match the impedance of the final sections of these transmission lines such that the energy in the trigger system is absorbed in a minimum amount of time after the switches close.

#### OIL DIELECTRIC RAIL SWITCHES

The discharge of the Blumlein transmission lines is initiated by three-electrode, oil-dielectric rail switches developed at Sandia Laboratories for this application.<sup>9</sup> A drawing of this switch is shown in Fig. 4, indicating the sharp-edged, 6.4 mm thick trigger blade. The edge is sharpened to about 0.1 mm radius. The electrodes are 120 cm wide.

#### Development Tests of Three-Electrode Rail Switches

The test set-up used for developing the switches is sketched in Fig. 5. The two Marx generators presently in Proto-I were used. In this arrangement the trigger pulse was generated by directly connecting the positively charged transmission line to an isolating resistor and the trigger blade. The trigger pulse rises to 2 MV in 30 ns. For normal operation of the switch, the trigger electrode is located approximately one-third of the distance across the gap and is resistively biased accordingly. For lowest jitter operation, the blade location is adjusted such that the wide side of the gap closes about 5 ns before the narrow side. When the wide side closes, the trigger transmission line is connected in series with the PFL. The series combination of the isolation resistor and the impedance of the trigger transmission line must be large enough to keep the voltage drop across the PFL minimal. In this test the trigger transmission line



impedance was 40  $\Omega$ , and the isolation resistor was 100  $\Omega$ . The isolation resistor cannot be arbitrarily large because it is in series with the approximately 200 pf capacitance of the trigger blade and can limit the rise-time of trigger electrode voltage.

Figure 6 is a plot of the switch closure time vs voltage between the main electrodes. The straight line is a least squares fit to the data. The r.m.s. deviation from this line is a measure of the switch jitter and is 1.3 ns for this experiment. The ratio of the trigger pulse amplitude to the PFL voltage was kept constant at 0.94 during this test. Experiments were performed to determine the minimum value of this ratio and to investigate effects of different blade configurations. Table I is a partial summary of the results of these experiments. These results show that if the blade location is adjusted for optimum operation, the ratio can be reduced to 0.44 and still maintain low jitter operation.

#### Proto-I Tests—Three-Electrode Switches

The arrangement in Proto-I has several features that could have increased the switch jitter from the experimental set-up. The main electrodes are firmly attached to the Blumlein electrodes. Mechanical tolerances in the electrode flatness and in the support system make the 6.9 cm main electrode spacings vary by  $\pm 0.25$  cm. These variations affect operation of the twelve switches. The isolation switches are needed to allow biasing of the trigger electrodes during charging of the PFL. The duration of time from application of the trigger pulse to closure of the switch was determined by monitoring the trigger pulse waveshape. An independent measurement of time that closure of the switches occurred was made with capacitive voltage monitors on each transmission line. These data are represented in the bottom two lines of Table II.

The jitter from the range is obtained by assuming a normal distribution. Both measurements indicate that the jitter is 2 ns at the 1.8-2.0 MV level.

#### Proto-I Tests—Two-Electrode Switches

Two-electrode rail switch<sup>10</sup> tests were also performed using Proto-I. Figure 7 is a sketch showing the experimental arrangement for these tests. One set of transmission lines was used as an intermediate storage capacitor. Three SF<sub>6</sub> trigatrons were used for switching the charged lines into the uncharged lines. Table III is a tabulation of the data from these experiments. It indicates that for charge times < 200 ns, low jitter operation exists. At 100 ns, significant numbers of channels and low jitter are achieved. The number of channels is fewer, but the electric fields are higher than in the three-electrode switch experiments; therefore, the risetimes are similar.

#### PULSE SHARPENING SWITCH

Figure 8 is a sketch showing a cross-section of the diodes, pulse sharpening switches, and the sections of transmission lines between the end of the Blumlein transmission lines and the diodes. The pulse sharpening switches were designed into the system for two reasons: the first was to attenuate the prepulse, and the second, as the name implies, to improve the risetimes of the output pulse by closing when the pulse nears peak value.

During the operation of Proto-I at the 2 MV level, the prepulse was < 30 kV and the pulse risetime about 10 ns. Therefore, the pulse sharpening switches were always mechanically closed. The prepulse was small because the inductance of three 4  $\mu$ H inductors in parallel that ground the center plate, and the inductance of ground connections from the upper and lower plates is of comparable value such that the prepulse is tuned to a minimum value.

A brief series of pulse sharpening switch experiments was performed on the test set-up described in the section on rail switches. The pulse sharpening switch was tested with several different gap spacings and electrode shapes. The three-electrode rail switch operation was degraded such that a 20 ns risetime pulse was applied to the pulse sharpening switch. When this pulse arrived at the switch, the displacement current that charged the switch capacity passed through the transmission line impedance generating a pulse in the line while the switch was open. Although several attempts were made to reduce the switch capacity, the amplitude of this pulse was always at least 38 percent of the peak voltage pulse. When the switch closed, the rise from this 0.38 amplitude to peak value was  $< 2$  ns, as shown in Fig. 9. Approximately 20 channels closed at electric fields of 2-4 MV/cm to give this fast risetime.

With the lower inductance of the intermediate storage capacitor discharge circuit and the capacitance between the lower PFL electrode and the tank, the circuit inductances cannot be tuned to give such a low value of prepulse as in the previous experiments. The calculated value of prepulse for 3 MV operation is 200 kV. Therefore, it will be necessary to use the pulse sharpening switch to decrease this level. The switch will be set to close at very low values of the output pulse since pulse sharpening should not be necessary. It may be desirable to adjust the prepulse to particular levels to aid in producing plasma within the diodes.

#### DIODES

The measured diode inductance varies from 16 nH with a 61 cm diameter cathode to 25 nH with a 20 cm diameter cathode. The cathodes were shorted at the diameters indicated for these tests. An additional 5 nH inductance

of the mismatched region between the pulse sharpening switch and the diode is in series with the diode inductance.

#### DIODE EXPERIMENTS

A series of diode experiments were carried out prior to installation of the three intermediate water capacitors with peak voltage of 2 MV. The primary purpose of the limited number of these phase 1 diode experiments was to determine conditions for self-pinching of the beams in the diode with a 24 ns pulse and 5-9 kJ of electron beam energy available in each diode. Two basic diode configurations were used with several variations on each. In the first, cathodes previously used on other accelerators were tested, and in the second configuration the diodes were filled with low density plasma. The basic diagnostics used were witness plate damage, pinhole camera, a PIN diode, and the diode voltage and current monitors.

#### SMALL DIAMETER CATHODES

Experiments were performed with cathodes listed in Table IV. When operated undermatched with peak voltage between 1.0 and 1.5 MV, and the corresponding currents of 360-240 kA, all of these cathodes showed some witness plate evidence of pinching. The smallest diameter pinch was produced by the '38' cathode. A photograph of this witness plate is shown in Fig. 10. Simulation of the anode witness plate damage with a hydrodynamic code<sup>11</sup> indicates that only 0.5 kJ was deposited in the 1 cm diameter pinch area. An interesting series of witness plate damage pattern with this particular cathode was obtained during the diode flashover experiments. In this case, the diode was effectively crowbarred at 18 ns in shot 86, and at 21 ns in shot 83. Photographs of these witness plates are shown in Fig. 11. Shot 86 shows a faint damage pattern over the complete



anode, and in shot 83 melting occurred over most of the central  $28 \text{ cm}^2$  of the anode. Shot 85 shows the complete pinch when crowbarring did not occur. One interpretation of these data is as follows: During the first part of the pulse, the electrons move straight across the anode-cathode gap. As the current approaches the critical current ( $8500 \text{ Sv r/d amps}$ ), the outermost electrons experience mild pinching such that the energy deposition is nearly all within the central  $28 \text{ cm}^2$  area. Recent experiments on the Nereus accelerator have shown that a deposition of  $1000\text{-}3000 \text{ J/gm}$  in the anode is required to form sufficient plasma for pinching.<sup>12</sup> The total beam energy was calculated from voltage and current traces and found to be  $5.5 \text{ kJ}$ . If  $4.5 \text{ kJ}$  of this energy is deposited over  $28 \text{ cm}^2$  with  $1 \text{ MeV}$  electrons, the anode dose would be between  $800\text{-}1500 \text{ J/gm}$  depending upon the angle of incidence of the electrons and would be sufficient to generate anode plasma. Hence, a reasonable explanation of the data would be that  $0.5 \text{ kJ}$  was deposited uniformly inside a  $6.4 \text{ cm}$  radius in the anode early in the pulse— $4.5 \text{ kJ}$  was deposited inside a  $3.0 \text{ cm}$  radius to form anode plasma and during the final portion of the pulse  $0.5 \text{ kJ}$  was subsequently deposited in the pinch region. The peak current ( $240 \text{ kA}$ ) in shot 83 exceeded the critical current ( $150 \text{ kA}$ ) by a factor of  $1.6$ . The current in '38' shell was measured to be  $14 \text{ kA}$ , and the total energy from this current is  $0.22 \text{ kJ}$ .

A numerical simulation<sup>13</sup> of a  $20 \text{ cm}$  diameter cathode indicating a similar beam behavior, as discussed above, is shown in Fig. 12. In this case, the anode-cathode gap was  $2 \text{ cm}$  and the peak current and voltage were  $280 \text{ kA}$  and  $1.4 \text{ MV}$ , respectively. Trajectory a is with  $220 \text{ kA}$  electron current only and shows a slight decrease in beam radius at the anode compared to the cathode radius. Trajectory b is with  $250 \text{ kA}$  of electron current and  $30 \text{ kA}$  ion current flowing in region  $5 < R < 10 \text{ cm}$ , and a slight pinch occurs. Trajectory c has  $50 \text{ kA}$  of ion current flowing in  $R < 10 \text{ cm}$ , and a tight pinch is obtained. These three trajectories can be considered as time sequences in the diode. The experiment

showed a slight pinch; therefore, it is concluded that insufficient time or beam energy was available to generate the required plasma to allow for ion production and flow in the central 5 cm radius area necessary for a good pinch.

As mentioned above, since the cathodes are grounded, the current distribution on the cathode can be measured with Rogowski coils. Although current distributions at the anode have been reported previously, these data are the first indicating the current distribution at the cathode. With the 12.7 cm diam '38' cathode, the total cathode current was 240 kA and the '38' shell carried 14 kA. An additional ring of 20 cm o.d. and 15 cm i.d. was added to this cathode, as shown in the lower diode in Fig. 13. The gap spacing was 1.3 cm and peak diode voltage was 1.2 MV. A tabulation of the peak measured current values and a comparison with numerical code calculations with ions assumed to be emitted over the complete anode is shown in Table V. The code indicated that 60 kA of this current consisted of ion flow, but there is no direct experimental confirmation of this prediction at this time.

All of the small diameter cathodes were operated with mean electric fields in the anode-cathode gaps  $> 500$  kV/cm, and the metal cathodes sprayed with an aerosol carbon mixture emitted uniformly in these cases.

#### LARGE DIAMETER CATHODES ( $> 20$ cm Diameter)

Some experiments were run with large diameter cathodes (o.d. from 20-60 cm). The anode-cathode gaps were correspondingly larger with mean electric fields as low as 200 kV/cm. Damage patterns and TLD maps indicated the current density at the anode was very nonuniform azimuthally (as much as a factor of six as shown by the TLD map with these low fields). These results indicate that for operation



at such low fields, it will be necessary to have additional means to provide for a uniform plasma emitter. Uniform emission was obtained with razor blade cathodes with mean electric fields of 260 kV/cm. Because this type of cathode produces a higher temperature electron beam, it is unlikely that it could be successfully pinched to a small diameter.<sup>15</sup>

#### PLASMA FILLED DIODE EXPERIMENTS

Since beams generated in standard cathode-anode arrangements require a substantial portion of the beam energy to create anode plasma with resultant delays in pinch formation, beam focusing experiments were attempted with a low density plasma injected into the diode prior to application of the high voltage pulse.<sup>16</sup> The plasma also makes operation with large anode-cathode gaps possible. Upon application of the diode voltage, a collisionless sheath is formed in the plasma at the cathode surface. Across this sheath a space charged limited flow of electrons and ions occur. Two techniques were successfully used for placing this plasma in the anode-cathode gap. Both experimental arrangements are sketched in the upper diode in Fig. 13. In the first arrangement, the plasma is formed with an arc first created in a coaxial plasma gun and then allowed to expand into the diode. In the second case, a 15 J laser beam is deposited on a carbon-coated anode, and the blow-off forms the plasma that then expands into the gap.

In the gun-injected plasma experiment, the plasma source was the same one as used in previous experiments.<sup>16</sup> The source was usually located 15 cm above the cathode, and the plasma was observed to expand at the rate of 1.3 cm/ $\mu$ s. The cathode was a wire mesh with either a 56 cm o.d. and 25 cm i.d., or a 28 cm o.d. and a 12.7 cm i.d. The anode-cathode gaps were varied from 2.5 cm to 5.4 cm. The vast majority of the experiments were run with 5.4 cm anode-cathode spacing;

the ion density was varied to control the impedance. The ion density was typically about  $3 \times 10^{12} \text{ cm}^{-3}$  and was varied by controlling the time between the discharge of the plasma source and the application of the electron beam accelerator voltage to the diode. Diode impedance at peak current could be varied from a short circuit to  $10 \text{ }\Omega$ ; thus, the voltage and current of Proto-I could be adjusted through an effective operating range of the 0.8-2 MV and 440-260 kA without changing the diode geometry. Since the cathode is an annulus, current could flow between the plasma gun and the anode. This current was measured to be 5 kA. The diode current exceeded the critical current for pinching by as much as a factor of 7.

The same impedance control can be achieved using a laser interacting with a carbon-coated anode to generate the plasma. The laser beam was defocused to 25 cm diameter, giving an irradiance at the anode of  $2 \text{ MW/cm}^2$  to create a plasma with a few times  $10^{12}$  ion density expanding at  $0.3 \text{ cm}/\mu\text{s}$ . Plasmas with higher ion densities generated with more intense laser beams shorted the diode when allowed to fill the anode-cathode gap.

Numerical simulation<sup>16</sup> of a plasma-filled diode with a 28 cm o.d. and 10 cm i.d. cathode, and a 5 cm anode-cathode gap provided agreement with the measured 330 kA peak current when the virtual anode-cathode spacing was 2 cm, as shown in Fig. 14. This calculation indicated that 250 kA was electron current and 80 kA was ion flow. This has not been confirmed experimentally. The trajectories indicate that one would expect the beam to pinch.

The electron beams did pinch with either plasma source and either cathode arrangement, but the pinch had a 3.8 cm diameter. A photograph of the witness plate damage for a 1.9 MV, 310 kA beam is shown in Fig. 15. Integration of the voltage and current waveshapes indicate that the diode electron and ion beam

energy was 12 kJ. If 26 percent of the current is ion flow as indicated by the numerical simulation, then the electron beam is 230 kA and about 9 kJ. Simulations of the hydrodynamic response of the targets indicate that  $\sim 6$  kJ was deposited in the damage region. The pinch diameter limitation was consistently 3.8 cm. When the 230 kA electron beam is 3.8 cm in diameter, the electron density is a few times  $10^{12} \text{ cm}^{-3}$ , about the same as the background ion density. Thus, electrostatic forces are thought to prevent the beam from collapsing further ; the associated electric fields are not large enough to move ions into the pinch region from the surrounding area in a few nanoseconds. To increase the current density within the pinch, it may be necessary to provide a higher density ( $\sim 10^{15} \text{ cm}^{-3}$ ) plasma on axis in conjunction with the low density plasma ( $\sim 10^{12} \text{ cm}^{-3}$ ). These plasma could be generated with the apparatus drawn in Fig. 14, where the plasma gun provides the low density plasma throughout the volume and the laser is focused to a small spot on the anode. Such an experiment will be carried out in the near future at the 3 MV level after installation of the water capacitors is completed.

In the above plasma source experiments, the electron beam pinched from either 28 or 56 cm diameter cathodes to a 3.8 cm diameter, and about 6 kJ out of a possible 9 kJ were deposited in the pinch area. This implies that either the electrons pinch from the outer edge of the cathode throughout the complete pulse or the pinch collapse velocity exceeds  $10^9 \text{ cm/s}$ . The diode operation was essentially the same whether or not the center 12.7 cm diam part of the cathode mesh was removed, indicating agreement with theoretical predictions that the beam is primarily emitted from the outer edge of the cathode.

## CONCLUSION

A description of the Proto-I accelerator has been given along with results of the first phase of diode and switching experiments. Several hundred shots have been fired at the 2 MV level with an average of 10 channels closing in the oil dielectric rail switches. The switch jitter is 2 ns and 10-90 risetimes of the diode current were measured to be 10 ns. Although the experiments confirmed earlier predictions<sup>2</sup> that preinjected plasma would be required to obtain pinching during the relatively short pulse, only mild pinches (6 kJ of beam in 3.8 cm diam) were obtained in the diode experiments. This is thought to be due to insufficient charge neutralization near the diode axis. Techniques for improving the pinch current density are being investigated. Experimental current measurements have been shown to agree with numerical calculations for three different diode configurations.

## REFERENCES

1. Yonas, G., et al, Nuclear Fusion 14, 1974, p. 731.
2. Chang, J., et al, Fifth Conference on Plasma Physics and Controlled Nuclear Fusion Research, International Atomic Energy Agency, Tokyo, Japan, November 11-15, 1974.
3. Prestwich, K. R., IEEE Trans. on Nucl. Sci. NS-22, No. 3, June 1975, p. 975.
4. Martin, T. H., and Prestwich, K. R., Proceedings of the International Conference on Energy Storage, Compression and Switching, Asti, Italy (November 1974) - to be published.
5. Martin, T. H., et al, Proceedings of the International Topical Conference on Electron Beam Research and Technology, Albuquerque, New Mexico (November 1975) - to be published.
6. Tucker, W. K., Sandia Report SC-DR-72-0506.
7. Martin, T. H., IEEE Trans. on Nucl. Sci. NS-20, No. 3, June 1973, p. 289.
8. Bernstein, B., and Smith, I., IEEE Trans. on Nucl. Sci. NS-20, No. 3, June 1973, p. 294.
9. Prestwich, K. R., Proceedings of the International Conference on Energy Storage Compression and Switching, Asti, Italy (1974) - to be published.
10. Johnson, D. L., Proceedings of the International Conference on Energy Storage, Compression and Switching, Asti, Italy (1974) - to be published.
11. Widner, M. M., and Thompson, S. L., Sandia Report SAND-74-381.
12. Swain, et al, "The Characteristics of a Medium Current Relativistic Electron Beam Diode," submitted to the Journal of Applied Physics for publication.
13. Poukey, J. W., Appl. Phys. Lett. 26, No. 4, February 15, 1975.

References (continued)

14. Miller, P. A., et al, Proceedings of the First International Topical Conference on Electron Beam Research and Technology (November 1975) - to be published.
15. Hadley, G. R., et al, Proceedings of the First International Topical Conference on Electron Beam Research and Technology (November 1975) - to be published.
16. Miller, P. A., et al, Phys. Rev. Lett. 35, No. 14, October 6, 1975, p. 940.



TABLE I

Multichannel, Triggered, Oil Switch Test Data

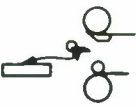
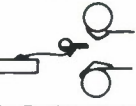

ELECTRODES	BIAS	# TESTS	VOLTAGE RANGE MV	AVERAGE NUMBER CHANNELS	AVERAGE OUTPUT RISETIME ns	AVERAGE SWITCH RISETIME ns	RELATIVE TRIGGER VOLTAGE	CLOSURE TIME V-MV, T - ns $\sigma$ - ns
STRAIGHT SHARP EDGE 	0.31	38	1.3 - 1.9	10	13		0.94	T = 57 - 15V $\sigma$ = 1.3
	0.28	14	1.6 - 1.8	12	14		1.06	T = 35 $\sigma$ = 1.6
STRAIGHT SHARP EDGE 	0.30	10	1.5 - 2.0	7	14	10	0.92	T = 63 - 16V $\sigma$ = 1.6
	0.36	48	1.4 - 2.0	9	11	8	0.92	T = 67 - 15V $\sigma$ = 2.1
SERRATED BLADE 20 POINTS 	0.28	15	1.6 - 2.0	11	11	8	0.83	T = 33 $\sigma$ = 1.6
	0.32	5	1.8 - 2.0	10	12	8	0.69	T = 32 $\sigma$ = 1.4
	0.28	12	1.6 - 2.0	8	12	10	0.60	T = 39 $\sigma$ = 1.6
	0.19	9	1.8 - 2.1	8	12	9	0.44	T = 37 $\sigma$ = 1.3

TABLE II

Triggered Switch Closure Times

V (MV)	1.6	1.7	1.8	1.9	2.0
CLOSURE TIMES (ns)	45	44	44	39	39
MEASURED SWITCH JITTER (ns)	3	3	3	3	2
CLOSURE TIME RANGE (ns)	11	10	9	8	8
JITTER FROM RANGE (ns)	3	3	3	2	2

TABLE III

## Untriggered Multichannel Switch Data

CHARGE TIME (ns)	RANGE OF CLOSURE TIMES (ns)	SINGLE SWITCH JITTER (ns)	NUMBER BRIGHT CHANNELS	SWITCH RISE TIME (ns)
90	3.9	1.6	4.2	8.8
120	4.8	2.1	4.1	9.4
130	5.5	2.6	3.2	9.7
170	7.3	3.2	2.5	11.0

TABLE IV

## Small Diameter Cathodes

	<u>o.d. (cm)</u>	<u>i.d. (cm)</u>
'38'	12.5	2.5
	20.0	2.5
TAPERED HOLLOW <sup>14</sup>	12.5	2.5
	20.0	10.0
FLAT	20.0	10.0
	20.0	7.5
	20.0	10.0

TABLE V

## Cathode Current Distribution

R(cm)	20 - 15	12.5 - 2.5	'38 shell'
MEASURED CURRENT (kA)	200	60	4
CODE CURRENT (kA)	210	50	4

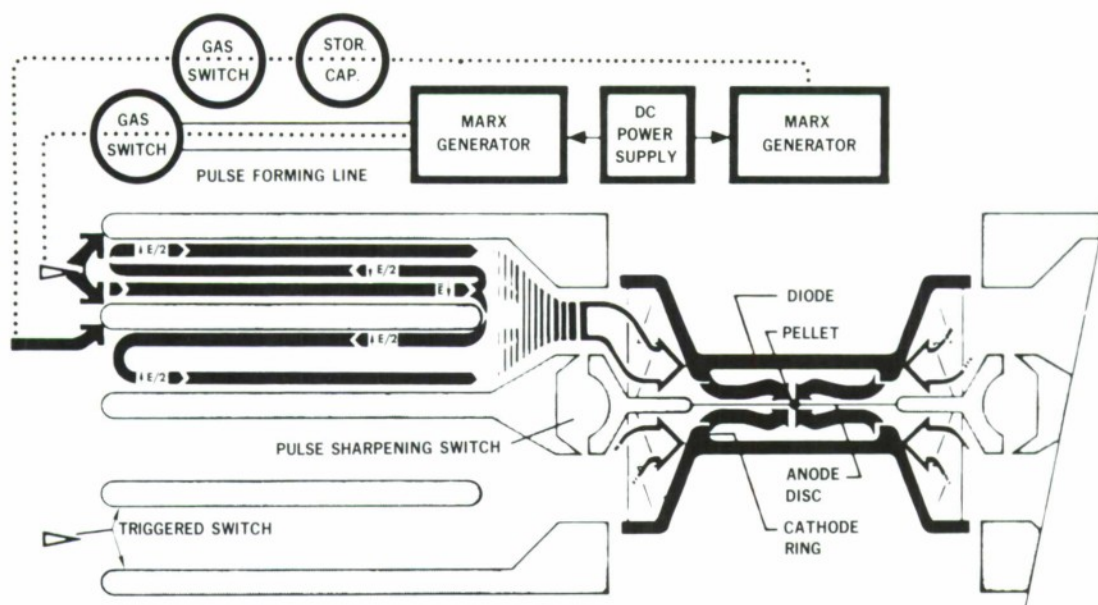


Figure 1. Proto-I Block Diagram

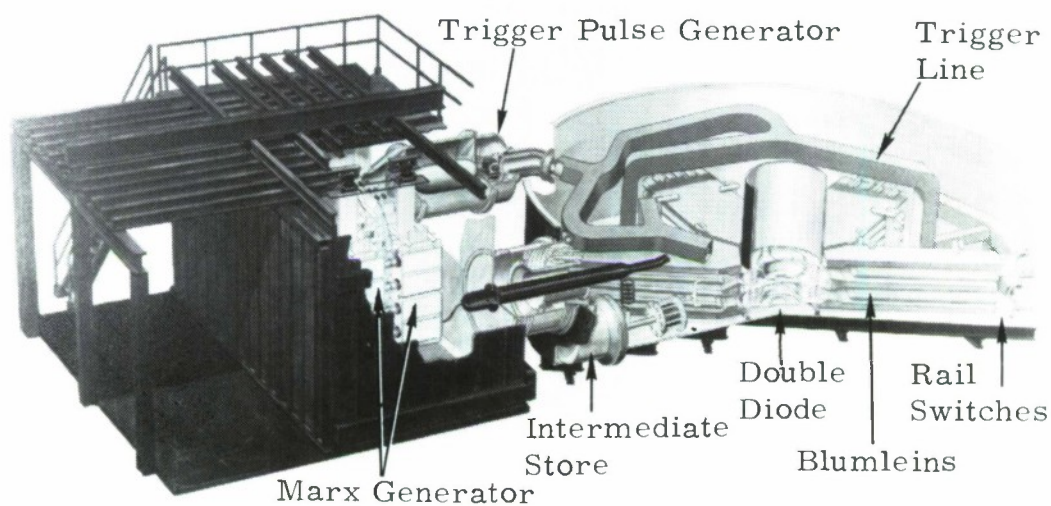


Figure 2. Proto-I

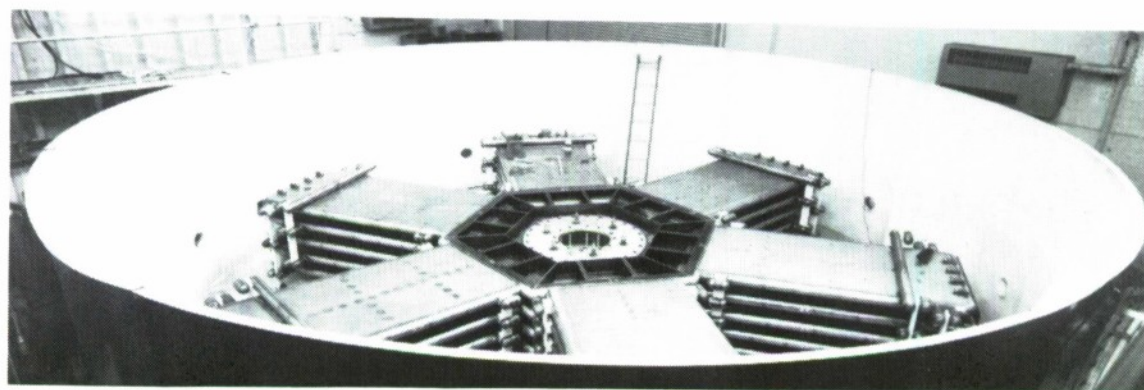


Figure 3. Proto-I Transmission Lines and Load Resistor

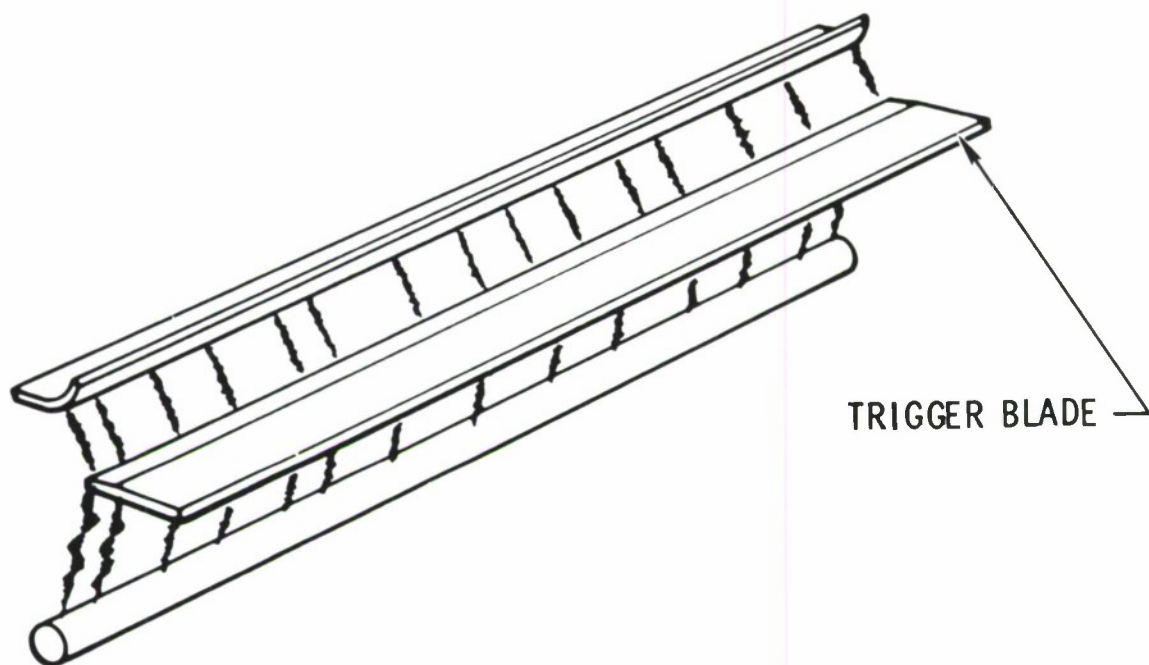


Figure 4. Oil Switch

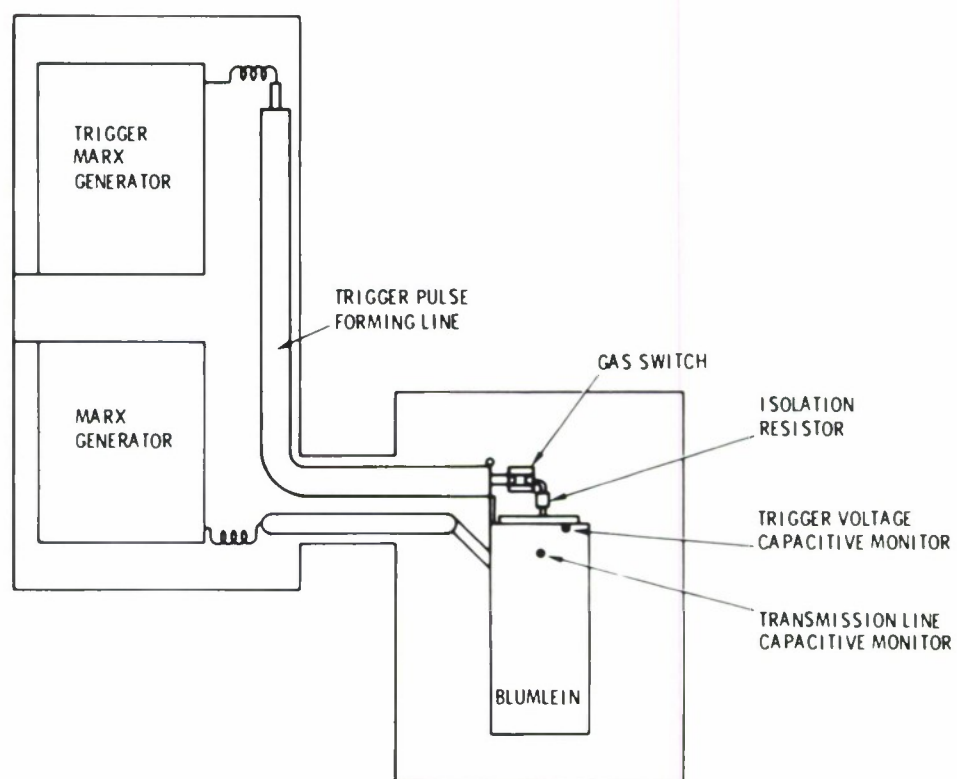


Figure 5. Multichannel Oil Switch Test Set-Up

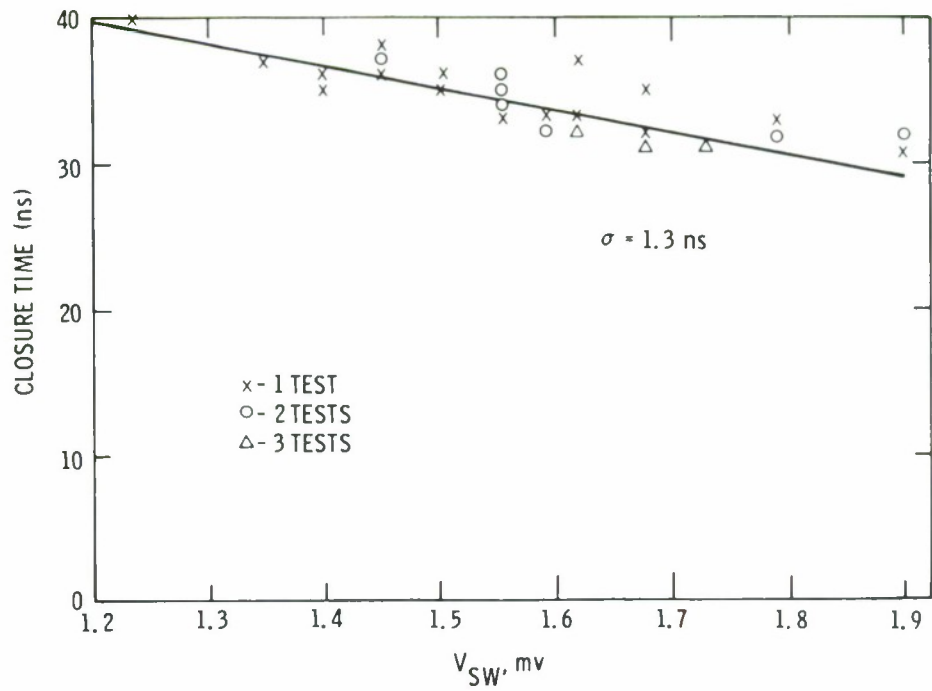


Figure 6. Triggered Oil Switch Test Set-Up

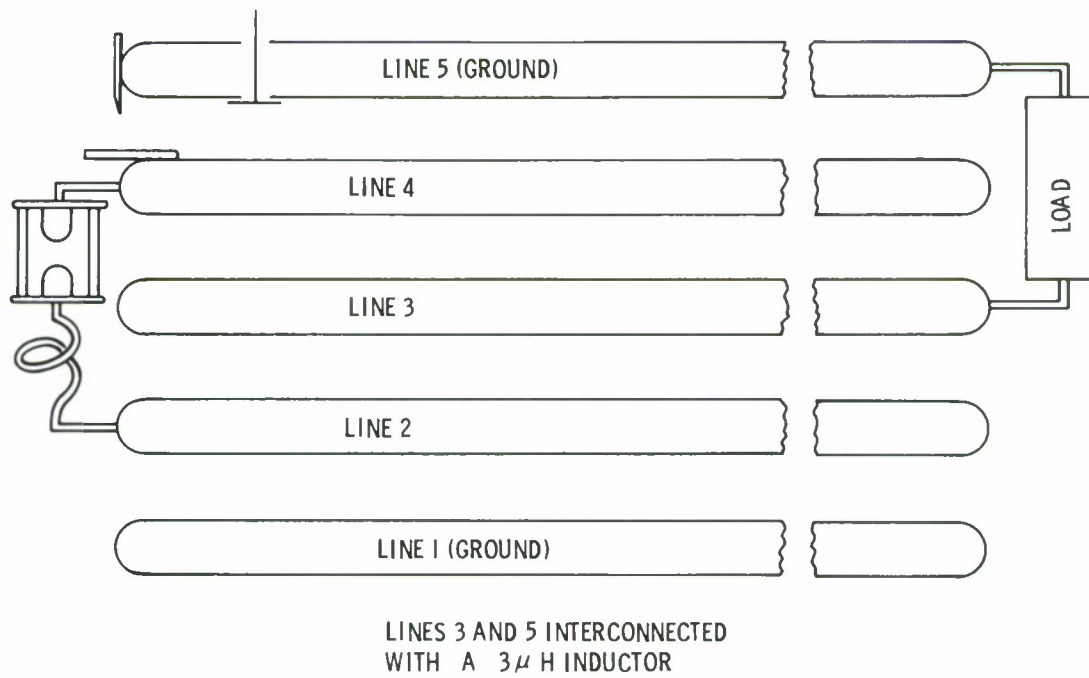


Figure 7. Two-Electrode Switch Test Set-Up

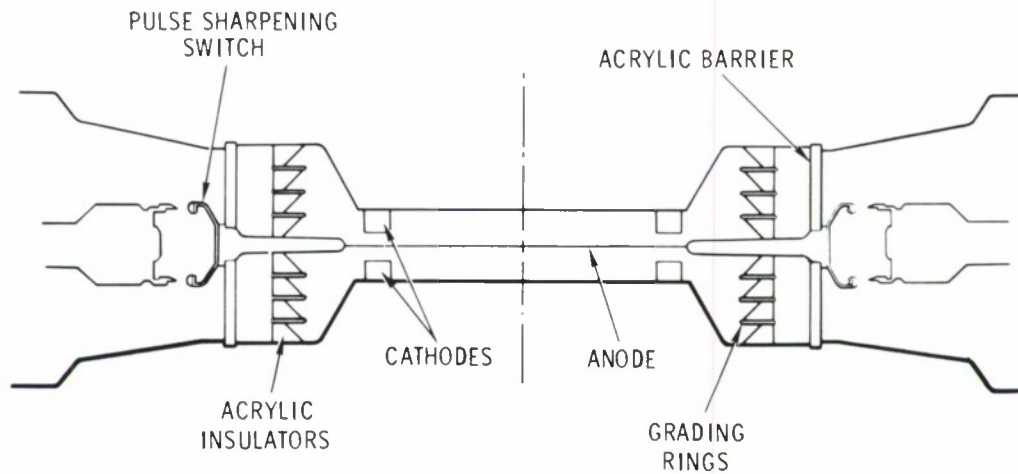


Figure 8. Proto-I Diode and Pulse Sharpening Switch

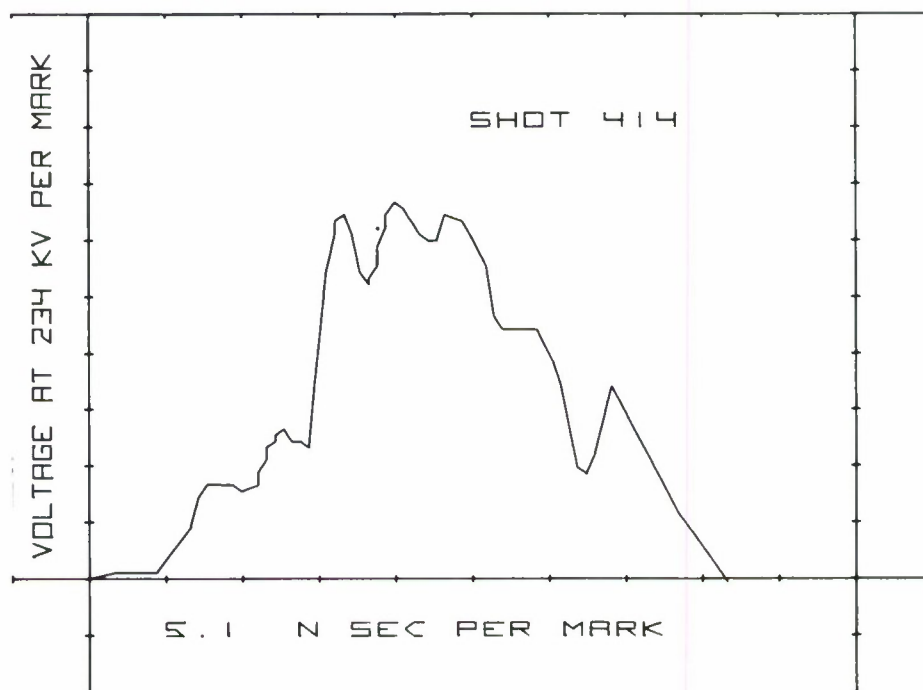


Figure 9. Output Voltage Waveshape from Pulse Sharpening Experiment





Figure 10. Anode Witness Plate Damage for 12.3 cm Diameter '38' Cathode Experiment

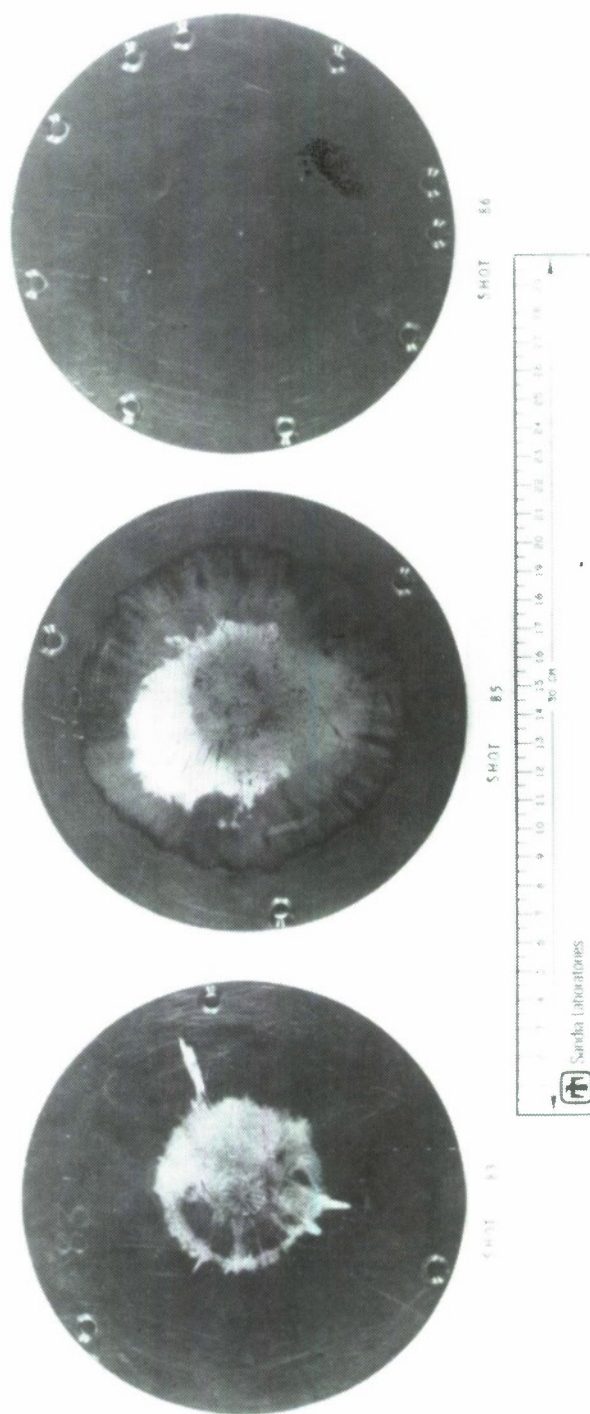


Figure 11. Witness Plate Damage for Crowbarred Shots

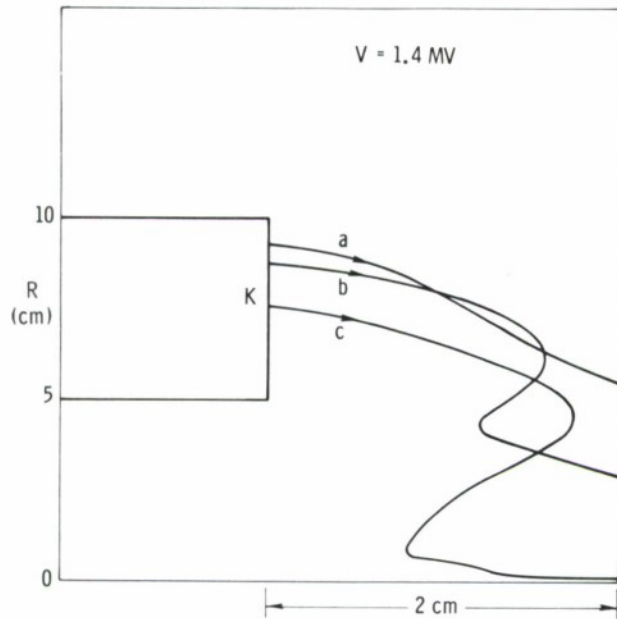


Figure 12.  
Numerical Simulation of Proto-I Diode  
Experiment with 20 cm Diameter  
Hollow Cathode

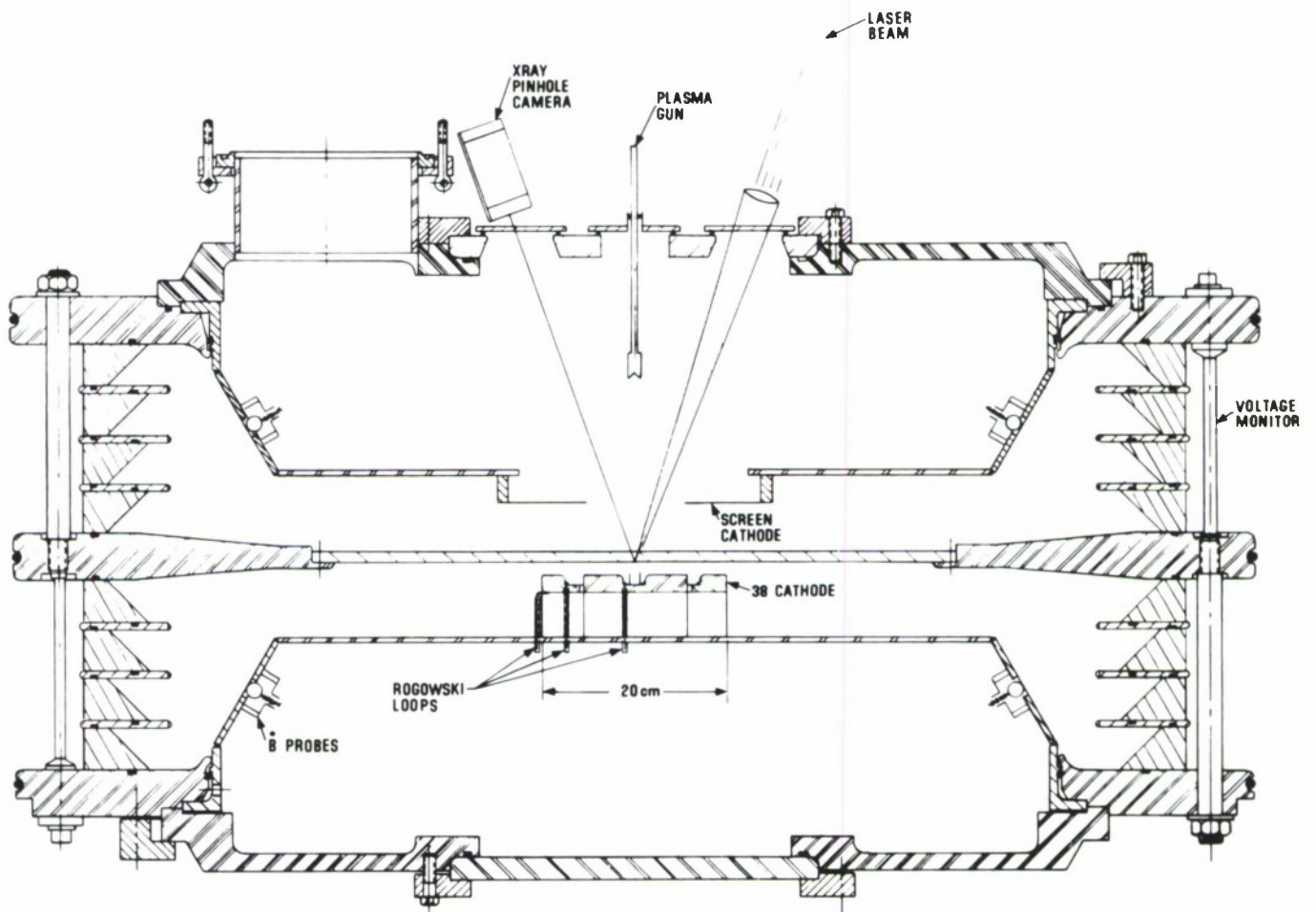


Figure 13. Proto-I Plasma-Filled Diode Experimental Set-Up

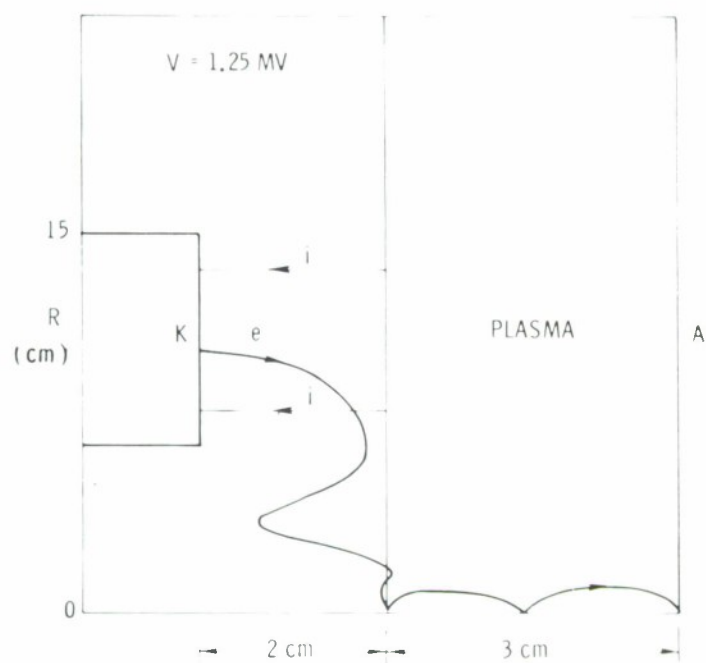


Figure 14. Numerical Simulation of Plasma-Filled Diode

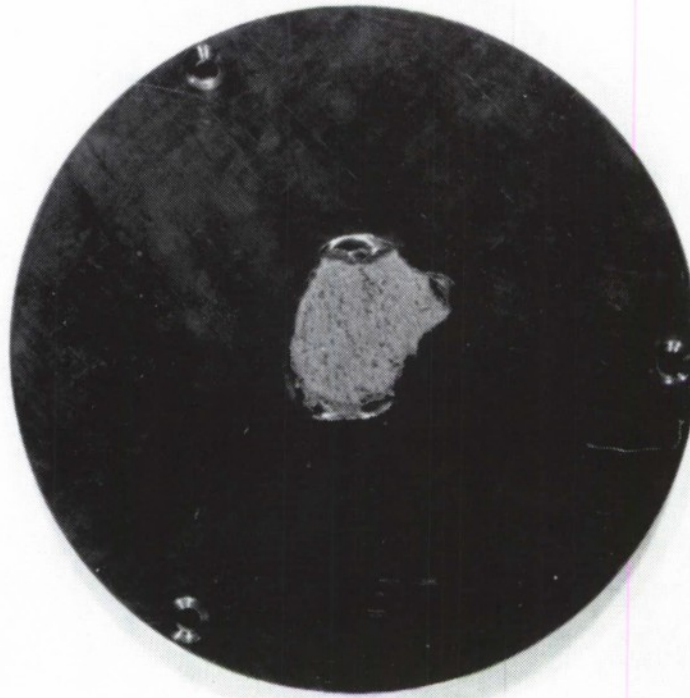
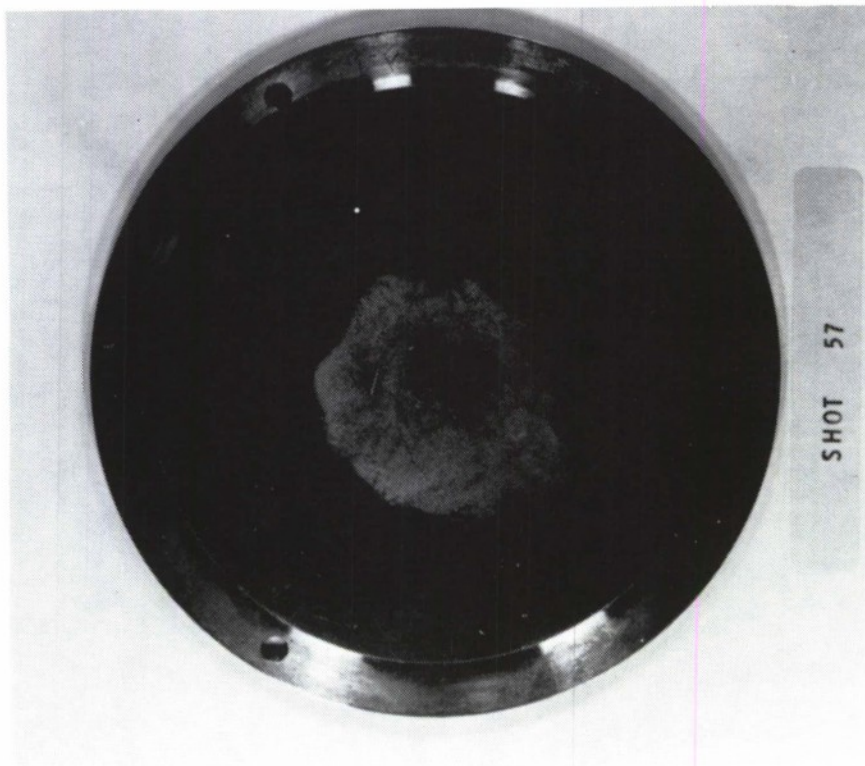


Figure 15. Witness Plate Damage for Pinched Beam in Plasma-Filled Diode Experiment



## PROTO-II - A SHORT PULSE WATER INSULATED ACCELERATOR\*

T. H. Martin, J. P. VanDevender, D. L. Johnson, D. H. McDaniel, M. Aker

Sandia Laboratories, Albuquerque, New Mexico 87115

### ABSTRACT

A new accelerator, designated Proto-II, is presently under construction at Sandia Laboratories. Proto-II will have a nominal output of 100 kJ into a two-sided diode at a voltage of 1.5 MV and a total current of over 6 MA for 24 ns. This accelerator will be utilized for electron beam fusion experiments and for pulsed power and developmental studies leading to a proposed further factor of five scale-up in power. The design of Proto-II is based upon recent water switching developments<sup>1</sup> and represents a 10-fold extrapolation of those results. Initial testing of Proto-II is scheduled to begin in 1976.

Proto-II power flow starts with eight Marx generators which charge 16 water-insulated storage capacitors. Eight triggered, 3 MV, SF<sub>6</sub> gas-insulated switches next transfer the energy through oil-water interfaces into the first stage of 16 parallel lines. Next, the 16 first stages transfer their energy into the pulse forming lines and fast switching sections. The energy is then delivered to two converging, back-to-back, disk-shaped transmission lines. Two back-to-back diodes then form the electron beams which are focused onto a common anode.

\*This work is supported by the Energy Research and Development Administration.

## INTRODUCTION

The requirements for high power ( $\sim 10^{14}$  W) and high current ( $\sim 100$  MA) accelerators for electron beam fusion applications has led to the research and development of a new generation of accelerators. Previous research on energy storage and switching in water<sup>1</sup> has permitted the design of a water-insulated and switched, two-sided accelerator. This accelerator, Proto-II, is now under construction at Sandia and is projected to have a 1.5 MV, 3 MA, 24 ns, 50 kJ output in each of two inwardly directed electron beams. The total 100 kJ output will be obtained with a peak power approaching 10 TW. The relevant data leading to the design of Proto-II and its application will be presented.

## OVERALL DESIGN

Proto-II is shown in Fig. 1. The center 7.9 m diameter tank contains the pulse forming lines, fast switches, transmission lines, and diodes. The Marx generators and intermediate water storage capacitors are located in the annulus formed between this tank and the outer 13.4 m diameter tank. Both tanks are 2.8 m high with 1.2 m diameter high voltage feedthroughs located at eight evenly spaced locations around the inner tank circumference.

When the eight Marx generators are charged to the appropriate voltage, signals from four low-jitter, 400 kV sources are used to trigger the first row of each generator.

The eight Marx generators then charge a total of 16 intermediate, water dielectric, storage capacitors with a typical  $V = V_0(1 - \cos \omega t)/2$  waveshape. When these water capacitors are fully charged, eight trigatron-type gas switches connecting the capacitors to the feedthroughs are triggered. The energy then passes through the interfaces into the water tank charging the first set of energy storage lines around the tank circumference in 240 ns. Circumferential interconnections between Marx generators, water capacitors and lines smooth



out voltage transients and provide a uniform voltage waveform to the first set of lines. The first lines then self-break into the second set of lines in 16 water spark channels. Then the second set is charged in 70 ns, and the second switch breaks with approximately 200 channels. The launched wave now travels down the converging transmission line transformers into the diode region. The transmission line transformers are adjustable and allow transforming impedances which are variable by a factor of 6 to optimize the accelerator output for specific experiments. The object of initial experiments will be to determine the dependence of pinch velocity and final pinch radius on diode impedance and plasma characteristics.

The electron beam forming section consists of two back-to-back diodes, each of which is nominally 180 cm in diameter and consists of a stack of Lucite rings and metal voltage grading rings. The cathode is located directly inside the insulator stack.

The accelerator will be assembled to provide a positive pulse output relative to ground. However, in many aspects a negative polarity output is easier to produce. Proto-II has been designed with interchangeable electrodes to provide the added capability.

#### MARX GENERATORS

The primary energy stores for Proto-II are eight parallel, oil-insulated Marx generators. The generators are similar to those used in Hydra<sup>2</sup> and Proto-I<sup>3</sup> with modifications to allow for an increased charge voltage from 60 kV to 100 kV. Each generator consists of thirty-two 0.7  $\mu$ F, 100 kV capacitors arranged in 4 rows of 8 capacitors, with 16 triggered midplane, SF<sub>6</sub> insulated spark gap switches, and can store up to 112 kJ at 3.2 MV. Plus-minus d.c. charging is utilized to minimize the number of spark gaps and to allow the midplane electrodes to be biased at ground potential.

Copper sulfate solution resistors are used throughout the generator for the charging, trigger, and ground.

Tests of a single Marx have been carried out, giving agreement with circuit analysis of the electrical schematic shown in Fig. 2. When connected to a 15 nF load, the actual ringing gain was 1.02, and the time to a peak voltage of 3.25 MV across the load was 750 ns.

Triggering of the generators is accomplished by applying a fast rise-time, 400 kV pulse to the four spark gap switches in the first row of each generator. The remaining switches are provided a trigger voltage by connecting the midplane trigger electrodes from four to eight stages back in the generator by means of resistors. The erection time of the Marx generator is 300 ns with a standard deviation of 30 ns. For eight generators, this will produce an average spread of 86 ns which, in turn, will result in a 3 percent voltage difference on the separately charged 15 nF loads.

A generator inductance of 6.7  $\mu$ H was determined from short circuit shots. A series resistance of 1.5  $\Omega$  was also determined from the short circuit case; however, on ringover tests into the 15 nF load which had a higher frequency of oscillation, a 3  $\Omega$  series resistance was measured. The difference is accountable to the skin effect in the generator current paths. The effective 560  $\Omega$  parallel resistance results from the charge, ground, and trigger resistors within the generator.

#### WATER CAPACITORS

Eight pairs of 7.5 nF water capacitors will be used as intermediate energy stores on Proto-II. The polarity effect in water<sup>4</sup> dictates that the center electrode be negative. Since the pulse forming lines require a positive charge voltage, the center electrodes are grounded to the tank and

the outer electrodes are charged positively by the Marx generator. Tests to 3.1 MV have been performed on a 90 percent scale model of the capacitor with no breakdowns. Electric field strength on the inner and outer cylinder for a 3 MV charge are 0.23 MV/cm and 0.135 MV/cm, respectively, permitting 36 kJ to be stored in a relatively low-inductance configuration.

### SF<sub>6</sub> GAS SWITCH

Energy is transferred from the water capacitors to the first set of lines through eight, triggered SF<sub>6</sub> insulated gas switches. A stacked insulator design is used based on testing at 3 MV on Sandia's Hydra accelerator and by the Physics International Company.<sup>5</sup> Triggering of the switches is accomplished with a +200 kV, fast risetime pulser applied to a pin on the negative electrode. Tests of trigatron switches in similar configuration have given a standard deviation in switching times of 1 ns and would predict an average spread in trigger times for the eight switches to be less than 3 ns. The trigger pulse is fed to the switch through a 10  $\mu$ H inductor which holds the triggered side of the switch at ground potential during the charging of the water capacitor.

### WATER-INSULATED LINES

The output from each set of water storage capacitors is fed through the trigatron switch and the oil/water interface to two sets of lines. The stray capacity in each of the eight interfaces and feeds is approximately 1.5 nF. The electrical characteristics of one set of lines are given in Fig. 3. The basic configuration is similar to the Ripple experiment,<sup>1</sup> but the lines are modified for a positive output. The gaps retain the field-enhanced negative electrode that gave a larger average breakdown field in the Ripple experiments. The field-enhancement was calculated with the FFEARS<sup>6</sup> field mapping code and the field enhancement decreased by a factor of two when

the edge was placed on line 2 instead of line 1. This modification degraded the overall performance, so points were used in gap 1 to increase the field enhancement.

#### GENERAL PRINCIPLES AND DESIGN DATA

In the design of 10 to 20 ns pulse duration, low impedance lines in water, the key to success lies in minimizing stray capacities and rapidly charging the self-breaking water switches. The rapid charging (30 to 300 ns) reduces the jitter in breakdown times to an acceptable fraction of the pulse width which will allow many lines to be fired in parallel and also minimizes the potentially severe (20 to 50 percent) energy losses in forming the spark channels in the gaps. Since the oil/water interface and the high voltage feeds to the lines are transit-time isolated from line 2 during its 60 to 70 ns charging time, reducing the energy stored in the stray capacities improves the overall efficiency. Since the capacity of line 1 is small (6 to 8 nF) for short pulse duration accelerators, the effect of the 1.5 nF strays is more severe than it is for longer pulse devices. The capacities  $C_{g1}$  and  $C_{g2}$  across gaps 1 and 2, respectively, must also be minimized since they cause a prepulse which degrades the performance of the next component in the network. For instance, the  $\sim 20$  ns prepulse on gap 2 coupled by  $C_{g1}$  resulted in gap 2 breaking prematurely if the prepulse exceeded  $\sim 500$  kV for a 2.5 cm spacing in gap 2. In some configurations, gap 2 would actually break before gap 1. The capacity  $C_{g1}$  was minimized by moving line 1 and line 2 apart and using one or more long points in gap 1. The increased inductance also improved the energy transfer between line 1 and line 2, which is consistent with the results of a SCEPTRE<sup>7</sup> simulation of the network, as shown in Fig. 3. The increased current per channel reduced the average water switch resistance of



the first gap and again increased the energy transfer between line 1 and line 2. Experiments<sup>8</sup> with six different gap configurations indicated that the resistance of water arcs in self-breaking water switches can range from 2 to 50  $\Omega$  per channel,\* 50 ns after the current begins to flow in the channel. The charge times on these 5 to 10 cm gaps ranged from 200 to 400 ns for peak voltages of 1 to 3 MV. Decreasing the charge time and increasing the mean field in the gap minimizes the gap resistance and the energy loss in the gap.

The stray capacity  $C_{g1}$  causes a 50 ns prepulse on the load. Preliminary experiments with Proto-I indicate that even short duration prepulse can cause uneven cathode emission and  $C_{g2}$  must be minimized. Prepulse isolation switches are, therefore, incorporated in the transmission lines. The capacity  $C_{g2}$  was minimized by reducing the thickness of the lines across gap 2.

The voltage waveform on the first line, the second line, and the output lines were taken using the prototype lines charged by the Ripple Marx. Typical traces are shown in Fig. 4. The charge time to peak voltage,  $\pi\sqrt{LC}$ , on the first line was 360 ns instead of the 240 ns expected in Proto-II. The (10 to 90 percent) risetime of the output pulse into a 2  $\Omega$  line is 8 ns. The risetime is dominated by the jitter in the closure of the 16 channels in the first water gap. This jitter is related to the fact that line 2 is charged in 50 ns while the wave (initiated from the single point feed on the center line) requires 40 ns to go from the center to the edge and back. Thus, the voltage waveform varies considerably along the length of the gap during the charging. The different voltage histories along the gap lead to approximately

\* The results of subsequent experiments on the high resistance of arcs in water are not consistent with values  $r > 6$  ohms at 45 ns for each channel in a 3-channel gap. Experiments are underway to elucidate the discrepancy.

a 6 ns spread in the closure times of the channels in gap 2. This spread is seen as a contribution to the risetime by the output monitor which averages the signal across the center 50 percent of the output line. The single point configuration in gap 1 leads to a 3 ns longer risetime than a multi-point gap would, but it gives 25 percent more energy in the pulse.

The time delay between the first and last output pulse from the 16 pulse forming lines also increases the effective risetime and pulse width at the diode. Consequently, minimizing the total jitter between the trigger signals to the eight gas switches (the last triggered stage of the accelerator) and the output pulse is important. With only one point in the first gap of each line, the total jitter of the accelerator voltage pulse is approximately equal to that of the first gap. With a 360 ns charge time, the output has a jitter of  $\sigma = 5$  ns r.m.s. deviation for a 1/8" rod conditioned by 20 to 30 shots. A detailed look at the data suggests that  $\sim 5$  percent transients on the charging waveform affect the jitter by 50 percent (or the breakdown time by  $\sim 1$  percent). Consequently, the total jitter from the sixteen Proto-II lines which are charged from water capacitors with a cleaner waveform and in a shorter time is expected to have a  $\sigma_{\text{rms}}$  of 2 ns. The expected delay from the first to the last pulse for sixteen lines is  $3.7 \sigma = 7.4$  ns. Thus, the output waveform is expected to have a 10 to 90 percent risetime of  $\sim 11$  ns.

A computer simulation of the pulse forming network was performed with the SCEPTRE<sup>7</sup> code. The circuit parameters were those given in Fig. 3. The overall efficiency of energy in the output compared to energy stored in the water capacitors was 49 percent. Of the remaining 51 percent (at the end of the main output pulse), 34 percent of the energy was dissipated in the switches, while 5 percent was left in line 1 and 12 percent was left in the stray capacity of the interface, feeds, the water store, and the spark gap.



## PREPULSE SWITCHES

The output waveshape of the Ripple lines is shown in Fig. 4. The nominal prepulse level rises sharply to 12 percent of the matched output voltage then slowly peaks at 18 percent with a total pulse length of 50 ns before the pulse arrives. The prepulse has a duration which corresponds to the line 2 charging cycle. The prepulse switch is physically located to provide transit time isolation from the second water switch. If this isolation is not provided, multiple reflections will occur and cause larger voltage transients and, subsequently, require a higher voltage prepulse switch. The minimum capacity obtainable was provided by the extended Lucite prepulse switch housing. Modeling experiments showed the fast rising pulse front will be attenuated by 94 percent while the lower frequency pulse will be attenuated by 98 percent, giving a prepulse level of less than 10 kV in the matched configuration. The rail switches will use 1.9 cm diameter rods 66 cm long with a gap spacing of 1.27 cm immersed in  $\text{SF}_6$ . This prepulse switch closely parallels a similar switch using spherical electrodes on the Sandia Hydra accelerator.

## TRANSMISSION LINE TRANSFORMERS

The disk transmission line geometry permits the use of a variable line transformer with only trivial modifications to the machine. The output impedance is readily changed by moving the transmission lines apart at the diode while maintaining a constant spacing at the input end. This capability extends the range of output voltages available to the experimenter without sacrificing output power. In addition, the primary limitation on the total output power of a short pulse duration e-beam is the power that can be transmitted through the diode. The problem is that the risetime  $\tau_d$  of the

current pulse into a diode with inductance  $L_{\text{diode}}$  and impedance  $Z_o$  from a line with impedance  $Z_o$  is

$$\tau_d = \frac{L_{\text{diode}}}{2Z_o} \quad , \quad (1)$$

and  $\tau_d$  must be less than the pulse duration for efficient energy transfer. The inductance,  $L_{\text{diode}}$ , can be made arbitrarily small by increasing the radius of the cathode, but very large radius beams will certainly be difficult to pinch to a few millimeters radius. This limitation probably means that cathodes will have to be limited to a radius of 1 meter although further work is underway to clarify this limitation.<sup>9</sup> Recent data on Proto-I<sup>10</sup> indicates that the maximum allowable electrical stress on the vacuum insulator interface should be 143 kV/cm, which yields an inductance of about 3 nH/MV. The output impedance of a perfect line transformer is

$$Z_o = \frac{V_o^2}{V_i^2} Z_i \quad , \quad (2)$$

where  $Z_i$ ,  $V_i$ ,  $Z_o$ , and  $V_o$  are the impedances and voltages at the input and output ends of the transformer, respectively. Upon combining Eqs. (1-2) one finds

$$\tau_d = \frac{3 \times 10^{-15} V_i^2}{2Z_i V_o} \quad . \quad (3)$$

Thus, for a given power,  $V_i^2/Z_i$ , and vacuum insulator stress, the risetime is inversely proportional to  $V_o$ .

As can be seen, for a given  $V_i$  and  $Z_i$ ,  $V_o$  can be varied to achieve a given  $\tau_d$  to extract the accelerator energy. The impedance or voltage will then be increased if the diode insulator, cathode, or electron beam is more inductive than presently envisioned.

The Proto-II transforming lines which are 147 cm long are articulated to accommodate a single gas-Lucite prepulse isolation switch in the center line. If a higher voltage diode is desired, the maximum impedance is about 1.5  $\Omega$  output, this yields a theoretical voltage gain of 2.45 ( $\sim$  3.6 MV). A double hinge joint configuration is used to allow the lines to be adjusted to approximate satisfactorily an exponentially varying impedance transformer. A comparison of the impedance variation of this line with that of an exponential line for  $Z_o/Z_i = 6$  showed a deviation of only 4 percent.

A one-third size model was constructed in water to study the transforming efficiencies of various disk-shaped converging lines. The diode was simulated by a 20 cm diameter polyethylene disk and the voltage output was measured at the disk center. The results are shown in Fig. 5. The test transformer section is shorter and deviates further from the exponential line than the Proto-II line but gives reasonably good efficiencies. The Proto-II adjustable lines will also allow large area, short pulse water breakdown to be studied, and these experiments will provide needed data in this critical area of accelerator technology.

#### DIODE

Due to the small amount of information available for vacuum surface flashover for 20 ns pulses, breakdown tests were conducted on small samples, 5 cm diameter, 1.2 cm tall, 45° post cones, and on the Proto-I diode.<sup>10</sup> These results indicate that the AWRE<sup>4</sup> and later Sandia scaling laws for vacuum surface flashover were still valid at these short time scales. Hence, the design of the Proto-II diode is based on these results.

The initial tube for the Proto-II diode is designed to work with a 0.25  $\Omega$  load and is a conventional, stacked insulator, grading structure with

a total height of 15.6 cm and a radius of 86.3 cm with an initial cathode radius of 76.2 cm. Various diode geometries will be employed to study diode pinch dynamics and focusing limitations. The height of the tube was dictated by the vacuum surface flashover strength, and the cathode diameter was determined from considerations of an inductance which would allow us to operate at a nominal level of 100 kJ. The tube is designed for a 2 MV pulse for 20 ns to provide a safety factor with the standard  $45^\circ$  insulator section. It was decided to employ a standard  $45^\circ$  angle design due to the lack of data available as a function of angle at large areas for these short pulses. As seen in Fig. 6, it was necessary to flare out the lines from 3.81 cm separation at  $r = 101.6$  to the 15.6 cm height of the tube. This leads to an inductance of 2.1 nH in the water feed. The inductance of the vacuum section of the tube is calculated to be 4.1 nH.

In order to provide greater flexibility in the operation of the accelerator, three other specific variations of the 15.6 cm high diode have been made: The first modification is the addition of grading rings with outer flux excluders to eliminate the 2.1 nH inductance in the water. The other two variations use the transforming properties of the transmission lines and match an impedance of 0.5 and 0.75  $\Omega$ , respectively, at the radius  $r = 101.6$  cm. The impedance variations increase the efficiency and, hence, lower the amount of energy reflected from the diode back down the pulse forming lines. To estimate the tube performance, output waveforms from the Ripple test were used in a computer simulation with the circuit shown in Fig. 7.  $R_L$  is the source impedance at a radius of 101.6 cm,  $L_W$  is the inductance in the water,  $L_V$  is the inductance in the vacuum, and  $R_D$  is a fixed diode resistance.  $V_C$  is the charge voltage in the single-sided 0.25  $\mu$  pulse

forming section. For the case of a fixed insulator height and maintaining a constant voltage across the insulator stack, Fig. 8 tabulates the single-sided total inductance, the tube risetime, the energy efficiency, and the power and energy outputs relative to the 0.25  $\mu$  system without flux excluders. The reference system used for Figs. 8 and 9 is a nominal total, double-sided energy output of 133 kJ in 22 ns, and the power level of 7 TW. It should be noted that the energy efficiency shown is for the diode and not for the overall accelerator.

The figures and computer solutions show that the diode inductance results in risetimes that seriously degrade the efficiency and increase the pulse duration at these power levels. The effect of the transformer section is evident in both figures, showing the decreased diode risetime and better efficiencies.

The diode support structure is adjustable to allow the diode insulator height to be changed for higher output voltage operation. The maximum ratio of the output impedance to the input impedance of the transformer is 6:1. Figure 9 tabulates the various tube parameters as a function of impedance for a constant line 1 charge voltage with the energy and power outputs referred to the 0.25  $\mu$  system.

The efficiency of the diode for various cathode diameters was calculated for the 0.25  $\mu$  system without flux excluders. The A-K gap spacings were calculated as a function of diameter by assuming parapotential flow for maintaining a matched impedance. The graph in Fig. 10 shows the results for inductance and relative energy as a function of cathode diameter.



The results of the computer simulation in Figs. 8 and 9 demonstrate the increased efficiency that can be achieved as diode risetime decreases as a result of transforming to higher impedances. As seen in Fig. 10, the effect of using smaller diameter cathodes will be to raise the diode inductance, hence, increasing the diode risetime and reducing the efficiency. In order to improve the diode performance above the nominal 100 kJ output of the reference tube diode, one must decrease the diode risetime by decreasing the inductance of the tube. This will require a significant improvement in the vacuum flashover strength of the insulator-grading stack. The Proto-I and Proto-II accelerators will be used to investigate the possibility of increasing this breakdown strength. Some of the possibilities which will be investigated are: (1) effects of using angles of greater than  $45^\circ$  with uniform grading across the insulator surface; (2) the effect of surface coatings on the grading rings and the insulators; (3) the effect of the bulk resistivity of the insulating material, and (4) the limits on magnetic insulation flashover. The effect of magnetic insulators is in the region of the insulator surface. Another alternative to lower the effective tube inductance would be to locate the insulator at still larger diameters and to make use of magnetically insulated vacuum feeds to provide power flow to the cathode. With this in mind, experiments to suppress electron emission in vacuum and on the limitations of magnetic insulation will also be conducted.

#### SUMMARY

The purpose of Proto-II is to develop new switching and high voltage technology. This will provide data on the limitations on maximum power capability for accelerators of this type. It will investigate the low



impedance diode operation with short pulses to determine pinch formation and minimum pinch size. Proto-II will then be used for pellet experiments at approximately 10 TW.

There are several questions that must be answered using this accelerator. The pulsed power flow through liquids, dielectric interfaces, and vacuum feeds can be investigated. New diode physics occurring at high power levels and large radii will be investigated. Proto-II provides considerable experimental flexibility by generating a low impedance short pulse with variable polarity output which can be modified by the line transformer to a range of output impedances to accelerate electrons or ions. Proto-II will also serve as the test bed for the nominally five times larger Electron Beam Fusion Accelerator (EBFA) presently being proposed.

## REFERENCES

1. J. P. VanDevender and T. H. Martin, IEEE Trans. on Nucl. Sci. NS-22, No. 3, p. 979 (June 1975).
2. T. H. Martin, IEEE Trans. on Nucl. Sci. NS-20, No. 3, p. 289 (June 1973).
3. K. R. Prestwich, IEEE Trans. on Nucl. Sci. NS-22, No. 3, p. 975 (June 1975).
4. J. C. Martin, SSWA/JCM/704/49, AWRE, Aldermaston, Berkshire, England (April 1970).
5. S. Mercer et al, Proceedings of the International Conference on Energy Storage, Compression and Switching, Asti, Italy (1974) - to be published.
6. J. W. Boers, 11th Symposium on Electron, Ion, and Laser Beam Technology (R. F. M. Thornley, Editor), San Francisco Press, Inc., 1971, pp. 167-175.
7. H. W. Mathers, SCEPTRE (System for Circuit Evaluation and Prediction of Transient Radiation Effects), Network Computer Analysis (George W. Zoorist, Editor), Boston Technical Publishers, Inc., Cambridge, Mass. (1969), pp. 169-196.
8. J. P. VanDevender, "Resistive Phase of High Voltage Water Switches," to be published.
9. G. R. Hadley, T. P. Wright, A. V. Farnsworth, Jr., "Pinching Limits and Scaling Laws for High Current Diodes," Proceedings of the First International Conference on Electron Beam Research and Technology, Albuquerque, New Mexico, November 1975 - to be published.

REFERENCES - continued:

10. K. R. Prestwich, P. A. Miller, D. H. McDaniel, J. W. Poukey, and M. M. Widner, "Proto-I Diode and Switching Studies," Proceedings of the First International Conference on Electron Beam Research and Technology, Albuquerque, New Mexico, November 1975 - to be published.

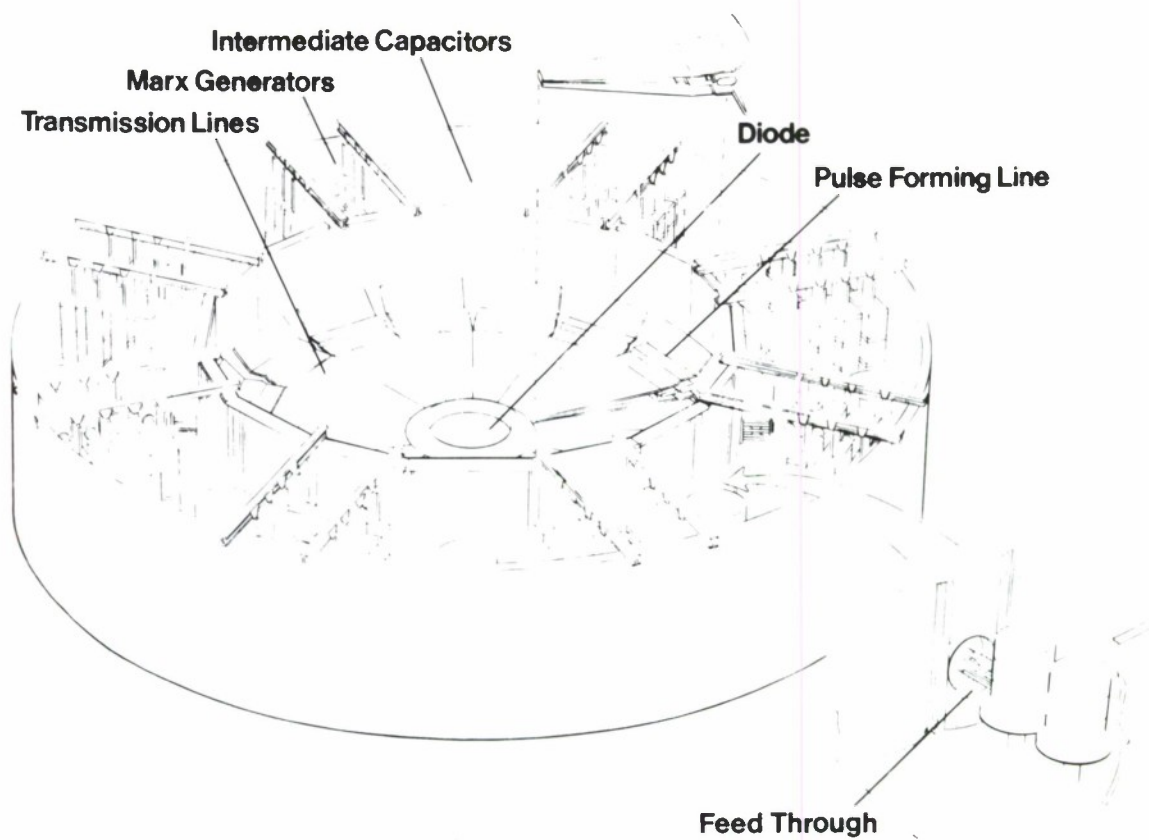
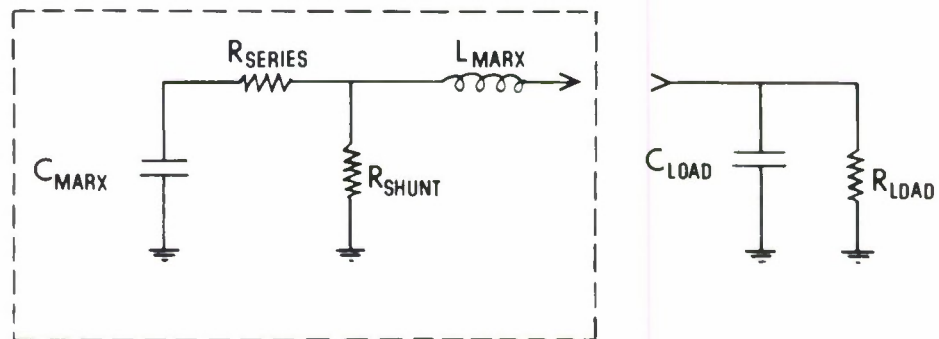


Figure 1. Proto-II



$$C_{\text{MARX}} = 22 \text{ nF}$$

$$L_{\text{MARX}} = 6.7 \mu\text{H}$$

$$R_{\text{SERIES}} = 3.0 \Omega$$

$$R_{\text{SHUNT}} = 560 \Omega$$

$$C_{\text{LOAD}} = 15 \text{ nF}$$

$$R_{\text{LOAD}} = 500 \Omega$$

Figure 2. Computer Model of Proto-II Marx

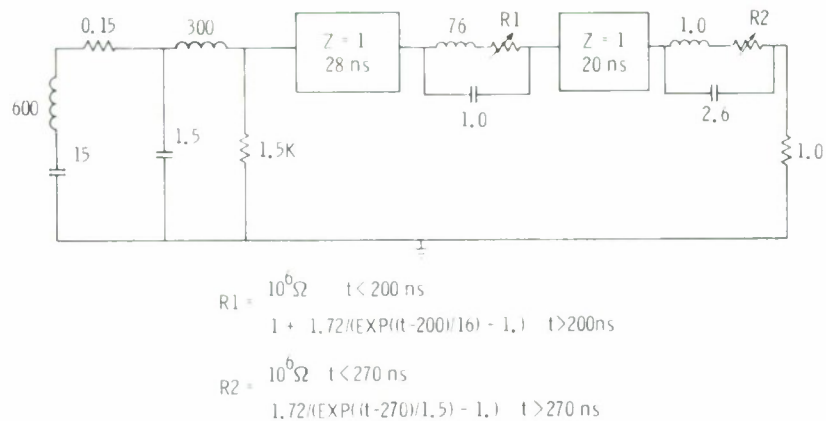


Figure 3. Computer Model of Proto-II Line

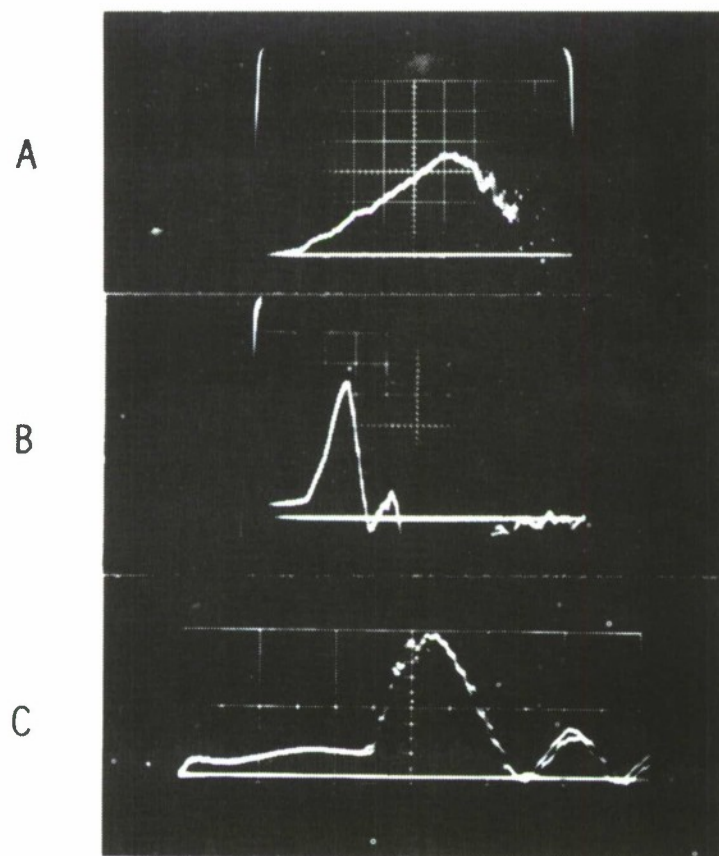


Figure 4. Ripple Voltage Waveshapes

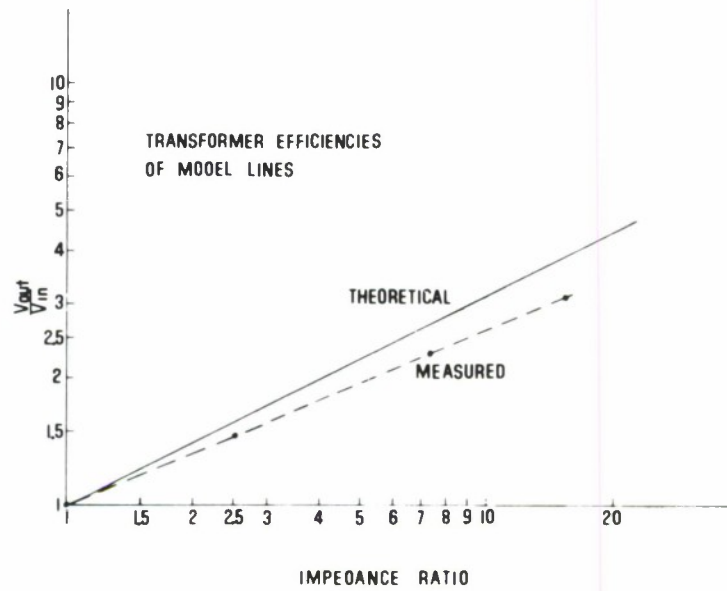


Figure 5. Transformer Efficiencies of Model Lines

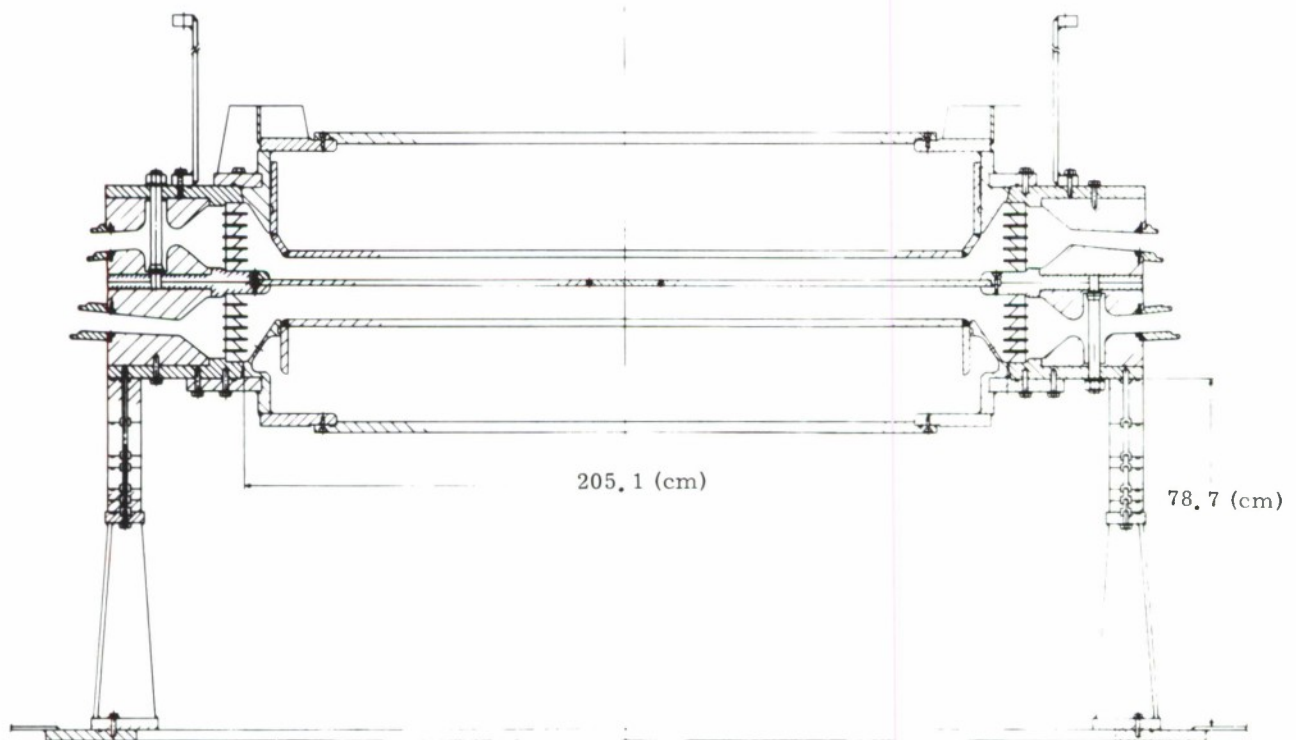


Figure 6. Proto-II Diode



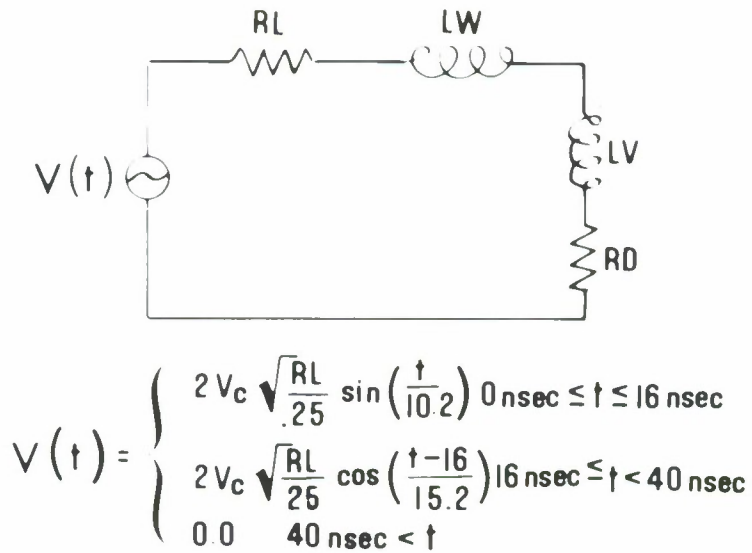


Figure 7. Computer Model of Proto-II Diode

SINGLE SIDE LOAD	$L_T$ ( nH )	$T_r$ ( ns )	$E_{out}$ ( relative )	$P_A$ ( relative )	$E_{eff}$ ( % )
0. 25 $\Omega$ w/F. E.	4. 14	8. 28	1. 17	1. 25	78. 9
0. 25 $\Omega$	6. 17	12. 34	1. 0	1. 0	67. 2
0. 50 $\Omega$	6. 44	6. 44	0. 63	0. 72	84. 8
0. 75 $\Omega$	6. 67	4. 45	0. 45	0. 52	90. 7

CONSTANT INSULATOR VOLTAGE - MATCHED ACCELERATOR OUTPUT

Figure 8. Constant Insulator Voltage - Matched Accelerator Output

$Z_{\text{load, line}}$ ( $\Omega$ )	$L_t$ ( $\mu\text{H}$ )	$T_T$ (ns)	$E_A$ (relative)	$P_0$ (relative)	$V_{A-K}$ (relative)	$E_{\text{eff}}$ (%)
0.25	6.17	12.34	1.0	1.0	1.0	67.2
0.50	9.22	9.22	1.13	1.21	1.55	76.2
0.75	11.90	7.93	1.19	1.30	1.97	80.0
1.50	21.40	7.13	1.23	1.36	2.86	82.0

CONSTANT CHARGE VOLTAGE - MATCHED ACCELERATOR OUTPUT

Figure 9. Constant Charge Voltage - Matched Accelerator Output

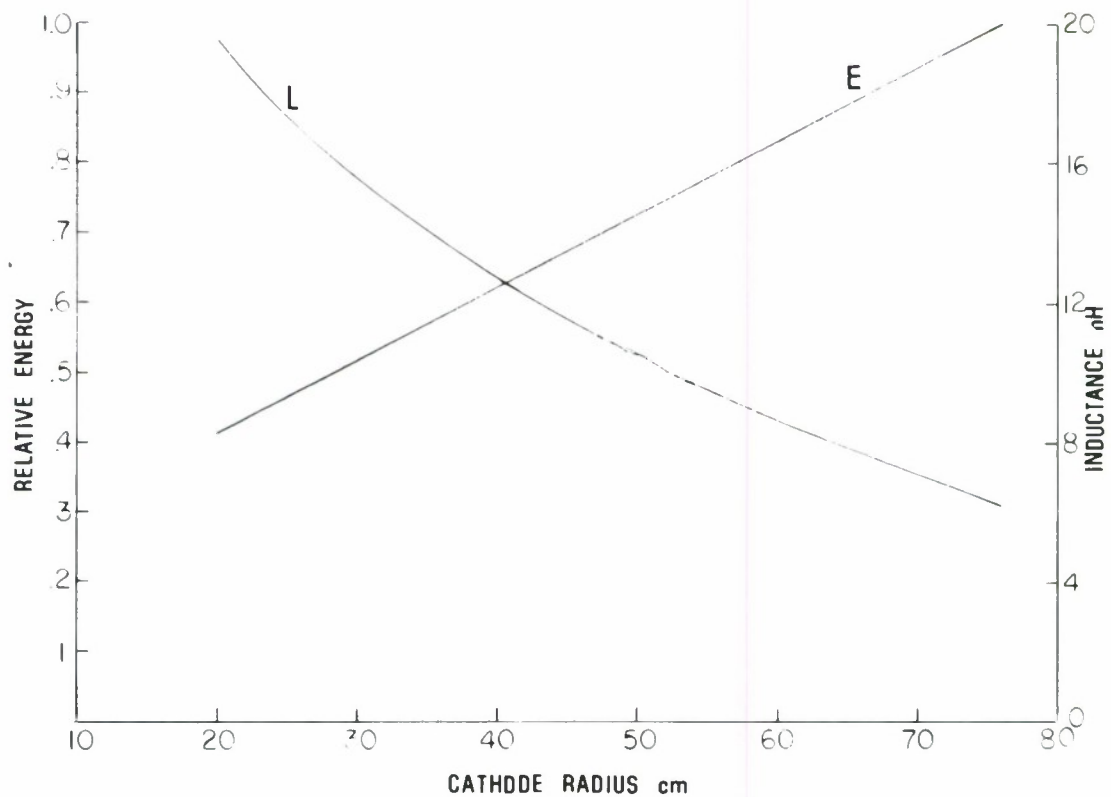


Figure 10. Relative Energy Output and Inductance vs Cathode Radius

APPROACHES TO THE GENERATION OF  
HUNDRED MEGAMPERE, SHORT PULSE ELECTRON BEAMS\*

Ian D. Smith

Physics International Company, 2700 Merced St., San Leandro,  
California 94577

ABSTRACT

Calculations of breakeven pellets imply the need for electron beams with total current of the order of  $10^8$  Amperes, voltages of a few megavolts and durations of about 10 nsec. The rate of increase of current far exceeds what has been achieved in existing accelerator tubes when driving small radius loads. The problem is in reducing the inductance of the accelerator tube and the surrounding dielectric. Several approaches are explored which are compatible with the use of electrostatically charged pulse generator circuits like those in common use. The technology improvements or developments necessary to achieve breakeven in systems with one or two beams are described.

---

\*Work supported in part by Sandia Laboratories, Albuquerque and by the Defense Nuclear Agency.

## INTRODUCTION

The requirements for electron beam pellet fusion are estimated from pellet calculations to be in the range of a few hundred terawatts at one to three megavolts, for a duration of about ten nanoseconds.<sup>(1)</sup> The voltage, duration and implied energy (a few megajoules) are in or near the range found in existing machines, but the power and the implied current are substantially greater. The power exceeds the 20 TW delivered by AURORA<sup>(2)</sup> by about one order of magnitude. The implied current is in the range one-hundred to a few hundred megamperes, and this is by far the most challenging aspect, since present systems deliver a maximum of about 1 MA per accelerator tube<sup>(3,4)</sup> and at this level already need careful design in order to avoid excessive inductance in the load region. The aim of this paper is to discuss some ways in which existing beam accelerator technology might be used to achieve currents exceeding 100 MA, despite the difficulties posed by the very high power densities and very low inductances needed near the load.

It is possible to design high current accelerators using principles different from those commonly in use. Of the other possible approaches, some avoid the difficulties that form the subject of this discussion. The matrix, Table 1, gives a fairly general classification of approaches based on: (1) the form in which the required energy is last stored before delivery to the beam (electrostatic, magnetostatic or particle energy), and (2) the medium (material or vacuum) in which the energy is stored. The well-developed technology exemplified by AURORA uses electrostatic energy stored in materials, e. g., liquid dielectrics. The energy is delivered to the final beam through the use of closing switches. The use of magnetic energy stored

in material media and delivered using opening switches (exploding foils) is also known<sup>(5, 6)</sup> though less highly developed. It is subject to much the same difficulties in achieving high currents as when electrostatic storage is used, since the chief problem is in reducing the inductance associated with the need for a material/vacuum interface around the acceleration region. Thus the results of this paper will have some application for the approach also. The remaining approaches, on the right of Table 1, avoid the need for a highly stressed material/vacuum interface because the energy is stored in vacuo, and can be immediately adjacent to the beam acceleration region. However, so far these approaches are all in their infancy, at best. Electrostatic storage in vacuo is not promising because vacuum breakdown limits the technique to fairly low energy and power densities. Magnetic storage in vacuo has been the subject of some development<sup>(7)</sup> but vacuum opening switches producing voltages in the desired range present great difficulties. Electron beam storage has also been investigated<sup>(8)</sup> but is at an early stage.

The first step in adapting existing technology to the needs of electron beam fusion is shown in Figure 1. This shows the Sandia Laboratories "PROTO II" accelerator, now in construction. The large power (7 TW) and current (6 MA at 1 to 1.5 MV) are obtained by using an annular pulse line, whose dimensions are large so that its discharge must be initiated independently at many points around the circumference. Charging and switching technology allow this parallel simultaneous operation of what are, in effect, many independent circuits.

To reach the comparatively small radius at which the beam is accelerated, the wave formed by discharging the pulse line propagates radially inwards in a constant impedance region we refer to as the "dielectric feed". As the center is approached, power and current densities increase and it is here that limitations imposed by breakdown can be reached. This is especially true where the wave enters the vacuum region; but the dielectric feed itself can pose some problems.

We begin by examining the design of the dielectric feed, and then proceed to some possible designs of the vacuum region. For numerical illustration purposes, we will assume a requirement to deliver 200 TW at 3 MV to a pair of cathodes (back-to-back) of radius 60 cm, and examine in each case how this might be achieved.

### Dielectric Feed

The degree of difficulty in the dielectric feed depends on the radius to which it must converge the power before delivering it to the vacuum tube. Under certain circumstances, the vacuum interface may immediately surround the cathode, so that the vacuum feed may converge to about 60 cm radius. Figure 2 shows, as a function of the dielectric constant of the feed dielectric, the electric field required to produce the current density in this case, assuming that the feed is matched by the tube impedance. Mismatching can reduce this field at the expense of some wasted energy, but the reduction is by a factor of less than two. The points entered on the graph are the maximum allowable fields suggested by present data for three different dielectrics, oil, water and biaxially oriented polypropylene film. The values for the liquids correspond to a fairly short pulse (10-20 nsec) and lower fields would obtain for longer pulses. The breakdown of polypropylene is time independent; however, the use of a solid dielectric such as polypropylene is unattractive because its dielectric failure is not self-healing.

Figure 2 shows that water comes closest to satisfying the requirements, but that much improvement is needed over present dielectric stress levels. Furthermore, if the same power is required at lower voltage (say 1 MV) the problem is exacerbated, because it is essentially one of current density. An alternative to requiring dielectrics capable of much higher stress levels does exist however, and this is to relieve the current density requirement by providing wider conductors; this implies a convolution of the flat geometry of the disk previously considered.



One such convolution is shown in Figure 3. It consists of an array of parallel plate transmission lines of constant width, spacing and impedance, with the conductors at right angles to the plane of the disk or load. This is not necessarily the best way to convolute the feed, but it is simple to build and easily lends itself to approximate analyses of its limitations. The limit on the output of such an array is set by the degradation of the pulse-shape in the region where the plates attached to the load; this effect will limit the plate width useful for a given pulse duration. For example, it is clear that if the electrical transit time from the edges of each line to the center exceeds the pulse duration, then the energy traveling at the edge of the line is completely wasted. Suppose that this transit time is allowed to be one-half the pulse duration of  $t$  nanoseconds; let the matched line-voltage be  $V$  (MV) the width  $w$  (cm) the field  $E$  (MV/cm) and the dielectric constant  $\epsilon$ . The transit time condition gives  $w = \frac{c t}{\epsilon^{1/2}}$ , where  $c = 30$  cm/ns. The line separation is  $s = V/E$  (cm). The impedance is given by

$$Z = \frac{120 \pi s}{\epsilon^{1/2} w} = \frac{4 \pi s}{t} \text{ (ohms)} . \quad (1)$$

The maximum output power is

$$\frac{V^2}{Z} = \frac{E^2 t}{4 \pi} \cdot s \text{ (TW)} . \quad (2)$$

Neglecting the transmission line conductor thickness, this power can be delivered to a width of load conductor equal to  $s$  if the lines are closely packed. Therefore, the transmission line array can deliver a power per unit width equal to

$$\frac{E^2 t}{4 \pi} \text{ (TW/cm)} . \quad (3)$$

Applying this result to the previous example where 200 TW is to be delivered to two 1.2 m. diameter tubes, it is seen that if the pulse duration is 20 nsec the field must be about 600 kV/cm, a field that can be sustained in liquid dielectrics for short pulses.

The properties of a convoluted feed consisting of a simple transmission line array differ in several important respects from those of the flat disk feed. First, the fields required are much lower. Second, the limit is one of power density and not current density, so that if the same power is required at a lower voltage, the fields needed are the same. Third, the longer the pulse, the higher the power limit. Fourth, dielectric constants do not strongly affect the limiting power (because the larger the dielectric constant, the narrower must be the lines) and hence field strength is the main indicator of dielectric performance.

The last statement suggests that oil is superior to water in such a design, since its field strength tends to be about 50 percent greater. However, several factors tend to offset this. First, the above analysis is a simplification; the pulse degradation will be affected not only by the transit time across the line, but by the degree to which the current is required to converge, as represented by the aspect ratio  $w/s$  of the line. Second, the area effect and polarity effect in water breakdown<sup>(9)</sup> can be used to raise the operating field somewhat compared with oil. Third, the overall compactness of water designs makes them more attractive.

#### Vacuum Tube with Simple Disk Geometry

This is shown in concept form in Figure 4. Current enters the vacuum at a material/vacuum interface where the spacing is large to avoid flashover, necessitating a cross-sectional area  $A \text{ cm}^2$  in the radial plane. Away from the interface, the spacing may be much smaller ( $d \text{ cm}$ ) in the vacuum region surrounding the cathode of radius  $r_c$ . Total inductance is minimized by placing the interface at a radius  $r_1 = A/d$ , unless this is

less than  $r_c$ , when the insulator is placed immediately outside the cathode, eliminating the close-spaced "vacuum feed." By using a very large radius cathode, the inductance can be made as small as necessary for any given large current and short pulse duration, but a large radius cathode may not produce a tight enough pinch or even allow the current to pinch onto the axis in the time available. It is, therefore, possible that the inductance problem may force an approach in which the desired current and the pinch onto the pellet are only achieved in the last 10-20 nsec of substantially longer, slower rising pulse. This entails a reduction of efficiency. An exercise was carried out to find what pulse durations are allowed by various design stresses in the vacuum tube in the case of a 100 TW, 3 MV, 60 cm radius cathode.

Certain assumptions must be made about the pulse shape and the inductive voltage drop, i.e., the difference between generator and cathode voltages. It was assumed that the interface voltage is maintained at 4 MV until peak power is reached and then returns to zero. This requires shaping the generator pulse as shown in Figure 5. A load waveform is produced with exponential rise and fall with time constant  $L/Z$ , where  $L$  is the inductance inside the interface and  $Z$  the load impedance. The FWHM of the power pulse is about  $1.0 L/Z$  and the duration of the interface voltage is about  $1.4 L/Z$ . The flat-topped interface waveform was chosen because the insulator flashover process is only weakly time dependent. An inductive drop of 1 MV was chosen as a compromise between minimizing rise time and excess generator power.

Table 2 shows some results in terms of the maximum insulator area compatible with three pulse durations, 10, 25 and 60 nsec, for various values of the electric field in the vacuum feed, which is assumed to have a constant spacing. For comparison, present experience suggests that the vacuum feed field can be of the order of 1 MV/cm. For the area of the 4 MV insulator, 400-600 cm<sup>2</sup> is suggested by scaling

from a recently tested design that uses thin multiple stages of acrylic, fitted with external flux excluders. Present technology thus implies the use of durations of about 200 nsec, or for a 60 nsec duration a cathode radius of 2 m. Table 2 shows that to drive a 60 cm radius cathode with a 60 nsec pulse requires a field in the feed of about 3 MV/cm or an insulator area of only 200 cm<sup>2</sup>, whereas to achieve a 25 nsec pulse requires both improvements simultaneously. In general, supplying the same power at reduced voltage leads to more stringent requirements because of the way in which the vacuum region scales.

It is clear that the use of this configuration, which is attractive because it is simple and provides excellent access to the pellet, implies the need for considerable improvement in both vacuum breakdown (as it applies to the feed) and interface flashover. Breakdown processes occurring in the feed are relatively well understood. They involve electron emission from cathode protrusions, and explosion of such protrusions to produce plasmas that emit strongly and close the vacuum gap. Possibilities of improvement certainly exist through the use of dielectric coatings and magnetic fields to suppress electron emission and electron and plasma motion.

The interface flashover process is poorly understood in detail. Present interface designs have been the result of largely empirical optimization. Their breakdown is widely thought to begin with electron emission from the insulator surface, but the steps by which this leads to the formation of a highly conducting plasma are largely the subject of speculation. The author believes that a large increase in breakdown fields will require new and more complex designs, such as the use of semi-conducting interfaces, strong magnetic fields or gas-free, bakable insulator surfaces. Such techniques are difficult enough that they cannot be applied empirically, but rather need a detailed understanding of the breakdown mechanisms. In view of the critical nature of the interface region, a careful investigation of the breakdown process is in any case very much in order.



### Use of Vacuum Transmission Lines

As previously noted, the field required to deliver 200 TW to a 1.2 m. diameter load through the use of a tightly packed array of transmission lines has been estimated to be about 600 kV/cm, which is within the range of fields that can be supported in vacuo for short pulses. The use of coated cathode electrodes allows fields of the order of 1 MV/cm, and magnetic insulation can permit such fields even on rough electrodes.

As an example of a design based on this approach, we suppose that two 100 TW, 3 MV, radius 60 cm cathodes are to be driven by 4 MV transmission lines with a field of 1.5 MV/cm in the uniform field region. Approximately one-hundred such transmission lines can be spaced around the circumference, and to provide the required driving impedance of 6 ohms necessitates a width of 1.8 m.

The transit time across the line is 6 nsec, so that the load rise time should be compatible with a pulse in the 10 nsec range. It is possible in fact, to estimate a stray inductance of about 50 nH in association with current convergence at the end of each line; therefore, if the generator is again designed to maintain a constant 4 MV, in this case at the end of the transmission lines, the e-fold rise time of the load voltage is about  $50/6$  or roughly 8 nsec. This is also the minimum FWHM of the power pulse.

The inductance of the material/vacuum interface has not been considered because in principle it can be made very small by providing each transmission line with an interface of matching width. This may require that the transmission lines extend out to radius of several metres to provide space for the interfaces; in this distance the width of the lines could be flared to provide even greater insulator width, or to reduce the field in the vacuum. It is also possible to extend the transmission lines out to large enough radius -- of the order of 10 m. -- to connect with a simple insulator of the type used in the disk-tube described above.

Clearly, the multiple vacuum transmission line configuration has disadvantages in the complexity of the vacuum structure, with its requirements of closely held spacings, and in the restricted access to the pellet. There are no insuperable mechanical difficulties however; the best approach is probably to enclose the whole transmission line structure in a vacuum vessel, and to make the conductors from relatively thin sheet metal, placed in tension along the length of the transmission lines.

### Electron Beam Coupling

It is attractive to consider the use of many separate accelerators from which beams are transported and combined at the pellet, so that the current per accelerator is low enough to avoid difficulties in the vacuum or the dielectric feed. Electron beams can be transported efficiently over considerable distances, but unfortunately cannot be delivered to the pellet at the necessary current density. Nevertheless, a way still remains to utilize transported beams if their particle energy can, after transport, be converted back to high currents flowing at high potential -- a process that is the inverse of that occurring in the accelerating diode. Given the existence of an "inverse diode," the power recovered from many beams can be closely coupled in vacuo (i. e., with no material interface present) to a single cathode, which generates the final super-pinched beam just as in more conventional schemes. The advantage offered by beam transport is that beam currents are neutralized by highly conducting background plasma, making it possible to converge large total currents into small regions without introducing a large inductance. Success of such an approach depends on having an inverse diode that is both efficient and compact enough that many inverse diodes can be juxtaposed with a small load cathode to form a low inductance circuit.



The coupling of beam particle energy to a load is illustrated in Figure 6. The beam passes through a thin foil window from the plasma-filled transport channel into a vacuum region, the inverse diode. The beam is decelerated by the electric fields set up by its own space charge, then strikes the collector electrode. The load is placed in the current return path between collector and window.

The one-dimensional flow of mono-energetic non-relativistic electrons normal to two conducting surfaces at different potentials is extensively analyzed in reference 10, where several flow regimes are described. The regime best suited to the inverse diode is where the beam current density and the accelerating and load voltages are chosen so that the potential has the form of the full line in Figure 7. The advantages of this regime are that all the beam current flows through the load, the load potential can approach that used to accelerate the beam, and a potential minimum exists that prevents electrons emitted from the collector from returning to the window (except for high energy secondaries, which will not be numerous from a low-Z collector). Thus the device is quite efficient; the residual kinetic energy of electrons at the collector is a loss comparable in magnitude to that caused by inductive drop in present accelerating tubes.

The potential can also have the form of the broken line in Figure 7, with no minimum; in principle, all the injected current still flows through the load, but in practice electrons will be accelerated back to the window because of the direction of the field at the collector. In fact, plasma is likely to be formed at the collector and the reverse electron current will rise to a space-charge limited value, i. e., one which reduces the field at the collector to zero. The efficiency of the device is then reduced.

A map of these two regimes is shown in Figure 8, based on material in reference 10. This can be used to show, for example, that if the load is assumed to have constant impedance and the injected beam current rises gradually at constant voltage, then at the start of the pulse the inverse diode almost immediately enters and stays within the preferred regime in which there is a potential minimum. Attention will have to be paid in practice to the real time-history of the load characteristic as well as that of the accelerating voltage and current of the injected beams, especially since excessive load impedance or injected current can lead to the setting-up of yet another regime in which almost all the injected beam is reflected to the window. It might be necessary, for example, to "turn-on" the load cathode with a separately applied low energy prepulse, or to add capacitance in parallel with the load. Other considerations include stabilizing the injected beam against repulsion from the load current; for this purpose, a longitudinal magnetic guide field used in the transport channel can be extended through the inverse diode.

To minimize inductance, the inverse diodes used to couple the several beams should form an annular array around the load cathode, Figure 9. The vacuum volume can be closed at large radius by an insulator whose size is unimportant -- indeed, an inductive metal closure might be better, as it would speed pumpdown and eliminate flashover considerations and the need for cleaning.

For a numerical example, two 3 MV, 100 TW, 60 cm radius load cathodes are each assumed to be driven by injected beams of  $20 \text{ kA/cm}^2$  at 4 MV. Assuming the inverse diodes occupy 50 percent of the available area, they must extend out to a radius of about 76 cm. Using the non-relativistic treatment as an approximation, we find that a spacing of about 1.8 cm in the inverse diode gives a load voltage of 3 MV and a potential barrier of 120 kV. We calculate an effective inductance of about 0.3 nH for the annulus in which the inverse diodes are located. By analogy with the previous treatment of pulse shaped, this inductance is consistent with a rise time of less than 5 nsec to peak current.

The beam in this example would be generated by diodes with about 1 cm anode cathode gap, assuming no compression in transport. For very short pulses, smaller anode cathode gaps should be practical; the inductance calculated varies with the cube of the assumed anode cathode gap, and if the beam is compressed during transport the inductance varies with the three-halves power of the compression ratio. Thus much lower inductances may be possible. In general, it is clear that the success of this approach, with its elimination of the material/vacuum interface around the final cathode, would increase feasible beam currents by a very large factor.

## CONCLUSION

Beam accelerator approaches in which the pulse is generated in a material medium present difficulties in converging the energy to small vacuum loads. If current pulses rising in 10-20 nsec to the 100 MA range are to be delivered to cathodes about 1 m. or less in diameter using design stress levels consistent with present experience, then highly convoluted configurations -- such as strip transmission line arrays -- must be employed in the vacuum and perhaps also in the dielectric regions of the accelerators. Alternatively, ways may be developed to withstand much higher stresses in liquids, on vacuum interfaces and in vacuum. Such developments are especially desirable to simplify the design of the vacuum region. The use of transported electron beams and "inverse diodes," which reconvert particle energy to current that drives the load cathode, represents a method by which existing technology might achieve much higher currents and shorter pulses.

## REFERENCES

1. M. A. Sweeney, M. J. Clauser, "Low-Z Ablation Targets for Electron Beam Fusion," Applied Physics Letters, Vol. 27, No. 9, p. 483, November 1975.
2. B. Bernstein, I. Smith, AURORA, An Electron Accelerator, IEEE trans. on Nucl. Sci., NS-18, No. 3, p. 294, 1971.
3. J. D. Shipman, Jr., The Electrical Design of the NRL GAMBLE II Pulse Generator, IEEE trans. on Nucl. Sci., NS-18, No. 4, p. 453, 1971.
4. G. B. Frazier, The OWL II Pulsed Electron Beam Generator, Presented at the Thirteenth Symposium for Electron, Ion, and Photon Technology, Colorado Springs, Colorado, May 22, 1975.
5. J. DiMarco and L. Burkhardt, J. Appl. Phys. 41, 3894 (1970).
6. J. Benford, H. Calvin, I. Smith, and H. Aslin, "High-Power Pulse Generation Using Exploding Fuses," presented Torino, Italy, November 1974, Physics International Company.
7. "Fast Switching of Vacuum Magnetic Energy Stores," Physics International Company, August 1975, DNA-3680-F-2
8. W. Clark, P. Korn, A. Mondelli, and N. Rostoker, Electron Beam Storage Device for Controlled Fusion, Annals of N. Y. Academy of Sciences, Vol. 251, p. 568, 1975.
9. P. D. A. Champney, Impulse Breakdown of Deionized Water with Assymetric Fields, AWRE Report SSWA/PDAC/6610/103 (October 13, 1966).
10. C. E. Fay, et al., "On the Theory of Space Charge Between Parallel Plane Electrodes," Bell System Technical Journal, 17 (1938).

TABLE 1  
CLASSIFICATION OF ACCELERATOR APPROACHES

	Energy Stored In Materials	Energy Stored In Vacuo
Electrostatic Energy	Well Developed	Not Promising
Magnetostatic Energy	Slightly Developed	Under Development
Particle Energy	Infeasible	Under Development

TABLE 2  
INSULATOR AREA AND VACUUM FIELD REQUIRED  
FOR A SIMPLE DISK TUBE AT  $10^{14}$  WATTS, 3MV, WITH A 60 CM  
RADIUS CATHODE

Pulse Duration (nsec)	10	25	60
	Insulator Area Allowed ( $\text{cm}^2$ )		
Vacuum Feed Field (MV/cm)			
1	35	88	210
2	35	88	247
4	35	93	689
10	35	300	



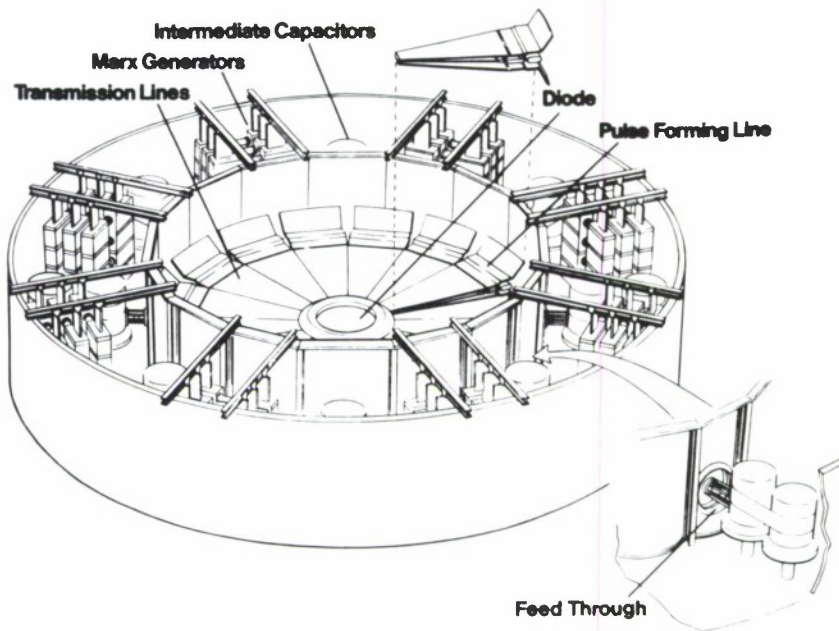


Figure 1. Configuration of electron beam pellet fusion accelerator (Sandia Laboratories PROTO II)

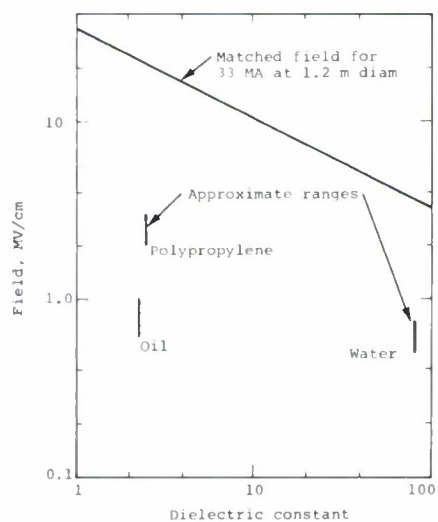


Figure 2. Field required to deliver 100 TW at 3 MV to 1.2 m. diameter load

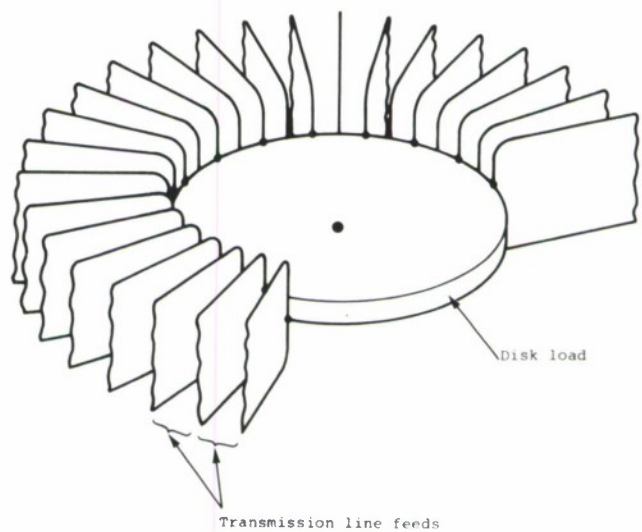


Figure 3. Convoluted feed using multiple transmission lines



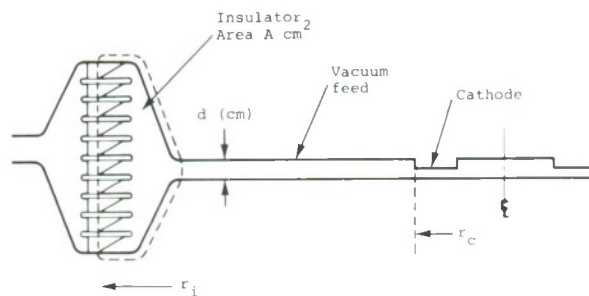


Figure 4. Schematic of simple flat disk tube

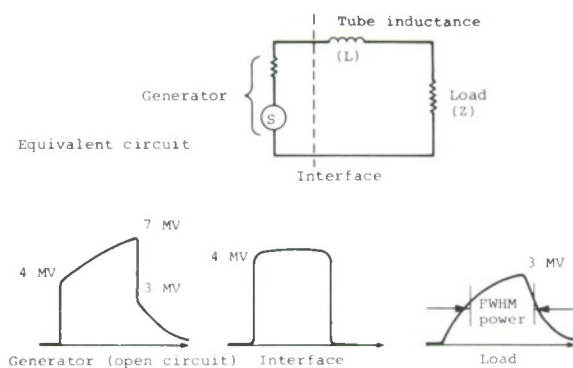


Figure 5. Derivation of time histories of interface and load voltage

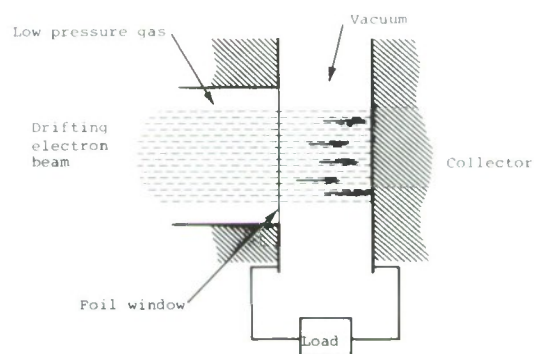


Figure 6. Electron beam used to drive external load via inverse diode

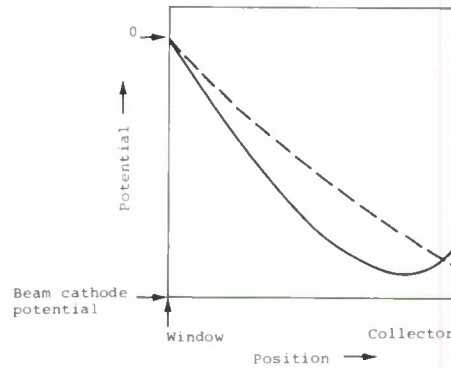


Figure 7. Potential plots for inverse diode

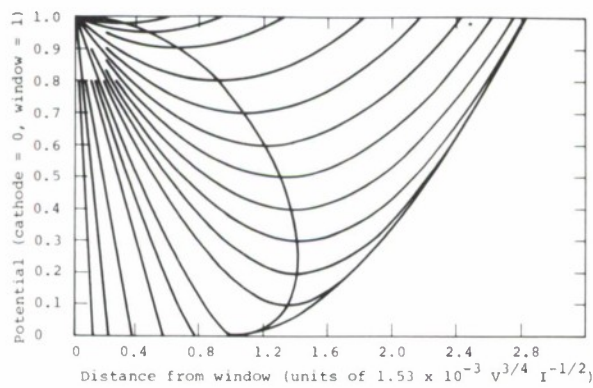


Figure 8. Potential distributions as a function of normalized position and current density

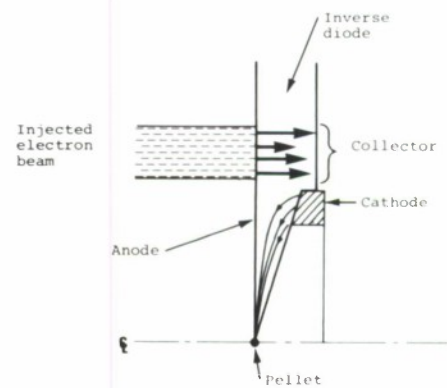


Figure 9. Use of an annular inverse diode to drive a focused load diode

# ELECTRON BEAM POWER FROM INDUCTIVE STORAGE\*

by

M. Cowan, G. J. Rohwein, E. C. Cnare

E. L. Neau, J. A. Mogford, W. K. Tucker, D. L. Wesenberg

Sandia Laboratories, Albuquerque, NM 87115

## ABSTRACT

When the energy required of electron beams greatly surpasses present capability, it will be advantageous to use inductive rather than capacitive storage for the prime energy source. This paper deals with development of technology for charging a storage inductor and for switching and transforming its stored energy for generation of an electron beam. A chemically powered generator which compresses magnetic flux provided by a superconducting coil is utilized along with high efficiency pulse transformers. Design concepts and experimental results are presented.

---

\*This work was supported by the U. S. Energy Research and Development Administration.

## ELECTRON BEAM POWER FROM INDUCTIVE STORAGE

### I. Introduction

For fusion applications electron beams may require such high energy that power supplies based on inductive storage will be most practical. Work to develop some of the technology needed to produce electron beams from inductive/capacitive stores is being carried out and this paper will report progress and indicate future plans.

The general design strategy is to use a chemically powered generator as the prime source for charging intermediate inductive and water-capacitor stores. High power transformers will be required and it may also be necessary to employ circuit breakers or fuses to interrupt high currents. A simplified diagram of a possible system which would employ these elements is shown in Figure 1. The first three inductors from the right constitute the chemically powered pulse generator which will be described in the next section. The next two inductors indicate a high power transformer, the development of which is the subject of the third section. The pulse from the generator rises in 300  $\mu$ s, charging the initial inductive store (the primary of the transformer) with 100 MJ. The fuse operation interrupts the primary

current in 6  $\mu$ s charging the water-dielectric capacitor with an energy  $\geq 10$  MJ. Generation of the electron beam from energy stored in the water capacitor could then employ state-of-the-art technology.<sup>1</sup> Performance of the fuse or opening switch is crucial to the success of this system example; however, switching technology will not be addressed here. Opening switches or fuses which provide time compression factors  $\gtrsim 40$  have been described elsewhere.<sup>2</sup> The last section deals with plans for continued development of the chemically powered generators and high-power transformers.

## II. The Chemically Powered Generator

The chemically powered generator called PULSAR is of the magnetic flux compression type and employs a superconducting coil to provide the working flux.<sup>3</sup> This type of generator operates by achieving a sufficiently fast forced reduction of the inductance of a circuit.<sup>4</sup> PULSAR is one of the first flux compression generators to operate without self-destruction.<sup>5</sup>

### A. Operating Modes

There are two PULSAR operating modes, axial and radial. In the axial mode, illustrated in Figure 2, the forced reduction in inductance is achieved by driving a conducting piston, the armature, through a nested coil arrangement. The outer coil

is superconducting while the inner one is of normal conductor and is connected in series with the load. Prior to armature arrival, current in the normal coil is zero while the superconducting coil carries a steady current providing flux in the normal one by mutual inductance. When the armature passes through the two coils, the pulse delivered to the load may have an energy even greater than that originally stored in the superconducting coil and yet the superconducting coil experiences only a small current change and returns to its original current soon after the armature has passed. This operating mode of PULSAR could be applied to any pulsed fusion reactor as a topping stage to improve fusion-to-electric energy conversion. A similar scheme for this purpose but without the superconducting-normal coil arrangement of PULSAR has been proposed by Velikhov of the Soviet Union.<sup>6</sup>

In the radial mode, illustrated in Figure 3, the inductance reduction is caused by radial expansion of an expendable, thin-walled aluminum tube. To prevent damage to the coils, the kinetic energy of this expanding armature and the original flux can be limited so that peak magnetic induction never exceeds 20T. In large scale systems it should be possible to avoid physical impact; however, with present experimental sizes the initial flux between the armature and compression coil is insufficient to stop



the armature upon compression and shocks resulting from impact must be dealt with. The strain rate of the expanding armature must be limited to  $\sim 10^4 \text{ s}^{-1}$  which is well below rates commonly used in self-destructive flux compression generators. The radial mode is best for the high power requirements of electron beam fusion but the use of an expendable armature limits operation to a few pulses per day. Either mode of PULSAR could have application as a "starter" for pulsed fusion reactors.

#### B. Experimental Hardware

Experiments to date have used normal compression coils with an inner diameter of 0.3 m and have substituted a capacitor bank and a normal electromagnet for the superconductor. Figure 4 shows hardware used in an experiment in the radial mode.

The flux compression coil is imbedded near the center of a fiber glass-epoxy structure which is about 1 m long and has a bore of 0.3 m. The coil itself is 0.3 m long with 6 turns and an inductance of 7.2  $\mu\text{H}$ . Coaxial cables are shown which connect the coil to a single turn load (not shown) of 0.55  $\mu\text{H}$ . A steel ring 0.38 m long and 51 mm thick is slipped over the coil structure to prevent damage from shocks generated by impact of the expanding armature. The electromagnet is physically isolated from the steel ring by a small gap. It has 98 turns (3200  $\mu\text{H}$ ) and is fed by a 3 mF capacitor. The armature is 1100-0 aluminum 330 mm long with

wall thickness 1.25 mm. It is expanded at strain rates  $\sim 10^4 \text{ s}^{-1}$  by a small diameter stick of explosive which is detonated simultaneously along its axis. This is much lower than previous experience with flux compression generators. At these low strain rates it is more difficult to achieve the maximum strain ( $\sim 50\%$ ) required for reasonably efficient operation. From an experimental program utilizing magnetically and explosively expanded tubes it was found that tubes of 1100 aluminum made by spinning and fully annealed give satisfactory performance. It is apparently important to minimize grain size and the number of impurity centers.

Figure 5 shows the experimental arrangement for a PULSAR experiment in the axial mode. The coil and electromagnet are the same ones which are shown in Figure 4. For the axial mode the armature is a thick-walled aluminum tube which is propelled by the smooth bore cannon through the coils at 750 m/s. No steel tube was used for the two axial experiments which were the first performed with the hardware. After the axial tests, the compression coil structure was machined to a smaller outer diameter to accept the steel ring for radial tests.

### C. Measured and Calculated Performance

Numerical analysis of circuits like those shown in Figure 6 establish performance expectations for PULSAR experiments. Only

the three basic elements are shown in this figure; however we also include circuits for the steel ring and the aluminum bobbin on which the superconductor is wound when they are to be considered. This bobbin carries most of the current transient protecting the superconductor. Proper time dependence of the various coupling coefficients accounts for armature motion, and the armature kinetic energy is consistently varied as magnetic energy is produced. Since the original PULSAR experiments<sup>3</sup> the coil has been redesigned to insure uniform axial distribution of current. Also, it is wound with thin copper material so that DC resistance may be used. However, axial drift and radial diffusion in the armature must be accounted for. This is done by conceptually dividing it axially and radially into many pieces and assigning resistance and both self and mutual inductance to each piece. Although several experiments have been carried out in the axial mode, only one has been done in the radial mode. The data from this one radial shot are shown in Figure 7. By the deadline for submission of this paper we had not finished calculations to compare with these data. Such comparison has been made for all axial shots and in all cases agreement has been close. One of these is shown as an example in Figure 8. Notice that there is negative current in the load circuit prior to arrival of the armature. This is due to the fact that a pulsed electromagnet

is substituting for the superconductor but also because there is a one ms uncertainty in timing for the axial mode.

### III. High Power Transformers

Work is underway to develop pulse transformer designs capable of operation in the  $10^6\text{V}$ - $10^7\text{A}$  range. A spiral strip rather than a helically wound design has been chosen because of its higher power density capacity and inherent capacitive voltage grading through the winding stack. This latter characteristic is particularly important when the transformer is subjected to very fast high voltage transients generated by discharge of a pulse forming line.

#### A. Design Considerations

For maximum performance the transformer must be designed specifically for its intended application. Important considerations are voltage stress endurance, magnetic force resistance, electrical matching to other elements of the circuit and service life. Spiral windings with polyester insulating sheet impregnated with castor oil have been reliably stressed to 20 kV/mm and linear current densities of 15 MA/m have been successfully demonstrated with urethane impregnated transformers. These are not expected to be the limits of performance. Matching electrical characteristics of a transformer to a given circuit generally requires parameter

space investigation using a transient circuit analysis code. The SCEPTRE code<sup>7</sup> has been used for this purpose during transformer development. No life expectancy data, per se, have been taken, but no apparent degradation has been observed in development designs although some have been pulsed more than 500 times.

## B. Design Evolution

Initial designs were simple spiral windings impregnated with either castor oil, water, or solid urethane and with no means for shaping electric fields. An example of one of these is shown in Figure 9. The copper strip is 100 mm wide with overall width of the lucite case being 350 mm. The primary diameter is 150 mm. The turn-to-turn insulation which is multilayered polyester film is 300 mm wide. There are five turns in the secondary and the open volume inside the case and secondary winding is impregnated with urethane. The secondary output was connected to a spark gap as shown in the figure. Operated directly by the 20 kV, 12 kJ capacitor bank the peak primary current was one MA and peak secondary voltage was 50 kV. With an exploding foil fuse in the primary, peak secondary voltage was 300 kV and pulse width 0.5  $\mu$ s. The best of these early designs used a water fill and operated satisfactorily to 600 kV.

Later designs achieved improved performance using a castor oil fill and variously shaped concentric shields both inside and outside the windings to shape the electric fields. An example of



one of the first of these is shown in Figure 10. The copper strip is 100 mm wide and the input strip to the 175 mm diameter primary is visible in the figure. The field-shaping shield which also serves as the case flares to a 400 mm diameter and the overall width (flare-to-flare) is 425 mm. Operated directly by the 20 kV, 12 kJ capacitor bank the secondary peak voltage was 200 kV, but with an exploding foil fuse in the primary it was 1.2 MV into a 500  $\Omega$  load. Figure 11 shows this design connected to the bank and equipped with a ring grading arrangement to accommodate a voltage probe. A very similar design was utilized in a small electron beam generator called Trace I which has been described previously.<sup>8</sup> The initial energy store in Trace I is a 14.5  $\mu$ F, 20 kV capacitor, and dual resonance is used to charge the water transmission line. Figure 12 shows the Trace I arrangement.

The most recent design is shown in Figure 13. This transformer is designed to transfer charge from a 120 kV capacitor bank to a 1.5 MV water line using a direct ringing transfer. The capacitor bank will be made up of a back-to-back arrangement of Scyllac-type 60 kV capacitors and for the first tests only 2 (7 kJ) will be used. Later tests will use 14 capacitors in the bank. The primary is 600 mm in diameter and the case length is 1.2 m. There are 20 turns in the secondary, and the winding width is 300 mm.



#### IV. Future Plans

The first superconducting magnet for the PULSAR generator development has been constructed and will be delivered during November 1975. It will be used to demonstrate that the superconductor does not quench during pulse generation and to work out proper operational procedures for the use of much larger superconducting magnets in this role. During 1976 we will be able to specify the design for a 22 MJ superconducting magnet which could be operational in 1977 and would be used with a complete power amplifying system for electron beam production. By 1978 we should be able to design a system to meet break-even energy requirements.

Figure 14 lists some of the properties of the future PULSAR generators. Values for the largest system, the break-even system, are open to revision but the system indicated should lead to an electron beam energy  $\geq 10$  MJ. Notice that for larger generators a greater fraction of  $E_{SC}$ , the energy stored in the superconducting magnet, appears as energy in the load  $E_L$ . The PULSAR load in a system like the one shown in Figure 1 would be the primary of the transformers. Also, it should be pointed out that  $E_L/t_p$  is much lower than peak power since  $t_p$  is the total operating time and current rise is nearly exponential. Transformers for use with the 1.8 m PULSAR system are only about twice as large as the present 1.5 MV design shown in Figure 13. A modest effort during the next two years should produce successful designs for use with the largest PULSAR generators.

## References

1. K. R. Prestwich, et al., "PROTO-I Diode and Switching Studies," These Proceedings.
2. M. Friedman and M. Ury, "High Voltage Pulse Generator Using a Novel Opening Switch for the Interruption of Current Flowing through an Inductor, Bull. Am. Phys. Soc. 18, 660 (1973).
3. M. Cowan, et al., "Multimegajoule Pulsed Power Generation from a Reusable Compressed Magnetic Field Device," Proceedings of the International Conference on Energy Storage, Compression, and Switching, Torino, Italy, November 5-7, 1974.
4. H. Knoepfel, Pulsed High Magnetic Fields, Amsterdam: North-Holland Publishing Co., 1970.
5. R. Hahn, et al., "Magnetic Compressive Generators Using Gaseous Explosive," Proceedings of the International Conference on Energy Storage, Compression, and Switching, Torino, Italy, November 5-7, 1974.
6. Y. P. Velikhov, et al., "Feasibility of MHD Conversion of Pulsed Thermonuclear Reactor Energy," FTD-HT-23-200-74, Foreign Technology Division WP-AFB, Ohio, November 1973.
7. J. C. Bowers and S. R. Sedone, SCEPTRE: A Computer Program for Circuit and System Analysis, Prentice-Hall, Inc., 1971.
8. G. J. Rohwein, "TRACE I, A Transformer-Charged Electron Beam Generator," IEEE Transactions on Nuclear Science, Vol. NS-22, No. 3, June 1975.

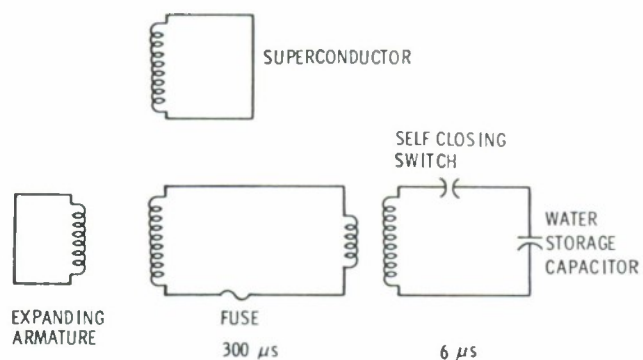


Figure 1. Pulse system for inductive power

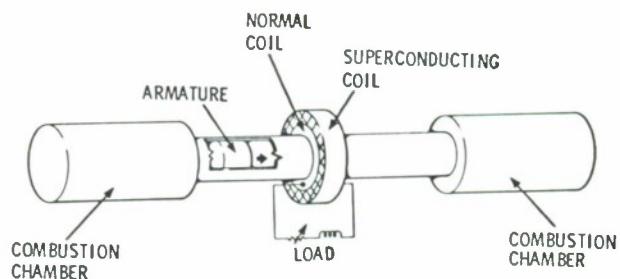


Figure 2. Chemically powered PULSAR generator (axial mode)

Figure 3  
PULSAR generator (radial mode)

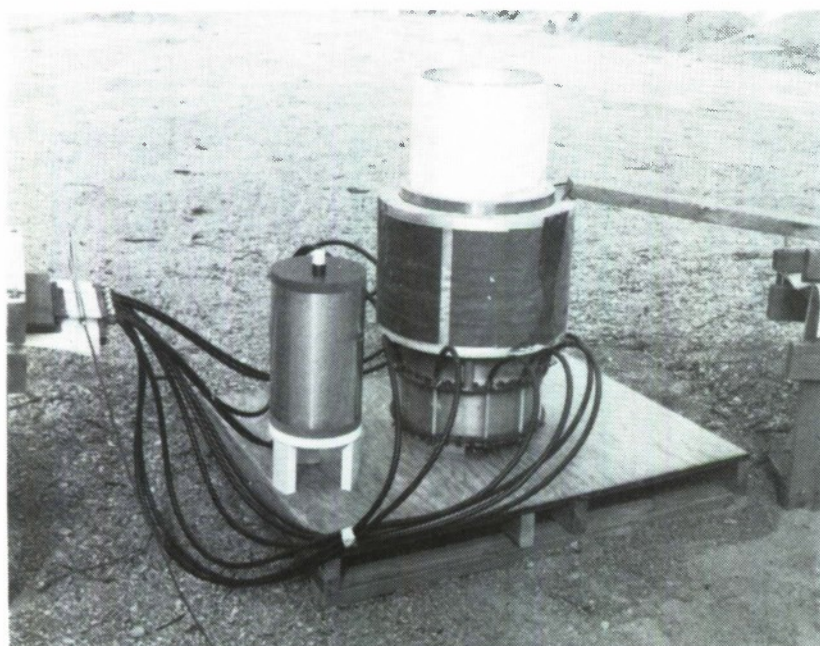
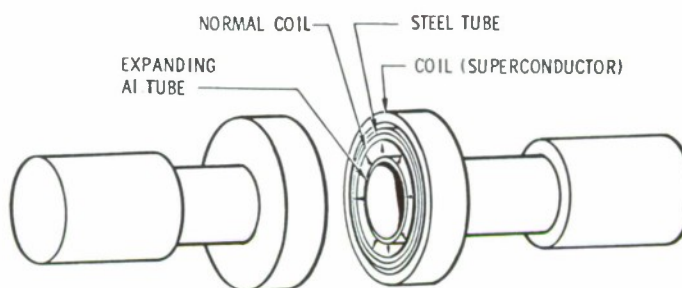


Figure 4  
Experimental apparatus for PULSAR experiment in the radial mode

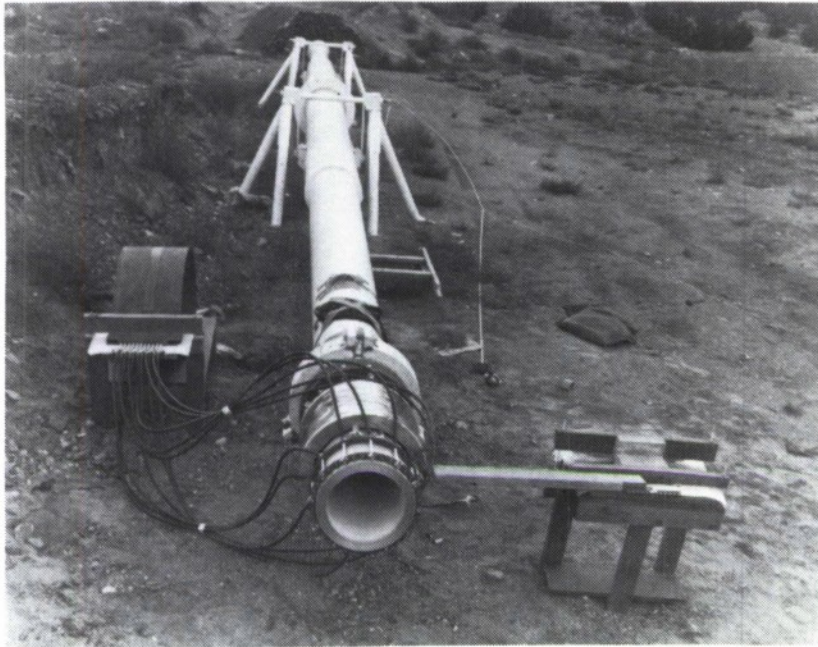


Figure 5  
Experimental apparatus for  
PULSAR experiment in the  
axial mode

Figure 6  
Circuits used to simulate PULSAR  
operation

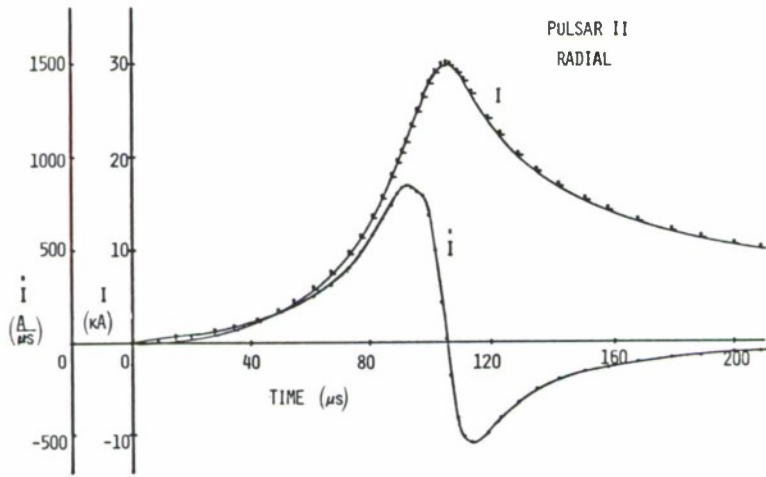
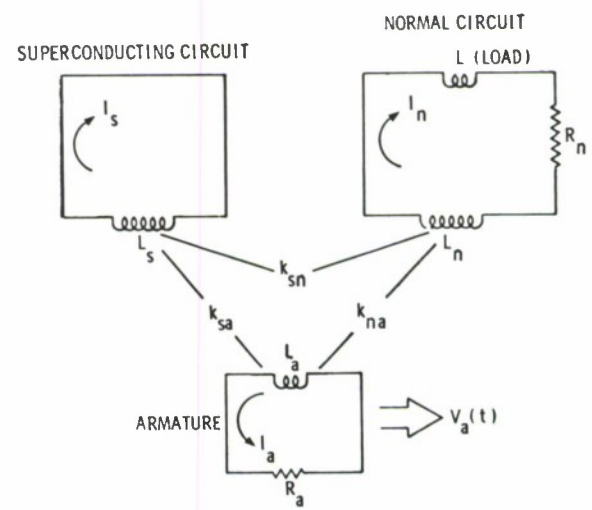


Figure 7  
Data from radial mode  
experiment



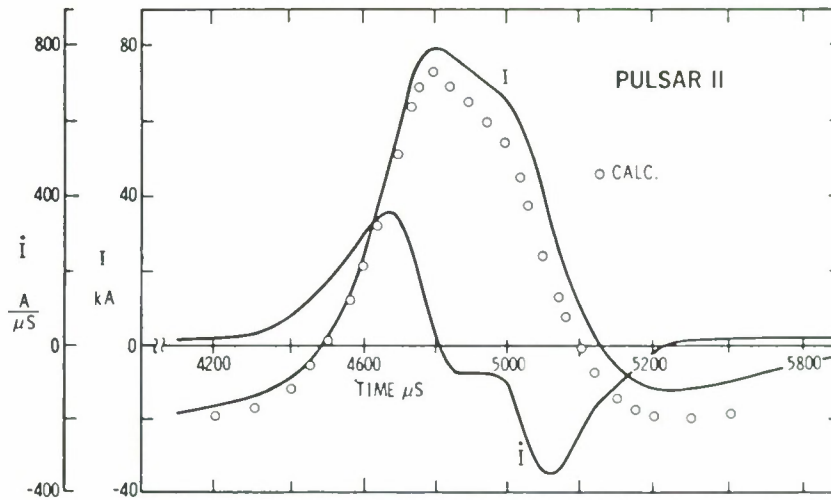


Figure 8. Comparisons between data and calculations for axial PULSAR experiment

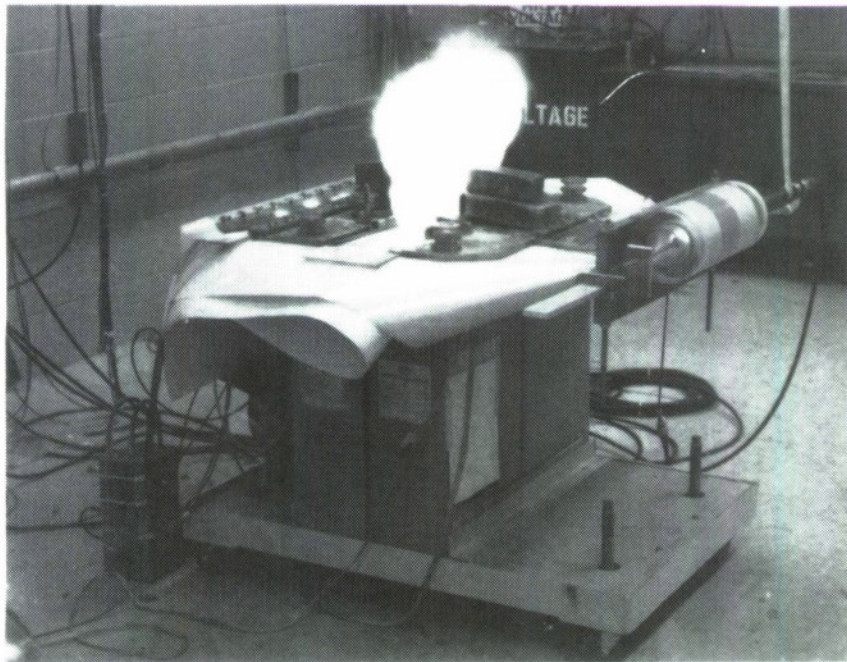


Figure 9. One of the early transformer designs being operated with an exploding foil fuse in the primary circuit

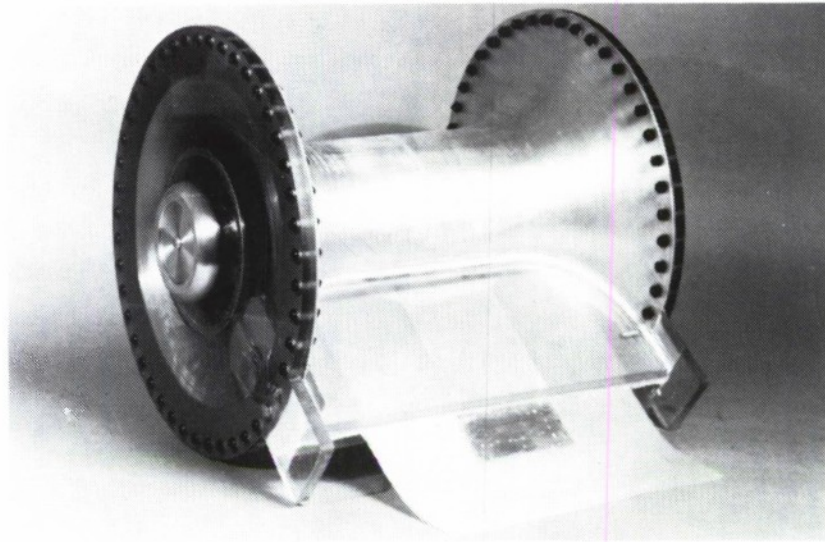


Figure 10. An experiment with one of the first transformers to employ circuits for electrical field shaping

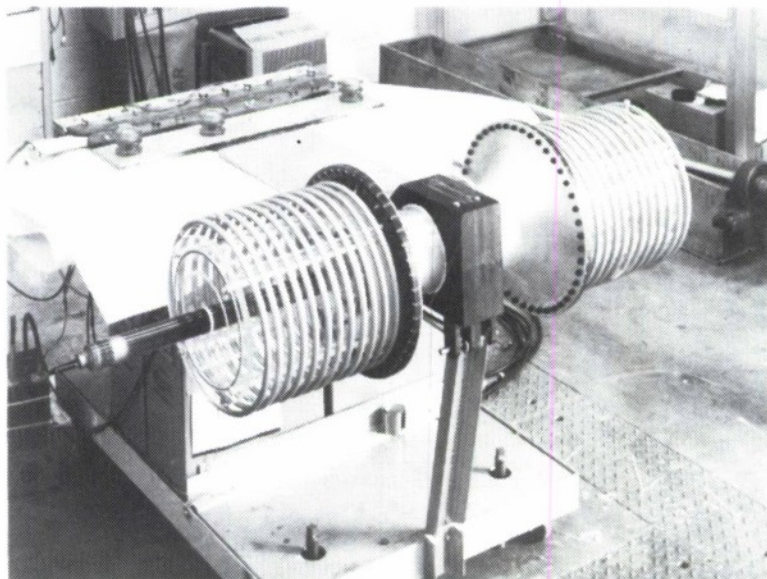


Figure 11. Transformer of Figure 10 equipped with ring grading arrangement to accommodate a voltage probe and a load



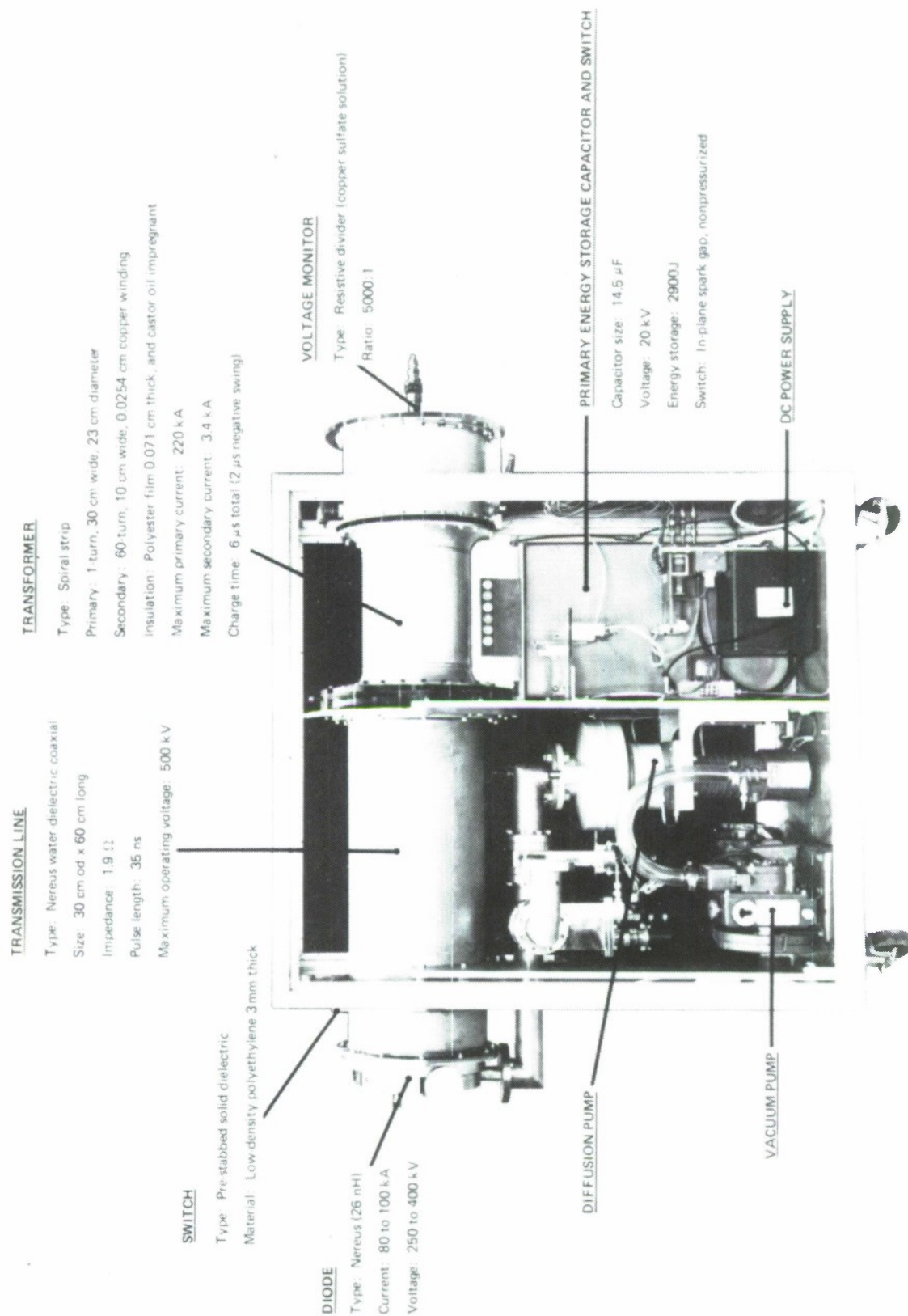


Figure 12. Trace 1 electron beam generator

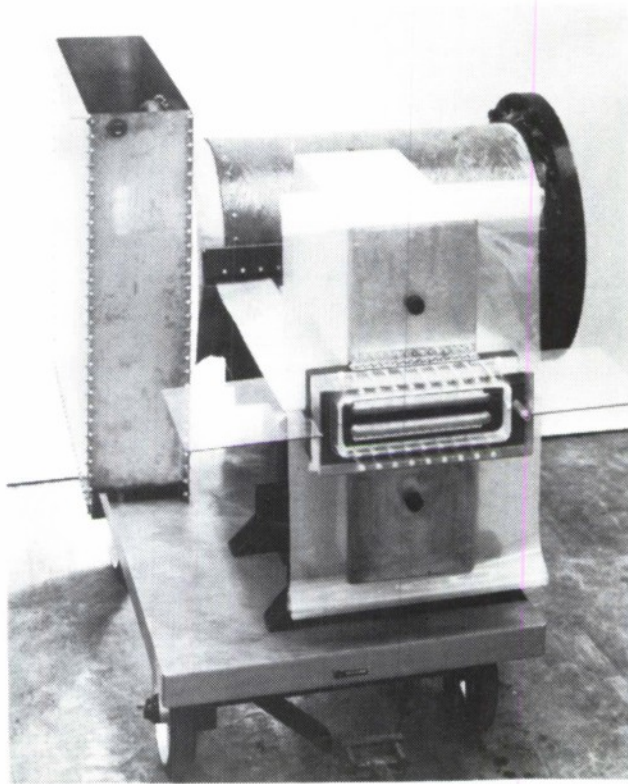


Figure 13. 1.5 MV transformer

DIAMETER (m)	$E_{KE}$ (J)	$E_{SC}$ (J)	$E_L$ (J)	$V$ (m/s)	$m$ (kg)	$t_p$ (ms)
0.3	180 k	200 k	14 k	750	0.6	0.03
1.8	22 M	22 M	10 M	750	40.0	0.15
3.6	224 M	110 M	100 M	800	700.0	0.3

Figure 14. Comparison of radial PULSAR systems. Column headings are left to right: The bore of the compression coil; kinetic energy of the armature; energy stored in the superconductor; energy delivered to the load; expansion velocity for the armature; armature mass; pulse time.

A LOW VOLTAGE MULTI-ELECTRON BEAM  
APPROACH TO PELLET HEATING

By

R. G. Little  
W. R. Neal  
and  
J. R. Uglum

SIMULATION PHYSICS INC.  
BURLINGTON, MA 01803

ABSTRACT

This paper presents analysis relating to the feasibility of using low voltage (100 keV) pulsed electron beams for fusion pellet heating. The rationale behind the multi-module approach is developed. Analysis pertaining to the identification of specific module characteristics is presented, and 100 keV electron beam physics is discussed. The results of the analysis are that near state-of-the-art pulsed power technology is adequate for module fabrication and that the feasibility of the concept depends upon the ability to transport and focus the electron beams.

This work supported by Lawrence Livermore Laboratory

## SECTION 1

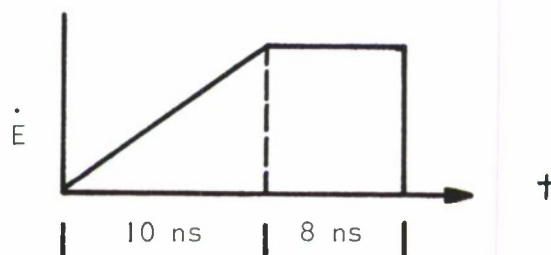
### INTRODUCTION

This paper presents analysis performed to assess the feasibility of using low voltage pulsed electron beams for fusion pellet heating. Other electron beam fusion work considers single or perhaps a two beam <sup>(1)</sup> approach at voltage  $>1$  MeV. This paper addresses the feasibility of using many electron beams, in the 100 keV range, fired simultaneously from multiple modules, distributed over  $4\pi$  geometry, onto a centrally located pellet.

The approach to the study was to use theoretical analysis and, where available, engineering data to conceptually design a break-even system.

The electron beam break-even specifications <sup>(2)</sup> addressed are as follows:

- Pellet Diameter = 4 mm
- E-beam Voltage = 100 kV
- Average Current =  $4 \times 10^7$  amps
- Total Beam Energy = 50 kJ
- Peak Power =  $4 \times 10^{12}$  watts
- Power Pulse Shape:



Although recent analysis indicates that the total energy requirement is more likely 200 kJ, the results of the study for the 50 kJ level can in most cases be extrapolated.

Based upon consideration of power flow in the electron beam generator and diode critical current criteria, multi-module machine concepts are developed. The range considered is from 30 to 150 modules where each module produces its own 100 kV electron beam at currents from 0.3 - 1.3 MA.

The status of pulsed power technology is such that fabrication of the described modules is quite feasible. Also the necessary synchronous triggering capability has been demonstrated. The principal area of concern in the concept is that of transport and focusing the electron beams. It has not yet been demonstrated that these requirements can be fulfilled.

## SECTION II

### MULTI-MODULE SYSTEM DESIGN CONSIDERATIONS

#### 2.1 GENERAL

A number of criteria must be considered in the design of a multi-module system which delivers 50 kJ of 100 kV electrons to a fusion pellet with pulse width of 13 nsec fwhm. These considerations begin with diode critical current criteria and the geometrical aspects of multiple beams in order to determine the effect of the choice of the number of modules upon the diode and beam requirements. Synchronous module switching is considered. Once the choice of the number of modules has been made, rise-time requirements and energy flow analysis determine the parameters of the energy store. In order to achieve a 10 ns risetime, present pulsed power technology points to a 2 ohm store. Since diode impedances are considerably less, the pulsed power modules must have an impedance transformer.

#### 2.2 DIODE PHYSICS

The diode parameters are not uniquely determined from the final beam requirements and must be selected after studying what options and trade-offs exist.

##### 2.2.1 Diode Critical Current

The energy requirement of 50 kJ of 100 kV electrons in about 13 nsec implies an average total current,  $I_{tot}$ , of



$$I_{\text{tot}} \approx \frac{50 \text{ kJ}}{100 \text{ kV} * 13 \text{ ns}} = 38.5 \text{ MA}$$

or, in round numbers,  $I_{\text{tot}} \approx 40 \text{ MA}$ .

The diode critical current, is defined as that diode current which generates a magnetic field strong enough to make the outermost diode electrons arrive at the anode with a purely tangential motion, that is, the magnetic radius of curvature,  $r_M$ , is equal to the anode-cathode gap spacing,  $g$ . Beam coolness and focusing requirements force consideration of an annular electron beam.

The expression for critical current for an annular diode is given by: (3)

$$I_{\text{CRIT}}^{\text{ANN}} = I_{\alpha} \frac{\bar{R}}{g} \sqrt{\gamma^2 - 1}$$

$$\approx 5.6 \frac{\bar{R}}{g} \text{ kA} \quad (\text{for } V_B = 100 \text{ kV}),$$

where

$$I_{\alpha} = \text{Alfvén current, } 8.517 \text{ kA}$$

$$\bar{R} = \text{Mean radius of the annulus}$$

$$g = \text{Anode-cathode gap spacing}$$

$$\gamma = 1 + \frac{e V_B}{m_0 C^2} = 1.196 \quad (\text{for } V_B = 100 \text{ kV})$$

Also, the Child-Langmuir current for an annular diode can be shown to be

$$I_{CL}^{ANN} = \frac{4\sqrt{2}}{9} I_{\alpha} \frac{\bar{R} \Delta R}{g^2} (\gamma - 1)^{3/2}$$

$$\approx 0.46 \frac{\bar{R} \Delta R}{g^2} \text{ kA} \quad (\text{for } 100 \text{ kV}).$$

Setting

$$I_{CRIT}^{ANN} = I_{CL}^{ANN}$$

gives

$$\frac{\Delta R}{g} \approx 12.$$

Adequate diode turn on response is achieved if the anode-cathode gap electric field strength is about 0.5 MV/cm or higher:<sup>(4)</sup>

$$E_{A-k} \approx \frac{V_B}{g} = \frac{m_0 c^2}{e} \frac{\gamma - 1}{g} \geq 500 \text{ kV/cm}$$

$$\approx \frac{m_0 c^2 / e}{1 \text{ cm}}.$$

Therefore

$$g \lesssim (\gamma - 1)$$

$$\approx 0.196 \text{ cm at } 100 \text{ kV}.$$

To minimize gap closure effects, choose

$$g \equiv 0.2 \text{ cm}$$

then

$$\Delta R = 12 g = 2.4 \text{ cm} ,$$

which results in a diode current equal to the critical diode pinch current with

$$I_{CL}^{ANN} \simeq 28 \bar{R} \text{ (cm) kA}$$

for  $V_B = 100 \text{ kV}$ .

### 2.2.2 Geometric Aspects of Multiple Beams

To help estimate the number of beam modules required, consider the surface of the beam compression chamber (of radius  $R_{CC}$ ) to be uniformly covered with annular cathodes. The solid angle subtended by one such cathode is

$$\Omega_c = 2 \pi (1 - \cos \theta) ,$$

where

$$\theta = \tan^{-1} (\bar{R}/R_{CC})$$

so that (neglecting, for simplicity, the inter-annular "waste" space)  
the number of cathodes that can fit on the chamber surface is given by

$$N \approx \frac{4\pi}{\Omega_c} = \frac{2}{1 - \cos \theta}.$$

Because

$$\cos (\tan^{-1} \chi) \equiv \frac{1}{\sqrt{1 + \chi^2}},$$

one finds that

$$N \approx \frac{2}{1 - \frac{1}{\sqrt{1 + (\bar{R}/R_{cc})^2}}}$$

which, upon inversion, yields

$$\frac{\bar{R}}{R_{cc}} \approx \sqrt{\left(\frac{N}{N-2}\right)^2 - 1}.$$

Since the space-charge limited diode current from a single cathode  
is

$$I_{CL}^{ANN} = 28 \frac{\text{kA}}{\text{cm}} \bar{R}$$

and the total current of all N cathodes is

$$I_{tot} = N I_{CL}^{ANN}$$

then given a module number, N, the module current is,

$$I_{CL}^{ANN} = I_{tot}/N$$

from which the appropriate beam radius,  $\bar{R}$ , is obtained from

$$\bar{R} = I_{CL}^{ANN} / 28 \frac{kA}{cm}$$

which, together with the ratio,  $\bar{R}/R_{cc}$ , calculable from N alone, gives the corresponding beam compression chamber radius,  $R_{cc}$ .

Representative values for 40 MA total current at 100 kV are given in Table I.

## 2.3 ENERGY STORE

### 2.3.1 Store Parameters

The energy store is also not uniquely determined by the final beam parameters, but in any event, a high energy density material is necessary from system power requirements. Both water and solid dielectrics were considered. The following develops the parameters for a solid dielectric store.

The length,  $\ell$ , of the store is uniquely determined by the desired pulsewidth,  $\tau_p$

$$\ell = \frac{C}{\sqrt{\epsilon_r}} \frac{\tau_p}{2}$$

which, for  $\epsilon_r \approx 2.5$  and  $\tau_p \approx 13$  nsec, yields

$$\ell = 123 \text{ cm}.$$

The thickness,  $d$ , in units of  $\ell$  is given by<sup>(3)</sup>

$$d/\ell = \alpha \sqrt{\frac{Z_s}{Z_D}},$$

where

$$\alpha = \left( \frac{2 V_B/\ell}{K} \right)^{5/4} L^{5/32} \left( 2\pi\ell^3 \frac{60 \Omega}{\sqrt{\epsilon_r} Z_D} \right)^{1/8}.$$

For  $K \approx 3$  MV/cm,<sup>(5)</sup> a shot lifetime  $L \approx 1000$  shots,  $V_B = 100$  kV and 40 modules

$$\alpha \approx 3.91 \times 10^{-3}$$

so that for  $Z_s = 2 \Omega$

$$d \approx 0.481 \sqrt{\frac{Z_s}{Z_D}} \approx 2.15 \text{ cm}.$$



Similarly, the radius,  $r$ , in units of  $\ell$  is given by

$$r/\ell = \beta \sqrt{\frac{Z_D}{Z_S}} ,$$

where

$$\beta = \frac{\alpha 60 \Omega}{\sqrt{\epsilon_r Z_D}} \approx 1.484$$

so that

$$r \approx 182 \sqrt{\frac{Z_D}{Z_S}} \approx 40.8 \text{ cm} .$$

### 2.3.2 Synchronous Switching and Risetime Considerations

Trigatron gas switching with nanosecond risetime has been achieved by many groups.<sup>(6-7)</sup> Even tenths of nanosecond jitter is possible with laser switching. This makes the possibility of firing many modules synchronously quite feasible. Figure 1 presents the results of a probability analysis<sup>(3)</sup> where probability distributions for less than all units firing are shown for arrays from 1 to 150 modules. An example of what the analysis shows is that 80% of the modules in a 100 module array can be expected to fire with a jitter of slightly more than twice the jitter of one module, i.e., 2 times 1 nanosecond. This is likely to be acceptable for pellet heating if the beams are overlapped at the target, which is assumed in this analysis.

Multiple channel switching for reduced inductance has also been accomplished. However, even with multiple channels and careful front end design, it is unlikely that total store inductance can be reduced to less than 10 nh. It is this consideration that results in choosing the energy store impedance to be 2 ohms.

#### 2.4 TRANSMISSION LINE TRANSFORMER

Since the store impedance is chosen to be 2 ohms and the diode impedances for the arrays considered are typically tenths of ohms, an impedance transformer must be employed for maximum power transfer. A transmission line transformer with water as the dielectric is chosen on the basis of transfer efficiency, voltage hold-off and compactness. It can be shown<sup>(3)</sup> that the relations to follow hold for an exponentially tapered line.

The radii of the line at either end are given by

$$R_{in} = R_{out} e^{-[\sqrt{\epsilon_r} Z_o / 60 \Omega]},$$

where  $R_{out}$ , the outer radius of the transformer is chosen to be the diameter of the store, which is also equal to that of the diode for compactness, and  $Z_o$  is the impedance of the transformer at that end.

The length of the transformer line is determined mainly by the fractional droop,  $f$ , tolerable for a pulse of duration,  $\tau_p$ :

$$l \geq \frac{c \tau_p \ln^2 (Z_D/Z_S)}{2 f \sqrt{\epsilon_r}} .$$

## 2.5 SPECIFIC MODULE PARAMETERS

Figure 2 shows the major elements of the pulsed power module developed here. These elements are a charging system which ultimately would be repetitive, a solid dielectric energy store which is multi-channel switched into a water dielectric transformer at the output of which is a large narrow-annulus cathode. The annular electron beam is extracted through a thin anode structure where it is transported and focused in a biconic structure. It is the transport and focusing of the generated electron beam which is the most difficult part of the concept as will be further discussed.

Using the relationships presented, the specific module parameters for arrays of 40 and 150 are presented in Table 2.

## 2.6 ELECTRON BEAM TRANSPORT AND FOCUSING

Thus far there has been no demonstration of the feasibility of transporting and focusing electron beams with such difficult requirements. **Strong** electric and magnetic field forces are associated with these beams

and both must be neutralized. The charge and current neutralization can be expressed as neutralization factors,  $f_Q$  and  $f_I$ , respectively, and, for a uniform density cylindrical beam, incorporated into the radial force expression as

$$F = \frac{e\rho}{2\epsilon_0} r \left[ (1 - f_Q) - (1 - f_I) \frac{v^2}{c^2} \right] = Kr.$$

Thus, for a charge-neutralized ( $f_Q \approx 1$ ) but current unneutralized ( $f_I \ll 1$ ) beam, the K-value is negative and the beam will converge or "pinch". Fully neutralized ( $f_Q \approx 1 \approx f_I$ ), the K-value is very small and parallel transport of the beam can occur.

In order to achieve both charge and current neutralization in transporting the electron beam to the pellet, we propose the approach shown schematically in Figure 3. The two basic concepts, based upon experimental observations, used in this approach are:

- (1) Control of space charge forces by the use of solid dielectric surfaces.<sup>(8)</sup>
- (2) Control of magnetic field forces with conducting structures internal to the beam.<sup>(9)</sup>

Specifically, the concept is as follows. The annular diode cold electron beam is injected into a collapsing annular structure formed by two concentric cones. The surfaces of the cones are lined with a dielectric layer whose thickness is greater than the electron beam range.

The background gas pressure in the double cone geometry is less than that required for space charge neutralization. Electrons injected into the structure expand under space charge forces and impinge upon the

surface of the outer dielectric. The voltage builds up on this surface until dielectric breakdown or flashover occurs. Either mechanism produces a high density ionized gas at the surface of the dielectric. This gas provides the ions required for space charge neutralization.

Once space charge neutralization has been achieved, magnetic field collapse of the beam occurs. Two effects keep the beam from collapsing upon the inner cone. Initially charge buildup on the inner dielectric surface repels the collapsing beam electrostatically. Subsequently, a return current flows in the conducting inner cone due to the back emf associated with the rising portion of the beam. This return current also repels the beam and should be sufficient to result in a net current such that the beam can propagate. As the beam propagates further down the collapsing annulus it again expands, impinging upon the outer dielectric wall and releasing ions; thus the process repeats itself until the beam collapses upon the pellet.

The effect of the solid dielectric liner warrants further discussion. First, it provides ions for space charge neutralization and could in fact be an unlimited source of ions. The exceedingly high electron current density requires a copious supply of ions for space charge neutralization. The required background gas pressure for such neutralization would not allow the beam to penetrate more than a few cm. This is to be contrasted with the solid dielectric liner which should provide the right quantity of ions as the beam is compressed to higher and higher current densities. This is because if the beam is not space charge neutralized, it expands, impinging upon the solid dielectric and creating more ionization through dielectric breakdown and impact collisions, until it is neutralized.

The second feature of the solid dielectric is that before strong ionization occurs it exerts electrostatic (trapped charge) forces on the beam unlike all other transport and focusing techniques which rely strictly on magnetic field force control.

A final comment on the dielectric liner configuration is that it is found to be a copious source of ions accelerated in the direction of beam propagation. The energy deposited in the surface of the dielectric due to flashover far exceeds that associated with presently considered multiple beam transit in an anode foil.<sup>(10)</sup> Also, directionality of the ion component can be achieved with geometrical tailoring of the dielectric guide. This approach should therefore be further pursued for ion acceleration studies.

Although the ideas presented here, to use dielectrics for space charge neutralization and center conductors for current neutralization, are based upon experimental observations; whether or not they can be used for this severe requirement is yet to be demonstrated.



### SECTION III

#### SUMMARY

This paper has presented an analysis of the utility of using pulsed low voltage electron beams for fusion pellet heating. The results can be summarized as follows:

- (1) Near state-of-the-art pulsed power technology can be used to provide the required electron beam module.
- (2) Feasibility of a 100 keV pulsed electron beam approach to pellet heating rests primarily with the ability to transport and focus the electron beams to attain the required power density.

An approach to electron beam transport and focusing, based upon the use of solid dielectric surfaces for space charge neutralization and an internal conductor for current neutralization, was presented. Also, the utility of a solid dielectric guide as a copious source of ions for ion acceleration studies was discussed.

## REFERENCES

1. Yonas, G., Poukey, J.W., Prestwich, K.R., Freeman, J.R., Toepfer, A.J. and Clauser, M.J., Nuclear Fusion 14, 731 (1974).
2. Bangerter, R.O., Lawrence Livermore Laboratory, Private Communication, July 1975.
3. Neal, W.R., Little, R.G. and Uglum, J.R., "Analysis of Low Voltage Electron Beam Requirements for Fusion Pellet Heating", Simulation Physics Final Report FR-20024, Contract No. 8837805, Lawrence Livermore Laboratory, November 1975.
4. Parker, R.K., Anderson, R.E., and Duncan, C.V., J. Appl. Phys. 45, 2463 (1974).
5. Martin, J.C., AFWL PEP Circuit and Electromagnetic System Design, Note #4 (1973).
6. Milde, H. and Moriarty, J., "Switching of Fast High Voltage Pulse Generators", High Voltage Technology Seminar, Vol. II, Sept. 1969.
7. Uglum, J.R., Little, R.G., and Face, S.H., "Electron Beam IEMP Simulation Development", Simulation Physics Final Report FR-75-10039, Defense Nuclear Agency Contract No. DNA001-75-C-0136, August 1975.
8. Little, R.G., Uglum, J.R. and Lowell, R.A., "Cavity IEMP Enhancement by Dielectric Walls", Proceedings of the IEEE Nuclear and Space Radiation Effects Conference, July 1975, to be published.
9. Little, R.G. and McNeill, W., "Effects of Acceleration and Drift Region Configurations upon the Propagation of Intense Relativistic Electron Beams", IEEE Transactions on Nuclear Science, Vol NS-18, No. 3, June 1971.
10. See, for example: Swain, D.W., Goldstein, S.A., Kelly, J.G., and Hadley, G.R., J. Appl. Phys. Vol. 46, No. 10, October 1975.

TABLE I

Effect of Number of Modules upon Diode Parameters and Beam and  
Compression Chamber Size

N	$I_{CL}^{(ann)}$ (kA)	$Z_D(\Omega)$	$I_{CL}^{(ann)} = I_{crit}^{(diode)}$	
			$\bar{R}(\text{cm})$	$R_{cc}(\text{cm})$
30	1333	0.075	47.9	125
35	1143	0.088	41.1	116
40	1000	0.100	36.0	110
50	800	0.125	28.8	98.7
60	667	0.150	24.0	90.6
80	500	0.200	18.0	79.0
100	400	0.250	14.4	70.9
125	320	0.313	11.5	63.5
150	267	0.375	9.59	58.1

TABLE II

Characteristics of Major Components of 100 keV Electron Module for 40 and 150 Element Arrays

SOLID DIELECTRIC ENERGY STORE	WATER TRANSFORMER	DIODE	ELECTRON BEAM
ELEMENT OF 40 MODULE ARRAY			
$Z_S = 2 \Omega$	$Z_{in} = 2 \Omega$	$Z_D = 0.1 \Omega$	$V_B = 100 \text{ kV}$
$V_S = 900 \text{ kV}$	$Z_{out} = 0.1 \Omega$	$V_D = 100 \text{ kV}$	$I_B = 1 \text{ MA}$
$I_L = 225 \text{ kA}$	$\ell = 200 \text{ cm}$	$I_D = 1 \text{ MA}$	$v/\gamma = 90$
$E_S = 1.3 \cdot \text{kJ}$	$R_{2in} = R_{2out} = 40 \text{ cm}$	$\bar{R} = 40 \text{ cm}$	$J = 8 \text{ MA/cm}^2$
$\ell = 123 \text{ cm}$	$R_{1in} = 29.6 \text{ cm}$	$\Delta R = 2.2 \text{ cm}$	
$r = 40 \text{ cm}$	$R_{1out} = 39.4 \text{ cm}$	$g = 0.2 \text{ cm}$	
$d = 2.2 \text{ cm}$			
ELEMENT OF 150 MODULE ARRAY			
$Z_S = 2 \Omega$	$Z_{in} = 2 \Omega$	$Z_D = 0.375 \Omega$	$V_B = 100 \text{ kV}$
$V_S = 460 \text{ kV}$	$Z_{out} = 0.375 \Omega$	$V_D = 100 \text{ kV}$	$I_B = 0.267 \text{ MA}$
$I_L = 115 \text{ kA}$	$\ell = 100 \text{ cm}$	$I_D = 0.267 \text{ MA}$	$v/\gamma = 24$
$E_S = 0.35 \text{ kJ}$	$R_{2in} = R_{2out} = 18 \text{ cm}$	$\bar{R} = 18 \text{ cm}$	$J = 2.1 \text{ MA/cm}^2$
$\ell = 123 \text{ cm}$	$R_{1in} = 13.3 \text{ cm}$	$\Delta R = 1.28 \text{ cm}$	
$r = 18 \text{ cm}$	$R_{1out} = 16.9 \text{ cm}$	$g = 0.2 \text{ cm}$	
$d = 0.94 \text{ cm}$			

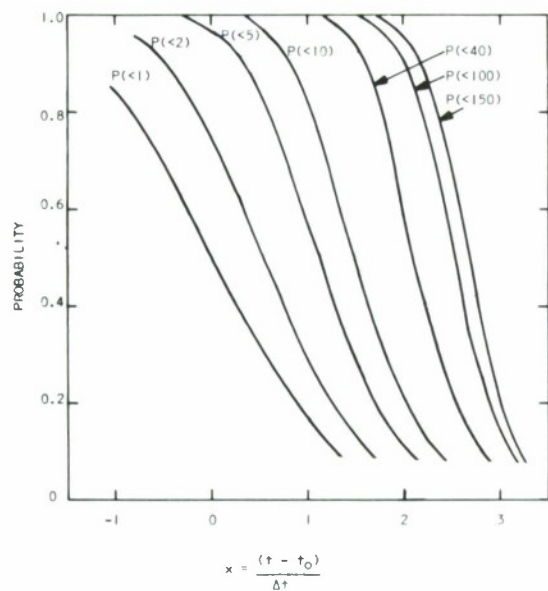


Figure 1. Probability distribution that less than all units have fired in an N-module array

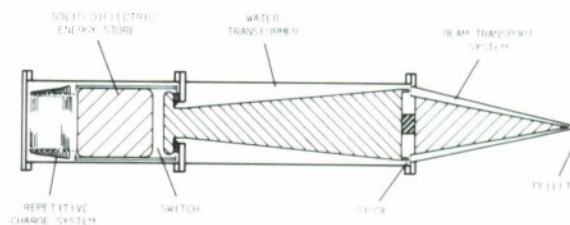


Figure 2. Conceptual design for electron beam module showing the major elements of the system.

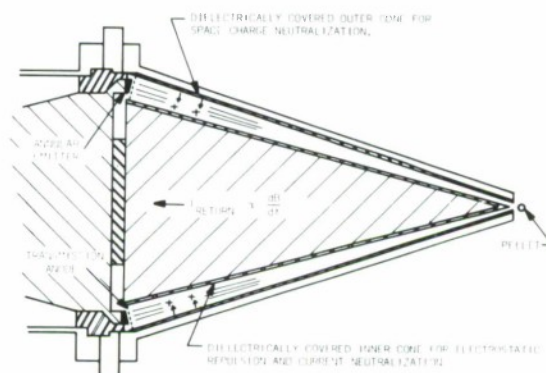


Figure 3. Concept for transport and focusing of electron beams utilizing solid dielectric surfaces for space charge neutralization and a center conductor for current neutralization

TONUS-2 -- INTENSE ELECTRON BEAM GENERATOR

WITH STORED ENERGY OF 0.2 MJ

V. M. Bistritsky, A. N. Didenko, I. S. Gleiser,  
G. A. Sterligov, B. V. Okulov, A. G. Gerlitsin,  
Yu. P. Usov, V. I. Tsvetkov, A. A. Shatanov

Institute for Nuclear Physics, 634050, Tomsk-50, P. O. Box 25, USSR

ABSTRACT

Details of construction, technology and some aspects of future applications of the intense electron beam generator TONUS-2 with disk-type transmission line is the subject of this paper.



The construction of the intense electron beam generator TONUS-2 is going on at the Research Institute for Nuclear Physics under the auspices of the Polytechnical Institute with the intention to carry on investigation of new methods of particle acceleration, generating of powerful x-ray and SRF-pulses, interaction of the intense beam with plasmas, etc. [1].

In spite of various modifications of parameters, constructions and purposes of utilization a common scheme of the intense beam generator has been developed consisting of the initial energy storage, usually a capacitor bank in the form of the Marx generator, pulse forming line with low impedance and electron gun.

The pulse generator TONUS-2 can be used not only in the nanosecond beam range, but also in the microsecond beam range with the energy up to 1.5 MV, and this feature provides its application in various fields.

The general structure of the beam generator is shown schematically in Fig. 1. The initial energy storage is the low inductive Marx generator with a 200 kJ stored energy. It has 18 stages fulfilled on the base of capacitors with the operational voltage of 100 kV and capacitance of 0.4  $\mu\text{F}$ . The whole Marx generator is constructed on the wooden carrying frame and immersed in transformer oil in the steel tank of 20 m<sup>3</sup> volume. The Marx generator is switched by using intense current gas gaps. During the work in the microsecond beam range the load of the Marx generator is the coaxial electron gun with magnetic isolation (see Fig. 2d).

Initial experiments for production and transport of the intense hollow annular beam has been carried on by using the generator TONUS-2 with the coaxial electron gun and magnetic isolation. The parameters of the beam were:

the duration - 80 ns, the applied voltage - 1 MV. The dependence of the net current in the circuit of the back current vs the strength of the magnetic field  $B$  is shown in Fig. 3 which has a similar dependence to that of a static magnetron. The beam current  $I_b$  measured by the Faraday cup was increasing up to the certain limit and after it was decreasing. The reason for this was the decrease of the whole current  $I_w$  and losses in the liner.

We must note that when the beam current was maximum, the energy transmission was not maximum. This was due to the voltage drop from the whole current which considerably more than  $I_b$ . The currents shown in Fig. 3 were normalized on the 1 MV voltage when Child-Langmuir law was fulfilled. For practical applications the photo (see Fig. 3) where  $I_b$  is near the value of  $I_w$  can be recommended. So for  $B = 10.8$  kG and cathode and anode diameters 68 mm and 90 mm accordingly and the length of the transport  $L = 500$  mm,  $I_b/I_w = 0.35$ . Furthermore, with the rising of the magnetic field strength the thickness of the hollow annular electron beam is diminishing and the energetic spectrum of the electron beam become more narrow.

In Fig. 3a, the "autograph" of the hollow annular electron beam made on the plastic ( $B = 14.5$  kG.  $L = 500$  mm with the hollow annular beam thickness of 2 mm) is shown. In that experiment, the unnormalized current was equal to  $I_b = 32$  kA. For purposes of the comparison the "autograph" of the beam with  $B = 1.4$  kG is shown in Fig. 3b which was the case of insufficient magnetic isolation.

The results of our evaluations based on [3] and measurements with the reference to constructional peculiarities of the Marx generator permit us to expect the generation of the beam up to 10 kA in the several microsecond

duration range. Low impedance pulse forming lines of pulsed beam generators are usually constructed in coaxial or strip-line forms. Strip forming lines can be made with the less impedance and smaller dimensions in the comparison with coaxial lines. The most important deficiencies of strip lines are considerable losses of the energy due to edges and difficulties of matching the line with the electron gun.

The forming device of TONUS-2 is forming as two parallel disk Blumlein forming lines connected in parallel. The transverse section of the device is shown in Fig. 1. The lines have one common cathode disk 2 and by means of it we can avoid the appearance of the high voltage pulse on the outer electrodes 3 of lines which are body of the beam generator.

The switching of the device is fulfilled with the aid of the command-triggered 3-electrode gas gaps 5 with the jitter not more than 2 ns [2]. The gas switches are spread along the circumference of disks 4. The minimum number of gas switches in TONUS-2 (which is equal to 36) is calculated from the condition of the isotropic radial propagation of electromagnetic waves to the electron gun, placed in the centre of the forming device. The wave impedance of the disc line on the radius  $R$  can be calculated from the expression given in Fig. 1 where  $h$  - the distance between two adjoint electrode-disks,  $\epsilon$  - the dielectric constant of the isolation of lines. In the device being under construction the distance between electrodes is constant and the ratio of the inner radius of disks to the outer one is 0.4. This value approximately corresponds to the case of exponential law of the impedance along the radius. Accordingly, the coefficient of the energy transmission to the load is equal to 0.9 [4]. The construction of

the forming device was chosen after the computer simulation of various disk-lines with and without the constant impedance and various media.

For dimensions of the forming device shown in Fig. 1 and the use of the purified water as the dielectric medium, the exit impedance of the device is 2.5 ohm, the length of the pulse is 40 ns and electron energy is 1.5 MV.

The forming device is separated from the electron gun by a sectional isolator. Such a construction of the forming device permits us to realize several modes of operation. In order to generate an isotropic x-ray field with high intensity in the considerable volume, the electron gun is operated as a coaxial diode the outer cylinder of which is the cathode as it is shown in Fig. 1. The anode target has the thickness approximately equal to the range of the electron in the material of the anode. Evaluations show that the mean x-ray dose inside of the anode cavity will be more than  $10^3$  R. The high density of the x-ray radiation except special interests makes feasible an experimental investigation of the reaction  $\gamma + \gamma \rightarrow e^+ + e^-$  [5], which is unfeasible in suggestions of the colliding x-ray beam experiments due to the great divergence of the x-ray radiation with the energy of 1 MV and because of that to the necessity of the severe collimation of x-ray radiation. Our estimates give approximately one event for the reaction on every  $10^2$  pulses of the beam generator for traditional schemes of the colliding beam experiment and one event on every pulse of the generator in the case of the suggested coaxial geometry of the gun due to the high coefficient of utilizing of the invergent x-radiation in the anode cavity.

As is shown in Fig. 2a, the injection of electrons in the anode cavity from several parallel guns can be applied to generate an electron ring with



high intensity. In this case the guns are situated on the inner circumference of the cathode and the axes of these guns make an angle of  $7^\circ$  with the direction of tangent lines in the injection points.

Such a location of electron guns secures the necessary "missing" of electron beams during their injection in the magnetic field of betatron type inside the anode cavity.

Furthermore, with the intense injection currents it is possible to utilize so-called phenomenon of "mirror capture" and this way of generation of annular intense currents is evidently more attractive than what we have in Astron type and "adgezators" devices [6,7].

The phenomenon of acceleration of the cathode plasma and connected with it the high degree of pinching of the electron beam in the planar diode in the interelectrode gap makes such densities of the current up to  $10 \text{ MA/cm}^2$  attainable. Generation of such densities is very interesting from the point of view of the controlled thermonuclear yield [8].

To investigate above-mentioned phenomenon the construction of the diode of the planar type with two cathodes in the form of disks and one common anode which is situated between them (see Fig. 2b) is suggested. In this case we change the polarity of the charging voltage of the Marx generator and accordingly to these changes the polarity of the generated pulse. The planar diode with the annular cathode can be used for the transmission of the electron beam outside of the forming device.

The transition of the high voltage pulse from the cathode disk to the diode can be fulfilled along vacuum coaxial lines with the magnetic auto-isolation (see Fig. 2b).

At the present time the construction of the Marx generator and the coaxial gun for the microsecond range beam experiments is under completion.

#### REFERENCES

1. V. M. Bistritsky, A. N. Didenko, Yu. P. Usov, V. I. Tsvetkov, IV Vsesoujznaja konferencia po uskoriteliam, Moskva, 1974.
2. I. Z. Gleyzer, A. N. Didenko, L. P. Dronova, A. G. Gerlitsin, G. I. Kotliarevsky, B. V. Okulov, N. S. Rudenko, G. E. Remnev, V. S. Pak, V. I. Smetanin, V. A. Tuzov, Yu. P. Usov, A. A. Shatanov, Atomnaya energiya 36, 5, 378 (1974).
3. M. Friedman, M. Ury. Rev. Sci. Instrum. 43, 11, 1659 (1972).
4. M. V. Babykin, A. V. Bartov, Preprint IAE-2253 (1972).
5. P. L. Csonka, CERN, 67-75 (1967).
6. A. N. Didenko, A. V. Petrov, A. I. Rjabchikov, V. A. Tuzov, Yu. P. Usov, Pisma v Zhurnal Tech. Fiz., 1, 11, 538 (1975).
7. A. C. Smith, S. E. Swannack, LPS, 139 (1973).
8. G. Yonas, SLA-73-5067 (1974).



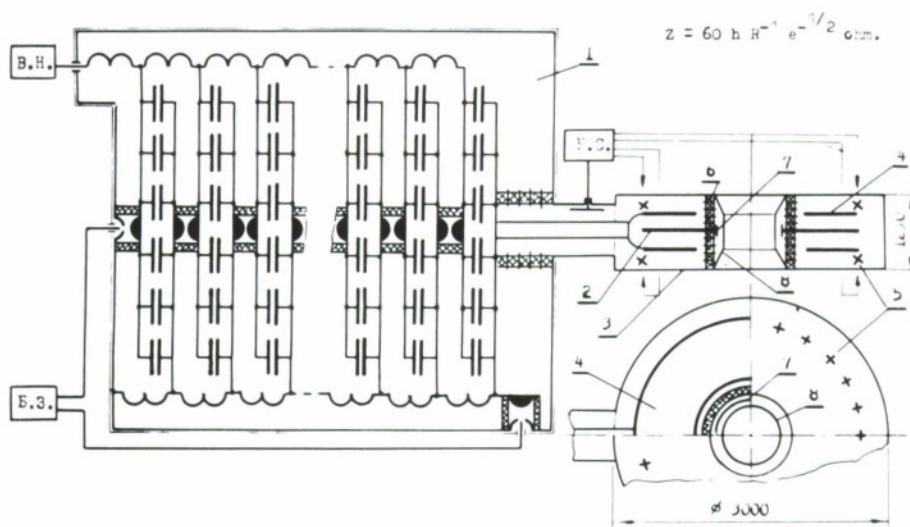


Figure 1. The scheme of beam generator.

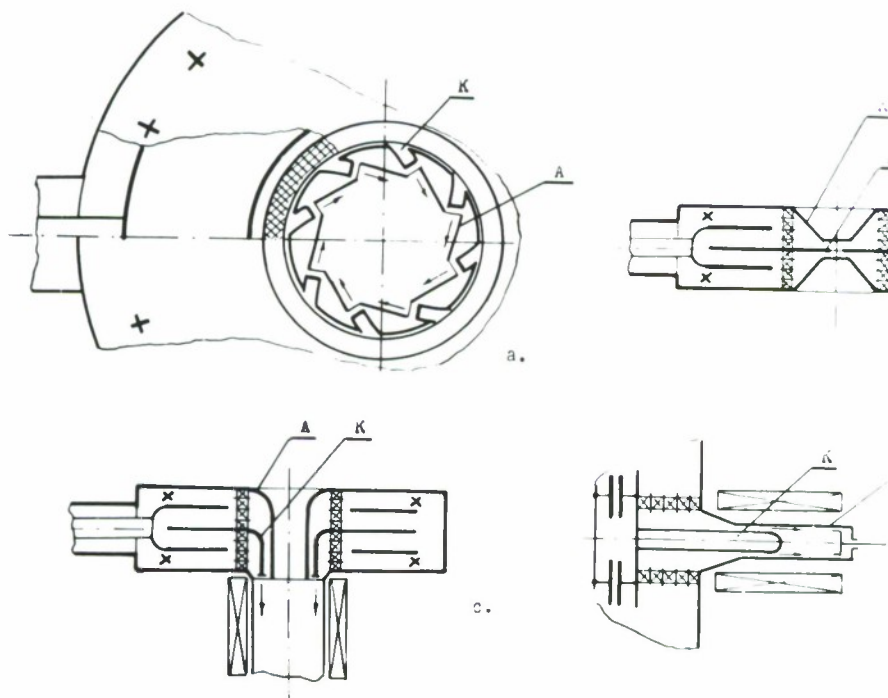


Figure 2. Possible versions of beam generator's gun.

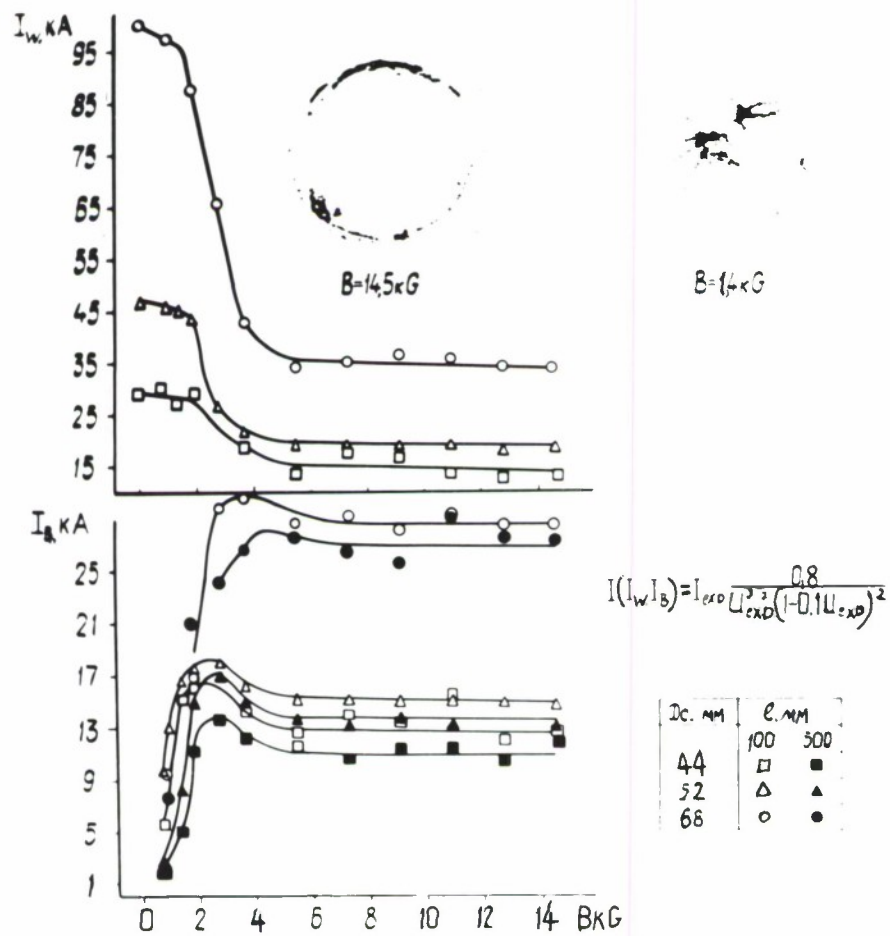


Figure 3. The currents  $I_w$  and  $I_b$  vs the strength of the magnetic field.

NANOSECOND SWITCHING OF HIGH POWER LASER  
ACTIVATED SILICON SWITCHES\*

O. S. Zucker, J. R. Long and V. L. Smith  
Lawrence Livermore Laboratory, University of California  
Livermore, California 94550

and

D. J. Page and J. S. Roberts  
Westinghouse Research Laboratories  
Pittsburgh, Pennsylvania 15235

Abstract

Light activated multilayered silicon semiconductor devices have been used to switch at Megawatt power levels with nanosecond turnon time. Current rate of rise of 700 KA/NS at 10 KAMP, with 1 kV across the load, has been achieved.

\*Work performed under the auspices of the U.S. Energy Research and Development Administration under contract No. W-7405-Eng-48.

## NANOSECOND SWITCHING OF HIGH POWER LASER ACTIVATED SILICON SWITCHES

### Introduction

To achieve high power, energy compression devices depend on switches as the primary nonlinear element required for time compression.<sup>1</sup>

The most important characteristics of a switch required for energy compression applications are: Power handling capacity, impedance, rise time, repetition rate capability and life time. Another consideration for large systems is the ability of many switches to function simultaneously. The power handling capability of a switch is defined here as the maximum voltage the switch will hold times the maximum current the switch will pass. The ratio of this voltage and current is defined as the impedance.

The light activated silicon switch (LASS) represents a combination of switch parameters which is unique and potentially better than currently available switches. The LASS meets all the switch requirements for energy compression. Solid dielectric switches currently handle the highest power and have good rise time. However, they are single shot devices and have simultaneity problems. The best currently available repetitive device is the high pressure spark gap. It can carry up to 1 MA per channel (.1  $\mu$ sec), hold off 500 kV/cm (100 psi), the inductance is around .05 nH/kV (25 nH at 500 kV), and the simultaneity is in the nanosecond regime.<sup>2</sup> The LASS device has the potential of lower inductance, higher repetition rate, longer life, and improved simultaneity over the high pressure spark gap.

This report describes the results of initial tests with research silicon devices which demonstrate significant improvements in current rate of rise over existing silicon switches (thyristor).

### The Device

Semiconductor switches come in many forms such as transistors, thyristors, triacs, and several modified forms of these. However, the same principle of switching is common to all. In the blocking or open circuit state, a region within the device, usually a p-n junction, is depleted of mobile charge and acts as an insulator. The voltage applied to this insulating region sweeps out the mobile charge and preserves the insulating state.

To convert this region to the conducting state, charge is injected into this depleted region, usually from a second p-n junction as in a transistor or from two p-n junctions, one on each side, in the case of a thyristor. The injected charge is made large enough ( $\approx 10^{18}/\text{cm}^3$ ) to reduce the impedance of the depleted region so that a substantial amount of current can flow. Usually the voltage drop of the device in conduction is less than two volts.

There is a limit to the speed that such devices can switch. The injection of charge from the p-n junction is a relatively slow process and is limited by the transit-time for the carriers to traverse the space between the injecting p-n junction and the depleted junction. This time varies with the device design, but for high power transistors and thyristors is about a microsecond. If the current is allowed to rise within the device before sufficient charge has been injected, the impedance will be high enough to either cause a substantial loss of efficiency or will result in the thermal destruction of the device.

The current method of transforming the depleted region into the conducting state is by photon absorption. In this case the mobile charge, electrons and holes, is created in-situ and can be accomplished as fast as the light enters the device. A suitable laser having an output photon energy closely matched to the band-gap of silicon can be used to efficiently accomplish this process.

A typical power device has a volume of silicon in the active region of  $10^{-2} \text{ cm}^3$ . If this volume is to be filled with carriers to the normal



on-state density of  $10^{18}/\text{cm}^3$  and each electron hole pair requires an energy of 1.1 eV, the total energy required will be:

$$\begin{aligned} E &= \text{volume} \times \text{density} \times \text{photon energy (1.09 eV)} \\ &= 10^{-2} \times 10^{18} \times 1.09 \times 1.6 \times 10^{-19} \\ &= 1.75 \text{ mJ.} \end{aligned}$$

This amount of energy is readily obtained by available lasers. The calculation assumes complete conversion of photons to electron hole pairs and no recombination during the illumination time. The choice of wavelength, such as using a  $\text{Nd}^{+++}$  doped YAG laser having an output of  $1.06\mu$ , which is closely matched to the band gap of silicon, ensures efficient conversion of photons to electron-hole pairs. The carrier lifetime in power devices is usually longer than 10 microseconds, so negligible recombination will take place during illumination, which usually occurs for a few nanoseconds. Turning off such devices is accomplished in single junction (back biased diode) or dual junction (transistor) by sweeping out the carriers in the reverse direction to allow the development of a depletion region.

### The Experiment

The experiments performed with the LASS were to determine first if the device would respond with risetime in the nanosecond regime, and second to attempt to achieve high rates of current rise. The first experiment utilized a  $50 \Omega$  charged line. The line was switched with the LASS into another  $50 \Omega$  line. A "Q-Switched" Nd doped YAG laser ( $1.06\mu$ ) was used to illuminate the switch wafer. A photograph of the laser output on an S-1 cathode photo diode is shown in Figure 1. The laser output was approximately 3-5 mJ/pulse. The fixture used to mount the switch wafer in a  $50 \Omega$  structure is shown in Figure 2, along with an electrical schematic of the test. Typical results are shown in Figure 3. The line was charged to 1500 volts (near avalanche) and the output pulse was approximately 750 volts with a rise time of 4 ns (10-90%). This output represents 15 amps in 4 ns or 3.75 kA/ $\mu\text{sec}$ . However, the important point is the switch turned completely on in nanoseconds.



In an additional experiment two  $50\ \Omega$  cables were connected in parallel to obtain a  $25\ \Omega$  circuit. The result is shown in Figure 4. The output is essentially the same as the  $50\ \Omega$  case but at twice the current.

In order to obtain significantly higher rates of current rise and current, a fixture was designed which would accommodate several strip transmission lines in parallel. The LASS in this case is designed to short the transmission line at one end. The fixture design and test schematic are shown in Figure 5. When the switch closes a pulse propagates down the line and a current flows in the switch equal to the voltage of the pulse across the characteristic impedance of the transmission line.

The strip transmission line used in the experiment is three flat conductors separated by insulation. The characteristic impedance calculated from the geometry and presumed dielectric constant was  $1.4\ \Omega$ . Due to the uncertainties in this calculation (and the close spacing which made the skin effect potentially important), a measurement of the impedance was made. The experimental schematic is shown in Figure 6, and the result in Figure 7. From this experiment, a value of  $1.25\ \Omega$  was used as the characteristic impedance of the strip transmission lines.

The experimental results for eight strip lines in parallel are shown in Figure 8. The voltage pulse shown is the pulse on the transmission line. The voltage at the switch end of the line does not go to zero implying the existence of some impedance in the switch and/or connections to the switch. We believe this impedance is resistance in the LASS due to the very small area of the device we can illuminate the present experiment. The interpretation of the amount of current flowing is independent of these considerations since it is determined simply by a measured voltage pulse on a known impedance transmission line.

With eight transmission lines in parallel charged to 1300 volts, a pulse of 1110 volts was measured on the transmission line. The rise time was 12 ns. The eight lines in parallel represent an impedance of  $.156\ \Omega$ . Therefore, 1110 volts across  $.156\ \Omega$  in 12 ns yields a current rate of rise of  $640\ \text{kA}/\mu\text{s}$  and a peak current of 7100 amperes. The same experiment with 12 lines in parallel gave the result  $760\ \text{kA}/\mu\text{sec}$  at 9800 amps peak current, Figure 9. The results of all experiments are shown in Table 1.

For comparison purposes two copper washers separated by mylar were inserted in place of the LASS in the test fixture. A nail was driven through the washers to short circuit the transmission lines. This is an example of the classic "hammer switch" and can be taken as a basis of comparison. The result is shown in Fig. 10, and the waveshape is seen to be poorer to the previous results.

To review the demonstrated results of the LASS:

1. Power - 10 MW
2. Impedance -  $.1 \Omega$
3. Risetime - 3 - 14 ns
4. Repetition rate - not tested but line is recharged in approximately 1 millisecond.

The other switch requirements for high power applications were long life and simultaneity. Silicon switches have demonstrated long life in similar service where only the speed of response is slower. The nature of the triggering (or turning on) mechanism makes it possible to predict that perfect simultaneity can be achieved by insuring that the light pulse reaches all switches at the same time.

## Conclusions and Potential Applications

### Immediate Applications

There are several applications of the LASS device which can be immediately pursued. The device used in the above experiments utilized a total area of  $.1 \text{ cm}^2$  out of a total available area of  $2.5 \text{ cm}^2$ . The reason is that during the time of our experiment diffusion does not take place and thus only the area illuminated can conduct. Thus with only 50% efficiency our experimental device could conduct 125 kA if fully illuminated. These devices have been fabricated in diameters of 5 or 7.5 cm so that area extrapolation to mega-ampere devices should be straightforward.

The device should lend itself very easily to the design of improved MARX Generators. The inductance of the device is arbitrarily low (.1 nH/kV or less) since practically all the magnetic flux can be external to the device. Triggering arrays of switches is particularly easy since laser triggering provides both high voltage isolation and perfect simultaneity (sub-nanosecond laser pulses are readily available). Thus the erection and discharge times of MARX Generators can be substantially reduced providing higher fields and higher power densities in liquid dielectric transmission line or Blumlein applications.

The discharge of megajoule capacitor banks on a repetitive basis can be considered feasible. The coulomb transfer of the LASS is in excess of 10 coulombs which is adequate. The primary limitation to high repetition rate is cooling of the devices. The flat large area geometry and the dissipation rate of between .1 and 1% of transferred energy make these devices particularly promising. For example a 1 kV - 100 kA switch can deliver  $10^8$  watts instantaneous power. If the dissipation is 1 MW and we can cool the device by convection or heat sinking at a 1 kW rate then the duty cycle could be  $10^{-3}$ . This result implies a 1 kHz repetition rate for 100 MW - 1  $\mu$ s pulse or a 100 kHz rate for a 100 MW - 10 ns pulse. Currently available silicon switches typically have junction cooling rates of 100 W/cm<sup>2</sup>.

There are many more conventional applications (e.g., Radar Modulators) for which the LASS would be useful.

### Potential Applications

One interesting potential development would be to modify the geometry of the device to improve the coupling of the device to the circuit. The self-inductance associated with the switch could be significantly reduced. Another possibility of geometrical modification is to integrate either a GaAs Laser or Amplifier intimately coupled optically to the device to supply the light pulse. The device could then be triggered electrically or by a relatively weak light pulse which would maintain electrical isolation of the trigger.

Another possibility is the generation of megawatt wide-band microwave power.

Turn-on with picosecond laser pulses in intrinsic silicon has been demonstrated by Johnson and Auston of Bell Laboratories<sup>3</sup>. There is no reason to suspect that turn-on in junction devices would be slower than in bulk intrinsic material. A crude estimate of the turn-on time is the light transit time in the depletion layer which is about 1 - 2 ps.

The turn-off characteristics in single and dual junction devices should be similar to performance of the storage or snapoff diode. These diodes generate gigahertz harmonics when the charge in the depletion layer is swept out and the diode snaps off. In a typical application such a bulk biased junction, biased at 1 kV, would be turned on with a picosecond rise time laser pulse. Depending on the waveguide impedance, amps to kiloamps could be conducted. When the light turns off the carriers are swept out and the device snaps off. This snapoff can be timed extremely accurately since both the number of carriers and the recombination rates are known. Thus a resonant cavity could be excited with precise phasing. This phasing could be controlled by varying the spacing between the laser pulses. This can be done quite easily with electro-optic techniques. Thus megawatts per device of microwave power can be generated at extremely broad bandwidth. We could construct phased array radar sources of very high powers.

Finally, the use of these devices as programmed nonlinear elements in waveguides would make possible energy compression of microwave energy at unprecedented powers.



### Acknowledgement

We would like to thank Henry Chau for his help with the laser and Al Myers for his technical assistance.

### References

1. O. S. F. Zucker and W. H. Bostick, "Theoretical and Practical Aspects of Energy Storage and Compression", Proc. of the Int'l. Conf. on Energy Storage, Compression, and Switching, Torino, Italy, 11/5-7/74.
2. Private communication with Philip Champney, Physics International Corp. (1975).
3. A. M. Johnson and D. H. Auston, "Microwave Switching by Picosecond Photoconductivity", IEEE Journal of Quantum Electronics, Vol. QE-11 No. 6, June 1975.

TABLE 1  
Summary of results

Z ( $\Omega$ )	V (volts)	I = V/Z (amps)	$\tau$ $\times 10^{-9}$ sec	I = I/ $\tau$ $\times 10^9$ (kA/ $\mu$ s)	P = VI (MW)
50	750	15	4	3.75	0.011
25	750	30	4	7.5	0.022
0.156	1110	7115	11	647	7.9
0.104	1020	9820	13	755	10

Z = Line impedance

V = Pulse voltage

I = Peak current

$\tau$  = Rise time

I = Rate of current rise

P = Power, load

↑  
On line

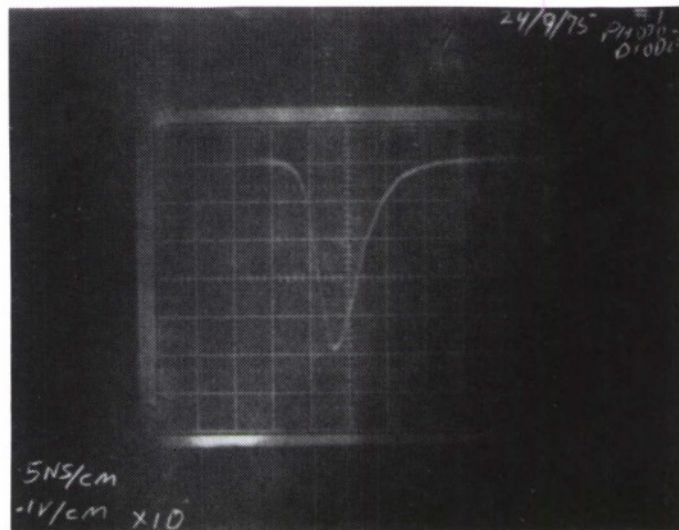


Figure 1: Oscilloscope trace of laser pulse used to trigger the LASS.



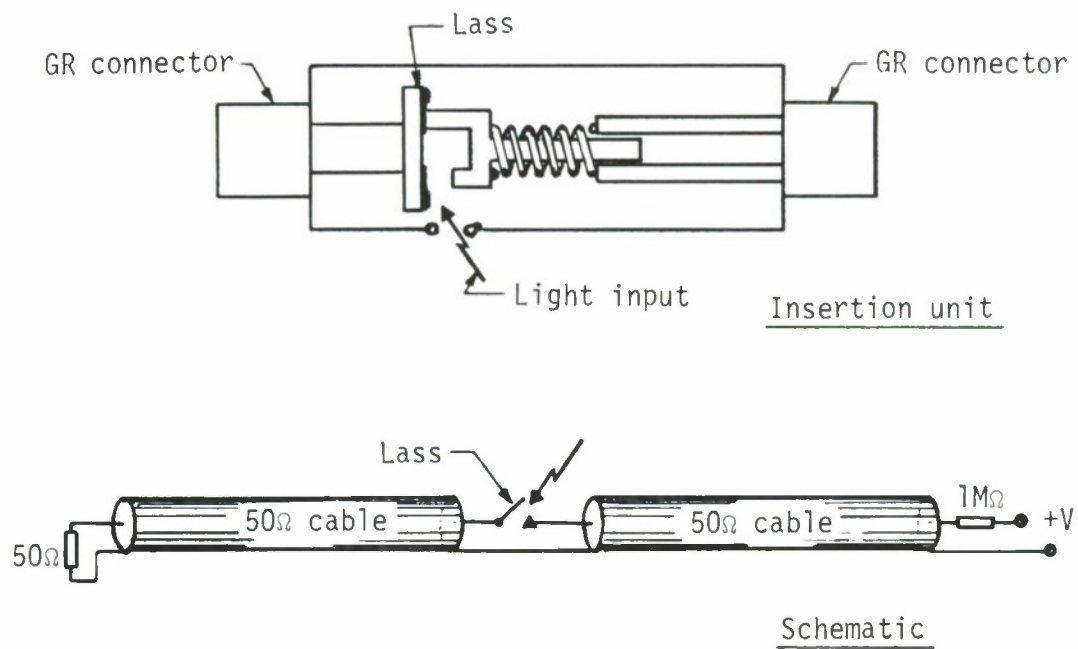
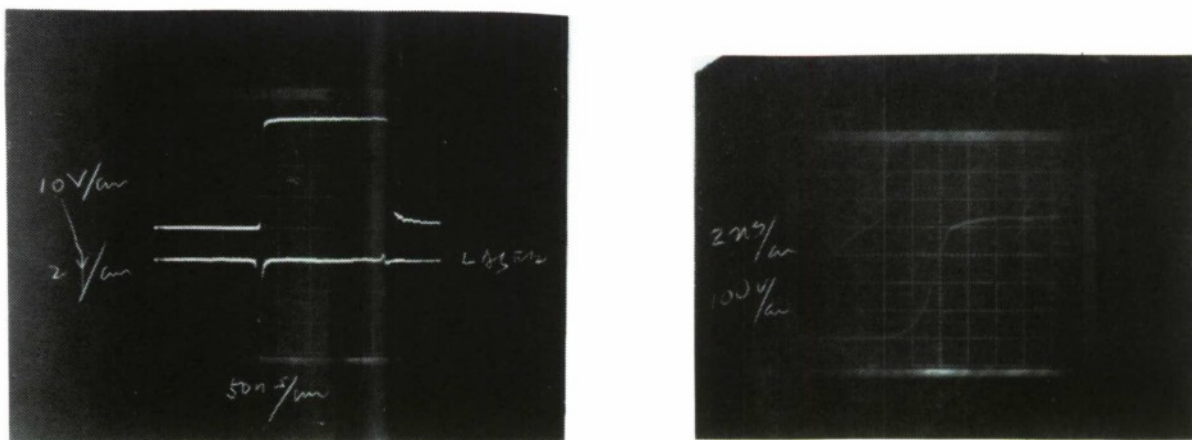


Figure 2: Fixture diagram and schematic for 50  $\Omega$  experiment.



- a) 50 ns/div sweep-bottom trace laser pulse
- b) Rise time at 2 ns/div

Figure 3: Pulse output of 50  $\Omega$  experiment

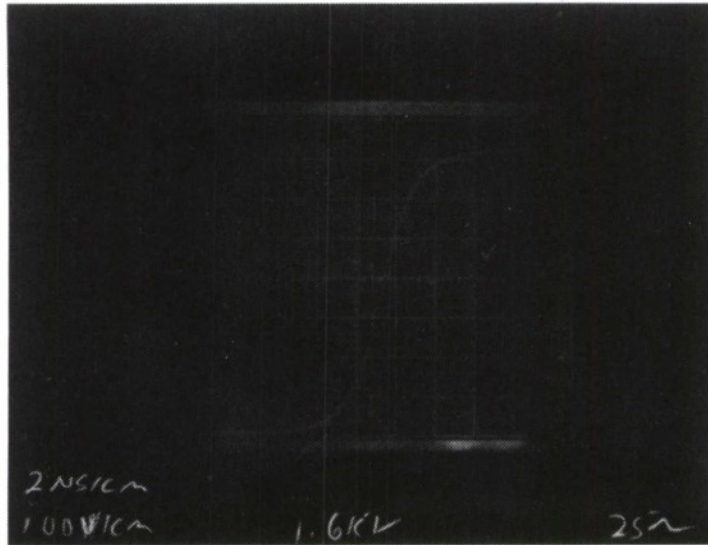


Figure 4: Pulse output of  $25\ \Omega$  experiment - rise time - 2 ns/div

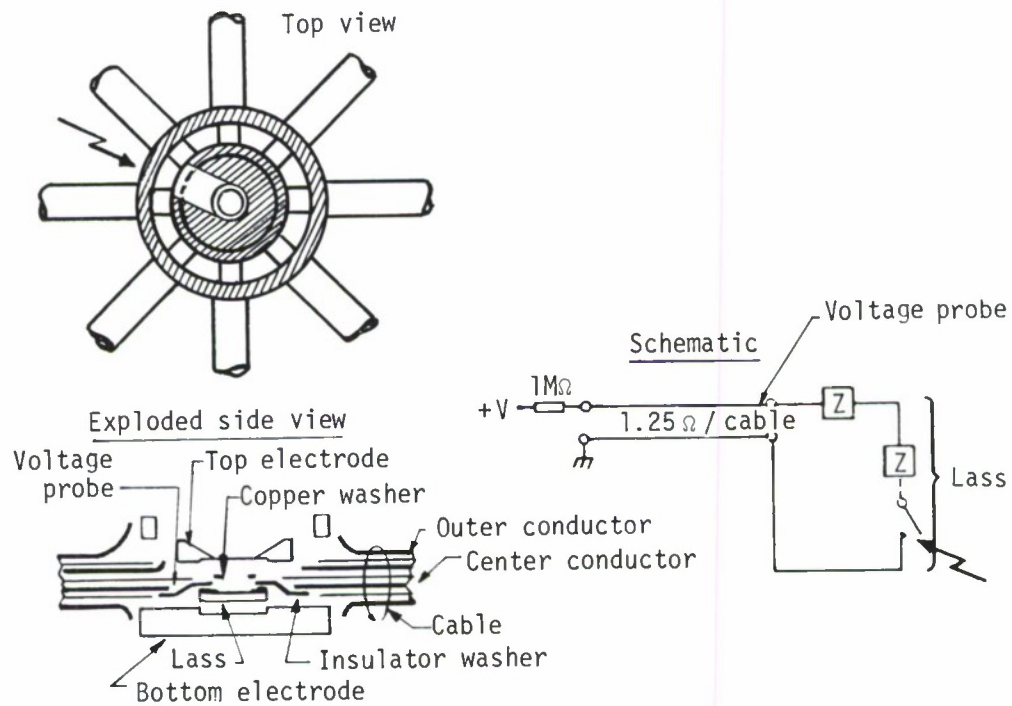


Figure 5: Shorting fixture diagram and schematic of strip line experiment

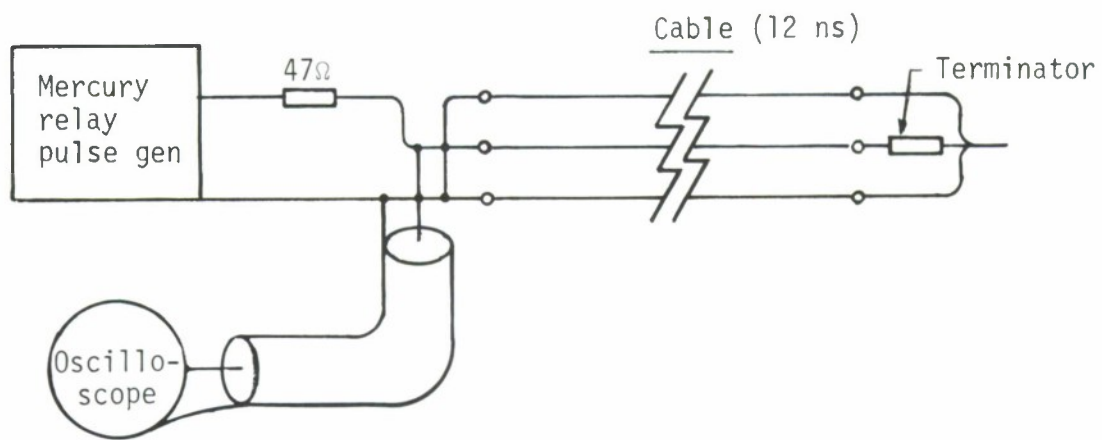


Figure 6: Cable characterization circuit

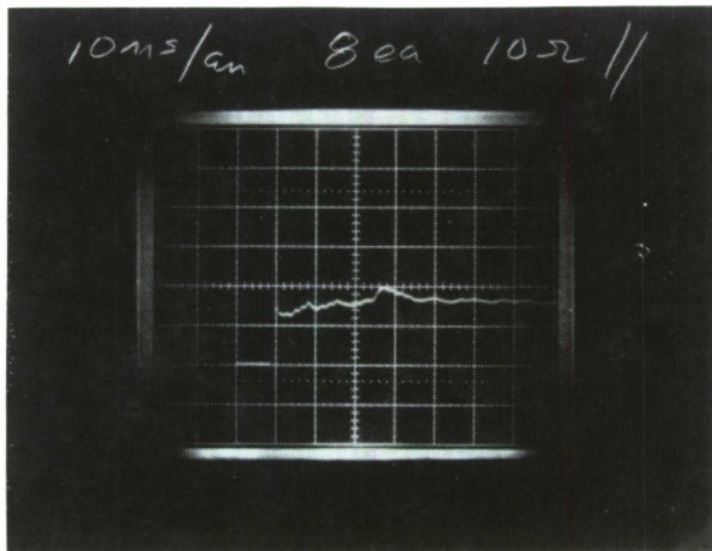
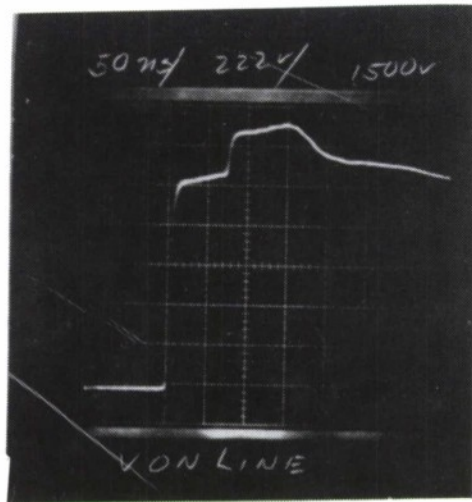
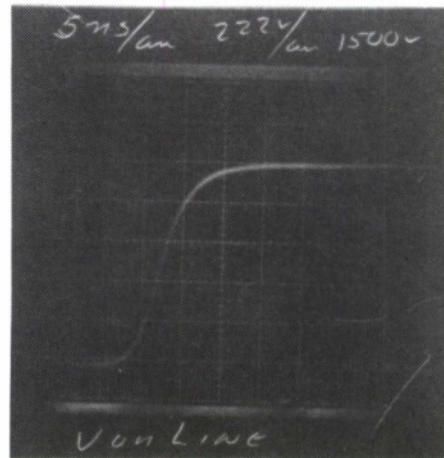


Figure 7: Result of cable characterization test showing minimum reflected pulse

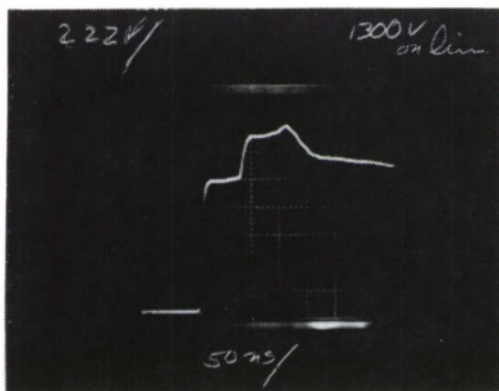


a) 50 ns/div sweep

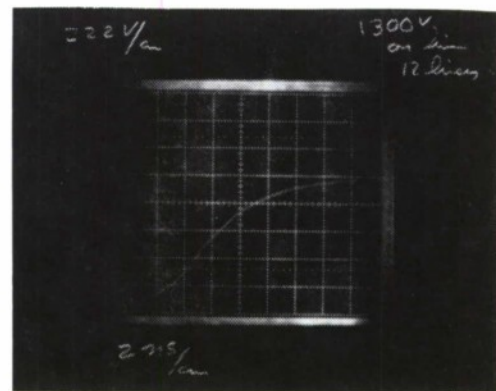


b) 5 ns/div sweep

Figure 8: Transmission line pulse with 8 parallel lines



a) 50 ns/div sweep



b) 2 ns/div sweep

Figure 9: Transmission line pulse with 12 parallel lines

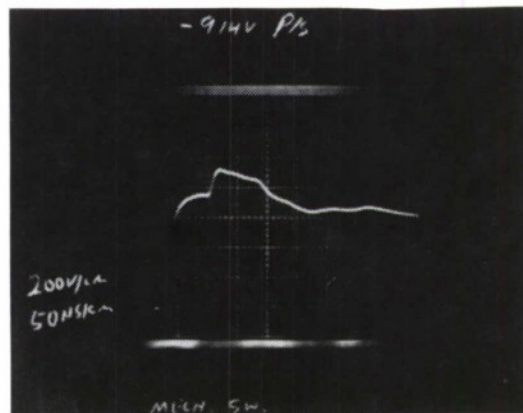


Figure 10: Transmission line pulse with dielectric switch in place of LASS.

# **CHAPTER 4**

## **ION BEAMS**

EXPERIMENTAL INVESTIGATIONS OF POSITIVE ION  
FLOW IN A DOUBLE DIODE

Marco Di Capua, Robert Huff and John Creedon  
Physics International Company  
San Leandro, California 94577

ABSTRACT

The double diode, or reflex triode, has been investigated experimentally. This device consists of a semitransparent anode located between two cathodes in a configuration which produces multiply reflected electrons combined with positive ion flow. The effects of the strength of the applied axial magnetic field, anode materials, and anode thickness were systematically explored. The voltage-current characteristics of the diode are consistent with a theoretical model which includes the energy loss and scattering of electrons in the anode. Decreasing the anode thickness causes a decrease in anode voltage and an increase in ion production. Conventional operation is observed in diodes when the number of multiple reflections is reduced either by removing the axial magnetic field or by increasing the thickness of the anode.



## 1. INTRODUCTION

The generation of intense positive ion beams with vacuum diodes opens exciting possibilities in the fusion field. Developments of the last few years have shown that, with slight modifications, the vacuum diodes which generate relativistic electron beams can accelerate intense positive ion beams as well. These ion beams can be used advantageously for many of the same applications as electron beams.

There are two basic requirements for efficient ion generation: an ion source in the form of a hot dense plasma must be created at the anode, and the ratio of the ion current from the anode to the electron current from the cathode must be enhanced by some means. The anode plasma can be produced by the electron flow from the cathode or by some external source of energy such as a laser. One way of reducing the electron current while maintaining the ion current is to use a magnetic field which is transverse to the electron flow.<sup>1,2</sup>

Another method of enhancing the ratio of ion to electron current is to use the reflex triode or double diode configuration shown in Figure 1.<sup>3-5</sup> A semitransparent anode is located between two cathodes so that the electrons make many passes through the

anode before coming to rest. A recent theoretical and experimental investigation of this device indicates that it might be possible to generate very intense positive ion beams with the reflex triode arrangement.<sup>6,7</sup> The experiments reported here were designed to test some of the conclusions of this theory.

## 2. EXPERIMENTAL APPARATUS

The double diode used in these experiments is shown in Figure 2. It consists of a 20-cm-diameter anode holder located symmetrically between the two cathodes (shown at the right and left of the figure). These cathodes are composed of stainless steel meshes woven from 1 mil wire; they have a 60% transparency. The meshes are stretched, on the anode side, over the ends of 10-cm-diameter stainless steel hollow cylinders. The magnet coils on the outside of the vacuum vessel provide a pulsed field with a maximum strength of  $0.20 \text{ Wb/m}^2$  in the anode-cathode region. Both the fiberglass vessel and the anode and cathode hardware were designed to allow penetration of the field on the time scale of the magnet pulse. The figure also shows the self-integrating Rogowski coils<sup>8</sup> used to measure the net current in each cathode. The voltage was monitored by a resistive monitor whose signal was combined with the signal of a  $\dot{B}$  pick-up loop to eliminate the

contribution of the inductive effects in the diode.<sup>9</sup> A redundant voltage divider connected directly to the anode holder provided another measurement of accelerating potential.

The Pulserad 738 accelerator, used in this experiment, consists of an oil-immersed 38-stage Marx generator which charges, at positive polarity, a coaxial oil dielectric transmission line to a maximum voltage of  $\sim 3.3$  MV. This transmission line, which has a nominal impedance of  $8.5 \Omega$ , delivers a current pulse of  $\sim 70$  nsec FWHM to the anode of the reflex triode. This transmission line is connected to the load through a gas switch.

### 3. THEORY

The theoretical investigation of space charge limited ion and electron flow in the reflex triode has indicated that the energy loss and scattering of the electrons as they pass through the anode have a very important effect on the characteristics of this device.<sup>6,7</sup> The analytic technique which has been developed enables one to decouple the energy loss and scattering processes in the anode from the space charge flow problem in the anode-cathode region. It should be possible to calculate the energy and angular distribution of the multiply scattered electrons by the numerical methods which are available, and thus to solve the

reflex triode problem exactly. This problem is presently being investigated; however, it is possible to draw some conclusions about this device without a numerical solution of the scattering problem.

Several radically different assumptions about the energy distribution for the flux density of the scattered electrons lead to basically the same results for space charge limited ion flow. The problem has been formulated in terms of a parameter  $\eta$  which is essentially the average number of times that an electron penetrates the anode. Without a numerical solution of the scattering problem, it is difficult to determine  $\eta$  exactly; however, it is possible to make reasonable estimates. If  $R$  is the residual range (c.s.d.a. range<sup>10</sup>) of electrons accelerated by a potential  $V$  and  $\tau$  is the anode thickness, then for  $R > \tau$

$$1 < \eta < R/\tau .$$

A value of  $\frac{1}{2} (R/\tau)$  gives a rough estimate for  $\eta$  when  $R \gg \tau$ .

For electron distributions appropriate for foil anodes, all of the examples which have been investigated indicate that there is a critical number of penetrations  $\eta_c$  for which there will be

a large increase in both the ion current and the total current of the diode. For foil anodes, the calculated value of  $\eta_c$  was between 4 and 16 for all cases considered.<sup>6,7</sup>

The sharp increase in current, which occurs as  $\eta$  approaches  $\eta_c$ , has a very important effect on the voltage-current characteristics of the reflex triode. As the anode voltage  $V$  of the reflex triode increases, the range of the electrons increases, and thus the number of penetrations  $\eta$  for a given anode thickness increases. As a consequence, there is a critical value of voltage  $V_C$  for which  $\eta = \eta_c$ . For space charge limited ion flow, the sharp increase in current which occurs as  $V$  approaches  $V_C$  results in a large current range for which the reflex triode is essentially a constant voltage device with  $V \cong V_C$ . The curve marked  $I_{S1}$  in Figure 3 illustrates the resulting shape of the voltage-current characteristics for a reflex triode with anode thickness  $\tau_1$  and  $V_C = V_{C1}$ .

The value of  $\eta_c$  predicted by the theory was found to be relatively insensitive to the energy distribution for the flux density of the multiply reflected electrons. For a constant value of  $\eta_c$ , reducing the anode thickness means that lower voltage electrons will make the critical number of transits through the anode; i.e.,  $V_C$  decreases as  $\tau$  decreases. The curve marked  $I_{S2}$  in Figure 3 represents the shape of the voltage current characteristics for an anode thickness  $\tau_2$  ( $V_C = V_{C2}$ ) which is less than  $\tau_1$ .



For any diode, the operating voltage and current are determined by the intersection of the load line of the generator and the characteristic curve of the device. The load line is represented by the dotted line in Figure 3. The constant voltage nature of the characteristics illustrated in Figure 3 means that, for a wide range of generator parameters, the operating potential of a reflex triode is given approximately by  $V_C$ .

Conventional operation of a diode without multiple reflections is illustrated by the curves marked  $I_{\ell c}$  and  $I_{bp}$  in Figure 3.  $I_{\ell c}$  represents the ordinary Langmuir-Child solution.<sup>11</sup>  $I_{bp}$  is the current resulting from Langmuir's<sup>12</sup> bipolar solution, which includes counterstreaming electrons and positive ions but no multiple reflections.

#### 4. EXPERIMENTAL RESULTS

Table 1 summarizes the experimental conditions reported here. The charging voltage listed in Table 1 is the potential to which the pulse forming line was charged; this potential is thus the open circuit voltage of the generator. Figures 4a and 4b show the voltage waveform and the voltage current characteristics for experiment 1 with an  $857 \text{ mg/cm}^2$  aluminum anode. This anode thickness is greater than the range of the electrons so that the reflex triode device operates as two separate conventional diodes.



Current begins to flow when the anode potential becomes sufficiently large to initiate the emission process at the cathode. (The zero of the time scale on all waveforms in this paper corresponds to the beginning of the current pulse.) The current then climbs rapidly to the full operating value of approximately 55 kA. The arrows in Figure 4b indicate the direction of increasing time. All current levels quoted in this paper are the average of the current measured in the two diodes that make up the reflex triode. When the voltage begins to fall, the operating point of the diode follows a three halves power curve quite closely. The dotted curve in Figure 4b represents the expression

$$I = kV^{3/2}$$

relating the anode current  $I$  to the anode potential  $V$  in terms of the perveance  $k$ . The perveance that agrees with the measured values in Figure 4b is about twice what one would calculate for plane parallel electron flow by using the Langmuir-Child current density and the area and spacing of the cathode. This discrepancy is due either to fringing effects at the edge of the cathode or to positive ion flow.

For experiment 2 of Table 1 the waveform of Figure 4c illustrates the drop in operating voltage from  $\sim 900$  kV to  $\sim 450$  kV, which occurs when the thickness of the anode is decreased to

71 mg/cm<sup>2</sup> of Mylar while the charging voltage and geometrical configuration are held constant. The dotted line in Figure 4c represents a voltage for which the ratio of the residual range  $R$  to the anode thickness  $\tau$  is 2.0. The voltage drop from 900 kV to 450 kV is consistent with the theoretical predictions; however, the value of  $\eta_c$  inferred from Figure 4c is less than 2 and is lower than any of the values which have been calculated.<sup>6,7</sup> The voltage current characteristics of Figure 4d indicate the constant voltage nature of the device.

Figure 4e (experiment 3 of Table 1) illustrates the change in the voltage waveform that occurs when the anode thickness is decreased to 1.78 mg/cm<sup>2</sup> of aluminized Mylar. Initially there is a very large peak in the voltage corresponding to a transient condition for which there are a large number of multiple reflections and no positive ions. About 10 nsec after the beginning of the pulse, the voltage begins to fall and reaches a low value at approximately 25 nsec. The dotted line in Figure 4e represents a voltage for which  $R/\tau = 4.6$ . As before, the operating voltage is pulled down until the electrons make only a small number of transits through the anode. Further agreement with the theory is illustrated by the constant voltage region of the voltage current characteristics shown in Figure 4f.

It is conceivable that the low voltage operation shown in Figure 4e is caused by plasma motion instead of positive ion flow. However, for the 2.5-cm anode-cathode spacing used in this experiment, the plasma velocity required to explain the waveform of Figure 4e is almost 100 cm/ $\mu$ sec. This velocity is an order of magnitude greater than the largest velocities which have been observed.<sup>13,14</sup>

Figure 5 shows the measured values of voltage and energy delivered to the diode for aluminum anodes of three different thicknesses (experiments 4, 5, and 6 of Table 1). Before ion flow begins, most of the energy delivered to the diode is deposited in the anode. The anode thickness ( $857 \text{ mg/cm}^2$ ) used for experiment 4 (Figures 5a and 5b) is the same as that used for experiment 1, and is more than a range thick. The difference in operating voltage in Figures 4a and 5a is caused by a shift in the load line of the generator due to the lower charging voltage.

Figures 5c and 5d illustrate the results for an anode thickness of  $41 \text{ mg/cm}^2$  (experiment 5). Initially the voltage is as high or higher than in Figure 5a. When the energy density deposited in the anode reaches a value of about 650 J/g, the anode voltage begins to drop. The dotted line in Figure 5c represents a value of  $R/\tau = 3.3$ .

Figures 5e and 5f illustrate the results obtained with an anode thickness of  $6.86 \text{ mg/cm}^2$  (experiment 6). Initially the voltage reaches a very large value. When the energy deposited in the anode reaches a value of approximately  $1 \text{ kJ/g}$ , there is a sharp drop in the voltage to a low operating value. The dotted line in Figure 5e represents a ratio  $R/\tau = 2.7$ . It is interesting to note that the shapes of Figures 4e and 5e are quite similar.

The mechanism of plasma production at the anode of a high  $v/\gamma$  diode is not well understood. The heating of the anode by the electron beam should cause the release of adsorbed gases. These gases can be ionized by the beam electrons or by the large electric fields which are present. For any reasonable plasma temperature, the energy per unit mass in the anode plasma is orders of magnitude greater than the average energy density deposited in the anode foil. One of the most plausible mechanisms for heating this plasma is the  $I^2R$  heating of that portion of the return conduction current which flows in the anode plasma. Comparison of Figures 4 and 5 indicates that the mechanism for plasma production is apparently somewhat different for Mylar than for aluminum. The anode plasma for a  $71 \text{ mg/cm}^2$  Mylar foil seems to form very early in the pulse compared to a  $41 \text{ mg/cm}^2$  aluminum foil. This difference may be due to the high conductivity of aluminum.

The experiments of Figures 4 and 5 were all done with the maximum value of the  $B_z$  field. If the  $B_z$  field is reduced to zero, then the voltage waveform for thin anodes becomes almost the same as that observed for thick anodes. Without the  $B_z$  field the electrons rapidly scatter out of the anode-cathode region and the effect of the multiple reflections is greatly reduced.

Figure 6 shows the diode voltage waveforms and the measured ion currents for two different thicknesses of Mylar anodes (experiments 2 and 7 of Table 1). The detector for the ions was a Faraday cup located 113 cm from the anode. Permanent magnets were located near the entrance of this device in order to sweep electrons out of the ion beam. The calibration of this Faraday cup is questionable so that the actual value of the ion current density is unknown. However, the time of arrival of the ion pulse gives an approximate measurement of the transit time from the diode to the Faraday cup. If it is assumed that appreciable ion production begins about 25 nsec after the beginning of the voltage pulse (Figures 6a and 6c), then the delay time of approximately 135 nsec in Figure 6b corresponds to a proton energy of 366 keV, and the 375 nsec delay in Figure 6b corresponds to a proton energy of 47 keV. These energies agree roughly with the operating potential in Figures 6a and 6c for  $t > 25$  nsec.



The conclusions of this study are:

1. As predicted by theory, the operating voltage of the reflex triode decreases with anode thickness.

2. For aluminum anodes, the decrease in anode potential (and presumably the onset of ion flow) begins when the average energy density deposited in the anode reaches a value which is approximately 1 kJ/g.

3. The time of flight for the positive ions agrees roughly with values calculated for protons with energies corresponding to the operating voltage of the reflex triode.

4. For the low values of the self-magnetic field in these experiments, an external magnetic field is necessary to keep electrons from scattering out of the anode cathode region.

5. The values of  $\eta_c$  deduced from the present data are somewhat smaller than the values which have been calculated from theory.



#### ACKNOWLEDGEMENTS

The authors gratefully acknowledge the advice of Dr. Stanley Humphries of Cornell University during the execution of the experiments. The authors also extend thanks to Ian Smith and Dr. Vernon Bailey for many helpful suggestions in the preparation of this manuscript; to Albert York for his generous contribution in the preparation and execution of the experiment; and to Vern Buck for his contribution in the reduction of the data.

## REFERENCES

1. R. N. Sudan and R. V. Lovelace, Phys. Rev. Lett. 31, 1174 (1973).
2. A. Theodore Forrester, J. Appl. Phys. 46, 2051 (1975).
3. S. Humphries, Jr., J. J. Lee, and R. N. Sudan, J. Appl. Phys. 46, 187 (1975).
4. S. Humphries, Jr., R. N. Sudan, and W. C. Condit, Jr., Appl. Phys. Letters 26, 667 (1975).
5. R. Huff and I. Smith, Bull. Amer. Phys. Soc. II, 19, 870 (1974).
6. J. M. Creedon, I. D. Smith, and D. S. Prono, Phys. Rev. Letters 35, 91 (1975).
7. D. S. Prono, J. M. Creedon, I. Smith, and N. Bergstrom, J. Appl. Phys. 46, 3310 (1975).
8. D. G. Pellin and P. W. Spence, Rev. Sci. Instr., 42, 1699 (November 1971).

9. D. G. Pellinen and I. Smith, Rev. Sci. Instr., 43, 299, (February 1972).
10. S. M. Seltzer, M. J. Berger, Nucl. Instrum. & Methods, 119, 157 (1974); M. J. Berger, S. M. Seltzer, NASA SP-3012, 1964.
11. P. T. Kirstein, G. S. Kino, W. E. Waters, Space Charge Flow (McGraw Hill, New York, 1967).
12. I. Langmuir, Phys. Rev. 33, 954 (1929).
13. L. Bradley, G. Kuswa, Phys. Rev. Lett. 29, 1441 (1972).
14. L. P. Mix, J. G. Kelly, G. W. Kuswa, D. W. Swain, and J. N. Olsen, J. Vac. Sci. Tech. 10, 951 (November/December 1973).

TABLE 1 SUMMARY OF EXPERIMENTAL CONDITIONS

Experiment Number	Anode Material	$\tau$ Anode Thickness (mg/cm <sup>2</sup> )	Cathode Radius (cm)	Anode-Cathode Spacing (cm)	Charging Voltage (MV)	V Operating Anode Potential (kV)	R Residual Range Corresponding to V (mg/cm <sup>2</sup> )	R/ $\tau$
1	Aluminum	857.00	5	2.5	3.2	900*	483.00	< 1.0
2	Mylar	71.00	5	2.5	3.3	450*	143.00	2.0
3	Aluminized Mylar	1.78	5	2.5	3.3	75*	8.11	4.6
4	Aluminum	857.00	5	2.1	2.0	650	319.00	< 1.0
5	Aluminum	41.00	5	1.8	2.2	350	135.00	3.29
6	Aluminum	6.86	5	1.8	2.3	100	18.6	2.71
7	Aluminized Mylar	1.78	5	1.8	2.3	75*	8.11	4.6

\* Anode potentials measured with the voltage divider connected directly to the anode holder.

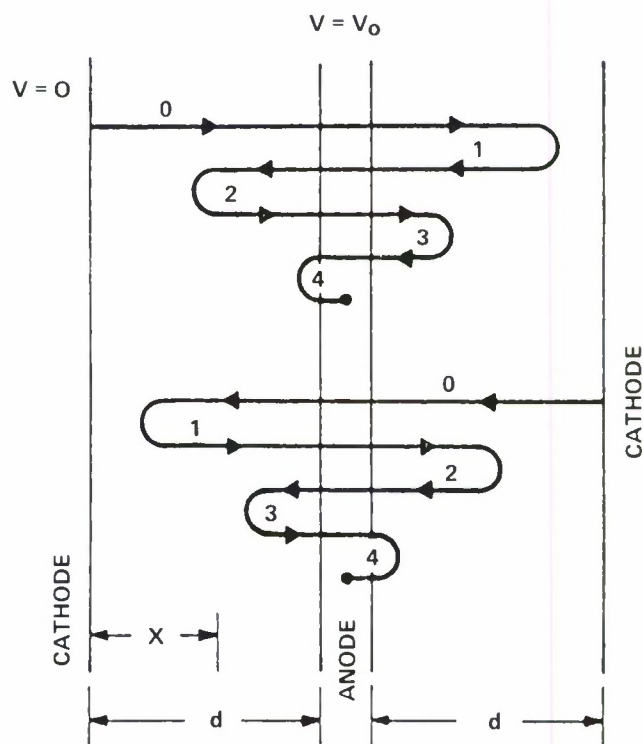


Figure 1. Reflex triode configuration. A semitransparent anode is located between two cathodes so that the electrons make many passes before coming to rest.

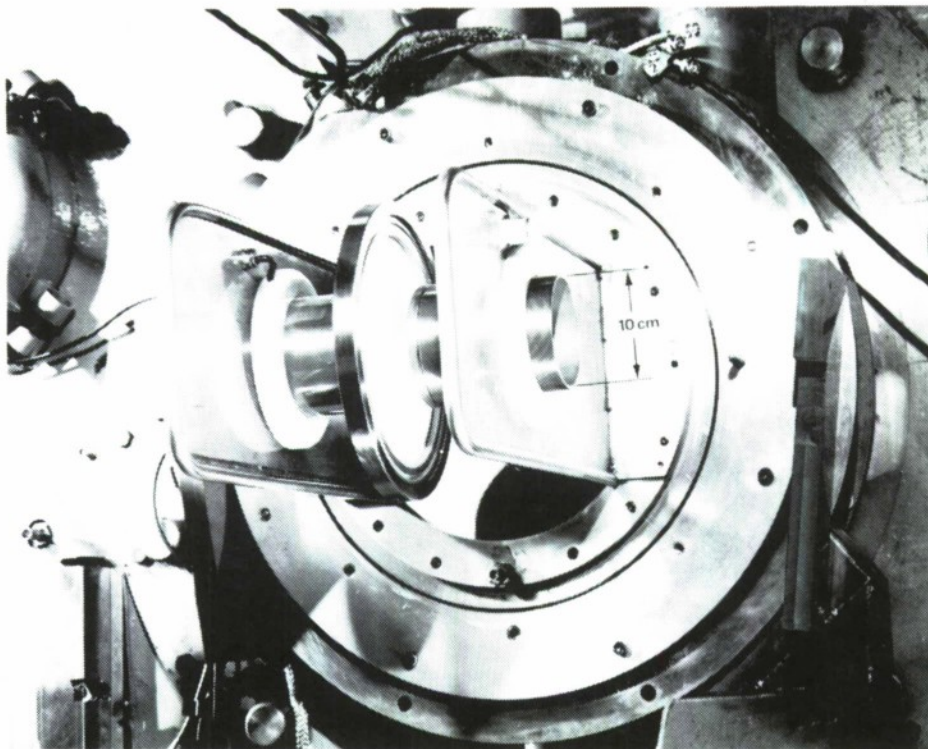


Figure 2. Experimental apparatus. Anode is located symmetrically between two cathodes. Current monitor for left cathode is shown.

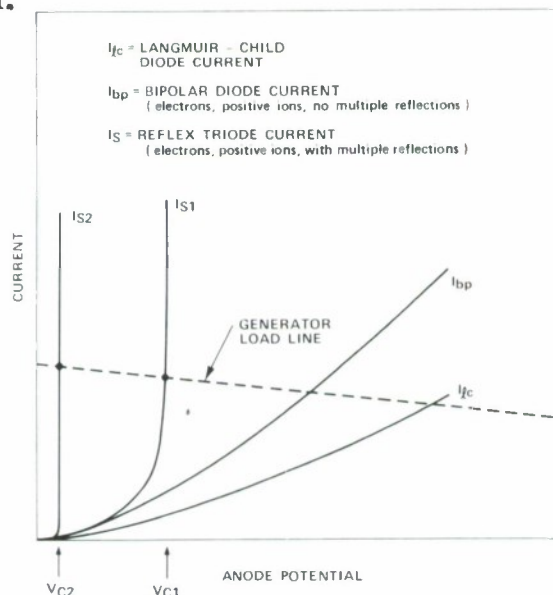


Figure 3. Theoretical voltage-current characteristics for diodes. The curve marked  $I_{LC}$  is the ordinary Langmuir-Child current for a diode.  $I_{bp}$  represents the total current for Langmuir's bipolar solution for counterstreaming electrons and positive ions when there are no multiple reflections. The curves marked  $I_S$  represent the characteristics of a reflex triode for two different anode thicknesses. The dotted line represents the load line of the generator.

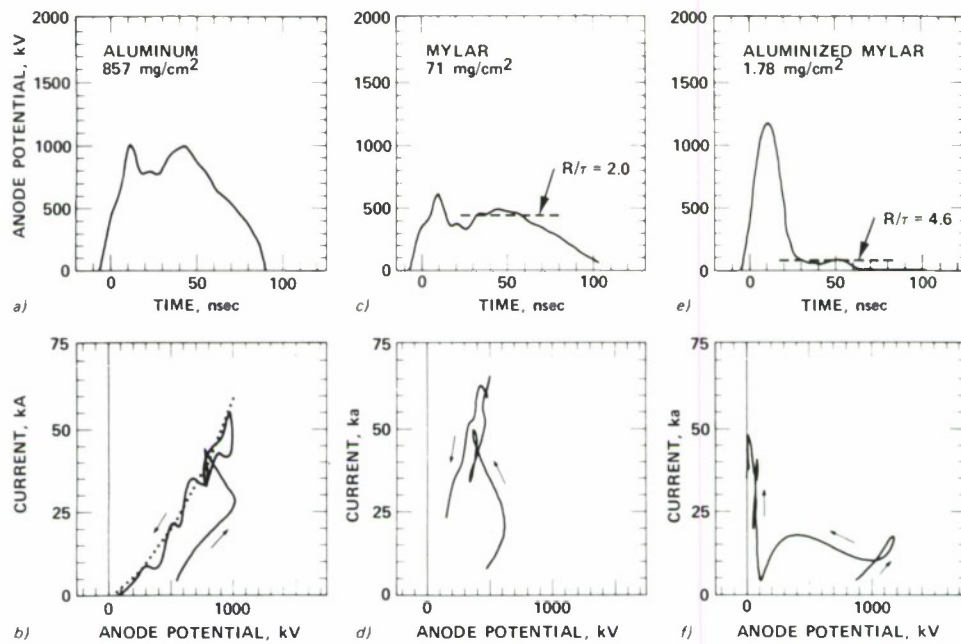


Figure 4. Voltage signatures and voltage current characteristics for reflex triodes with thick aluminum and fractional range Mylar anodes. The arrows in Figures 4b, 4d, and 4f indicate the direction of increasing time.

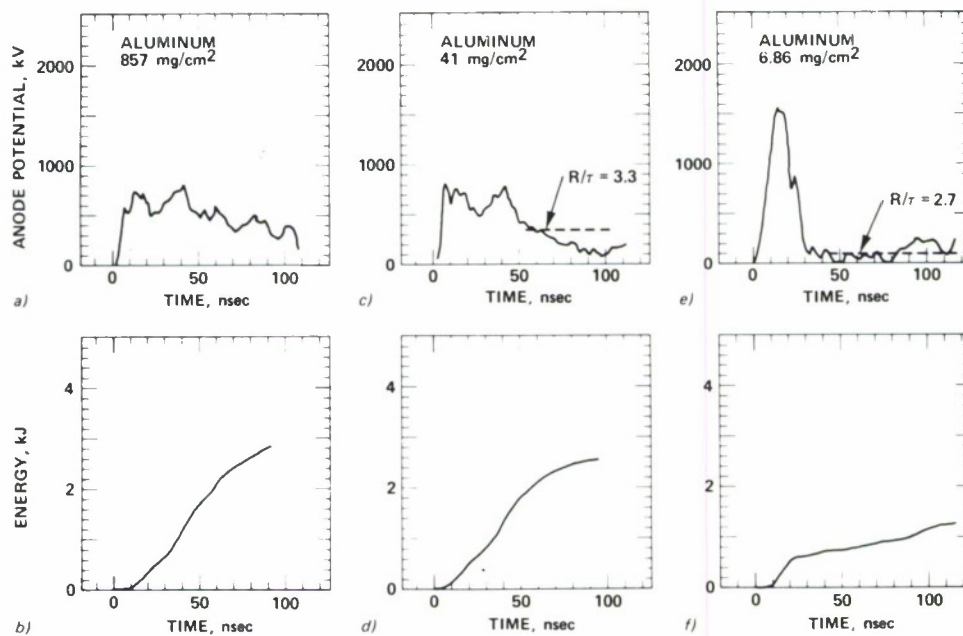


Figure 5. Voltage waveforms and deposited energy for aluminum anodes.



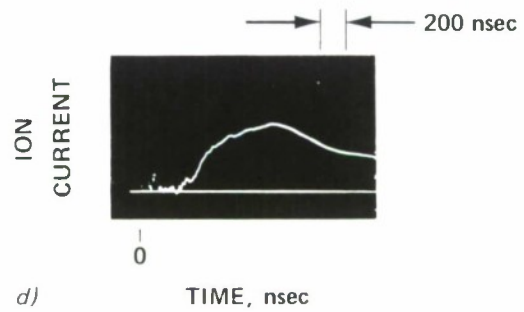
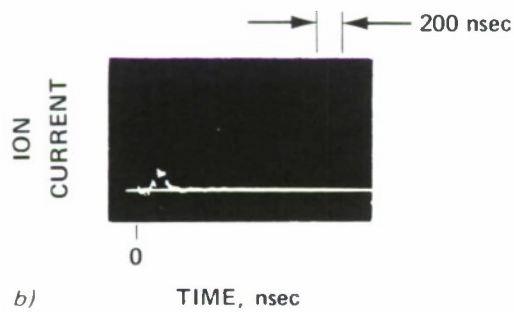
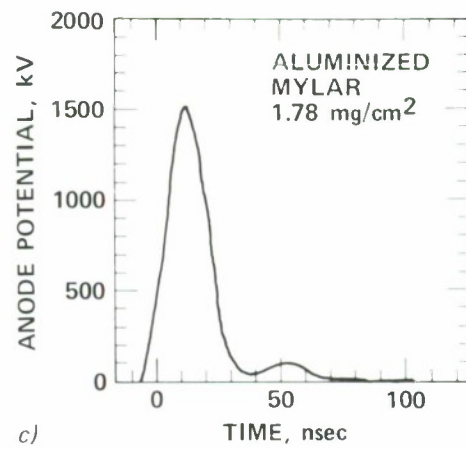
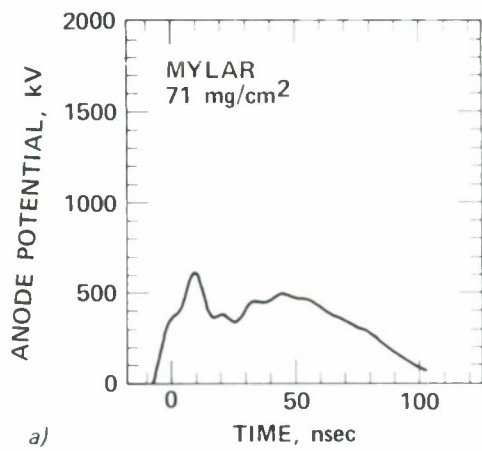


Figure 6. Voltage and ion current waveforms for different anode thicknesses.

INTENSE, PULSED, ION-DIODE SOURCES AND THEIR APPLICATION  
TO MIRROR MACHINES\*

D. S. Prono, J. W. Shearer, and R. J. Briggs  
University of California, Lawrence Livermore Laboratory  
Livermore, California 94550

ABSTRACT

Startup conditions for future mirror fusion experiments require a rapidly formed target plasma of  $\sim 0.5$  coulomb of ions with energy of 50 to 100 keV. Theory suggests that very intense ion-flux emission satisfying these requirements can be extracted from a pulsed ion diode. Developing such sources would be an ideal CTR application of the high-power, single-shot capability of pulsed power technology. Recent experimental results are reviewed in which  $\sim 2 \text{ kA/cm}^2$  of  $\text{D}^+$  at  $\sim 50 \text{ keV}$  was extracted. In the experiment, an intense relativistic electron beam undergoes many transits through a solid but range-thin anode foil. With each transit the electrons lose energy, causing their trajectories to collapse toward the anode surface. In so doing, the increased space charge extracts an intense ion flux from the anode foil's plasma. Observations are reported on the importance of diode stability. The general agreement between theoretical scaling laws and experimental results is also presented.

---

\* Work performed under the auspices of the U.S. Energy Research and Development Administration under Contract No. W-7405-Eng-48.

## I. INTRODUCTION

Recent theories have indicated that significant ion currents can flow within the diode of a relativistic electron-beam generator. Basically, there are two diode operational modes that yield enhanced ion flow: pinched electron flow<sup>1-3</sup> and a reflex diode with collapsing electron trajectories due to beam energy loss with successive transits of the foil.<sup>4</sup> In the first case, electron flow is prevented by the beam's self-magnetic field; in the latter, electron flow is restricted by the electrostatic fields of a virtual cathode created by the nonpropagating beam. In both cases, the increased electron space charge across the anode surface is neutralized by the extraction of intense ion flow from the anode plasma. This paper presents recent experimental results investigating the second of these intense ion-flux generators. In brief, a relativistic electron-beam (REB) diode (which normally operated at a peak diode voltage of 850 kV and peak electron diode current of 350 kA) was converted to an operational mode of ~50-kV diode voltage and a total diode current of 750 kA, of which 36 kA was  $D^+$  ions.

## II. APPLICATION OF ION DIODES TO CTR MAGNETIC MIRROR CONFINEMENT

Intense ion beams from pulsed diodes could be useful in the initial formation of a mirror-confined fusion plasma. As an example, consider the proposed parameters of the next generation confinement experiment, MFX (Mirror Fusion Experiment), shown in Table I.

Table I. MFX Parameters.

Central magnetic field $\sim 20$ kG	$n \sim 3 \times 10^{13} \text{ cm}^{-3}$
$\beta \gtrsim 0.5$	$T_i \sim 50 \text{ keV}$
$n\tau \sim 10^{12}$	Volume $\sim 10^5 \text{ cm}^3$

This plasma could be maintained by modest currents from long pulse length (or D.C.) neutral beams; however, the "startup" sequence is critical since many low density states of mirror plasmas are not sufficiently stable.<sup>5</sup> A number of possible approaches are being considered at present, such as the creation of a target plasma by laser irradiation of a pellet as being studied in the present Baseball II facility. The attractive feature of the ion diode approach is the short time scale of the ion injection ( $\sim 200$  ns). Instabilities of the intermediate density and temperature states of the plasma are of little concern with such a fast injection process. In contrast, buildup with D.C. sources requires on the order of a millisecond with the 1500-A, 60-keV sources being considered for MFX.

To begin assessing the feasibility of this alternative startup approach, we performed an experiment to investigate the phenomena of intense ion currents in REB diodes.

### III. THE EXPERIMENT

The REB generator used was the Physics International OWL II machine; a schematic of the experiment is shown in Figure 1. The cathode stalk was hollow to house ion diagnostics. These diagnostics included a radial array of Faraday cups (located at  $r = 0, 1.5$  and  $3.0$  cm) and a large

Faraday cup located 15 or 25 cm in back of the radial array. Each Faraday-cup collector was equipped with a thermistor, which thus gave calorimetric information. The 15- to 25-cm staggered Faraday cup gave ion energy by time-of-flight analysis. A planar circular cathode of  $45 \text{ cm}^2$  was used; small holes on the cathode allowed ion flow to reach the Faraday-cup calorimeter detectors. The cathode's surface was made of deuterated titanium with a 24% loading ( $\sim 1 \text{ D}_2$  molecule for every 4 titanium atoms). A "transit-time-isolator," developed by Physics International, enabled Faraday-cup and calorimetric signals to be brought from the cathode even though the cathode was pulsed to a high negative potential. The concentric anode stalk was equipped with two Rogowskii belts to monitor cathode current, one at the anode base and the other 1 cm from the anode foil. In all cases, both Rogowskii belts gave equal readings, indicating no cathode shank emission.

The circular anode foils ( $102 \text{ cm}^2$ ) were of varying material and thickness: 1- and 0.5-mil titanium ( $11.4$  and  $5.7 \text{ mg/cm}^2$ ), and 1-, 0.25-, and 0.1-mil aluminized Mylar ( $3.4$ ,  $0.86$ , and  $0.34 \text{ mg/cm}^2$ ). The cathode side of the anode foil was covered with a light layer of pump oil when proton flow was sought, and with a 0.1- to 0.2-mil layer of  $\text{CD}_2$  (deuterated polyethelene) when a deuterium ion current was desired. In the latter case, the deuterium ions accelerated onto the deuterated cathode surface furnished a D-D reaction yielding neutrons. These neutrons were detected externally by a geiger tube and a silver-activated scintillation counter, thereby furnishing another means of diagnosing ion flux. Downstream of the anode foil was a circular metallic drift tube in which the virtual cathode was formed; this drift tube, 1 m long by  $177 \text{ cm}^2$ , was in contact with the anode extension near the anode foil



location. External field coils supplied a uniform 16-kG field over the entire anode-cathode extension and also along the drift tube.

Three key features uniquely characterize this experimental arrangement from other similar experiments. First, the ion diagnostics are located in the diode, not downstream of the anode. This is critical because with a virtual cathode, the electron flow is asymmetric. That is, there is a high electron flow from the real cathode to anode, but no net electron flow from the virtual cathode to anode--this asymmetry also affects ion flow. Second, the function of the long drift tube is that no physical barrier should be within several diameters of the anode, else the field topology is altered and a virtual cathode will not be formed. Third, the high currents ( $\geq 750$  kA) flowing from the cathode produce a self-field of  $\sim 40$  kG on beam edge, and this field is only partially balanced by the externally applied 16 kG field. Therefore, the experiment was midway between a pinched-flow mode and an axially uniform flow.

It is important to summarize our basic diagnostics:

- 1) The total diode current,  $I_D$ , was monitored by Rogowskii belts.
- 2) The tube voltage,  $V_T$ , was detected by a capacitive voltage monitor.
- 3) The time derivative of the net diode current was sensed by a nonintegrated induction loop giving a  $\dot{B}_\theta$  signal; this signal was electronically added to  $V_T$  to give the "corrected diode voltage,"  $V_C$ .
- 4)  $V_C$ , the actual voltage appearing across the diode, is the tube voltage minus the inductive component ( $V_C = V_T - L \dot{I}_D = V_T - K \dot{B}_\theta$ , where  $K$  is a constant depending on geometry).
- 5) The neutron diagnostics determine total deuterium current flow.



- 6) The calorimeters give total energy onto the cathode Faraday-cup collectors.
- 7) The radial array of Faraday cups gives ion-current density (current through small holes in the cathode) as a function of radius.
- 8) The axially staggered Faraday cup gives ion energy (by time-of-flight), which is compared to  $V_c$ .

#### IV. EXPERIMENTAL RESULTS

The essence of the experiment was to observe diode behavior and ion flow as a function of foil thickness when a virtual cathode is present. The theory proposed in Ref. 4 indicates that when the foil thickness decreases, the average number of transits,  $\eta$ , that a beam electron makes through the anode foil should increase. Increases in  $\eta$  thus cause an increase in electron space charge across the anode and correspondingly increase both electron and ion current. The average number of anode transits is defined as

$$\eta = \frac{1}{\rho\tau} \left( \frac{R}{3} \right), \quad (1)$$

where  $\rho$  is the anode density,  $\tau$  is the anode foil thickness, and  $R$  is the residual range.<sup>6</sup> The 1/3 factor is suggested by the data of Ref. 6 as being the correction required to convert residual range into a median range.

In Figure 2 we show how diode characteristics,  $I_D$  and  $V_c$ , change when a virtual cathode is present and the anode foil thickness is varied. Infinite anode thickness implies a condition where  $\eta = 1$  (i.e., normal diode behavior). We note that there is a general increase in diode current and decrease in diode voltage. Figures 3a and 3b show actual

oscilloscope traces of  $I_D$ ,  $V_C$ , and Faraday-cup signals for cases of anode foil being 0.5-mil titanium with a pump oil coating ( $H^+$  ion flow) and 0.1-mil aluminized Mylar with a  $CD_2$  coating ( $D^+$  ion flow). The "r = 1.5 cm Faraday cup" signal comes from the sensor located directly behind the cathode plate; "staggered Faraday cup" signals come from the sensor that is 25 cm behind the "r = 1.5 cm" detector. Important points to note on these traces are:

- 1) There is a 40- to 50-ns early transition phase during which the diode behaves normally. The termination of this transition is marked by a sharp drop in  $V_C$  and an increase in the slope of  $I_D$ . The transition phase is that time required to deposit sufficient energy into the anode foil such that the anode plasma can freely supply space-charge-limited ion flow.
- 2) Following the transition period,  $V_C$  remains roughly constant at a value that is characteristic of foil thickness.
- 3) Ion flow initiates at the termination of the transition phase.
- 4) Energy analysis (assuming appropriate  $H^+$  or  $D^+$  species) of the time-of-flight between "near" and "far" Faraday cups gives ion energy in good agreement with  $V_C$ .
- 5) There is structure on the Faraday cup signals which probably results from energy modulation apparent on  $V_C$  and/or heavy ion impurities. At this time our diagnostics cannot discriminate between these two possibilities.

The data of Figure 2 are compared to the theory (Ref. 4) in Figure 4.  $J_e$ , the electron-current density, was determined as  $(I_D - I_+)/A$ , where  $I_D$  is the observed peak total diode current,  $I_+$  is the measured ion current, and  $A$  is the 45-cm<sup>2</sup> cathode area (we assume uniform flow).  $J_0$ , the

Child-Langmuir current, was calculated using the average  $V_c$  value after the transition phase and assuming a gap spacing 0.5 times the initial A-K gap of 0.95 cm (the 0.5 factor accounts for diode closure). If we assume a likely energy spectrum of the reflected electrons within the diode gap, the theory in Ref. 4 suggests a  $J_e/J_0$  vs.  $\eta$  dependence shown as the solid line in Figure 4. The dashed lines encircle data points characterizing machine performance for a given foil thickness. For low  $\eta$  values there is a large discrepancy between theory and experiment. At present, we believe this discrepancy is due to an over-simplified theoretical model. One possible modification is that whereas the theoretical model is based on a continuous electron energy spectrum extending from zero to full diode voltage, in reality the spectrum is probably truncated at both extremes. However, as the simplified theory suggests, the data show a pronounced steeping of  $J_e/J_0$  vs.  $\eta$  as  $\eta$  approaches a critical value.

Ion-current density dependence on  $\eta$  is shown in Figure 5. Conditions of  $H^+$  and  $D^+$  ion flow are denoted by different symbols. Again, the dashed lines encircle data for a given foil thickness; however, this time the 0.5-mil titanium and 0.25-mil aluminized Mylar shots are divided into an upper and lower region. The lower regions characterized ion flow when diode instability was present.

Experimentally, the observed features of diode instability were:

- 1) Diode voltage,  $V_c$ , showed h.f. oscillations in the 100- to 300-MHz band.
- 2) The oscillation frequency was correlated to anode foil thickness ( $f \propto \frac{1}{\tau}$ ).
- 3) Intense ion flow only occurred when h.f. oscillations were quiescent.

- 4) The ion flux detected during the instability showed severe energy modulation (the staggered time-of-flight Faraday cup showed a temporally broadened pulse).

Diode instability occurred whenever the virtual cathode was formed in vacuum, regardless of foil materials (although for thicker foils with low  $\eta$  values, the instability was less pronounced). In retrospect, diode instability for vacuum diodes should have been anticipated.<sup>7</sup>

Experimentally, we found that significant suppression of the instability occurred when the virtual cathode was formed in a very low pressure gas ( $\sim 20$  microns of hydrogen). The gas pressure cannot be higher because then the beam ionization time would be short compared to pulse length (i.e., the virtual cathode would be "shorted out" by the plasma and beam propagation would result). We do not understand at present why a slight gas fill around the virtual cathode causes stabilization, but one possible effect is that a virtual cathode partially neutralized by ions would be less likely to exhibit fast spatial fluctuations.

For conditions where  $\text{CD}_2$  coated the cathode side of the anode foil, we are able to compare the measurements of ion flow as given by our Faraday-cup, calorimetry, and neutron diagnostics. This comparison is given below in Table II. The effective area assumed for deducing ion current density from the neutron count was  $30 \text{ cm}^2$ , and an ion pulse duration of 30 ns was used. Because of the anode debris blow-off, the calorimeters usually give abnormally high signals, but for the thinnest foils used this effect was less pronounced. In general, the agreement between the various diagnostics is within a factor of 2. However, the neutron count estimates are still very preliminary and have a large possible error.

Table II. Comparison of Diagnostics Measuring  $D^+$  Current Density.

Anode foil	$A/cm^2$ as diagnosed by		
	Faraday cup	Neutron detection	Calorimeter
0.5 -mil Ti	15	25	--
0.5 -mil Ti	30	52	--
1 -mil Mylar	140	98	--
0.25-mil Mylar	460	340	--
0.1 -mil Mylar	1150	900 to 1280	3380
0.1 -mil Mylar	1380	850 to 1206	2230

A final aspect of the experimental results was that the ion-current density, as diagnosed by the radial array of Faraday cups immediately behind the cathode, was observed to be annular, not uniform. For thicker foils, whether the virtual cathode was in vacuum or gas, the Faraday cup at 1.5-cm radius read 2 to 5 times higher than the  $r = 0$  or  $r = 3$  cm cups. For the thinnest foils, this degree of nonuniformity increased to more than an order of magnitude. Again, we do not have a complete explanation for this observation, but some possible candidates are as follows. Perhaps our electron-current emission across the cathode was not uniform but peaked at larger radii due to electrons emitted along the cathode shank and carried into the diode region along  $B_z$  lines. The partial pinching due to high self-fields would thus cause the peak electron fluence to be located at some radius less than the cathode radius. An analogue to this condition would be electron flow from a hollow cathode. A second possible explanation involves a partially



pinched but uniform beam and return-current heating of the anode plasma. If ions are emitted only from that area of the anode plasma that has been sufficiently heated by radial return currents, then the optimum region of heating would be at the radius of the partial pinch and not in the center or at the cathode radius.

## V. SUMMARY AND CONCLUSIONS

In our experiment, an REB diode was made to operate in an extremely low-voltage, high-current mode. Electron currents in excess of 80 times Child's-law current (space-charge-limited flow) were observed. Deuterium currents densities of  $0.05 J_e$  were monitored; this exceeds by a factor of 3 the normal Langmuir value of  $0.0165 J_e$ . Although this is only a modest increase, we feel that more serious attention to anode-foil fabrication will minimize impurities causing heavy ion currents and significantly increase  $D^+$  flow. Having already achieved  $D^+$  current densities  $> 1 \text{ kA/cm}^2$  is in itself a promising step.

The qualitative features of simple theory<sup>4</sup> have been substantiated. Both electron and ion flow increase sharply as  $\eta$  approaches a critical value. A disruptive diode instability that quenches ion flow was observed and found to be stabilized by adding low-pressure gas in the virtual cathode region. Why the presence of this gas and its associated tenuous plasma afford stabilization is not known. Equally unexplained is the annular radial profile of ion flow.



## ACKNOWLEDGMENT

We gratefully acknowledge numerous staff members of Physics International Company, whose advice and assistance contributed greatly to this experiment.

## REFERENCES

1. J. W. Poukey, Appl. Phys. Lett. 26, 145 (1975).
2. S. A. Goldstein and R. Lee, Phys. Rev. Lett. 35, 1079 (1975).
3. S. A. Goldstein and J. Guillory, Phys. Rev. Lett. 35, 1160 (1975).
4. D. S. Prono, J. M. Creedon, I. Smith, and N. Bergstrom, J. Appl. Phys. 46, 3310 (1975). See also earlier work on reflex triodes by S. Humphries, Jr. et al., J. Appl. Phys. 46, 137 (1975).
5. J. H. Foote, Instability-Threshold Data from the Baseball II Vacuum Buildup Experiment, Lawrence Livermore Laboratory Rept. UCID-16664 (1974).
6. S. M. Seltzer and M. J. Berger, Nuclear Inst. and Methods 119, 157 (1974).
7. C. K. Birdsall and W. B. Bridges, Electron Dynamics of Diode Regions (Academic Press, New York, 1966), pp. 68-118.

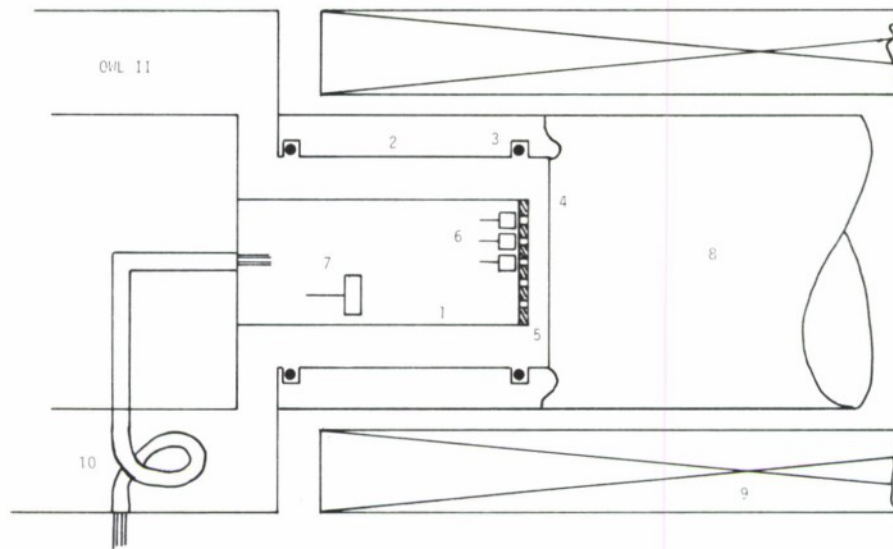


Figure 1. Schematic of experimental arrangement as described in the text. Components are: 1) cathode stalk, 2) anode stalk, 3) Rogowskii belts, 4) anode foil, 5) deuterated-titanium cathode tip with small holes to pass ion flow, 6) radially located Faraday cups with calorimeters, 7) axially staggered Faraday cup with a calorimeter, 8) drift tube, 9) external  $B_z$  coils, and 10) transit time isolator.

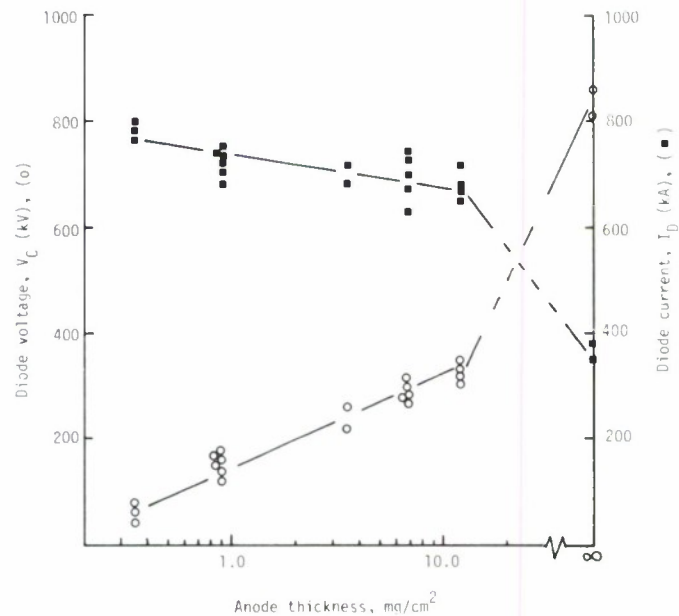


Figure 2. Characteristic diode voltage and current caused variations of anode foil thickness when a virtual cathode is formed.

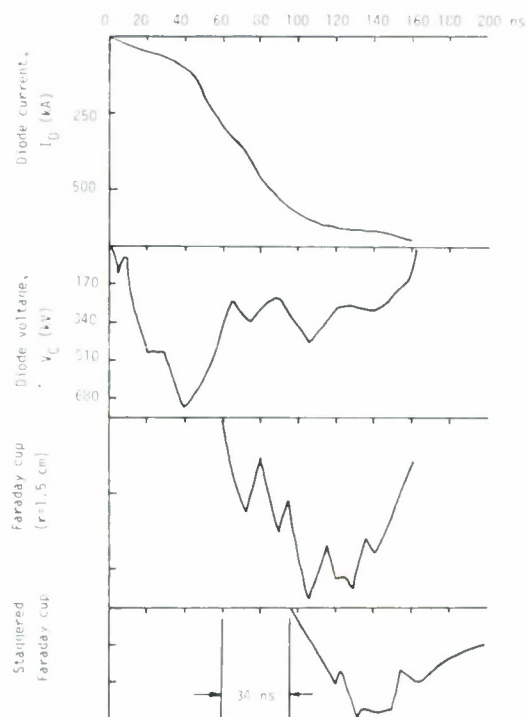


Figure 3a. Oscilloscope waveforms of diode current, diode voltage,  $r = 1.5$  cm Faraday cup, and staggered Faraday cup. The anode foil is 0.5-mil titanium coated with pump oil for  $H^+$  emission. The drift tube is filled with  $\sim 20$  microns of hydrogen.

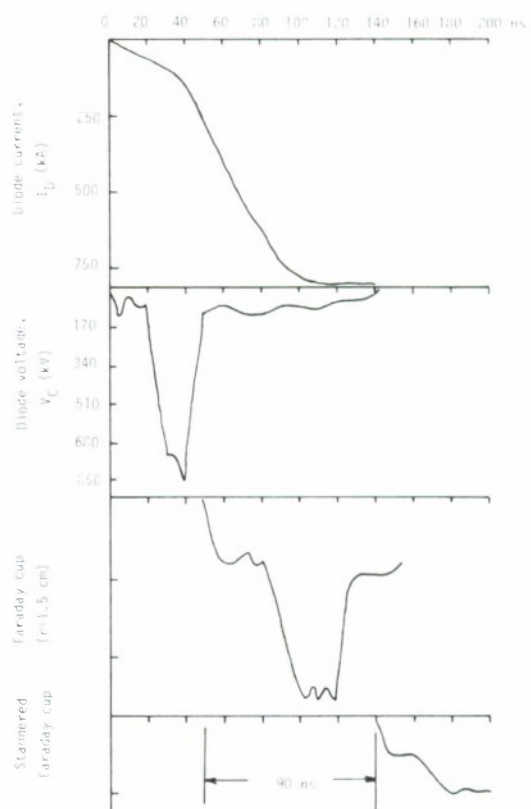


Figure 3b. Oscilloscope waveforms of diode current, diode voltage,  $r = 1.5$  cm Faraday cup, and staggered Faraday cup. The anode foil is 0.1-mil aluminized Mylar coated with  $CD_2$  for  $D^+$  emission. The drift tube is filled with  $\sim 20$  microns of hydrogen.

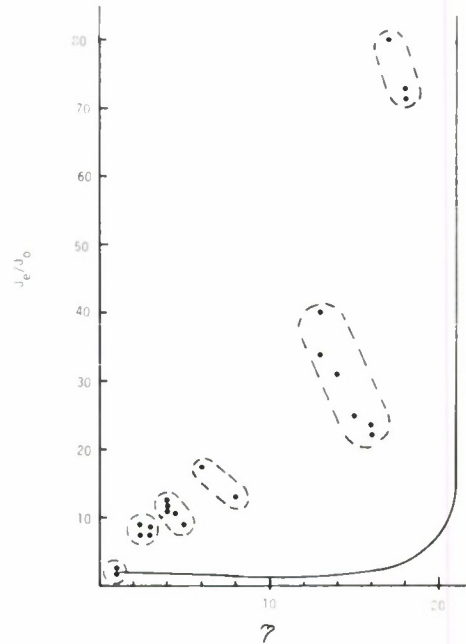


Figure 4.  $J_e/J_0$  vs.  $\eta$ . The dashed lines enclose data points characterizing equal thickness foils and the solid curve is from the simple theory given in Ref. 4.

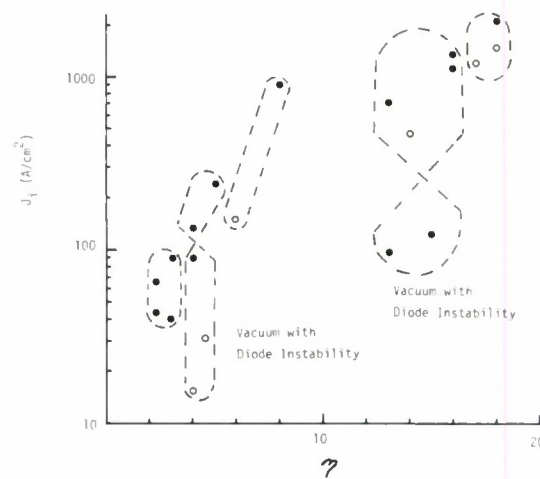


Figure 5. Ion-current density,  $J_i$ , vs.  $\eta$ . Anode foils covered with pump oil yielding  $H^+$  emission are denoted by  $\bullet$  data points; anode foils covered with  $CD_2$  for  $D^+$  emission are denoted by  $o$  data points. Dashed lines again enclose data for anode foils of equal thickness, but here we indicate which shots were with the virtual cathode in vacuum, resulting in diode instability.

CONVERSION OF INTENSE ELECTRON BEAM ENERGY INTO

CONVERGING ION FLUXES - THEORETICAL STUDIES \*

John Guillory and Shyke A. Goldstein  
University of Maryland  
Department of Physics and Astronomy  
College Park, Maryland 20742

ABSTRACT

Various designs of relativistic electron beam diodes allow the production of very intense converging ion pulses<sup>†</sup> for bombardment of, e.g., pellet or rod targets placed inside a mesh anode. Ions formed by ionization of anode mesh material are accelerated by the self-consistent space charge produced by electrons from the cathode and target. In the conventional region of the diode before the anode, the self-pinching of the electron flow largely decouples the ion acceleration region from the electron source, so that the space charge does not quench the electron current. The steady-state equations for the magnetic field-free ion-acceleration regions of such diodes are analyzed in several geometries, and the formation and effects of virtual cathodes are discussed. Efficient conversion (>50%) of electron current into ion current is predicted.

---

\* Work supported by ONR and NSF.

<sup>†</sup> Shyke A. Goldstein and John Guillory, Univ. Md. preprint #505P013, and Bull. Am. Phys. Soc. 20, 585 (1975).

The power requirements for initiation of pellet fusion implosions by direct use of intense electron beams are formidable. Present estimates appear to be in the range of  $3 \times 10^{14}$  W.<sup>1</sup> In addition, the power must be delivered at relatively low voltages ( $\leq 1$  MeV) to avoid preheat of the target, and this poses formidable problems in the design of appropriate electron beam diodes. Intense ion beams with energy densities comparable with presently available electron beams would of course alleviate those difficulties by having much shorter range, no bremsstrahlung, and much lower power requirements. Present estimates of required ion power are in the range of  $3 \times 10^{13}$  W and below.<sup>2</sup> Until recently, no technique for achieving such intense ion beams had appeared, although it has been known for some time that intense electron beams can accelerate small bursts of ions.<sup>3,4,5</sup> Various ion-diode schemes have been discussed<sup>6,7</sup> but focusing of the ions to adequate current densities has appeared difficult.

Recent theoretical work,<sup>8,9</sup> concurrent with that reported in this paper, has revolutionized the understanding of high power electron diodes and predicted intense ion currents in the diodes of present machines. These ion currents have now been detected.<sup>10</sup> Electron flux risetimes at the anode center have also been found to be much shorter than once expected, allowing production of ion pulses with fast risetimes ( $\sim 2$  ns). The way has thus been opened for application of such ion pulses to pellet fusion and other tasks requiring interaction of intense ion beams with solids.



This paper describes some of the physics of a scheme for using the intense electron beam diode behavior to produce intense pulses of ions incident on a floating target.<sup>11</sup> It appears theoretically that ions may be accelerated to several MeV by space charge between the anode and target plasmas, and may flow with currents larger than half the primary electron current in the diode. These ions arrive at the target accompanied by electrons which are much reduced in energy (and therefore much shortened in range). The conversion of electron beam energy to ion energy is predicted to be quite efficient. Applications to pellet compression and emission of radiation appear possible. Fusion reactions between accelerated ions (e.g., deuterons) and the target may also be of interest.

One possible diode geometry for producing such ion pulses is that of Fig. 1. The anode plane, between two hollow cylindrical cathodes, has its central region replaced by a spherical mesh. Regions I and II of Fig. 1 are idealized as initially vacuum regions. The target, III, is assumed floating. Recent experiments with a simple small spherical obstacle centered on the anode plane indicate quite uniform electron fluence over the surface of the sphere.<sup>12</sup> The electron and plasma dynamics bringing this about may be illustrated qualitatively as in Fig. 2, and experimentally the  $E \times B$  motion appears to predominate over  $\nabla B$  effects, since electron fluence is present over the entire hemisphere.

We consider first a spherical anode portion made of wire mesh with a small fraction of the area covered by the wires (fraction  $P \ll 1$ ). A thin foil would suffice if virtual cathode formation proves unimportant, but theoretically the all-or-nothing absorption of electron energy at the wires is a useful simplification. Electrons from the cathode follow the anode plane down toward the center as anode plasma is formed on the plane,

and they converge suddenly (typically  $\sim 3$  nsec) on the central spherical portion.<sup>13</sup> Drift motion carries them partway around the hemisphere, and they fall in, creating space charge in region II. Initially, this space charge reflects the electrons back into region I, but because of the electric and magnetic fields in region I, they are returned to region II, and thus make several passes through the mesh. The anode mesh becomes ionized in the process and emits ions into region II in a field-emission process which quickly becomes space-charge limited, i.e., the electric field at the quasineutral dense plasma surface vanishes:  $E(R_2) = 0$ . In actual fact, an expanding layer of positive charge is formed on the plasma surfaces, which reduces the field to zero at some small depth in the mesh plasma. The structure of the anode mesh plasma is shown in Fig. 3 (which however omits the explicit representation of the ion layer and  $E$  field dependence at the plasma surfaces.). The ions are accelerated inwards (and also outwards) by the space-charge field of the electrons.

The initial time-dependent dynamics can be solved analytically but are of less interest here. The intermediate-time history (a few ion crossing times for region II) is a problem for computation. In what follows we treat the steady-state flow of ions and electrons self-consistently. In the steady state the primary electrons are only slowed down in region II and reach the absorber III with a small fraction of their initial energy. The ions are accelerated by the electric field in the electron-rich region II. The net current into region III is zero because additional space-charge accumulation reduces the arrival of one or the other species; the charging process is thus self-adjusting.

On the surface of region III the electric field is zero because

of plasma formation. This boundary emits electrons into region II. These "secondary" electrons cross the anode mesh with multiple reflections back from region I and simply add to the population of electrons in region II. In the present steady-state analysis we solve Poisson's equation assuming that all charge flow is spherically symmetric and only electric fields exist in region II with the boundary conditions

$$E(R_2) = E(R_3) = 0. \quad (1)$$

No magnetic fields are generated in region II because of spherical symmetry and zero total current. The total ion current is computed as a fraction of the electron current,  $I_p$ , incident on the sphere.

The work reported here differs from current work by several other groups<sup>14-16</sup> in the following important respects: (1) Because no axial magnetic field is used in the electron-beam diode, focusing of the electrons is achieved, and hence current densities obtainable are orders of magnitude larger. In addition the geometry in this Letter is such that the ion flux is focused naturally and used immediately on the target. (2) In the usual "reflex triode", reflection of the primary electrons reduces the electron current significantly by space-charge effects; in the present work, both the geometry of Fig. 1 and the magnetic field in Fig. 2 serve to isolate these secondary electrons from the cathode emission surface in region I, thus alleviating this disadvantage of reflex triode ion-generation schemes. Primary electrons are not reflected, and thus the mathematical treatment is different.

The current circuit for the diode is closed by the planar portion of the anode, which takes electrons from the spherical mesh to compensate for

its loss of ions. The treatment is relativistic for the electrons and we distinguish between two electron groups: (1) primary electrons and (2) secondary electrons followed for many reflections. In group (1) the electrons are slowed down in energy but very little in velocity and their radial velocity is nearly  $c$  - the velocity of light in vacuo. Their assumed current is denoted  $I_p$ . In group (2) the electrons leave the surface of region III with small thermal velocity, assumed zero. Their velocity as a function of radius is computed from energy conservation. After being reflected from region I, those electrons not absorbed by the mesh approach very near the surface of region III because they suffered only a small energy loss. The points of closest approach are idealized to be on the surface of region III.

The average number of times,  $N_2$ , these electrons appear in region II is computed by assuming a probability  $P$  of being absorbed in the wires of the anode mesh each time an electron crosses the anode mesh. Thus,

$$N_2 = 1 + 2 \sum_{s=1}^{\infty} (1-P)^{2s} \approx \frac{1}{P} - \frac{1}{2} \quad (\text{for } P \ll 1). \quad (2)$$

The current of these electrons is denoted by  $I_s$ .

The velocity of the ions is computed from energy conservation assuming zero velocity at  $R_2$ . The ion current,  $I_i$ , is related to the electron currents by zero total current into region III:

$$|I_i| = |I_p| - |I_s|. \quad (3)$$

For simplicity, one may idealize to the case of purely radial electron motion in region II (even though in actuality electrons may enter with random azimuthal velocities).

One can then write Poisson's equation (multiplied by  $R^2 c$ ) as

$$\begin{aligned} \frac{d}{dR} \left( R^2 \frac{dV}{dR} \right) = G(V) \equiv & \frac{I_p}{[1 - (\gamma_D + V)^{-2}]^{1/2}} + \frac{N_2 I_s}{[1 - (\gamma_0 + V)^{-2}]^{1/2}} \\ & + \frac{I_p - I_s}{[(2mZ/M)(\gamma_0 - 1 - V)]^{1/2}} \end{aligned} \quad (4)$$

with  $V$  measured in units of  $mc^2/e$ ,  $V(R_2) = 0$ ,  $V(R_3) = -V_0$ ,  $\gamma_0 \equiv 1 + V_0$  and  $\gamma_D = 1 + V_D$  with  $V_D$  the (normalized) diode voltage.  $I_p$  and  $I_s$  are positive magnitudes. The mass of the accelerated ions is  $M$  and they are ionized  $Z$  times.

Eq. (4) is in the form of a turning-point problem. Certain approximations (non-relativistic ions, highly relativistic primary electrons, i.e.,  $\beta \sim 1$  for all  $R$ ) allow simplification of  $G(V)$ . Choosing  $R_2 - R_3 \ll R_2$  allows simplification of the left hand side. The ion current,  $I_p - I_s$ , is determined by the conditions  $dV/dR = 0$  at  $R_2, R_3$ . An exact first integral of the approximate equation gives for this case

$$\frac{I_i}{I_p} = \frac{N_2(\gamma_0 + 1)^{1/2} + (\gamma_0 - 1)^{1/2}}{N_2(\gamma_0 + 1)^{1/2} + (2M/mZ)^{1/2}}. \quad (5)$$

For protons accelerated to 2 MeV and for  $P = 0.03$  in Eq. (2), this gives

$$I_i/I_p = 0.56.$$

The second integration of (4) gives an implicit expression for the floating target potential  $V_0 \equiv \gamma_0 - 1$ :

$$\begin{aligned} \frac{R_2 - R_3}{R_2} \left( \frac{2I_p e}{mc^3} \right)^{1/2} = & \int_1^{\gamma_0} d\gamma \left\{ \gamma - 1 + N_2 \left( 1 - \frac{I_i}{I_p} \right) (\gamma^2 - 1)^{1/2} \right. \\ & \left. + \frac{I_i}{I_p} \left( \frac{2M}{mZ} \right)^{1/2} [(\gamma_0 - \gamma)^{1/2} - (\gamma_0 - 1)^{1/2}] \right\}^{-1/2}. \end{aligned} \quad (6)$$



In Fig. (4), the resulting  $\gamma_o$  is shown as a function of the left hand side of Eq. (6), using  $N_2 = 10$  and  $N_2 = 32.8$  ( $P = 0.03$ ). The ions in this case were protons.  $V_o$  is thus determined self-consistently and must be less than the diode voltage. (This places a lower bound on  $R_3$  in order to avoid virtual cathodes in region II.) It is easily seen that only when the primary current ( $I_p$ ) is larger than  $m_o c^3/e$  ( $=17000$  A) will the induced voltage be in the range of megavolts. Either the accelerating voltage ( $\gamma_o$ ) or the left-hand side of Eq. (6) may be considered as the independent variable.

If the azimuthal velocity spread of the primary electrons is taken into account at the anode, one can make a small but perhaps important correction to the  $I_p/\beta c$  term on the right side of (4). This will be described elsewhere.

If the anode mesh region is replaced by a thin foil, secondary electrons lose a small but rather well-defined amount of energy on each pass through the foil, and the resulting striations in space charge density may cause bifurcation of the solution for  $V(R)$  near the target, where these electrons return with slightly reduced energy. In this case we expect fluctuations in the potential and the currents.

Spherical symmetry is not essential to the functioning of the ion acceleration technique just discussed. Fig.(5) shows a cylindrical system (also with floating target) which should behave in very much the same way. Utilization of such a rod target for ion bombardment may have certain advantages as a radiation source, especially if coherent effects are envisioned<sup>17,18</sup>. A planar system with basically the same physics is shown in Fig. (6) and is amenable to simple experiments. The



current-free target and acceleration region and their isolation, by beam pinching, from the cathode emission region are essential, as is the driving energy of the primary electrons as they pass through the anode plasma.

Because of the high efficiency of electron beam diodes and the demonstrated high efficiency of the conversion to ion energy, such systems as, for example that of Fig. (6), also hold considerable promise as sources of intense ions for ion ring experiments and ion-beam heating of plasmas.

## REFERENCES

1. M. J. Clauser, Phys. Rev. Lett. 34, 570 (1975) and M. J. Clauser and M. A. Sweeney, these proceedings.
2. M. J. Clauser, Phys. Rev. Lett. 35, 848 (1975) and J. D. Lindl, R. O. Bangerter and D. Meeker, these proceedings.
3. S. Graybill, IEEE Trans. Nucl. Sci. NS-18, 3, 438 (1971).
4. J. Rander, B. Ecker, G. Yonas, and D. Drickey, Phys. Rev. Lett. 24, 283 (1970).
5. B. Ecker et al, Proc. IEEE Conf. on Electron Beam Technol., 1973.
6. M. Friedman, IEEE Trans. Nucl. Sci. 19, 184 (1972).
7. J. M. Creedon, I. D. Smith, and D. S. Prono, Phys. Rev. Lett. 35, 91 (1975) and D. S. Prono et al, J. Appl. Phys. (to be published).
8. S. A. Goldstein, R. C. Davidson, J. G. Siambis, and R. Lee, Phys. Rev. Lett. 33, 1471 (1974) and these proceedings.
9. S. A. Goldstein and R. Lee, Phys. Rev. Lett. 35, 1079 (1975).
10. A. E. Blaugrund, G. Cooperstein, J. R. Boller, and S. A. Goldstein, Bull. Am. Phys. Soc. 20, 1252 (1975).
11. S. A. Goldstein and J. Guillory, Phys. Rev. Lett. 35, 1160 (1975).
12. A. J. Toepfer, Bull. Am. Phys. Soc. 19, 856 (1974).
13. A. E. Blaugrund, G. Cooperstein, and S. A. Goldstein, these proceedings.
14. S. Humphries Jr., J. J. Lee, and R. N. Sudan, J. Appl. Phys. 46, 187 (1975).
15. J. M. Creedon, I. D. Smith, and D. S. Prono, Phys. Rev. Lett. 35, 91 (1975).
16. T. M. Antonsen Jr., and E. Ott, Cornell University Report No. LPS 166, 1975 (unpublished).
17. G. Chapline and L. Wood, Phys. Today 28, 40 (1975).
18. A. V. Vinogradov and I. I. Sobel'man, Sov. Phys. JETP 36, 1115 (1973).

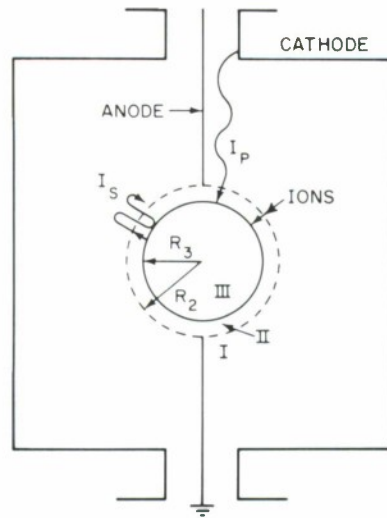


Figure 1. Diode geometry consisting of a spherical anode mesh (radius  $R_2$ ) with the target (III) floating inside it. The two cylindrical hollow cathodes are the source of the primary electrons ( $I_p$ ). Ions are emitted from the plasma mesh and accelerated inwards by the electron-rich cloud of the secondary electrons ( $I_s$ ) which are reflected many times.

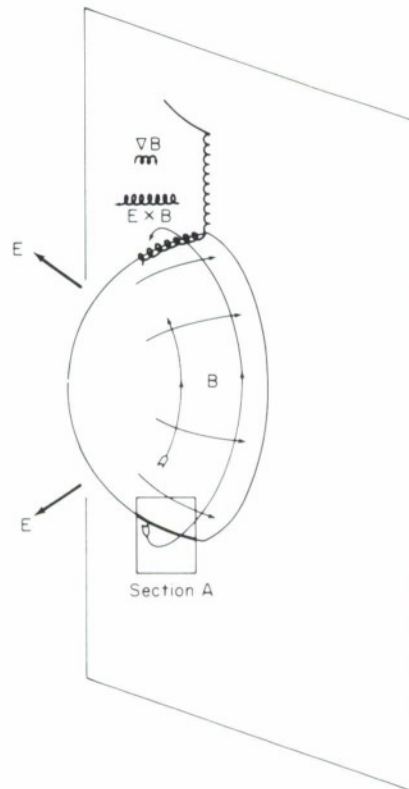


Figure 2. Magnetic field and drift motion of relativistic primary electrons at a hemispherical anode bulge.

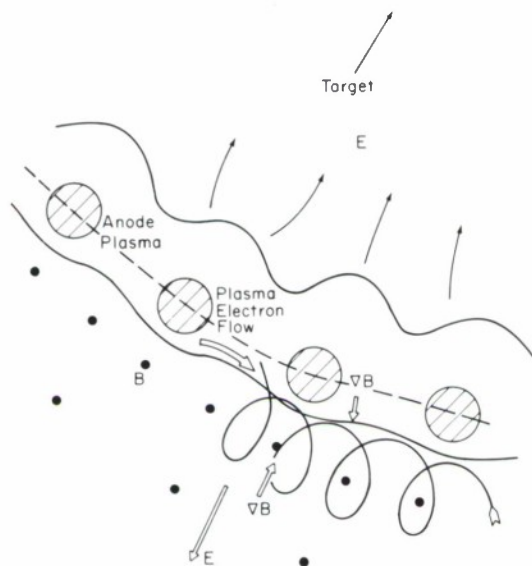


Figure 3. Hypothetical anode mesh plasma structure, section at A of Fig. 2. Electric field increases from zero at the neutral anode plasma boundary. Surface layer of plasma current shields the magnetic field,  $B$ , from the interior of the anode mesh.

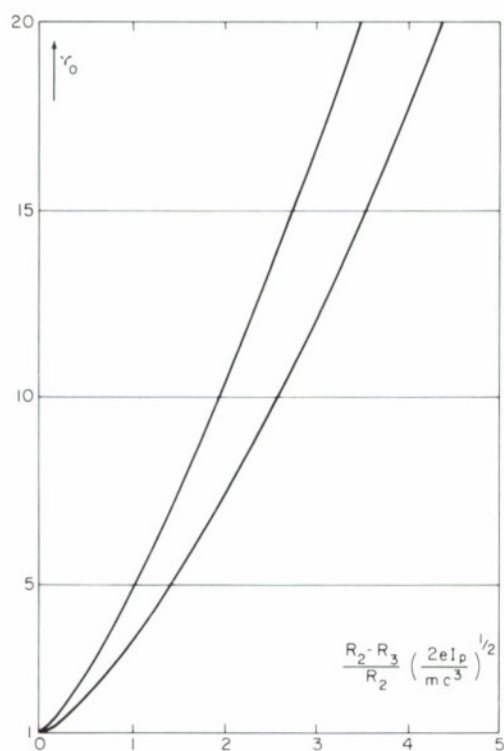


Figure 4. Floating potential of target (as measured by  $\gamma_0 = 1 + V_0$ ) as a function of diode current parameter (left hand side of Eq. 6), for  $N_2 = 33$  (left hand curve) and  $N_2 = 10$  (right hand curve). The ions in this case were protons.

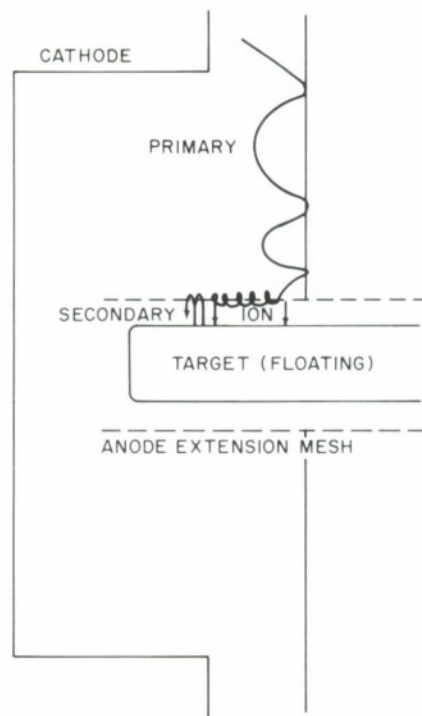


Figure 5. Cylindrical ion implosion onto rod target.

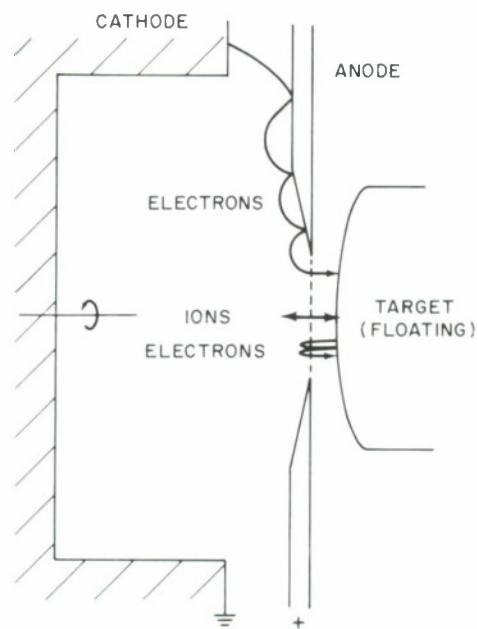


Figure 6. "Planar ion source.

## INJECTION, COMPRESSION AND STABILITY OF INTENSE ION-RINGS\*

R. N. Sudan  
Laboratory of Plasma Studies

Cornell University, Ithaca, N.Y. 14853

### Abstract

Recent advances in pulsed high power ion beam technology make possible the creation of intense ion-rings with strong self-magnetic fields by single pulse injection. Such ion rings have several uses in controlled fusion, e.g., to produce a min  $|B|$  magnetic geometry with a mirror ratio much higher than is possible with external conductors. For even stronger ion rings a min  $|B|$  geometry with closed lines of force (ASTRON type) can be created. For this purpose, since the ion energies required are much higher than are available from high power sources, magnetic compression can be utilized to increase the ion energy. The success of this scheme depends critically on the stability of the ion ring. The low frequency perturbations of the ring-plasma system is examined by means of a generalization of the energy principle which established sufficient conditions for stability. The high-frequency micro-instabilities and their nonlinear consequences are discussed in terms of conventional techniques.

\* Experimental work supported by ONR Contract N00014-75-C-0358 and the theoretical work by ERDA Contract AT(11-1) 3170.



## INTRODUCTION

Developments in technology can breathe new life into old concepts. High-power, pulsed, high voltage technology gave rise to relativistic electron-beams (E-beams) which have had much impact in several fields of research. This same technology is in principle also capable of producing intense ion beams efficiently with a minimal amount of modification to the diode structure. Encouraged by some progress (see Table I) made towards the experimental realization of this idea at Cornell,<sup>1</sup> a strong interest in the technology of intense ion beam production appears to emerge at several laboratories (see Conference proceedings) because of their potential applications.

Such intense ion-beams can be put to several uses depending upon the limits to which their power and energy content can be pushed. A few of these applications are listed below: -

- 1) D-T Pellet Fusion<sup>2</sup>
- 2) Long  $\theta$ -Pinch Plasma Heating<sup>3</sup>
- 3) Novel Laser Systems<sup>4</sup>
- 4) Two-Component Target Plasma
- 5) Proton Ring Fusion System.<sup>5</sup>

Clauser<sup>2</sup> has demonstrated that the heating of D-T pellets for break-even requires an order of magnitude less power if electron beams are substituted by ion-beams. Furthermore since intense ion-beams are intrinsically electrostatically and magnetically neutral because they transport an equal number of electrons, propagation in vacuum is possible without the need of an ambient plasma. The focusing of these beams is therefore

geometrical in nature and determined by the beam emittance. A significant advantage is that the pellet need not be physically within the diode structure. However considerable further development in technology is needed to show if the required pulse currents of 10 MA are feasible at low emittance.

If ion beams at the required power are available then a case can also be made for their application to the long  $\theta$ -pinch system envisaged by Dawson et al<sup>6</sup> and by Budker.<sup>7</sup> Here the main advantage of the ion beam over E-beam heating is that the heating process with ions is likely to be almost entirely classical and therefore well defined and calculable, while for E-beams collective processes are important and as yet these are not entirely well understood.

#### Proton Ring Fusion System<sup>5</sup>

An application that makes a less ambitious demand on ion-beam technology is the Proton-Ring fusion system, which is in fact a revival of the Astron concept with the two important modifications. Christofilos of course realized that synchrotron radiation from an E-layer would make the system untenable but that protons would overcome this limitation. He envisaged the Astron as a steady state system in which the long E-layer was continually being replenished by particle injection. On the other hand, the experiments at Livermore displayed severe limitations on E-layer build up by stacking of a sequence of injected pulses of 5 MeV,  $\lesssim 800A$  relativistic electrons.<sup>8</sup> This was attributed to an increase of axial energy spread<sup>9</sup> as more pulses were trapped resulting in an increased E-layer length with almost the same current

per unit length.<sup>10</sup> The success of single pulse injection in producing reversed E-layers<sup>11</sup> leads one to the belief that the same technique should be successful for proton-layers. It is possible that self-fields play an important role in this injection process. We define a field reversal factor  $\zeta = \delta B / B_0$ , where  $\delta B$  is the change in the magnetic field on axis and  $B_0$  is the applied field. It is readily seen that  $\zeta \approx N(e^2/mc^2)R_L/R^2$ , where  $R_L$  is the ion Larmor radius in the applied field,  $R$  is the mean radius of the ring and  $N$  is the total number of protons in the ring. For  $R \sim R_L$  and  $\zeta \sim 1$  we require  $N \sim (mc^2/e^2) R_L$  protons. If this many protons are provided in a single pulse, then the total energy input is  $\sqrt{2}(mc^2/e^2)^{3/2}E^{3/2}/B$ , where  $E$  the particle energy is of the order 1-10 MeV. Since this energy is insufficient to heat the confined plasma to thermonuclear temperatures for breakeven conditions, it was suggested that adiabatic magnetic compression could be utilized to increase the beam energy. Furthermore the field reversal factor  $\zeta$  increases because  $R$  decreases with increasing  $B$ . These two modifications, viz., pulsed injection followed by magnetic compression, are the key features of the proton ring scheme.

As the strength of a proton ring is built up either by injection or compression, there is at first a region where the plasma is  $\int dl/B$  stable but the lines of force are open, Fig. (1a). At a particular strength  $\zeta \sim r/R$ , where  $r$  is the minor ring radius, the net magnetic field becomes zero inside the ion ring and any increase in strength beyond this point gives a configuration which is  $\int dl/B$  stable with closed lines of force, Fig. (1b). Even at strengths below field reversal, a proton ring is a useful device since it provides a  $\int dl/B$  stable region with a large mirror ratio which is otherwise difficult to achieve with external means, viz., Joffe bars or Ying Yang coils etc.

## INJECTION AND EQUILIBRIA

The conditions for the satisfactory formation of proton rings by injection through a magnetic cusp are less stringent than for electron beams largely because of the much slower axial velocities of protons (for the same energy) which allows for the more efficient use of resistive trapping. The neutralizing electrons accompanying the ions are of course incapable of crossing the cusp lines of force non-adiabatically like the ions. A small amount of plasma or an appropriate electron emission source in the cusp removes this requirement since each ion emerging from the cusp can drag along a new ion. Humphries<sup>12</sup> has considered injection through a magnetic cusp followed by an axially increasing magnetic field. From the conservation of canonical angular momentum and particle energy, he shows that the ion bunch emerging from the cusp will have a directed axial velocity  $\sim v_0 (a_1/2R_1)^{1/2}$  with a velocity spread  $\Delta v_{||}$  of the same order. Here  $R_1$  and  $a_1$  are the mean injection radius and width of the annular ion source and  $v_0$  is ion injection speed. The bunch is axially contained by self-magnetic forces if  $\Delta v_{||}/v_0 < \zeta^{1/2}$ . Since  $\zeta \propto R_L^{-1} \propto B$ , the self-fields become more important as ions move into the strong field region until the containment condition is satisfied. Finally this self-contained bunch enters a magnetic mirror and the excess axial momentum is damped out by resistive walls.

With respect to the equilibrium there exist several calculations in the literature. It is of course not always possible to comment on the accessibility of these equilibria from the injection conditions. The injec-



tion and trapping of relativistic electrons to form a long cylindrical E-layer has been treated by Lovelace et al.<sup>13</sup> who show that, for this case, the radial thickness appears to increase with injection as  $\zeta^{1/2}$ . To study ion injection and also ring compression including the presence of a background plasma for a variety of magnetic configurations Friedman et al.<sup>14</sup> have developed a numerical (r,z) code which treats the ring ions as individual particles, and the response of the background plasma obeys Ohm's law. The electric field is given by  $\underline{E} = -\hat{\theta} \partial A_{\theta} / \partial t - \nabla_{\perp} \phi$ , where  $A_{\theta}$  and  $\phi$  are the vector and scalar potentials and  $\nabla_{\perp} = \hat{r} \partial / \partial r + \hat{z} \partial / \partial z$ . The electrostatic component of the electric field is determined through the charge neutrality condition  $\nabla \cdot \underline{j} = 0$ , where  $\underline{j}$  is the sum of the plasma and ring currents.

For the purpose of discussion on the low frequency stability of proton rings which is considered in the next section, I discuss a couple of limiting cases of the proton-ring equilibria.

### Long Layer

For an equilibrium distribution  $\exp[-(H - \Omega P_{\theta})/T]$ , where  $H$  and  $P_{\theta}$  are the particle Hamiltonian and canonical momentum, respectively. Marx<sup>15</sup> obtained the following equilibria for an infinitely long layer  $\partial/\partial z = \partial/\partial \theta = 0$  following techniques originally developed by Pfirsch.<sup>16</sup>

$$n(r) = n_0 \operatorname{sech}^2[(r^2 - r_0^2)/2\delta_0^2]$$

$$j_{\theta}(r) = n e r \Omega$$

$$(e/mc)B_z(r) = \Omega\{1 + 2(T/m\delta_0^2\Omega^2)\tanh[(r^2 - r_0^2)/2\delta_0^2]\}$$

$$(eB_o/mc) = \Omega + (2T/m)^{1/2}(\omega_o/c)$$

$$\delta_o^2 = (c/\omega_o)(2T/m)/\Omega ; \omega_o^2 = 4\pi m_o e^2/m$$

and  $\zeta = \delta B/B_o = [1 + \tanh[(r_o \omega_o/c)(E/T)^{1/2}]/[1 + (c/r_o \omega_o)(E/T)^{1/2}]$  ,  
 where  $E = \frac{1}{2} m r_o^2 \Omega^2$  .

### Bicycle-Tire Equilibrium

Ott and Sudan<sup>17</sup> obtained an equilibrium for a toroidal self-pinch with large inverse aspect ratio  $R/r$  where the equilibrium major radius is larger than the Larmor radius because of diamagnetic effects by the factor

$$R/R_L = 1 + (N e^2/mc^2 R) \ln(8R/r) .$$

For a Bennet pinch of circular cross-section with the same type of distribution as the long layer, the density and self-magnetic field vary in the usual manner,

$$n(\rho) \propto (1 + \rho^2)^2$$

$$B(\rho) = \sqrt{2} (1 + \rho^2)^{-1} ,$$

where  $\rho$  is the normalized radial distance from the pinch axis.



## LOW FREQUENCY STABILITY

Lovelace<sup>18</sup> has considered the low-frequency magnetohydrodynamic stability of high current, high energy density ion rings (bicycle-tire configuration) embedded in a dense plasma. In this analysis based on the dynamical equations for the plasma and the ions, the toroidal beam is approximated by a straight model and subject to rigid body displacements in directions transverse to the mean momentum. A sufficient condition for stability against kink modes with displacement  $\sim \exp i(m\phi + n\theta)$ ,  $m \neq \pm 1$ ,  $n \neq 0$  excluding the  $n=1$  precession mode is

$$\beta_e \equiv 4\pi m n v_o^2 / B_o^2 < 2/g^2$$

where  $g$  is a numerical factor of order unity. For  $\zeta \sim 1$ ,  $\beta_e \geq (2/\pi g)(R/a)^2$ .

In collaboration with Rosenbluth<sup>19</sup> I have examined the same problem from the viewpoint of a generalized "Energy Principle". The system composed of the plasma and ion ring with distribution  $f$  has constants of motion which are combined to form

$$C = \epsilon - \Omega L_z + \int d^3x \, d^3v \, G(f) ,$$

where the total energy,

$$\epsilon = \int d^3x \left\{ \frac{1}{2} n m u^2 + \frac{P}{\gamma-1} + \frac{|E|^2 + |B|^2}{8\pi} + \frac{1}{2} \int d^3v \, m v^2 f \right\} ,$$

is composed of the plasma kinetic energy, pressure energy, electromagnetic energy and the ring kinetic energy, respectively. The  $z$ -component of the total angular momentum is

$$L_z = \int d^3x \, \hat{z} \cdot \left\{ n m \underline{r} \times \underline{u} + \underline{r} \times \frac{(\underline{E} \times \underline{B})}{4\pi c} + m \int d^3v \, \underline{r} \times \underline{v} f \right\} ,$$

and the quantity  $\int d^3x \, d^3v \, G(f)$  is a constant of motion by virtue of Liouville's

theorem. In what follows we limit our discussion to a pressureless cold plasma. The motion of the plasma is governed by the continuity equations for both electrons and ions, the ion momentum equation

$$n_i m \frac{d\mathbf{u}}{dt} = n_i e (\mathbf{E} + \mathbf{u} \times \mathbf{B})$$

the electron force balance,

$$\mathbf{E} + \mathbf{u}_e \times \mathbf{B} = 0$$

flux conservation,

$$\frac{\partial B}{\partial t} = \nabla \times \mathbf{u}_e \times \mathbf{B}$$

and the Vlasov equation for the ring ions. We now cause a perturbation  $\delta f$  in  $f$  which gives rise to perturbations  $\delta \mathbf{E}$  and  $\delta \mathbf{B}$  in the electric and magnetic fields. From these perturbations we compute the displacement of the electron and ion fluids  $\xi_e$  and  $\xi_i$  and compute the variation  $\delta C$  to second order in  $\xi$ . The vanishing of the first order variation arises from satisfying the correct equilibrium conditions, viz.,

$$\mathbf{u}_e = \mathbf{u} = \mathbf{E} = 0$$

$$-r\mathbf{B} = \hat{\theta} \times \nabla r A_\theta$$

$$n_e = n_b + n_i \quad (\text{charge neutrality})$$

$$\mathbf{J} \times \mathbf{B} = T \nabla n_b - n_b m r \Omega^2 \hat{r} \quad (\text{beam force balance})$$

with  $f_0 \sim \exp - (H - \Omega P_\theta)/T$  and  $J = n_b e r \Omega \hat{\theta}$ . The first order displacements

are obtained from  $\delta \mathbf{B} = \nabla \times \delta \mathbf{A}$

$$\delta \mathbf{A} = \xi_e \times \mathbf{B} = \xi_i \times \mathbf{B} - \frac{m_i c}{e} \frac{\partial \xi_i}{\partial t}$$

and the density perturbations are given by

$$\delta n_e = -\nabla \cdot n_e \xi_e \quad \text{and} \quad \delta n_i = -\nabla \cdot n_i \xi_i.$$

We now assume that  $\xi_{\perp} \equiv (\underline{\xi} \cdot \underline{B})/B$  so adjusts itself as to maintain charge neutrality, i.e.,

$$\delta n_b \equiv \int d^3v \delta f = \delta n_e - \delta n_i.$$

Following Newcomb's<sup>20</sup> techniques and a considerable amount of algebra we finally arrive at

$$\delta C = \delta W_{\text{MHD}} + \delta W_c + \delta W_b > 0$$

as a sufficient condition for stability, neglecting diamagnetic terms of  $O(\omega/\omega_c)$ , where  $\omega_c$  is the ion cyclotron frequency;

$$\delta W_{\text{MHD}} = \frac{1}{2} \int d^3x \left\{ \frac{(\delta B)^2}{4\pi} - \underline{\xi}_{\perp} \cdot \underline{J} \times \underline{\delta B} + \underline{\xi}_{\perp} \cdot \underline{J} \times \underline{B} \nabla \cdot \underline{\xi}_{\perp} \right\}$$

$$\delta W_c = \frac{1}{2} \int d^3x \underline{\xi}_{\perp} \cdot \underline{J} \times \underline{B} \left( \frac{mr\Omega^2}{T} \right) (\underline{\xi}_{\perp} \cdot \hat{r})$$

$$\delta W_b = \frac{e^2}{2T} \int d^3x \int d^3v f_0 |g|^2$$

$$g \equiv i(1\Omega - \omega) \int_{-\infty}^t dt' \underline{\xi}(t') \cdot \underline{v}(t') \times \underline{B}(t'),$$

where  $\underline{\xi} = \tilde{\underline{\xi}}(r, z) \exp i(1\theta - \omega t)$  and the integral in  $g$  is an orbit integral.

The term  $\delta W_{\text{MHD}}$  is the conventional  $\delta W$  as if the ring current  $\underline{J}$  was carried by inertialess particles, the term  $\delta W_c$  is the destabilizing term that arises from the centrifugal force in the ring and  $\delta W_b$  is a positive definite term that emerges from the particle dynamics and corresponds in some sense to the  $P(\nabla \cdot \underline{\xi})^2$  of the conventional MHD energy principle.

The application of this generalized "energy principle" to the stability of the two limiting equilibria discussed earlier is under study. Treating the long layer ( $\partial/\partial z = 0$ ) for  $\ell = 0$  one recovers the usual tearing mode; for  $\ell = 1$ ,  $\nabla \cdot \underline{\xi} = 0$ , the destabilizing term  $\delta w_c$  and the stabilizing term cancel each other exactly and stability is ensured by  $\delta w_{\text{MHD}} = \int \frac{d^3x}{4\pi} k^2 B^2 |\xi_r|^2$ , where  $k$  is the mode number in the  $z$  direction. For  $\ell > 2$  the layer is apparently stable to all modes. A similar exhaustive survey of modes for the bicycle-tire equilibrium is not yet complete.

### High Frequency Stability

For frequencies above the ion cyclotron frequency and wavelengths smaller than the ion Larmor radius, the cylindrical geometry of the system should play a less important role and the infinite medium analysis may have some relevance. In this limit the modified two-stream instability discussed at length by Ott,<sup>21</sup> et al. may appear if the threshold conditions with respect to beam temperature etc. are met. However, the net effect of this instability is to heat the plasma electrons at the expense of the ion energy. Stability against this fast growing mode is achieved if the beam has a temperature  $(T/mv_0^2) > (n_b/n)^{2/3}$ , where  $n_b$  and  $n$  are the beam and plasma densities, respectively, and  $v_0$  is the directed beam velocity.

## CONCLUSION

In view of the above discussion I feel that we are now in a position to test experimentally the feasibility of producing ion rings with a significant field reversal factor  $\xi \sim 10\%$ . To this end the Cornell Ion-Beam group plans to use the Neptune C+ machine (500 kV, 250 kA, 50 nsec) as a source of protons for injection experiments in the very near future.

## Acknowledgements

I am indebted to Drs. R. Ferch, S. Humphries, C. Kapatnakos, R. V. Lovelace, E. Ott and M. N. Rosenbluth for many discussions on the various facets of this subject.

## REFERENCES

1. S. Humphries, J. J. Lee and R. N. Sudan, Appl. Phys. Lett. 25, 20 (1974); S. Humphries, J. J. Lee and R. N. Sudan, J. Appl. Phys. 46, 187 (1975); S. Humphries, R. N. Sudan and W. C. Condit, Appl. Phys. Lett. 26, 667 (1975) and P. Dreike, C. Eichenberger, S. Humphries and R. N. Sudan, LPS Report No. 172, Laboratory of Plasma Studies, Cornell University, Ithaca, N.Y. July 1975 (to appear in Appl. Phys. Lett. (1975)).
2. M. J. Clauser, Phys. Rev. Lett. 34, 570 (1975).
3. E. Ott (private communication).
4. A. Ali, NRL Memo Report, 3060, Naval Research Laboratory, Washington, D. C.
5. R. N. Sudan and E. Ott, Phys. Rev. Lett. 33, 355 (1974); H. H. Fleischmann and T. Kammash, Nucl. Fusion (to be published).
6. J. Dawson, et. al. Proc. Fourth Intl. Conf. on Plasma Phys. and Controlled Thermonuclear Fusion Res., Madison, Wisc. (IAEA, Vienna, 1971) Vol. I, p. 673.
7. G. I. Budker, Proc. VI European Conf. of Plasma Phys. and Controlled Fusion, Moscow, Aug. 1973, Vol. II.
8. N. C. Christofilis and T. K. Fowler, Phys. Fluids, 16, 715 (1971).
9. R. E. Hester, et al. Phys. Fluids 18, 96 (1975).
10. H. Berk and L. D. Pearlstein, Phys. Fluids 15, 2396 (1972).



11. M. L. Andrews, et al. Phys. Rev. Lett. 27, 1428 (1971); M. L. Andrews, et al. Proc. Fourth Intl. Conf. on Plasma Phys. and Controlled Thermonuclear Fusion, Madison, Wisc., (IAEA, Vienna, 1971) Vol. I, p. 169.
12. S. Humphries, LPS Report No. 156, Laboratory of Plasma Studies, Cornell University, Ithaca, N.Y. (1974) (to be published in Plasma Physics).
13. R. V. Lovelace, T. Fessenden, R. N. Sudan and H. H. Fleischmann, Phys. Fluids 17, 2081 (1974).
14. A. Friedman, A. Drobot, R. L. Ferch and R. N. Sudan, Bull. Am. Phys. Soc. Ser. II, 20, 1331 (October 1975).
15. K. D. Marx, Phys. Fluids 11, 357 (1968).
16. D. Pfirsch, Z. Naturforsch 17a, 861 (1962); see R. C. Davidson, Theory of Non-neutral Plasmas, W. A. Benjamin, Reading, Mass. (1974) p. 123.
17. E. Ott and R. N. Sudan, Phys. Fluids 14, 1226 (1971).
18. R. V. Lovelace, Phys. Rev. Lett. 35, 162 (1975).
19. Manuscript in preparation.
20. A discussion of this method is given by T. K. Fowler in "Advances in Plasma Physics", A. Simon and W. B. Thompson, Editors (Interscience, New York, 1968) Vol. 1, p. 201.
21. E. Ott, J. McBride, J. Orens and J. Boris, Phys. Rev. Lett. 28, 88 (1972); J. McBride, E. Ott, J. Boris and J. Orens, Phys. Fluids 15, 2367 (1972).

TABLE I

← Reflex Triode →

Machine	100 KV Marx (1)	500 KV 7 $\Omega$ Blumlein (2)	150 KV Blumlein (2)	5 MW CREB (3)	Mag. Ins. Coax. (4)
Ion Energy	~ 100 keV	300 keV	130 keV	3 MeV	$\lesssim$ 200 kV
Ion Current	2 X 250 A	2 X 2050 A	2 X 3,300 A	~ 5 kA	4 kA
Current Density	~ 10A/cm <sup>2</sup>	8.3A/cm <sup>2</sup>	20A/cm <sup>2</sup>	> 30A/cm <sup>2</sup>	> 50A/cm <sup>2</sup>
Efficiency		9%	42%	< 20%	~100%
$\tau$ (nsec)	~50	~ 50	~ 50	130	50
Type of Ion	p	p	p	Al <sup>++</sup>	p

- (1) S. Humphries, J. J. Lee and R. N. Sudan, Appl. Phys. Lett. 25, 20 (1974).  
 (2) S. Humphries, J. J. Lee and R. N. Sudan, J. Appl. Phys. 46, 187 (1975).  
 (3) S. Humphries, R. N. Sudan and W. Condit, Appl. Phys. Lett. 26, 667 (1975).  
 (4) P. Dreike, C. Eichenberger, S. Humphries and R. N. Sudan, LPS #172 (July 1975).

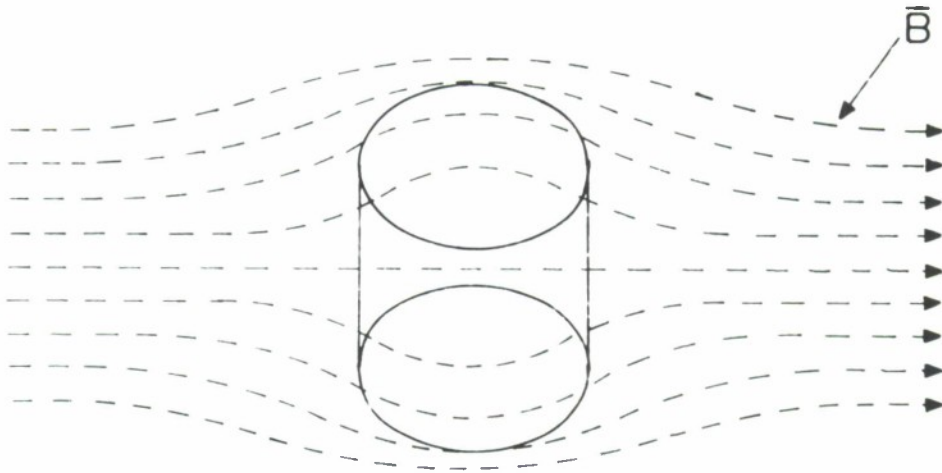


Figure 1. Ion ring with open lines of force

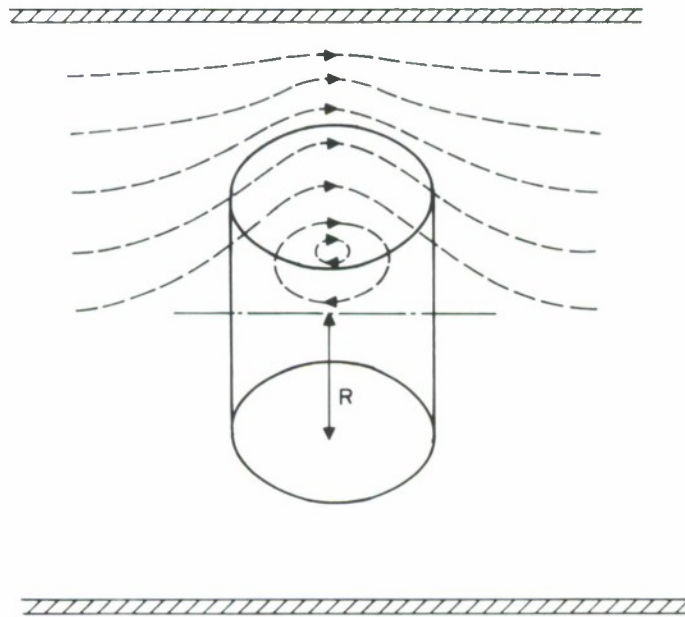


Figure 2. Ion ring with closed lines of force

# ION BEAM GENERATION AND FOCUSING\*

by

P. A. Miller, C. W. Mendel, D. W. Swain and S. A. Goldstein

Sandia Laboratories, Albuquerque, New Mexico 87115

## ABSTRACT

Calculations have shown that efficiently generated and focused ion beams could have significant advantages over electron beams in achieving ignition of inertially-confined thermonuclear fuel. Efficient ion beam generation implies use of a good ion source and suppression of net electron current. Net electron flow can be reduced by allowing electrons to reflex through a highly transparent anode or by use of transverse magnetic fields (either beam self-fields or externally applied fields). Geometric focusing can be achieved if the beam is generated by appropriately shaped electrodes. Experimental results are presented which demonstrate ion beam generation in both reflexing and pinched-flow diodes. Spherically shaped electrodes are used to concentrate a proton beam, and target response to proton deposition is studied.

\*This work was supported by the U.S. Energy Research and Development Administration.

## I. INTRODUCTION

An outgrowth of electron beam research has been the recent use of electron beam accelerators to generate intense pulsed ion beams. These ion beams offer several potential advantages over electron beams for achieving ignition of inertially-confined thermonuclear fuel. Target calculations indicate that breakeven may be accomplished at lower power levels with ion beams because of the reduced bremsstrahlung production and the improved energy deposition profile.<sup>1</sup> Furthermore, much lower currents (at higher voltages) may be used to achieve the required power with ions than with electrons because of the difference in ion and electron ranges. This reduced current requirement makes accelerator design considerably less difficult.<sup>2</sup> Finally, since the ions are non-relativistic, bunching in space could be used to shorten ion pulses and obtain higher peak powers at the target than at the accelerator.<sup>3,4</sup> Because of these potential advantages of ion beams for pellet fusion, studies are in progress to find means to generate efficiently and to focus intense ion beams.

In ordinary, one-dimensional, bi-polar diodes, the ion current is a factor  $\sqrt{m_e/M_i}$  lower than the electron current. This represents an ion beam generation efficiency of  $\sim 2\frac{1}{2}$  percent for protons. This may be improved upon by employing either of two basic concepts: either the overall electron flow may be reduced by transverse magnetic fields (self-generated<sup>5</sup> or externally applied<sup>6</sup>), or the net electron current may be reduced by allowing the electrons to recirculate through the diode without being collected by a "thick" anode.<sup>7,4</sup> In Sections II and III of this paper are described experiments which utilize these different concepts to obtain ion current generation efficiencies of several times  $\sqrt{m_e/M_i}$ .



Focusing of ion beams may be conceptually achieved by use of shaped electrodes. Since the ions are deflected only slightly by the transverse electric and magnetic fields in the anode-cathode gap, almost-spherically shaped electrodes seem suitable. An experiment testing this idea is presented in Section IV.

In addition, techniques for diagnosing intense ion beams are being developed. Spatially and temporally resolved bremsstrahlung measurements and passive witness plates have been the major means for diagnosing e-beam pinches. Other means must be used to study focused ion beams. In Section IV, preliminary target response measurements are reported and compared with code calculations.

## II. ION FLOW IN A PINCHED DIODE

Code calculations by Poukey<sup>5</sup> have shown that, in high power, high aspect ratio diodes which generate pinched electron beams, proton beams can be generated with high efficiency. This occurs because the transverse self-magnetic field inhibits electron flow across the anode-cathode gap. An experiment was carried out with Hydra to test certain aspects of this result. Calculations were performed for the case of a planar diode with a 10 cm diameter cathode at 400 kV using a 0.6 cm anode-cathode gap and assuming the anode to be a proton source. The calculation indicated a total current of 150 kA; 20 kA of this were protons with peak density of  $4 \text{ kA/cm}^2$  on axis, and the total proton current inside a 1.2 cm radius was 4 kA.

Experimental measurements have been made with both flat and conical<sup>8</sup> cathodes; similar results were obtained in the two cases for ion flow on axis. Sample voltage and current waveforms for the conical cathode case are shown in Fig. 1. Two different means of ion diagnostics were employed.



The first involved neutron production. An  $8 \times 10^{-3}$  cm thick, 1.2 cm radius disk of  $\text{CD}_2$  was centered on the anode to provide a source of deuterons. A target of  $\text{LiCl}$  was used on the cathode and the total neutron production was recorded by silver activation counters. The total charge indicated in the deuteron beam by the yield was 1.5 to  $3 \times 10^{-4}$  Coulomb. Using a nominal value of 60 ns for the ion pulse length (see below), the corresponding central deuteron current was 2.5 to 5 kA, in agreement with the calculation. The experimental measurement is, of course, a lower bound on ion current, since any protons from anode contaminants were not measured.

The second ion detection system used ion Faraday cups. The ion beam was intercepted by an aperture plate with a hole in it, typically with an area of  $10^{-3} \text{ cm}^2$ . Two different ion collection schemes were employed to measure the apertured beam current. The first used a grid biased 300 V negative to strip the electrons from the ion beam. The ions were then collected by a flat plate just behind the grid. The grid also served to return secondary electrons to the collector so that their flow should not have given an erroneous signal. This system was checked with the C.W. proton beam from a Pelletron accelerator at 100 kV and the indicated current was roughly half of the beam current. A change in responsivity was found as the beam voltage was varied. In light of these results, and considering the possibility of significant collective effects occurring at high currents, the Faraday cup results may be no more accurate than a factor of two. A second scheme used a deep cup biased negatively, placed right behind the aperture plate. In this case, somewhat higher signals were obtained than with the gridded collector. A typical ion current signal obtained behind the center of the cathode is shown in Fig. 1. An ion current density of roughly  $2 \text{ kA/cm}^2$  is indicated, which agrees with the code and neutron count

results. It can be seen that the ion current is delayed from the start of the main pulse. This was a general feature found in this and other work.<sup>9</sup> Apparently, energy deposition levels near 1 kJ/gm are required before the anode becomes a space charge limited source of ions.

Activation analysis is potentially useful for accurate proton current measurements. However, it is difficult to do with unattenuated beams of the type encountered here. Energy deposition levels are such that all material which would be activated would also be vaporized, necessitating debris collection for counting.

There is good agreement between the calculations and the experimental results for ion current, although the code results were found to depend significantly on the assumed anode plasma thickness (not measured). The ion current density on axis was roughly 50 times the value for simple one-dimensional flow and is thus an encouraging result.

### III. PLASMA-FILLED ION DIODE

A second means to achieve efficient ion beam generation involves using a "thin" anode and recirculating electrons. In previous work,<sup>7,10</sup> solid or mesh anodes have been used and external magnetic fields have been applied to prevent radial electron loss. These fields may be incompatible with the tight beam focusing necessary for pellet irradiation. Fig. 2 shows the schematic of an experiment performed without external magnetic fields using a plasma anode and using plasma sheaths as anode-cathode gaps. In operation, the region between the two cathodes is filled with plasma from a gun or a laser pulse on a target. Then the electrodes are pulsed to high voltage, causing sheaths to develop over the cathodes. Space charge limited

ion and electron currents flow across the sheaths, with the sheaths receding in time to provide the ion current.<sup>11</sup> The electrons oscillate between the two cathodes and, in principle, absorb almost no energy from the system. Two ion beams are thus generated efficiently, with one being available for focusing. Electrode curvature is designed so that the electrons are on stable orbits and are not quickly lost radially from the system. This is potentially an important aspect of the device since it eliminates the need for external magnetic fields in the gap.

In Fig. 3 is shown a model which can be used to analyze the system. Between the two cathodes (K and R) flows a circulating electron current  $J_C$ , with  $\delta$  being the probability of losing an electron in transit. This circulating current is replenished by a current  $J_e$ , and ion currents  $J_R$  and  $J_K$  flow to the cathodes. Sheath thicknesses are  $X(t)$  and  $Y(t)$ , and the plasma is assumed to be field free. It can be shown that for  $\delta \ll 1$ , the ratio of ion to net diode current is given by

$$\frac{J_R + J_K}{J_N} = \left[ 1 + \frac{\delta}{2\sqrt{m_e/M_i}} \right]^{-1} .$$

This is the expected result that the electrons must make of the order of  $\sqrt{M_i/m_e}$  transits to give efficient ion beam generation.

In the experiment, the total ion current was not measured directly. Instead, a relationship between voltage and current was found which allowed determination of  $\delta$ . Define  $Q_N$  as the total charge delivered to the diode by time  $t$ :

$$Q_N = \int_0^t I_N dt .$$

Also define  $Q_i$  as the charge depleted from both sheaths,  $Q_i = 2n_0 e A Y(t)$  where  $n_0$  is the plasma density,  $X = Y$  is assumed, and  $A$  is the electrode area. Assuming space charge limited flow,  $Y(t)$  can be calculated from the measured perveance. We can then define a function  $Q_O = (\delta + 2\sqrt{m_e/M_i}) \cdot Q_i$  which can be shown to be a function only of the measured perveance. It can then be shown that

$$\frac{Q_O}{Q_N} = 2\sqrt{m_e/M_i} \cdot \left[ 2\sqrt{m_e/M_i} + \delta \right]^{-\frac{3}{2}}.$$

Thus, the ratio  $Q_O/Q_N$  gives a measure of  $\delta$ .

The experiment used a Nereus accelerator operating at roughly 100 kV, 50 kA and employed 15 cm<sup>2</sup> electrodes. The plasma was generated by a laser beam hitting a thin target on one cathode. The timing was such that any hydrogen contaminants should have dissipated from the anode region prior to the beam pulse and the plasma should have been predominantly carbon and aluminum. One cathode was pulsed negative; the other was floating and observed to follow the driven cathode in voltage, as expected. Measured  $Q_O$  and  $Q_N$  values are plotted for several times and several shots in Fig. 4. Also shown are lines of constant  $Q_O/Q_N$  and lines which the data would follow if reflexing were not occurring, for different possible ions in the plasma. It can be seen that substantial improvement (roughly factor of 5) over normal ion beam generation efficiency is occurring.

The experiment apparently verifies the essential aspects of the model. Considerations of stability and magnetic field effects suggest that much larger ion diodes of this type should be feasible.



#### IV. FOCUSING ION DIODE

In a third experiment designed to study geometric focusing, a diode with electrodes shaped like sectors of spheres was employed. The experimental geometry is shown in Fig. 5. In principle, the ions from the anode plasma should cross the gap and be focused near the focal point, the focal size being determined by the accuracy of the electrode surfaces, finite cathode grid effects, and plasma effects in the gap. The ion beam should pick up neutralizing electrons as it goes through the cathode plasma. The anode, which was pulsed positive by the Hydra accelerator, consisted of copper, stainless steel, or Mylar. The cathode through which the ion beam was extracted, was made from screen wire with meshes from 5 to 25 lines per cm. The electrodes had radii of curvature of  $7\frac{1}{2}$  cm. Anode-cathode gaps from 0.7 to 1.3 cm were used. The solid anodes were generally coated with "schmaltz" proton sources to facilitate anode plasma generation.

Sample experimental data are shown in Fig. 6. In one set of measurements, a Faraday cup was used to determine ion current density as a function of position along the axis of the diode. As indicated in Fig. 6, the Mylar anode provided a good source of protons throughout most of the pulse, while the solid anodes did not until late in the pulse. The difference may be due to plasma generation by surface flashover on the Mylar. The absolute amplitude of the ion signals at the focus indicated peak current densities of 2 to 3 kA/cm<sup>2</sup>. Figure 7 shows the variation of the peak ion current density with distance from the focal point for the case of a Mylar anode. Also shown is calculated current density, assuming uniform ion current density over the cathode surface with  $I_i/I_e = \sqrt{m_e/M_i}$ . The agreement in curve shapes suggests that geometric focusing is occurring, though the agreement in amplitudes may not be significant. The peak in the data indicates a focal size of the order of 1 cm<sup>2</sup>.

At ion current densities well above a few  $\text{kA/cm}^2$ , it is expected that problems will occur in the use of Faraday cups. The development of new alternative diagnostics seems desirable. In this work, a study was made of the dynamic response of a target placed in the focal region. The rear surface of a grounded aluminum foil  $3 \times 10^{-4}$  cm thick was observed with photodiodes, a framing camera, and a streaking spectrograph. The foil was somewhat less than an ion range thick, and thus should have received nearly uniform energy deposition throughout its thickness.<sup>12</sup> For  $1 \text{ kA/cm}^2$  of 400 kV protons incident, roughly  $0.3 \text{ TW/gm}$  should have been deposited. The one-dimensional Lagrangian hydro-code CHART D<sup>13</sup> was used to study the foil response to such energy depositions. The calculated temperature and rear surface position are shown in Fig. 8. Here, rear surface means the outer zones which contained a few percent of the foil mass. Operationally, this is a reasonable definition. The temperature was fairly uniform through out the foil and the foil should have been optically thick. A 50 ns input pulse has been used.

In Fig. 6 is shown the output of an absolutely calibrated avalanche photodiode which observed the foil in the range 1 micron to  $4000 \text{ \AA}$ . Assuming the source to be a blackbody radiator, we obtain the data in Fig. 8. The area assumed was  $\frac{1}{14} \text{ cm}^2$  which was the spot size observed in framing photographs. A part of a streaked spectrum is shown in Fig. 9. On it are seen absorption lines from ground state and excited aluminum atoms, and a short wavelength cutoff of  $\sim 2500 \text{ \AA}$ , in general agreement with features expected to be seen from an expanding foil at  $\sim \frac{1}{2} \text{ eV}$ .

It was found experimentally that when an obstruction was placed a distance behind the foil, a second burst of light (somewhat longer than the first and about  $\frac{1}{14}$  its amplitude) was generated at late times. If this is



assumed to be due to the temperature and density jumps which occur when the expanding foil hits the obstruction, then the time of occurrence of the light burst gives a rear surface velocity indication. In Fig. 8 are shown rear surface positions measured in this fashion. It should be noted that, since the foil was a bit less than a range thick, the obstruction was also irradiated with protons, and thus may have been expanding in time somewhat. This effect would give an erroneously fast velocity.

Several points of disagreement are evident between the code and experimental results. The observed rear surface velocity is indicative of higher energy deposition than is the radiation output, and the radiation output does not decay as quickly as anticipated. Framing photographs of the foil showed, at times, a diffuse light coming from areas of the foil away from the focus. The structure of the diffuse light varied in time and from shot to shot. This suggests that the single temperature model for the radiation may be bad, as may be the one-dimensional expansion approximation. From all this we conclude that this diagnostic method shows promise insofar as it indicates energy deposition levels of the same magnitude as indicated by the Faraday cups. However, it needs further study before it can be relied upon.

## CONCLUSION

Experiments have been described which test concepts for efficient ion beam generation and focusing for the purpose of pellet compression. Agreement with theory for reflexing and pinched diode behavior is satisfactory at present. In planar pinched-flow diodes, ion current densities 50 times the normal one-dimensional flow values have been achieved. Efficiencies of ten percent or more have been attained in pinched and reflexing diodes.

Focusing and target response studies have shown results in general as anticipated, with many questions yet to be answered. Focusing has been used to obtain ion current densities roughly 20 times the density at the cathode. Clearly, experiments at much higher powers are needed to see whether or not present results scale as favorably as theory predicts.

# REFERENCES

1. M. J. Clauser, Phys. Rev. Lett. 35, 848 (1975); M. J. Clauser and M. A. Sweeney, paper in session I of this conference.
2. T. H. Martin, private communication.
3. F. Winterberg, Nature 251, 44 (1974); Annals N.Y. Acad. Sci. 251 679 (1975).
4. J. T. Verdeyen, D. A. Swanson, B. E. Cherrington, and W. L. Johnson, Appl. Phys. Lett. 27, 380 (1975).
5. J. W. Poukey, Appl. Phys. Lett. 26, 145 (1975); 13th Symposium on Electron, Ion, and Photon Beam Technology, Colorado Springs, Colorado, May (1975); also see paper in Session II of this conference.
6. R. N. Sudan and R. V. Lovelace, Phys. Rev. Lett. 31, 1174 (1973).
7. S. Humphries, Jr., R. N. Sudan, and W. C. Condit, Jr., Appl. Phys. Lett. 26, 667 (1975).
8. A. E. Blaugrund and G. Cooperstein, Phys. Rev. Lett. 34, 461 (1975).
9. D. W. Swain, S. A. Goldstein, J. G. Kelly, G. R. Hadley, J. Appl. Phys. 46 (to be published).
10. J. M. Creedon, I. D. Smith, and D. S. Prono, Phys. Rev. Lett. 35, 91 (1975).
11. P. A. Miller, J. W. Poukey, and T. P. Wright, Phys. Rev. Lett. 35, 940 (1975).
12. Handbuch der Physik, ed. by S. Flugge, Vol. 24 (1958).
13. S. L. Thomson, Sandia Laboratories Report SIA-73-0477 (1973).

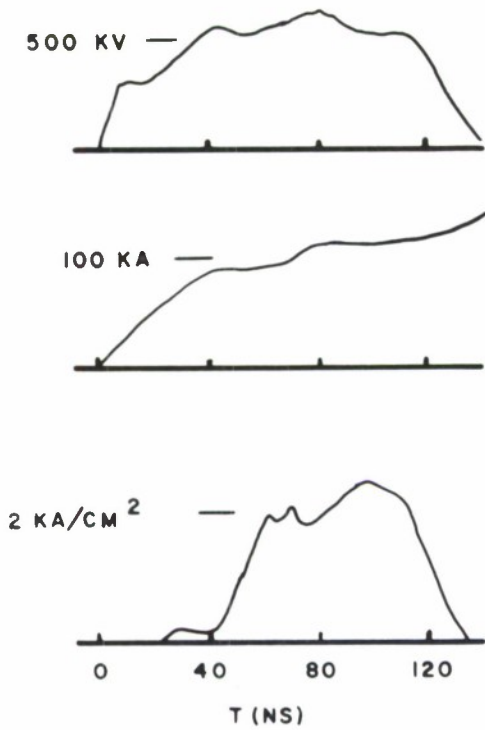


Figure 1. Inductively corrected diode voltage, diode current, and Faraday cup waveform.

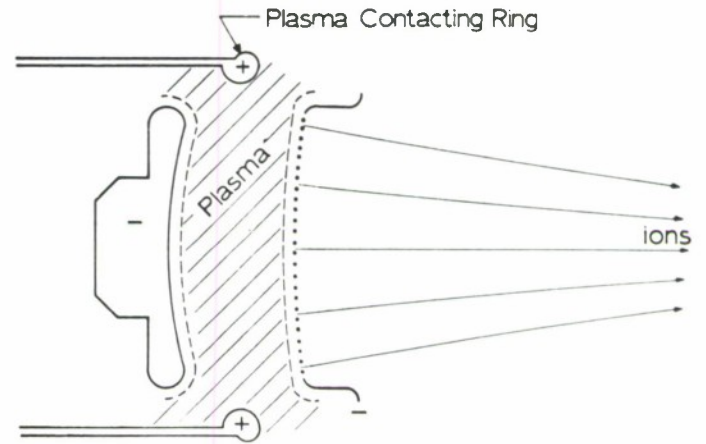


Figure 2. Schematic of plasma-filled ion diode.

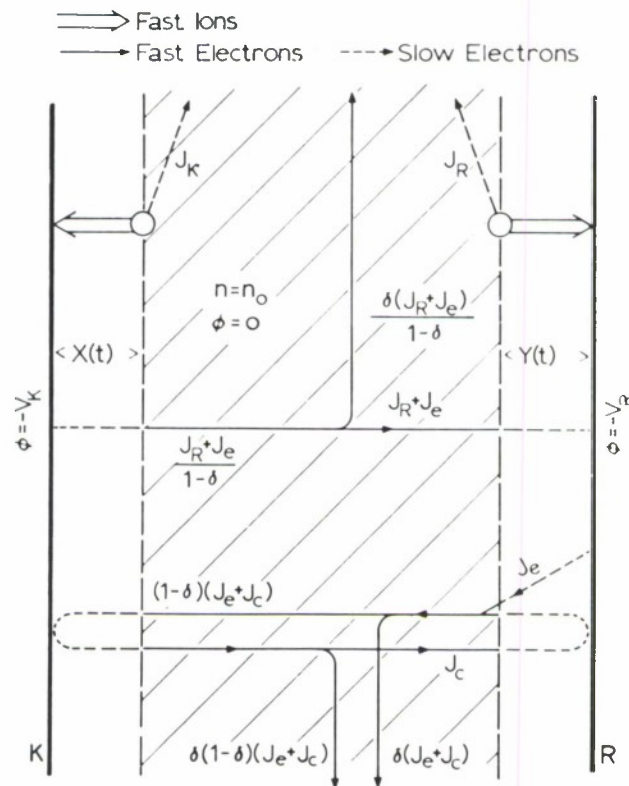


Figure 3. Basic model for the diode calculations.

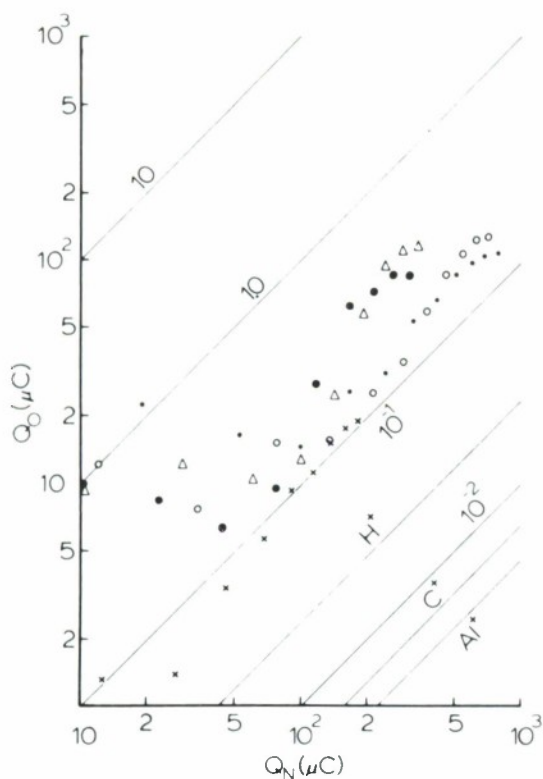


Figure 4. Data from 4 shots indicating  $Q_O/Q_N \approx 0.2$ .

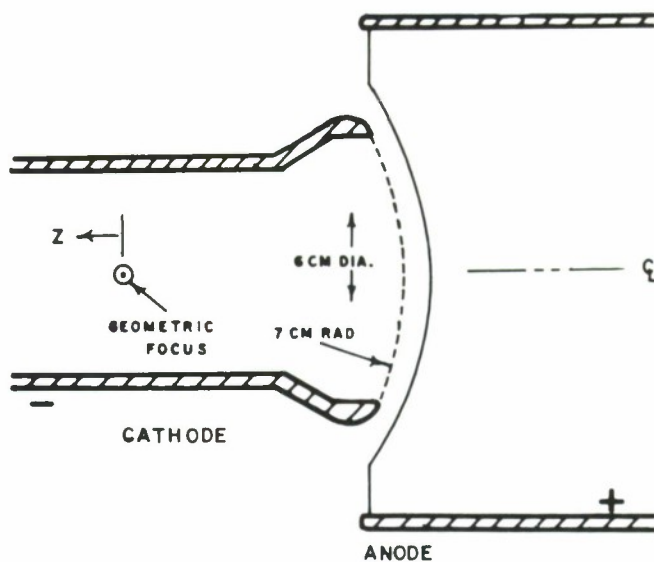


Figure 5. Schematic of focusing ion diode.

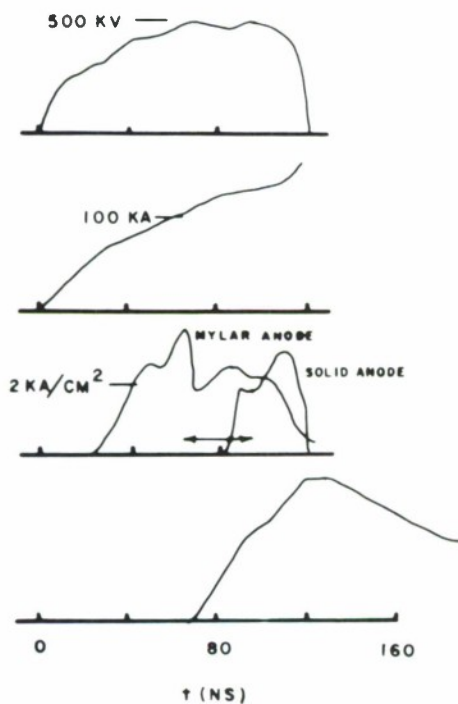


Figure 6. Sample waveforms: inductively corrected diode voltage, current, Faraday cup signals for different anodes, and photodiode output.

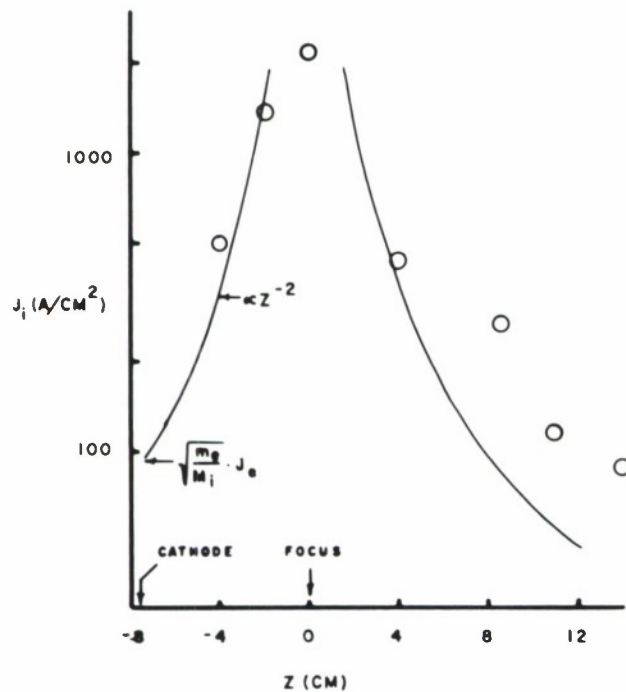
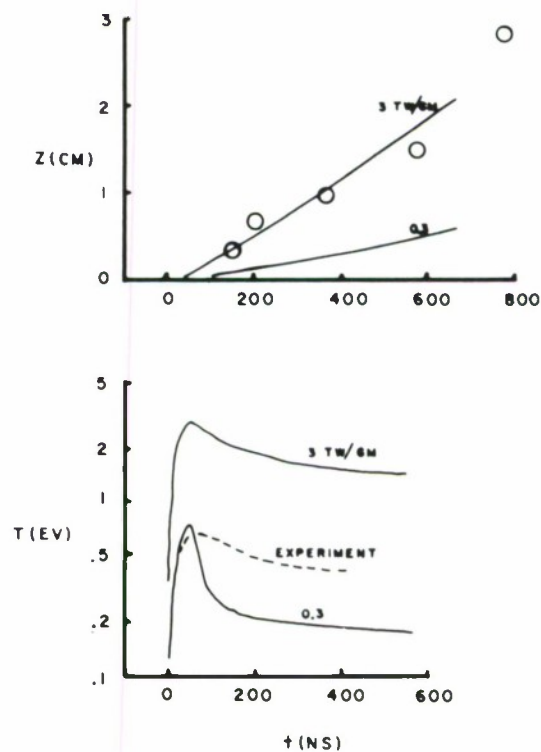


Figure 7. Measured ion current density as a function of axial position.

Figure 8. Calculated rear surface position and foil temperature vs time for two energy inputs (solid lines); and sample measured values of rear surface position and radiation temperature.





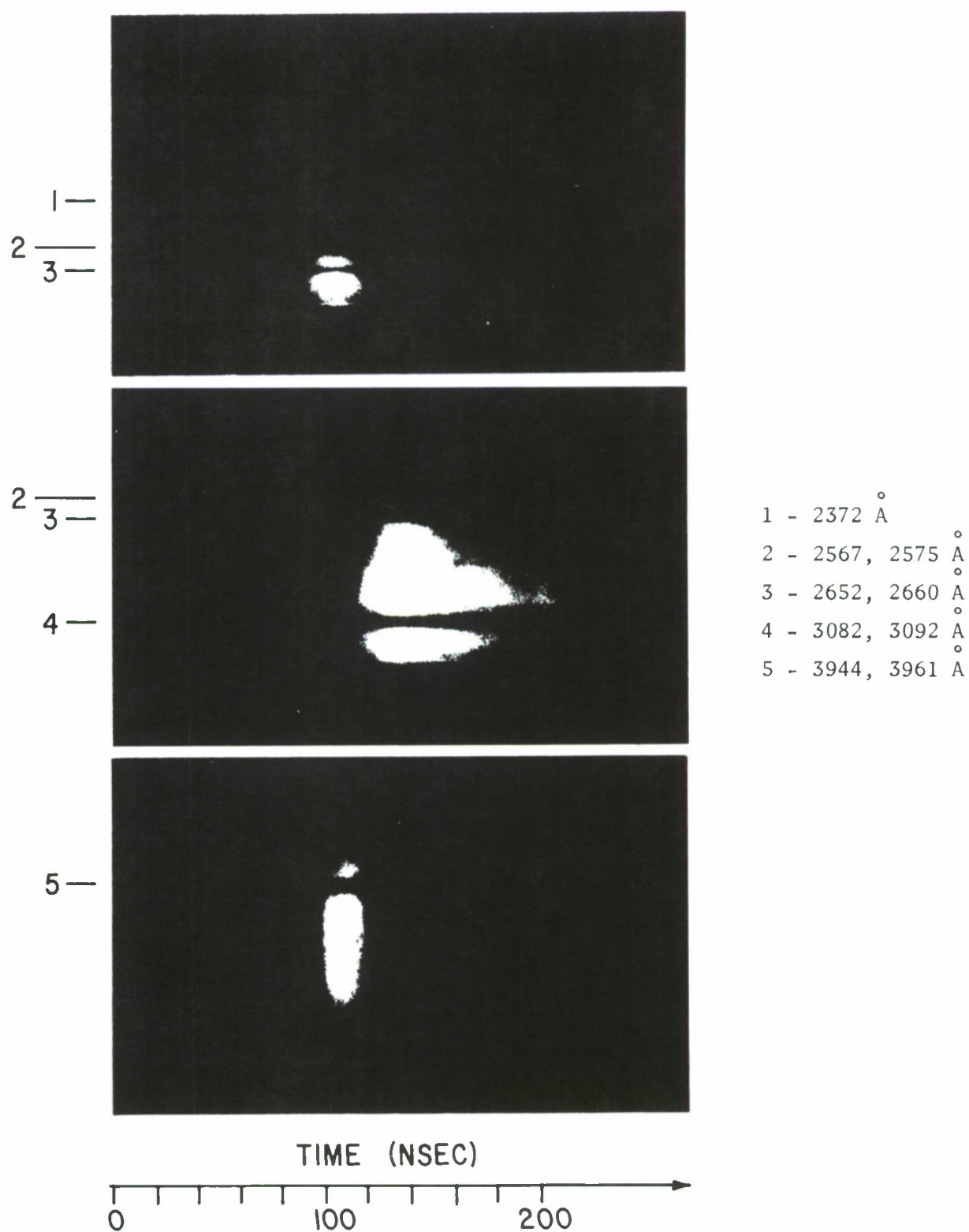


Figure 9. Composite of streaked spectra showing the following absorption lines from neutral aluminum:

## STUDIES OF A REFLEX TRIODE

J. Golden\*, C.A. Kapetanacos and Roswell Lee  
Naval Research Laboratory, Washington, D.C. 20375

and

Shyke A. Goldsteint  
University of Maryland, College Park, MD 29742

### ABSTRACT

The ion current of a reflex-triode has been studied as a function of the anode thickness, when a 400 kV positive pulse is applied to such an anode. The 11.4-cm-OD anode consists of solid polyethylene (or polycarbonate) film of thickness,  $\delta$ , between 2 and 150  $\mu\text{m}$  interwoven between 0.7 mm diameter meter wires spaced 0.7 cm apart. It is observed that the ion current increases with decreasing thickness for  $12 < \delta < 120 \mu\text{m}$  and remains practically constant for thinner films. Contrary to the predictions of a recent theoretical model, the ion current does not exhibit resonance-like behavior. For  $\delta \leq 25 \mu\text{m}$ , the results are in agreement with a macroscopic model, which predicts that the ratio of the ion current to the cathode current is given by  $0.5 [1 + (2\eta + 1)^{-1} (m_i/m_e)^{1/2}]^{-1}$ , where  $\eta$  is the average number of passes of a typical electron through the anode. The above theoretical estimates are based on time averages of space charge limited flows. Refinements of the theory are included in a new, one-dimensional, multi-species, particle simulation code.

## I. INTRODUCTION

The wide range of potential application of intense, pulsed ion beams has recently motivated experimental<sup>1,2</sup> and theoretical<sup>3-7</sup> work on their production and propagation.

Among the various schemes proposed so far for the production of ion beams, the reflex triode appears to have attracted most of the experimental efforts. This device consists of a positively biased, semi-transparent anode and a grounded cathode. Electrons emitted from the cathode are accelerated toward the anode. In general, most of the electrons reaching the anode pass through it and travel up the potential hill, where they form a virtual cathode. As the electrons oscillate between the real and virtual cathodes, they create plasma from the plastic film or plastic filaments mounted on the anode. The ions are drawn from the anode plasma and are accelerated by the positive anode potential toward the real and virtual cathodes.

The reduction in the axial velocity of the oscillating electrons because of elastic and inelastic scattering on a solid plastic anode can cause concentration of electrons close to the anode and this drastically influences the space charge distribution in the anode-cathode gap, as well as the ion current density. It is expected, therefore, that the ion current depends on the thickness of the plastic film anode.

In this paper, we report results from studies of the total number of protons in the beam (and thus the proton current) as a function of

the anode thickness, when a  $\sim 400$ -keV, 50-nsec-duration positive pulse is applied to the anode of a reflex triode. It is observed that the number of accelerated protons increases initially as the anode thickness decreases from 150 to about 12  $\mu\text{m}$ , but remains practically constant for thinner films.

In a recent theoretical work Creedon et al<sup>3</sup> have studied in detail the effect of elastic and inelastic scattering of electrons by a solid anode on the ion current density. The general trend of the ion current density as a function of anode thickness predicted by ~~their~~ model appears to be in agreement with the experimental results. However, the prophesied resonance-like behavior in the ion current density, when the number of transits of a typical oscillating electron through the anode approaches a critical value, is not borne out of the experimental results.

In addition to experimental results, the paper contains an analytic estimate for the ratio of ion to cathode current and results from a one-dimensional, multi-species, particle simulation code.

## II. DESCRIPTION OF THE EXPERIMENT

A schematic of the experiment is shown in Figure 1a. Electrons emitted from the 11.4-cm OD, 1.9-cm-thick annular carbon cathode are accelerated by the 50-nsec-duration positive voltage pulse that is applied to the anode, pass through it and form a virtual cathode. The anode is constructed from solid polyethylene (or polycarbonate) film of thickness between 2 to 150  $\mu\text{m}$  interwoven between 0.7-mm-diameter metal wires spaced 0.7 cm apart as it is shown in Figure 1b. Such an arrangement has the advantage that the symmetry of the anode is preserved. The protons are extracted out of the plasma formed from the plastic by the oscillating electrons. The protons that are accelerated toward the virtual cathode pass through it and enter the drift region. Both the triode and the drift region are immersed in a uniform magnetic field ( $B_0$ ), which can be varied from 0 to 23 kG. If not otherwise specified, the results reported here were taken at  $B_0 \approx 6$  kG. The 14.4-cm-ID vacuum chamber has been constructed of 1.5 mm thick 304 stainless steel and is magnetically transparent to the 13 msec rise time magnetic field. All the results reported here were taken at a pressure below 0.4 m Torr.

The anode voltage is measured using a capacitive voltage divider, which is located on the water side of the diode insulator. The anode current is monitored with a 15-m  $\Omega$  current shunt and the cathode current with a small pickup loop that is located on the surface of the cathode stalk. When the anode-cathode gap is short-circuited, the shapes of

waveforms from the two current monitors are identical. Such shots are used to calibrate the pickup loop according to the current shunt.

Several diagnostic tools (calorimetry, biased Faraday cups, magnetically shielded Rogowski coils, scintillators and so on) are used to determine the number of protons in the beam. However, it was found that the only reliable diagnostic is the nuclear activation technique. This technique not only gives information about the total number of protons in the beam, but also allows an unambiguous identification of protons. Briefly, this activation technique consists of measuring the radioactivity induced on a 3-mm-thick boron nitride (BN) target by the drifting protons. The number of protons is inferred from the measured number of  $\gamma$ -rays associated with the annihilation of positrons ( $\beta^+$ ), which are produced from the decay of  $^{15}\text{O}$ . This oxygen is generated by the resonant reaction  $^{14}\text{N} (p, \gamma) ^{15}\text{O}$  that has a threshold of about 270 keV. After bombardment, the activated target is quickly removed from the vacuum system and placed between two 12.5-cm-diameter NaI crystals that are facing each other and separated by 2.5 cm. In the coincidence counting the only  $\gamma$ -rays recorded are those with energy between 0.45–0.55 MeV.



### III. EXPERIMENTAL RESULTS

Figure 2 gives the number of protons in the beam (measured by the activation technique) as a function of the anode thickness,  $\delta$ . Each point in the figure is the average over several shots. The ratio,  $R$ , of the number of protons observed for  $\delta < 12 \mu\text{m}$  to the number of protons measured for  $\delta > 120 \mu\text{m}$  is about 10. In reality,  $R$  is less than 10, because it is observed that the voltage on the anode remains relatively flat for most of the pulse duration when  $\delta < 25 \mu\text{m}$ , but drops relatively fast for the thicker anodes.

For the triangular shaped, 50 nsec duration proton pulse, the peak ion current can be computed from  $i_p = 6.4 \times 10^{-12} N$ , where  $N$  is the measured number of protons. The peak of the curve ( $\sim 7.5 \times 10^{14}$  protons) corresponds to a current of about 4.5 kA and to an ion current density of  $\sim 85 \text{ A/cm}^2$ . For a simple diode (electron only) at anode voltage  $V_0 = 400 \text{ kV}$  and anode-cathode separation  $d = 1.35 \times 10^{-2} \text{ m}$ , the Child-Langmuir current density  $J_0$  is computed to be about  $3.22 \times 10^2 \text{ A/cm}^2$ . The ion current density in a bipolar flow is given by  $J_i = 1.86 J_0 \left(\frac{\gamma+1}{2}\right)^{1/2} (M_e/M_i)^{1/2}$ , where  $\gamma$  is the relativistic factor. For protons, this equation gives  $J_i = 17 \text{ A/cm}^2$ , which is by a factor of 5 lower than that observed experimentally. Corrections to  $J_0$  associated with the circumferential edges of the hollow cathode and plasma motion can account only for a fraction of this difference.

Time delay of plasma production cannot account for the different number of protons observed at various anode thicknesses. Spectroscopic observations have established that the anode plasma is always produced within

15 to 25 nsec after the initiation of the voltage pulse for all thicknesses tested. In addition, extrapolation of time-of-flight data at 10 cm and 50 cm from the anode indicate beam production prior to 20 ns after the initiation of the voltage pulse.

In order to determine the number of transits performed by a typical oscillating electron as a function of anode thickness, a calculation has been performed assuming that the oscillating electrons undergo: (a) elastic scattering, (b) inelastic scattering, and (c) stopping collisions with the wires that support the plastic film.

The elastic scattering produces an increase in the transverse energy at the expense of the axial energy. The root-mean-square angle of scatter (with respect to the normal) is given by the Fermi<sup>8</sup> formula, i.e.,

$$\sqrt{\langle \Delta \theta^2 \rangle} = \left( \frac{8\pi n_0 \ell R_0^2}{\beta^4 \gamma^3} D(Z^2 + Z) \ln \frac{a_0 \gamma \beta^2}{2Z^{4/3} R_0} \right)^{1/2},$$

where  $Z$  is the atomic number,  $n_0$  is the density of the material,  $R_0$  is the classical electron radius,  $a_0$  is the Bohr radius,  $D$  is the number of atoms per molecule, and  $\ell$  is the thickness of material traversed.

After  $\eta$  transits the mean angle of an electron velocity vector to the normal to the anode is  $\sqrt{\langle \theta^2 \rangle_\eta}$ , where

$$\langle \theta^2 \rangle_\eta = \sum_{\eta} \langle \Delta \theta^2 \rangle.$$

The inelastic loss is obtained using a piecewise interpolation of the data of M. J. Berger and S. M. Seltzer<sup>9</sup> for the range as a function

of energy. As an electron crosses the anode for the  $\eta$ -time, its range is reduced by  $\ell_\eta = \delta / \cos \sqrt{\langle \theta^2 \rangle_\eta}$ . The new range is  $R_\eta = R_{\eta-1} - \ell_\eta$ , where  $R_{\eta-1}$  is the range corresponding to the remaining energy of the electron after its  $\eta-1$  crossing of the anode. The remaining energy is computed from the tables<sup>9</sup> using  $R_\eta$ .

For electrons with energies of 400 keV, the elastic scattering appears to be more important than inelastic. This is illustrated in Fig. 3 which shows the reduction in the energy associated with the axial velocity of an electron as a function of anode thickness,  $\delta$ .

The number of transits  $\eta$ , required for the axial energy to become zero or for  $\sqrt{\langle \theta^2 \rangle_\eta}$  to reach  $90^\circ$  are shown in Fig. 4. These results, are given approximately by the empirical relation  $\eta \sim 24.05/\delta^{0.97}$ . In addition, it was found at the time when the electrons are stopped as a result of the elastic scattering, the energy loss due to inelastic scattering is less than two-thirds of the initial energy provided that  $\delta \leq 175 \mu\text{m}$ .

The oscillating electrons are also reduced because they suffer collisions with the wires supporting the plastic film. On a given pass, there is a chance that an electron collides with a wire. In the case without an applied magnetic field, the probability for collision is the ratio of the wire diameter,  $d_1$ , to the spacing  $d_2$ , i.e.,  $d_1/d_2$ . The average number of transits is the inverse of it, i.e.,  $d_2/d_1$ . In the presence of an applied magnetic field, the loss rate is modified because only electrons whose guiding centers pass within a gyro-radius of a wire have a chance to collide with it. Scattering at the anode allows a random

walk so that eventually any given electron might get close enough to strike a wire. Under the present experimental conditions  $d_1 \sim 0.7$  mm,  $d_2 \sim 7$  mm, and  $B_0 \geq 6$  kG, the electron gyro-radius,  $a$ , is less than or comparable to  $d_1$ . Therefore, if an electron guiding center is within a gyroradius of the wire, the chance for collision with it is nearly unity. The average number of transits necessary for an electron to random walk to a wire is

$$\eta = \frac{1}{d_2 - 2a} \int_0^{d_2 - 2a} \left( \frac{x_0}{a} \right)^2 dx_0 = \frac{1}{3} \frac{(d_2 - 2a)^2}{a^2},$$

where  $x_0$  is the initial distance of closest approach of the guiding center to the wire and the average step size is  $a$ . If  $a \leq d_1$  then  $\eta \geq \frac{1}{3} \left( \frac{d_2 - 2d_1}{d_1} \right)^2 \approx 21$ . In the case of 400-keV electrons, the number of transits for anode thicknesses less than 20  $\mu$ m should be limited by collisions of electrons with the anode wires.

This conclusion is supported by the observation that the ion current increases by about 20-30%, when the spacing of the wires in the anode increased from 7 to 15 mm and  $B_0$  to 11.5 kG. The maximum ion current density obtained under these conditions is in excess of 100 A/cm<sup>2</sup>.

The various currents flowing in a reflex triode are shown pictorially in Fig. 5 and are identified in Table I. Both the cathode current ( $I_c$ ) and the current flowing in the anode and measured by the shunt resistor ( $I_{sh}$ ), are proportional to the electron current absorbed by the anode ( $I_e^a$ ). The measured peak cathode current as a function

of anode thickness is shown in Fig. 6. It is observed that this peak cathode current increases linearly with  $\delta$  up to  $\delta \approx 75 \mu\text{m}$ , but remains constant for thicker anodes. The  $I_c^{\text{peak}}$  is probably associated with the relatively rapid drop of the voltage pulse observed with the thicker anodes.

Anode and cathode current waveforms for various anode thicknesses are shown in Fig. 7. When the plastic is absent (Fig. 7a) or very thin (Fig. 7b) the cathode current rises faster than the anode current. However, no appreciable difference in the rise time of anode and cathode current is observed for the thicker anodes ( $\delta > 25 \mu\text{m}$ ). Electron losses along the magnetic field before the plasma is formed can account for the fast rise of cathode current when  $\delta$  is small. This phenomenon is presently not well understood.



#### IV. COMPARISON WITH THEORY

Recently, the production of ion pulses in the double-diode configuration has attracted considerable theoretical attention.<sup>3,5</sup> The double-diode is very similar to the reflex-triode and is different from it to the extent that it has two real cathodes instead of one real and one virtual.

One of these theoretical models<sup>3</sup> predicts that the ion current exhibits resonance-like behavior, when the number of passes  $\eta$ , of an oscillating electron through the anode is equal to a critical number  $\eta_c$ , determined from the condition that the electric field in the anode-cathode gap should always be greater or equal to zero. Based on the sharp increase of the ion current at  $\eta = \eta_c$ , the authors predict that such a device can produce 1-MeV ion beams at current densities of about 18 kA/cm<sup>2</sup>.

Contrary to the predictions of this theoretical model, no resonance-like behavior is observed in the ion current experimentally, as it is manifested from the results of Fig. 2. It should be noticed that for the thinnest anodes used (see Figs. 2 and 4), the number of passes,  $\eta$ , of a typical electron through the anode is considerably greater than  $\eta_c$  predicted by all spectral distributions tested in Ref. 3. It is therefore, very unlikely that the ion current resonance will appear at anode thicknesses less than 2  $\mu\text{m}$ .

Further insight in the nature of the ion current discontinuity may be obtained by considering a double-diode, in which the distribution of potential between the anode and cathode is as shown schematically in Fig. 8. The potential  $V$  is flat between  $x_2$  and  $x_3$  and has a value  $\Delta V$ , which is equal to the reduction in the energy of an electron (associated with its motion parallel to x-axis) while it crosses the anode for the



first time. As a consequence of this, the oscillating electrons do not contribute to the negative space charge at  $x < x_3$ . Note that space charge limited flow for both ion and electrons requires that the electric field at  $x=0$  and  $x=D$  must be equal to zero. If  $\Delta V^*$  is the magnitude of the potential at  $x=x_1$ , then the electron ( $J_e$ ) and ion ( $J_i$ ) current density components at  $x=x_1$  and  $x=x_2$  are given by

$$J_i (x=x_1) = ze n_i (x=x_1) \sqrt{\frac{2ez(V_0 - \Delta V^*)}{m_i}}, \quad (1)$$

$$J_e (x=x_1) = en_e (x=x_1) \sqrt{\frac{2e\Delta V^*}{m_e}}, \quad (2)$$

$$J_i (x=x_2) = ze n_i (x=x_2) \sqrt{\frac{2ez(V_0 - \Delta V)}{m_i}}, \quad (3)$$

and

$$J_e (x=x_2) = en_e (x=x_2) \sqrt{\frac{2e\Delta V}{m_e}}, \quad (4)$$

where  $n_e, n_i$  are the electron and ion densities and  $ze$  is the ion charge. Since  $d^2V/dx^2$  is equal to zero at  $x=x_1$  and  $x=x_2$ , Poisson's equation demands that  $n_e(x=x_1) = n_i(x=x_1)$  and  $n_e(x=x_2) = n_i(x=x_2)$ . These two conditions, together with Eqs. (1) to (4) and the fact that the ratio  $J_i/J_e$  must be the same for any  $x < x_3$ , give

$$\sqrt{\left(\frac{V_o}{\Delta V^*} - 1\right)} = \sqrt{\left(\frac{V_o}{\Delta V} - 1\right)},$$

i.e.,  $\Delta V = \Delta V^*$ , which is in contradiction with the assumed potential distribution of Fig. 8.

The preceding arguments clearly demonstrate that solutions to Poisson's equation as those of Fig. 8 violate the condition that  $J_i/J_e = \text{const.}$  across the anode-cathode gap and therefore are not acceptable.

It is easy now to show that the potential distribution of Creedon et al for  $\eta = \eta_c$  is similar to that of Fig. 8. Specifically, the function  $G(\varphi)$  that is defined in their Eq.(3) and is proportional to the square of the electric field becomes approximately zero at least in one point between  $0 < x < D$ , for  $\phi = \Delta V/V_o = 1/\eta = 1/\eta_c$ . Thus, the condition  $J_i/J_e = \text{const.}$  is violated for all finite values of  $J_i$  and  $J_e$ . Of course, infinite currents cannot be realized in an actual laboratory device.

In general, when the number of transits of a typical electron in the anode-cathode gap is high, only time dependent solutions are appropriate. For this reason, we have started a study of electron and ion flows in a double diode using a new computer code. This code treats the emission of electrons and ions from plasmas, includes the effect of the elastic and inelastic scattering on the motion of the electrons and follows the orbits of both electrons and ions in the self-consistent electric field developed under a given diode voltage. Preliminary results from the numerical simulation show that the increase in the ratio of ion to electron current with decreasing anode thickness is similar to that observed experimentally. The distribution of the potential in the anode-cathode gap is considerably different than that of a bipolar flow and, for thin anodes, becomes under some conditions non-monotonic.

## V. AN ESTIMATE OF $I_i/I_c$

Under steady state conditions, with  $I_{e\parallel}^w \simeq I_i^+$  (current neutralized ion beam),  $I_{e\perp}^w \cong 0$  (strong external magnetic field) and  $I_i^+ \simeq I_i^- \simeq I_i$ , the cathode current  $I_c$  of a reflex triode (see Fig. 5) is given by

$$I_c = 2I_i + I_e^a \quad . \quad (5)$$

The average time a typical electron spends from the time of its emission from the cathode until it gets absorbed in the anode is

$$\tau = \ell / \langle v_e \rangle = (2\eta + 1)D/2 \langle v_e \rangle, \quad (6)$$

where  $\ell$  is the total length traveled by the electron,  $\eta$  is the number of times the electron crosses the anode,  $D$  is the anode-cathode distance,  $\langle v_e \rangle$  is the average electron velocity parallel to x-axis, and the factor  $\frac{1}{2}$  accounts for the gradual reduction of the electron path. The electron current absorbed by the anode is equal to

$$I_e^a = \frac{Q_e^a \langle v_e \rangle}{\ell} \quad , \quad (7)$$

where  $Q_e^a$  is the absorbed charge by the anode within the time interval  $\tau$ .

Similarly, we have for the ion current

$$I_i = \frac{Q_i \langle v_i \rangle}{D} \quad , \quad (8)$$

where  $\langle v_i \rangle$  is the average ion velocity and  $2Q_i$  is the total ion charge in the triode. For space-charge limited flow, the total charge inside the triode should be nearly zero, i.e.,

$$2Q_i = Q_e^a + Q_e^w, \quad (9)$$

where  $Q_e^w$  is the electron charge required to neutralize the drifting ion beam and thus is equal to  $Q_i$ .

Combining Eqs. (5) to (9), and using  $\langle v_e \rangle / \langle v_i \rangle = (m_i/m_e)^{1/2}$ , it is obtained

$$\frac{I_i}{I_c} = 0.5 \left[ 1 + \left( m_i / m_e \right)^{1/2} (2\eta + 1) \right]^{-1}. \quad (10)$$

Equation (10) predicts an appreciable increase of  $I_i/I_c$  with  $\eta$ . For example, for  $\eta=1$ , the ratio is  $I_i/I_c \simeq 1/30$  and increases to 0.5 for  $\eta \rightarrow \infty$ . Equation (10) is shown in Fig. 9 as solid line. The experimental results of Fig. 2 normalized according to  $I_c$  of Fig. 6 are plotted also in the same figure. Although there is a fair agreement between Eq. (10) and experiment for  $\delta < 25 \mu\text{m}$ , the ratio  $I_i/I_c$  is considerably smaller than that predicted from Eq. (10) for thicker anodes. As stated previously, the voltage pulse falls rather rapidly during the life time of the pulse for  $\delta > 25 \mu\text{m}$ . This effect has a double-fold reduction in the ion current, because not only does  $I_i$  decrease with decreasing voltage, but also because a substantial fraction of the protons in the beam may have insufficient energy to be recorded by the reaction  $^{14}\text{N}(p, \gamma)^{15}\text{O}$ , which has a threshold energy of 277 keV. It is rather unlikely that the leveling-off of the  $I_c$  can counterbalance the reduction of  $I_i$ .

## VI. CONCLUSIONS

In this paper, we have studied the effect of the anode thickness  $\delta$  on the ion current, when a 400-kV, 50-nsec positive pulse is applied on the anode of a reflex triode, in the presence of an externally applied magnetic field. The results indicate that the ion current increases by about a factor of 10, when the anode thickness decreases from  $\sim 125 \mu\text{m}$  to less than or equal to  $12 \mu\text{m}$ . However, we have not observed any discontinuity in the ion current. For  $\delta < 12 \mu\text{m}$ , the ion current density is about  $85\text{A}/\text{cm}^2$ , appreciably higher than that predicted in the case of a bipolar flow.

Preliminary results from a computer simulation code exhibit an increase in the ratio of ion to electron current with decreasing  $\delta$  similar to that experimentally observed.

## ACKNOWLEDGEMENT

The authors wish to acknowledge helpful discussions on the subject with Dr. A.E. Robson and the technical assistance of Dr. W.M. Black and R.A. Covington.

## References

\*NRC Resident Research Associate at NRL.

†Supported by ONR.

1. S. Humphries Jr., J.J. Lee and R.N. Sudan, Appl. Phys. Lett. 25, 20 (1974); S. Humphries, Jr., J.J. Lee and R.N. Sudan, J. Appl. Phys. 4, 187 (1975).
2. C.A. Kapetanacos, J. Golden and F.C. Young, Experimental Results on the Formation of a 400 keV Proton Layer, Subm. to J. Nuclear Fusion; J. Golden and C.A. Kapetanacos, Production of Intense Deuteron Beams, to be published in Appl. Phys. Letters Jan. 1, 1976; J. Golden, C.A. Kapetanacos and S.A. Goldstein, Proc. of the Seven European Conf. on Contr. Fusion and Plasma Phys., Lausanne, 1975, p. 91.
3. J.M. Creedon, I.D. Smith and D.S. Prono, Phys. Rev. Lett. 35, 91 (1975).
4. R.N. Sudan and R.V. Lovelace, Phys. Rev. Lett. 31, 1174 (1974).
5. T.M. Antonsen, Jr. and E. Ott, Lab. of Plasma Studies Report #166, 1975.
6. S.A. Goldstein and J. Guillory, Phys. Rev. Lett. 35, 1160, 1975.
7. S.A. Goldstein and R. Lee, Phys. Rev. Lett. 35, 1079 (1975).
8. E. Fermi, Nuclear Physics, Univ. of Chicago Press, Chicago 1950, p. 36.
9. N.J. Berger and S.M. Seltzer, NASA Report #SP-3012, Washington, D.C., 1964.



TAB L E I

Various Currents Flowing in a Reflex  
Triode

$I_i^+$	=	ION CURRENT PROPAGATING TOWARD VIRTUAL CATHODE
$I_i^-$	=	ION CURRENT PROPAGATING TOWARD REAL CATHODE
$I_e^a$	=	ELECTRON CURRENT ABSORBED IN ANODE
$I_e^w$	=	ELECTRON CURRENT TO THE WALLS = $I_{e//}^w + I_{e\perp}^w$
$I_{e//}^w$	=	ION BEAM NEUTRALIZING ELECTRON CURRENT
$I_{e\perp}^w$	=	ELECTRON CURRENT LOST TO THE WALLS $\perp$ to $B_0$ .
$I_e^{p+}$	=	PLASMA ELECTRON CURRENT IN THE + DIRECTION
$I_e^{p-}$	=	PLASMA ELECTRON CURRENT IN THE - DIRECTION
$I_c$	=	CATHODE CURRENT
$I_{sh}$	=	SHUNT CURRENT

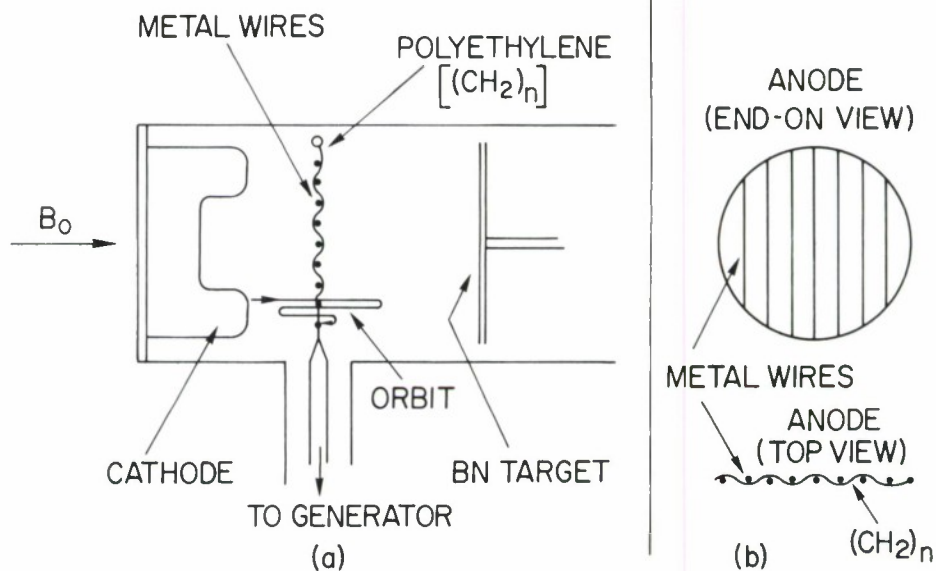


Figure 1. (a) Schematic of the experiment (top-view) and (b) details of the anode

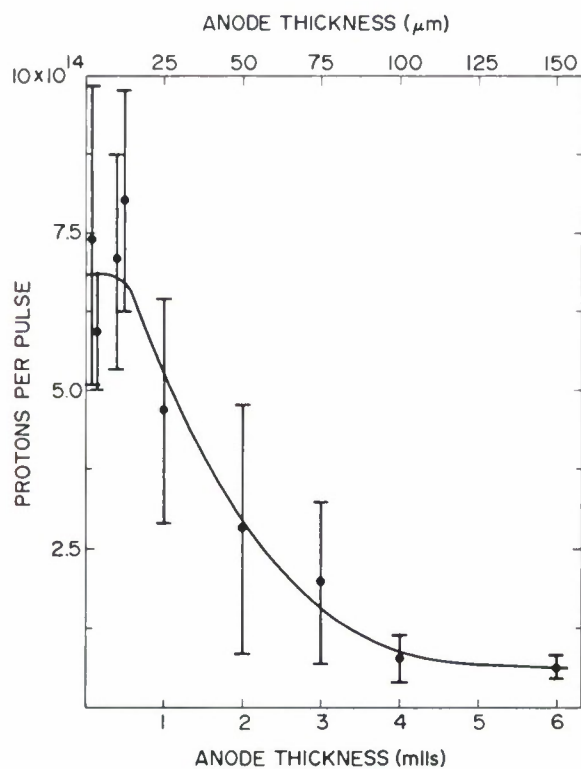


Figure 2

Number of protons in the beam, measured by the nuclear activation technique as a function of anode thickness. For the triangular shaped, 50-nsec-duration proton pulse, the peak ion current is computed from  $i_p = 6.4 \times 10^{-12} N$ , where  $N$  is the measured number of protons.

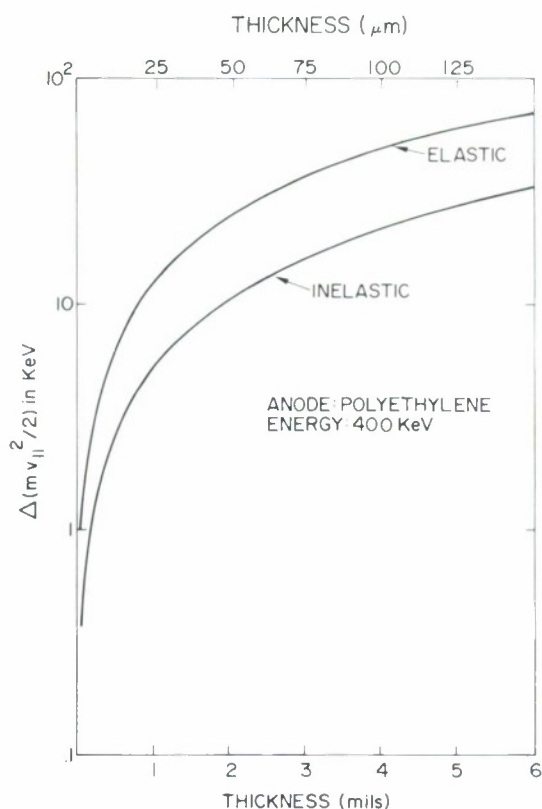
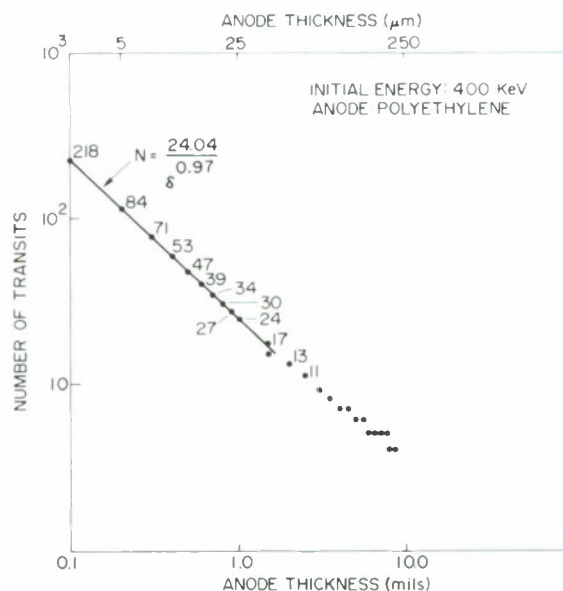


Figure 3

Reduction in the axial energy of a 400-keV electron, because of elastic and inelastic scattering in the anode, as a function of anode thickness

Figure 4

Number of transits a 400-keV initial energy electron can perform at various anode thicknesses. This number of transits was computed under the assumption that the velocity vector of the elastically scattered electron remains always in the source plane and therefore must be considered as a lower limit.



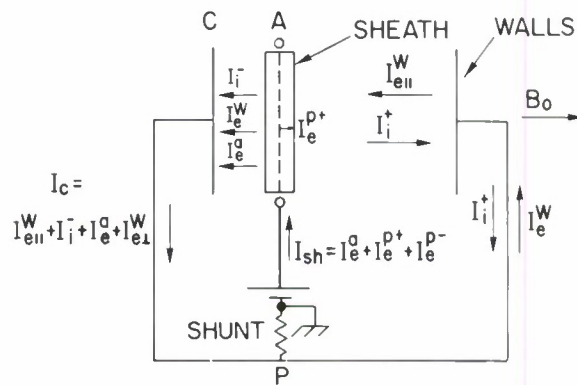


Figure 5. Currents flowing in reflex triode. These currents are identified in Table I.

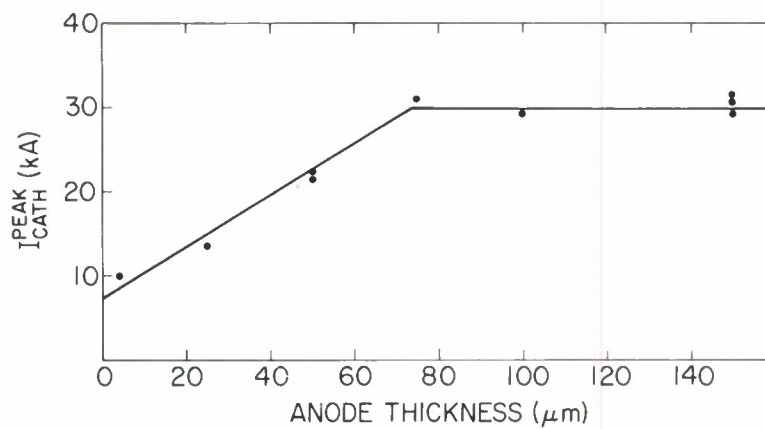


Figure 6. Observed peak cathode current vs. anode thickness at an applied magnetic field  $B_0 \approx 6\text{kG}$

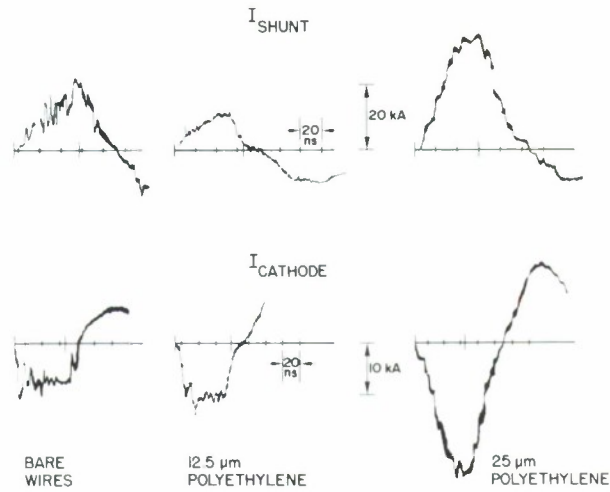


Figure 7. Anode and cathode current wave forms for various anode thicknesses.  $B_0 \approx 6\text{kG}$

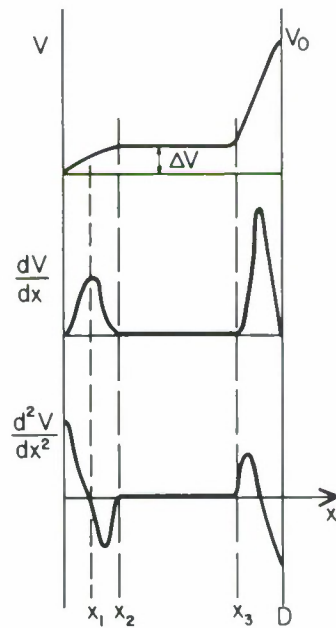


Figure 8. Distribution of potential (V), electric field ( $dV/dx$ ), and charge density  $\left[ \frac{d^2 V}{dx^2} = -e(n_i - n_e)/\epsilon_0 \right]$  in an anode-cathode gap

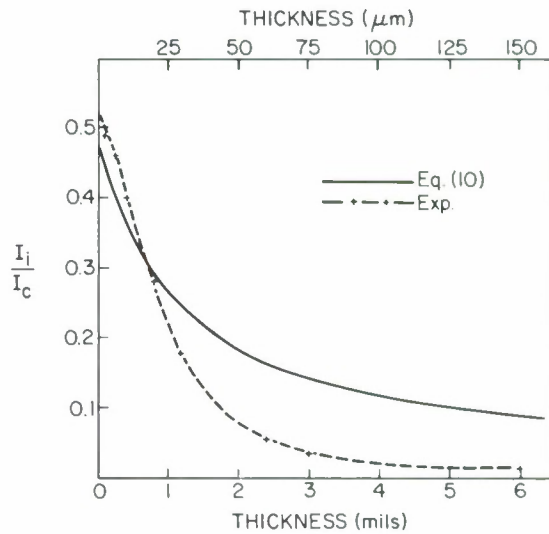


Figure 9. Ratio of ion to cathode current vs. anode thickness. The dashed line (experiment) is plotted from the results of Figures 2 and 3. The solid line is the prediction of Eq. (10).

USE OF ELECTRONIC SPACE CHARGE TO ACCELERATE, FOCUS  
AND BUNCH PLASMA IONS FOR PELLET FUSION\*

J.T. Verdeyen, W.L. Johnson, D.A. Swanson, and B.E. Cherrington  
Gaseous Electronics Laboratory, University of Illinois, Urbana, IL 61801

ABSTRACT

Prior experiments have shown that deep, nearly parabolic, potential wells can be created by the injection of electrons into a spherical diode. Furthermore, it has been demonstrated that a large fraction of the input power can be transferred from the electronic space charge to ion motion provided the electron collection probability is small. However, the instantaneous power required for pellet fusion is still beyond the capabilities of existing machines. By utilizing the spherically symmetric potential wells found previously, the instantaneous power delivered to a small target at the center can be magnified (or bunched) by factors of 10-100. The measurement of these potentials, the comparison with a realistic theory, and an extrapolation to higher voltages/energies will be presented. Recent experiments are described which imply that bunching is present in a planar diode. Although the experiments were performed at low voltages (kV), the extrapolation with constant perveance is straightforward.

\* Work supported by the DMA Division of ERDA. E(11-1) - 2765.



## I. INTRODUCTION

In our work on Inertial Electrostatic Plasma Confinement, we have shown<sup>(1-3)</sup> that deep and stable potential wells can be produced (and predicted) by injecting electrons into the interior of a highly open spherical anode. Obviously, such wells will attract and focus ions towards the center of the anode, a fact which is borne out by experiment and theory.<sup>(4,5)</sup> Even more important than the spatial focusing properties of these wells is the ability to "bunch" the arrival time of ions at the center.<sup>(6,7)</sup>

To appreciate the importance of this fact, let's consider the recent papers on laser,<sup>(8)</sup> - E-Beam,<sup>(9)</sup> - or Ion Beam<sup>(10,11)</sup> - pellet fusion. Although there are considerable differences in pellet design for the specific application, there are similarities in the energy requirement ( $\sim 100$  kJ), time scale (1-10 nsec), and power requirements ( $\sim 10^{14}$  watts). At present, only the E-Beam machines are close to these requirements. Humphreys, Lee and Sudan<sup>(12,13)</sup> have, however, demonstrated a 42% efficiency in transferring energy from an electron beam to the plasma ions emitted from an anode plasma. This result, when extrapolated to higher energy, makes Ion-Pellet fusion attractive, especially since Clauser<sup>(9)</sup> has estimated a factor of 6 less power required for an Ion-Pellet scheme than for an E-Beam system.

Unfortunately, the power level, time scale, and energy of existing machines still do not match the calculated conditions. Usually, the power level is too low and the pulse duration is too long; only the energy is adequate. Herein lies the importance of "Bunching." One can integrate a low input power over a long period of time, the pumping time,  $\tau_p$ , and then deliver the accumulated energy in a much shorter time,  $\Delta t$ . This is, of course, precisely the scheme used in radar pulse modulators or, more recently, in laser Q-switching and in the line-type E-Beam machines. In all cases, the instantaneous power delivered by the pulse is many times the power taken from the primary source.

There have been many schemes proposed to achieve this goal. A controlled rise-time of the anode voltage could achieve bunching, but only after a considerable drift distance.<sup>(14)</sup> Lavrent'ev and Kalmykov<sup>(7)</sup> discussed the use of a sequence of grids to establish the graded potential well structure to bunch ions extracted from the surrounding plasma. Unfortunately, the presence of the macroscopic grid structure will contribute angular momentum to the ion motion, thereby requiring large target diameters.

On the other hand, if an electronic space charge is used to focus and bunch ions, it is perfectly transparent to the ions - and would contribute no angular momentum during bunching - hence the limiting factor in the target size is the initial angular momentum of the plasma ions. But this is quite low in a glow - essentially that of the neutral gas background. Thus, one can hit a small target with ions accelerated by an electronic space charge.

In the following section, we will review the experimental evidence for the existence of the space charge wells, and then present a first order theory of the bunching achieved and energy delivered for a system scaled according to constant perveance ( $I/V^{3/2}$ ). However, these calculations do not account for the presence and motion of the plasma electrons, nor for the distortion of the space charge fields by the ions.

These effects are considered in Section III in a quasi-static analysis of an electron beam being injected through a partially transparent anode and then through a plasma layer which emits ions towards the virtual cathode (i.e., the center) and plasma electrons towards the anode. Although the calculations were done for planar geometry with only collection by the anode permitted, the results would be applicable to the spherical case, where only collection by the anode is possible.

Although the spherical geometry should be the best for the ultimate case, it is the most difficult to study experimentally. Thus, our recent experiments have been performed in planar geometry and at low voltages. Although any experiment is truly 3-dimensional in nature, we have excellent agreement with a 1-D analysis. Furthermore, experiments are described which indicate that "bunching" is occurring in this system.

## II. PRELIMINARY IDEAS

### A. Review of Prior Experiments on Negative Wells

The experimental device used on our IEPC studies is shown in Fig. 1. The hot cathode opposite the slot in the aluminum shell is pulsed negative by 100-300 V, thereby injecting electrons into the interior of the structure. The 93% open anode was held at a constant positive voltage of 500-2500 V. Even though the initial source of electrons is definitely not spherically symmetric, the accumulated scattering of the anode structure and the secondary electron production or photoelectric emission at the grounded cathode serves to generate a spherically symmetric electron injection after a few electron transit times.

The resulting potential wells are inferred from the scattering experienced by the beam from the oscilloscope gun. One drives the deflection  $90^\circ$  out of phase to obtain a circular Lissajou pattern on the screen prior to the injection of the electrons and prior to the application of the anode voltage. Of course, the anode voltage will contract the pattern, whereas the formation of a negative well will expand the circle. An example of this is shown in Fig. 2. The parameter which is independent of the well itself is the gun voltage,  $V_g$ . By varying the ratio of  $V_g/V_A$  one can infer the potential distribution within the anode structure.

The wells so formed have the general shape of a parabolic depression. This can be demonstrated in a dynamic fashion by disconnecting one set of deflection plates on the guns, thus generating a vertical scan, and by off-setting the probing beam to one side of the center of the well. This is shown in Fig. 3. The dashed lines show the equivalent circular Lissajou patterns with both deflection plates operative, whereas the solid lines show the scattering before (short) and after (long) electron injection. By doing this, one is varying the slope and position of the incoming ray, thereby sampling a different region of the potential well.

The fact that the two traces are parallel and that a line drawn through the extremes passes through the center, means that the scattering is proportional to the distance from the center. This indicates an electric field which increases with  $r$ ; hence, a parabolic well.

Such wells are a consequence of the angular momentum of the injected electrons.<sup>(2)</sup> As will become obvious shortly, the parabolic wells are not necessary to the bunching concept, but merely facilitate the analysis. If the electrons have only a small amount of angular momentum, then the resulting potential wells approach those predicted by Langmuir and Blodgett.<sup>(15)</sup>

#### B. Bunching in the Space Charge Wells

Let us now consider the transient behavior of an ion in the wells that can be formed with a given injected electron current. If one neglects the electron transient effects, then it is sufficient to specify the injected current, the energy associated with the angular momentum at the anode, and the spread in total energy of the electrons at the anode to solve for the potential. To express the results in the most general form, the perveance, i.e.,  $(I_e^+/V_a^{3/2})$ , expresses the injected current at a given voltage, and the spread in angular



energy and total energy,  $BB\emptyset$  and  $BBE$ , is normalized to the anode potential. Aside from relativistic effects, these solutions are scalable to any size, voltage, or current device through these normalized quantities.

Typical solutions are shown in Fig. 4 for two different values of the spread in angular momentum. The fact that we had observed parabolic wells in the past is indicative of substantial momentum of injected current for our low voltage system. At higher voltages, one could expect less scattering by the macroscopic grid structure; thus, one chooses a smaller value for the angular energy spread and expects a potential structure that more closely resembles the Langmuir solution. This is borne out in Fig. 4 with the appearance of a "virtual cathode" at the point of maximum curvature of the potential.

The dashed potential well labeled with a microperveance of 37.4 can be closely approximated by a parabola for the form

$$V(r) = V_A \left( 1 - f \left( 1 - \frac{r^2}{b^2} \right) \right) \quad (1)$$

with  $f = 0.55$  representing the depth of the potential well expressed as a fraction of the anode voltage. The main utility of this case lies in the simplicity of the analysis of the motion of a few ions which start from an arbitrary point  $Z_0$  inside the anode structure.

If one neglects the initial velocity of the ion, then it is trivial to show that all of the ions reach the center at the same time, irrespective of their initial position. Thus one is continuously transferring power from the electrons to the ions over a time scale of the ion transit time, but delivering it to the center - where a pellet might be located - in zero time.

The initial angular energy of ions limits the degree of focussing one can achieve with the parabolic well, whereas the spread in radial kinetic energy yields a slight amount of time defocussing or "debunching." Neither is serious as evidenced from the parameters as shown in Table I.<sup>(6)</sup> Here we computed the energy delivered to a target which is larger than 0.154 mm, by the ions extracted from an initial  $10^{11} \text{ cm}^{-3}$  plasma filling a 1 meter sphere and driven by a voltage pulse of 1 MV. There are two main points to gather from this idealistic case: (a) large quantities of energy can be delivered in a short period of time, and (b) reasonably small targets ( $\sim 1 \text{ mm}$ ) can be used and still have reasonable uniform illumination.

Of course, such an extreme in bunching is a consequence of the perfect parabolic well, a fact which was recognized by Lavrent'ev and Kalmykov.<sup>(7)</sup> But even the distinctly non-parabolic wells shown in Fig. 4 yield impressive bunching times. For instance, consider the case for a microperveance of 89.5 in Fig. 4, all of the ions located in angular region between  $r/b = 0.86$  and 1.0 arrive at the center within 2% of the time it takes for the first one to arrive. Furthermore, these initial ions carry 50% of the total energy associated with all of the ions.

For a given energy and time scale requirement, there is an optimum electron current to be injected. This is shown in Fig. 5, where we plot the arrival of energy (normalized to the maximum possible amount of ion kinetic energy) as a function of the time after the first ion arrives. (This time is shown in parentheses on the graph). We choose the same size device as in Table I. Notice that as more electron current is injected (higher perveance), the fraction of the energy delivered in a time interval,  $\Delta t$ , becomes larger. However, if too high a current is injected, the relative power delivered by the ions is considerably reduced.

The cause of this drop in power is due to the dependence of bunching on well shape. For the highest current case, the ions originating next to the anode reach the center first - followed by those originating at smaller radii. Although there may be larger energy delivered in the long run (since the injected current is larger), there is less energy in a fixed time interval.

In the above analysis, there are two assumptions which seriously limit the applicability of the theory. The motion of the plasma electrons has been ignored. They will, of course, move toward the anode uncovering the positive charge which modifies the space charge field of the injected beam which, in turn, modifies the motion of the ions. A complete analysis has not been performed as of this time, but the quasi-static analysis, presented in the next section, indicates that the general prediction of bunching remains valid.

### III. QUASI-STATIC ANALYSIS

The problem to be considered is shown in Fig. 6 along with a first order sketch of the variation of the potential and currents in space of the various constituents. We assume that an electron beam is injected through a transparent anode ( $\eta$  = transmission coefficient) and thus forms a space charge well in region  $x > 0$ . The presence of plasma located in the region defined by  $V_1 < V(x) < V_A$  must be accounted for in a self-consistent manner.

The plasma ion current will buildup with increasing distance and reach a limiting value of  $J_{i0}$  at the point  $V(x) = V_1$ , whereas the plasma electrons circulate through the transparent anode with a fraction  $(1 - \eta)$  being captured by the anode structure. Since most of the plasma electrons return after passing through the anode structure twice; i.e., one round trip, they partially neutralize the adverse effects of the ionic space charge. Beyond the point  $V(x) = V_1$ , the ion current is a constant.

The space charge of the beam electrons will depress the potential until some of these electrons are reflected back towards the anode; the remainder, the transmitted electrons, neutralize (more or less) the ions emitted from plasma region.

In order to handle this problem in a realistic fashion, we must assign a distribution function to all of the constituents, including the injected beam. Our previous experience<sup>(2)</sup> indicates that the exact shape of distribution function is not so important as the fact that there is a spread in injected energies. Therefore, we assume a rectangular energy spread of width  $\epsilon V_A$ . This choice allows for the natural transmittance of some of the beam electrons beyond the virtual cathode at a potential  $V_0 > 0$ , without any "ad hoc" assumption.<sup>(16)</sup>

The distributions are shown in Fig. 7. Note that in Fig. 7a, the negative velocity component of the injected electron terminates at a smaller magnitude than does the positive component. This is due to the escape of the electrons beyond the potential minimum  $V_0$ .



If the point of consideration is less than the distance,  $x_1$ , then the ions are uniformly distributed in velocity from 0, corresponding to ions generated at that point, to those that have originated near the anode and have been accelerated through the potential differences  $V_A - V(x)$ . If the point is beyond the plasma region,  $x > x_1$ , the energy spread of the ions is assumed to remain constant at  $e(V_A - V_1)$ . The two cases are shown in Fig. 7b by dash ( $x < x_1$ ) and solid ( $x > x_1$ ) curves. The plasma electrons exist only in the region  $0 < x < x_1$ . Furthermore, those electrons with a positive directed velocity are reduced in number by two multiples of  $\eta$  corresponding to the double pass through the anode.

One cannot be completely arbitrary in the choice of the distributions and currents. Obviously, for a static analysis, the net electrical current must be zero for any point  $x > 0$ . Thus the amount of ion current transmitted beyond  $x_c$  must be balanced by the amount of electron current that can pass the potential minimum  $V_0$ . But this, in turn, is related to potential minimum  $V_0$  and the energy spread of the electrons.

$$\frac{J_{i0}}{J_{eb}^+} = \frac{V_0}{eV_A} = \frac{\phi_0}{e}. \quad (2)$$

The remainder of the beam electrons are reflected, and for  $x < x_2$ ,  $J_{i0}$ ,  $J_{eb}^+$  and  $J_{eb}^-$  are constant. In the plasma region, the variation of the ion current with distance must be compensated by the variation of the circulating electron current. Since  $J_{eb}^+$  and  $J_{eb}^-$  are constant in that region also, we can relate  $J_{ep}^-$  and  $J_i$  by:

$$J_i(x) + (1-\eta^2) J_{ep}^-(x) = J_{eb}^+ \frac{\phi_0}{e}. \quad (3)$$

It is now a straightforward (but tedious) task to relate the plasma and beam densities to the potential variation and the distribution. These are given below:

$$J_i(x) = J_{i0} \left\{ \frac{1-\phi}{1-\phi_i} \right\} \quad (4a)$$

$$\frac{\rho_i(x)}{e_0} = \frac{2J_{i0}}{e_0 \left( \frac{2eV_A}{M} \right)^{1/2}} \left\{ \frac{(1-\phi)^{1/2} - (\phi_i - \phi)^{1/2} u(\phi_i - \phi)}{1-\phi_i} \right\} \quad (4b)$$

$$J_{ep}^-(x) = \frac{J_{io}}{1-\eta^2} \left\{ \frac{(\phi - \phi_1) u(\phi - \phi_1)}{1 - \phi_1} \right\} \quad (5a)$$

$$-\frac{\rho_{ep}(x)}{\epsilon_0} = 2 \left( \frac{1+\eta^2}{1-\eta^2} \right) \frac{J_{io}}{\epsilon_0 \left( \frac{2eV_A}{m} \right)^{1/2}} \left\{ \frac{(\phi - \phi_1)^{1/2} u(\phi - \phi_1)}{1 - \phi_1} \right\} \quad (5b)$$

$$J_{eb}^+(x) = J_{eb}^+ \left\{ 1 - (1 - \frac{\phi}{\epsilon}) u(\epsilon - \phi) \right\} \quad (6a)$$

$$-\frac{\rho_{eb}(x)}{\epsilon_0} = \frac{2J_{eb}^+}{\epsilon_0 \left( \frac{2eV_A}{m} \right)^{1/2}} \left\{ \frac{\phi^{1/2} - 2(\phi - \epsilon)^{1/2} u(\phi - \epsilon) + (\phi - \phi_0)^{1/2}}{\epsilon} \right\}. \quad (6b)$$

In these equations, liberal use has been made of the Heaviside step function  $u$ , to delete or include various terms in the appropriate regions, and all potentials have been normalized to the anode, viz.  $\phi_1 = V_1/V_A$ ;  $\phi_0 = V_0/V_A$ ;  $\phi = V(x)/V_A$ . Implicitly in the above development is the assumption that the potential is monotonically<sup>(17)</sup> decreasing in the plasma region so as to avoid the possibility of trapped particles. That situation requires even more regions (and step functions)! We have also implicitly assumed that the e-i pair production rate exactly balances the extraction rate in any elemental volume.

One can now proceed to Poisson's Equation to find the potential as a function of distance. It is convenient to normalize the distance to that of the virtual cathode for a monoenergetic beam of electrons injected into a vacuum (a distance which approximately equals the anode-cathode space for highly transparent anodes).

$$\bar{z} = x/x_{v.c.} \quad (7a)$$

$$\chi_c^2 = \frac{2}{9} \epsilon_0 \left( \frac{2e}{m} \right)^{1/2} \frac{V_A^{3/2}}{J_{eb}^+}. \quad (7b)$$

Thus Poisson's Equation becomes:

$$\begin{aligned}
\frac{d^2\phi}{dz^2} = & \frac{4}{9} \left( \frac{1+\eta^2}{1-\eta^2} \right) \frac{J_{io}}{J_{eb}^+} \left\{ \frac{(\phi-\phi_1)^{1/2} u(\phi-\phi_1)}{1-\phi_1} \right\} & \text{Plasma Electrons} \\
& - \frac{4}{9} \left( \frac{M}{m} \right)^{1/2} \frac{J_{io}}{J_{eb}^+} \left\{ \frac{(1-\phi)^{1/2} - (\phi_1-\phi)^{1/2} u(\phi_1-\phi)}{1-\phi_1} \right\} & \text{Plasma Ions (8)} \\
& + \frac{4}{9} \left\{ \frac{\phi^{1/2} - 2(\phi-\epsilon)^{1/2} u(\phi-\epsilon) + (\phi-\phi_0)^{1/2}}{\epsilon} \right\}. & \text{Beam Electrons}
\end{aligned}$$

The first integral is found in the usual fashion by multiplying by  $2d\phi/dz$  and using the indefinite integral. The integration constant is evaluated by forcing the field to vanish at  $\phi = \phi_0$  (see Fig. 6). Thus the square of the field obeys the following equation:

$$\begin{aligned}
\left( \frac{d\phi}{dz} \right)^2 = & \frac{16}{27} \left( \frac{1+\eta^2}{1-\eta^2} \right) \frac{J_{io}}{J_{eb}^+} \left\{ \frac{(\phi-\phi_1)^{3/2} u(\phi-\phi_1)}{1-\phi_1} \right\} \\
& - \frac{16}{27} \left( \frac{M}{m} \right)^{1/2} \frac{J_{io}}{J_{eb}^+} \left\{ \frac{(1-\phi_0)^{3/2} - (1-\phi)^{3/2} - (\phi_1-\phi_0)^{3/2} + (\phi_1-\phi)^{3/2} u(\phi_1-\phi)}{1-\phi_1} \right\} \\
& + \frac{16}{27} \left\{ \frac{\phi^{3/2} - \phi_0^{3/2} + (\phi-\phi_0)^{3/2} - 2(\phi-\epsilon)^{3/2} u(\phi-\epsilon)}{\epsilon} \right\}.
\end{aligned}$$

(9)

Obviously, numerical methods must be used if further progress is to be made on the potential function. However, considerable insight into the problem can be obtained without a solution to the potential function.

First, the electronic charge must exceed the ionic charge at  $\phi_0$ .

$$\rho_e(x=x_c) > \rho_i(x=x_c) \quad (10a)$$

or

$$\left( \frac{m}{M} \right) > \phi_0 \left\{ \frac{(1-\phi_0)^{1/2} - (\phi_1-\phi_0)^{1/2}}{1-\phi_1} \right\}^2. \quad (10b)$$

If the plasma is located close to the anode, then  $\phi_1 \rightarrow 1 - \delta$ , and Eq. (10b) simplifies to

$$\phi_0 < \frac{4m}{M} . \quad (11)$$

Notice that this requirement is on the magnitude of the potential minimum at the virtual cathode, not on the ratio  $\phi_0/\epsilon$  which is the ratio of ion current to electron current. This ratio is determined by the requirement that the field can, at most, vanish in the plasma region. The point at which this occurs depends upon the extent of the plasma,  $\phi_1$ , and the openness of the anode.

It is most convenient for numerical purposes to choose the openness factor to be related to the mass ratio by:

$$\frac{1 + \eta^2}{1 - \eta^2} \left( \frac{m}{M} \right)^{1/2} = 1 \quad (12)$$

or  $\eta = 0.9769$  for a  $(e - H^+)$  plasma. Table II gives the maximum values of the ratio  $\phi_0/\epsilon = J_i/J_{eb}^+$  for various choices of the plasma thickness, i.e.,  $\phi_1$ . Also shown in Table II is the value of the potential where the field vanishes for this choice of extracted ion current. Greater emphasis is placed on the values of  $\phi_1$  close to 1 since ions originating in this region will deposit the greatest amount of energy in the target pellet. Notice that the potential is depressed to an extremely small value, typically 0.2% of the anode potential, no matter what the energy spread of the injected electrons. However, there must be a finite spread in order to allow some of the electrons to pass the virtual cathode and neutralize the ion current. (18)

One can also estimate the fractional power transfer from the injected electrons to the ions. The amount of power delivered to the anode consists of the intercepted fraction of injected and return beam current and that contributed by the plasma electrons.

$$P_A = J_{eb}^+ V_A \left\{ (1-\eta) \left[ \frac{1+\eta}{\eta} - \frac{\phi_0}{\epsilon} \right] + \frac{1}{2} \frac{\phi_0}{\epsilon} (1-\phi_1) \right\}, \quad (13)$$

where the first term is that contributed by the beam and the second is that contributed by the plasma electrons.

The power delivered to the region  $V_o$  consists mainly of the energy carried by the ions plus a small amount carried by the transmitted electrons. After due allowance is made for the distribution of ion velocities, the result is:

$$P_{out} = J_{io} V_A \left\{ \phi_0 + \frac{1}{2} \left[ \frac{(1-\phi_0)^2 - (\phi_1 - \phi_0)^2}{1-\phi_1} \right] \right\}. \quad (14)$$

Hence the efficiency of power transfer is found to be

$$EFF. = \frac{J_{io}}{J_{eb}^+} \frac{\frac{1+\phi_1}{2}}{\frac{1-\eta^2}{\eta} + \eta \left( \frac{J_{io}}{J_{eb}^+} \right)}. \quad (15)$$

Note that the efficiency can approach 100% in this case if the transparency of anode is quite high. This result is not subject to the limitation of the convenient assignment of the openness expressed by Eq. (12); but for that value we obtain the efficiencies noted in the last column of Table II.

If the transmittance of the anode approaches unity, the efficiency can exceed 50% and approaches  $(1 + \phi_1)/2$ . This is in contrast to the limiting efficiency of 50% for a space charge limited emitter of ions at the anode. In that case, half of the ions go the wrong way - back to the real cathode - wasting half of the power. As we will see subsequently, the plasma electrons create a slight space charge depression near the anode and prevent the plasma ions from flowing to the real cathode - hence higher efficiencies.

The normalized self-consistent potentials found from a numerical integration of Eq. (9) is shown in Fig. 8. Recall that the quantity,  $J_{io}$ , is just a convenient way of specifying the plasma density (through Eqs. (4b) and (5b)) in the region  $\phi_1 < \phi < 1$ . The ratio of the "plasma" electron to ion density is given by:

$$\frac{|p_{ep}|}{|p_{ip}|} = \left(\frac{m}{M}\right)^{1/2} \left(\frac{1+\eta^2}{1-\eta^2}\right) \left\{ \frac{\phi(x) - \phi_1}{1 - \phi(x)} \right\}^{1/2}. \quad (16)$$

Hence, near the anode, the "plasma" is electron rich; whereas it is ion rich near  $\phi = \phi_1$ . The fact that the ratio goes to zero or infinite at the extremes of plasma region is a consequence of the neglect of thermal velocities of the plasma particles. Thus a true plasma condition is achieved at  $\phi = (1 + \phi_1)/2$ , for the openness relation given by Eq. (12). At that point the plasma density is  $\sim 5$  times the beam density for values of  $J_i/J_e$  close to the maximum value.

Notice that the shape of the space charge region beyond  $x_1$ , i.e.,  $\phi < \phi_1$ , is more or less the same for values of  $J_{io}/J_e$  close to the maximum value. Essentially the plasma short-circuits the space charge field yielding a region that can be labeled as the "positive column." This is, of course, identical to that found by Langmuir<sup>(19)</sup> in 1927.

It is also interesting and most important to note that the lifetime of a plasma electron at  $\phi_1$  is approximately the same as the time for an ion to make the transit between  $\phi_1$  and  $\phi_0$  for the openness condition prescribed by Eq. (12). After the ion moves through this region, its space charge is neutralized by the transmitted electron beam, and the corresponding electron is collected by the anode. Consequently, both can be ignored insofar as the space charge effects are concerned after this time.



Thus by the choice of a highly open anode, the plasma can act as a space charge emitter of ions in one direction increasing the efficiency of energy transfer from the beam. If the plasma density is higher than that indicated by this analysis, the potential would no longer be a single-valued function of  $x$  due to potential well formed by the circulating and trapped electrons. An anode sheath would form to limit the electron current to that of ions, just as it does in positive column of a simple gas discharge.

We can now relax the requirement that pair production balances the emission rate to obtain an estimate of the dynamic effects essential to the bunching problem. As the plasma ions are emitted to right and the plasma electrons are collected by the anode, the plasma region would recede towards the anode. (This would occur only if the ion-ionization is small, a condition which implies low neutral pressure.)<sup>(20)</sup> Thus, the field accelerating the ion changes in space and in time. Consequently, the ions traversing the space charge region does not gain the full kinetic energy corresponding to  $\phi_1 - \phi_0$ .

However, those ions emitted closer to the anode experience a much slower changing field and thus gain more energy. This is precisely what is required to achieve bunching. Similar effects have been predicted by the analysis of the expansion of a plasma into a vacuum,<sup>(21)</sup> where the space charge of the plasma electrons accelerate the ions. An ion "bunch" (see Fig. 5 of Ref. 21) is obtained.

#### IV. EXPERIMENTAL

Our prior experimental work in spherical geometry was discussed in Section II. Although this geometry is probably optimum from an application point-of-view, it is most difficult to study. Any probe inserted into the interior of the anode greatly affects the space charge fields (although a free-falling pellet would not!), and the electron-beam probing technique integrates effects along the entire path. Thus, for our initial experiments, we have chosen the planar geometry shown in Fig. 9.

The source of the electron current is a planar, temperature-limited hot cathode approximately 5 cm in diameter. Consequently, the region between the real cathode and the transparent anode is not limited by space charge and thus the injected current and the applied voltage are independent variables. This cathode is indirectly heated and is at ground (0 volts) potential for these experiments.

In order to achieve some resemblance to a one dimensional problem, we bias the electrode labeled (h.c.) negative with respect to the real cathode to prevent the electrons from escaping laterally. A moveable probe which can be biased with respect to the cathode is used to collect the electron (or ion) current emitted to the right.

Let us first show that this indeed approximates a 1-dimensional problem by considering experiments done under "hard" vacuum conditions ( $p \sim 10^{-7}$  Torr). If the probe position is fixed, but its voltage is varied from zero, very little current transmitted from the cathode reaches the probe; most of the current is collected by the screen as shown in Fig. 10. If the voltage of the probe exceeds a certain value, then the system abruptly switches, and the full injected current is transmitted. A further increase in probe potential does not change any of the currents.

If the probe voltage is decreased from the high value, the current remains at the saturated value. At some lower voltage, the probe current abruptly switches back to its small value and retraces the original curve. This same effect was seen by Humphries, Lee, and Sudan<sup>(12)</sup> by varying the position of the second cathode. It can also be seen in the plate characteristics of a 6L6 Beam power tube. Indeed, it was analyzed and discussed in 1937 by Salzberg and Haeff.<sup>(22)</sup>

The probe voltage to draw a constant probe current (but much less than the injected current) as a function of the probe position is shown in the top curve of Fig. 11. Note that the curve extrapolates to a minimum in potential which is quite small (2-5 V), compared to anode voltage (typically 800 V), and is located at a definite position, the virtual cathode.

This is precisely what one would expect from the one dimensional analysis presented in Section III. If the probe is located far enough away from the anode, a virtual cathode forms at a well defined distance from the anode. The minimum potential is very small and differs from zero by just enough to transmit the current demanded by the probe. Thus, in spite of three dimensional appearance of the problem, a one dimensional approximation can be achieved rather easily. The interpretation of these data is summarized in the sketch shown in Fig. 12. At low values of probe current, a well defined potential well exists, state A, whereas the potential is nearly monotonically decreasing for large transmitted currents, state B.

Incidentally, the data shown in Figs. 10 and 11 are very reproducible and stable, at least within a time resolution of  $\sim 50$  nsec, for a time interval of 100  $\mu$ sec, in spite of predictions to the contrary.<sup>(16)</sup> The same data were obtained whether the anode was pulsed or whether it was D. C.

The situation is modified slightly when the background pressure (of helium) is allowed to rise as shown in Fig. 11. Even though the pressure is far below that of a self-sustained discharge (with the probe being the cathode and the screen being the anode), some electron-ion pairs are created by the injected electrons. These secondary electrons join the primary electrons in creating negative space charge, whereas the ions can flow to the probe, or to the negatively biased electrode (h.c.). If the ions were formed near anode potential, they would be accelerated towards and collected by the probe. Those formed at a potential below  $V_p$  by the low energy electrons ( $< 100V$ ) will be trapped in any potential well formed by the electrons, eventually disappearing laterally towards the bias electrode (h.c.).

However, the presence of the positive ions does neutralize part of the electronic space charge raising (slightly) the potential minimum and allowing more electronic current to pass for a given probe voltage. However, the same general behavior is observed under the "soft" vacuum condition; there are still the two states as indicated in Fig. 12.

An interesting phenomenon is observed when the anode is pulsed with the probe being biased to the "B" shape sketched in Fig. 12. As shown in Fig. 13, the probe current decreases slightly with time due to secondary electron emission and ion collection. Then in a very narrow time interval, the probe current actually goes negative - and then the process repeats.

This is not a simple relaxation oscillation aided by the presence of the injected electrons. That occurs at much higher pressures. It is extremely sensitive to probe bias and occurs very close to the switching points. Its time scale is on the order of ion transit time. The phenomenon is not observed for voltage below or above the probe bias required for switching. The repetition frequency is not a circuit effect, but is strongly affected by the background pressure.

The potential appears to be switching between states A and B of Fig. 12 under these conditions. Since the potential variation is determined by the motion of the electrons, this can occur on very short time scale. This, in turn, could give rise to the apparent short burst of ions detected by the probe.

Very recent experiments have verified this qualitative picture. The planar probe of Fig. 12 was replaced with a double shield probe so as to distinguish between electrons and ions. Indeed, the sharp current reversal shown in Fig. 13 is due to the arrival of a "bunch" of ions, far in excess of that allowed by a simple bipolar analysis.

#### VI. SUMMARY AND CONCLUSION

Although these experiments have been performed at low voltages, in a small device, with minuscule energies, we feel that the results are applicable to the requirements of fusion devices. Space charge fields do scale with perveance, although real gas effect such as charge exchange and ion ionization do not. If bunching can be achieved with the large scale machines, pellet fusion could be achieved with existing technology.

## REFERENCES

1. D. A. Swanson, B. E. Cherrington and J. T. Verdeyen, Appl. Phys. Lett., 23, 125 (1973).
2. D. A. Swanson, B. E. Cherrington and J. T. Verdeyen, Phys. Fluids, 17, 1269 (June 1974).
3. J. T. Verdeyen, B. E. Cherrington, D. A. Swanson and D. J. Meeker, Annals of the New York Academy of Sciences, 251, 126, (1975).
4. D. A. Swanson, B. E. Cherrington and J. T. Verdeyen, Phys. Fluids, 16, 1939 (1973).
5. B. E. Cherrington, J. T. Verdeyen and D. A. Swanson, Annals of the New York Academy of Sciences, 251, 139 (1975).
6. J. T. Verdeyen, D. A. Swanson, B. E. Cherrington and W. L. Johnson, Appl. Phys. Lett., 27, 380 (1975).
7. O. A. Lavrent'ev and A. A. Kalmykov, Annals of the New York Academy of Sciences, 251, 152 (1975).
8. K. A. Brueckner and S. Jorna, Rev. Mod. Phys., 46, 325 (1974)
9. M. J. Clauser, Phys. Rev. Lett., 34, 570 (1975).
10. M. J. Clauser, Phys. Rev. Lett., 35, 848 (1975).
11. J. W. Shearer, Lawrence Livermore Laboratory, Report No. UCRL-76519 (to be published).
12. S. Humphries, J. J. Lee and R. N. Sudan, Appl. Phys. Lett., 25, 20 (1974).
13. S. Humphries, J. J. Lee and R. N. Sudan, J. Appl. Phys., 46, 187 (1975).



14. F. Winterberg, *Nature*, 251, 44 (1975).
15. I. Langmuir and K. B. Blodgett, *Phys. Rev. (Ser. 2)*, 22, 347 (1923).
16. Y. Y. Winograd, *Phys. Fluids*, 10, 1063 (1967).
17. D. S. Prono, J. M. Creedon, I. Smith and N. Bergstrom, *J. Appl. Phys.*, 46, 3310, (1975), also *Phys. Rev. Lett.* 35, 91 (1975).
18. This differs from Langmuir's classic result (Ref. 20) due to the presence of circulating beam electrons.
19. I. Langmuir, *Phys. Rev.*, 33, 954 (1929).
20. C. L. Olson, J. W. Poukey, *Phys. Rev.*, A9, 2631 (1974).
21. J. E. Crow, P. L. Auer and J. E. Allen, *J. Plasma Phys.*, 14, Part I, 65 (1975).
22. B. Salzberg and A. V. Haeff, *RCA Review*, 336 (1937).



TABLE I

Summary of Calculations on Parabolic Potential Wells

TERM	SYMBOL	FORMULA	VALUE *
pumping time (electron current injection)	$\tau_p$	$\frac{\pi b}{2} \left[ \frac{M}{2efV_a} \right]^{1/2}$	306 nsec
bunch time (thermal spreading)	$\Delta t$	$\left[ \frac{kT_i}{2efV_a} \right]^{1/2} \left[ \frac{M}{2efV_a} \right]^{1/2} \frac{b^2}{Z_0}$	25 psec
aiming error and/or location tolerance	$\Delta r$	$\left[ \frac{kT_i}{2efV_a} \right]^{1/2} b$	0.154 mm
energy to target	$W$	$\frac{4\pi b^3}{3} N_i \left[ \frac{3efV_a}{5} \right]$	22.1 kJ
power multiplication	$\tau_p/\Delta t$		$1.2 \times 10^4$

\*VALUES ARE FOR A 1 M RADIUS SPHERE, FILLED WITH A HELIUM PLASMA OF  $10^{11} \text{ cm}^{-3}$ , WITH  $T_i = 0.026 \text{ eV}$ , AND 1 MV APPLIED TO THE ANODE WITH  $F = 0.55$ .

TABLE II

Parameters Associated with the Beam-Plasma Problem of Fig. 6. The Openness of the Anode is Assumed to be 0.9769.

$\phi_1$	$\left[ \frac{M}{m} \right] \phi_0$	$\left[ \frac{\phi_0}{\epsilon} = \frac{J_{i0}}{J_{eb}^+} \right] (\text{MAX})$	$\phi \text{ (for } E = 0)$	EFF.
0.95	3.8909	0.05034	0.971	0.512
0.90	3.7892	0.05295	0.940	0.511
0.85	3.6859	0.05522	0.907	0.507
0.80	3.5810	0.05732	0.873	0.502
0.75	3.4744	0.05942	0.838	0.496
0.70	3.3659	0.06152	0.800	0.489

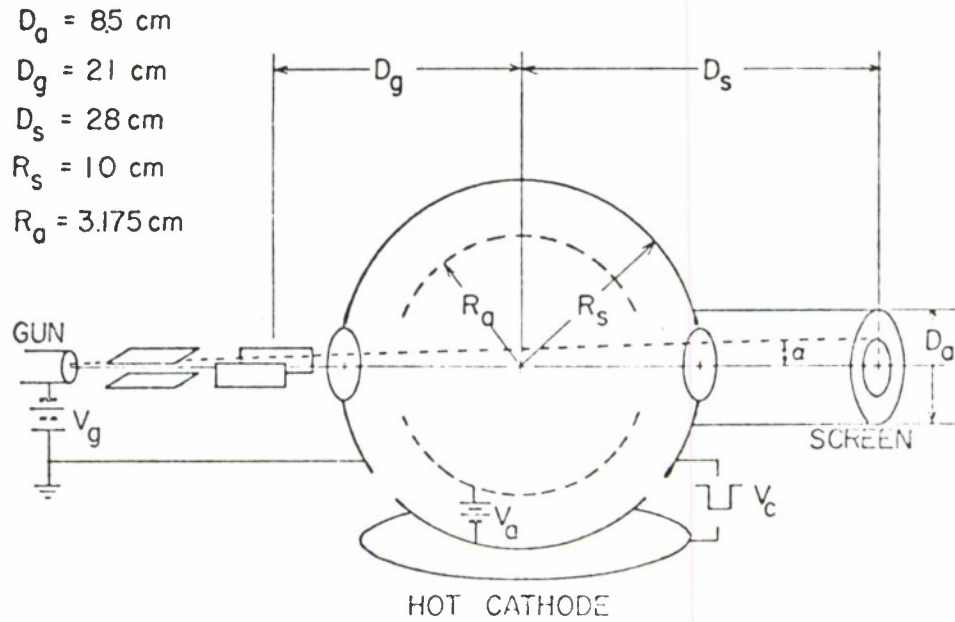


Figure 1. Schematic diagram of LEPC device. The spherically symmetric potential distribution generated by injecting electrons from a pulsed hot cathode into a mesh anode, is diagnosed by an electron beam injected through the system to a phosphor screen.

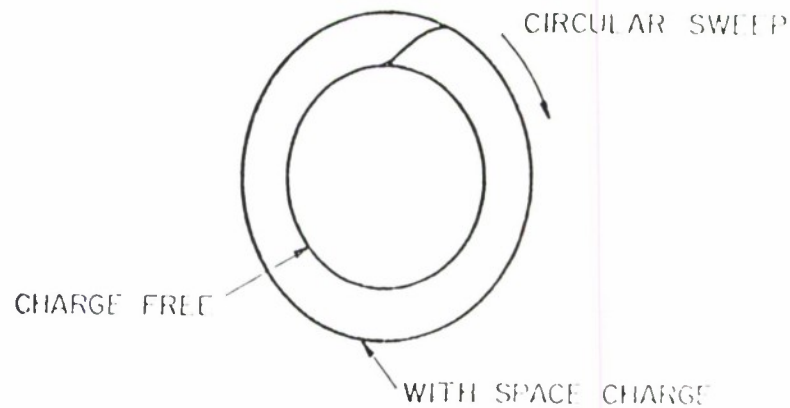


Figure 2. Basic kind of change observed in the circular Lissajous pattern (see Fig. 1) for the two cases of a pure electrostatic potential distribution (inner circle) and an electron injection potential distribution (outer circle).

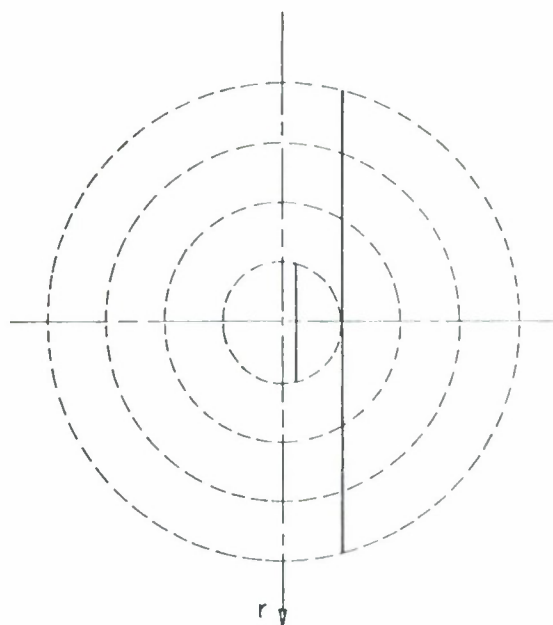


Figure 3. Basic kind of change observed in the diagnostic beam pattern where one set of deflection plates (see Fig. 1) are disabled. The short line is the case of a pure electrostatic potential distribution while the long line is the case of an electron injection potential distribution.

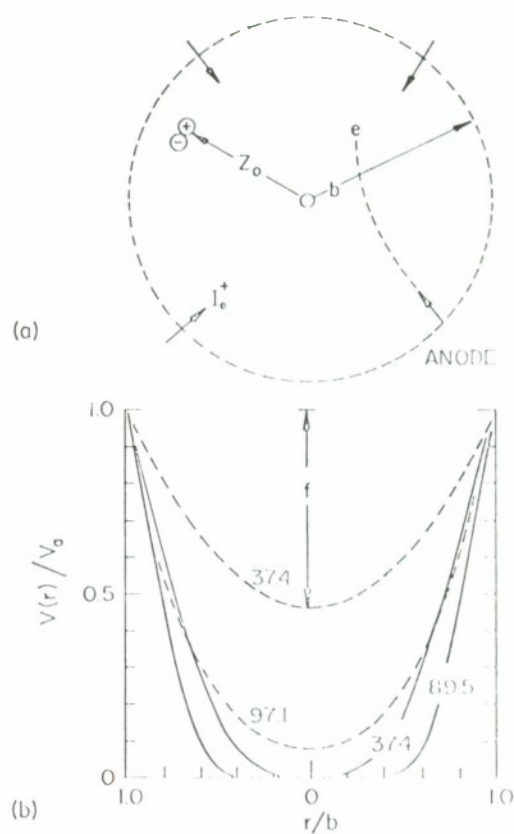


Figure 4. (a) Cross-sectional diagram of a spherical anode of radius  $b$  with an electron-ion pair located at  $r = z_0$ . (b) Plot of the theoretical potential distributions for two kinds of angular energy spreads. Dashed lines are for wide energy spreads and solid lines are for narrow energy spreads. Each curve is labeled by its micro-perveance.

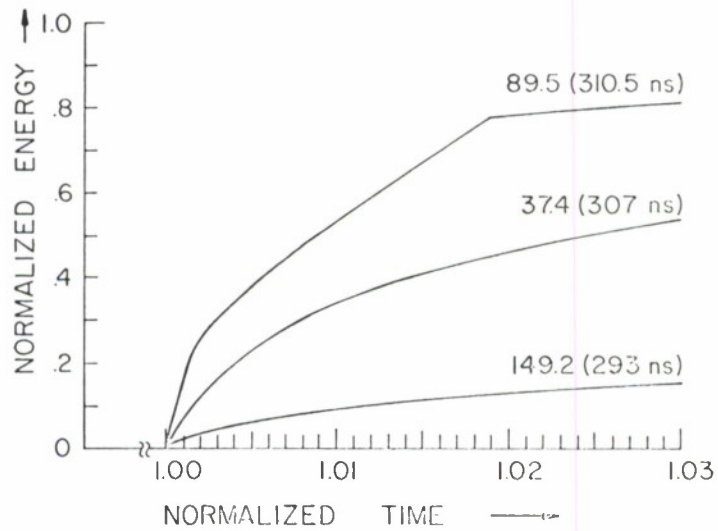


Figure 5. Energy delivered to pellet as a function of time. Energy is normalized to the total integrated energy delivered by all the ions. Curves are labeled in the micropervance of the associated potential distribution (see Fig. 4.). Time is normalized to the arrival of the first ion, given in parenthesis for a 1 meter, 1 MV device.

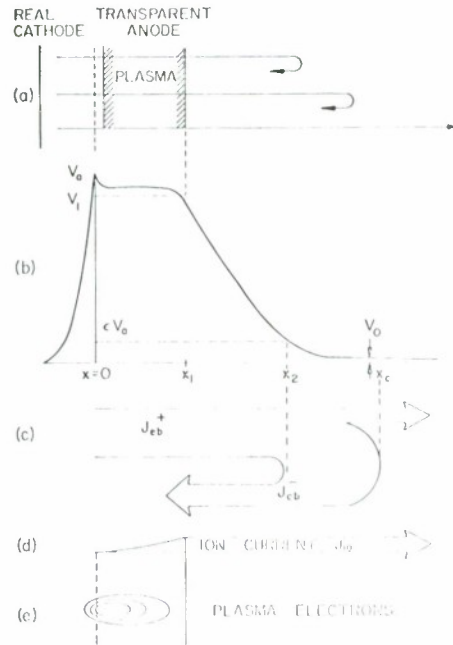


Figure 6. Conceptual representation of the planar model. (a) Plasma location with respect to real cathode and transparent anode. (b) Potential variation with plasma fixed in space. (c) Spatial electron current distribution. (d) Spatial ion current distribution. (e) Plasma electron orbits through the transparent anode.

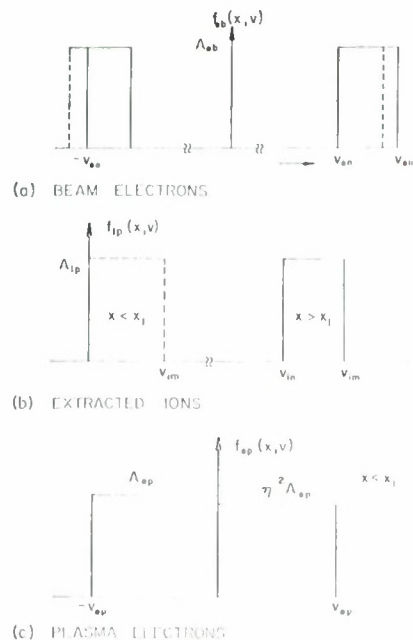


Figure 7. Velocity distributions. (a) Beam electron distribution. Electrons with energy less than  $v_{eo}$  are transmitted through the potential minimum. (b) Ion distribution. The dashed distribution is for positions within the plasma region; hence, some zero energy ions. The solid distribution indicates ions accelerated out at the edge of the plasma. (c) Plasma electron distribution.

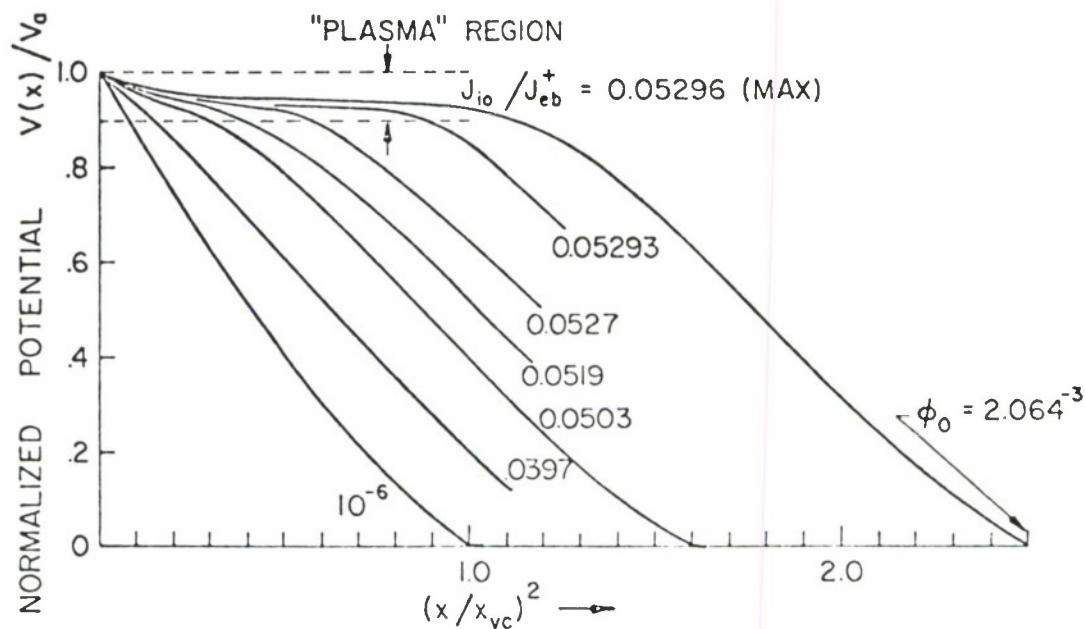


Figure 8. Potential variation predicted by model for various ratios of  $J_{io}/J_{eb}^+$ . The openness of the anode  $\eta = 0.979$  for a  $(e-H^+)$  plasma.

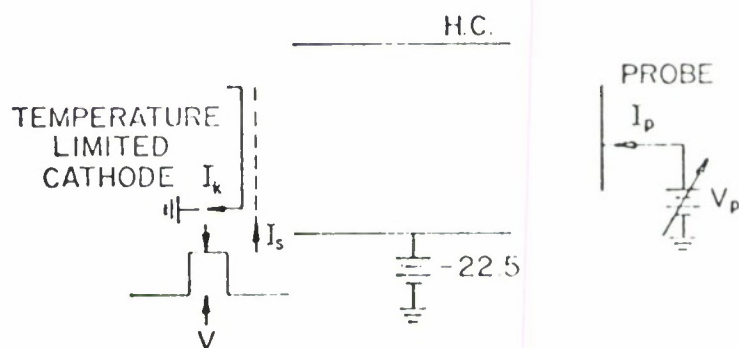


Figure 9. Experimental setup for planar experiment. The grounded cathode emits electrons through the positively pulsed screen into the cylindrical electrode (H.C.). A moveable probe collects the transmitted electrons.



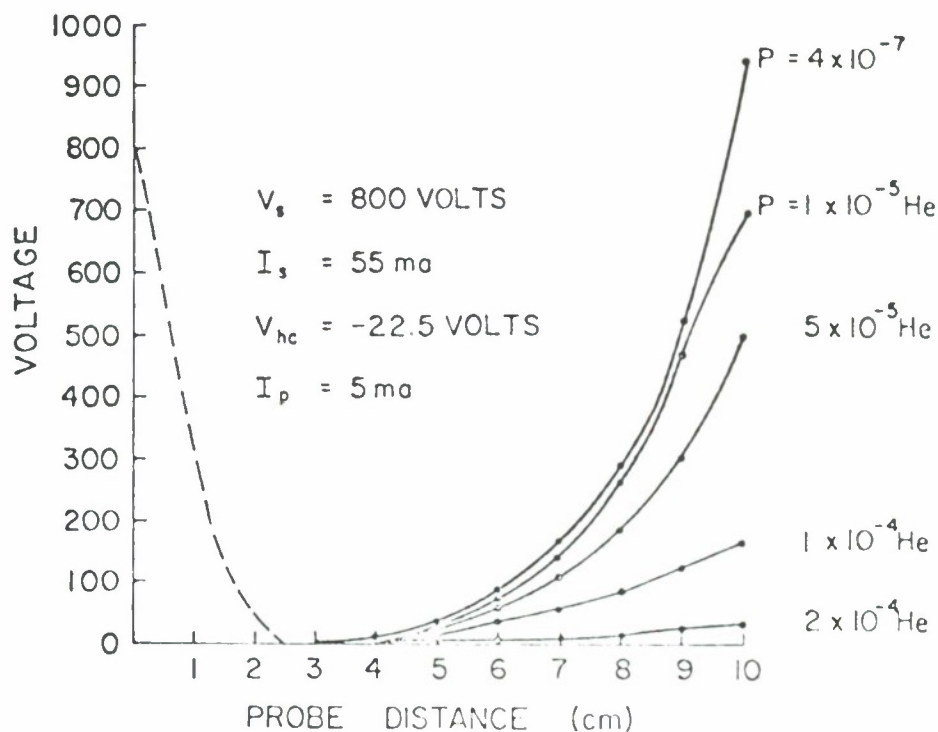


Figure 10. Probe voltage v's distance for constant probe current. The solid curves are for data taken at various pressures in helium. The dashed curve is the theoretical potential variation for an ideal planar diode.

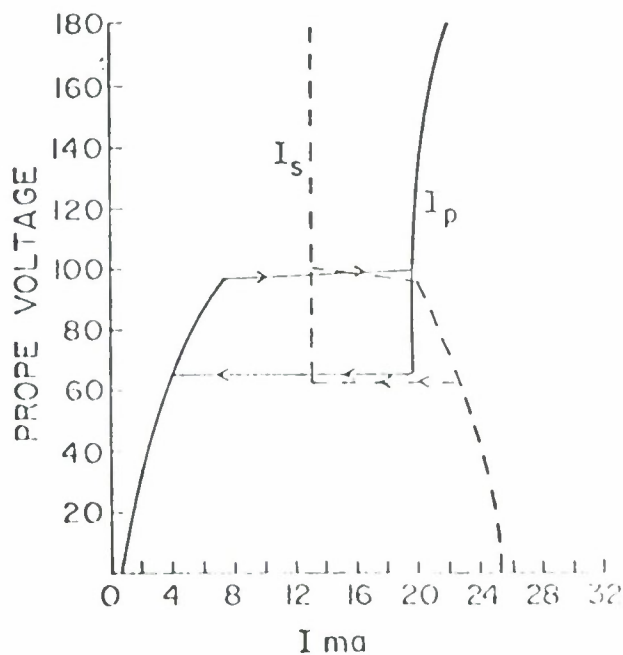


Figure 11. Switching behavior.  $I_s$  is the current drawn by the screen and  $I_p$  is the probe current. The current switches between them as the probe voltage is increased.

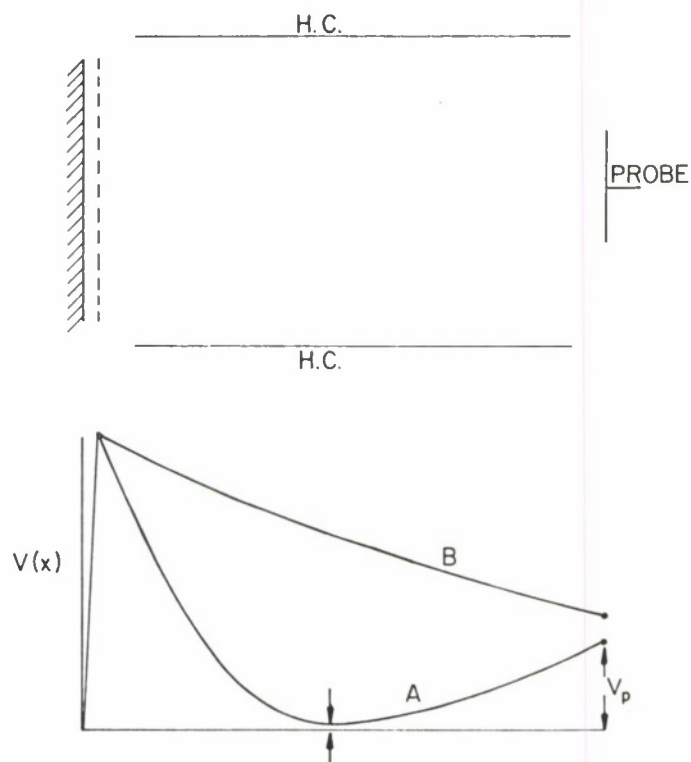


Figure 12. Potential shapes of system. The state B transmits the injected electrons while state A reflects most electrons from the cathode.

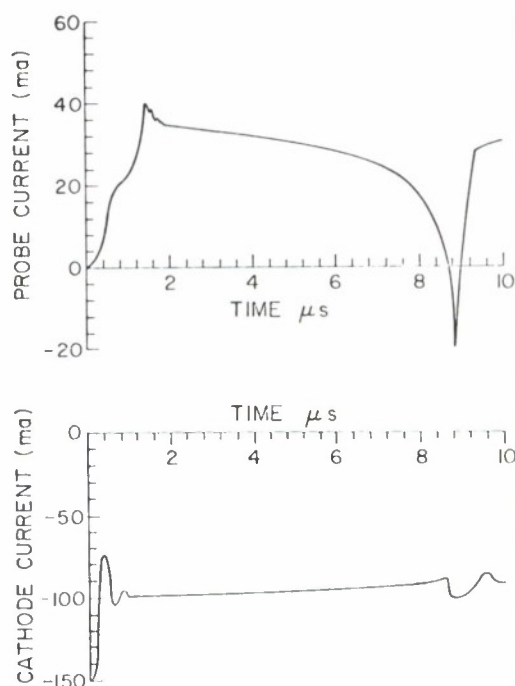


Figure 13. Pulsed behavior in soft vacuum. Upper waveform is the probe current showing the first in a series of negative pulses. Lower waveform is the cathode current which stays almost constant during switching.  $P = 3 \times 10^{-4}$  Torr He